Mathematical Problems in Engineering

New Advances in Distributed Control of Large-Scale Systems

Guest Editors: Dan Zhang, Wen-An Zhang, Zheng-Guang Wu, Kun Liu, Hui Zhang, and Yun-Bo Zhao

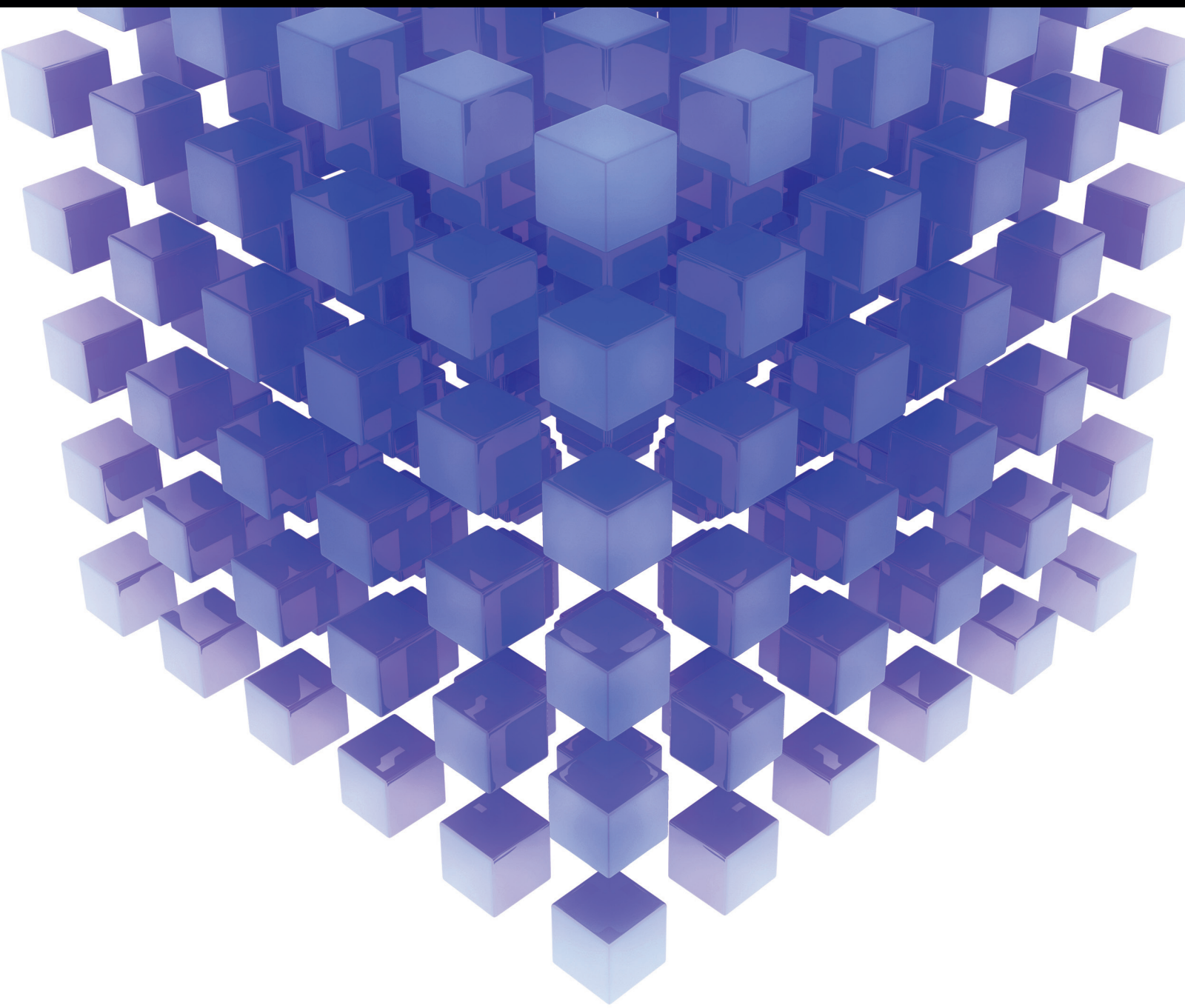

New Advances in Distributed Control of Large-Scale Systems

Mathematical Problems in Engineering

New Advances in Distributed Control of Large-Scale Systems

Guest Editors: Dan Zhang, Wen-An Zhang,
Zheng-Guang Wu, Kun Liu, Hui Zhang, and Yun-Bo Zhao

Copyright © 2015 Hindawi Publishing Corporation. All rights reserved.

This is a special issue published in "Mathematical Problems in Engineering." All articles are open access articles distributed under the Creative Commons Attribution License, which permits unrestricted use, distribution, and reproduction in any medium, provided the original work is properly cited.

Editorial Board

Mohamed Abd El Aziz, Egypt
Farid Abed-Meraim, France
Silvia Abrahão, Spain
Paolo Addesso, Italy
Claudia Adduce, Italy
Ramesh Agarwal, USA
Juan C. Agüero, Australia
Ricardo Aguilar-López, Mexico
Tarek Ahmed-Ali, France
Hamid Akbarzadeh, Canada
Muhammad N. Akram, Norway
Mohammad-Reza Alam, USA
Salvatore Alfonzetti, Italy
Francisco Alhama, Spain
Juan A. Almendral, Spain
Saiied Aminossadati, Australia
Lionel Amodeo, France
Igor Andrianov, Germany
Sebastian Anita, Romania
Renata Archetti, Italy
Felice Arena, Italy
Sabri Arik, Turkey
Fumihiro Ashida, Japan
Hassan Askari, Canada
Mohsen Asle Zaeem, USA
Francesco Aymerich, Italy
Seungik Baek, USA
Khaled Bahlali, France
Laurent Bako, France
Stefan Balint, Romania
Alfonso Banos, Spain
Roberto Baratti, Italy
Martino Bardi, Italy
Azeddine Beghdadi, France
Abdel-Hakim Bendada, Canada
Ivano Benedetti, Italy
Elena Benvenuti, Italy
Jamal Berakdar, Germany
Enrique Berjano, Spain
Jean-Charles Beugnot, France
Simone Bianco, Italy
David Bigaud, France
Jonathan N. Blakely, USA
Paul Bogdan, USA
Daniela Boso, Italy
Abdel-Ouahab Boudraa, France
Francesco Braghin, Italy
Michael J. Brennan, UK
Maurizio Brocchini, Italy
Julien Bruchon, France
Javier Buldu, Spain
Tito Busani, USA
Pierfrancesco Cacciola, UK
Salvatore Caddemi, Italy
Jose E. Capilla, Spain
Ana Carpio, Spain
Miguel E. Cerrolaza, Spain
Mohammed Chadli, France
Gregory Chagnon, France
Ching-Ter Chang, Taiwan
Michael J. Chappell, UK
Kacem Chehdi, France
Xinkai Chen, Japan
Chunlin Chen, China
Francisco Chicano, Spain
Hung-Yuan Chung, Taiwan
Joaquim Ciurana, Spain
John D. Clayton, USA
Carlo Cosentino, Italy
Paolo Crippa, Italy
Erik Cuevas, Mexico
Peter Dabnichki, Australia
Luca D'Acierno, Italy
Weizhong Dai, USA
Purushothaman Damodaran, USA
Farhang Daneshmand, Canada
Fabio De Angelis, Italy
Stefano de Miranda, Italy
Filippo de Monte, Italy
Xavier Delorme, France
Luca Deseri, USA
Yannis Dimakopoulos, Greece
Zhengtao Ding, UK
Ralph B. Dinwiddie, USA
Mohamed Djemai, France
Alexandre B. Dolgui, France
George S. Dulikravich, USA
Bogdan Dumitrescu, Finland
Horst Ecker, Austria
Ahmed El Hajjaji, France
Fouad Erchiqui, Canada
Anders Eriksson, Sweden
Giovanni Falsone, Italy
Hua Fan, China
Yann Favennec, France
Giuseppe Fedele, Italy
Roberto Fedele, Italy
Jacques Ferland, Canada
Jose R. Fernandez, Spain
Simme Douwe Flapper, Netherlands
Thierry Floquet, France
Eric Florentin, France
Francesco Franco, Italy
Tomonari Furukawa, USA
Mohamed Gadala, Canada
Matteo Gaeta, Italy
Zoran Gajic, USA
Ciprian G. Gal, USA
Ugo Galvanetto, Italy
Akemi Gálvez, Spain
Rita Gamberini, Italy
Maria Gandarias, Spain
Arman Ganji, Canada
Zhong-Ke Gao, China
Xin-Lin Gao, USA
Giovanni Garcea, Italy
Fernando García, Spain
Laura Gardini, Italy
Alessandro Gasparetto, Italy
Vincenzo Gattulli, Italy
Oleg V. Gendelman, Israel
Mergen H. Ghayesh, Australia
Anna M. Gil-Lafuente, Spain
Hector Gómez, Spain
Rama S. R. Gorla, USA
Oded Gottlieb, Israel
Antoine Grall, France
Jason Gu, Canada
Quang Phuc Ha, Australia
Ofer Hadar, Israel
Masoud Hajarian, Iran
Frédéric Hamelin, France
Zhen-Lai Han, China
Thomas Hanne, Switzerland
Takashi Hasuike, Japan

Xiao-Qiao He, China
María I. Herreros, Spain
Vincent Hilaire, France
Eckhard Hitzer, Japan
Jaromir Horacek, Czech Republic
Muneo Hori, Japan
András Horváth, Italy
Gordon Huang, Canada
Sajid Hussain, Canada
Asier Ibeas, Spain
Giacomo Innocenti, Italy
Emilio Insfran, Spain
Nazrul Islam, USA
Payman Jalali, Finland
Reza Jazar, Australia
Khalide Jbilou, France
Linni Jian, China
Zhongping Jiang, USA
Bin Jiang, China
Ningde Jin, China
Grand R. Joldes, Australia
Joaquim Joao Judice, Portugal
Tadeusz Kaczorek, Poland
Tamas Kalmar-Nagy, Hungary
Tomasz Kapitaniak, Poland
Haranath Kar, India
Konstantinos Karamanos, Belgium
C. M. Khalique, South Africa
Nam-Il Kim, Korea
Do Wan Kim, Korea
Oleg Kirillov, Germany
Manfred Krafczyk, Germany
Frederic Kratz, France
Jurgen Kurths, Germany
Kyandoghere Kyamakya, Austria
Davide La Torre, Italy
Risto Lahdelma, Finland
Hak-Keung Lam, UK
Antonino Laudani, Italy
Aime' Lay-Ekuakille, Italy
Marek Lefik, Poland
Yaguo Lei, China
Thibault Lemaire, France
Stefano Lenci, Italy
Roman Lewandowski, Poland
Qing Q. Liang, Australia
Panos Liatsis, UK
Wanquan Liu, Australia
Yan-Jun Liu, China
Peter Liu, Taiwan
Peide Liu, China
Jean J. Loiseau, France
Paolo Lonetti, Italy
Luis M. López-Ochoa, Spain
Vassilios C. Loukopoulos, Greece
Valentin Lychagin, Norway
Fazal M. Mahomed, South Africa
Yassir T. Makkawi, UK
Noureddine Manamanni, France
Didier Maquin, France
Paolo Maria Mariano, Italy
Benoit Marx, France
Geŕard A. Maugin, France
Driss Mehdi, France
Roderick Melnik, Canada
Pasquale Memmolo, Italy
Xiangyu Meng, Canada
Jose Merodio, Spain
Luciano Mescia, Italy
Laurent Mevel, France
Y. V. Mikhlin, Ukraine
Aki Mikkola, Finland
Hiroyuki Mino, Japan
Pablo Mira, Spain
Vito Mocella, Italy
Roberto Montanini, Italy
Gisele Mophou, France
Rafael Morales, Spain
Aziz Moukrim, France
Emiliano Mucchi, Italy
Domenico Mundo, Italy
Jose J. Muñoz, Spain
Giuseppe Muscolino, Italy
Marco Mussetta, Italy
Hakim Naceur, France
Hassane Naji, France
Dong Ngoduy, UK
Tatsushi Nishi, Japan
Ben T. Nohara, Japan
Mohammed Nouari, France
Mustapha Nourelfath, Canada
Sotiris K. Ntouyas, Greece
Roger Ohayon, France
Mitsuhiro Okayasu, Japan
Eva Onaindia, Spain
Javier Ortega-Garcia, Spain
Alejandro Ortega-Moñux, Spain
Naohisa Otsuka, Japan
Erika Ottaviano, Italy
Alkiviadis Paipetis, Greece
Alessandro Palmeri, UK
Anna Pandolfi, Italy
Elena Panteley, France
Manuel Pastor, Spain
Pubudu N. Pathirana, Australia
Francesco Pellicano, Italy
Haipeng Peng, China
Zhike Peng, China
Mingshu Peng, China
Marzio Pennisi, Italy
Matjaz Perc, Slovenia
Francesco Pesavento, Italy
Maria do Rosário Pinho, Portugal
Antonina Pirrotta, Italy
Vicent Pla, Spain
Javier Plaza, Spain
Jean-Christophe Ponsart, France
Mauro Pontani, Italy
Stanislav Potapenko, Canada
Sergio Preidikman, USA
Christopher Pretty, New Zealand
Carsten Proppe, Germany
Luca Pugi, Italy
Yuming Qin, China
Dane Quinn, USA
Jose Ragot, France
Kumbakonam Ramamani Rajagopal, USA
Gianluca Ranzi, Australia
Sivaguru Ravindran, USA
Alessandro Reali, Italy
Oscar Reinoso, Spain
Nidhal Rezg, France
Ricardo Riaza, Spain
Gerasimos Rigatos, Greece
José Rodellar, Spain
Rosana Rodriguez-Lopez, Spain
Ignacio Rojas, Spain
Carla Roque, Portugal
Aline Roumy, France
Debasish Roy, India
Rubén Ruiz García, Spain
Antonio Ruiz-Cortes, Spain
Ivan D. Rukhlenko, Australia
Mazen Saad, France

Kishin Sadarangani, Spain
Mehrdad Saif, Canada
Miguel A. Salido, Spain
Roque J. Saltarén, Spain
Francisco J. Salvador, Spain
Alessandro Salvini, Italy
Maura Sandri, Italy
Miguel A. F. Sanjuan, Spain
Juan F. San-Juan, Spain
Roberta Santoro, Italy
Ilmar Ferreira Santos, Denmark
José A. Sanz-Herrera, Spain
Nickolas S. Sapidis, Greece
Evangelos J. Sapountzakis, Greece
Andrey V. Savkin, Australia
Valery Sbitnev, Russia
Thomas Schuster, Germany
Mohammed Seaid, UK
Lotfi Senhadji, France
Joan Serra-Sagrista, Spain
Leonid Shaikhet, Ukraine
Hassan M. Shanechi, USA
Sanjay K. Sharma, India
Bo Shen, Germany
Babak Shotorban, USA
Zhan Shu, UK
Dan Simon, USA
Luciano Simoni, Italy
Christos H. Skiadas, Greece
Michael Small, Australia
Francesco Soldovieri, Italy
Raffaele Solimene, Italy
Ruben Specogna, Italy
Sri Sridharan, USA
Ivanka Stamova, USA
Yakov Strelniker, Israel
Sergey A. Suslov, Australia
Thomas Svensson, Sweden
Andrzej Swierniak, Poland
Yang Tang, Germany
Sergio Teggi, Italy
Alexander Timokha, Norway
Rafael Toledo, Spain
Gisella Tomasini, Italy
Francesco Tornabene, Italy
Antonio Tornambe, Italy
Fernando Torres, Spain
Fabio Tramontana, Italy
Sébastien Tremblay, Canada
Irina N. Trendafilova, UK
George Tsiatas, Greece
Antonios Tsourdos, UK
Vladimir Turetsky, Israel
Mustafa Tutar, Spain
Efstratios Tzirtzilakis, Greece
Filippo Ubertini, Italy
Francesco Ubertini, Italy
Hassan Ugail, UK
Giuseppe Vairo, Italy
Kuppalapalle Vajravelu, USA
Robertt A. Valente, Portugal
Pandian Vasant, Malaysia
Miguel E. Vázquez-Méndez, Spain
Josep Vehi, Spain
Kalyana C. Veluvolu, Korea
Fons J. Verbeek, Netherlands
Franck J. Vernerey, USA
Georgios Veronis, USA
Anna Vila, Spain
Rafael J. Villanueva, Spain
Uchechukwu E. Vincent, UK
Mirko Viroli, Italy
Michael Vynnycky, Sweden
Yan-Wu Wang, China
Yongqi Wang, Germany
Junwu Wang, China
Shuming Wang, Singapore
Desheng D. Wu, Canada
Yuqiang Wu, China
Xuejun Xie, China
Guangming Xie, China
Gen Qi Xu, China
Hang Xu, China
Xinggang Yan, UK
Luis J. Yebra, Spain
Peng-Yeng Yin, Taiwan
Ibrahim Zeid, USA
Qingling Zhang, China
Huaguang Zhang, China
Jian Guo Zhou, UK
Quanxin Zhu, China
Mustapha Zidi, France
Alessandro Zona, Italy

Contents

New Advances in Distributed Control of Large-Scale Systems, Dan Zhang, Wen-An Zhang, Zheng-Guang Wu, Kun Liu, Hui Zhang, and Yun-Bo Zhao
Volume 2015, Article ID 102469, 2 pages

A Fault Detection Filtering for Networked Control Systems Based on Balanced Reduced-Order, Da-Meng Dai
Volume 2015, Article ID 673201, 8 pages

Dynamic Responses of Continuous Girder Bridges with Uniform Cross-Section under Moving Vehicular Loads, Qingfei Gao, Zonglin Wang, Hongyu Jia, Chenguang Liu, Jun Li, Binqiang Guo, and Junfei Zhong
Volume 2015, Article ID 951502, 29 pages

A Novel Dynamic Method in Distributed Network Attack-Defense Game, Liu Xiaojian and Yuan Yuyu
Volume 2015, Article ID 356146, 7 pages

ACO-Initialized Wavelet Neural Network for Vibration Fault Diagnosis of Hydroturbine Generating Unit, Zhihuai Xiao, Xinying He, Xiangqian Fu, and O. P. Malik
Volume 2015, Article ID 354658, 7 pages

New Results on Passivity for Discrete-Time Stochastic Neural Networks with Time-Varying Delays, Wei Kang, Jun Cheng, and Xiangyang Cheng
Volume 2015, Article ID 341839, 10 pages

A Novel Consensus Protocol for Two-Dimension First-Order Multiagent Systems, Yibo Zhang, Jinfeng Gao, and Jia Ren
Volume 2015, Article ID 872475, 8 pages

Passive Control of Switched Singular Systems via Output Feedback, Shuhui Shi, Guoliang Wang, Jianhua Wang, and Hong Li
Volume 2015, Article ID 573950, 7 pages

Vector Control Algorithm for Electric Vehicle AC Induction Motor Based on Improved Variable Gain PID Controller, Gang Qin, Mushuang Liu, Jianxiao Zou, and Xiaoshuai Xin
Volume 2015, Article ID 875843, 9 pages

Synchronization of Hybrid Microgrids with Communication Latency, Jingang Lai, Hong Zhou, Wenshan Hu, Xiaoqing Lu, and Liang Zhong
Volume 2015, Article ID 586260, 10 pages

One-Step-Ahead Predictive Control for Hydroturbine Governor, Zhihuai Xiao, Suili Meng, Na Lu, and O. P. Malik
Volume 2015, Article ID 382954, 10 pages

Fast Consensus of Networked Multiagent Systems with Two-Hop Network, Jinfeng Gao, Bin Bu, Lihui Feng, and Minming Gu
Volume 2015, Article ID 953464, 7 pages

K-Nearest Neighbor Intervals Based AP Clustering Algorithm for Large Incomplete Data, Cheng Lu, Shiji Song, and Cheng Wu
Volume 2015, Article ID 535932, 9 pages

Fault Reconstruction Approach for Distributed Coordinated Spacecraft Attitude Control System, Mingyi Huo, Yanning Guo, and Xing Huo
Volume 2015, Article ID 364138, 9 pages

A Simulation Perspective: Error Analysis in the Distributed Simulation of Continuous System, Yao-fei Ma and Xiao Song
Volume 2015, Article ID 461513, 10 pages

Exponential Cluster Synchronization of Neural Networks with Proportional Delays, Nian Feng, Ye Wu, Weiping Wang, Lin Zhang, and Jinghua Xiao
Volume 2015, Article ID 523424, 10 pages

Stabilization of Networked Distributed Systems with Partial and Event-Based Couplings, Sufang Zhang, Wei Wang, and Chi Huang
Volume 2015, Article ID 342465, 11 pages

Robust Stabilization and H_∞ Control for Uncertain Neural Networks with Mixed Time Delays, Bin Wen, Hui Li, and Li Liang
Volume 2015, Article ID 690578, 13 pages

Design for Nonlinear Networked Control Systems with Time Delay Governed by Markov Chain with Partly Unknown Transition Probabilities, Yan-Feng Wang, Zu-Xin Li, Hui-Ying Chen, Li-Di Quan, and Xiao-Rui Guo
Volume 2015, Article ID 604246, 7 pages

Fault-Tolerant Control for Networked Control Systems with Limited Information in Case of Actuator Fault, Wang Yan-feng, Wang Pei-liang, Li Zu-xin, and Chen Hui-ying
Volume 2015, Article ID 785289, 7 pages

An Improved Information Hiding Method Based on Sparse Representation, Minghai Yao, Miao Qi, Yugen Yi, Yanjiao Shi, and Jun Kong
Volume 2015, Article ID 197215, 10 pages

Optimal Power Constrained Distributed Detection over a Noisy Multiaccess Channel, Zhiwen Hu and Zhenhua Xu
Volume 2015, Article ID 580289, 7 pages

Distributed Modeling and Control of Large-Scale Highly Flexible Solar-Powered UAV, Rui Wang, Zhou Zhou, Xiaoping Zhu, and Xiaoping Xu
Volume 2015, Article ID 195390, 13 pages

Novel Degree Constrained Minimum Spanning Tree Algorithm Based on an Improved Multicolony Ant Algorithm, Xuemei Sun, Cheng Chang, Hua Su, and Chuitian Rong
Volume 2015, Article ID 601782, 13 pages

A Method for Signal Coordination in Large-Scale Urban Road Networks, Bao-Lin Ye, Weimin Wu, and Weijie Mao
Volume 2015, Article ID 720523, 15 pages

On Fixed-Point Smoothing for Descriptor Systems with Multiplicative Noise and Single Delayed Observations, Xiao Lu, Xin Dong, Haixia Wang, and Baoye Song
Volume 2015, Article ID 658153, 8 pages

Robust Stability and Stabilization of Interval Uncertain Descriptor Fractional-Order Systems with the Fractional-Order α: The $1 \leq \alpha < 2$ Case, Yuanhua Li, Heng Liu, and Hongxing Wang
Volume 2015, Article ID 606048, 8 pages

A New Wavelet Threshold Determination Method Considering Interscale Correlation in Signal Denoising, Can He, Jianchun Xing, Juelong Li, Qiliang Yang, and Ronghao Wang
Volume 2015, Article ID 280251, 9 pages

Application of a New Wavelet Threshold Method in Unconventional Oil and Gas Reservoir Seismic Data Denoising, Guxi Wang, Ling Chen, Si Guo, Yu Peng, and Ke Guo
Volume 2015, Article ID 969702, 7 pages

A New Wavelet Thresholding Function Based on Hyperbolic Tangent Function, Can He, Jianchun Xing, Juelong Li, Qiliang Yang, and Ronghao Wang
Volume 2015, Article ID 528656, 10 pages

Hindawi Publishing Corporation
Mathematical Problems in Engineering
Volume 2015, Article ID 102469, 2 pages
http://dx.doi.org/10.1155/2015/102469

Editorial

New Advances in Distributed Control of Large-Scale Systems

Dan Zhang,[1] Wen-An Zhang,[1] Zheng-Guang Wu,[2] Kun Liu,[3] Hui Zhang,[4] and Yun-Bo Zhao[1]

[1] *Department of Automation, Zhejiang University of Technology, Hangzhou, China*
[2] *The National Laboratory of Industrial Control Technology, Institute of Cyber Systems and Control, Zhejiang University, Hangzhou, China*
[3] *ACCESS Linnaeus Centre and School of Electrical Engineering, KTH Royal Institute of Technology, Stockholm, Sweden*
[4] *The Merchant Marine College, Shanghai Maritime University, Shanghai, China*

Correspondence should be addressed to Dan Zhang; danzhang@zjut.edu.cn

Received 30 August 2015; Accepted 31 August 2015

Copyright © 2015 Dan Zhang et al. This is an open access article distributed under the Creative Commons Attribution License, which permits unrestricted use, distribution, and reproduction in any medium, provided the original work is properly cited.

With the rapid development of the modern industry, the scale of process system of industry becomes more huge, the system functions are more complex, and the geographical distribution of system tends to be more distributed. Representative systems are chemical industrial network, robotic systems, smart grids, sensor networks, and so on [1–3]. The rapid development of industry system inevitably imposes much difficulty on the control system design. Traditional control system design theory cannot be applied to these large-scale systems. The distributed control system integrates control, computation, communication technology, and so forth and adapts to the developing trend of industrial control system. However, insertion of communication networks into the control systems comes at the price of nonideal signal transmission: the data sent through the networks experience time delay or suffer transmission data losses [4]. So far, research attention has been paid to this area; see [5–9] and the references therein.

In this issue, some research works on large-scale systems and the related topics are reported. We are proud to notice that these limited numbers of research works have shown a great variety and in a sense give a fairly complete picture of the state-of-the-art research on large-scale systems. In addition, a brief tutorial on large-scale systems from the Editorial Board is also included in this special issue.

(1) Theoretical studies on the large-scale multiagent systems are reported here. For example, J. Gao et al. discussed the consensus of multiagent systems, Y. Zhang et al. studied the two-dimension first-order multiagent systems, R. Wang et al. discussed the modeling and control of highly flexible solar-powered UAVs, and M. Huo et al. focus on the fault reconstruction approach for distributed coordinated spacecraft attitude control system.

(2) Theoretical analysis on the time-delay, packet dropouts in the large-scale networked systems are reported. For example, D.-M. Dai discussed the fault detection for networked systems based on the reduced-order filter, X. Lu et al. studied the fix-point smoothing for descriptor systems with multiplicative noise and single delayed observations, W. Yanfeng et al. considered the fault-tolerant control for networked control systems with limited information in case of actuator fault, S. Zhang et al. focus on the stabilization of networked distributed systems with partial and event-based couplings, and Z. Hu and Z. Xu give some solution on the distributed detection over a noisy multiaccess channel.

(3) Other results on the large-scale systems, such as microgrids, electric vehicle hydroturbine, and neural networks, are also discussed. Interested readers are referred to the detailed papers reported in this issue.

We hope this special issue will be a useful reference for people working on this area, and more fruitful results will be obtained in the time ahead based on the published works.

Acknowledgment

We appreciate all the researchers for their valuable work on the large-scale systems.

Dan Zhang
Wen-An Zhang
Zheng-Guang Wu
Kun Liu
Hui Zhang
Yun-Bo Zhao

References

[1] J. B. Rawlings and B. T. Stewart, "Coordinating multiple optimization-based controllers: new opportunities and challenges," *Journal of Process Control*, vol. 18, no. 9, pp. 839–845, 2008.

[2] Y. Zheng, S. Li, and N. Li, "Distributed model predictive control over network information exchange for large-scale systems," *Control Engineering Practice*, vol. 19, no. 7, pp. 757–769, 2011.

[3] V. Sundarapandian, "Distributed control schemes for large-scale interconnected discrete-time linear systems," *Mathematical and Computer Modelling*, vol. 41, no. 2-3, pp. 313–319, 2005.

[4] L. Zhang, H. Gao, and O. Kaynak, "Network-induced constraints in networked control systems—a survey," *IEEE Transactions on Industrial Informatics*, vol. 9, no. 1, pp. 403–416, 2013.

[5] S. C. Xu and J. Bao, "Distributed control of plant-wide chemical processes with uncertain time-delays," *Chemical Engineering Science*, vol. 84, pp. 512–532, 2012.

[6] F. Kazempour and J. Ghaisari, "Stability analysis of model-based networked distributed control systems," *Journal of Process Control*, vol. 23, no. 3, pp. 444–452, 2013.

[7] M. Pajic, S. Sundaram, G. J. Pappas, and R. Mangharam, "The wireless control network: a new approach for control over networks," *Institute of Electrical and Electronics Engineers. Transactions on Automatic Control*, vol. 56, no. 10, pp. 2305–2318, 2011.

[8] P. Millán, L. Orihuela, C. Vivas, F. R. Rubio, D. V. Dimarogonas, and K. H. Johansson, "Sensor-network-based robust distributed control and estimation," *Control Engineering Practice*, vol. 21, no. 9, pp. 1238–1249, 2013.

[9] D. Zhang, R. Y. Ling, Q.-G. Wang, L. Yu, and Y. Feng, "Sensor-network-based distributed stabilization of nonlinear large-scale systems with energy constraints and random sensor faults," *Journal of the Franklin Institute*, vol. 352, no. 8, pp. 3345–3365, 2015.

Hindawi Publishing Corporation
Mathematical Problems in Engineering
Volume 2015, Article ID 673201, 8 pages
http://dx.doi.org/10.1155/2015/673201

Research Article

A Fault Detection Filtering for Networked Control Systems Based on Balanced Reduced-Order

Da-Meng Dai

College of Physics and Electronic Information Engineering, Wenzhou University, Wenzhou 325000, China

Correspondence should be addressed to Da-Meng Dai; daidameng1977@sina.cn

Received 15 January 2015; Revised 13 March 2015; Accepted 13 March 2015

Academic Editor: Hui Zhang

Copyright © 2015 Da-Meng Dai. This is an open access article distributed under the Creative Commons Attribution License, which permits unrestricted use, distribution, and reproduction in any medium, provided the original work is properly cited.

Due to the probability of the packet dropout in the networked control systems, a balanced reduced-order fault detection filter is proposed. In this paper, we first analyze the packet dropout effects in the networked control systems. Then, in order to obtain a robust fault detector for the packet dropout, we use the balanced structure to construct a reduced-order model for residual dynamics. Simulation results are provided to testify the proposed method.

1. Introduction

The background of the research is the increasing application of the wireless networks as medium in complex large-scale systems. In networked control systems (NCS), the control loops are close via communication networks. Hence, compared with traditional control systems, the NCS have many advantages, such as fewer system wiring, lower cost of maintenance, improvement of system flexibility, and application in the field of aerospace. So it has drawn more and more consideration in recent years. However, due to the insertion of the network, there appeared many challenging problems: the limited brand width of networked channel maybe cause impossibility of all information transmitted at the same time; due to the uncertainty, the information may be delayed or even dropped; the communication method of the networked system is the digital communication, so there may exist quantization error.

Since some packets have the probability of dropout in the channel, the detection of the faults may cause the false alarm for the NCS. Much work has been done to deal with this problem. In order to deal with the false alarm of the fault detection, the structure of standard model-based residual generator is suggested in [1], and then a residual evaluation scheme is developed to reduce the false alarm rate caused by the packet dropout. If the packets dropout is supposed to be finite, the dynamics of the observer error is modeled as a switched system. Also, the stability condition of observer is provided, and observer gain is obtained by solving LMI optimization problem [2]. Under the stochastic packet dropout in the network, the NCS are modeled as a Markovian jump linear system with four operation modes. Based on this model, the residual generator is developed and the fault detection is reformatted as a problem of H-infinity filter [3]. When the packets dropout is described as discrete-time Markov jumping linear systems (MJLS), the stationary MJLS and the nonstationary MJLS are studied for fault detection problems [4]; then the problem of robust fault detection filter design and optimization is investigated with random delays in [5]. Under the condition of a short sampling period, the limited resource, and computational capacity, a reduced-order fault detection filter algorithm is proposed in [6]. To deal with the fault detection problems of nonlinear discrete-time NCS, the discrete observer based on sliding mode is designed to guarantee the condition of the specified sliding surface. Focusing on the networked control system with long time delays and data packet dropout, according to conditions of data arrival of the controller, the state observers of the system are designed to detect the faults in [7]. The fault detection filter is designed so that the overall fault detection dynamics is exponentially stable in the mean square

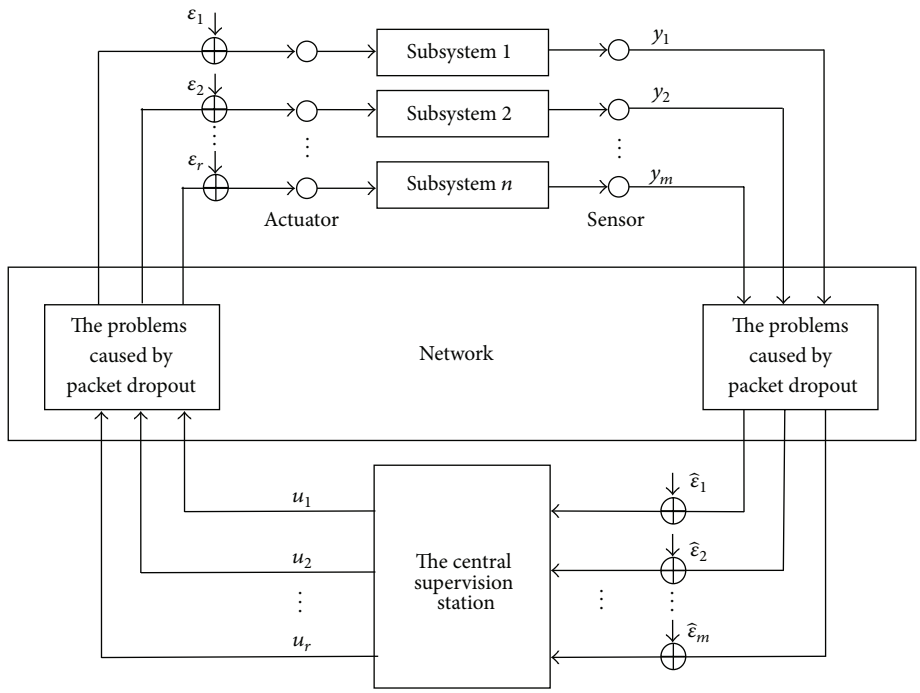

Figure 1: The structure of networked control systems.

with multiple communication delays and stochastic missing measurements.

Nth order linear time-invariant infinite impulse response system can be realized by infinite number methods, each has different sensitivity measurement. This property motivates us to seek a high performance realization in the fault detection for the NCS. Some results show that the characteristics of the parameterization play an important role in minimizing the output error [8, 9]. Since the balanced realization, introduced by [10], has a good noise rejection characteristic, this property should lead the fault detection systems exhibiting well robust to the data packet dropout for the NCS.

For the fault detection system, the big Hankel singular values are more robust to the data packet dropout compared with the small ones; that is, the data packet dropout is easier to disturb the small Hankel singular values than the big ones. So we can improve the robust performance of the fault detection by the reduce-order model, that is, removing the small Hankel singular values. In this paper, in order to minimize the influence of the data packet dropout on the fault detection, we first analyze the packet dropout effects in the NCS. Then, based on the balanced structure, we construct a reduced-order fault detection filter and obtain the residual dynamics, which minimizes the ratio of maximum-to-minimum eigenvalues of the Gramian matrices. It has low parameter sensitivity to the data packet dropout and the measurement noise and improves the robust to the false alarm. At last, the simulation results are provided to corroborate the analytical theory.

2. Problem Description

Figure 1 gives the structure of the NCS with the packet dropout. Assume that the dynamics of the subsystem to be monitored is a linear time-invariant system and can be described by the discrete model:

$$\begin{aligned} x(k+1) &= \mathbf{A}x(k) + \mathbf{B}[u(k) + \varepsilon(k)] + \mathbf{E}f(k), \\ y(k) &= \mathbf{C}x(k) + \mathbf{F}f(k), \end{aligned} \tag{1}$$

where x, u, and y denote the system state, control input signal, and measurable output signal, respectively. $\mathbf{A}$, $\mathbf{B}$, $\mathbf{C}$, $\mathbf{E}$, and $\mathbf{F}$ are known constant matrices with appropriate dimensions. f denotes the faults to be detected, and the measurement noise ε is zero mean white noise for the input signal of the NCS.

The networks are between the sensor and the controller, and they have the same sample time and are simultaneous. Since the communication is hold in the network environment, we assume that there exists packets loss in the communication link and the signal where the central catch is given as follow:

$$y^a(k) = \begin{cases} y(k) + \hat{\varepsilon}(k), & \text{if } \gamma(k) = 1, \\ \text{the last available measurement}, & \text{if } \gamma(k) = 0, \end{cases} \tag{2}$$

where $\gamma(k)$ describes the phenomenon of the packet dropout. $\gamma(k) = 1$ means that the measurement at time point k is correct, while $\gamma(k) = 0$ means that this measurement is lost. When $\gamma(k) = 0$, we use the last available measurement to

generate the residual signal. The measurement noise $\hat{\varepsilon}$ is zero mean white noise for the output signal of the NCS.

3. Fault Detection Filter

In this paper, we assume that the faults supervision stations and the central controller station are located together. Since the residual generator catches the input signal directly, in order to get the deviation, we must obtain the measurement output through the network. Hence, if there are some packets dropout which cause the network jam in the channel, some measurement output signal may be lost between the sensors and the supervision station. In order to obtain a robust residual generator and make the fault detection filter less sensitive to the packets dropout, we can remove the small Hankel singular values. So we design a reduced-order residual generator based on the balanced realization, and it is described as follow:

$$\begin{aligned} \hat{x}(k+1) &= \widehat{\mathbf{A}}\hat{x}(k) + \widehat{\mathbf{B}}u(k) + \mathbf{L}\left(y^a(k) - \hat{y}(k)\right), \\ r(k) &= \mathbf{W}\left(y^a(k) - \hat{y}(k)\right), \\ \hat{y}(k) &= \widehat{\mathbf{C}}\hat{x}(k), \end{aligned} \tag{3}$$

where $\hat{x}$ is the state of the fault detection filter, $\hat{y}$ is the output signal of the filter, and r is the residual signal. $\widehat{\mathbf{A}}$, $\widehat{\mathbf{B}}$, and $\widehat{\mathbf{C}}$ are the known matrices of the fault detection filter, which are deduced from the matrices $\mathbf{A}$, $\mathbf{B}$, and $\mathbf{C}$. $\mathbf{L}$ and $\mathbf{W}$ are vectors which ensure the stability and dynamics of the residual signal. The method used to select $\mathbf{L}$ and $\mathbf{W}$ in this paper is given by [11].

If we define that

$$\chi(k) = y^a(k) - \hat{y}(k), \tag{4}$$

in ideal conditions, the result of (4) is $\hat{\varepsilon}(k)$. Thus, we suppose that the packet is dropout when the square of (4) is more than $2\delta^2$; that is,

$$\begin{aligned} \chi^2(k) > 2\delta^2 &\Longrightarrow \gamma(k) = 0, \\ \chi^2(k) \le 2\delta^2 &\Longrightarrow \gamma(k) = 1, \end{aligned} \tag{5}$$

where δ^2 is the variance of the white noise $\hat{\varepsilon}$. In case of $\gamma(k) = 0$, we wish that the observation value is more close to the actual value, so we set the vector $\mathbf{L}$ to be zero; that is,

$$\mathbf{L} = 0, \quad \chi^2(k) \le 2\delta^2. \tag{6}$$

We use the threshold selector to evaluate the residual generator (3). The decision is made based on the following logic:

$$\begin{aligned} J_r > J_{\text{th}} &\Longrightarrow \text{A fault is detected}, \\ J_r \le J_{\text{th}} &\Longrightarrow \text{No fault}, \end{aligned} \tag{7}$$

where J_{th} is a threshold, and it is determined by the method in [1]. The residual evaluation function J_r is calculated by

$$J_r = \left(\frac{1}{L}\sum_{i=0}^{L-1} r(k-i)\right)^{1/2}. \tag{8}$$

4. Parameters of Residual Generator

In this section, based on balanced reduced-order model, we aim to find the optimal system parameters for the fault detection filter. Because it can minimize the effects of the measurement noises ε and $\hat{\varepsilon}$. That is to say, we need a robust fault detection system. We consider that the subsystem is a discrete SISO system. Thus, based on (1), we have

$$\begin{aligned} G(z) = \mathbf{C}(z\mathbf{I} - \mathbf{A})^{-1}\mathbf{B} &= \frac{q_N(z)}{p_N(z)} \\ &= \frac{b_0 + b_1 z^{-1} + \cdots + b_N z^{-N}}{1 + a_1 z^{-1} + \cdots a_N z^{-N}}, \end{aligned} \tag{9}$$

where the coefficients $b_0, b_1, \ldots, b_N$ and $a_1, a_2, \ldots, a_N$ denote the corresponding system input and output variables. In order to obtain the balanced reduced-order fault detection model of the NCS, using the result in [12, 13], we firstly construct the system $(\widetilde{\mathbf{A}}, \widetilde{\mathbf{B}}, \widetilde{\mathbf{C}})$ to be

$$\begin{aligned} \widetilde{\mathbf{A}} &= \begin{pmatrix} -a_1 & \cdots & -a_{N-1} & -a_N \\ 1 & \cdots & 0 & 0 \\ \vdots & \ddots & \vdots & \vdots \\ 0 & \cdots & 1 & 0 \end{pmatrix}, \\ \widetilde{\mathbf{B}} &= \begin{pmatrix} 1 \\ 0 \\ \vdots \\ 0 \end{pmatrix}, \qquad \widetilde{\mathbf{C}} = \begin{pmatrix} b_1 - b_0 a_1 \\ b_2 - b_0 a_2 \\ \vdots \\ b_N - b_0 a_N \end{pmatrix}. \end{aligned} \tag{10}$$

Given the polynomial as

$$\widetilde{p}_N(z) = z^N p_N(z) = z^N + a_1 z^{N-1} + \cdots + a_N \tag{11}$$

and the shift matrix $\mathbf{Z} = R^{N\times N}$ as

$$\mathbf{Z} = \begin{pmatrix} 0 & 1 & \cdots & 0 \\ \vdots & \vdots & \ddots & \vdots \\ 0 & 0 & \cdots & 1 \\ 0 & 0 & \cdots & 0 \end{pmatrix}, \tag{12}$$

then we can get the Schur-Cohn matrix:

$$\mathbf{H} = \widetilde{p}_N(\mathbf{Z})^T \widetilde{p}_N(\mathbf{Z}) - p_N(\mathbf{Z})^T p_N(\mathbf{Z}). \tag{13}$$

Define the matrix $\mathbf{M} = \{m_{i,j}\}_{N\times N}$ as

$$m_{i,j} = \sum_{\tau\ge 1} a_{i-\tau} c_{j+\tau-1} - \sum_{\tau\ge 1} c_{i-\tau} a_{j+\tau-1}, \tag{14}$$

where $a_0 = 1$, $c_0 = 0$, and $c_i = b_i - b_0 a_i$, $(1 \le i \le N)$.

Then we define

$$\mathbf{W}_{co} = \mathbf{H}^{-1}\mathbf{M} = \mathbf{V}\boldsymbol{\Lambda}\mathbf{V}^{-1}, \tag{15}$$

where $\mathbf{\Lambda}$ and $\mathbf{V}$ are the eigenvalue and eigenvector matrices of $\mathbf{W}_{co}$, respectively. The matrix $\mathbf{Q}$ is defined as

$$\mathbf{Q} = \mathbf{V}^{\mathbf{T}}\mathbf{M}\mathbf{V}, \tag{16}$$

in which the diagonal elements are $q_1, q_2, \ldots, q_N$. As a result, we define the matrix $\mathbf{F}$ as

$$\mathbf{F} = \operatorname{diag}\left(|q_1|^{-1/2}, |q_2|^{-1/2}, \ldots, |q_N|^{-1/2}\right). \tag{17}$$

From (15) and (17), we can obtain the transformation $\mathbf{T}_{\text{bal}}$ from controllable canonical to a balanced form as [12, 13]

$$\mathbf{T}_{\text{bal}} = \mathbf{V}\mathbf{F}. \tag{18}$$

Now, the balanced realization system $(\mathbf{A}_{\text{bal}}, \mathbf{B}_{\text{bal}}, \mathbf{C}_{\text{bal}})$ can be calculated as follow:

$$\begin{aligned} \mathbf{A}_{\text{bal}} &= \mathbf{T}_{\text{bal}}^{-1}\widetilde{\mathbf{A}}\mathbf{T}_{\text{bal}}, \\ \mathbf{B}_{\text{bal}} &= \mathbf{T}_{\text{bal}}^{-1}\widetilde{\mathbf{B}}, \\ \mathbf{C}_{\text{bal}} &= \widetilde{\mathbf{C}}\mathbf{T}_{\text{bal}}. \end{aligned} \tag{19}$$

The controllability Gramian $\mathbf{W}_c$ and the observability Gramian $\mathbf{W}_o$ of the system $(\mathbf{A}_{\text{bal}}, \mathbf{B}_{\text{bal}}, \mathbf{C}_{\text{bal}})$ are equal to each other. Consider

$$\mathbf{W}_c = \mathbf{W}_o = \operatorname{diag}(\sigma_1, \sigma_2, \ldots, \sigma_N), \tag{20}$$

where $\sigma_1 > \sigma_2 > \cdots > \sigma_{N-1} > \sigma_N > 0$. In order to obtain a balanced reduced-order system, we partition the system $(\mathbf{A}_{\text{bal}}, \mathbf{B}_{\text{bal}}, \mathbf{C}_{\text{bal}})$ as

$$G_{\text{bal}} \sim \left[\begin{array}{cc|c} \mathbf{A}^{11}_{(N-M)\times(N-M)} & \mathbf{A}^{12}_{(N-M)\times M} & \mathbf{B}^{1}_{(N-M)\times 1} \\ \mathbf{A}^{21}_{M\times(N-M)} & \mathbf{A}^{22}_{M\times M} & \mathbf{B}^{2}_{M\times 1} \\ \hline \mathbf{C}^{1}_{1\times(N-M)} & \mathbf{C}^{2}_{1\times M} & \mathbf{0} \end{array}\right]. \tag{21}$$

From (21), we obtain the reduced-order model for the networked control systems $(\mathbf{A}^{11}_{(N-M)\times(N-M)}, \mathbf{B}^{1}_{(N-M)\times 1}, \mathbf{C}^{1}_{1\times(N-M)})$, which is still a balanced realization. Using this result in (3), that is, setting the system $(\widehat{\mathbf{A}}, \widehat{\mathbf{B}}, \widehat{\mathbf{C}})$ to be $(\mathbf{A}^{11}_{(N-M)\times(N-M)}, \mathbf{B}^{1}_{(N-M)\times 1}, \mathbf{C}^{1}_{1\times(N-M)})$, the balanced reduced-order fault detection filter for the NCS is obtained, which minimizes the ratio of maximum-to-minimum eigenvalues of the Gramian matrices and has a good packets dropout rejection.

5. Simulation Results

In this section, we analyze the proposed algorithm in MATLAB. The first case of the NCS is the fourth-order system, and the matrices are given as

$$\begin{gathered} \mathbf{A} = \begin{bmatrix} -0.2571 & 0.2350 & 0.5290 & 0.1497 \\ -0.6290 & -0.2154 & 0.0990 & -0.2897 \\ 0.1059 & -0.2623 & -0.2553 & -0.5475 \\ 0.1690 & 0.5330 & 0.0760 & -0.2820 \end{bmatrix}, \\ \mathbf{B} = \begin{bmatrix} 0.1258 \\ 0.2175 \\ -0.5990 \\ -0.2430 \end{bmatrix}, \\ \mathbf{C} = \begin{bmatrix} 0.1190 & -0.2210 & 0.2307 & -0.6274 \end{bmatrix}, \\ \mathbf{E} = \begin{bmatrix} 0.5258 \\ 0.6175 \\ -0.59909 \\ -0.6430 \end{bmatrix}, \qquad \mathbf{F} = 0.3984. \end{gathered} \tag{22}$$

Since the dropout of the packets is random, we use two-state Markov jump system to describe the stochastic process [1]. And the parameter $\gamma(k) \in \{0, 1\}$ denotes the packet dropout or not, so the probability of the state transition can be described as

$$\begin{aligned} \lambda_{ij} &= \operatorname{Prob}\{\gamma(k+1) = j \mid \gamma(k) = i\}, \\ \sum_{j=0}^{1} \lambda_{ij} &= 1, \quad \forall i, j \in \{0, 1\}, \ \lambda_{ij} \geq 0. \end{aligned} \tag{23}$$

And the state transfer matrix of the Markov chain is given as

$$\left[\lambda_{ij}\right]_{i,j=0,1} = \begin{bmatrix} 0.5 & 0.5 \\ 0.3 & 0.7 \end{bmatrix}. \tag{24}$$

The measurement noises $\varepsilon(k)$ and $\widehat{\varepsilon}(k)$ are the Gaussian white noise with the variance 0.2. The fault signal is described as

$$f(k) = \begin{cases} 1 + 0.5\cos(4\pi k), & \text{for } k = 2000, 2001, \ldots, 5000, \\ 0, & \text{else.} \end{cases} \tag{25}$$

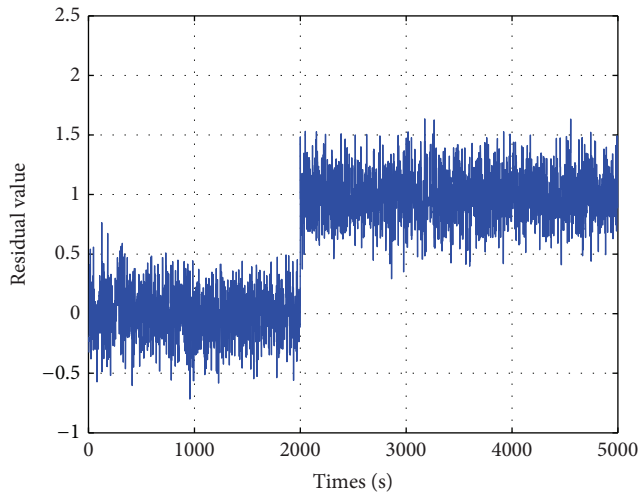

Figure 2: Residual signal of the initial system given by (22) using (25).

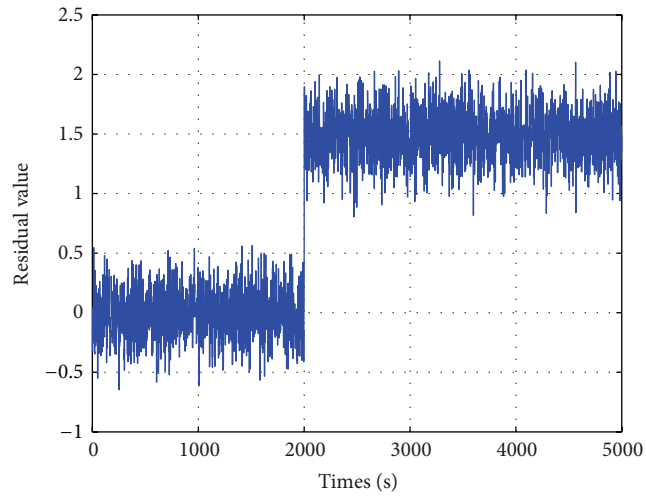

Figure 3: Residual signal of the reduced-order system given by (26) using (25).

By using (21), we can get the following system, in which the system matrices are

$$\widehat{\mathbf{A}} = \begin{bmatrix} -0.2571 & 0.5290 & 0.1497 \\ 0.1059 & -0.2553 & -0.5475 \\ 0.1690 & 0.0760 & -0.2820 \end{bmatrix},$$
$$\widehat{\mathbf{B}} = \begin{bmatrix} 0.1258 \\ -0.5990 \\ -0.2430 \end{bmatrix}, \tag{26}$$
$$\widehat{\mathbf{C}} = \begin{bmatrix} 0.1190 & 0.2307 & -0.6274 \end{bmatrix}.$$

The residual generators of the initial system given by (22) and the balanced reduced-order system given by (26) are shown in Figures 2 and 3, respectively. From Figures 2 and 3, we can conclude that the residual generator of the balanced reduced-order system gives the accurate fault alarm and has a good packets dropout and measurement noise rejection.

When the fault signal f is given as

$$f(k) = \begin{cases} 0.5 \sin k, & \text{for } k = 1500, 1501, \ldots, 5000, \\ 0, & \text{else}, \end{cases} \tag{27}$$

the measurement noise is

$$\widetilde{\varepsilon}(k) = 2e^{(-0.0006k)} n(k), \tag{28}$$

where $n(k)$ and $\varepsilon(k)$ are the Gaussian white noise with the variances 0.01 and 0.2, respectively. Figures 4 and 5 give the residual signal of the initial system and the balanced reduced-order system. We find that the balanced reduced-order residual generator show a good robust to the measurement noise and the packet dropout, and it also gives the accurate faults alarm.

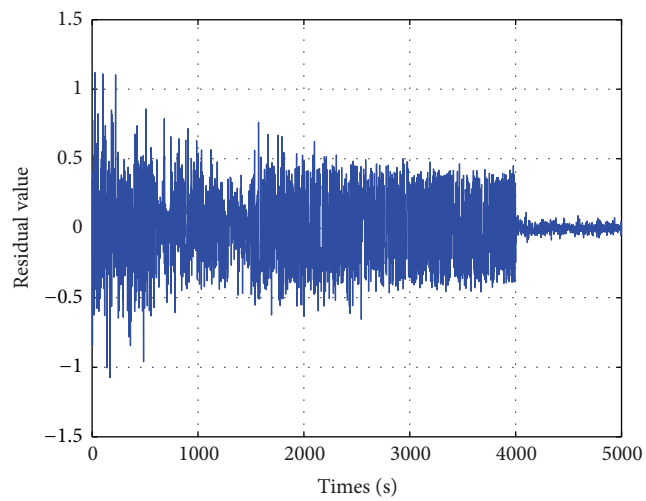

Figure 4: Residual signal of the initial system given by (22) using (27).

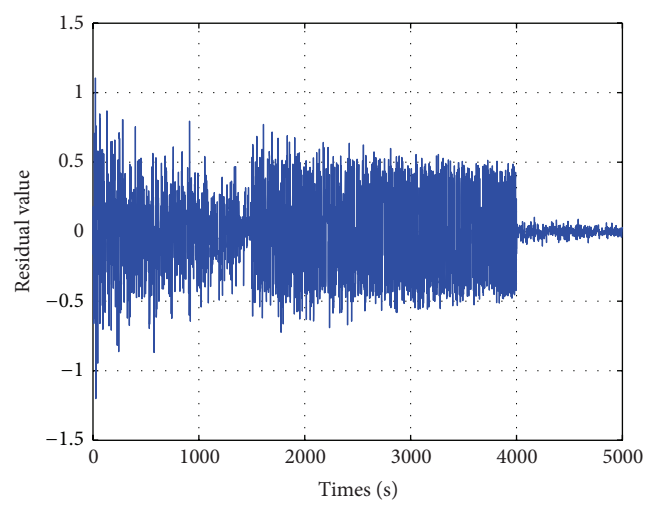

Figure 5: Residual signal of the reduced-order system given by (26) using (27).

The second case system is the fifth-order system, and the matrices of the NCS are given as follows:

$$\mathbf{A} = \begin{bmatrix} -0.6571 & 0.9250 & 0.8290 & 0.0497 & 0.8535 \\ -0.0290 & -0.5154 & 0.0990 & 0.0897 & 0.0636 \\ 0.1059 & -0.9623 & 0.2553 & -0.3750 & 0.2456 \\ 0.1690 & 0.2330 & 0.1760 & -0.0820 & 0.7493 \\ 0.0345 & -0.5433 & 0.6046 & 0.4237 & 0.3986 \end{bmatrix},$$

$$\mathbf{B} = \begin{bmatrix} 0.1258 \\ 0.2175 \\ -0.1990 \\ -0.2430 \\ 0.6673 \end{bmatrix}, \tag{29}$$

$$\mathbf{C} = \begin{bmatrix} 0.1190 & -0.2210 & 0.2307 & -0.6274 & 0.6490 \end{bmatrix},$$

$$\mathbf{E} = \begin{bmatrix} 0.8258 \\ 0.6175 \\ -0.7990 \\ -0.5430 \\ 0.8053 \end{bmatrix}, \qquad \mathbf{F} = 0.1984.$$

Based on (21), we can obtain the fourth-order system as follows:

$$\widehat{\mathbf{A}} = \begin{bmatrix} -0.6571 & 0.9250 & 0.0497 & 0.8535 \\ -0.0290 & -0.5154 & 0.0897 & 0.0636 \\ 0.1690 & 0.2330 & -0.0820 & 0.7493 \\ 0.0345 & -0.5433 & 0.4237 & 0.3986 \end{bmatrix},$$

$$\widehat{\mathbf{B}} = \begin{bmatrix} 0.1258 \\ 0.2175 \\ -0.2430 \\ 0.6673 \end{bmatrix}, \tag{30}$$

$$\widehat{\mathbf{C}} = \begin{bmatrix} 0.1190 & -0.2210 & -0.6274 & 0.6490 \end{bmatrix},$$

$$\widehat{\mathbf{E}} = \begin{bmatrix} 0.8258 \\ 0.6175 \\ -0.5430 \\ 0.8053 \end{bmatrix}, \qquad \widehat{\mathbf{F}} = 0.1984.$$

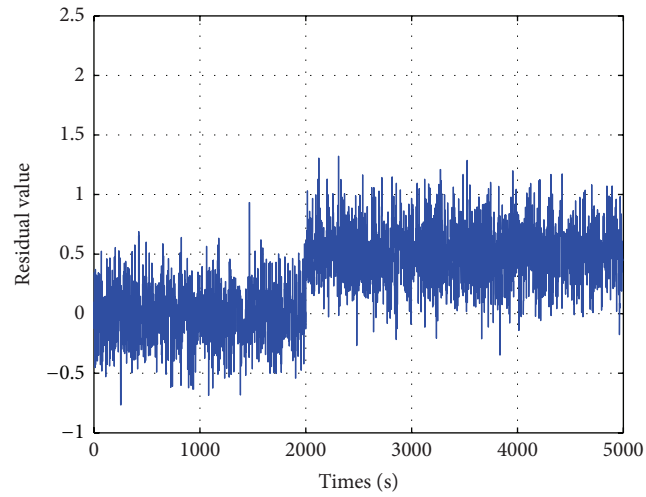

Figure 6: Residual signal of the initial system given by (29) using (25).

The same as (30), using (21), the third-order system can be obtained as

$$\widehat{\mathbf{A}}_2 = \begin{bmatrix} -0.6571 & 0.9250 & 0.8535 \\ -0.0290 & -0.5154 & 0.0636 \\ 0.0345 & -0.5433 & 0.3986 \end{bmatrix},$$

$$\widehat{\mathbf{B}}_2 = \begin{bmatrix} 0.1258 \\ 0.2175 \\ 0.6673 \end{bmatrix}, \tag{31}$$

$$\widehat{\mathbf{C}}_2 = \begin{bmatrix} 0.1190 & -0.2210 & 0.6490 \end{bmatrix},$$

$$\widehat{\mathbf{E}}_2 = \begin{bmatrix} 0.8258 \\ 0.6175 \\ 0.8053 \end{bmatrix}, \qquad \widehat{\mathbf{F}}_2 = 0.1984.$$

When the measurement noises $\varepsilon(k)$ and $\widehat{\varepsilon}(k)$ are the Gaussian white noise with the variance 0.2, the fault signal is described as (25). The residual signal $r(k)$ of the initial system given by (29) is shown in Figure 6, and the residual signal of the balanced reduced-order system given by (30) and (31) are shown in Figures 7 and 8, respectively. From Figures 6, 7, and 8, we find that the residual generator of the reduced-order system given by (30) and (31) shows more accurate alarm because the small Hankel singular values are removed and the robust of the systems (30) and (31) are improved. When the fault signal is described as (27) and the measurement noise is given as (28). Figures 9, 10, and 11 give the simulation results of the residual signal. From these three figures, we find that the residual signal of the initial system confuse with the noise at interval $[1000, 2000]$, while the balanced reduced-order systems given by (30) and (31) can easily distinguish the fault signal since they remove the small Hankel singular values and have the better measurement noise and packet dropout rejection.

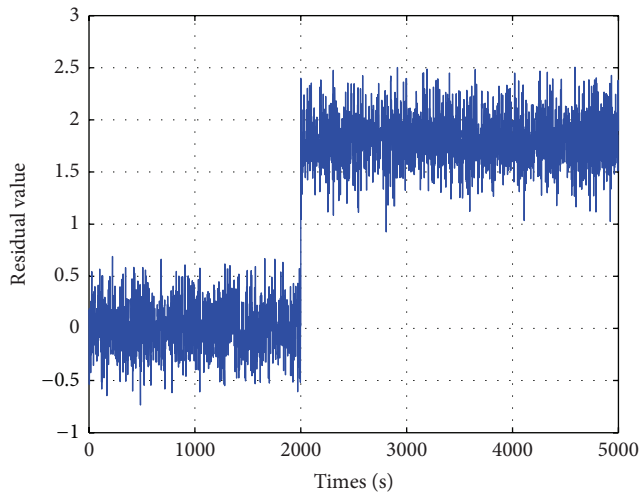

Figure 7: Residual signal of the reduced-order system given by (30) using (25).

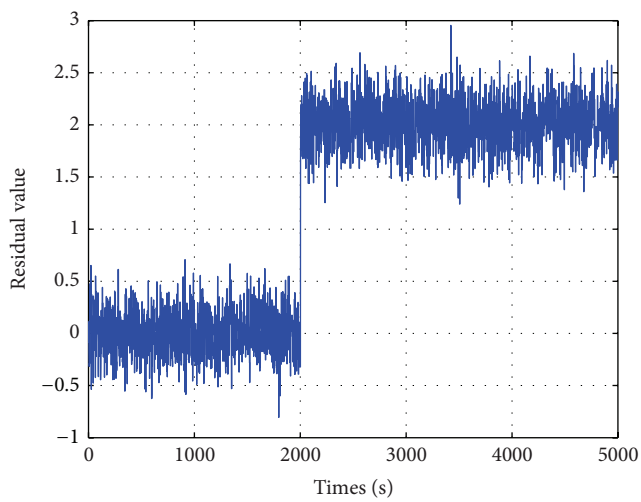

Figure 8: Residual signal of the reduced-order system given by (31) using (25).

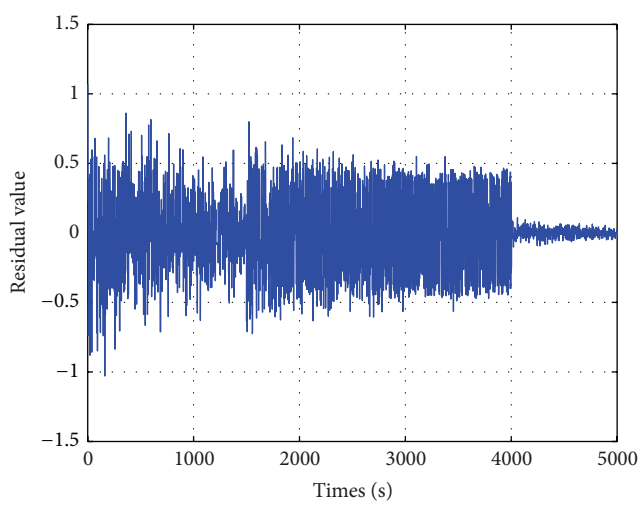

Figure 9: Residual signal of the initial system given by (29) using (27).

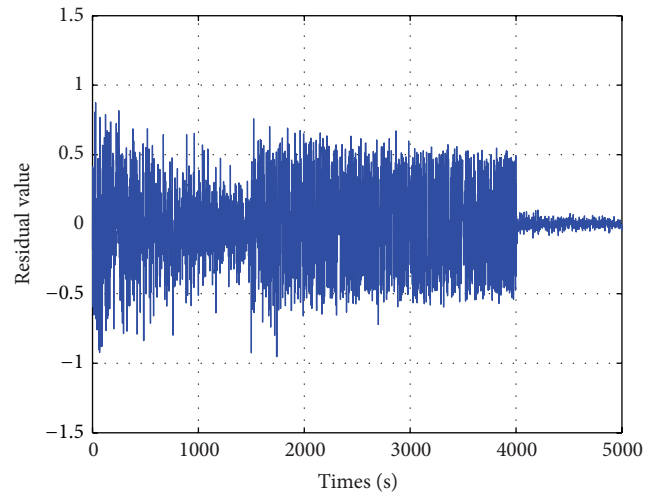

Figure 10: Residual signal of the reduced-order system given by (30) using (27).

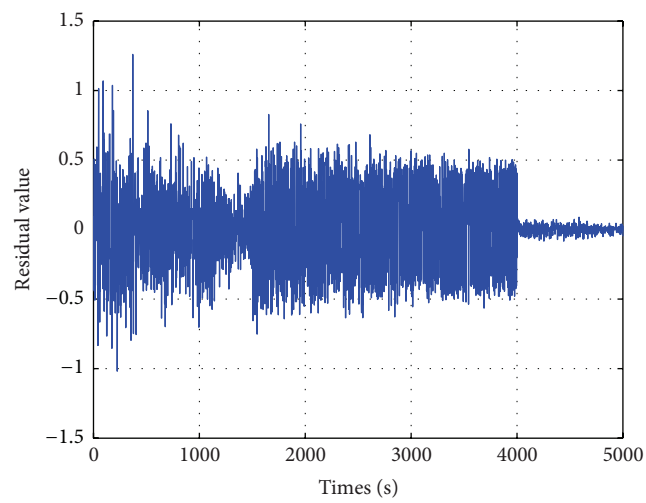

Figure 11: Residual signal of the reduced-order system given by (31) using (27).

6. Conclusions

The packets dropout is inevitable in the NCS; we analyze the effects of this phenomenon for the fault detection systems. Since the balanced reduced-order model minimizes the ratio of maximum-to-minimum eigenvalues of the Gramian matrices and has low parameter sensitivity to the data packet dropout and the measurement noise, we propose a new structure of the fault detection for the NCS based on the balanced realization, which lead this structure to have a good packets dropout and measurement noise rejection. Simulation results show that the proposed method has a good performance for the NCS. For future work, the intelligent design could be further included in the scheme to deal with the case of system learning. For future work, the intelligent design [14–16] could be further

included in the scheme to deal with the case of system learning.

Conflict of Interests

The author declares that there is no conflict of interests.

Acknowledgments

This work was supported in part by the Key Project of Natural Science Foundation of Zhejiang Province under Grant no. LZ14F010002 and in part by the Public Welfare Project of Zhejiang Province under Grants nos. 2012C21048 and 2012C23040.

References

[1] P. Zhang, S. X. Ding, P. M. Frank, and M. Sader, "Fault detection of networked control systems with missing measurements," in *Proceedings of the 5th Asian Control Conference*, pp. 1258–1263, Melbourne, Australia, July 2004.

[2] Z. Li, D. Sun, J. J. Zhen, and Y. T. Shi, "Fault detection for networked control system with data packet dropout," in *Proceedings of the IEEE International Conference on Automation and Logistics (ICAL '09)*, pp. 613–616, IEEE, Shenyang, China, August 2009.

[3] H. Huang, D. X. Xie, X. D. Han, D. F. Zhang, and Z. Q. Wang, "Fault detection for networked control system with random packet dropout," *Control Theory and Applications*, vol. 28, no. 1, pp. 79–86, 2011.

[4] W. Li, F. Jiang, Z. Wang, G. Zhou, and Z. Zhu, "Fault detection of Markov jumping linear systems," *Mathematical Problems in Engineering*, vol. 2012, Article ID 141867, 27 pages, 2012.

[5] W. L. Jiang, C. Y. Dong, E. Z. Niu, and Q. Wang, "Observer-based robust fault detection filter design and optimization for networked control systems," *Mathematical Problems in Engineering*. In press.

[6] Q. Wang, M.-M. Wang, and C.-Y. Dong, "Design of a kind of reduced-order fault detection filtering algorithm and its application in space vehicles," *Journal of Astronautics*, vol. 34, no. 1, pp. 61–68, 2013.

[7] X. Li, X. B. Wu, Z. L. Xu, and C. Huang, "Fault detection observer design for networked control system with long time-delays and data packet dropout," *Journal of Systems Engineering and Electronics*, vol. 21, no. 5, pp. 877–882, 2010.

[8] P. A. Regalia, *Adaptive IIR Filtering in Signal Processing and Control*, Marcel Dekker, New York, NY, USA, 1995.

[9] Y. F. Zhi, X. Zheng, and R. Li, "On the convergence behavior of affine projection algorithm with direction error," *Asian Journal of Control*, vol. 16, no. 2, pp. 530–538, 2014.

[10] B. C. Moore, "Principal component analysis in linear systems: controllability, observability, and model reduction," *IEEE Transactions on Automatic Control*, vol. 26, no. 1, pp. 17–32, 1981.

[11] P. M. Frank and X. Ding, "Frequency domain approach to optimally robust residual generation and evaluation for model-based fault diagnosis," *Automatica*, vol. 30, no. 5, pp. 789–804, 1994.

[12] K. Hochan, C. Chongho, O. Sangrok, and K. Kwangbae, "Minimal balanced realization of SISO systems using closed-form Gramians," in *Proceedings of the Proceedings of the 1995 American Control Conference*, vol. 3, pp. 1837–1841, IEEE, Seattle, Wash, USA, June 1995.

[13] Y. F. Zhi, P. G. Fan, and J. Zhang, "Adaptive IIR filtering based on balanced-realization," *Journal of Systems Engineering and Electronics*, vol. 24, no. 1, pp. 19–25, 2013.

[14] B. Xu, C. G. Yang, and Z. K. Shi, "Reinforcement learning output feedback NN control using deterministic learning technique," *IEEE Transactions on Neural Networks and Learning Systems*, vol. 25, no. 3, pp. 635–641, 2014.

[15] B. Xu, Z. K. Shi, C. G. Yang, and F. C. Sun, "Composite neural dynamic surface control of a class of uncertain nonlinear systems in strict-feedback form," *IEEE Transactions on Cybernetics*, vol. 44, no. 12, pp. 2626–2634, 2014.

[16] B. Xu, Z. K. Shi, and C. G. Yang, "Composite fuzzy control of a class of uncertain nonlinear systems with disturbance observer," *Nonlinear Dynamics*, 2015.

Hindawi Publishing Corporation
Mathematical Problems in Engineering
Volume 2015, Article ID 951502, 29 pages
http://dx.doi.org/10.1155/2015/951502

Research Article

Dynamic Responses of Continuous Girder Bridges with Uniform Cross-Section under Moving Vehicular Loads

Qingfei Gao,[1] Zonglin Wang,[1] Hongyu Jia,[2] Chenguang Liu,[1] Jun Li,[1,3] Binqiang Guo,[4] and Junfei Zhong[1]

[1] *School of Transportation Science and Engineering, Harbin Institute of Technology, Harbin 150090, China*
[2] *Department of Civil Engineering, Southwest Jiaotong University, Emei Campus, Emeishan 614202, China*
[3] *School of Architecture Engineering and Technology, Heilongjiang College of Construction, Harbin 150050, China*
[4] *Zhejiang Provincial Institute of Communications Planning, Design and Research, Hangzhou 310000, China*

Correspondence should be addressed to Qingfei Gao; gaoqingfei_1986@163.com

Received 13 November 2014; Accepted 26 November 2014

Academic Editor: Yun-Bo Zhao

Copyright © 2015 Qingfei Gao et al. This is an open access article distributed under the Creative Commons Attribution License, which permits unrestricted use, distribution, and reproduction in any medium, provided the original work is properly cited.

To address the drawback of traditional method of investigating dynamic responses of the continuous girder bridge with uniform cross-section under moving vehicular loads, the orthogonal experimental design method is proposed in this paper. Firstly, some empirical formulas of natural frequencies are obtained by theoretical derivation and numerical simulation. The effects of different parameters on dynamic responses of the vehicle-bridge coupled vibration system are discussed using our own program. Finally, the orthogonal experimental design method is proposed for the dynamic responses analysis. The results show that the effects of factors on dynamic responses are dependent on both the selected position and the type of the responses. In addition, the interaction effects between different factors cannot be ignored. To efficiently reduce experimental runs, the conventional orthogonal design is divided into two phases. It has been proved that the proposed method of the orthogonal experimental design greatly reduces calculation cost, and it is efficient and rational enough to study multifactor problems. Furthermore, it provides a good way to obtain more rational empirical formulas of the DLA and other dynamic responses, which may be adopted in the codes of design and evaluation.

1. Introduction

The dynamic response of bridges due to moving vehicular loads has been a subject of interest to engineers more than 100 years. Owning to the uncertain, transient, and nonlinear characteristics of the vehicle-bridge coupled vibration system, the phenomenon of dynamic response is one that requires fairly complex mathematical treatment to adequately characterize the motion and forces within the structure. However, for simplicity, it will instead be conceptual treatment using a common format, one that describes dynamic response as a fraction or multiple of the response that would be obtained if the same forces or loads were applied statically. This is, in fact, the same approach that most design specifications use to calculate the effects of dynamic live loading. When using such an approach, the amount of response above the static value is typically called the dynamic increment and is found by multiplying the static value by an "impact fraction." Alternatively, the total response can be expressed as a multiple of the static value using an impact factor [1]. In recognition of the complex behavior associated with the dynamic response from vehicular loading, several authors have observed that the term "impact" is too limited and therefore not descriptive of the actual behavior [2–5]. Instead, the current trend is to replace the term "impact fraction" with "dynamic load allowance," which represents the response from all types of vehicular dynamic effects, not solely impact. In this study, the term "dynamic load allowance" is adopted.

It has been proved that many different definitions of dynamic load allowance are adopted by various researchers and engineers [6, 7]. Based on the design theory of the bridge

in Chinese current code, the dynamic load allowance in this paper is defined as follows:

$$\mu(x_b) = \frac{y_{d,\max}(x_b, x_{v1})}{y_{s,\max}(x_b, x_{v2})} - 1, \quad (1)$$

where x_b is the location of the selected section, $\mu(x_b)$ denotes the dynamic load allowance of the selected section of the bridge, and $y_{d,\max}(x_b, x_{v1})$ and $y_{s,\max}(x_b, x_{v2})$, respectively, denote the maximum dynamic response and the maximum static response of the selected section. Furthermore, x_{v1} and x_{v2} mean the location of the vehicle when the dynamic response and the static response reach the maximum value. It should be noted that x_{v1} and x_{v2} are not the same in most of the time.

The dynamic response of a bridge to a crossing vehicle is a complex problem affected by the dynamic characteristics of both the bridge and the vehicle and by the bridge surface conditions [1]. Extensive research and development has been carried out to understand the vibration of bridges as a result of natural sources of vibration and to determine the dynamic allowance as a function of the fundamental frequency due to its uniqueness [8–11]. So it is important to find a reliable method to estimate the natural frequency of bridges. Komatsu et al. evaluated the natural vibration responses of straight and curved I- or box-girder bridges using Vlasov's beam theory [12, 13]. Cantieni conducted an experimental study to establish a reliable relationship between the fundamental frequency and maximum span length of bridges [14]. Meanwhile, Billing presented tables of natural frequencies for straight, continuous symmetric multispan uniform beams of two through six spans, for various span ratios [15]. Additionally, in order to reduce the significant difference between the estimation of the natural frequency obtained from the codes and theoretical methods or numerical simulation, Gao et al. proposed a numerical improved method for straight bridges [16, 17]. Also, the empirical expressions are established by Mohseni et al. using regression analysis, to determine the fundamental frequencies of skew continuous multicell box-girder bridges [18]. However, some limitations still exist for these methods to actually be used in practice.

Over the last 60 years, a significant amount of research has been conducted in the area of bridge dynamics, and this research has been both analytical and experimental in scope. Following the collapse of several railway bridges in Great Britain, the first study of vehicle-bridge interaction was conducted in 1849 by Willis [19]. A major experimental investigation of bridge impact loads was initiated in 1958 by American Association of State Highway Officials (AASHO). Eighteen simply supported bridges traversed by the two-axle trucks and the three-axle tractor-trailer combinations were investigated, each with a span of 15 m [20]. Wright and Green reported on a series of experimental investigations of vehicle-bridge interaction made on 52 highway bridges in Ontario from 1956 to 1957 [21]. Csagoly et al. conducted a second series of tests on bridges (11 bridges) in Ontario in 1969 to 1971 [22]. Page [23] and Leonard [24] reported on a series of dynamic tests conducted on highway bridges (30 bridges) by the Transport and Road Research Laboratory (TRRL) in England. Shepard and Sidwell [25], Shepard and Aves [26], and Wood and Shepard [27] reported on fourteen bridge tests conducted in New Zealand. In 1980, a third series of dynamic testing of highway bridges in Ontario was performed. The tests were conducted on 27 bridges of various configurations of steel, concrete, and timber construction [5, 28]. Cantieni presented results from the dynamic load tests of 226 highway bridges in Switzerland from the mid-1950s to the early 1980s [14, 29]. As for the numerical simulation, in 1970, Veletsos developed a numerical method for computing the dynamic response of highway bridges to moving vehicular loads [30]. Guant et al. investigated analytically the effects on bridge accelerations of several parameters, including the properties of the bridge and the vehicle as well as the initial conditions of the roadway [31]. Inbanathan and Wieland performed an analytical investigation of the dynamic response of a simply supported box girder bridge due to vehicle moving across the span [32]. Coussy et al. presented an analytical study of the influence of random surface irregularities on the dynamic response of bridges [33]. Recently, Bakht and Pinjarkar presented a literature review of bridge dynamics, with a particular focus on the dynamic testing of highway bridges [7]. And Paultre et al. presented a comprehensive review of analytical and experimental findings on bridge dynamics and the evaluation of the dynamic load allowance [19]. All these studies have proved that many of the parameters interact with one another, further complicating the issue, and consequently, many research studies have reported seemingly conflicting conclusions.

Therefore, the method of orthogonal experimental design in batches [34–38] has been proposed in this paper. It can be used for studying both the main effects and the interaction effects. Meanwhile, due to the processing in batches, it greatly reduces the calculation cost.

In this study, the natural frequencies of the simply supported girder bridge and the continuous girder bridge with uniform cross-section are firstly investigated based on the theoretical derivation and the numerical simulation. And then the effects of different parameters on the dynamic responses of the vehicle-bridge coupled vibration system are discussed by our own program VBCVA. Finally, the orthogonal experimental design method is proposed for the dynamic responses analysis, including the case without interaction and the case considering interaction.

2. Natural Frequencies of Multispan Continuous Girder Bridges

In civil and transportation engineering, dynamic characteristics of structures always consist of natural frequencies, corresponding vibration modes, and damping ratios. The natural frequency is one of the most important dynamic characteristics, due to its key role in determining dynamic responses of the structure under dynamic loads, such as wind, earthquake, and moving vehicles. Also, the impact factor or dynamic load allowance, which is used for considering the dynamic increments generated by moving vehicular loads, is

Table 1: Three different types of boundary of single-span bridge.

Boundary	Hinged and hinged	Fixed and hinged	Fixed and fixed
Schematic plot	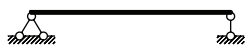	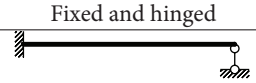	
Boundary description	$\begin{cases} \varphi_n(0) = 0 & \varphi_n''(0) = 0 \\ \varphi_n(L) = 0 & \varphi_n''(L) = 0 \end{cases}$	$\begin{cases} \varphi_n(0) = 0 & \varphi_n'(0) = 0 \\ \varphi_n(L) = 0 & \varphi_n''(L) = 0 \end{cases}$	$\begin{cases} \varphi_n(0) = 0 & \varphi_n'(0) = 0 \\ \varphi_n(L) = 0 & \varphi_n'(L) = 0 \end{cases}$

Note: $\varphi = 0$ means the deflection is zero, $\varphi' = 0$ means the rotation is zero, and $\varphi'' = 0$ means the moment is zero.

Table 2: The results of single-span bridges with different boundary conditions.

Boundary	Vibration modes	Frequency equation	First three frequencies
Hinged and hinged	$\varphi_n(x) = A_1 \sin \alpha_n x$	$\sin \alpha_n L = 0$	$\alpha_1 = \frac{\pi}{L}$ $\alpha_2 = \frac{2\pi}{L}$ $\alpha_3 = \frac{3\pi}{L}$
Fixed and hinged	$\varphi_n(x) = A_1[\sin \alpha_n x - \sinh \alpha_n x + \frac{\sinh \alpha_n L - \sin \alpha_n L}{\cos \alpha_n L - \cosh \alpha_n L}(\cos \alpha_n x - \cosh \alpha_n x)]$	$\tan \alpha_n L - \tanh \alpha_n L = 0$	$\alpha_1 = \frac{3.927}{L}$ $\alpha_2 = \frac{7.069}{L}$ $\alpha_3 = \frac{10.210}{L}$
Fixed and fixed	$\varphi_n(x) = A_1[\sin \alpha_n x - \sinh \alpha_n x + \frac{\cos \alpha_n L - \cosh \alpha_n L}{\sin \alpha_n L + \sinh \alpha_n L}(\cos \alpha_n x - \cosh \alpha_n x)]$	$3 - 2\cos \alpha_n L \cosh \alpha_n L = 0$	$\alpha_1 = \frac{4.739}{L}$ $\alpha_2 = \frac{7.853}{L}$ $\alpha_3 = \frac{10.996}{L}$

given as the function of natural frequencies in most codes and specifications for bridge design. In addition, the serviceability of bridges, especially for pedestrian bridges, is closely related to the natural frequency. Therefore, the natural frequency is firstly studied in this paper, and it is the basis of dynamic responses analysis.

2.1. Simply Supported Girder Bridges. The boundary of the simply supported girder bridge is assumed as pinned joint in both ends. However, according to inspections of existing bridges, we found that the ends could not completely rotate with the degeneration of rubber bearings. For convenience of engineers and researchers, three types of boundary are investigated, which are shown in Table 1.

As for the Euler beam with uniform cross-section, if the damping is ignored, the vibration governing equation can be simplified as

$$m\ddot{y} + EI\frac{\partial^4 y}{\partial x^4} = p(x,t), \tag{2}$$

where the p denotes the force and m, E, I, y, x, and t denote, respectively, the mass per unit length, elasticity modulus, moment of inertia, displacement, location, and time.

Based on the method of separation of variables, the solution can be listed as follows:

$$\omega_n = \alpha_n^2\sqrt{\frac{EI}{m}} \tag{3}$$

$$\begin{aligned} \varphi_n(x) = {} & A_1 \sin \alpha_n x + A_2 \cos \alpha_n x \\ & + A_3 \sinh \alpha_n x + A_4 \cosh \alpha_n x, \end{aligned} \tag{4}$$

where ω_n is the nth natural frequency (rad/s), φ_n is the nth vibration mode, and α_n is the constant parameter determined by both the cross-section and the boundary conditions. In addition, A_1, A_2, A_3, and A_4 are constant parameters, which are determined by the boundary condition.

Submitting (4) into different types of boundaries in Table 1, then the results can be seen in Table 2.

It can be seen from Table 2 that the natural frequency is higher when there are more constraints and the corresponding stiffness is higher. The nth natural frequency of the single-span bridge with different boundary conditions can be summarized as

$$f_n = \frac{\pi}{2}\left(\frac{n + 0.25b}{L}\right)^2\sqrt{\frac{EI}{m}}, \tag{5}$$

where b is used for denoting different boundary conditions and L is the span length. When the boundary is hinged and hinged, the parameter $b = 0$. As for the other two conditions, $b = 1$ and $b = 2$ in turn.

For common bridges, the moment of inertia I is positively correlated with the factor h^3 (h is the height of the beam), and the area A is positively correlated with the hight h. Therefore, the nth natural frequency f_n is negatively related to the span length L. And it successfully explains the phenomenon that most empirical formulas regressed by fielding test for estimating natural frequencies are negatively correlated with the span length L.

2.2. Continuous Girder Bridges with Uniform Spans. As for 2-span, 3-span, and 4-span continuous girder bridges with uniform cross-section and uniform spans, the natural frequency and corresponding vibration modes are given by Gao et al. [16]. Based on a similar method, more general frequency equation can be listed as follows:

$$\begin{vmatrix} -2G_n & H_n & 0 & \cdots & 0 & 0 \\ H_n & -2G_n & H_n & \cdots & 0 & 0 \\ 0 & H_n & -2G_n & H_n & 0 & 0 \\ \vdots & \vdots & \ddots & \ddots & \ddots & \vdots \\ 0 & 0 & 0 & H_n & -2G_n & H_n \\ 0 & 0 & 0 & \cdots & H_n & -2G_n \end{vmatrix} \begin{matrix} 1 \\ 2 \\ 3 \\ \vdots \\ n-1 \\ n \end{matrix} = 0, \quad (6)$$

where

$$G_n = \frac{\cosh \alpha_n L}{\sinh \alpha_n L} - \frac{\cos \alpha_n L}{\sin \alpha_n L}, \qquad H_n = \frac{1}{\sinh \alpha_n L} - \frac{1}{\sin \alpha_n L}. \quad (7)$$

For common bridges, the number of spans is not more than eight. Equation (6) is solved by the general software MATLAB, and the frequency equations and the natural frequencies are listed in Tables 3 and 4.

It can be seen from Table 4 that the first natural frequency of the multispan continuous girder bridge with uniform spans is completely the same as that of the corresponding simply supported girder bridge. Also, for bridges with different spans, the fundamental vibration modes are retained. However, the number of other vibration modes among fundamental vibration modes is more for the bridge with more spans.

In the Chinese code D60-2004 for bridge design, the impact factor is defined as the function of the natural frequency. For continuous girder bridges, the impact factor of the positive moment in mid-span is different from that of the negative moment in pier-top section, which is determined by the curvature of different modes. According to the analysis of vibration modes distribution, for positive moment in mid-span section, the first mode is significant for all bridges. However, for negative moment in pier-top section, the curvature of the second vertical vibration mode is larger for even-span bridges, and the curvature of the third vertical vibration mode is larger for odd-span bridges (Figure 1).

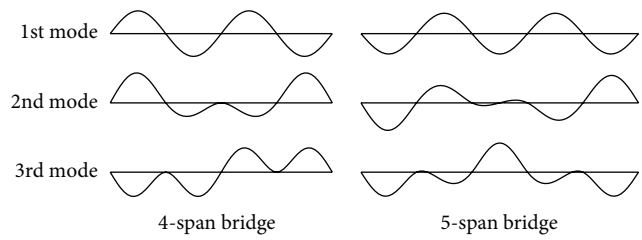

Figure 1: Vertical vibration modes distribution for bridges with different spans.

Table 3: Frequency equations of multispan continuous girder bridges with uniform spans.

Number of spans	Frequency equation
2	$G_n = 0$
3	$4G_n^2 - H_n^2 = 0$
4	$G_n(4G_n^2 - 2H_n^2) = 0$
5	$16G_n^4 - 12G_n^2H_n^2 + H_n^4 = 0$
6	$G_n(16G_n^4 - 16G_n^2H_n^2 + 3H_n^4) = 0$
7	$64G_n^6 - 80G_n^4H_n^2 + 24G_n^2H_n^4 - H_n^6 = 0$
8	$G_n(64G_n^6 - 96G_n^4H_n^2 + 40G_n^2H_n^4 - 4H_n^6) = 0$

So the second natural frequency in the even-span bridge and the third natural frequency in the odd-span bridge are selected for calculating the impact factor of negative moment in pier-top section. To make it clear, both of them are denoted as f_2. Based on Table 4, the empirical formula of f_2 can be given by

$$f_2 = \frac{1}{2\pi}\left(\frac{\lambda\pi}{L}\right)^2 \sqrt{\frac{EI}{m}} = \lambda^2 \frac{\pi}{2L^2}\sqrt{\frac{EI}{m}}, \quad (8)$$

where λ is the modified factor, and it can be gained by

$$\lambda = \begin{cases} 1.25 & s = 2 \\ 1 + 0.08 \times 2^{2-m} & s = 2m, \quad 2 \le m \le 4 \\ 1 + 0.36 \times 2^{2-m} & s = 2m - 1, \quad 2 \le m \le 4, \end{cases} \quad (9)$$

where s is the number of spans.

2.3. Continuous Girder Bridges with Nonuniform Spans. The multispan continuous girder bridge is usually seen in urban areas and other areas with special terrain. For urban bridges, when the road extends under the bridge, the span above the road will be larger than others. For bridges in special terrain areas, the piers cannot be constructed at the idealized location due to the bad terrain occasionally, so the spans should be nonuniformly arranged.

To our experience of bridge design, the length of side span is always smaller in the multispan continuous girder bridge with nonuniform spans. The span ratio r is introduced here. And it has been assumed that only the length of side span is different from others (Figure 2):

$$r = \frac{L_s}{L_m}, \quad (10)$$

Table 4: Natural frequencies of multispan continuous girder bridges with uniform spans.

Number of spans	Natural frequencies (Hz)
2	$f_n = \frac{1}{2\pi L^2}(\pi^2, 3.927^2, 4\pi^2, \ldots)\sqrt{\frac{EI}{m}}$
3	$f_n = \frac{1}{2\pi L^2}(\pi^2, 3.556^2, 4.298^2, 4\pi^2, \ldots)\sqrt{\frac{EI}{m}}$
4	$f_n = \frac{1}{2\pi L^2}(\pi^2, 3.393^2, 3.927^2, 4.463^2, 4\pi^2, \ldots)\sqrt{\frac{EI}{m}}$
5	$f_n = \frac{1}{2\pi L^2}(\pi^2, 3.309^2, 3.700^2, 4.153^2, 4.550^2, 4\pi^2, \ldots)\sqrt{\frac{EI}{m}}$
6	$f_n = \frac{1}{2\pi L^2}(\pi^2, 3.261^2, 3.556^2, 3.927^2, 4.298^2, 4.601^2, 4\pi^2, \ldots)\sqrt{\frac{EI}{m}}$
7	$f_n = \frac{1}{2\pi L^2}(\pi^2, 3.230^2, 3.460^2, 3.764^2, 4.089^2, 4.395^2, 4.634^2, 4\pi^2, \ldots)\sqrt{\frac{EI}{m}}$
8	$f_n = \frac{1}{2\pi L^2}(\pi^2, 3.210^2, 3.393^2, 3.645^2, 3.927^2, 4.208^2, 4.463^2, 4.655^2, 4\pi^2, \ldots)\sqrt{\frac{EI}{m}}$

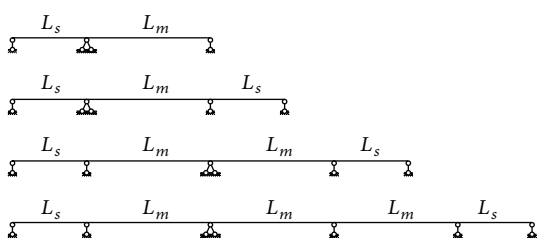

Figure 2: Schematic plots of multispan continuous girder bridges with nonuniform spans.

Table 5: Frequency equations of multispan bridges with nonuniform spans.

Number of spans	Frequency equation
2	$G_{ns} + G_{nm} = 0$
3	$(G_{ns} + G_{nm})^2 - H_{nm}^2 = 0$
4	$(G_{ns} + G_{nm})(G_{nm}^2 + G_{ns}G_{nm} - H_{nm}^2) = 0$
5	$G_{ns}^2(4G_{nm}^2 - H_{nm}^2) + G_{ns}G_{nm}(8G_{nm}^2 - 6H_{nm}^2) + (4G_{nm}^4 - 5G_{nm}^2H_{nm}^2 + H_{nm}^4) = 0$

where L_s is the length of side span and L_m is the length of middle span.

The frequency equation of this type of bridge can be given by

$$\begin{vmatrix} -G_{ns} - G_{nm} & H_{nm} & 0 & \cdots & 0 & 0 \\ H_{nm} & -2G_{nm} & H_{nm} & \cdots & 0 & 0 \\ 0 & H_{nm} & -2G_{nm} & H_{nm} & 0 & 0 \\ \vdots & \vdots & \ddots & \ddots & \ddots & \vdots \\ 0 & 0 & 0 & H_{nm} & -2G_{nm} & H_{nm} \\ 0 & 0 & 0 & \cdots & H_{nm} & -G_{ns} - G_{nm} \end{vmatrix} \begin{matrix} 1 \\ 2 \\ 3 \\ \vdots \\ n-1 \\ n \end{matrix} = 0. \tag{11}$$

When the number of spans is from 2 to 5, the frequency equations are listed in Table 5.

The empirical formulas for estimating natural frequencies of the bridge with nonuniform spans are listed as

$$f_1 = \frac{1}{2\pi}\left(\frac{\eta_1 \pi}{L}\right)^2 \sqrt{\frac{EI}{m}}, \tag{12a}$$

$$f_2 = \frac{1}{2\pi}\left(\frac{\eta_2 \pi}{L}\right)^2 \sqrt{\frac{EI}{m}}, \tag{12b}$$

where η_1 and η_2 are modified factors, which can be seen in Figure 3.

It can be seen from Figure 3(a) that all of modified factors are not less than 1.0. In other words, the first natural frequency of the multispan continuous girder bridge is larger than that of the corresponding simply supported girder bridge. Because the side span length is smaller than the middle span length, the stiffness has been increased by the side span. In addition, the modified factor η_1 of the bridge with two spans is completely the same as that of the bridge with four spans. This is due to the free rotation of the middle support of the bridge with four spans, and the first vibration mode of four-span bridge is equal of that of two two-span bridges.

It can be seen from the Figure 3(b) that the modified factor η_2 of 4-span bridge is almost the same as that of 5-span bridge. They are largely different from others and should be noted.

Finally, it has been emphasized that the empirical formulas and modified factors proposed in this paper can be used for estimating natural frequencies of bridges with uniform cross-section. Also, according to these formulas, the factors influencing natural frequencies are more clearly seen, which may give a better guideline for the design and evaluation of dynamic performance of bridges.

3. Dynamic Responses Analysis by Traditional Method

Research over the last 40 years has shown that the dynamic responses of bridges under moving vehicles are influenced by many parameters, such as the dynamic characteristics of the vehicle, the dynamic characteristics of the bridge, and variations in the surface conditions of the bridge and

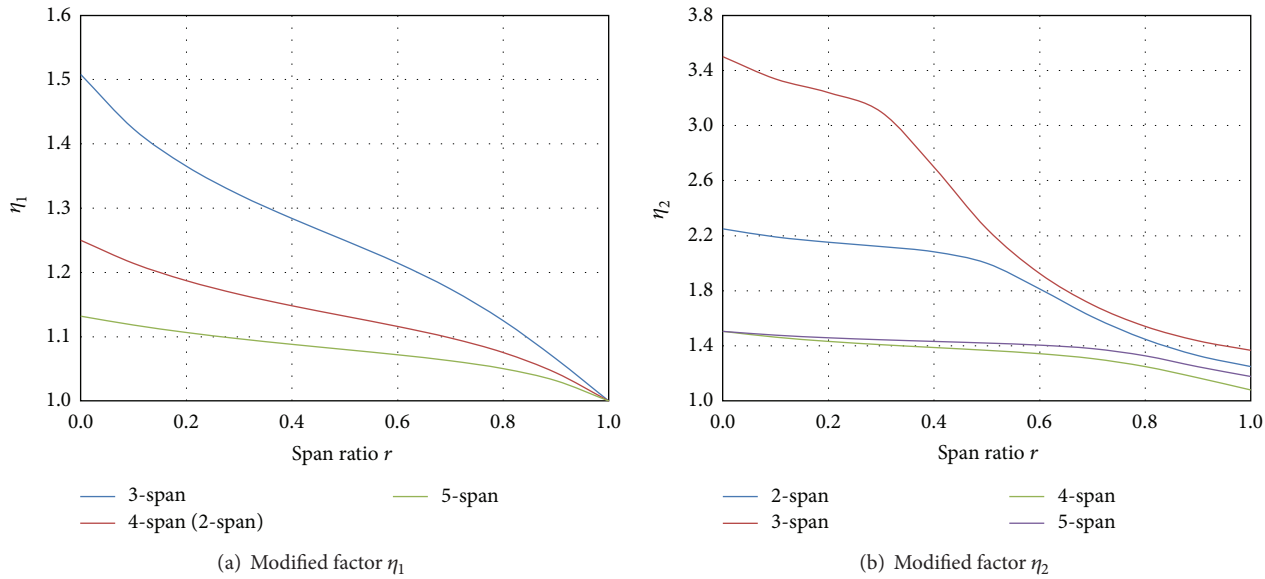

(a) Modified factor η_1 (b) Modified factor η_2

Figure 3: Modified factors of natural frequencies for the bridge with nonuniform spans.

approach roadways [1]. However, most of the studies focused on the dynamic load allowance in midspan of the bridge. In this part, the dynamic load allowances (DLAs) in the side span and the middle span are discussed, respectively, to obtain the differences of DLAs in variance sections. Also, for comfort analysis, the accelerations of the bridge and the vehicle are investigated.

Based on the existing research results, thirteen parameters are considered here. According to the traditional method, every parameter is studied, respectively. In other words, if this parameter is changing, all of the other parameters are fixed. Therefore, the fundamental model of bridge-vehicle coupled system is assumed at first, and then every parameter is varied from the basis of this model. They are listed in Tables 6, 7, and 8.

According to the numerical simulation, the effect of different parameters on the dynamic response of the vehicle-bridge system is investigated by our own program VBCVA (Vehicle-Bridge Coupled Vibration Analysis). It has to be noted that the pavement roughness model proposed by Hwang and Nowak has been adopted in this program [39].

3.1. Effect of Roughness. For actual bridges, the pavement roughness is an inevitable factor. The effect of roughness on dynamic responses of the vehicle-bridge system is shown in Figure 4.

It can be seen from Figure 4 that, with the deterioration of bridge pavement conditions, the DLA of the bridge, the acceleration of the bridge, and the acceleration of the bridge grow in a linear fashion. Moreover, the dynamic response of the middle span is smaller than that of the side span. In addition, the growth rate in the middle span is a little smaller than that of the side span.

A great deal of research shows that the bridge pavement is one of the most vulnerable components due to its smaller stiffness [40, 41]. The results obtained from this study show that the roughness may significantly promote the vibration of the bridge traversed by moving vehicular loads. This will set up a vicious circle of increasing vibration, poorer roughness, and increased stress. Additionally, the larger vibration acceleration of the vehicle induced by the poorer roughness will make the passengers uncomfortable. Therefore, we should pay more attention to the bridge pavement condition in actual operation. Prompt repair of the damaged bridge pavement will reduce the unnecessary cost.

3.2. Effect of Span Length. As for the continuous girder bridges with uniform cross-section, the common span length ranges from 20 m to 40 m. It has to be emphasized that the cross-sections of bridges with different span length are the same. The effect of span length on dynamic response of the vehicle-bridge system is shown in Figure 5.

It can be seen from Figure 5 that as the span length increases, the DLA of the middle span firstly decreases and then keeps steady, and the DLA of the side span is on the rise, which is largely different from the former one. But the change of the vibration acceleration in the middle span is the same as that of the vibration acceleration in the side span. Both of them slightly decrease and then increase. Additionally, the vibration acceleration of the vehicle rises at first and goes down later with the increasing of the span length.

For most dynamic responses in Figure 5, there is an extreme point with the increasing of the span length. It may be due to the resonance phenomenon between the bridge and the vehicle. The vibration natural frequency of the bridge with 25 m long span may be more close to that of the vehicle.

3.3. Effect of Span Ratio. From the aspect of mechanical characteristics due to the static load, the length of side span is not larger than that of middle span and not smaller than

Table 6: Parameters of the bridge in the fundamental model.

L (m)	W (m)	I (m^4)	A (m^2)	E (MPa)	ρ (kg/m^3)	ξ	X (cm)
40	12	3.54	7.08	34500	2600	0.05	2.0

L: length, W: width, I: moment of inertia, E: modules of elasticity, ρ: density, ξ: damping ratio, and X: maximum magnitude of the roughness.

Table 7: Parameters of the vehicle in the fundamental model.

Parameters	Value
Mass of truck body	31800 kg
Mass of front wheel	400 kg
Mass of middle/rear wheel	600 kg
Pitching moment of inertia	40000 kg·m^2
Rolling moment of inertia	10000 kg·m^2
Distance (front axle to center)	4.60 m
Distance (middle axle to center)	0.36 m
Distance (middle to rear axle)	1.40 m
Wheel base	1.80 m
Upper stiffness (front axle)	1200 kN·m^{-1}
Upper stiffness (middle/rear axle)	2400 kN·m^{-1}
Upper damping (front axle)	5 kN·s·m^{-1}
Upper damping (middle/rear axle)	10 kN·s·m^{-1}
Lower stiffness (front axle)	2400 kN·m^{-1}
Lower stiffness (middle/rear axle)	4800 kN·m^{-1}
Lower damping (front axle)	6 kN·s·m^{-1}
Lower damping (middle/rear axle)	12 kN·s·m^{-1}
Speed	80 km/h

Table 8: Parameters description and their values.

Index	Description	Values	Note
A	Pavement roughness	1 cm, 2 cm, 3 cm, 4 cm, 5 cm	Maximum magnitude
B	Length of the main span	20 m, 25 m, 30 m, 35 m, 40 m	
C	Ratio between side span and middle span	0.5, 0.6, 0.7, 0.8, 0.9, 1.0	Changing the side span
D	Number of spans	3, 4, 5, 6, 7	
E	Weight of the bridge	$(0.6, 0.8, 1.0, 1.2, 1.4) \times \rho$	Changing the density
F	Stiffness of the bridge	$(0.6, 0.8, 1.0, 1.2, 1.4) \times E$	Changing the modules
G	Damping ratio of the bridge	$(0.6, 0.8, 1.0, 1.2, 1.4) \times \xi$	
H	Weight of the vehicle	$(0.6, 0.8, 1.0, 1.2, 1.4) \times M_v$	Including body and tyres
I	Upper stiffness of the vehicle	$(0.6, 0.8, 1.0, 1.2, 1.4) \times k_s$	
J	Upper damping of the vehicle	$(0.6, 0.8, 1.0, 1.2, 1.4) \times c_s$	
K	Lower stiffness of the vehicle	$(0.6, 0.8, 1.0, 1.2, 1.4) \times k_t$	
L	Lower damping of the vehicle	$(0.6, 0.8, 1.0, 1.2, 1.4) \times c_t$	
M	Speed of the vehicle	20~120 km/h (step = 20 km/h)	

M_v: the whole weight of the vehicle, k_s: upper stiffness, c_s: upper damping, k_t: lower stiffness, and c_t: lower stiffness. The values of all the parameters are obtained from the fundamental model (Table 7).

half of the length of the middle span. So the span ratio of the side span and the middle span ranges from 0.5 to 1.0 in this study. The effect of span ratio on dynamic responses of the vehicle-bridge system is shown in Figure 6.

It can be seen from Figure 6 that the change of the DLA is almost the same as that of the acceleration of the bridge. In the side span, they slightly decrease and then increase and then keep steady. In the middle span, they firstly go up and then go down. In addition, the vibration acceleration of the vehicle body keeps steady at first, and then it goes down. Moreover, it can be found that all of these dynamic responses reach their extreme value when the span ratio is 0.9. In China, as for the fabricated girder bridge, the span ratio is equal to 1.0 in common. And, as for the cast in place, the span ratio usually ranges from 0.6 to 0.8.

To determine the span ratio in design of the bridge, both the static and dynamic characteristics should be paid attention to.

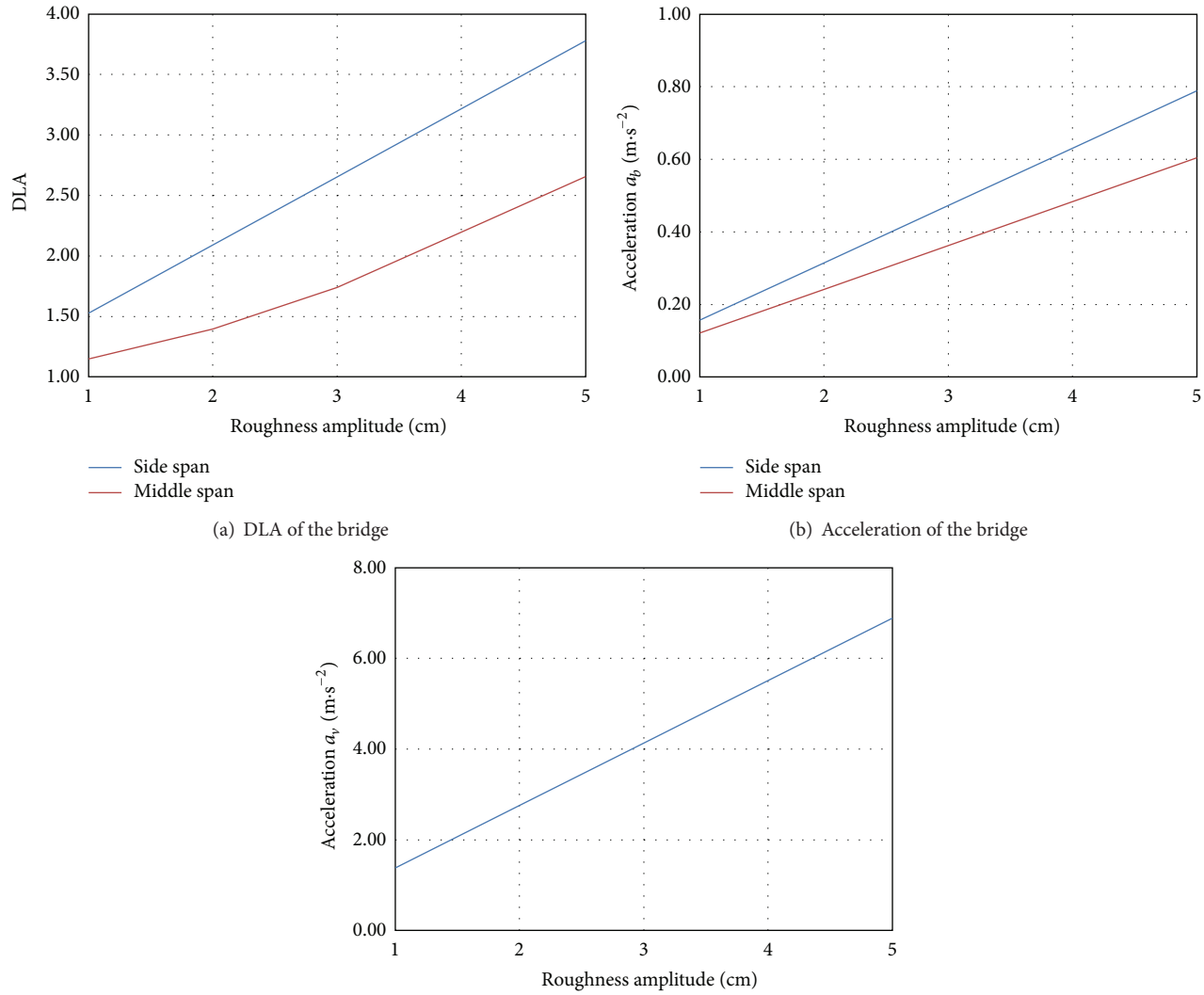

(a) DLA of the bridge

(b) Acceleration of the bridge

(c) Acceleration of the vehicle

Figure 4: Effect of roughness on dynamic responses of the vehicle-bridge system.

3.4. Effect of Spans Number. For middle- and small-span continuous girder bridges, the number of spans is always ranging from 3 to 7, owning to the expansion or contraction according to the change of temperature. The effect of spans number on dynamic responses of the vehicle-bridge system is shown in Figure 7.

It can be seen from Figure 7 that the effect of spans number on the DLA of the bridge is not significant, especially for the DLA in the side span. However, the vibration acceleration of the bridge decreases with the increasing of the spans number. Moreover, the change of the vibration acceleration in the side span is much more similar to that in the middle span. Additionally, the vibration acceleration of the vehicle body is little influenced by the spans number of the bridge, as the fundamental natural frequency stays the same for bridges with different number of spans.

Based on the conclusion in this study, the dynamic performance is better for the bridge with more spans. However, the expansion or contraction induced by the change of the temperature may be larger when there are more spans. As a result, it has to be synthetically considered in the design.

3.5. Effect of Bridge Weight. The bridge weight is changed according to amending the density of the material. This method can make sure that the area and the stiffness of the cross-section of the bridge are invariable. The effect of bridge weight on dynamic responses of the vehicle-bridge system is shown in Figure 8.

It can be seen from Figure 8 that as the bridge weight increases, the DLA in the side span keeps steady, while the DLA in the middle span jumpily decreases. However, the change of the vibration acceleration in the side span and that in the middle span are almost the same. They slightly increase and then decrease. Additionally, the vibration acceleration of the vehicle body goes up and down, and the range is small.

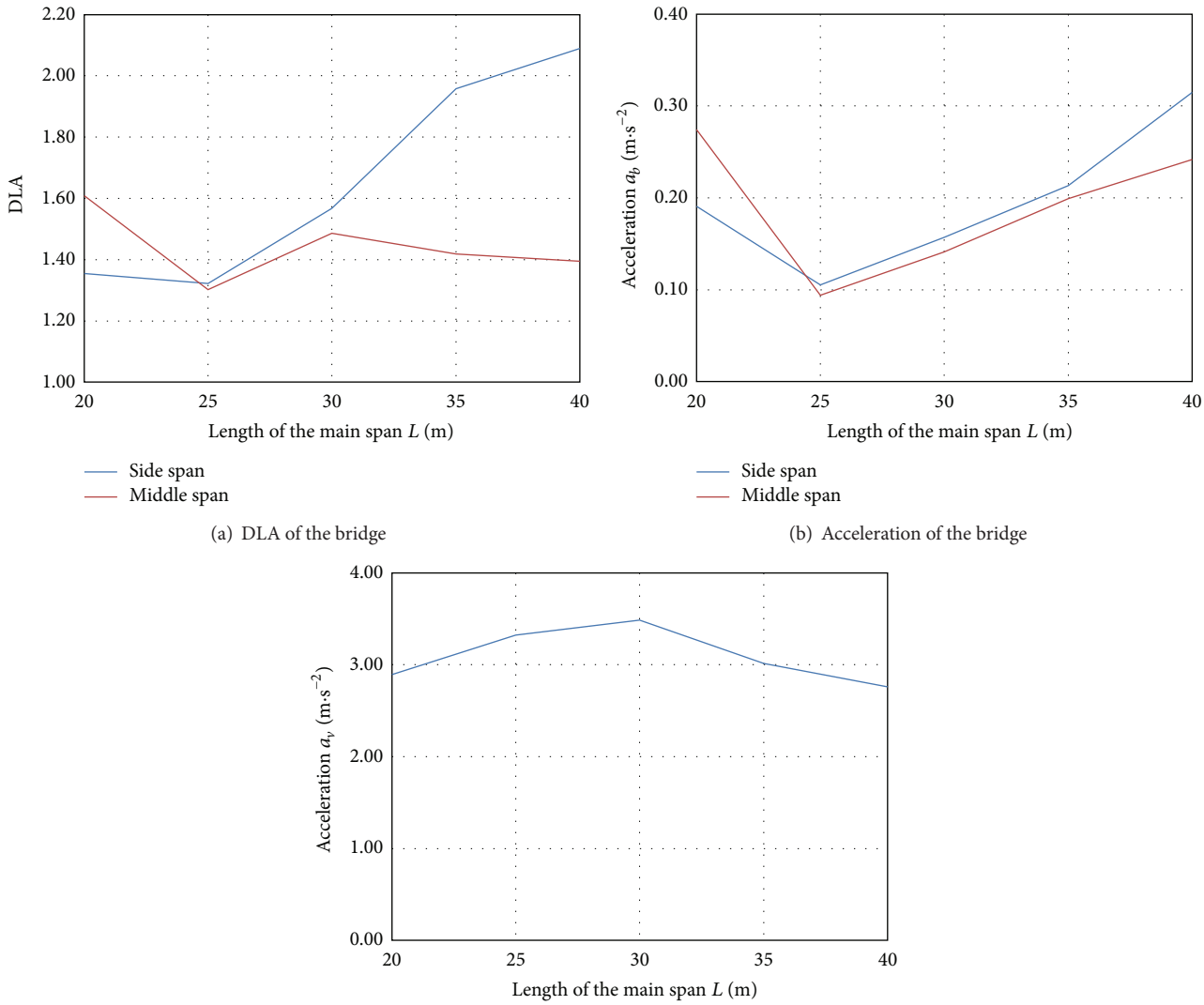

(a) DLA of the bridge

(b) Acceleration of the bridge

(c) Acceleration of the vehicle

Figure 5: Effect of span length on dynamic responses of the vehicle-bridge system.

In natural, it may be related to the dynamic characteristics of the bridge. The natural frequency is lower when the bridge weight is bigger. As for the vehicle-bridge coupled vibration system, the resonance phenomenon will appear when its natural frequencies are so approximate.

3.6. Effect of Bridge Stiffness. The bridge stiffness is changed according to amending the elasticity modules of the material. This method can make sure that the area and the weight of the bridge are invariable. The effect of bridge stiffness on dynamic responses of the vehicle-bridge system is shown in Figure 9.

It can be seen from Figure 9 that, with the increasing of the bridge stiffness, the DLA in the side span continues to rise, while the DLA in the middle span slightly decreases and then increases. However, the change of the vibration acceleration in the side span and that in the middle span are almost the same. They fluctuate and the range is small. Additionally, the bridge stiffness has little influence on the vibration acceleration of the vehicle body.

Similarly, the natural frequency is higher when the bridge stiffness is bigger. Also, as for the vehicle-bridge coupled vibration system, the resonance phenomenon will appear when its natural frequencies are so approximate.

3.7. Effect of Bridge Damping. As for the concrete structure, the damping ratio is assumed to be 0.05. In this study, it floats up and down at 40 percent. The effect of bridge damping on dynamic responses of the vehicle-bridge system is shown in Figure 10.

It can be seen from Figure 10 that the damping ratio has little influence on the DLA of the bridge. But the vibration acceleration of the bridge significantly decreases with the increasing of the damping ratio. Similarly, the vibration acceleration of the vehicle body continues to go down as the damping ratio increases.

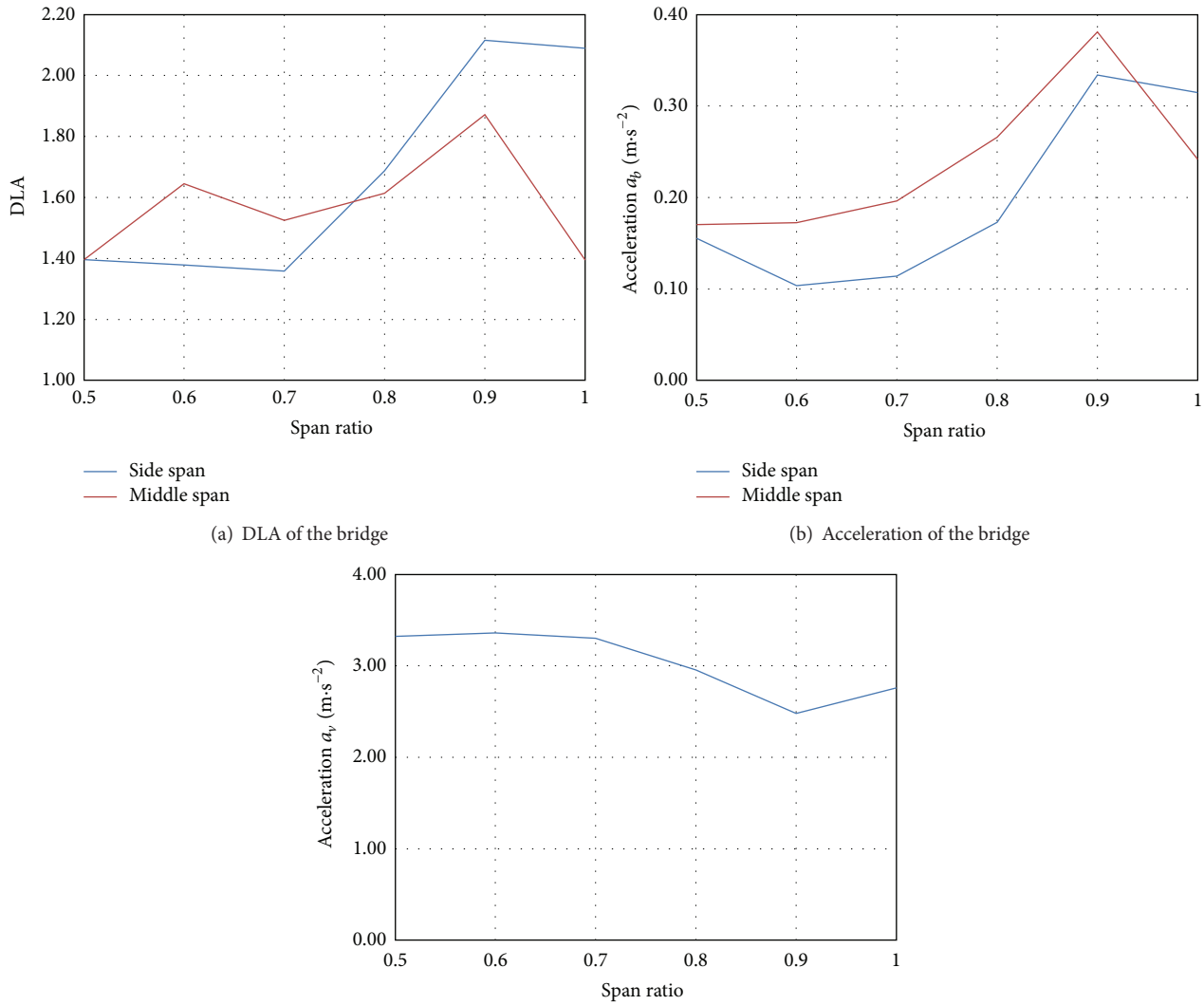

(a) DLA of the bridge

(b) Acceleration of the bridge

(c) Acceleration of the vehicle

Figure 6: Effect of span ratio on dynamic responses of the vehicle-bridge system.

Damping is one of the most important dynamic characteristics of the bridge. Up till now, it cannot be obtained by calculation. The only way to obtain the damping of the structure is by measuring in the fielding test. However, according to the results in this paper, the damping is not so important for calculating the DLA. But it is closely related to the vibration acceleration of the bridge and the vehicle, which may influence the inertia force of the bridge and the riding comfort. Therefore, the damping should still be noticed.

3.8. Effect of Vehicle Weight. To investigate the effect of the vehicle weight on dynamic responses of the bridge, the factor of the vehicle weight is introduced, and the fundamental weight is assumed to be 35 tons. In this study, the factor ranges from 0.6 to 1.4 at the step of 0.2. The effect of vehicle weight on dynamic responses of the vehicle-bridge system is shown in Figure 11.

It can be seen from Figure 11 that when the factor is smaller than 1.0, the DLA in the side span slightly decreases and then increases, while the DLA in the middle span firstly decreases and then keeps steady. When the factor is bigger than 1.0, the DLA in the side span decreases with the increasing of the vehicle weight, but the DLA in the middle span increases with the increasing of the vehicle weight. However, as the vehicle weight increases, the vibration acceleration in the side span goes down, while that in the middle span goes up. In addition, the vibration acceleration of the vehicle body decreases with the increasing of the vehicle weight.

Obviously, the effect of vehicle weight on dynamic responses in different positions is not the same. Limiting the vehicle weight can effectively reduce the static stress of the bridge, but its influence on the dynamic responses is not clearly enough. In particular, the change of the vibration acceleration in different positions of the bridge is completely the opposite.

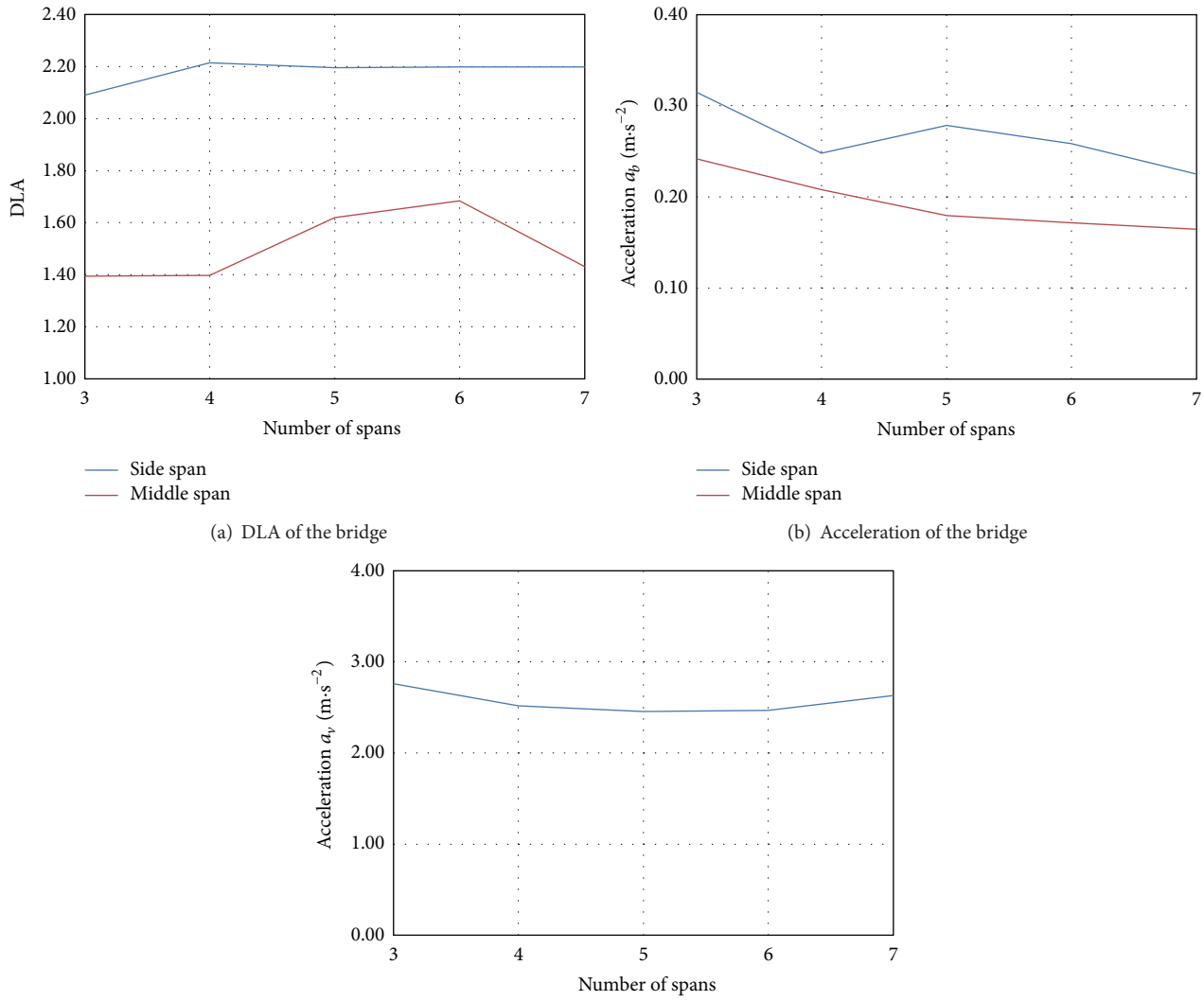

(a) DLA of the bridge

(b) Acceleration of the bridge

(c) Acceleration of the vehicle

Figure 7: Effect of spans number on dynamic responses of the vehicle-bridge system.

3.9. Effect of Upper Stiffness. To investigate the effect of the upper stiffness on dynamic responses of the vehicle-bridge system, the factor of the upper stiffness is introduced. In this study, the factor ranges from 0.6 to 1.4 at the step of 0.2. The effect of upper stiffness on dynamic responses of the vehicle-bridge system is shown in Figure 12.

It can be seen from Figure 12 that the DLA of the bridge almost goes down with the increasing of the upper stiffness of the vehicle. However, as the upper stiffness of the vehicle increases, the vibration acceleration of the bridge goes up. Moreover, the change of the acceleration in the side span is faster than that in the middle span. In other words, the effect of the upper stiffness on the dynamic response of the side span is much more sensitive. In addition, the vibration acceleration of the vehicle body continues to go up with the increasing of the upper stiffness of the vehicle.

As a result, the upper stiffness of the vehicle not only influences the dynamic responses of the bridge but also significantly affects the vibration acceleration of the vehicle body, which is closely related to the comfort of passengers and the safety of the goods. Therefore, to find the friendly stiffness of the vehicle is urgent and efficient in the area of riding comfort analysis.

3.10. Effect of Upper Damping. To investigate the effect of the upper damping on dynamic responses of the vehicle-bridge system, the factor of the upper damping is introduced. In this study, the factor ranges from 0.6 to 1.4 at the step of 0.2. The effect of upper damping on dynamic responses of the vehicle-bridge system is shown in Figure 13.

It can be seen from Figure 13 that all of the dynamic responses of the vehicle-bridge system decease with the increasing of the upper damping of the vehicle. The change of the DLA in the side span is faster than that in the middle span. However, the change of the vibration acceleration in the side span is almost the same as that in the middle span. It has to be

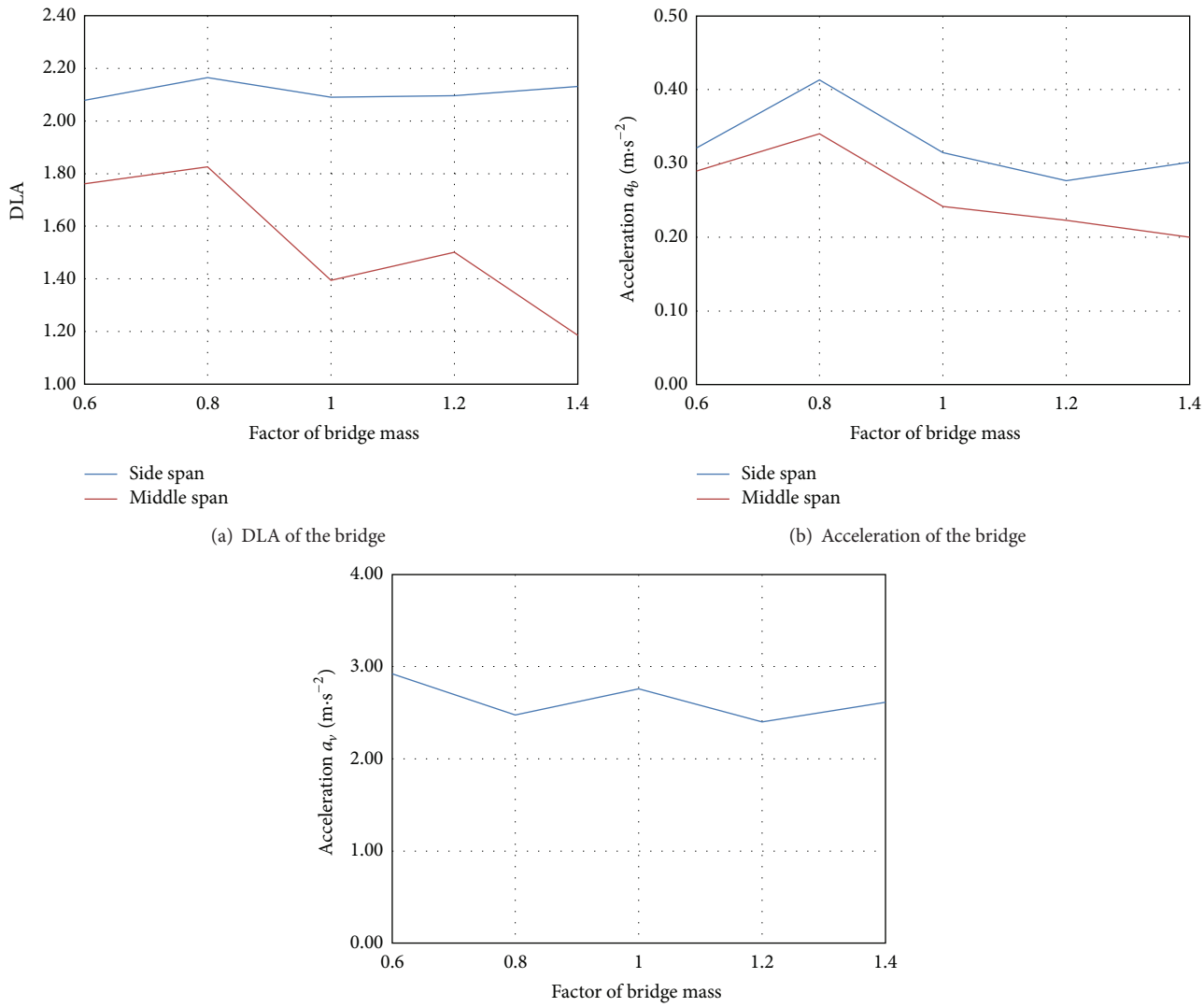

(a) DLA of the bridge

(b) Acceleration of the bridge

(c) Acceleration of the vehicle

Figure 8: Effect of bridge weight on dynamic responses of the vehicle-bridge system.

emphasized that the influence of the upper damping on the vibration acceleration of the vehicle is the most significant. In other words, the shock absorber system of the vehicle is so important in its design.

3.11. Effect of Lower Stiffness. To investigate the effect of the lower stiffness on dynamic responses of the vehicle-bridge system, the factor of the lower stiffness is introduced. In this study, the factor ranges from 0.6 to 1.4 at the step of 0.2. The effect of lower stiffness on dynamic responses of the vehicle-bridge system is shown in Figure 14.

It can be seen from Figure 14 that as the lower stiffness of the vehicle increases, the change of the DLA in the side span and that in the middle span are entirely the opposite. The former one slightly increases and then decreases, while the latter one slightly decreases and then increases. However, the vibration acceleration of the bridge goes up with the increasing of the lower stiffness. Moreover, the change of the vibration acceleration in the side span is faster than that in the middle span. Additionally, the vibration acceleration of the vehicle body goes up firstly and then keeps steady.

Comparing Figure 12 with Figure 14, it can be found that the effect of the upper stiffness is almost the same as the effect of the lower stiffness. Moreover, the former one is more significant than the latter one.

3.12. Effect of Lower Damping. To investigate the effect of the lower damping on dynamic responses of the vehicle-bridge system, the factor of the lower damping is introduced. In this study, the factor ranges from 0.6 to 1.4 at the step of 0.2. The effect of lower damping on dynamic responses of the vehicle-bridge system is shown in Figure 15.

It can be seen from Figure 15 that as the lower damping increases, all of dynamic responses of the vehicle-bridge system are falling. But the changing range of them is small.

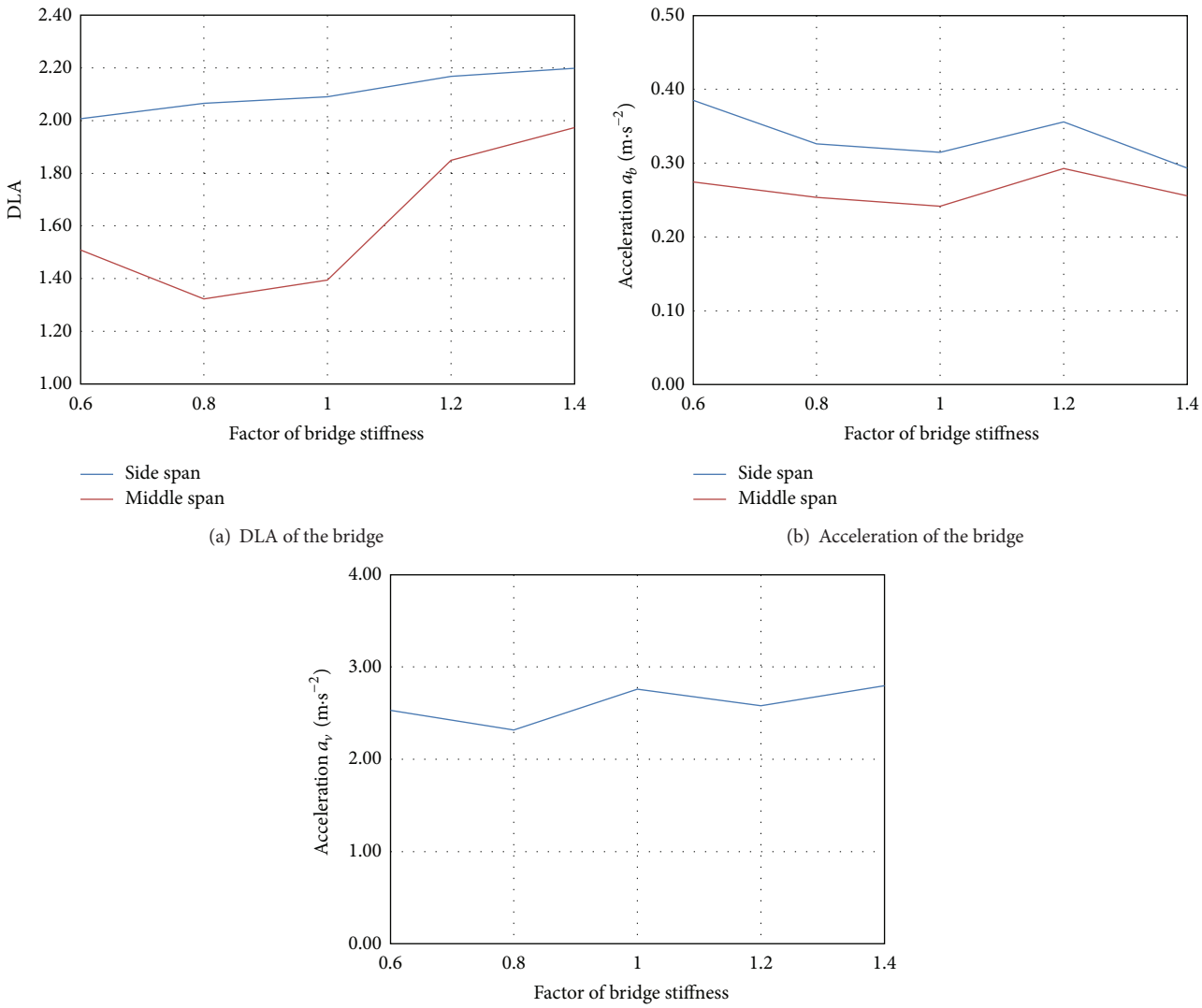

(a) DLA of the bridge

(b) Acceleration of the bridge

(c) Acceleration of the vehicle

Figure 9: Effect of bridge stiffness on dynamic responses of the vehicle-bridge system.

Also, the dynamic responses in the side span are significantly larger than those in the middle span, especially for the DLA.

Comparing Figure 13 with Figure 15, it can be found that the effect of the upper damping is almost the same as the effect of the lower damping. Moreover, the former one is more significant than the latter one.

3.13. Effect of Vehicle Speed. As for the loading truck, the speed ranges from 20 km/h to 120 km/h at the step of 20 km/h. The effect of vehicle speed on dynamic responses of the vehicle-bridge system is shown in Figure 16.

It can be seen from Figure 16 that as the speed increases, both the DLA in the side span and the DLA in the middle span increase firstly and then decrease. But the critical speeds of them are not the same, and the former one is bigger than the latter one. However, the vibration acceleration of the bridge goes up with the increasing of the vehicle speed. Similarly, the vibration acceleration of the vehicle body also increases.

Therefore, it has to be noted that limiting the speed directly is not a rational way to ensure the safety of the bridge, which is the common way during the maintenance of the old or damaged bridge.

Obviously, the effect of every parameter on the dynamic responses of the vehicle-bridge system can be studied by the program VBCVA. When one parameter is studied, the other parameters should be fixed. But, according to this method, the results may not occasionally be the same as the actual condition, because the interaction effects among different parameters are not considered.

4. Numerical Simulations Based on the Orthogonal Experimental Design

There are two ways for the analysis of factors influencing the dynamic responses of the vehicle-bridge coupled vibration system, full factorial designs and fractional factorial designs.

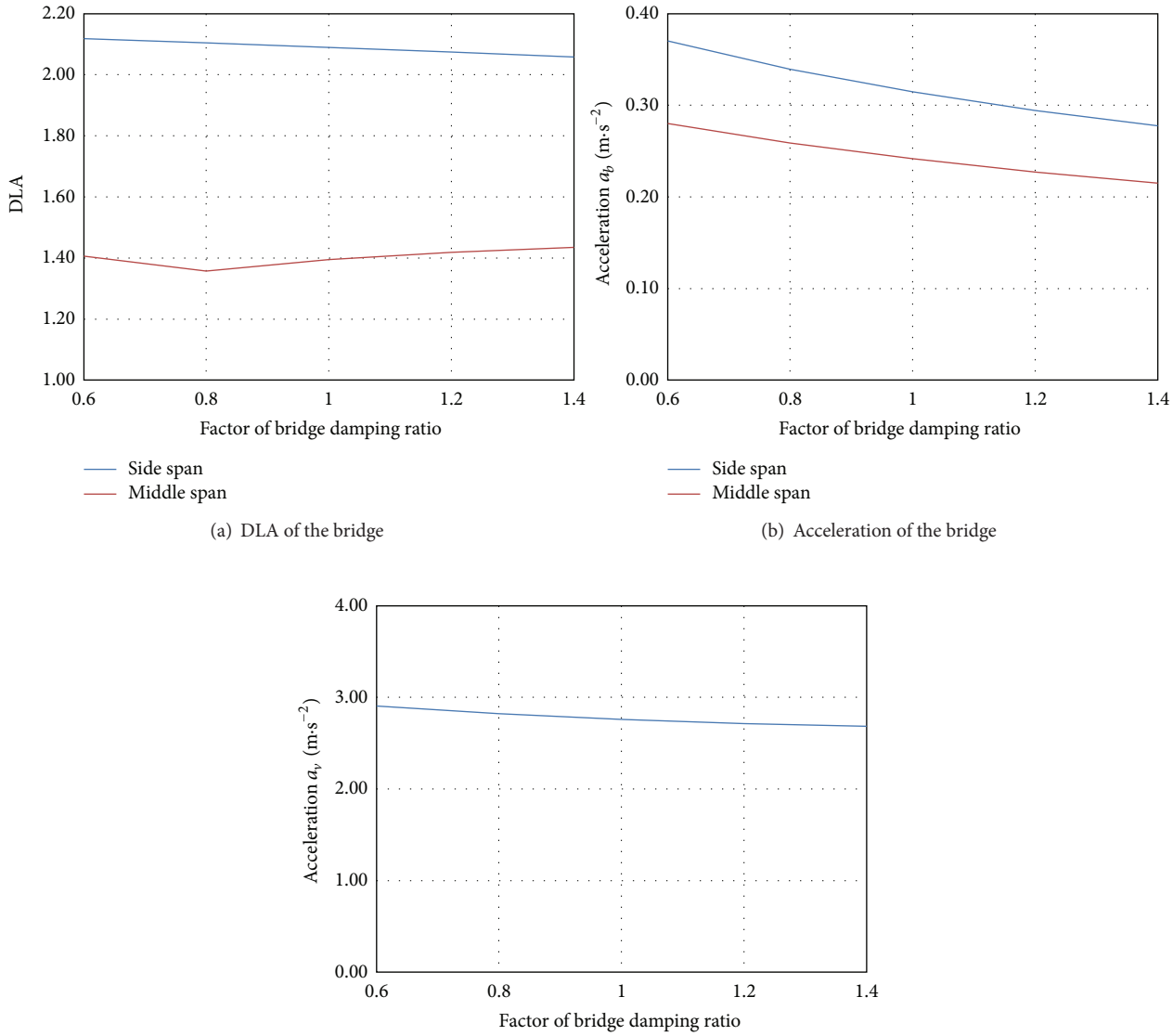

(a) DLA of the bridge

(b) Acceleration of the bridge

(c) Acceleration of the vehicle

Figure 10: Effect of bridge damping on dynamic responses of the vehicle-bridge system.

Full factorial designs reveal whether the effect of each factor depends on the levels of other factors in the experiment. This is the primary reason for multifactor experiments. One factorial experiment can show "interaction effects" that a series of experiments each involving a single factor cannot [42]. However, fractional factorial designs permit investigation of the effects of many factors in fewer runs than a full factorial design.

Data from fractional factorial designs are interpreted based on the following two assumptions. The first one is the sparsity of important effects. Only a few of the many possible effects are prominent. Even if many effects are nonzero, we expect a few to stand out as much larger than the rest. The other one is the simplicity of important effects. Main effects and/or two-factor interactions are more likely to be important than high-order interactions. This is also known as the hierarchical ordering principle.

Therefore, considering the high efficiency, the orthogonal experimental design, one common type of the fractional factorial design, is adopted in this study, including the numerical simulation without interaction and the numerical simulation with interaction.

4.1. Orthogonal Experimental Design. According to the orthogonal experimental design, two objectives can be attained. The first objective is to select fewer typical combinations for the test. And the other objective is to obtain the correct conclusions by the scientific method based on the limited combinations. The orthogonal experimental design consists of the design of test plan and the process of test data.

As for the design of test plan, the main procedures are listed as follows [43]. Firstly, the objective and the test index are clearly proposed. Secondly, the factors and their levels are

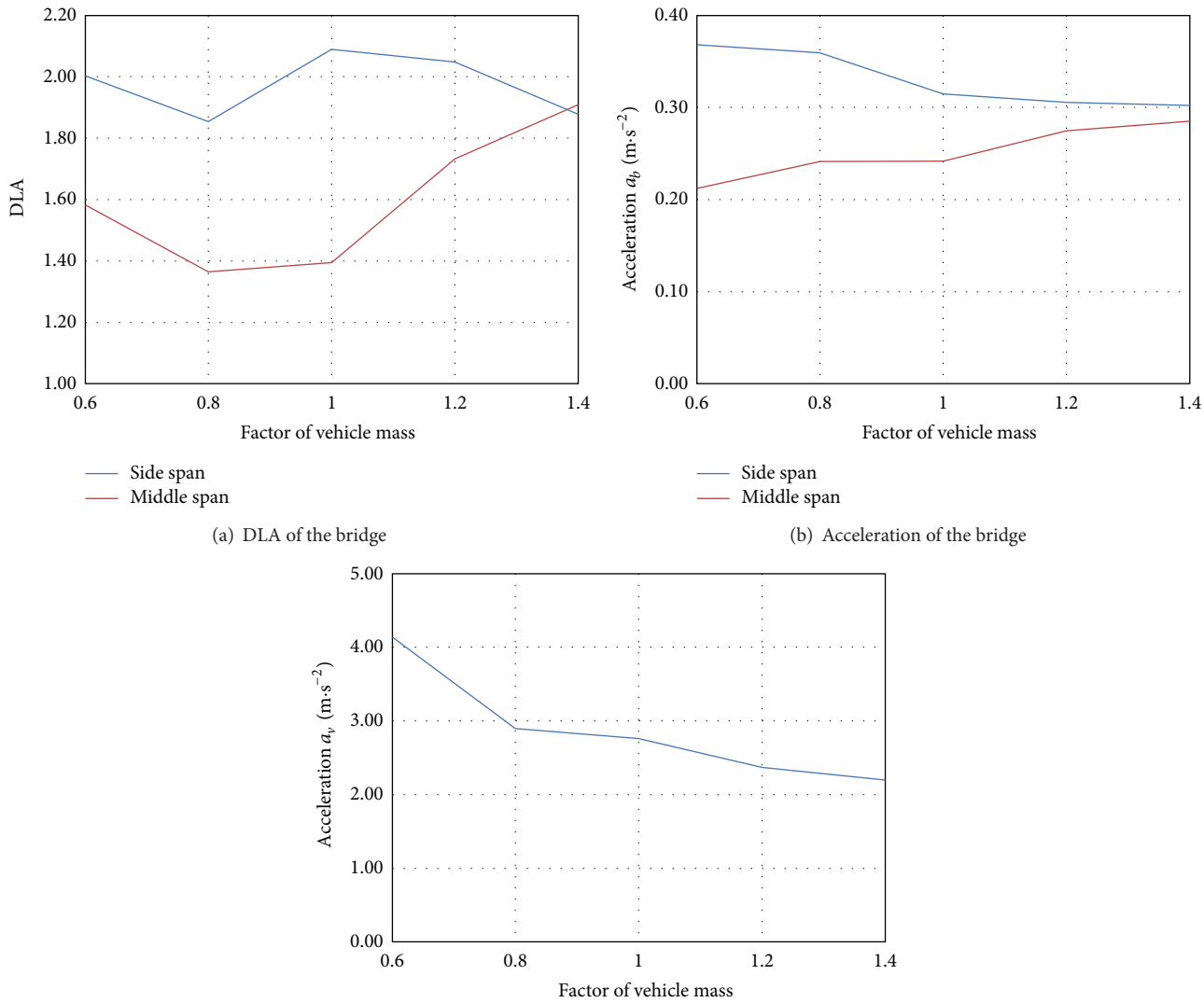

(a) DLA of the bridge

(b) Acceleration of the bridge

(c) Acceleration of the vehicle

Figure 11: Effect of vehicle weight on dynamic responses of the vehicle-bridge system.

determined based on the comprehension in this research field other than the knowledge of statistics. Thirdly, the rational orthogonal table is selected, including the table considering interaction and the table without interaction. Fourthly, the table header is designed. Finally, the test plan is formed.

As for the process of the test data, two methods are adopted, including the range analysis and the variance analysis [44]. The range analysis is much simpler and more convenient. However, the test error cannot be estimated, and the reliability of the results cannot be determined. Also, it cannot be applied in the fields of regression analysis and regression design. But the variance analysis can remedy the defects above.

The method of range analysis is also called the visual analysis method and the R (the abbreviation of the range) method. It consists of two procedures, calculation and judgment. The diagram can be seen in Figure 17.

In Figure 17 the K_{jm} is the sum of the test index with the mth level in the jth column and k_{jm} is the average of the K_{jm}. In addition, the R_j is the difference between the maximum and the minimum value of the k_{jm}:

$$R_j = \max\left(k_{j1}, k_{j2}, \ldots, k_{jm}\right) - \min\left(k_{j1}, k_{j2}, \ldots, k_{jm}\right). \tag{13}$$

The R_j is represented for the changing amplitude of the test index with the changing of the levels of the jth factor. Therefore, it can be concluded that the influence of the jth factor on the test index is much more significant if the value of R_j is bigger. Sometimes, for more clarity, the trend plot is given.

Variance analysis is more rigorous. There are four steps to realize the variance analysis [45, 46].

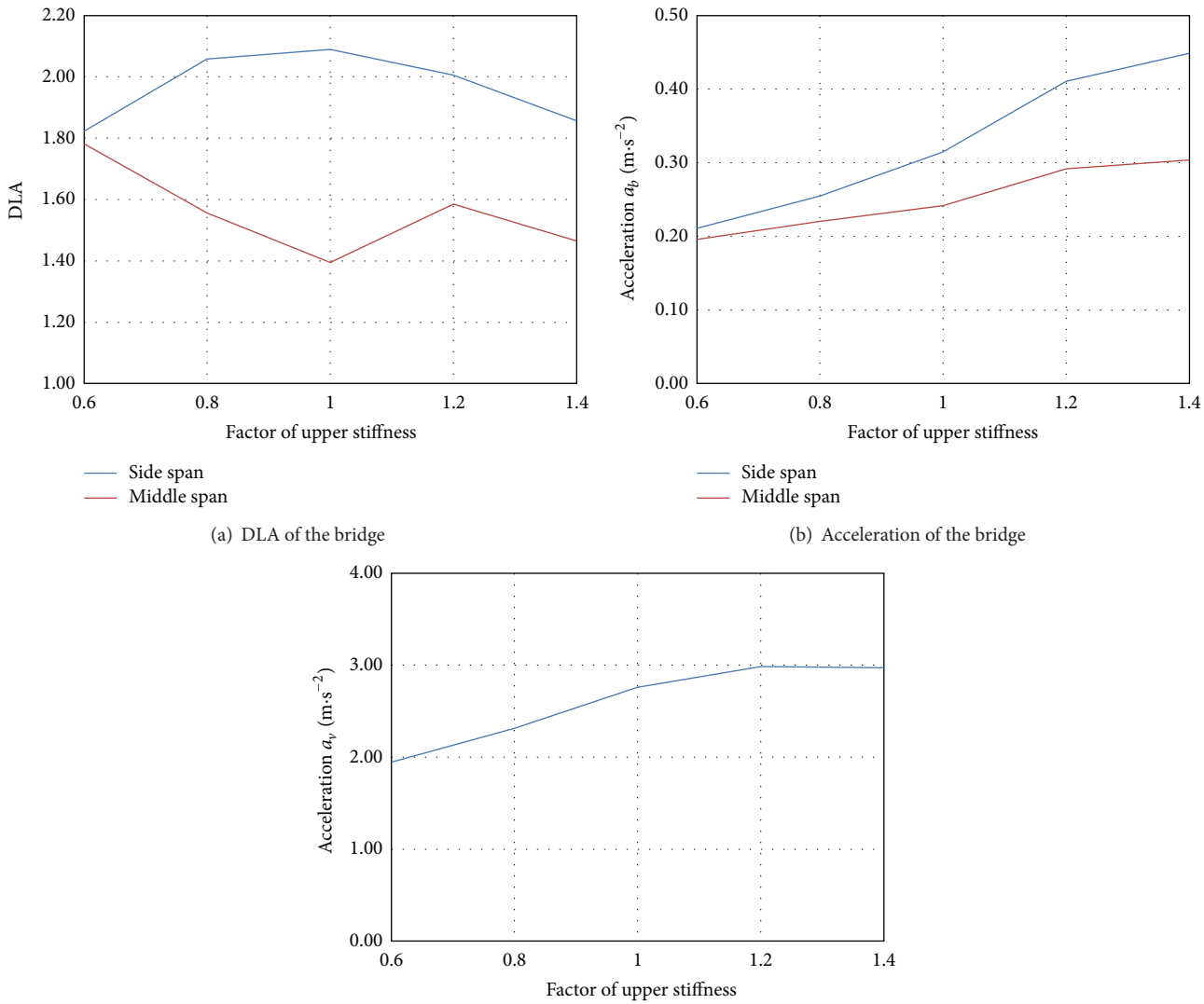

(a) DLA of the bridge

(b) Acceleration of the bridge

(c) Acceleration of the vehicle

Figure 12: Effect of upper stiffness on dynamic responses of the vehicle-bridge system.

Step 1. As for every factor, calculate the sum of square of deviations (S_j), the degree of freedom (dof, f_j), and the variance estimation (σ_j).

Step 2. Estimate the variance of the error (σ_e).

Step 3. Obtain the test static F and compare F with its critical value F_α for given significance level α.

Step 4. For simplicity, the variance analysis table is listed, including the process and the results. Consider

$$S = \sum_{i=1}^{a} (y_i - \overline{y})^2 = \sum_{i=1}^{a} y_i^2 - \frac{1}{a}\left(\sum_{i=1}^{a} y_i\right)^2,$$

$$S_j = \frac{a}{b}\sum_{k=1}^{b} (\overline{y}_{jk} - \overline{y})^2 = \frac{a}{b}\sum_{k=1}^{b} y_{jk}^2 - \frac{1}{a}\left(\sum_{i=1}^{a} y_i\right)^2,$$

$$F_j = \frac{\sigma_j}{\sigma_e} = \frac{S_j/f_j}{S_e/f_e} \tag{14}$$

in which y_i is the index result of the ith run and y_{jk} is the index result of the jth factor with the kth level. Also, S_e and f_e denote, respectively, the sum of square of deviations and the degree of freedom of the error. It has to be noted that the error has resulted from all of the vacant columns in the orthogonal array. Also, the accuracy increases with the increasing dof of the error [47]. Therefore, if the significance level of one factor is larger than 0.25, it can be included as the error.

In this study, the orthogonal table $L_{27}(3^{13})$ is used for the numerical simulation without interaction, while the orthogonal table $L_{16}(2^{15})$ is used for the numerical simulation with interaction.

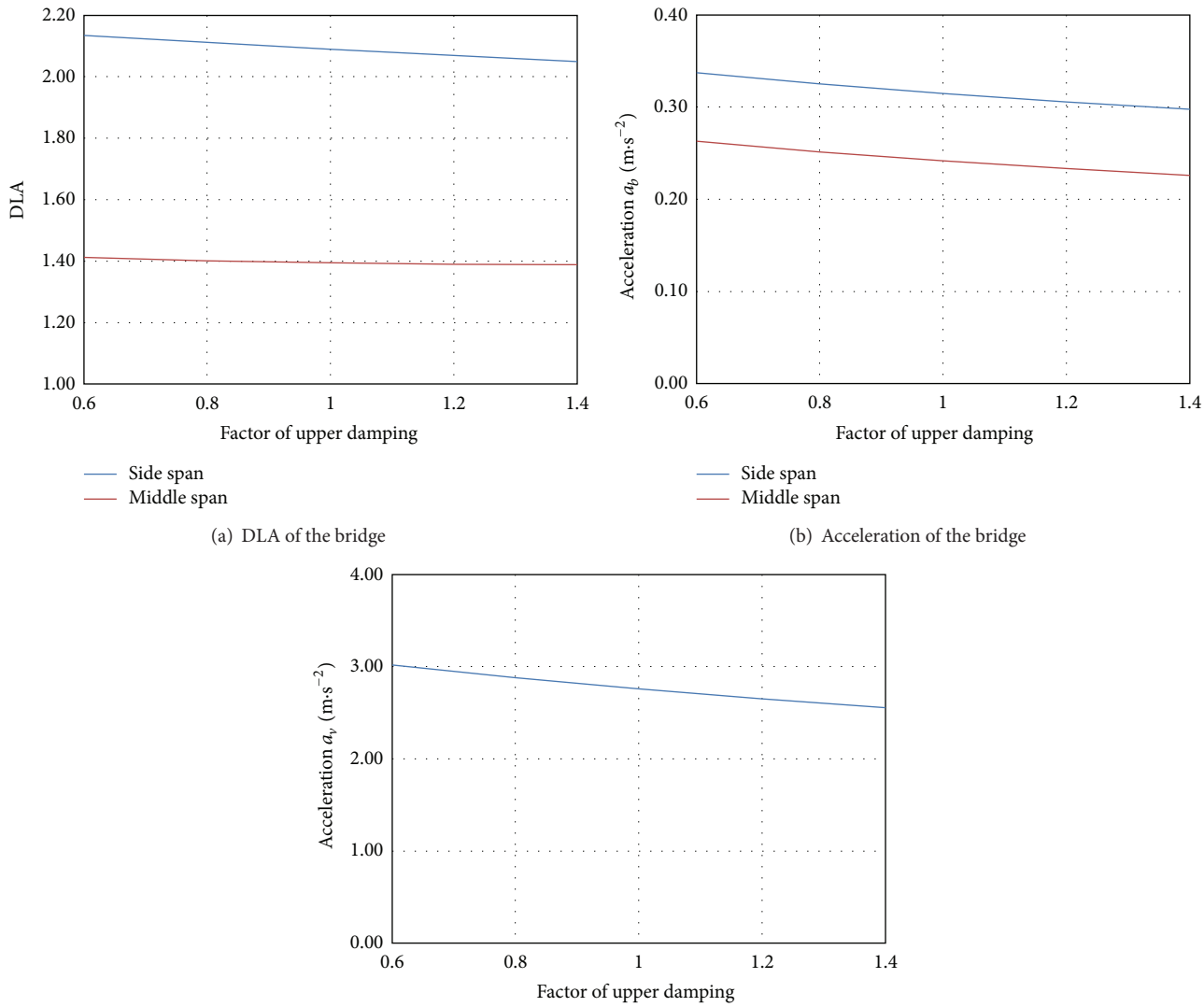

(a) DLA of the bridge

(b) Acceleration of the bridge

(c) Acceleration of the vehicle

Figure 13: Effect of upper damping on dynamic responses of the vehicle-bridge system.

4.2. Numerical Simulation without Interaction. There are thirteen factors possibly affecting dynamic responses of the vehicle-bridge coupled vibration system. A large number of studies [8] have proved that the roughness is the most significant factor. Therefore, the roughness is not arranged in the orthogonal table. The other twelve factors are arranged in the orthogonal table, once in a column. And the residual column is thought as the test error.

The results obtained from the VBCVA are listed in Table 9. The range analysis of the data can be seen in Table 10 and Figure 18. The variance analysis of the data is shown in Table 11.

It can be concluded that the influence of factors on different indices is listed as follows.

(i) For DLA in the side span of the bridge, consider

$$B > H > C > J > D > E > K > F > I > L > G > M. \quad (15)$$

(ii) For DLA in the middle span of the bridge, consider

$$D > C > E > H > I > G > B > K > L > M > J > F. \quad (16)$$

(iii) For vibration acceleration in the side span of the bridge, consider

$$D > B > E > J > M > I > C > F > K > G > L > H. \quad (17)$$

(iv) For vibration acceleration in the middle span of the bridge, consider

$$D > B > C > E > J > M > I > H > G > F > L > K. \quad (18)$$

(v) For vibration acceleration of the vehicle body, consider

$$H > I > K > B > C > J > D > L > F > E > G > M. \quad (19)$$

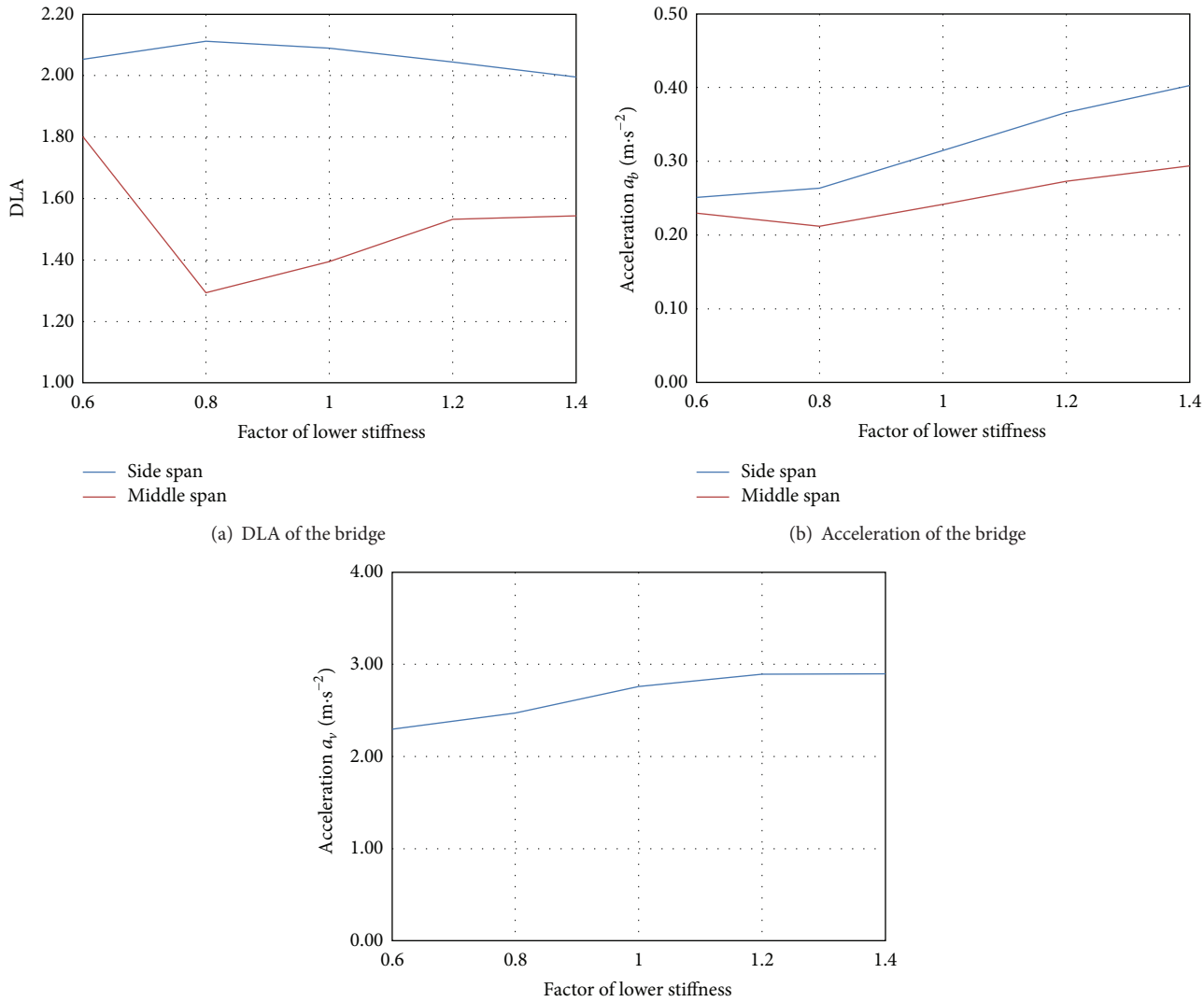

(a) DLA of the bridge

(b) Acceleration of the bridge

(c) Acceleration of the vehicle

Figure 14: Effect of lower stiffness on dynamic responses of the vehicle-bridge system.

It has to be noted that the roughness is assumed as the significant factor. Obviously, among other factors, the most important factors affecting the different dynamic responses are not the same.

4.3. Numerical Simulation with Interaction. As mentioned earlier, the interaction almost exists in all of physical phenomena. When the interaction is so small, it can be ignored in application. However, as for research, we do not know whether the interaction can be ignored or not at first.

Based on the results from the above section, eight most important factors influencing the DLA are selected, and some interactions between them are investigated. They are the pavement roughness (A), the length of the main span (B), the ratio between the side span and the middle span (C), the number of spans (D), the weight of the bridge (E), the weight of the vehicle (H), the upper stiffness of the vehicle (I), and the upper damping of the vehicle (J). Meanwhile, due to the calculation cost and the existing orthogonal array, the number of levels is determined as two for each factor. To avoid the mixture, the most important factor is arranged at first. It can be seen in Table 12.

The results obtained from the VBCVA are listed in Table 13. The range analysis of the data can be seen in Table 14. The variance analysis of the data is shown in Table 15.

It can be concluded that the influence of factors on different indices is listed as follows.

(i) For DLA in the side span of the bridge, consider

$$\begin{aligned} &A > I > B \times C > D > J > H > D \times C > E > A \times D \\ &\quad > B > A \times C > A \times B > D \times B > C. \end{aligned} \tag{20}$$

(ii) For DLA in the middle span of the bridge, consider

$$\begin{aligned} &B > A > D > D \times B > A \times B > H > E > A \times D \\ &\quad > J > B \times C > I > D \times C > C > A \times C. \end{aligned} \tag{21}$$

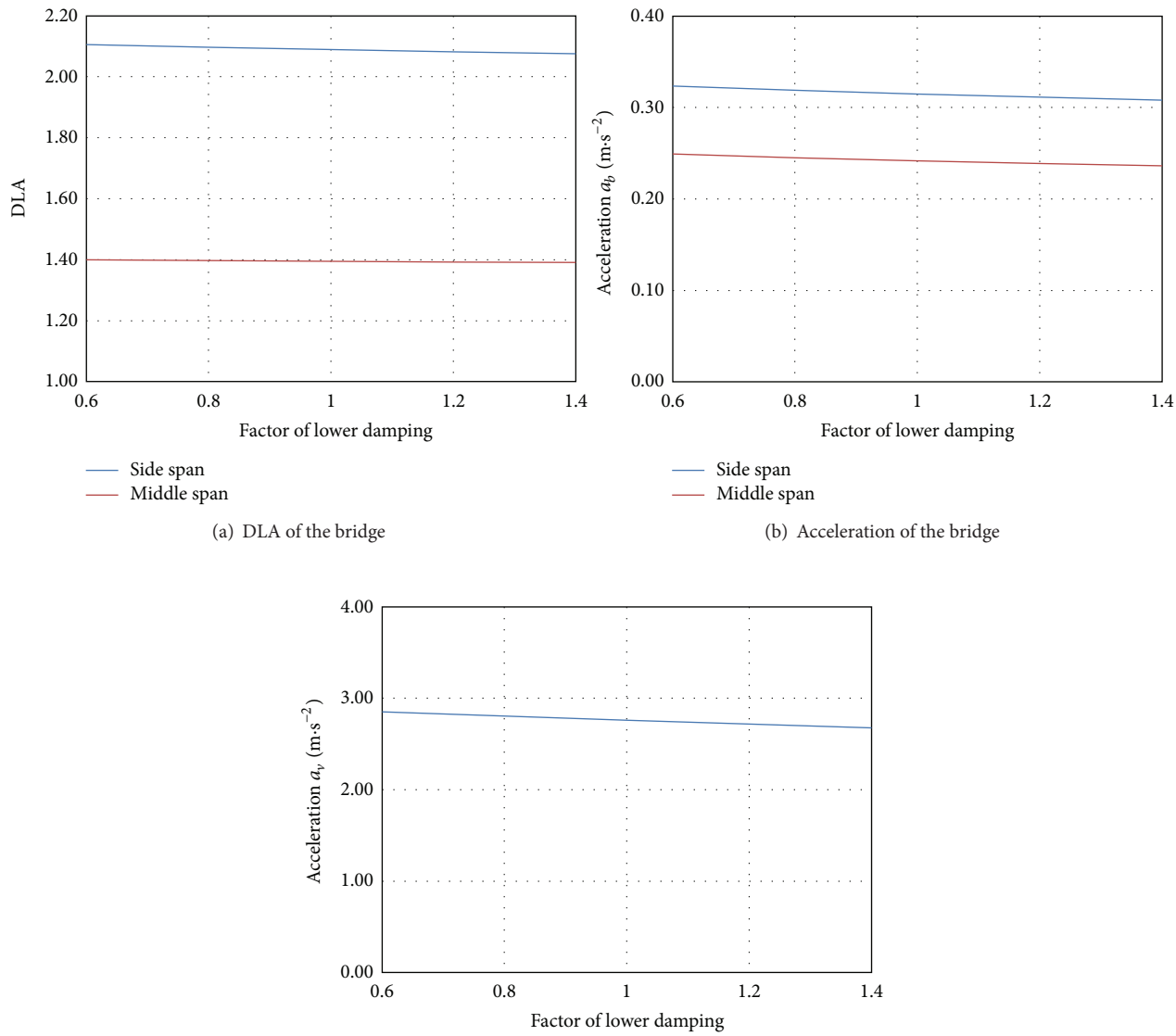

(a) DLA of the bridge

(b) Acceleration of the bridge

(c) Acceleration of the vehicle

Figure 15: Effect of lower damping on dynamic responses of the vehicle-bridge system.

(iii) For vibration acceleration in the side span of the bridge, consider

$$\begin{aligned} &B \times C > A > D > C > I > J > B > E > A \times D \\ &\quad > A \times B > D \times C > A \times C > D \times B > H. \end{aligned} \tag{22}$$

(iv) For vibration acceleration in the middle span of the bridge, consider

$$\begin{aligned} &A > B > A \times B > B \times C > I > H > D > D \times B \\ &\quad > A \times D > J > E > A \times C > D \times C > C. \end{aligned} \tag{23}$$

(v) For vibration acceleration of the vehicle body, consider

$$\begin{aligned} &A > I > H > B > D \times C > D \times B > J > A \times B \\ &\quad > B \times C > A \times D > D > A \times C > E > C. \end{aligned} \tag{24}$$

Similarly, for different indices, the most important factors are not the same. Also, it should be noted that some interactions are not ignored.

4.4. Comparison with the Current Code. In the current code of China (General Code for Design of Highway Bridges and Culverts) [48], the dynamic load allowance (μ) is defined as the function of the natural frequency. It is given by

$$\mu = \begin{cases} 0.05 & f < 1.5\,\text{Hz} \\ 0.1767 \ln f - 0.0157 & 1.5\,\text{Hz} \le f \le 14\,\text{Hz} \\ 0.45 & f > 14\,\text{Hz}, \end{cases} \tag{25}$$

where f is the fundamental natural frequency of the bridge. Its unit is Hz.

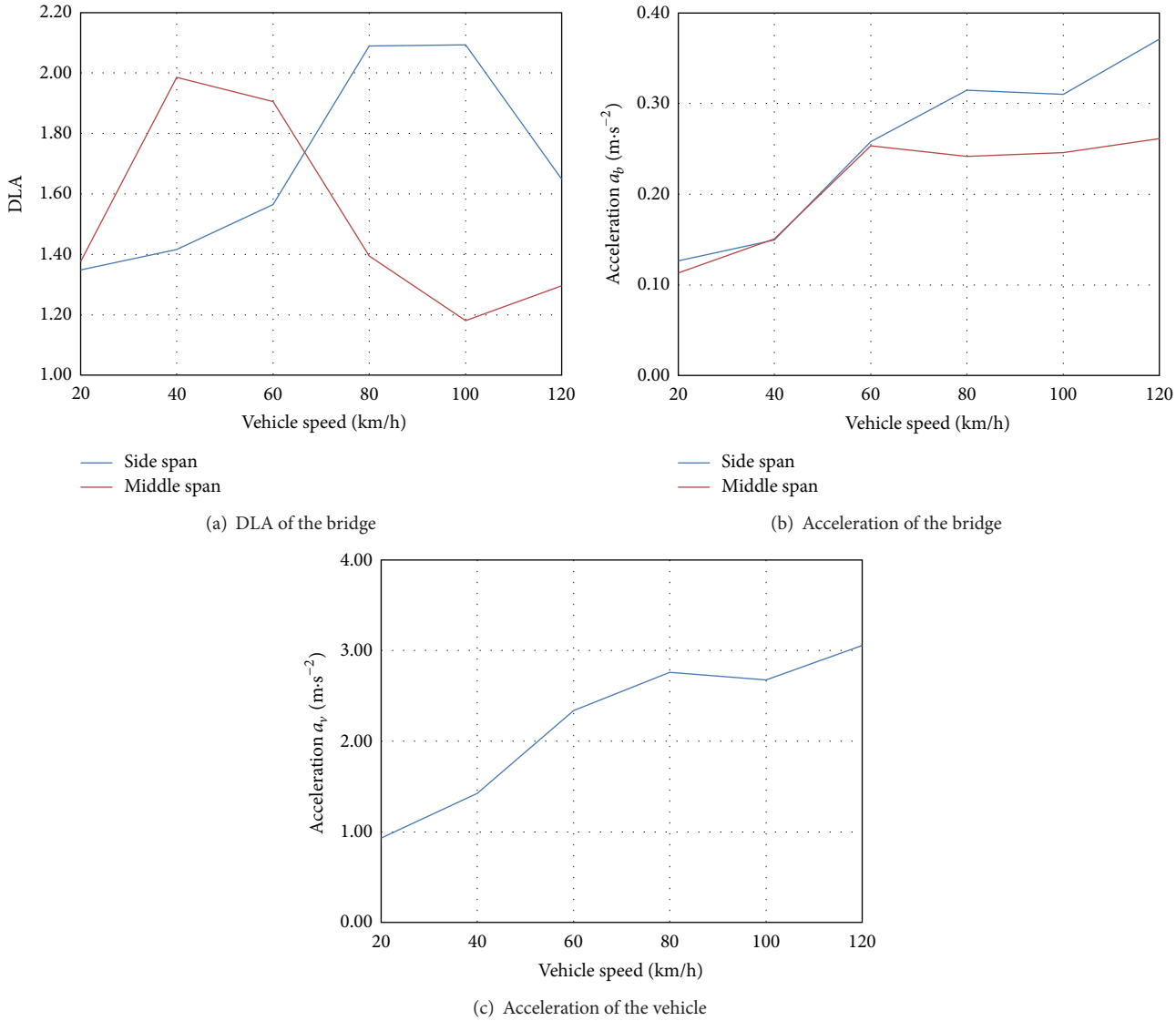

(a) DLA of the bridge

(b) Acceleration of the bridge

(c) Acceleration of the vehicle

Figure 16: Effect of vehicle speeds on dynamic responses of the vehicle-bridge system.

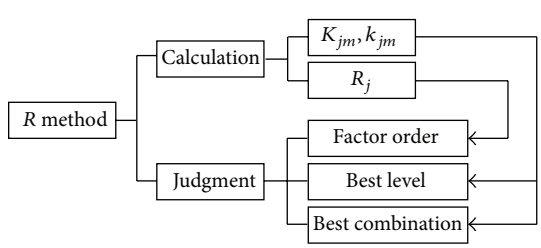

Figure 17: The diagram of the R method.

The DLA calculated by the program VBCVA is compared with the DLA obtained based on the current code in China. The results are shown in Figure 19.

It can be seen from Figure 19 that the differences between them are large, especially for the cases of the frequency from 2 Hz to 4 Hz. It may be related to the natural frequency of the vehicle. In other words, the dynamic load allowance defined in the current code may be not rational enough. To better consider the dynamic effects induced by moving vehicles in the design phase, some revisions may be needed in the future.

Table 9: Results of numerical simulation without interaction.

Run	f_1 (Hz)	DLA_s	DLA_m	a_{bs} (m/s^2)	a_{bm} (m/s^2)	a_v (m/s^2)
1	14.82	1.431	2.436	0.2499	0.7623	3.4869
2	16.57	1.156	2.574	0.3564	1.1550	2.9201
3	18.16	1.275	2.317	0.2758	0.8258	3.0941
4	8.85	1.302	1.107	0.3288	0.2249	4.1458
5	9.90	1.523	1.775	0.1865	0.1588	4.8916
6	10.84	1.287	1.283	0.2236	0.1858	2.6550
7	5.31	1.772	1.600	0.0899	0.1211	3.9578
8	5.94	1.175	1.045	0.1257	0.1683	3.0282
9	6.50	1.429	1.515	0.1237	0.1288	2.3746
10	4.21	1.218	1.751	0.2646	0.1737	2.7197
11	4.70	1.489	2.152	0.1145	0.1109	3.7590
12	5.15	1.719	1.661	0.1441	0.0963	4.5308
13	4.60	1.326	1.380	0.0784	0.1045	2.1844
14	5.14	1.685	1.699	0.1005	0.1617	4.4917
15	5.63	1.323	1.329	0.1537	0.1436	2.7863
16	4.01	1.434	1.520	0.2780	0.1964	2.5608
17	4.49	1.491	1.815	0.1407	0.1176	3.6745
18	4.91	1.412	1.264	0.1521	0.1462	2.6360
19	2.42	1.293	1.190	0.0866	0.2490	2.5880
20	2.71	1.413	1.649	0.1057	0.2816	2.7028
21	2.96	1.522	2.226	0.0794	0.3196	3.0362
22	2.61	1.979	1.949	0.3605	0.4664	3.6195
23	2.92	1.319	2.116	0.3079	0.4740	2.9401
24	3.20	1.886	2.257	0.1505	0.2254	2.8719
25	2.53	1.818	1.965	0.4168	0.2730	2.1650
26	2.82	1.904	1.214	0.2497	0.2277	2.0962
27	3.09	2.981	2.232	0.5926	0.3882	3.7986

Table 10: Range analysis of numerical simulation without interaction.

Index	B	C	D	E	F	G	H	I	J	K	L	M
DLA_s	0.418	0.322	0.256	0.247	0.187	0.070	0.328	0.164	0.281	0.244	0.079	0.049
DLA_m	0.248	0.421	0.513	0.369	0.132	0.265	0.309	0.284	0.139	0.187	0.179	0.161
a_{bs} (m/s^2)	0.103	0.055	0.175	0.099	0.052	0.037	0.015	0.063	0.088	0.047	0.031	0.074
a_{bm} (m/s^2)	0.276	0.245	0.299	0.240	0.044	0.046	0.047	0.084	0.093	0.015	0.016	0.090
a_v (m/s^2)	0.526	0.477	0.401	0.309	0.342	0.141	1.099	0.640	0.457	0.595	0.394	0.083

5. Conclusions

In this study, the natural frequencies of the simply supported girder bridge and the continuous girder bridge with uniform cross-section are firstly investigated based on the theoretical derivation and the numerical simulation. And then the effects of different parameters on the dynamic responses of the vehicle-bridge coupled vibration system are discussed by our own program VBCVA. Finally, the orthogonal experimental design method is proposed for the dynamic responses analysis, including the case without interaction and the case considering interaction. The conclusions obtained in this study are summarized as follows.

(1) The empirical formulas on natural frequency of the single-span bridge with different boundary conditions are obtained based on the theoretical derivation. It can be used for the simply supported girder bridge, especially for some old bridges, where bearing and

Table 11: Various analysis of numerical simulation without interaction.

(a) Dynamic load allowance in the side span (DLA_s)

Factor	S_j	dof	Initial			Modification		
			σ_j	F	α	σ_j	F	α
B	0.8830	2	0.4415	11.01	0.10	0.4415	9.95	0.01
C	0.4764	2	0.2382	5.94	0.25	0.2382	5.37	0.05
D	0.3311	2	0.1656	4.13	0.25	0.1656	3.73	0.10
E	0.2776	2	0.1388	3.46	0.25	0.1388	3.13	0.10
F	0.1697	2	0.0848	2.12	>0.25	—	—	
G	0.0237	2	0.0119	0.30	>0.25	—	—	
H	0.5193	2	0.2596	6.48	0.25	0.2596	5.85	0.05
I	0.1290	2	0.0645	1.61	>0.25	—	—	
J	0.3551	2	0.1775	4.43	0.25	0.1775	4.00	0.05
K	0.2684	2	0.1342	3.35	0.25	0.1342	3.02	0.10
L	0.0327	2	0.0163	0.41	>0.25	—	—	
M	0.0121	2	0.0060	0.15	>0.25	—	—	
Error	0.0802	2	0.0401			0.0444		
Sum	**3.5581**	**26**						

(b) Dynamic load allowance in the middle span (DLA_m)

Factor	S_j	dof	Initial			Modification		
			σ_j	F	α	σ_j	F	α
B	0.2762	2	0.1381	4.07	0.25	0.1381	2.36	0.25
C	0.8983	2	0.4492	13.23	0.10	0.4492	7.67	0.01
D	1.2312	2	0.6156	18.13	0.10	0.6156	10.52	0.01
E	0.6344	2	0.3172	9.34	0.10	0.3172	5.42	0.05
F	0.1002	2	0.0501	1.48	>0.25	—	—	
G	0.3232	2	0.1616	4.76	0.25	0.1616	2.76	0.25
H	0.5709	2	0.2855	8.41	0.25	0.2855	4.88	0.05
I	0.3674	2	0.1837	5.41	0.25	0.1837	3.14	0.10
J	0.0934	2	0.0467	1.38	>0.25	—	—	
K	0.1627	2	0.0814	2.40	>0.25	—	—	
L	0.1598	2	0.0799	2.35	>0.25	—	—	
M	0.1183	2	0.0592	1.74	>0.25	—	—	
Error	0.0679	2	0.0340			0.0585		
Sum	**5.0039**	**26**						

(c) Vibration acceleration in the side span (a_{bs})

Factor	S_j	dof	Initial			Modification		
			σ_j	F	α	σ_j	F	α
B	0.0477	2	0.0239	16.99	0.10	0.0239	12.57	0.01
C	0.0135	2	0.0068	4.82	0.25	0.0068	3.57	0.10
D	0.1598	2	0.0799	56.92	0.05	0.0799	42.10	0.01
E	0.0531	2	0.0266	18.92	0.10	0.0266	13.99	0.01
F	0.0121	2	0.0061	4.31	0.25	0.0061	3.19	0.10
G	0.0069	2	0.0034	2.44	>0.25	—	—	
H	0.0010	2	0.0005	0.37	>0.25	—	—	
I	0.0181	2	0.0091	6.45	0.25	0.0091	4.77	0.05
J	0.0465	2	0.0232	16.56	0.10	0.0232	12.25	0.01
K	0.0114	2	0.0057	4.05	0.25	0.0057	2.99	0.25

(c) Continued.

Factor	S_j	dof	Initial			Modification		
			σ_j	F	α	σ_j	F	α
L	0.0045	2	0.0022	1.60	>0.25	—	—	
M	0.0249	2	0.0125	8.88	0.25	0.0125	6.57	0.05
Error	0.0028	2	0.0014			0.0019		
Sum	**0.4024**	**26**						

(d) Vibration acceleration in the middle span (a_{bm})

Factor	S_j	dof	Initial			Modification		
			σ_j	F	α	σ_j	F	α
B	0.3544	2	0.1772	30.63	0.05	0.1772	47.46	0.01
C	0.3096	2	0.1548	26.76	0.05	0.1548	41.46	0.01
D	0.5061	2	0.2531	43.74	0.05	0.2531	67.78	0.01
E	0.3331	2	0.1666	28.79	0.05	0.1666	44.61	0.01
F	0.0093	2	0.0046	0.80	>0.25	—	—	
G	0.0115	2	0.0057	0.99	>0.25	—	—	
H	0.0102	2	0.0051	0.88	>0.25	—	—	
I	0.0315	2	0.0158	2.72	>0.25	0.0158	4.22	0.05
J	0.0403	2	0.0202	3.48	0.25	0.0202	5.40	0.05
K	0.0012	2	0.0006	0.10	>0.25	—	—	
L	0.0011	2	0.0006	0.10	>0.25	—	—	
M	0.0402	2	0.0201	3.48	0.25	0.0201	5.39	0.05
Error	0.0116	2	0.0058			0.0037		
Sum	**1.6601**	**26**						

(e) Vibration acceleration of the vehicle body (a_v)

Factor	S_j	dof	Initial			Modification		
			σ_j	F	α	σ_j	F	α
B	1.3451	2	0.6726	12.43	0.10	0.6726	17.11	0.01
C	1.0364	2	0.5182	9.58	0.10	0.5182	13.18	0.01
D	0.8230	2	0.4115	7.60	0.25	0.4115	10.47	0.05
E	0.4458	2	0.2229	4.12	0.25	0.2229	5.67	0.05
F	0.6294	2	0.3147	5.81	0.25	0.3147	8.01	0.05
G	0.0936	2	0.0468	0.86	>0.25	—	—	
H	5.4978	2	2.7489	50.79	0.05	2.7489	69.93	0.01
I	1.8752	2	0.9376	17.32	0.10	0.9376	23.85	0.01
J	0.9799	2	0.4899	9.05	0.10	0.4899	12.46	0.01
K	1.5926	2	0.7963	14.71	0.10	0.7963	20.26	0.01
L	0.8165	2	0.4082	7.54	0.25	0.4082	10.38	0.05
M	0.0340	2	0.0170	0.31	>0.25	—	—	
Error	0.1082	2	0.0541			0.0393		
Sum	**15.2776**	**26**						

boundary conditions are no longer the same as the design state.

(2) The empirical formulas on the first two natural frequencies of the continuous girder bridge with odd span are given by the numerical simulations. Similarly, the empirical formulas on the first and the third natural frequencies of the continuous girder bridge with even span are obtained. They can be used for calculating the dynamic load allowance in the mid-span cross-section and the pier-top cross-section based on the current code of bridge design in China, respectively. Also, according to these formulas, the factors influencing natural frequencies are more clearly seen, which may give a better guideline for

Table 12: Design of the table header.

Column	1	2	3	4	5	6	7	8	9	10	11	12	13	14	15
Factor	A	D	A × D	B	A × B	D × B	E	C	A × C	D × C	H	B × C	I	J	Non

Table 13: Results of numerical simulation with interaction.

Run	f_1 (Hz)	DLA_s	DLA_m	a_{bs} (m/s^2)	a_{bm} (m/s^2)	a_v (m/s^2)
1	7.40	1.212	1.123	0.2164	0.0981	1.6398
2	6.34	1.170	1.163	0.0726	0.0651	1.6830
3	3.73	1.259	1.583	0.0565	0.1310	1.4709
4	3.20	1.192	1.181	0.0802	0.1128	1.2788
5	5.15	1.184	1.149	0.1469	0.0606	1.2814
6	4.95	1.279	1.363	0.0505	0.0857	1.8366
7	3.25	1.195	1.629	0.0770	0.1351	1.6609
8	3.12	1.245	1.783	0.0932	0.1486	1.3401
9	6.61	1.504	1.410	0.3277	0.1753	3.2438
10	5.67	1.355	1.421	0.1105	0.1190	3.2590
11	4.17	1.343	1.426	0.1617	0.2024	2.4870
12	3.57	1.496	2.011	0.2926	0.3618	3.2189
13	5.76	1.638	1.404	0.2203	0.2013	3.4707
14	5.53	1.299	1.488	0.1322	0.1227	2.7466
15	2.90	1.357	3.016	0.1019	0.3588	2.9297
16	2.79	1.685	2.495	0.2080	0.3878	2.8570

Table 14: Range analysis of numerical simulation with interaction.

Index	A	D	A × D	B	A × B	D × B	E	C	A × C	D × C	H	B × C	I	J
DLA_s	0.242	0.044	0.026	0.016	0.005	0.004	0.027	0.004	0.005	0.030	0.034	0.112	0.130	0.043
DLA_m	0.462	0.376	0.157	0.576	0.231	0.305	0.199	0.021	0.019	0.038	0.220	0.067	0.059	0.099
a_{bs} (m/s^2)	0.095	0.036	0.021	0.026	0.019	0.008	0.023	0.034	0.016	0.018	0.008	0.103	0.033	0.026
a_{bm} (m/s^2)	0.136	0.029	0.024	0.114	0.059	0.026	0.012	0.005	0.008	0.008	0.030	0.041	0.040	0.017
a_v (m/s^2)	1.503	0.020	0.031	0.240	0.067	0.103	0.011	0.004	0.017	0.145	0.241	0.032	0.310	0.088

the design and evaluation of dynamic performance of bridges.

(3) The dynamic responses in the side span, including the DLA and the vibration acceleration, are always largely different from those in the middle span. In addition, the effects of different factors on different dynamic responses of the vehicle-bridge system are various. In other words, the effects of factors on dynamic responses are dependent on both the selected position and the type of the responses (DLA or vibration acceleration).

(4) Based on the traditional method, when one factor is studied, the others should be fixed. Some significant factors affecting the dynamic responses of the vehicle-bridge system are roughly identified and selected. They are the pavement roughness, the length of the main span, the ratio between the side span and the middle span, the number of spans, the weight of the bridge and the vehicle, and the upper stiffness and damping of the vehicle.

(5) The orthogonal experimental design is introduced in this study for the dynamic responses analysis of the vehicle-bridge coupled vibration system. To efficiently reduce the experimental runs, the conventional orthogonal design is divided into two phases. In the first phase, the main effects (single factor) are analyzed without any interaction effects. Based on the results from the first phase, the interaction effects of some of the most important factors are discussed in the second phase. It has been proved that the interaction effects cannot be ignored.

In the end, it has to be emphasized that the proposed method of the orthogonal experimental design greatly reduces calculation cost. And it is efficient and rational enough to study multifactor problems. The proposed method is used for not only the analysis of influence factors but also the analysis of regression. And it can be applied in all types of bridges, other than just the girder bridge. Furthermore, it provides a good way to obtain more rational empirical formulas of the DLA and other dynamic responses, which may be adopted in the codes of design and evaluation.

Table 15: Various analysis of numerical simulation with interaction.

(a) Dynamic load allowance in the side span (DLA_s)

Factor	S_j	dof	Initial			Modification		
			σ_j	F	α	σ_j	F	α
A	0.2348	1	0.2348	25.47	0.25	0.2348	24.58	0.01
D	0.0077	1	0.0077	0.83	>0.25	0.0077	0.80	>0.25
A × D	0.0028	1	0.0028	0.30	>0.25	0.0028	0.29	>0.25
B	0.0011	1	0.0011	0.12	>0.25	0.0011	0.11	>0.25
A × B	0.0001	1	0.0001	0.01	>0.25	—	—	
D × B	0.0001	1	0.0001	0.01	>0.25	—	—	
E	0.0029	1	0.0029	0.32	>0.25	0.0029	0.31	>0.25
C	0.0001	1	0.0001	0.01	>0.25	—	—	
A × C	0.0001	1	0.0001	0.01	>0.25	—	—	
D × C	0.0036	1	0.0036	0.39	>0.25	0.0036	0.37	>0.25
H	0.0045	1	0.0045	0.49	>0.25	0.0045	0.47	>0.25
B × C	0.0506	1	0.0506	5.49	>0.25	0.0506	5.30	0.10
I	0.0675	1	0.0675	7.33	0.25	0.0675	7.07	0.05
J	0.0074	1	0.0074	0.80	>0.25	0.0074	0.78	>0.25
Error	0.0092	1	0.0092			0.0095		
Sum	**0.3924**	**15**						

(b) Dynamic load allowance in the middle span (DLA_m)

Factor	S_j	dof	Initial			Modification		
			σ_j	F	α	σ_j	F	α
A	0.8551	1	0.8551	5.63	>0.25	0.8551	4.44	0.10
D	0.5659	1	0.5659	3.72	>0.25	0.5659	2.94	0.15
A × D	0.0991	1	0.0991	0.65	>0.25	0.0991	0.51	>0.25
B	1.3252	1	1.3252	8.72	0.25	1.3252	6.88	0.05
A × B	0.2134	1	0.2134	1.40	>0.25	0.2134	1.11	>0.25
D × B	0.3714	1	0.3714	2.44	>0.25	0.3714	1.93	0.15
E	0.1582	1	0.1582	1.04	>0.25	0.1582	0.82	>0.25
C	0.0017	1	0.0017	0.01	>0.25	—	—	
A × C	0.0015	1	0.0015	0.01	>0.25	—	—	
D × C	0.0057	1	0.0057	0.04	>0.25	—	—	
H	0.1941	1	0.1941	1.28	>0.25	0.1941	1.01	>0.25
B × C	0.0179	1	0.0179	0.12	>0.25	—	—	
I	0.0138	1	0.0138	0.09	>0.25	—	—	
J	0.0395	1	0.0395	0.26	>0.25	0.0395	0.21	>0.25
Error	0.1520	1	0.1520			0.1926		
Sum	**4.0147**	**15**						

(c) Vibration acceleration in the side span (a_{bs})

Factor	S_j	dof	Initial			Modification		
			σ_j	F	α	σ_j	F	α
A	0.0363	1	0.0363	59.14	>0.25	0.0363	0.67	0.10
D	0.0052	1	0.0052	8.46	>0.25	0.0052	0.10	0.15
A × D	0.0018	1	0.0018	3.01	>0.25	0.0018	0.03	>0.25
B	0.0027	1	0.0027	4.32	0.25	0.0027	0.05	0.05
A × B	0.0015	1	0.0015	2.39	>0.25	0.0015	0.03	>0.25
D × B	0.0003	1	0.0003	0.45	>0.25	0.0003	0.01	0.15
E	0.0021	1	0.0021	3.44	>0.25	0.0021	0.04	>0.25
C	0.0045	1	0.0045	7.36	>0.25	—	—	

(c) Continued.

Factor	S_j	dof	Initial			Modification		
			σ_j	F	α	σ_j	F	α
A × C	0.0011	1	0.0011	1.77	>0.25	—	—	
D × C	0.0013	1	0.0013	2.12	>0.25	—	—	
H	0.0003	1	0.0003	0.42	>0.25	0.0003	0.00	>0.25
B × C	0.0423	1	0.0423	68.95	>0.25	—	—	
I	0.0043	1	0.0043	7.01	>0.25	—	—	
J	0.0027	1	0.0027	4.43	>0.25	0.0027	0.05	>0.25
Error	0.0006	1	0.0006			0.0541		
Sum	**0.1069**	**15**						

(d) Vibration acceleration in the middle span (a_{bm})

Factor	S_j	dof	Initial			Modification		
			σ_j	F	α	σ_j	F	α
A	0.0745	1	0.0745	178.69	0.05	0.0745	27.12	0.01
D	0.0035	1	0.0035	8.29	0.25	0.0035	1.26	>0.25
A × D	0.0022	1	0.0022	5.35	>0.25	0.0022	0.81	>0.25
B	0.0518	1	0.0518	124.28	0.10	0.0518	18.86	0.01
A × B	0.0141	1	0.0141	33.75	0.25	0.0141	5.12	0.10
D × B	0.0027	1	0.0027	6.58	0.25	0.0027	1.00	>0.25
E	0.0006	1	0.0006	1.38	>0.25	—	—	
C	0.0001	1	0.0001	0.25	>0.25	—	—	
A × C	0.0003	1	0.0003	0.66	>0.25	—	—	
D × C	0.0002	1	0.0002	0.59	>0.25	—	—	
H	0.0037	1	0.0037	8.81	0.25	0.0037	1.34	>0.25
B × C	0.0067	1	0.0067	16.00	0.25	0.0067	2.43	0.25
I	0.0064	1	0.0064	15.36	0.25	0.0064	2.33	0.25
J	0.0011	1	0.0011	2.71	>0.25	—	—	
Error	0.0004	1	0.0004			0.0027		
Sum	**0.1683**	**15**						

(e) Vibration acceleration of the vehicle body (a_v)

Factor	S_j	dof	Initial			Modification		
			σ_j	F	α	σ_j	F	α
A	9.0320	1	9.0320	436.16	0.05	9.0320	323.17	0.01
D	0.0016	1	0.0016	0.08	>0.25	—	—	
A × D	0.0039	1	0.0039	0.19	>0.25	—	—	
B	0.2298	1	0.2298	11.10	0.25	0.2298	8.22	0.05
A × B	0.0180	1	0.0180	0.87	>0.25	0.0180	0.65	>0.25
D × B	0.0423	1	0.0423	2.04	>0.25	0.0423	1.51	>0.25
E	0.0005	1	0.0005	0.02	>0.25	—	—	
C	0.0001	1	0.0001	0.00	>0.25	—	—	
A × C	0.0011	1	0.0011	0.06	>0.25	—	—	
D × C	0.0842	1	0.0842	4.06	>0.25	0.0842	3.01	0.25
H	0.2321	1	0.2321	11.21	0.25	0.2321	8.31	0.05
B × C	0.0041	1	0.0041	0.20	>0.25	0.0041	0.15	>0.25
I	0.3842	1	0.3842	18.55	0.25	0.3842	13.75	0.01
J	0.0312	1	0.0312	1.50	>0.25	0.0312	1.11	>0.25
Error	0.0207	1	0.0207			0.0279		
Sum	**10.0859**	**15**						

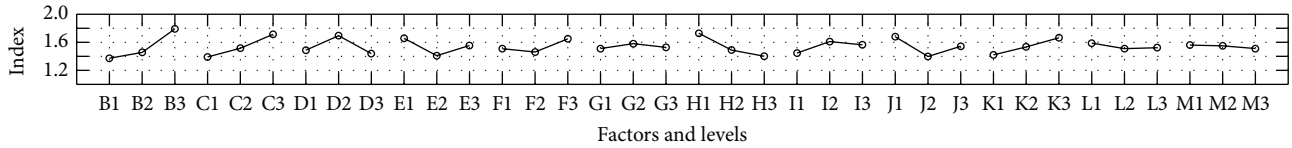

(a) Trend plot between factors and the DLA in side span

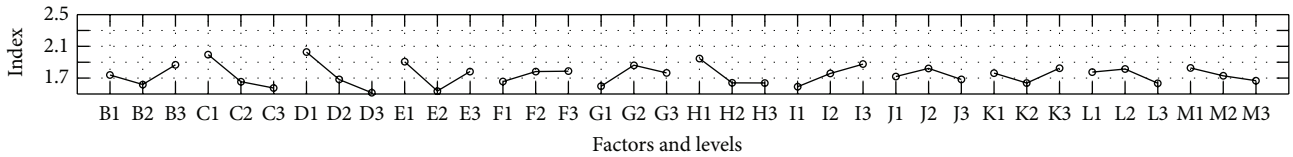

(b) Trend plot between factors and the DLA in middle span

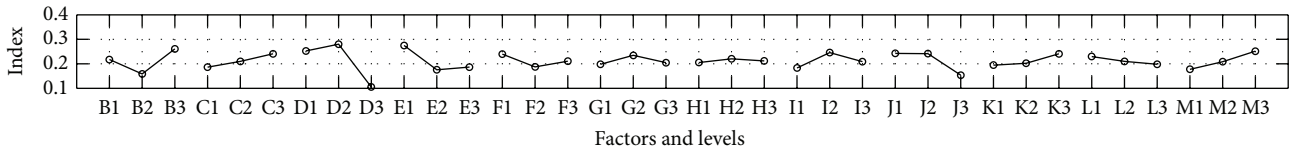

(c) Trend plot between factors and the acceleration in side span

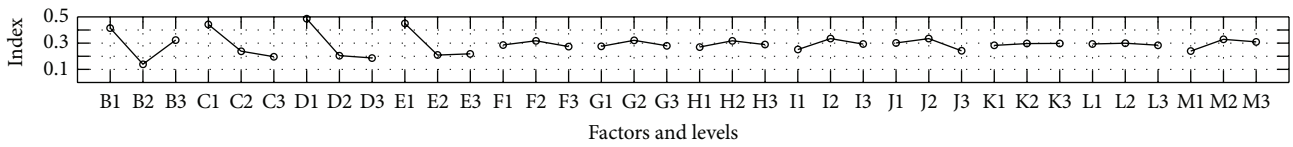

(d) Trend plot between factors and the acceleration in middle span

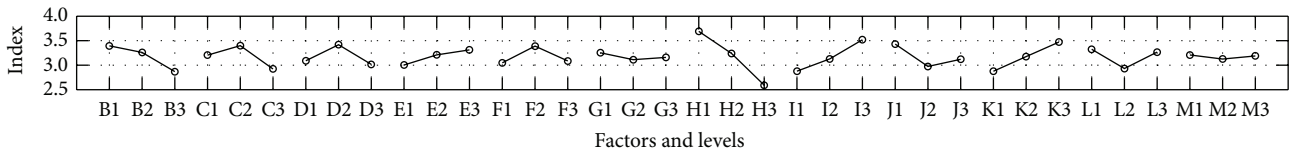

(e) Trend plot between factors and the acceleration of the vehicle body

Figure 18: Trend plot between the factors and the tested index.

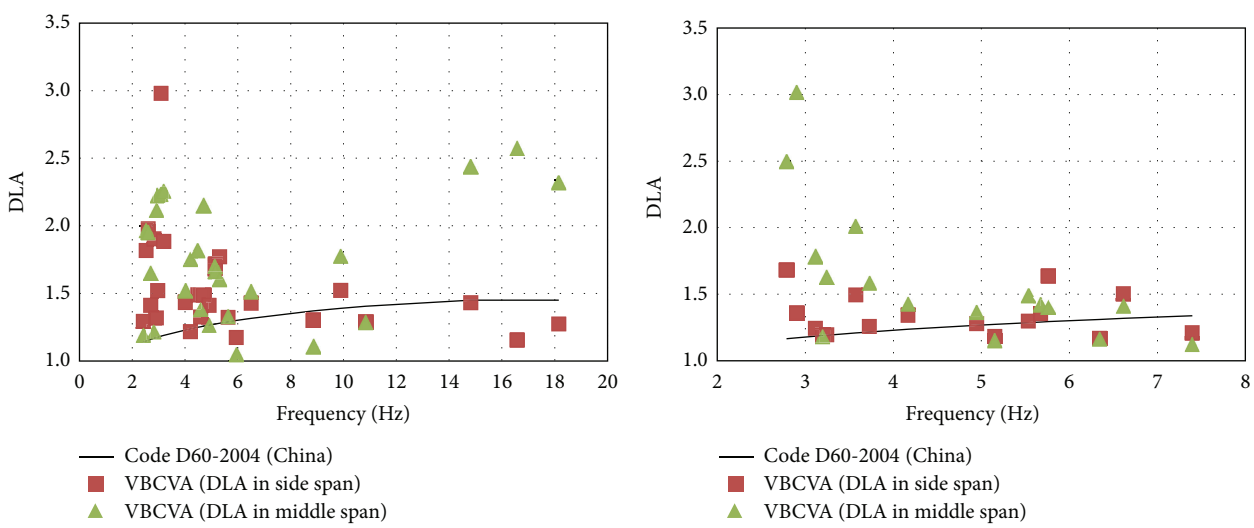

(a) The sample without interaction

(b) The sample with interaction

Figure 19: Comparison with the current code.

Conflict of Interests

The authors declare that there is no conflict of interests regarding the publication of this paper.

Acknowledgments

The research reported herein was sponsored by the China Scholarship Council (the 2013 China State-Sponsored Postgraduate Study Abroad Program), the National Natural Science Foundation of China (nos. 51308465, 50678051, and 51108132, U1234208), and the Fundamental Research Funds for the Central Universities (no. 2682014CX004EM). The authors would like to express their deep gratitude to all the sponsors for the financial aid.

References

[1] D. I. McLean and M. L. Marsh, *Dynamic Impact Factors for Bridges*, Transportation Research Board, Washington, DC, USA, 1998.

[2] ASCE Committee on Loads and Forces on Bridges of the Committee on Bridges of the Structural Division, "Bridge loading: research needed," *ASCE Journal of the Structural Division*, vol. 108, no. 5, pp. 1012–1020, 1982.

[3] ASCE Committee on Loads and Forces on Bridges of the Committee on Bridges of the Structural Division, "Recommendation design loads for bridges," *Journal of the Structural Division*, vol. 107, no. 7, pp. 1161–1213, 1981.

[4] P. F. Csagoly and R. A. Dorton, "The development of the Ontario Highway Bridge Design Code," *Transportation Research Record*, no. 655, pp. 1–12, 1978.

[5] J. R. Billing and R. Green, "Design provisions for dynamic loading of highway bridges," *Transportation Research Record*, vol. 950, pp. 94–103, 1984.

[6] D. B. Ashebo, *Evaluation of dynamic loads for highway bridges [Ph.D. thesis]*, The Hong Kong Polytechnic University, Hong Kong, 2006.

[7] B. Bakht and S. G. Pinjarkar, *Dynamic Testing of Highway Bridges—A Review*, Ministry of Transportation, Ontario, Canada, 1989.

[8] OHBDC, *Ontario Highway Bridge Design Code*, Ontario Ministry of Transportation and Communications, Ontario, Canada, 1983.

[9] M. Samaan, J. B. Kennedy, and K. Sennah, "Impact factors for curved continuous composite multiple-box girder bridges," *Journal of Bridge Engineering*, vol. 12, no. 1, pp. 80–88, 2007.

[10] K. M. Sennah, X. Zhang, and J. B. Kennedy, "Impact factors for horizontally curved composite box girder bridges," *Journal of Bridge Engineering*, vol. 9, no. 6, pp. 512–520, 2004.

[11] J. Senthilvasan, D. P. Thambiratnam, and G. H. Brameld, "Dynamic response of a curved bridge under moving truck load," *Engineering Structures*, vol. 24, no. 10, pp. 1283–1293, 2002.

[12] S. Komatsu and H. Nakai, "Fundamental study on forced vibration of curved girder bridges," *Transactions of the Japan Society of Civil Engineers*, vol. 2, pp. 37–42, 1970.

[13] K. M. Sennah, *Load distribution factor and dynamic characteristics of curved composite concrete deck-steel cellular bridges [Ph.D. thesis]*, University of Windsor, Ontario, Canada.

[14] R. Cantieni, *Dynamic Load Testing of Highway Bridges*, Transportation Research Board, Washington, DC, USA, 1984.

[15] J. R. Billing, *Estimation of the Natural Frequencies of Continuous Multi-Span Bridges*, Ontario Ministry of Transportation and Communications, Ontario, Canada, 1979.

[16] Q. F. Gao, Z. L. Wang, Y. Liu, and B. Q. Guo, "Modified formula of estimating fundamental frequency of girder bridge with uniform cross-section," *Advanced Engineering Forum*, vol. 5, pp. 177–182, 2012.

[17] Q. Gao, Z. Wang, and B. Guo, "Modified formula of estimating fundamental frequency of girder bridge with variable cross-section," *Key Engineering Materials*, vol. 540, pp. 99–106, 2013.

[18] I. Mohseni, A. K. A. Rashid, and J. Kang, "A simplified method to estimate the fundamental frequency of skew continuous multicell box-girder bridges," *Latin American Journal of Solids and Structures*, vol. 11, no. 4, pp. 649–658, 2014.

[19] P. Paultre, O. Chaallal, and J. Proulx, "Bridge dynamics and dynamic amplification factors—a review of analytical and experimental findings," *Canadian Journal of Civil Engineering*, vol. 19, no. 2, pp. 260–278, 1992.

[20] AASHO, *The AASHO Road Test*, Highway Research Board, Washington, DC, USA, 1962.

[21] D. T. Wright and R. Green, *Highway Bridge Vibrations, Part II, Ontario Test Program*, Queen's University, Ontario, Canada, 1963.

[22] P. F. Csagoly, T. I. Campbell, and A. C. Agarwall, *Bridge Vibration Study*, Ministry of Transportation and Communications, Ontario, Canada, 1972.

[23] J. Page, *Dynamic Wheel Measurements on Motorway Bridges*, Transport and Road Research Laboratory, London, UK, 1976.

[24] D. R. Leonard, *Dynamic Tests on Highway Bridges*, Transport and Road Research Laboratory, London, UK, 1974.

[25] R. Shepard and G. K. Sidwell, "Investigations of the dynamic properties of five concrete bridges," in *Proceedings of the 4th Australian Conference on the Mechanics of Structures and Materials*, pp. 261–268, University of Queensland, Brisbane, Australia, 1973.

[26] R. Shepard and R. J. Aves, "Impact factors for simple concrete bridges," in *Proceedings of the Institution of Civil Engineers*, vol. 55, pp. 191–210, 1973.

[27] J. H. Wood and R. Shepard, "Vehicle induced vibrations," Road Research Unit Bulletin 44, 1979.

[28] J. R. Billing, "Dynamic loading and testing of bridges in Ontario," *Canadian Journal of Civil Engineering*, vol. 11, no. 4, pp. 833–843, 1984.

[29] R. Cantieni, *Dynamic Load Tests on Highway Bridges in Switzerland—60 Years of Experience*, Federal Laboratories for Testing of Materials, EMPA, Dübendorf, Switzerland, 1983.

[30] A. S. Veletsos, "Analysis of dynamic response of highway bridges," *ASCE Journal of the Engineering Division*, vol. 93, no. 5, pp. 593–620, 1970.

[31] J. T. Guant, T. Aramraks, M. J. Gutzwiller, and R. H. Lee, *Highway Bridge Vibration Studies*, Transportation Research Board, Washington, DC, USA, 1977.

[32] M. J. Inbanathan and M. Wieland, "Bridge vibrations due to vehicle moving over rough surface," *Journal of Structural Engineering*, vol. 113, no. 9, pp. 1994–2008, 1987.

[33] O. Coussy, M. Said, and J.-P. van Hoove, "The influence of random surface irregularities on the dynamic response of bridges under suspended moving loads," *Journal of Sound and Vibration*, vol. 130, no. 2, pp. 313–320, 1989.

[34] W. Cui, X. Li, S. Zhou, and J. Weng, "Investigation on process parameters of electrospinning system through orthogonal

experimental design," *Journal of Applied Polymer Science*, vol. 103, no. 5, pp. 3105–3112, 2007.

[35] F. Kaitai and M. Changxing, *Orthogonal and Uniform Experimental Design*, Tsinghua University Press, Beijing, China, 2001.

[36] W. F. Kuhfeld, R. D. Tobias, and M. Garratt, "Efficient experimental design with marketing research applications," *Journal of Marketing Research*, vol. 12, pp. 545–557, 1994.

[37] S. Chen, X. Hong, and C. J. Harris, "Sparse kernel regression modeling using combined locally regularized orthogonal least squares and D-optimality experimental design," *IEEE Transactions on Automatic Control*, vol. 48, no. 6, pp. 1029–1036, 2003.

[38] A. H. Jesus, Z. Dimitrovová, and M. A. G. Silva, "A statistical analysis of the dynamic response of a railway viaduct," *Engineering Structures*, vol. 71, pp. 244–259, 2014.

[39] E. S. Hwang and A. S. Nowak, "Simulation of dynamic load for bridges," *Journal of Structural Engineering*, vol. 117, no. 5, pp. 1413–1434, 1991.

[40] W. Huang, X. Zhang, and G. Hu, "New advance of theory and design on pavement for long-span steel bridge," *Journal of Southeast University (Natural Science Edition)*, vol. 32, no. 3, pp. 480–487, 2002 (Chinese).

[41] P. K. Chatterjee, T. K. Datta, and C. S. Surana, "Vibration of continuous bridges under moving vehicles," *Journal of Sound and Vibration*, vol. 169, no. 5, pp. 619–632, 1994.

[42] R. Mee, *A Comprehensive Guide to Factorial Two-Level Experimentation*, Springer, Berlin, Germany, 2009.

[43] L. Q. Ren, *Optimum Design and Analysis of Experiments*, Higher Education Press, Beijing, China, 2nd edition, 2003, (Chinese).

[44] J. Cheng, H. Zhu, S. Zhong, F. Zheng, and Y. Zeng, "Finite-time filtering for switched linear systems with a mode-dependent average dwell time," *Nonlinear Analysis: Hybrid Systems*, vol. 15, pp. 145–156, 2015.

[45] T. P. Ryan, *Modern Engineering Statistics: Solutions Manual to Accompany*, John Wiley & Sons, Hoboken, NJ, USA, 2000.

[46] D. C. Montgomery, *Design and Analysis of Experiments*, John Wiley & Sons, Hoboken, NJ, USA, 2008.

[47] D. Zhang and L. Yu, "Exponential state estimation for Markovian jumping neural networks with time-varying discrete and distributed delays," *Neural Networks*, vol. 35, pp. 103–111, 2012.

[48] Ministry of Communication of the People's Republic of China, *JTG D60-2004 General Code for Design of Highway Bridges and Culverts*, China Communication Press, Beijing, China, 2004, (Chinese).

Hindawi Publishing Corporation
Mathematical Problems in Engineering
Volume 2015, Article ID 356146, 7 pages
http://dx.doi.org/10.1155/2015/356146

Research Article

A Novel Dynamic Method in Distributed Network Attack-Defense Game

Liu Xiaojian[1] and Yuan Yuyu[2]

[1] *College of Computer Science and Technology, Beijing University of Posts and Telecommunications, Beijing 100876, China*
[2] *College of Software Engineering, Beijing University of Posts and Telecommunications, Beijing 100876, China*

Correspondence should be addressed to Liu Xiaojian; chn1989lxj@163.com

Received 5 January 2015; Revised 4 March 2015; Accepted 4 March 2015

Academic Editor: Hui Zhang

Copyright © 2015 L. Xiaojian and Y. Yuyu. This is an open access article distributed under the Creative Commons Attribution License, which permits unrestricted use, distribution, and reproduction in any medium, provided the original work is properly cited.

We analyze the distributed network attack-defense game scenarios, and we find that attackers and defenders have different information acquisition abilities since the ownership of the target system. Correspondingly, they will have different initiative and reaction in the game. Based on that, we propose a novel dynamic game method for distributed network attack-defense game. The method takes advantage of defenders' information superiority and attackers' imitation behaviors and induces attackers' reaction evolutionary process in the game to gain more defense payoffs. Experiments show that our method can achieve relatively more average defense payoffs than previous work.

1. Introduction

Modern organizations embed information and communication technologies (ICT) into their core processes as means to facilitate the collection, storage, processing, and exchange of data to increase operational efficiency, improve decision quality, and reduce costs [1]. In this way, distributed system is becoming widely used. Despite the significant benefits of distributed system, the system also places the processing tasks at the risk due to "distributed vulnerability." Traditional approaches to improve security generally consider only system vulnerabilities and attempt to defend all the attacks through system upgrading. No matter if the assuming attacks come, the defending resources have to be inputted. In distributed system, these keeping upgrading approaches will result in a huge waste of defending resource. Regarding this, game theory has been applied in network security.

In traditional game theory, equilibrium is achieved through players' analysis and reasoning based on common view about game rules, players' reason, and payoff matrix. Generally, the game players are the interactional individuals. Even as group-player, the members should be consubstantial with the same rational characteristics, strategies, and payoffs. However, this strong rational assumption of traditional game theory is receiving more and more criticism from game theory experts and economists [2].

In reality, there exist a large number of game problems between individual-player and group-player. For example, in distributed network attack-defense game scenarios, system officers, as defenders of the system, are consubstantial and can be regarded as individual-player (we use singular form to indicate individual-player and use plural form to indicate group-player). The defender has more information about system, game structure, and payoff matrix. Even if they temporarily lack knowledge, the defender has more resources to fill in the blank. So the defender is easier to make rational decision. On the other hand, attackers are regarded as group-player, because of their different information acquisition abilities and rational characteristics. In the game process, attackers will perform in an incomplete rational way and tend to imitate high payoff strategy behaviors. The process of imitation can be regarded as evolutionary process. As the theory of learning stated, the equilibrium is the results of the long-term process that players with incomplete rationality seek for optimization [3]. In distributed network attack-defense game scenarios, game players, especially attackers as group-player, dynamically adjust their strategies based on game situation and press on towards dynamic equilibrium.

In this paper, we propose a dynamic method in distributed network attack-defense game scenarios. The method takes advantage of defenders' information superiority and attackers' imitation behaviors and induces attackers' evolutionary process to gain more defense payoffs.

The contribution of this paper is as follows. First, we describe distributed network attack-defense game as one-many game, regarding defender as individual-player and attackers as group-player. This way is more realistic. Moreover we formulate the game group-player's behaviors as evolutionary process. Based on the above, we propose a dynamic game method to achieve optimization of defense benefit.

The remainder of this paper is structured as follows. In Section 2, we discuss related work. In Section 3, we describe the problem and distributed network attack-defense game scenarios. In Section 4, we discuss group-players' behaviors in the game and model the behaviors into the imitation evolutionary process. In Section 5, we propose the dynamic game method with a strategy sequence generation algorithm and a parameter analysis method. In Section 6, experiments are performed to verify the proposed method. Finally, in Section 7, we present our conclusions and make recommendations for future works.

2. Related Work

Game theory is a study of mathematical models of conflict and cooperation between intelligent rational decision-makers [4]. In 1928, von Neumann proved the basic principle of game theory, which formally declared the birth of game theory. Due to the superiority of understanding and modeling conflict, game theory has recently been used in the field of computer network security. Reference [5] proposes a model to reason the friendly and hostile nodes in secure distributed computation using game theoretic framework. Reference [6] presents an incentive-based method to model the interactions between a DDoS attacker and the network administrator and a game-theoretic approach to infer intent, objectives, and strategies (AIOS). References [7, 8] also focused on DDos attack and defense mechanisms using game theory. Reference [9] modeled the interactions between an attacker and the administrator as a two-player stochastic game and computed Nash equilibrium using a nonlinear program. However, these researches all assume that both players in the game are consubstantial even individuals. Obviously this assumption cannot cover all the realistic situations. This paper extends this assumption to one-many game to be more realistic.

In the field of dynamic game, [10, 11] focused on the same scenarios as this paper. Reference [10] modeled the interaction of an attacker and the network administrator as a repeated game and found the Nash equilibrium via simulation. Reference [11] models the interaction between the hacker and the defender as a two-player, zero-sum game and explained how min-max theorem for this game is formulated. They concluded by suggesting that to solve this problem linear algorithms would be appropriate. Reference [12] modeled the mission deployment problem as repeated game and computed Nash equilibrium using improved PSO. They all do not consider the attackers' group behaviors. This paper precisely takes advantage of the attackers' group behaviors and in this way defender can gain more payoffs. More related works about applying game theory in network security can be referred to [13].

3. Distributed Network Attack-Defense Game

Given the flexibility that software-based operation provides, it is unreasonable to expect that attackers will demonstrate a fixed behavior over time [14]. Instead, on the one hand, attackers dynamically change their strategy in response to the dynamics of the configuration of the target system or defense strategy. On the other hand, relative to the defenders, attackers vary in degree of information acquisition abilities and rational characteristics.

We simplify attackers into two categories: senior attacker and junior attacker. Senior attacker has greater ability to acquire game information than junior attacker. As a result, senior attacker can react as soon as game situation changes and junior attacker generally follows senior attacker's behavior because of his weaker information acquisition ability.

Different from attackers, defenders, as system officers, are consubstantial and have more information about system, game structure, and payoff matrix. Even if they temporarily lack knowledge, they have more resources to fill in the blank. So the defenders are easier to gain the whole view of game situation.

Similar to Stackelberg model [15], there are senior and junior players in the distributed network attack-defense game. Moreover, distributed network attack-defense game is one-many game, as is stated above. Attackers are group-players, containing a minority of senior players and a majority of junior players. Defender is individual and senior player.

In distributed network attack-defense game, there are three game stages classified based on players' behaviors.

Stage 1. Attackers, as group-players, select different pure strategies randomly and format the proportion distribution of various kinds of pure strategies. Generally, the first game stage will not last too long and it will be terminated by defender's behavior.

Stage 2. Defender, as individual-player, behaves based on the proportion distribution of attack strategies. In our opinion, defender can gain more payoffs through misleading and guiding attacker group distribution structure, as in Section 5.

Stage 3. Senior attackers react to the game situation, and junior attackers follow senior attacker's behaviors to gain more payoffs. Junior attackers' behavioral pattern can be modeled as imitation dynamics model, as in Section 4.

Then, the game situation will repeat between the second stage and the third stage infinitely, unless in some special situation which we will discuss in Section 5.1.

4. Imitation Dynamics Model

As discussed above, attacker group presents imitation dynamics pattern in distributed network attack-defense

game. Different from general imitation dynamics model, minority of senior attackers can lead the imitation actions. In this section, we model attacker imitation dynamics in distributed network attack-defense game considering the effect of senior attackers.

Stage 1. As attackers select pure strategies randomly, proportion distribution of various kinds of pure strategies obeys uniform distribution. Let attacker's pure strategy space be S^a $(S^a1, \ldots, S^an)$ and let the number of the attackers be N. The Proportion Vector (PV) of attacker group choosing strategy S^ai at time t is denoted by $P^ai(t)$. In this stage, $P^ai(t)$ is equal to $1/n$. n is the number of attack strategies. In the attacker group, the proportion of senior attackers is denoted by θ. So there are $P^ai(t) \cdot \theta$ senior attackers choosing S^ai. Similarly, defender's pure strategy space is denoted by S^d $(S^d1, \ldots, S^dn)$ and the game situation when attacker chooses S^ai and defender chooses S^dj is denoted by S_{ij}, corresponding to attacker's payoff $S_{ij} \cdot U^a$ and defender's payoff $S_{ij} \cdot U^d$.

Stage 2. Defender behaves based on the proportion distribution of attack strategies. There are two cases to be considered: first defense behavior and follow-up defense behavior. Before the first time defender behaves, senior attackers randomly choose attack strategies and the distribution of senior attackers obeys uniform distribution like junior attackers. After the first time defender behaves, senior attackers always concentrate on the best response strategy no matter how defense strategy changes because of their quick reaction capability and the distribution of senior attackers obeys concentrated distribution.

Stage 3. Senior attackers react to the game situation immediately. Let senior attackers react in vector at time t be $\alpha(t)$. In the first defense behavior case, uniform distribution of the senior attackers concentrates on the best response attack strategy, suppose S^ai:

$$\begin{aligned}\alpha(t) &= \left(-P^a1(t) \cdot \theta, \ldots, \left(1 - P^ai(t)\right) \cdot \theta, \ldots, -P^an(t) \cdot \theta\right).\end{aligned} \tag{1}$$

In the follow-up defense behavior case, suppose that best response attack strategy changes from S^aj to S^ai. Then concentrated distribution of senior attackers accordingly changes from S^aj to S^ai:

$$\alpha(t) = (0, \ldots, \theta, \ldots, -\theta, \ldots, 0). \tag{2}$$

Let $\beta(t)$ be the PV after senior attackers' reaction at time t:

$$P^a(t+1) = \beta(t) = P^a(t) + \alpha(t). \tag{3}$$

For junior attackers, they imitate senior attacker's behaviors to gain more payoffs in the imitation probability λ. The distribution of junior attackers concentrates on the best response strategy gradually. Let imitation vector be $\gamma(t)$.

Table 1: Game payoff matrix.

		Defender		
		S^d1	S^d2	S^d3
Attacker	S^a1	4, 1	5, 5	3, **6**
	S^a2	2, 2	1, **9**	**4**, 2
	S^a3	**5**, 3	**7**, 4	3, **5**

Similar to the first defense behavior case, uniform distribution of the junior attackers concentrates on the best response attack strategy, suppose S^ai:

$$\begin{aligned}\gamma(t) &= \left(-P^a1(t) \cdot \lambda, \ldots, \left(1 - P^ai(t)\right) \cdot \lambda, \ldots, -P^an(t) \cdot \lambda\right).\end{aligned} \tag{4}$$

In the follow-up defense behavior case, suppose that best response attack strategy changes from S^aj to S^ai. Then concentrated distribution of junior attackers accordingly changes from S^aj to S^ai:

$$\gamma(t) = \left(0, \ldots, +P^aj(t) \cdot \lambda, \ldots, -P^aj(t) \cdot \lambda, \ldots, 0\right). \tag{5}$$

Correspondingly, the Proportion Vector (PV) of attacker group is updated as

$$P^a(t+1) = P^a(t) + \gamma(t). \tag{6}$$

Imitation probability λ is affected by additional game information obtained by junior attackers beyond their own information acquisition ability. In this paper, we assume that the additional game information is obtained from two aspects. One is revealing game information initiatively by defender. The more game information is revealed, the higher value of λ can be. So λ can reach maximum value of 1 if plenty of game information was revealed by defender. The other aspect is internal communication among attacker group which is the natural attribute of group and cannot be controlled by external behaviors. So λ has a constant minimum value, suppose λ_0. As a result, the following is obtained:

$$\lambda_0 < \lambda < 1. \tag{7}$$

As mentioned above, defender has a partially ability to control junior attackers' imitation rate through revealing game information purposefully. The game information revealing strategy will be discussed in Section 5.2.1.

5. Dynamic Game Method

We now present a dynamic game method for achieving the optimization of defense benefit. The proposed method is a two-step procedure which involves defense strategy sequence generation algorithm (SSGA) (Section 5.1) and parameter analysis method (Section 5.2) used to set parameters in dynamic game method.

Consider a simple game payoff matrix L as in Table 1.

Input: A game situation S_{ij} and a game payoff matrix M
Output: A suitable ring containing S_{ij} as key inducing point
(1) **Initial** $R(SP(S^d key, S^d assist), S_k, S_a)$;
(2) **If** S_{ij} is Vertex **then**
(3) **return** null;
(4) **else**
(5) $R \cdot SP \cdot S^d key = S^d j$;
(6) $R \cdot S_k = S_{ij}$;
(7) $a \leftarrow$ the line of vertex of row j;
(8) **for** $(m = 1; m <= n; m{+}{+})$
(9) **if** S_{im} is Vertex && $S_{am} \cdot U^d > S_a \cdot U^d$
(10) $R \cdot SP \cdot S^d assist = S^d m$;
(11) $R \cdot S_a = S_{am}$;
(12) **else** continue;
(13) **end for**
(14) **end if**
(15) **return** R;

Algorithm 1: $Ring_Idenfy(S_{ij}, M)$.

Obviously, defender wishes to keep game situation in $S_{22} = (S^a 2, S^d 2)$ within which he can gain global best payoff of 9. However, this desire seems unrealizable since if defender chooses strategy $S^d 2$, attackers will choose strategy $S^a 3$ as response to gain more payoffs. What we propose is a novel dynamic game method to keep game situation in global best situation as long as possible in which way defender can gain more payoffs.

5.1. Strategy Sequence Generation Algorithm. Strategy sequence generation algorithm (SSGA) produces a strategy pair which will be chosen in sequence circularly by defender to keep game situation in global best situation. Two parameters will be attached to the strategy pair and we will discuss them in Section 5.2.

We firstly define some notions which are necessary in SSGA.

Vertex. It is the best response game situation of attackers. In Table 1, $S_{31} = (S^a 3, S^d 1)$, $S_{32} = (S^a 3, S^d 2)$, and $S_{23} = (S^a 2, S^d 3)$ are vertices. Obviously, there is one and only one vertex in a row of game payoff matrix and, in imitation process, attacker group will gather to the vertex of the row. In this way, we can redefine Nash equilibrium as game situation which is both the vertex and the best response game situation of defender.

Inducing Point. It is game situation which is not *Vertex* and has *Vertex* in the same line. Among inducing points, two inducing points are determined seriously by SSGA: *key inducing point* with higher defense payoff which defender wishes to keep as long as possible, for example, $S_{22} = (S^a 2, S^d 2)$ in Table 1, and *assist inducing point* which is used to adjust the contribution of attacker group and assist to keep game situation in key inducing point. We have the following trivial result of the number of inducing points in a game payoff matrix:

$$N^2 - \sum_{Xi>0} \left[(Xi - 1) \cdot N + Xi\right], \tag{8}$$

where Xi is the number of vertices in ith line in game payoff matrix.

Ring. A triple $Ring((S^d key, S^d assist), S_k, S_a) \cdot (S^d key, S^d assist)$ is a defense strategy pair which will be chosen in sequence circularly; S_k is inducing point of the ring which is in the same line of vertex of $S^d key$; S_a is inducing point which is in the same line of vertex of $S^d assist$. The defense payoffs of S_k, S_a decide which one is key inducing point and which is the order of strategy pair. In Table 1, $((S^d 2, S^d 3), S_{22}, S_{33})$ is a ring of the responding payoff matrix.

The number of rings in a game payoff matrix can be computed as

$$C_N^2 - \sum_i^N C_{Xi}^2. \tag{9}$$

It is easy to prove that, unless all the vertices concentrate upon one same line, there must exist at least one ring. A ring identification algorithm is as in Algorithm 1.

In lines 9–11, we select higher defense payoff inducing point and corresponding vertex as the ring result in accordance with original intention.

Based on ring identification algorithm, a global ring selecting algorithm is as in Algorithm 2 to work out a global best ring.

The global ring selecting algorithm works out a ring R which is used in the following method discussion. However, let us consider a special case in which the game has Nash equilibrium with corresponding defense payoff larger than key inducing point's defense payoff. In this case, it is easy to make the conclusion that Nash equilibrium is the better choice. So in this paper, we do not consider this case.

5.2. Parameter Analysis Method. Based on the above discussion, a dynamic game scheme is *DGS* (*Ring*, *Leakage_factor*, and *Duration)*, meaning that how long the time to hold each

```
Input: A game payoff matrix M
Output: A global best ring
(1) Initial L ← the sequence of inducing point in descending order of S_ij · U^d
(2) Initial *p = L;
(3) While p != null
(4)     If Ring_Idenfy(p, M) != null
(5)         return Ring_Idenfy(p, M);
(6)     else
(7)         p = p.next;
(8)     end if
(9) end while
(10) return null
```

Algorithm 2: $G_ring_select(M)$.

strategy in strategy *Ring* is with which degree of information leakage. Since we have discussed *Ring* in the last section, in this section, we discuss the parameters in the dynamic game scheme, mainly *Duration* and *Leakage_factor*.

5.2.1. Leakage Factor. The parameter *Leakage_factor* indicates to what degree defender should reveal information in each strategy duration to induce the behavior of attacker group. As definition of *Ring* in Section 5.1, there are two strategies in a *Ring*, corresponding to two inducing points. Therefore, the parameter *Leakage_factor* should also have two subparameters.

Leakage_Factor. A two-tuple *Leakage_factor* (L_k, L_a) is a pair of percentage figures corresponding to each strategy in *Ring* and also key inducing point and assisting inducing point. Note that the percentage figures are independent of each other, since they are used during different strategy durations. *Leakage_factor* equaling 0 means that defender does not reveal game information intentionally; oppositely, *Leakage_factor* equaling 1 means that defender reveals plenty of game information; others mean that defender reveals game information partially.

As mentioned above, imitation probability λ is affected by revealed game information. The more game information is revealed, the higher value of λ will be, meaning higher imitation speed of junior attackers. Obviously, we can simply suppose that there is positive correlation between λ and *Leakage_factor*. Since the functional relationship $\lambda = f(Leakage_factor)$ is not the focus of this paper, we just have the following assumptions:

$$\begin{aligned} f(L) &= \lambda_0, \quad \text{if } L = 0 \\ f(L1) &\geq f(L2), \quad \text{if } L1 \geq L2 \\ f(L) &= 1, \quad \text{if } L = 1. \end{aligned} \tag{10}$$

There are two cases to be considered: duration of $S^d key$ and duration of $S^d assist$.

In duration of $S^d key$, the concentrated distribution of junior attackers changes game situation from key inducing point S_k to the *Vertex* of the same row. Based on our purpose, we wish to keep game situation in key inducing point as long as possible. As the result, defender should decrease *Leakage_factor* to 0 by revealing no game information intentionally, corresponding to minimum imitation probability of λ_0 and the lowest imitation speed of junior attackers.

In duration of $S^d assist$, the concentrated distribution of junior attackers changes game situation from assist inducing point S_a to the *Vertex* of the same row. Based on our purpose, assist inducing point is used to adjust the contribution of attacker group and assist in keeping game situation in key inducing point. So we wish the concentrated distribution of junior attackers ready rapidly to be induced to key inducing point. As a result, defender should increase *Leakage_factor* to 1 by revealing plenty of game information, corresponding to maximum imitation probability of 1 and the highest imitation speed of junior attackers.

5.2.2. Duration. The parameter *Duration* indicates how long the time to hold each strategy in strategy *Ring* is. Similar to *Leakage_factor*, the parameter *Duration* should also have two subparameters.

Duration. A two-tuple *Duration* (D_k, D_a) is a pair of durations corresponding to each strategy in *Ring* and also key inducing point and assisting inducing point.

Before analyzing the parameter of *Duration*, a computational method of the average payoff of game players should be given. Let $E(t)$ be average payoff of players at time t. $E(t)$ can be deduced through payoff variation. Suppose the best response attack strategy changes from $S^a j$ to $S^a i$:

$$E(t) = E(t-1) + (Ui - Uj) \cdot P^a j(t-1) \cdot \lambda, \tag{11}$$

where the second part indicates the payoff increment by junior attackers imitation behavior which means there is the proportion $P^a j(t-1) \cdot \lambda$ of attackers changing strategy from $S^a j$ to $S^a i$, the corresponding payoff increment. The Proportion Vector (PV) strategy $S^a j$ varies as

$$P^a j(t) = P^a j(t-1) \cdot \lambda. \tag{12}$$

Let $E(t0) = e0$ be the initial payoff. The average payoff of players at time t is as follows:

$$\begin{aligned} E(t) &= e0 + \frac{(Ui - Uj) \cdot Pj(t0) \cdot \lambda \cdot \left(1 - (1-\lambda)^t\right)}{1 - (1-\lambda)} \\ &= e0 + (Ui - Uj) \cdot Pj(t0) \\ &\quad - (Ui - Uj) \cdot Pj(t0) \cdot (1-\lambda)^T. \end{aligned} \tag{13}$$

Then the sum of player payoff in the duration of T can be deduced as

$$\begin{aligned} SoE(T) &= e0 \cdot T + (Ui - Uj) \cdot P^a j(t0) \cdot T \\ &\quad - \frac{(Ui - Uj) \cdot P^a j(t0) \cdot (1-\lambda) \cdot \left(1 - (1-\lambda)^T\right)}{1 - (1-\lambda)}. \end{aligned} \tag{14}$$

Suppose that there is a dynamic game scheme $DGS(((S^d key, S^d assist), S_k, S_a), (L_k, L_a), (D_k, D_a))$ and let the cost of changing defense strategy be C. In duration of $S^d assist$, defender lets $Leakage_factor$ change to 1 by revealing plenty of game information, corresponding to maximum imitation probability of 1 discussed above which means attackers converge instantaneously. So we suppose that D_a is 0 and that defender gains no payoffs in duration of $S^d assist$. Then the average of defender payoff in the duration of a *Ring* can be

$$AoR = \frac{(SoE(D_k) - 2 * C)}{D_k}. \tag{15}$$

We can achieve the highest AoR by controlling the only variable D_k through solving the equation of $d(AoR)/d(D_k) = 0$.

6. Experimental Results

6.1. Numerical Example. In this section, we provide a numerical test to illustrate the implementation of the proposed method. In the example, we suppose that the game payoff matrix, the imitation probability, and the cost of changing defense strategy are determined since these are not the focus of this paper. Let λ_0 be 0.1 and the game payoff matrix as Table 1.

Using SSGA, we figure out a pair of defense strategies and a dynamic game scheme $(((S^d 2, S^d 3), S_{22}, S_{33}), (L_k, L_a), (D_k, D_a))$. As mentioned above, we want to keep game situation in S_{22} as long as possible. So let $L_k = 0, L_a = 1$ and correspondingly $\lambda = \lambda_0$ and $\lambda = 1$. As a result, the dynamic game scheme should be $(((S^d 2, S^d 3), S_{22}, S_{33}), (0, 1), (D_k, 0))$. The influence of D_k on AoR is as in Figure 1.

The result of the equation $d(AoR)/d(D_k) = 0$ is $D_k \approx 4.734$. When $D_k < 4.734$, defender changes strategies frequently by which lots of costs $C = 2$ are introduced. So we can see in Figure 1 that, with the increase of D_k, AoR grows rapidly. When $D_k > 4.734$, the cost of changing defense strategy is not main impact factor on AoR anymore because of low frequency of defense strategy replacement. In this case, attackers change their convergence from S_{22} to S_{32} gradually in the process where defender's payoff decreases. That means that longer duration results in low AoR, as seen in the figure.

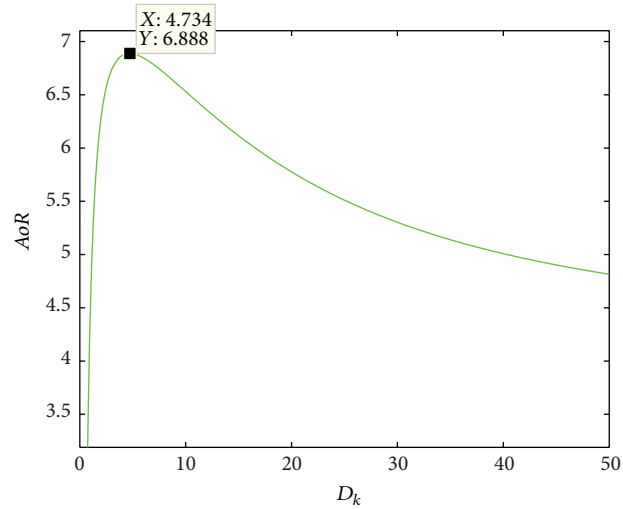

Figure 1: The influence of D_k to AoR.

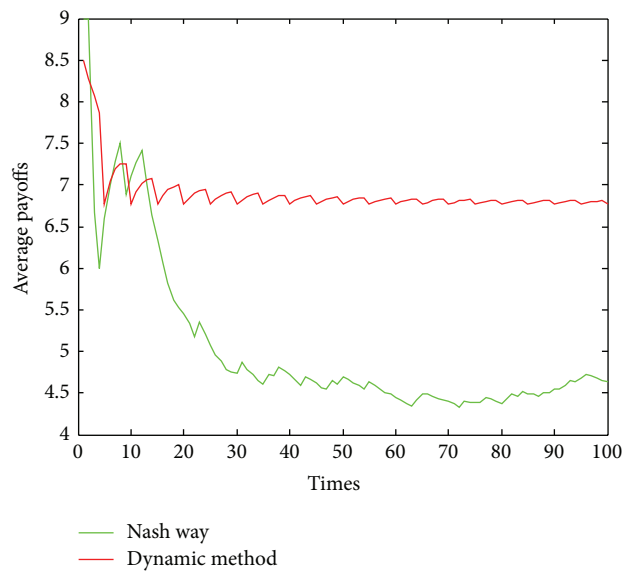

Figure 2: The comparison of average payoffs.

6.2. Effectiveness. In this section, we verify the effectiveness of proposed method. Reference [12] proposed a game strategy optimization approach solving mission deployment problem. A Nash way to choose game strategy is figured out using particle swarm optimization (PSO). Although reference [12] had different assumption and problems with this paper, the method itself is comparable. We compare the average defender payoffs achieved by two methods, shown in Figure 2.

We can see in Figure 2 that the graphic of dynamic method shows the vibration waveform and amplitude

decreases. In every vibration cycle, average payoffs increase firstly with a declining slope. This is because of the fact that the dynamic regulation of attacker group leads to the decreasing growth rate of defender payoff. Then average payoff decreases rapidly caused by the cost of changing strategies. In Nash way, the average payoff fluctuates seriously in the earlier stage because the average payoff is still unstable as average values [12]. Then, after about 30 times, the average payoff is tending towards stability, about 4.5. It is clear that the dynamic method can achieve obviously higher average payoff. The Nash way seeks for an optimization approach by safeguarding a Nash equilibrium game situation. This is driven by minimizing the possible losses. On the other hand, in this paper, our dynamic method applies a different thinking by seeking for the global best payoff in the game. So our method can greatly improve the payoffs.

7. Conclusions

In this paper, we model distributed network attack-defense game as one-many game and formulate the game group-player's imitation behaviors as evolutionary process. Taking advantage of defenders' information superiority and attackers' imitation behaviors, we propose a dynamic game method to help defender gain more payoffs through inducing attackers' evolutionary process. The experiments prove the effectiveness of the proposed method. In our future research, we will apply the proposed method in other areas to verify the effectiveness, such as state estimation, dynamics control, resources allocation, or information management [16–18].

On the other hand, this paper is based on the assumption that players in the game are seeking for the increasing of their own payoffs and do not care about opponents'. However, in the reality, there are different types of attack. For example, there exists such case where attackers are seeking for destroying opponent's system. In this kind of attack, attackers concentrate more on the decreasing of opponent's payoffs than the increasing of their own payoffs. So the attack type will affect defense mode. Our future work will be driven towards these problems.

Conflict of Interests

The authors declare that there is no conflict of interests regarding the publication of this paper.

Acknowledgment

This work is supported by Project 042500318 which is supported by National Nature Science Foundation of China.

References

[1] M. R. Grimaila, R. F. Mills, M. Haas, and D. Kelly, *Mission Assurance: Issues and Challenges*, Air Force Institute of Technology, Center for Cyberspace Research, Wright-Patterson AFB, Ohio, USA, 2010.

[2] K. Binmore, "Foundation of game theory," in *Advances in Economic Theory: Sixth World Congress*, J. Laffont, Ed., vol. 1, pp. 1–31, Cambridge University Press, Cambridge, UK, 1992.

[3] D. Fudenberg and D. K. Levine, "Learning in games," *European Economic Review*, vol. 42, no. 3–5, pp. 631–639, 1998.

[4] R. B. Myerson, *Game Theory*, Harvard University Press, Cambridge, Mass, USA, 1991.

[5] P. F. Syverson, "Different look at secure distributed computation," in *Proceedings of the 10th IEEE Computr Security Foundations Workshop (CSFW '97)*, pp. 109–115, IEEE, June 1997.

[6] P. Liu, W. Zang, and M. Yu, "Incentive-based modeling and inference of attacker intent, objectives, and strategies," *ACM Transactions on Information and System Security*, vol. 8, no. 1, pp. 78–118, 2005.

[7] J. Mirkovic and P. Reiher, "A taxonomy of ddos attack and ddos defense mechanisms," *ACM SIGCOMM Computer Communication Review*, vol. 34, no. 2, pp. 39–53, 2004.

[8] J. Xu and W. Lee, "Sustaining availability of web services under distributed denial of service attacks," *IEEE Transactions on Computers*, vol. 52, no. 2, pp. 195–208, 2003.

[9] K.-W. Lye and J. M. Wing, "Game strategies in network security," *International Journal of Information Security*, vol. 4, no. 1-2, pp. 71–86, 2005.

[10] T. Alpcan and T. Başar, "A game theoretic analysis of intrusion detection in access control systems," in *Proceedings of the 43rd IEEE Conference on Decision and Control (CDC '04)*, pp. 1568–1573, December 2004.

[11] X. Z. You and Z. Shiyong, "A kind of network security behavior model based on game theory," in *Proceedings of the 4th International Conference on Parallel and Distributed Computing, Applications and Technologies (PDCAT '03)*, pp. 950–954, IEEE, August 2003.

[12] L. Xiaojian, Y. Yuyu, F. Binxing, and G. Yi, "A strategy optimization approach for mission deployment in distributed systems," *Mathematical Problems in Engineering*, vol. 2014, Article ID 404681, 8 pages, 2014.

[13] S. Roy, C. Ellis, S. Shiva, D. Dasgupta, V. Shandilya, and Q. Wu, "A survey of game theory as applied to network security," in *Proceedings of the 43rd Hawaii International Conference on System Sciences (HICSS '10)*, pp. 1–10, IEEE, Honolulu, Hawaii, USA, January 2010.

[14] M. H. R. Khouzani, S. Sarkar, and E. Altman, "A dynamic game solution to malware attack," in *Proceedings of the IEEE INFOCOM*, pp. 2138–2146, April 2011.

[15] K. Basu, "Stackelberg equilibrium in oligopoly: an explanation based on managerial incentives," *Economics Letters*, vol. 49, no. 4, pp. 459–464, 1995.

[16] M. H. Manshaei, Q. Zhu, T. Alpcan, T. Basar, and J.-P. Hubaux, "Game theory meets network security and privacy," *ACM Computing Surveys*, vol. 45, no. 3, article 25, 2013.

[17] C. Leboucher, R. Chelouah, P. Siarry, and S. le Ménec, "A swarm intelligence method combined to evolutionary game theory applied to the resources allocation problem," *International Journal of Swarm Intelligence Research*, vol. 3, no. 2, pp. 20–38, 2012.

[18] A. Fielder, E. Panaousis, P. Malacaria, C. Hankin, and F. Smeraldi, "Game theory meets information security management," in *ICT Systems Security and Privacy Protection*, vol. 428 of *IFIP Advances in Information and Communication Technology*, pp. 15–29, Springer, Berlin, Germany, 2014.

Hindawi Publishing Corporation
Mathematical Problems in Engineering
Volume 2015, Article ID 354658, 7 pages
http://dx.doi.org/10.1155/2015/354658

Research Article

ACO-Initialized Wavelet Neural Network for Vibration Fault Diagnosis of Hydroturbine Generating Unit

Zhihuai Xiao,[1] Xinying He,[1] Xiangqian Fu,[1] and O. P. Malik[2]

[1] *School of Power and Mechanical Engineering, Wuhan University, Wuhan, Hubei 430072, China*
[2] *Department of Electrical and Computer Engineering, University of Calgary, Calgary, AB, Canada T2N 1N4*

Correspondence should be addressed to Zhihuai Xiao; xiaozhihuai@126.com

Received 24 November 2014; Accepted 12 January 2015

Academic Editor: Yun-Bo Zhao

Copyright © 2015 Zhihuai Xiao et al. This is an open access article distributed under the Creative Commons Attribution License, which permits unrestricted use, distribution, and reproduction in any medium, provided the original work is properly cited.

Considering the drawbacks of traditional wavelet neural network, such as low convergence speed and high sensitivity to initial parameters, an ant colony optimization- (ACO-) initialized wavelet neural network is proposed in this paper for vibration fault diagnosis of a hydroturbine generating unit. In this method, parameters of the wavelet neural network are initialized by the ACO algorithm, and then the wavelet neural network is trained by the gradient descent algorithm. Amplitudes of the frequency components of the hydroturbine generating unit vibration signals are used as feature vectors for wavelet neural network training to realize mapping relationship from vibration features to fault types. A real vibration fault diagnosis case result of a hydroturbine generating unit shows that the proposed method has faster convergence speed and stronger generalization ability than the traditional wavelet neural network and ACO wavelet neural network. Thus it can provide an effective solution for online vibration fault diagnosis of a hydroturbine generating unit.

1. Introduction

Nowadays, hydroturbine generating units are becoming larger, more complicated, and more integrated, which not only makes regulation and operation of the hydroturbine generating unit complicated but also increases the probability of occurrence of faults. Therefore, it is of great significance to research effective fault diagnosis methods that give early alert before faults happen or avoid deterioration of existing faults resulting in great economic losses.

About 80% of the hydroturbine generating unit faults reveal characteristics in vibration signals [1]. Vibration signals of a hydroturbine generating unit, a complicated and nonlinear system, are generally influenced by multiple hydraulic, mechanical, and electrical/electronic factors [2]. These factors may interact with each other, which makes it difficult to construct by theoretical analysis a one-to-one relationship between the vibration feature and the cause of the fault. All these factors lead to the difficulty of fault diagnosis for a hydroturbine generating unit.

Taking the characteristics of hydroturbine generating unit vibration signals into consideration, nonlinear diagnosis models are often utilized to realize effective mapping from vibration feature sets to fault sets [3–6]. Neural network [7] has perfect self-organization, adaptive learning, and remembrance abilities. It can realize complicated relationship mapping in nonlinear systems and has become a dominant method in the area of hydroturbine generating unit fault diagnosis. Feedforward neural network trained by back propagation method is one of the most widely used methods [3–5]. However, such a neural network has drawbacks, for example, slow convergence speed and inclination to be trapped in local minima [8]. Wavelet neural network, a kind of feedforward network proposed in 1992 [9] on the basis of wavelet analysis theory by substituting excitation function for wavelet function, has developed fast [10–12]. However, even though by combining time-frequency localization ability of wavelet analysis and self-learning ability of neural network a wavelet neural network has strong approximation, fault tolerance, and classification abilities, it cannot avoid drawbacks of

slow convergence speed and high sensitivity to initialization parameters [13]. Therefore, optimizing parameters of wavelet neural networks by heuristic optimization algorithms is becoming an important research topic [14–16].

Ant colony optimization (ACO) algorithm is one kind of the heuristic optimization algorithms. It has perfect global optimization characteristics, strong robust ability, and great distributed computing system. ACO wavelet neural network, which uses ACO to learn parameters of wavelet neural network, preserves the advantages of ACO and does not have the drawbacks of sensitivity to initializing parameters. However, its training speed is still slow according to the information in the literature. Therefore, an ACO-initialized wavelet neural network is proposed in this paper and used in the vibration fault diagnosis of a hydroturbine generating unit. This method employs ACO to train the parameters of a wavelet network and the obtained parameters are taken as the initialization parameters. Vibration frequency features of a hydroturbine generating unit are taken as the inputs and fault types are taken as the outputs of the wavelet neural network. A fault diagnosis model of the hydroturbine generating unit based on ACO-initialized wavelet neural network is constructed. Fault diagnosis results show that, compared with the traditional wavelet neural network and ACO wavelet neural network, not only can the method proposed in this paper increase the speed of convergence but it also has strong generalization ability.

2. Vibration Types and Characteristics of Hydroturbine Generating Units

According to disturbing force types of vibration signals, vibration types can be divided into hydraulic vibration, mechanical vibration, and electrical vibration [2].

2.1. Hydraulic Vibration. Hydraulic vibration is caused by water flow and machinery. There are many factors which lead to this kind of vibration such as hydraulic imbalance, draft tube pressure pulsation, nonuniformity in the path of circulating water flow, nonuniform gap of runner wearing ring, Karman vortex street, clearance jet, cavity erosion, and wrong in cam relationship. The characteristic of this type of vibration is that vibration frequency is different for each vibration source.

2.2. Mechanical Vibration. Mechanical vibration is aroused by improper installation of the unit, drawbacks of the unit structure, or damage in the component of the running unit. There are many factors which lead to this kind of vibration such as imbalance of the rotating part of the unit, misalignment of the axis, defects in the bearing, rotor-to-stator rub, and looseness of the connection. The characteristic of this kind of vibration is that vibration frequency is the rotation frequency or a multiple of the rotation frequency.

2.3. Electrical Vibration. Electrical vibration is caused by nonuniformity of magnetic flux density, unbalance of electromagnetic pull, and stator core looseness. There are many factors which lead to this kind of vibration such as the rotor pole coil turn-to-turn short circuit, nonuniform air gap between rotor and stator, wrong polarity order of the core, out of round of rotor inside or stator outside, and unbalance of current among three phases. The characteristic of this kind of vibration is that vibration frequency is the rotation frequency or the frequency of the polar in the hydropower generator.

It can be seen from the above that vibration signals are the synthesis of results aroused by hydraulic vibration, mechanical vibration, and electrical vibration. It has highly nonlinear characteristic. Hydroturbine generating unit fault diagnosis based on neural network method is used to extract features of these vibration signals and neural network is used to map these features to corresponding fault type in order to realize the fault diagnosis for hydroturbine generating unit.

3. Wavelet Neural Network

Wavelet neural network is a kind of neural network that is constructed based on wavelet analysis theory. As wavelet analysis theory ensures the $L^2(R)$ approximation ability, wavelet function can substitute for excitation function of the neural network to form a new kind of feedforward neural network model.

3.1. Structure of Wavelet Neural Network. Structure of a wavelet neural network is shown in Figure 1, where M, n, and N are number of input layer nodes, hidden layer nodes, and output layer nodes, respectively. $\mathbf{x}$ (x_k, $k = 1, 2, \ldots, M$), $\mathbf{o}$ (o_j, $j = 1, 2, \ldots, n$), and $\mathbf{y}$ (y_i, $i = 1, 2, \ldots, N$) are vectors of input layer, hidden layer, and output layer, respectively. W_{jk} ($j = 1, 2, \ldots, n$; $k = 1, 2, \ldots, M$) is weight parameter between input layer and hidden layer. V_{ij} ($i = 1, 2, \ldots, N$; $j = 1, 2, \ldots, n$) is weight parameter between hidden layer and output layer. $\mathbf{b}$ (b_j, $j = 1, 2, \ldots, n$) and $\mathbf{a}$ (a_j, $j = 1, 2, \ldots, n$) are translation parameters and scaling parameters, respectively. h is wavelet function.

Suppose that $\text{net}_j = \sum_{k=1}^{M} W_{jk} x_k$; then the model of wavelet network can be expressed as

$$y_i = \sum_{j=1}^{n} V_{ij} h\left(\frac{\text{net}_j - b_j}{a_j}\right). \tag{1}$$

3.2. Training Method of Wavelet Neural Network. Suppose that the error function of a wavelet neural network is

$$E = \frac{1}{2}\sum_{l=1}^{L}\sum_{i=1}^{N}\left(d_i^l - y_i^l\right)^2. \tag{2}$$

Here, L is the number of training samples and $\mathbf{d}$ (d_i, $i = 1, 2, \ldots, N$) is the object output vector.

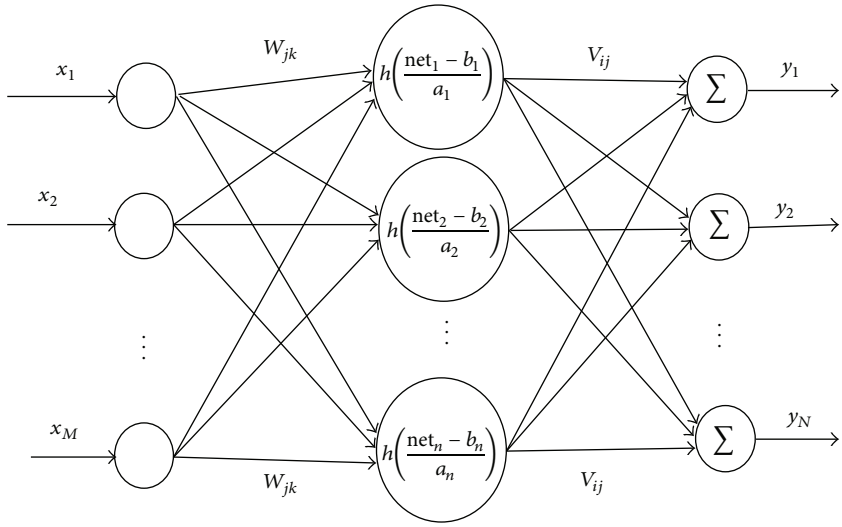

Figure 1: Structure of wavelet neural network.

Generally, the training method of a wavelet neural network is the gradient descent method, for which the equations for parameters adjustment are shown in

$$\begin{aligned} V_{ij}^{\text{new}} &= V_{ij}^{\text{old}} - \eta \frac{\partial E}{\partial V_{ij}} \\ W_{jk}^{\text{new}} &= W_{jk}^{\text{old}} - \eta \frac{\partial E}{\partial W_{jk}} \\ a_j^{\text{new}} &= a_j^{\text{old}} - \eta \frac{\partial E}{\partial a_j} \\ b_j^{\text{new}} &= b_j^{\text{old}} - \eta \frac{\partial E}{\partial b_j}. \end{aligned} \tag{3}$$

Here, η is learning factor. Gradient of parameters are shown in

$$\begin{aligned} \frac{\partial E}{\partial V_{ij}} &= -\sum_{l=1}^{L} \left(d_i^l - y_i^l\right) h\left(\frac{\text{net}_j^l - b_j}{a_j}\right) \\ \frac{\partial E}{\partial W_{jk}} &= -\sum_{l=1}^{L}\sum_{i=1}^{N} \left(d_i^l - y_i^l\right) V_{ij} h'\left(\frac{\text{net}_j^l - b_j}{a_j}\right) \frac{1}{a_j} x_k^l \\ \frac{\partial E}{\partial a_j} &= \sum_{L=1}^{l}\sum_{i=1}^{N} \left(d_i^l - y_i^l\right) V_{ij} h'\left(\frac{\text{net}_j^l - b_j}{a_j}\right) \frac{\left(\text{net}_j^l - b_j\right)}{a_j^2} \\ \frac{\partial E}{\partial b_j} &= \sum_{l=1}^{L}\sum_{i=1}^{N} \left(d_i^l - y_i^l\right) V_{ij} h'\left(\frac{\text{net}_j^l - b_j}{a_j}\right) \frac{1}{a_j}. \end{aligned} \tag{4}$$

4. ACO-Initialized Wavelet Neural Network

4.1. Theory of ACO-Initialized Wavelet Neural Network. ACO algorithm [15] is a kind of heuristic global optimization algorithm which takes ant seeking food theory as its basic theory and seeks the optimization in the solution space of an objective function. Pheromone is the intermediary by which ants communicate with each other. When an ant seeks food, it will secrete pheromone to mark trace and determine forward direction according to the amount of pheromone on the trace which has direct ratio relationship with the number of ants which have passed this trace. At the beginning, ants will choose trace randomly. Because the number of ants in a shorter trace is larger than in a longer one, more pheromone will be left in the shorter trace and hence the probability of the shorter trace being chosen will be larger. This is the positive feedback mechanism. As the iteration times increases, the whole ant colony will eventually restrain itself to a shorter trace which represents the optimized solution.

The specific theory of ACO-initialized wavelet neural network is that the parameters waiting to be initialized are treated as the nodes in the seeking traces, and then all of the ants need to choose the nodes to reach the food source. During the food seeking process, error function of the wavelet neural network is taken as the evaluation function to adjust the amount of pheromone and guide the direction of the ants.

4.2. Procedure of ACO-Initialization of the Wavelet Neural Network. The procedure of ACO-initialization of the wavelet neural network is similar to the procedure of ACO wavelet neural network [15]. The difference is that the former method employs ACO algorithm to train the neural network and then the parameters after the initial training are taken as the initialization parameters of the wavelet neural network. The initial training time is not very large and does not need to reach certain error precision. The error precision of the wavelet network is determined by the further training process. In the latter method, ACO algorithm is used to train the wavelet neural network until the error precision or certain training time is reached.

Suppose there are m parameters waiting to be initialized, which include weight parameters, scaling parameters, and

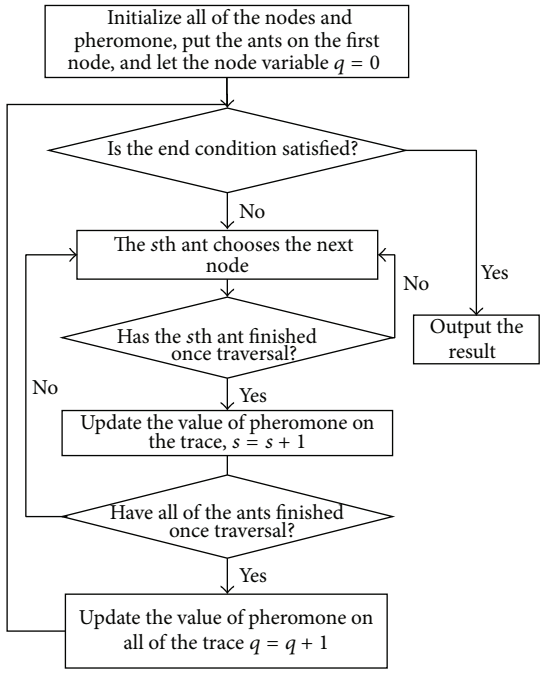

Figure 2: Flowchart of ACO-initialized wavelet network.

translation parameters. Then, these parameters are lined up and form a vector, $\mathbf{P}$ $(P_i, i = 1, 2, \ldots, m)$, in which K random numbers corresponding to each of the elements are chosen to form m sets I_{Pi} $(i = 1, 2, \ldots, m)$. Suppose the total number of ants is S. Each ant takes off from I_{Pi} first. Then it chooses elements from each of the sets independently and randomly according to the law of probability transfer. The ant will reach the food source when all of the sets are chosen. After that, the pheromone of each set will be adjusted. This process is repeated until the error precision or certain training time is reached.

Flowchart of the ACO-initialized wavelet neural network is shown as in Figure 2. The specific procedure is as follows.

(1) Relevant parameters initialization: set pheromone of each element in set I_{Pi} as $\tau_j(I_{Pi})(0) = C$ $(j = 1, 2, \ldots, K)$.

(2) Determine whether the stop condition (the error precision or certain training time) is reached or not. If so, output the optimization solution and stop the iteration; otherwise turn to the third step.

(3) The jth element is chosen from set I_{Pi} according to the law of probability transfer shown as follows for ant s $(s = 1, 2, \ldots, S)$:

$$\text{Prob}\left(\tau_j^s\left(I_{Pi}\right)\right) = \frac{\tau_j\left(I_{Pi}\right)}{\sum_{u=1}^{K} \tau_u\left(I_{Pi}\right)}. \tag{5}$$

(4) After the sth ant finished all of the nodes in the chosen process, the chosen parameters will be input into the wavelet neural network and the error calculated. Then calculate the amount of pheromone corresponding to the sth ant and the jth nodes:

$$\Delta\tau_j^s\left(I_{Pi}\right) = \begin{cases} \dfrac{Q}{E^s} & \text{The } s\text{th ant chooses the } j\text{th elements} \\ & \text{in set } I_{Pi} \text{ during this circulation} \\ 0 & \text{otherwise,} \end{cases} \tag{6}$$

where Q is a constant which is used to adjust the pheromone adjustment speed and E^s is the error calculated by inputting the parameters into wavelet neural network after the sth ant finished all of the nodes traversal.

(5) After all of the ants finished choosing once, adjust all of the elements in set I_{Pi} according to the following equation, record the optimized value, and turn to step (2):

$$\tau_j\left(I_{Pi}\right)(t + m) = \rho\tau_j\left(I_{Pi}\right)(t) + \Delta\tau_j\left(I_{Pi}\right). \tag{7}$$

Here, ρ $(0 < \rho < 1)$ represents the durability of pheromone and $1 - \rho$ represents the disappearing degree between t and $t + m$.

5. Hydroturbine Generating Fault Diagnosis Example

5.1. Selection of Fault Features. Vibration signals of a hydroturbine generating unit are the synthesized reflection of hydraulic, mechanical, and electric vibration factors and so on. The method, which takes amplitude of vibration signals frequency components as feature vector and employs neural network to realize the mapping from vibration feature set to fault set, is a common method for hydroturbine generating unit fault diagnosis. In this paper, the amplitudes of vibration signals frequency components $0.4 \sim 0.5f$, $1f$, $2f$, $3f$, and $> 3f$ are chosen to form the feature vector, and 3 fault conditions (vortex with eccentric, unbalance and misalignment) and normal condition of hydroturbine generating unit are taken as fault types waiting to be recognized. Here, the letter "f" represents the fundamental frequency of hydroturbine generating unit. ACO-initialized wavelet neural network is employed to diagnose vibration fault of the hydroturbine generating unit. Three-layer model, namely, input layer, hidden layer, and output layer, is selected to form the structure of the wavelet neural network. To make the structure simpler and the result of the neural network more intuitive, multi-input and single-output structure is employed. According to the characteristics of the training samples, the number of input nodes is chosen as 5 which is equal to the number of feature parameters; the number of output nodes is 1. The number of hidden layer nodes is chosen as 8 according to experience. Define the objective values 1, 2, 3, and 4 as the values corresponding to vortex with eccentric, unbalance, misalignment, and normal machinery conditions, respectively. Choose 2 groups of feature samples for each of the 4 conditions as training samples and 1 group of feature samples for each of the 4 conditions as testing samples. The normalized training and testing feature samples are shown in Tables 1 and 2, respectively [5, 8].

Table 1: Training samples.

Fault types	(0.4–0.5)f	1f	2f	3f	>3f	Object values
Vortex with eccentric	**0.88**	**0.22**	**0.02**	**0.04**	**0.06**	**1**
Vortex with eccentric	0.85	0.25	0.06	0.02	0.01	1
Unbalance	0.04	0.98	0.10	0.02	0.02	2
Unbalance	0.03	0.96	0.12	0.04	0.03	2
Misalignment	0.02	0.41	0.43	0.34	0.15	3
Misalignment	0.02	0.45	0.42	0.28	0.29	3
Normal	0.01	0.02	0.01	0.05	0.04	4
Normal	0.10	0.03	0.02	0.03	0.04	4

Table 2: Testing samples.

Fault types	(0.4–0.5)f	1f	2f	3f	>3f	Object values
Vortex with eccentric	**0.82**	**0.28**	**0.05**	**0.04**	**0.03**	**1**
Unbalance	0.02	0.91	0.08	0.01	0.02	2
Misalignment	0.01	0.48	0.48	0.36	0.20	3
Normal	0.10	0.03	0.02	0.03	0.04	4

Table 3: Diagnosis results of three methods.

Fault types	Wavelet neural network	ACO wavelet neural network	ACO-initialized wavelet neural network	Object values
Vortex with eccentric	**1.1073**	**1.0925**	**1.0955**	**1**
Unbalance	1.8307	2.1806	2.0564	2
Misalignment	2.7499	2.8566	2.9255	3
Normal	3.9745	3.9700	3.9723	4

5.2. Model Parameters Selection and Diagnosis Results. In this example, the number of iterations is set as 10, the number of ants in an ant colony is set as 10, Q is set as 1, ρ is set as 0.6, and the random number N is set as 20. Wavelet basis function is set as commonly used Morlet wavelet function $h(t) = \cos(1.75t)\exp(-(1/2)t^2)$, learning factor η is set as 0.05, and the objective error E is set as 0.01.

In order to prove the effectiveness of the ACO-initialized wavelet neural network, ACO wavelet neural network and traditional wavelet neural network are chosen as comparison methods in the same computer and with the same parameters. Figures 3 and 4 show the training line of the traditional wavelet neural network and the ACO-initialized wavelet neural network, respectively. It can be seen from these figures that the traditional neural network needs 958 training times to reach the objective error, while the ACO-initialized wavelet neural network needs only 63 training times to reach the objective error.

Using the testing samples in Table 2 to test the obtained ACO-initialized wavelet neural network, the ACO wavelet neural network, and the traditional wavelet neural network, Table 3 shows the test results.

Table 4 demonstrates the diagnosis error and training time of the three kinds of networks. Here, the training time of the ACO-initialized wavelet neural network is the sum of 10 times ACO initializing training time (0.4531 s) and wavelet neural network training time (0.1563 s). The unit of the numbers in Table 4 is second.

Table 4: Error and training time of three methods.

Diagnosing methods	Wavelet neural network	ACO wavelet neural network	ACO-initialized wavelet neural network
Diagnosing error	**0.0517**	**0.0313**	**0.0093**
Training time/s	2.3438	9.3281	0.6094

5.3. Analysis of the Diagnosis Results. According to Tables 3 and 4 and Figures 3 and 4, analysis of the results can be obtained as follows.

(1) All three kinds of neural networks can recognize fault types of the hydroturbine generating unit.

(2) Compared with the traditional neural network, ACO wavelet neural network has higher generalization ability, but it needs more computer time to finish the training process.

(3) The training time of the ACO-initialized wavelet neural network is 0.6094 s, and its diagnosing error

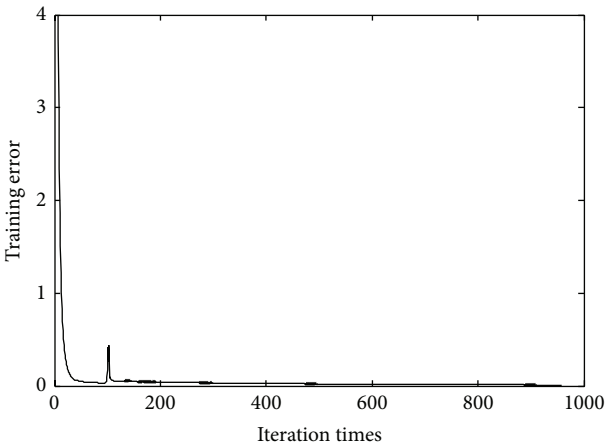

Figure 3: Training curve of wavelet network.

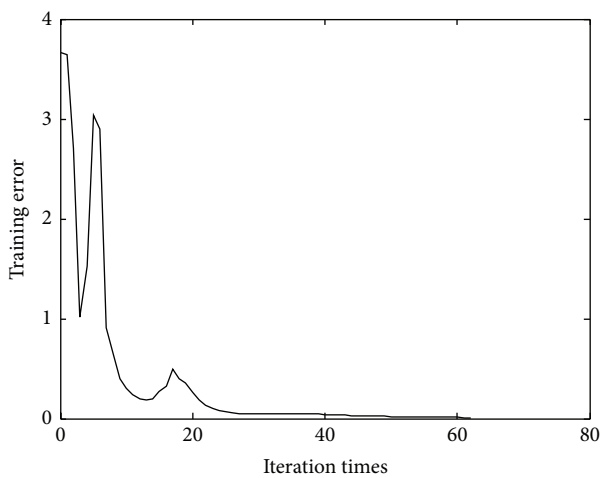

Figure 4: Training curve of ACO-initialized wavelet network.

is 0.0093. Compared with the other two types of neural networks, the proposed network not only has higher generalization ability but also increases the convergence speed. Thus, the ACO-initialized wavelet neural network is more suited to online vibration fault diagnosis for hydroturbine generating unit.

6. Conclusions

Wavelet neural network is sensitive to initial parameters. In other words, when the parameters are initialized improperly, the convergence speed of the neural network will become slower and its generalization ability will become worse. This constrains its application in the hydroturbine generating unit fault diagnosis. In this paper, the advantages of both ACO algorithm and wavelet neural network are combined and the parameters optimized by the ACO algorithm are used as the initialized parameters of the wavelet neural network. The wavelet neural network is trained further and the trained wavelet neural network is applied to vibration fault diagnosis of a hydroturbine generating unit. The method proposed in this paper can determine the initial parameters of the wavelet neural network and also has the time-frequency location property of wavelet neural network and global optimization ability of the ACO algorithm. By using the extracted features of amplitude of frequency components of hydroturbine generating unit vibration signals, the traditional wavelet neural network, the ACO wavelet neural network, and the ACO-initialized wavelet neural network are compared with each other. The results show that the ACO-initialized wavelet neural network has stronger generalization ability and faster convergence speed and thus is more suitable to diagnose the vibration faults of a hydroturbine generating unit online.

Conflict of Interests

The authors declare that there is no conflict of interests regarding the publication of this paper.

Acknowledgment

The authors acknowledge the supports from the National Natural Science Foundation of China under Grant no. 51379160.

References

[1] D.-L. Zhao, W. Ma, W.-K. Liang, and X.-Q. Luo, "Data fusion fault diagnosis and simulation of hydroelectric units vibration," *Proceedings of the Chinese Society of Electrical Engineering*, vol. 25, no. 20, pp. 137–142, 2005 (Chinese).

[2] D. Shen, F. Chu, and S. Chen, "Diagnosis and identification of vibration accident for hydro-generator unit," *Journal of Hydrodynamics*, vol. 15, no. 1, pp. 129–133, 2000 (Chinese).

[3] X. Fu, G.-L. Liu, and J. Jiang, "Application of BP neural networks to condition monitoring and fault diagnosis system of hydro-generator units," *Engineering Journal of Wuhan University*, vol. 35, no. 1, pp. 24–28, 2002 (Chinese).

[4] R. Jia, L. Bai, X. Luo, and F. Liu, "Expert system on fault diagnosis based on neural network for hydropower units," *Journal of Hydroelectric Engineering*, vol. 23, no. 6, pp. 120–123, 2004.

[5] X. Yang, J. Xie, and C. Sun, "Neural network method for vibration fault diagnosis of hydroelectric generating set," *Journal of Hydraulic Engineering*, supplement 1, pp. 94–97, 1998 (Chinese).

[6] W. Peng, P. Guo, and X. Luo, "Research on vibration fault diagnosis of hydro-turbine generating unit based on LS-SVM and information fusion technology," *Journal of Hydroelectric Engineering*, vol. 26, no. 6, pp. 137–142, 2007.

[7] D. Zhang and L. Yu, "Exponential state estimation for Markovian jumping neural networks with time-varying discrete and distributed delays," *Neural Networks*, vol. 35, pp. 103–111, 2012.

[8] W. Peng and X. Luo, "Research on vibration fault diagnosis of hydro-turbine generating unit based on wavelet neural network," *Journal of Hydroelectric Engineering*, vol. 26, no. 1, pp. 123–128, 2007 (Chinese).

[9] Q. Zhang and A. Benveniste, "Wavelet networks," *IEEE Transactions on Neural Networks*, vol. 3, no. 6, pp. 889–898, 1992.

[10] R. Cheng and Y. Bai, "A novel approach to fuzzy wavelet neural network modeling and optimization," *International Journal of Electrical Power & Energy Systems*, vol. 64, pp. 671–678, 2015.

[11] Z. Zainuddin and O. Pauline, "Modified wavelet neural network in function approximation and its application in prediction of time-series pollution data," *Applied Soft Computing Journal*, vol. 11, no. 8, pp. 4866–4874, 2011.

[12] J. Cao, Z. Lin, and G.-B. Huang, "Composite function wavelet neural networks with extreme learning machine," *Neurocomputing*, vol. 73, no. 7-9, pp. 1405–1416, 2010.

[13] T.-S. Wang and L.-P. Zhang, "Application of immune wavelet network model to fault diagnosis of hydro-turbine generating units," *Journal of Hydraulic Engineering*, vol. 40, no. 6, pp. 762–767, 2009 (Chinese).

[14] L. Zuo, L.-G. Hou, D.-M. Gao, X.-H. Peng, and W.-C. Wu, "Fault diagnosis of analog circuit based on PSO-WNN," *Journal of Beijing University of Technology*, vol. 36, no. 3, pp. 306–309, 2010 (Chinese).

[15] D. Feng, *Application Research of Ant Colony Algorithm and Wavelet Network in Complexity Science*, Tianjin University, Tianjin, China, 2008, (Chinese).

[16] L. Liu, Y. Li, and W. Wang, "Fault diagnosis study on the vibration of hydropower units based on GA neural network and evidence theory fusion," *Journal of Hydroelectric Engineering*, vol. 27, no. 5, pp. 163–167, 2008.

Hindawi Publishing Corporation
Mathematical Problems in Engineering
Volume 2015, Article ID 341839, 10 pages
http://dx.doi.org/10.1155/2015/341839

Research Article

New Results on Passivity for Discrete-Time Stochastic Neural Networks with Time-Varying Delays

Wei Kang,[1,2] Jun Cheng,[3] and Xiangyang Cheng[4]

[1] *School of Mathematical Sciences, University of Electronic Science and Technology of China, Chengdu 611731, China*
[2] *School of Information Engineering, Fuyang Teachers College, Fuyang 236041, China*
[3] *School of Electrical and Information Technology, Yunnan Minzu University, Kunming 650500, China*
[4] *School of Business, Fuyang Teachers College, Fuyang 236041, China*

Correspondence should be addressed to Wei Kang; kangwei0830@163.com

Received 30 November 2014; Accepted 24 December 2014

Academic Editor: Yun-Bo Zhao

Copyright © 2015 Wei Kang et al. This is an open access article distributed under the Creative Commons Attribution License, which permits unrestricted use, distribution, and reproduction in any medium, provided the original work is properly cited.

The problem of passivity analysis for discrete-time stochastic neural networks with time-varying delays is investigated in this paper. New delay-dependent passivity conditions are obtained in terms of linear matrix inequalities. Less conservative conditions are obtained by using integral inequalities to aid in the achievement of criteria ensuring the positiveness of the Lyapunov-Krasovskii functional. At last, numerical examples are given to show the effectiveness of the proposed method.

1. Introduction

Neural networks have been greatly applied in many areas in the past few decades, such as static processing, pattern recognition, and combinatorial optimization [1–3]. In practice, time-delays are frequently encountered in neural networks. As the finite signal propagation time and the finite speed of information processing, the existence of the delays may cause oscillation, instability, and divergence in neural networks. Moreover, stochastic perturbations and parameter uncertainties are two main resources which could reduce the performances of delayed neural networks. Due to the importance in both theory and practice, the problem of stability for stochastic delayed neural networks with parameter uncertainties is one of hot issues. Therefore, there have been lots of important and interesting results in this field [3–17].

It should be noticed that most neural networks are focused on continuous-time case [3, 7–12]. However, discrete-time systems play crucial roles in today's information society. Particulary, when implementing the delayed continuous-time neural networks for computer simulation, it needs to formulate discrete-time system. Thus, it is necessary to research the dynamics of discrete-time neural networks. In recent years, a lot of important results have been published in the literatures [13–17]. Kwon et al. [14] discussed the stability criteria for the discrete-time system with time varying delays. Wang et al. [16] researched the exponential stability of discrete-time neural networks with distributed delays by means of Lyapunov-Krasovskill functional theory and linear matrix inequalities technology. In [17], the authors are concerned with the robust state estimation for discrete neural networks with successive packet dropouts, linear fractional uncertainties, and mixed time-delays.

On the other hand, passivity is a significant concept that represents input-output feature of dynamic systems, which can offer a powerful tool for analyzing mechanical systems, nonlinear systems, and electrical circuits [18]. The passivity theory was firstly presented in the circuit analysis [19]. During the past several decades, the passivity theory has found successful applications in various areas such as complexity, signal processing, stability, chaos control, and fuzzy control. Thus, the problem of passivity for time-delay neural networks has received much attention and lots of effective approaches have been proposed in this research area [20–27]. The authors [21, 22] discussed the problem of passivity for neural networks with time-delays. Recently, Lee et al. [23] further studied the problem of dissipative analysis for neural networks with times-delays by using reciprocally convex approach and

linear matrix inequality technology. Very recently, in [24], the problem of passivity criterion of discrete-time stochastic bidirectional associative memory neural networks with time-varying delays has been developed. In [25], some delay-dependent sufficient passivity conditions have been obtained for stochastic discrete-time neural networks with time-varying delays in terms of linear matrix inequalities technology and free-weighting matrices approach. A less conservative passivity criterion for discrete-time stochastic neural networks with time-varying delays was derived in [26]. However, there is still a room for decreasing the conservatism.

Motivated by the above discussion, the problem of passivity for discrete-time stochastic neural networks with time-varying delays is studied. The major contribution of this paper lies in that, first of all, different from the traditional way, a new inequality is introduced to deal with terms $\sum_{i=k-\tau_m}^{k-1} \eta^T(i)T_1\eta(i)$ and $\sum_{i=k-\tau_M}^{k-\tau_m-1} \eta^T(i)T_1\eta(i)$. This method can effectively reduce the conservatism. Secondly, we do not need all the symmetric matrices in the Lyapunov functional to be positive definite and take advantage of the relationships of $\tau(k)-\tau_m$ and $\tau_M-\tau(k)$. New passivity conditions are presented in terms of matrix inequalities. Finally, numerical examples are given to indicate the effectiveness of the proposed method.

Notations. Throughout this paper, the superscripts "-1" and "T" stand for the inverse and transpose of a matrix, respectively; $P>0$ ($P\geqslant 0$, $P<0$, $P\leqslant 0$) means that the matrix P is symmetric positive definite (positive semidefinite, negative definite, and negative semidefinite); $E\{\cdot\}$ stands for the mathematical expectation operator with respect to the given probability measure; $\|\cdot\|$ refers to the Euclidean vector norm; $(\Omega,\mathscr{F},\mathscr{P})$ denotes a complete probability space with a filtration containing all p-null sets and is right conditions; $N[a,b]$ denotes the discrete interval given $N[a,b]=\{a,a+1,\ldots,b-1,b\}$; R^n denotes n-dimensional Euclidean space; $R^{m\times n}$ is the set of $m\times n$ real matrices; $*$ denotes the symmetric block in symmetric matrix; $\lambda_{\max}(Q)$ and $\lambda_{\min}(Q)$ denote, respectively, the maximal and minimal eigenvalue of matrix Q.

2. Problem Statement and Preliminaries

Consider the following DSNN with time-varying delays:

$$\begin{aligned} x(k+1) &= Ax(k)+B_1g(x(k))+B_2g(x(k-\tau(k)))\\ &\quad +u(k)+\delta(x(k),x(k-\tau(k)))\,\omega(k),\\ y(k) &= g(x(k)),\\ x(j) &= \psi(j),\quad j=-\tau_M,-\tau_M+1,\ldots,0, \end{aligned} \tag{1}$$

where $x(k)=[x_1(k),x_2(k),\ldots,x_n(k)]^T\in R^n$ is the neuron state vector of the system; $y(k)$ is the output of the neural networks; $u(k)=[u_1(k),u_2(k),\ldots,u_n(k)]^T$ is the input vector; $\psi(j)$ is the initial condition; $A=\operatorname{diag}(a_1,a_2,\ldots,a_n)$ is the state feedback coefficient matrix; B_1 and B_2 are the connection weight matrices and the delayed connection weight matrices, respectively; $g(x(k))=[g_1(x_1(k)),g_2(x_2(k)),\ldots,g_n(x_n(k))]^T\in R^n$ represents the neuron activation functions; $\tau(k)$ denotes the known time-varying delay and satisfies $0<\tau_m\leq\tau(k)\leq\tau_M$; δ is diffusion coefficient vector and $\omega(k)$ is a scalar Brownian motion defined on the probability space $(\Omega,\mathscr{F},\mathscr{P})$ with

$$\begin{aligned} E\{\omega(k)\} &= 0,\\ E\{\omega(k)\,\omega(k)\} &= 1,\\ E\{\omega(i)\,\omega(j)\} &= 0,\quad (i\neq j). \end{aligned} \tag{2}$$

Assumption 1. The neuron activation function $g(\cdot)$ satisfies

$$l_s^-\leqslant\frac{g_s(a)-g_s(b)}{a-b}\leqslant l_s^+,\quad g_s(0)=0,\ s=1,2,\ldots,n, \tag{3}$$

for all $a,b\in R$, $a\neq b$, where l_s^- and l_s^+ are known real constants.

Remark 2. In Assumption 1, l_s^- and l_s^+ can be positive, negative, or zero. Moreover, when $l_s^-=0$, then $l_s^+>0$.

Assumption 3. $\delta(x(k),x(k-\tau(k)))$ is the continuous function satisfying

$$\begin{aligned} &\delta^T(x(k),x(k-\tau(k)))\,\delta(x(k),x(k-\tau(k)))\\ &\quad\leq\rho_1x^T(k)\,x(k)+\rho_2x^T(k-\tau(k))\,x(k-\tau(k)), \end{aligned} \tag{4}$$

where ρ_1,ρ_2 are known constant scalars.

The following lemmas and definition will be used in proof of main results.

Lemma 4. *For integers $\tau(k)$ and vector function $x(k+\cdot):N[-\tau_M,-\tau_m]\mapsto R^n$, $\eta(k)=x(k+1)-x(k)$, for any positive semidefinite matrix*

$$X=\begin{bmatrix} X_{11} & X_{12} & X_{13}\\ X_{12}^T & X_{22} & X_{23}\\ X_{13}^T & X_{23}^T & X_{33}\end{bmatrix}\geq 0, \tag{5}$$

the following inequality holds:

$$\begin{aligned} &-\sum_{i=k-\tau(k)}^{k-1}\eta^T(i)\,X_{33}\eta(i)\\ &\quad\leq\sum_{i=k-\tau(k)}^{k-1}\left[x^T(k)\ \ x^T(k-\tau(k))\ \ \eta^T(i)\right]\\ &\qquad\cdot\begin{bmatrix} X_{11} & X_{12} & X_{13}\\ X_{12}^T & X_{22} & X_{23}\\ X_{13}^T & X_{23}^T & 0\end{bmatrix}\begin{bmatrix} x(k)\\ x(k-\tau(k))\\ \eta(i)\end{bmatrix}. \end{aligned} \tag{6}$$

Proof. In fact, we have

$$\begin{aligned}0 &\le \sum_{i=k-\tau(k)}^{k-1}\left[x^T(k)\ \ x^T(k-\tau(k))\ \ \eta^T(i)\right]\\ &\qquad\cdot\begin{bmatrix}X_{11} & X_{12} & X_{13}\\ X_{12}^T & X_{22} & X_{23}\\ X_{13}^T & X_{23}^T & X_{33}\end{bmatrix}\begin{bmatrix}x(k)\\ x(k-\tau(k))\\ \eta(i)\end{bmatrix}\\ &= \sum_{i=k-\tau(k)}^{k-1}\Bigg(\eta^T(i)X_{33}\eta(i)\\ &\qquad+\left[x^T(k)\ \ x^T(k-\tau(k))\ \ \eta^T(i)\right]\\ &\qquad\cdot\begin{bmatrix}X_{11} & X_{12} & X_{13}\\ X_{12}^T & X_{22} & X_{23}\\ X_{13}^T & X_{23}^T & 0\end{bmatrix}\begin{bmatrix}x(k)\\ x(k-\tau(k))\\ \eta(i)\end{bmatrix}\Bigg).\end{aligned} \tag{7}$$

Thus, one can easily obtain

$$\begin{aligned}&-\sum_{i=k-\tau(k)}^{k-1}\eta^T(i)X_{33}\eta(i)\\ &\quad\le \sum_{i=k-\tau(k)}^{k-1}\left[x^T(k)\ \ x^T(k-\tau(k))\ \ \eta^T(i)\right]\\ &\qquad\cdot\begin{bmatrix}X_{11} & X_{12} & X_{13}\\ X_{12}^T & X_{22} & X_{23}\\ X_{13}^T & X_{23}^T & 0\end{bmatrix}\begin{bmatrix}x(k)\\ x(k-\tau(k))\\ \eta(i)\end{bmatrix}.\end{aligned} \tag{8}$$

The proof is completed. □

Remark 5. The new inequality was proposed in [5, 6] for continuous-time systems; it is worth noting that we firstly extend this method to study discrete-time neural networks in this paper.

Lemma 6 (see [4, 13]). *Let $M \in R^{n\times n}$ be a positive-definite matrix, $X_i \in R^n$; then*

$$\begin{aligned}&-(m-n)\sum_{i=k-m}^{k-n-1}X_i^T M X_i\\ &\quad\leqslant -\left(\sum_{i=k-m}^{k-n-1}X_i\right)^T M\left(\sum_{i=k-m}^{k-n-1}X_i\right).\end{aligned} \tag{9}$$

Lemma 7 (see [24]). *Let $A = A^T, D, E$ be real matrices with appropriate dimensions, with matrix $F(k)$ satisfying $F^T(k)F(k) \le I$; there exists a scalar $\varepsilon > 0$ such that*

$$A + DF(t)E + E^T F^T(t) D^T \le A + \varepsilon DD^T + \varepsilon^{-1}E^T E. \tag{10}$$

Lemma 8 (see [3]). *For any constant matrices Ω, Υ_1, Υ_2 with appropriate dimensions, and a function $\tau(k)$ satisfying $\tau_m \le \tau(k) \le \tau_M$, then*

$$\Omega + (\tau(k)-\tau_m)\Upsilon_1 + (\tau_M - \tau(k))\Upsilon_2 < 0, \tag{11}$$

if and only if

$$\begin{aligned}&\Omega + (\tau_M-\tau_m)\Upsilon_1 < 0,\\ &\Omega + (\tau_M-\tau_m)\Upsilon_2 < 0.\end{aligned} \tag{12}$$

Definition 9 (see [25]). The system (1) is said to be passive if there exists a scalar $\gamma > 0$ satisfying

$$2\sum_{i=0}^{k_0}E\left\{y^T(i)u(i)\right\} \ge -\gamma\sum_{i=0}^{k_0}E\left\{u^T(i)u(i)\right\}, \tag{13}$$

for all $k_0 \in N$ and for all solution of (1) with $\psi(0) = 0$.

3. Main Results

In this section, the passivity of discrete-time stochastic neural networks with time-varying delays will be investigated by use of the new integral inequality and Lyapunov method. In the paper, some of symmetric matrices in Lyapunov-Krasovskii functional are not necessarily required to be positive definite.

Denote

$$\begin{aligned}L_1 &= \operatorname{diag}\{l_1^- l_1^+, \ldots, l_n^- l_n^+\},\\ L_2 &= \operatorname{diag}\left\{\frac{l_1^- + l_1^+}{2}, \ldots, \frac{l_n^- + l_n^+}{2}\right\},\\ \tau_{Mm} &= \tau_M - \tau_m,\\ \eta(k) &= x(k+1) - x(k).\end{aligned} \tag{14}$$

Main results are given in the following theorems.

Theorem 10. *Under Assumptions 1 and 3, the discrete-time stochastic neural network (1) is passive, if there exist matrices P, $R_1, R_2, Q = \begin{bmatrix}Q_{11} & Q_{12}\\ * & Q_{22}\end{bmatrix} > 0$, $T_1 > 0$, $T_2 > 0$, $X = \begin{bmatrix}X_{11} & X_{12} & X_{13}\\ * & X_{22} & X_{23}\\ * & * & X_{33}\end{bmatrix} \ge 0$, $Y = \begin{bmatrix}Y_{11} & Y_{12} & Y_{13}\\ * & Y_{22} & Y_{23}\\ * & * & Y_{33}\end{bmatrix} \ge 0$, $Z = \begin{bmatrix}Z_{11} & Z_{12} & Z_{13}\\ * & Z_{22} & Z_{23}\\ * & * & Z_{33}\end{bmatrix} \ge 0$, the positive diagonal matrices $S_k = \operatorname{diag}\{s_{1k}, s_{2k}, \ldots, s_{nk}\}$ $(k = 1, 2)$, and scalars $\lambda > 0$, $\gamma > 0$, such that the following matrix inequalities hold:*

$$\begin{aligned}&\begin{bmatrix}T_1 + \dfrac{\tau_m}{\tau_M}P & -T_1\\ * & T_1 + \tau_m R_1\end{bmatrix} > 0,\\ &\begin{bmatrix}T_2 + P & -T_2\\ * & T_2 + \tau_M R_2\end{bmatrix} > 0,\end{aligned} \tag{15}$$

$$\begin{aligned}&T_1 - X_{33} \ge 0,\\ &T_2 - Y_{33} \ge 0,\\ &T_2 - Z_{33} \ge 0,\\ &\Theta \le \lambda I,\end{aligned} \tag{16}$$

$$\begin{aligned}&\Omega + \Upsilon_1 < 0,\\ &\Omega + \Upsilon_2 < 0,\end{aligned} \tag{17}$$

where

$$\Theta = P + \tau_m T_1 + \tau_{Mm} T_2,$$

$$\Omega = \begin{bmatrix} \Omega_{11} & \cdots & \Omega_{17} \\ * & \ddots & \vdots \\ * & * & \Omega_{77} \end{bmatrix},$$

$$\Upsilon_1 = \begin{bmatrix} d_{11} & \cdots & d_{17} \\ * & \ddots & \vdots \\ * & * & d_{77} \end{bmatrix},$$

$$\Upsilon_2 = \begin{bmatrix} e_{11} & \cdots & e_{17} \\ * & \ddots & \vdots \\ * & * & e_{77} \end{bmatrix},$$

$$\begin{aligned}
\Omega_{11} &= (\tau_{Mm} + 1) Q_{11} + R_1 + \tau_m X_{11} + X_{13} + X_{13}^T \\
&\quad + \tau_m (A - I) T_1 (A - I) + \tau_{Mm} (A - I) T_2 (A - I) \\
&\quad + \rho_1 \lambda I + APA - P - S_1 L_1, \\
\Omega_{12} &= \tau_m X_{12} - X_{13} + X_{23}^T, \\
\Omega_{15} &= (\tau_{Mm} + 1) Q_{12} + L_2 S_1 + \tau_m (A - I) T_1 B_1 \\
&\quad + \tau_{Mm} (A - I) T_2 B_1 + A^T P B_1, \\
\Omega_{16} &= \tau_m (A - I) T_1 B_1 + \tau_{Mm} (A - I) T_2 B_1 + APB_1, \\
\Omega_{17} &= \tau_m (A - I) T_1 + \tau_{Mm} (A - I) T_2 + AP, \\
\Omega_{22} &= -R_1 + R_2 + \tau_m X_{22} - X_{23} - X_{23}^T + Y_{13} + Y_{13}^T, \\
\Omega_{23} &= -Y_{13} + Y_{23}^T, \\
\Omega_{33} &= -Q_{11} - S_2 L_1 + \rho_2 \lambda I - Y_{23} - Y_{23}^T + Z_{13} + Z_{13}^T, \\
\Omega_{34} &= -Z_{13} + Z_{23}^T, \\
\Omega_{36} &= -Q_{12} + L_2 S_2, \\
\Omega_{44} &= -R_2 - Z_{23} - Z_{23}^T, \\
\Omega_{55} &= B_1^T P B_1 + \tau_m B_1^T T_1 B_1 + \tau_{Mm} B_1^T T_2 B_1 \\
&\quad + (\tau_{Mm} + 1) Q_{22} - S_1, \\
\Omega_{56} &= B_1^T P B_2 + \tau_m B_1^T T_1 B_2 + \tau_{Mm} B_1^T T_2 B_2, \\
\Omega_{57} &= B_1^T P + \tau_m B_1^T T_1 + \tau_{Mm} B_1^T T_2 - I, \\
\Omega_{66} &= B_2^T P B_2 + \tau_m B_2^T T_1 B_2 + \tau_{Mm} B_2^T T_2 B_2 \\
&\quad - Q_{22} - S_2, \\
\Omega_{67} &= B_2^T P + \tau_m B_2^T T_1 + \tau_{Mm} B_2^T T_2, \\
\Omega_{77} &= P + \tau_m T_1 + \tau_{Mm} T_2 - \gamma I, \\
d_{22} &= Y_{11}, \\
d_{23} &= Y_{12}, \\
d_{33} &= Y_{22}, \\
e_{33} &= Z_{11}, \\
e_{34} &= Y_{12}, \\
d_{44} &= Z_{22}, \quad \textit{elsewhere}, \\
\Omega_{ij} &= 0, \\
d_{ij} &= 0, \\
e_{ij} &= 0, \\
i, j &= 1, 2, \ldots, 8.
\end{aligned} \tag{18}$$

Proof. Define a new augmented of Lyapunov-Krasovskii functional as follows:

$$V(k) = V_1(k) + V_2(k) + V_3(k) + V_4(k), \tag{19}$$

where

$$\begin{aligned}
V_1(k) &= x^T(k) P x(k), \\
V_2(k) &= \sum_{i=k-\tau_m}^{k-1} x^T(i) R_1 x(i) + \sum_{i=k-\tau_M}^{k-\tau_m-1} x^T(i) R_2 x(i), \\
V_3(k) &= \sum_{i=k-\tau(k)}^{k-1} \begin{bmatrix} x(i) \\ g(x(i)) \end{bmatrix}^T \begin{bmatrix} Q_{11} & Q_{12} \\ * & Q_{22} \end{bmatrix} \begin{bmatrix} x(i) \\ g(x(i)) \end{bmatrix} \\
&\quad + \sum_{j=-\tau_M}^{-\tau_m-1} \sum_{i=k+j}^{k-1} \begin{bmatrix} x(i) \\ g(x(i)) \end{bmatrix}^T \begin{bmatrix} Q_{11} & Q_{12} \\ * & Q_{22} \end{bmatrix} \begin{bmatrix} x(i) \\ g(x(i)) \end{bmatrix}, \\
V_4(k) &= \sum_{j=-\tau_m}^{-1} \sum_{i=k+j}^{k-1} \eta^T(i) T_1 \eta(i) \\
&\quad + \sum_{j=-\tau_M}^{-\tau_m-1} \sum_{i=k+j}^{k-1} \eta^T(i) T_2 \eta(i).
\end{aligned} \tag{20}$$

Firstly, we show that the Lyapunov-Krasovskii functional $V(k)$ is positive definite. By using Lemma 6, one can obtain

$$\begin{aligned}
&\sum_{j=-\tau_m}^{-1} \sum_{i=k+j}^{k-1} \eta^T(i) T_1 \eta(i) \\
&\quad \geq \sum_{j=-\tau_m}^{-1} \frac{-1}{j} \left(\sum_{i=k+j}^{k-1} \eta(i) \right)^T T_1 \left(\sum_{i=k+j}^{k-1} \eta(i) \right) \\
&\quad = \sum_{j=-\tau_m}^{-1} \frac{-1}{j} \begin{bmatrix} x(k) \\ x(k+j) \end{bmatrix}^T \begin{bmatrix} T_1 & -T_1 \\ * & T_1 \end{bmatrix} \begin{bmatrix} x(k) \\ x(k+j) \end{bmatrix} \\
&\quad \geq \frac{1}{\tau_m} \sum_{i=k-\tau_m}^{k-1} \begin{bmatrix} x(k) \\ x(i) \end{bmatrix}^T \begin{bmatrix} T_1 & -T_1 \\ * & T_1 \end{bmatrix} \begin{bmatrix} x(k) \\ x(i) \end{bmatrix},
\end{aligned}$$

$$\begin{aligned}
&\sum_{j=-\tau_M}^{-\tau_m-1}\sum_{i=k+j}^{k-1}\eta^T(i)T_2\eta(i)\\
&\quad\geq \sum_{j=-\tau_M}^{-\tau_m-1}\frac{-1}{j}\left(\sum_{i=k+j}^{k-1}\eta(i)\right)^T Z_2\left(\sum_{i=k+j}^{k-1}\eta(i)\right)\\
&\quad= \sum_{j=-\tau_M}^{-\tau_m-1}\frac{-1}{j}\begin{bmatrix}x(k)\\x(k+j)\end{bmatrix}^T\begin{bmatrix}T_1 & -T_1\\ * & T_1\end{bmatrix}\begin{bmatrix}x(k)\\x(k+j)\end{bmatrix}\\
&\quad\geq \frac{1}{\tau_M}\sum_{i=k-\tau_M}^{k-\tau_m-1}\begin{bmatrix}x(k)\\x(i)\end{bmatrix}^T\begin{bmatrix}T_2 & -T_2\\ * & T_2\end{bmatrix}\begin{bmatrix}x(k)\\x(i)\end{bmatrix},
\end{aligned}\tag{21}$$

$$\begin{aligned}
&x^T(k)Px(k)\\
&\quad=\sum_{i=k-\tau_m}^{k-1}\frac{1}{\tau_M}x^T(k)Px(k)\\
&\qquad+\sum_{i=k-\tau_M}^{k-\tau_m-1}\frac{1}{\tau_M}x^T(k)Px(k).
\end{aligned}\tag{22}$$

Then, it follows from (19)–(21) that

$$\begin{aligned}
V(k)\geq{}&\sum_{i=k-\tau_m}^{k-1}\frac{1}{\tau_M}x^T(k)Px(k)+\sum_{i=k-\tau_M}^{k-\tau_m-1}\frac{1}{\tau_M}x^T(k)Px(k)\\
&+\sum_{i=k-\tau_m}^{k-1}x^T(i)R_1x(i)+\sum_{i=k-\tau_M}^{k-\tau_m-1}x^T(i)R_2x(i)\\
&+\frac{1}{\tau_m}\sum_{i=k-\tau_m}^{k-1}\begin{bmatrix}x(k)\\x(i)\end{bmatrix}^T\begin{bmatrix}T_1 & -T_1\\ * & T_1\end{bmatrix}\begin{bmatrix}x(k)\\x(i)\end{bmatrix}\\
&+\frac{1}{\tau_M}\sum_{i=k-\tau_M}^{k-\tau_m-1}\begin{bmatrix}x(k)\\x(i)\end{bmatrix}^T\begin{bmatrix}T_2 & -T_2\\ * & T_2\end{bmatrix}\begin{bmatrix}x(k)\\x(i)\end{bmatrix}\\
\geq{}&\frac{1}{\tau_m}\sum_{i=k-\tau_m}^{k-1}\begin{bmatrix}x(k)\\x(i)\end{bmatrix}^T\begin{bmatrix}T_1+\frac{\tau_m}{\tau_M}P & -T_1\\ -T_1 & T_1+\tau_mR_1\end{bmatrix}\begin{bmatrix}x(k)\\x(i)\end{bmatrix}\\
&+\frac{1}{\tau_M}\sum_{i=k-\tau_M}^{k-\tau_m-1}\begin{bmatrix}x(k)\\x(i)\end{bmatrix}^T\begin{bmatrix}T_2+P & -T_2\\ -T_2 & T_2+\tau_mR_2\end{bmatrix}\begin{bmatrix}x(k)\\x(i)\end{bmatrix}.
\end{aligned}\tag{23}$$

From condition (15), there exists a scalar $\delta_1 > 0$, for any $x(k)\neq 0$, such that

$$V(k)\geq\delta_1\|x(k)\|^2>0.\tag{24}$$

Now, taking the forward difference of $V(k)$ along the trajectories of system (1), it yields that

$$\begin{aligned}
&E\{\Delta V_1(k)\}\\
&\quad=E\left\{(\eta(k)+x(k))^TP(\eta(k)+x(k))-x^T(k)Px(k)\right\}\\
&\quad=E\left\{\eta^T(k)P\eta(k)+2x^T(k)P\eta(k)\right\},\\
&E\{\Delta V_2(k)\}\\
&\quad=E\left\{x^T(k)R_1x(k)-x^T(k-\tau_m)(R_1-R_2)x(k-\tau_m)\right.\\
&\qquad\left.-x^T(k-\tau_M)R_2x(k-\tau_M)\right\},\\
&E\{\Delta V_3(k)\}\\
&\quad\leq E\left\{(\tau_{Mm}+1)\begin{bmatrix}x(k)\\g(x(k))\end{bmatrix}^T\begin{bmatrix}Q_{11} & Q_{12}\\ * & Q_{22}\end{bmatrix}\begin{bmatrix}x(k)\\g(x(k))\end{bmatrix}\right.\\
&\qquad-\begin{bmatrix}x(k-\tau(k))\\g(x(k-\tau(k)))\end{bmatrix}^T\begin{bmatrix}Q_{11} & Q_{12}\\ * & Q_{22}\end{bmatrix}\\
&\qquad\left.\cdot\begin{bmatrix}x(k-\tau(k))\\g(x(k-\tau(k)))\end{bmatrix}\right\}\\
&\quad=E\left\{(\tau_{Mm}+1)x^T(k)Q_{11}x(k)+2x^T(k)Q_{12}g(x(k))\right.\\
&\qquad+g^T(x(k))Q_{22}g(x(k))\\
&\qquad-x^T(k-\tau(k))Q_{11}x(k-\tau(k))\\
&\qquad-2x^T(k-\tau(k))Q_{12}g(x(k-\tau(k)))\\
&\qquad\left.-g^T(x(k-\tau(k)))Q_{22}g(x(k-\tau(k)))\right\},\\
&E\{\Delta V_4(k)\}\\
&\quad=E\left\{\eta^T(k)(\tau_mT_1+\tau_{Mm}T_2)\eta(k)-\sum_{i=k-\tau_m}^{k-1}\eta^T(i)T_1\eta(i)\right.\\
&\qquad\left.-\sum_{i=k-\tau(k)}^{k-\tau_m-1}\eta^T(i)T_2\eta(i)-\sum_{i=k-\tau_M}^{k-\tau(k)-1}\eta^T(i)T_2\eta(i)\right\},\\
&E\left\{-\sum_{i=k-\tau_m}^{k-1}\eta^T(i)T_1\eta(i)-\sum_{i=k-\tau(k)}^{k-\tau_m-1}\eta^T(i)T_2\eta(i)\right.\\
&\qquad\left.-\sum_{i=k-\tau_M}^{k-\tau(k)-1}\eta^T(i)T_2\eta(i)\right\}\\
&\quad=E\left\{-\sum_{i=k-\tau_m}^{k-1}\eta^T(i)(T_1-X_{33})\eta(i)\right.\\
&\qquad-\sum_{i=k-\tau(k)}^{k-\tau_m-1}\eta^T(i)(T_2-Y_{33})\eta(i)
\end{aligned}$$

$$-\sum_{i=k-\tau_M}^{k-\tau(k)-1}\eta^T(i)(T_2-Z_{33})\eta(i)-\sum_{i=k-\tau_m}^{k-1}\eta^T(i)X_{33}\eta(i)$$
$$\left.-\sum_{i=k-\tau(k)}^{k-\tau_m-1}\eta^T(i)Y_{33}\eta(i)-\sum_{i=k-\tau_M}^{k-\tau(k)-1}\eta^T(i)Z_{33}\eta(i)\right\}. \tag{25}$$

Form the new inequality of Lemma 4, one can get

$$\begin{aligned}
&-\sum_{i=k-\tau_m}^{k-1}\eta^T(i)X_{33}\eta(i)\\
&\le\sum_{i=k-\tau_m}^{k-1}\left[x^T(k)\ \ x^T(k-\tau_m)\ \ \eta^T(i)\right]\\
&\qquad\cdot\begin{bmatrix}X_{11}&X_{12}&X_{13}\\X_{12}^T&X_{22}&X_{23}\\X_{13}^T&X_{23}^T&0\end{bmatrix}\begin{bmatrix}x(k)\\x(k-\tau_m)\\\eta(i)\end{bmatrix}\\
&=x^T(k)\left(\tau_mX_{11}+X_{13}^T+X_{13}\right)x(k)\\
&\quad+x^T(k)\left(\tau_mX_{12}-X_{13}+X_{23}^T\right)x(k-\tau_m)\\
&\quad+x^T(k-\tau_m)\left(\tau_mX_{12}^T-X_{13}^T+X_{23}\right)x(k)\\
&\quad+x^T(k-\tau_m)\left(\tau_mX_{22}-X_{23}^T-X_{23}\right)x(k-\tau_m),\\
&-\sum_{i=k-\tau(k)}^{k-\tau_m-1}\eta^T(i)Y_{33}\eta(i)\\
&\le\sum_{i=k-\tau(k)}^{k-\tau_m-1}\left[x^T(k-\tau_m)\ \ x^T(k-\tau(k))\ \ \eta^T(i)\right]\\
&\qquad\cdot\begin{bmatrix}X_{11}&X_{12}&X_{13}\\X_{12}^T&X_{22}&X_{23}\\X_{13}^T&X_{23}^T&0\end{bmatrix}\begin{bmatrix}x(k-\tau_m)\\x(k-\tau(k))\\\eta(i)\end{bmatrix}\\
&=x^T(k-\tau_m)\left((\tau(k)-\tau_m)Y_{11}+Y_{13}^T+Y_{13}\right)x(k-\tau_m)\\
&\quad+x^T(k-\tau_m)\left((\tau(k)-\tau_m)Y_{12}-Y_{13}+Y_{23}^T\right)x(k-\tau(k))\\
&\quad+x^T(k-\tau(k))\left((\tau(k)-\tau_m)Y_{12}^T-Y_{13}^T+Y_{23}\right)x(k-\tau_m)\\
&\quad+x^T(k-\tau(k))\left((\tau(k)-\tau_m)Y_{22}-Y_{23}^T-Y_{23}\right)x(k-\tau(k)),\\
&-\sum_{i=k-\tau_M}^{k-\tau(k)-1}\eta^T(i)Z_{33}\eta(i)\\
&\le\sum_{i=k-\tau_M}^{k-\tau(k)-1}\left[x^T(k-\tau(k))\ \ x^T(k-\tau_M)\ \ \eta^T(i)\right]\\
&\qquad\cdot\begin{bmatrix}X_{11}&X_{12}&X_{13}\\X_{12}^T&X_{22}&X_{23}\\X_{13}^T&X_{23}^T&0\end{bmatrix}\begin{bmatrix}x(k-\tau(k))\\x(k-\tau_M)\\\eta(i)\end{bmatrix}\\
&=x^T(k-\tau(k))\left((\tau_M-\tau(k))Z_{11}+Z_{13}^T+Z_{13}\right)x(k-\tau(k))\\
&\quad+x^T(k-\tau(k))\left((\tau_M-\tau(k))Z_{12}-Z_{13}+Z_{23}^T\right)x(k-\tau_M)\\
&\quad+x^T(k-\tau_M)\left((\tau_M-\tau(k))Z_{12}^T-Z_{13}^T+Z_{23}\right)x(k-\tau(k))\\
&\quad+x^T(k-\tau_M)\left((\tau_M-\tau(k))Z_{22}-Z_{23}^T-Z_{23}\right)x(k-\tau_M).
\end{aligned} \tag{26}$$

It is easy to get

$$\begin{aligned}
&E\left\{\eta^T(k)\Theta\eta(k)\right\}\\
&\quad=E\left\{\left[(A-I)x(k)+B_1g(x(k))+B_2g(x(k-\tau(k)))\right.\right.\\
&\qquad\left.+u(k)+\delta(x(k),x(k-\tau(k)))\omega(k)\right]^T\\
&\qquad\cdot\Theta\left[(A-I)x(k)+B_1g(x(k))\right.\\
&\qquad\quad+B_2g(x(k-\tau(k)))\\
&\qquad\quad\left.\left.+u(k)+\delta(x(k),x(k-\tau(k)))\omega(k)\right]\right\}.
\end{aligned} \tag{27}$$

From Assumption 3 and inequality (16), we have

$$\begin{aligned}
&\delta(x(k),x(k-\tau(k)))\Theta\delta(x(k),x(k-\tau(k)))\\
&\quad\le\lambda\left[\rho_1x^T(k)x(k)+\rho_2x^T(k-\tau(k))x(k-\tau(k))\right].
\end{aligned} \tag{28}$$

From Assumption 1, it follows that

$$\begin{aligned}
&\left(g_i(x_i(k))-l_i^+x_i(k)\right)\left(g_i(x_i(k))-l_i^-x_i(k)\right)\le0,\\
&\left(g_i(x_i(k-\tau(k)))-l_i^+x_i(k-\tau(k))\right)\\
&\quad\cdot\left(g_i(x_i(k-\tau(k)))-l_i^-x_i(k-\tau(k))\right)\le0.
\end{aligned} \tag{29}$$

Thus, for the diagonal matrices $S_k=\operatorname{diag}\{s_{1k},s_{2k},\ldots,s_{nk}\}$ $(k=1,2)$, one can receive the following inequalities:

$$\begin{aligned}
&-\begin{bmatrix}x(k)\\g(x(k))\end{bmatrix}^T\begin{bmatrix}S_1L_1&-S_1L_2*&S_1\end{bmatrix}\begin{bmatrix}x(k)\\g(x(k))\end{bmatrix}\ge0,\\
&-\begin{bmatrix}x(k-\tau(k))\\g(x(k-\tau(k)))\end{bmatrix}^T\\
&\quad\cdot\begin{bmatrix}S_2L_1&-S_2L_2*&S_2\end{bmatrix}\begin{bmatrix}x(k-\tau(k))\\g(x(k-\tau(k)))\end{bmatrix}\ge0.
\end{aligned} \tag{30}$$

Combining (25)–(30), it yields

$$\begin{aligned} &E\left\{\Delta V(k)-2y^T(k)u(k)-\gamma u^T(k)u(k)\right\} \\ &\quad\le E\left\{\alpha^T(k)\left(\Omega+\left(\tau(k)-\tau_m\right)\Upsilon_1+\left(\tau_M-\tau(k)\right)\Upsilon_2\right)\alpha(k)\right. \\ &\qquad -\sum_{i=k-\tau_m}^{k-1}\eta^T(i)\left(T_1-X_{33}\right)\eta(i) \\ &\qquad -\sum_{i=k-\tau(k)}^{k-\tau_m-1}\eta^T(i)\left(T_2-Y_{33}\right)\eta(i) \\ &\qquad \left.-\sum_{i=k-\tau_M}^{k-\tau(k)-1}\eta^T(i)\left(T_2-Z_{33}\right)\eta(i)\right\}, \end{aligned} \tag{31}$$

where

$$\begin{aligned} \alpha^T(k)=&\left[x^T(k),x^T\left(k-\tau_m\right),x^T(k-\tau(k)),x^T\left(k-\tau_M\right),\right. \\ &\left.g^T(x(k)),g^T(x(k-\tau(k))),u^T(k)\right]. \end{aligned} \tag{32}$$

From (15)–(17), observing that $T_1-X_{33}\ge 0$, $T_2-Y_{33}\ge 0$, and $T_2-Z_{33}\ge 0$, one can conclude that

$$E\left\{\Delta V(k)-2y^T(k)u(k)-\gamma u^T(k)u(k)\right\}\le 0. \tag{33}$$

Then,

$$\begin{aligned} 2\sum_{i=0}^{k_0}E\left\{y^T(i)u(i)\right\}\ge&\sum_{i=0}^{k_0}E\left\{\Delta V(i)\right\} \\ &-\gamma\sum_{i=0}^{k_0}E\left\{u^T(i)u(i)\right\}. \end{aligned} \tag{34}$$

By the definition of $V(k)$ and inequality (23), one can find that

$$\sum_{i=0}^{k_0}E\left\{\Delta V(i)\right\}=E\left\{V\left(k_0+1\right)-V(0)\right\}\ge 0. \tag{35}$$

So, one can have

$$2\sum_{i=0}^{k_0}E\left\{y^T(i)u(i)\right\}\ge-\gamma\sum_{i=0}^{k_0}E\left\{u^T(i)u(i)\right\}, \tag{36}$$

for all $k_0\in N$. This completes the proof. □

Remark 11. It should be pointed out that the new inequality is introduced to deal with $\sum_{i=k-\tau_m}^{k-1}\eta^T(i)T_1\eta(i)$ and $\sum_{i=k-\tau_M}^{k-\tau_m-1}\eta^T(i)T_1\eta(i)$, which is immensely different from traditional ways. This method can effectively reduce the conservatism of the results.

Remark 12. In this paper, not all the matrices in the Lyapunov functional need to be positive definite. In fact, the conditions in (15) assure the positive definiteness of the Lyapunov functional; this is greatly different from traditional ways for passivity researches of discrete-time neural network, because the traditional methods always need Lyapunov matrices to be positive definite.

Remark 13. It can be seen that the term $\sum_{i=k-\tau_M}^{k-\tau_m-1}\eta^T(i)T_1\eta(i)$ is divided into two parts; the aim is to make full use of the relationship of $\tau_M-\tau(k)$ and $\tau(k)-\tau_m$, and then, taking advantage of the integral inequality and Lemma 8, new passivity conditions are obtained in terms of LMIs.

Corollary 14. *Under Assumptions 1 and 3, the discrete-time stochastic neural network (1) is passive, if there exist scalars $\lambda>0$, $\gamma>0$, matrices $P>0$, $R_1>0$, $R_2>0$, $Q=\begin{bmatrix}Q_{11}&Q_{12}\\ *&Q_{22}\end{bmatrix}>0$, $T_1>0$, $T_2>0$, $X=\begin{bmatrix}X_{11}&X_{12}&X_{13}\\ *&X_{22}&X_{23}\\ *&*&X_{33}\end{bmatrix}\ge 0$, $Y=\begin{bmatrix}Y_{11}&Y_{12}&Y_{13}\\ *&Y_{22}&Y_{23}\\ *&*&Y_{33}\end{bmatrix}\ge 0$, $Z=\begin{bmatrix}Z_{11}&Z_{12}&Z_{13}\\ *&Z_{22}&Z_{23}\\ *&*&Z_{33}\end{bmatrix}\ge 0$, and the positive diagonal matrices $S_k=\operatorname{diag}\{s_{1k},s_{2k},\ldots,s_{nk}\}$ $(k=1,2)$, such that linear matrix inequalities (16) and (17) hold.*

Now, we will consider the stochastic discrete-time neural networks with time-varying delay and parameter uncertainties as follows:

$$\begin{aligned} x(k+1)=&\left(A+\Delta A(k)\right)x(k) \\ &+\left(B_1+\Delta B_1(k)\right)g(x(k)) \\ &+\left(B_2+\Delta B_2(k)\right)g(x(k-\tau(k)))+u(k) \\ &+\delta(x(k),x(k-\tau(k)))\omega(k), \end{aligned} \tag{37}$$

where $\Delta A(k)$, $\Delta B_1(k)$, and $\Delta B_2(k)$ denote the parameter uncertainties that are assumed to be of the form

$$\left[\Delta A(k)\quad\Delta B_1(k)\quad\Delta B_2(k)\right]=MF(k)\left[E_1\quad E_2\quad E_3\right], \tag{38}$$

where M, E_i $(i=1,2,3)$ are known constant matrices, and $F(k)$ is the unknown matrix valued function subject to

$$F(k)^TF(k)\le I. \tag{39}$$

Theorem 15. *Under Assumptions 1 and 3, the discrete-time stochastic uncertain neural network (37) is robustly passive, if there exist scalars $\lambda>0$, $\gamma>0$, $\varepsilon>0$, matrices P, R_1, R_2, $Q=\begin{bmatrix}Q_{11}&Q_{12}\\ *&Q_{22}\end{bmatrix}>0$, $T_1>0$, $T_2>0$, $X=\begin{bmatrix}X_{11}&X_{12}&X_{13}\\ *&X_{22}&X_{23}\\ *&*&X_{33}\end{bmatrix}\ge 0$, $Y=\begin{bmatrix}Y_{11}&Y_{12}&Y_{13}\\ *&Y_{22}&Y_{23}\\ *&*&Y_{33}\end{bmatrix}\ge 0$, $Z=\begin{bmatrix}Z_{11}&Z_{12}&Z_{13}\\ *&Z_{22}&Z_{23}\\ *&*&Z_{33}\end{bmatrix}\ge 0$, and the positive*

diagonal matrices $S_k = \mathrm{diag}\{s_{1k}, s_{2k}, \ldots, s_{nk}\}$ $(k = 1, 2)$, *such that the following matrix inequalities hold:*

$$\begin{bmatrix} T_1 + \frac{\tau_m}{\tau_M} P & -T_1 \\ * & T_1 + \tau_m R_1 \end{bmatrix} > 0,$$

$$\begin{bmatrix} T_2 + P & -T_2 \\ * & T_2 + \tau_M R_2 \end{bmatrix} > 0,$$

$$T_1 - X_{33} \geq 0,$$

$$T_2 - Y_{33} \geq 0,$$

$$T_2 - Z_{33} \geq 0,$$

$$\Theta \leq \lambda I,$$

$$\begin{bmatrix} \Sigma + \Upsilon_i & \Xi_1 & \sqrt{\tau_m}\Xi_2 & \sqrt{\tau_{Mm}}\Xi_3 & 0 & \varepsilon\Xi_4 \\ * & -P & 0 & 0 & PM & 0 \\ * & * & -T_1 & 0 & \sqrt{\tau_m}T_1 M & 0 \\ * & * & * & -T_2 & \sqrt{\tau_{Mm}}T_2 M & 0 \\ * & * & * & * & -\varepsilon I & 0 \\ * & * & * & * & * & -\varepsilon I \end{bmatrix} < 0, \quad (i = 1, 2), \tag{40}$$

where

$$\Xi_1 = \begin{bmatrix} PA & 0 & 0 & 0 & PB_1 & PB_2 & P \end{bmatrix}^T,$$

$$\Xi_2 = \begin{bmatrix} T_1(A - I) & 0 & 0 & 0 & T_1 B_1 & T_1 B_2 & T_1 \end{bmatrix}^T,$$

$$\Xi_3 = \begin{bmatrix} T_2(A - I) & 0 & 0 & 0 & T_2 B_1 & T_2 B_2 & T_2 \end{bmatrix}^T,$$

$$\Xi_4 = \begin{bmatrix} E_1 & 0 & 0 & 0 & E_2 & E_3 & 0 \end{bmatrix}^T,$$

$$\Theta = P + \tau_m T_1 + \tau_{Mm} T_2,$$

$$\Sigma = \begin{bmatrix} \Sigma_{11} & \Sigma_{12} & 0 & 0 & (\tau_{Mm} + 1) Q_{12} + L_2 S_1 & 0 & 0 \\ * & \Sigma_{22} & -Y_{13} + Y_{23}^T & 0 & 0 & 0 & 0 \\ * & * & \Sigma_{33} & -Z_{13} + Z_{23}^T & 0 & -Q_{12} + L_2 S_2 & 0 \\ * & * & * & -Z_{23} - Z_{23}^T - R_2 & 0 & 0 & 0 \\ * & * & * & * & (\tau_{Mm} + 1) Q_{22} - S_1 & 0 & -I \\ * & * & * & * & * & -Q_{22} - S_2 & 0 \\ * & * & * & * & * & * & \Sigma_{77} \end{bmatrix}, \tag{41}$$

$$\Sigma_{11} = (\tau_{Mm} + 1) Q_{11} + R_1 + \tau_m X_{11} + X_{13} + X_{13}^T + \rho_1 \lambda I - P - S_1 L_1,$$

$$\Sigma_{12} = \tau_m X_{12} - X_{13} + X_{23}^T,$$

$$\Sigma_{22} = -R_1 + R_2 + \tau_m X_{22} - X_{23} - X_{23}^T + Y_{13} + Y_{13}^T,$$

$$\Sigma_{33} = -Q_{11} - S_2 L_1 + \rho_2 \lambda I - Y_{23} - Y_{23}^T + Z_{13} + Z_{13}^T,$$

$$\Sigma_{77} = P + \tau_m T_1 + \tau_{Mm} T_2 - \gamma I.$$

Υ_1, Υ_2 *are the same as defined in Theorem 10.*

Proof. By replacing A, B_1, B_2 in (17) with $A + \Delta A(k)$, $B_1 + \Delta B_1(k)$, $B_2 + \Delta B_2(k)$, respectively, then using Lemma 7, the desired results can be obtained immediately. The proof is completed. □

4. Numerical Examples

In this section, some numerical examples are proposed to show the effectiveness of the results obtained in this paper.

Example 1. Consider the system (1) with the following parameters:

$$A = \begin{bmatrix} 0.8 & 0 \\ 0 & 0.9 \end{bmatrix},$$

$$B_1 = \begin{bmatrix} 0.001 & 0 \\ 0 & 0.005 \end{bmatrix},$$

$$B_2 = \begin{bmatrix} -0.1 & 0.01 \\ -0.2 & -0.1 \end{bmatrix},$$

$$\rho_1 = 0.003,$$
$$\rho_2 = 0.002. \tag{42}$$

The activation functions are taken as

$$f_1(x) = f_2(x) = \tanh(0.5x). \tag{43}$$

It can be verified that

$$L_1 = \begin{bmatrix} 0 & 0 \\ 0 & 0 \end{bmatrix}, \quad L_2 = \begin{bmatrix} 0.25 & 0 \\ 0 & 0.25 \end{bmatrix}. \tag{44}$$

In this example, if $\tau_m = 3$ and $\tau_M = 12$, the optimal passivity performance obtained is $\gamma = 12.2439$ by the method in [25] and $\gamma = 5.4007$ by the method in [26], while by Theorem 10 in this paper, the optimal passivity performance $\gamma = 3.9546$. The comparisons of γ are listed in Table 1, when $\tau_m = 3$, $\tau_M = 8, 9, 10, 11, 12$. Then, when we assume $\tau_M = 13$, the optimal passivity performance γ obtained by Theorem 10 for different τ_m can be found in Table 2. It can be seen that our results are less conservative than the ones in [25, 26].

Example 2. Consider the system (1) with the following parameters:

$$A = \begin{bmatrix} 0.4 & 0 \\ 0 & 0.5 \end{bmatrix}, \quad B_1 = \begin{bmatrix} 0.001 & 0 \\ 0 & 0.005 \end{bmatrix}, \quad B_2 = \begin{bmatrix} -0.1 & 0.01 \\ -0.2 & -0.1 \end{bmatrix}, \quad \rho_1 = \rho_2 = 0.003. \tag{45}$$

The activation functions are taken as

$$f_1(x) = f_2(x) = \tanh(x). \tag{46}$$

It can be verified that

$$L_1 = \begin{bmatrix} 0 & 0 \\ 0 & 0 \end{bmatrix}, \quad L_2 = \begin{bmatrix} 0.5 & 0 \\ 0 & 0.5 \end{bmatrix}. \tag{47}$$

For this example, when $\gamma = 3$ and $\tau_m = 1$, by Theorem 10, we can get that the upper bound of the time-varying delay is $\tau_M = 8$. When $\gamma = 4$ and $\tau_m = 1$, by Theorem 10, we can get $\tau_M = 10$; we can obtain upper bound of τ_M for different γ and τ_m, which are summarized in Table 3. It can be found from Table 3 that, for the same τ_m, a larger passivity performance γ corresponds to a larger τ_M; with the same τ_M, a smaller passivity performance γ corresponds to a larger τ_m.

Table 1: Optimal passivity performance γ for different τ_M.

Methods	8	9	10	11	12
Theorem 1 [25]	3.9708	4.8691	6.2501	8.3991	12.2439
Corollary 2 [26]	2.9660	3.3483	3.8428	4.4968	5.4007
Theorem 10	2.8481	3.2154	3.5172	3.7438	3.9546

Table 2: Optimal passivity performance γ for different τ_m.

Methods	4	5	6	7	8
Theorem 1 [25]	16.1853	13.2125	11.0130	9.2978	7.9134
Corollary 2 [26]	6.1649	5.6743	5.2451	4.8664	4.5300
Theorem 10	4.4126	4.3752	4.2563	4.1871	4.0802

Table 3: Allowable upper bounds of τ_M for different γ and τ_m.

τ_m	1	3	5	7	9
$\gamma = 3$	8	10	12	14	16
$\gamma = 4$	10	12	14	16	18
$\gamma = 6$	12	13	15	17	19

5. Conclusions

In this paper, the problem of passivity analysis for discrete-time stochastic neural networks with time-varying delays has been investigated. The presented sufficient conditions are based on the Lyapunov-Krasovskii functional, a new inequality and linear matrix inequality approach. Numerical examples are given to demonstrate the usefulness and effectiveness of the proposed results. Finally, it should be worth noticing that the proposed method in this paper may be extensively applicable in many other areas, such as Markov jump neural networks, Markov jump neural networks with incomplete transition descriptions, and switched neural networks, which deserves further investigation.

Conflict of Interests

The authors declare that there is no conflict of interests regarding the publication of this paper.

Acknowledgments

This work is supported by National Natural Science Foundation of China (Grants nos. 61273015 and 61473001), the Natural Science Research Project of Fuyang Normal College (2013FSKJ09), and the Teaching Reform Project of Fuyang Normal College (2013JYXM48).

References

[1] M. M. Gupta, L. Jin, and N. Homma, *Static and Dynamic Neural Networks: From Fundamentals to Advanced Theory*, John Wiley & Sons, New York, NY, USA, 2003.

[2] J. J. Hopfield, "Neurons with graded response have collective computational properties like those of two-state neurons," *Proceedings of the National Academy of Sciences of the United States of America*, vol. 81, no. 10 I, pp. 3088–3092, 1984.

[3] D. Yue, Y. Zhang, and E. Tian, "Improved global robust delay-dependent stability criteria for delayed cellular neural networks," *International Journal of Computer Mathematics*, vol. 85, no. 8, pp. 1265–1277, 2008.

[4] S. Xu, J. Lam, B. Zhang, and Y. Zou, "A new result on the delay-dependent stability of discrete systems with time-varying delays," *International Journal of Robust and Nonlinear Control*, vol. 24, no. 16, pp. 2512–2521, 2014.

[5] P.-L. Liu, "Delay-dependent global exponential robust stability for delayed cellular neural networks with time-varying delay," *ISA Transactions*, vol. 52, no. 6, pp. 711–716, 2013.

[6] P. L. Liu, "A delay decomposition approach to robust stability analysis of uncertain systems with time-varying delay," *ISA Transactions*, vol. 51, no. 6, pp. 694–701, 2012.

[7] J. Sun and J. Chen, "Stability analysis of static recurrent neural networks with interval time-varying delay," *Applied Mathematics and Computation*, vol. 221, pp. 111–120, 2013.

[8] D. Zhang and L. Yu, "Exponential state estimation for Markovian jumping neural networks with time-varying discrete and distributed delays," *Neural Networks*, vol. 35, pp. 103–111, 2012.

[9] P. G. Park, J. W. Ko, and C. Jeong, "Reciprocally convex approach to stability of systems with time-varying delays," *Automatica*, vol. 47, no. 1, pp. 235–238, 2011.

[10] C. Lin, Q.-G. Wang, and T. H. Lee, "A less conservative robust stability test for linear uncertain time-delay systems," *IEEE Transactions on Automatic Control*, vol. 51, no. 1, pp. 87–91, 2006.

[11] R. Lu, H. Wu, and J. Bai, "New delay-dependent robust stability criteria for uncertain neutral systems with mixed delays," *Journal of the Franklin Institute. Engineering and Applied Mathematics*, vol. 351, no. 3, pp. 1386–1399, 2014.

[12] J. Cheng, H. Zhu, S. Zhong, F. Zheng, and Y. Zeng, "Finite-time filtering for switched linear systems with a mode-dependent average dwell time," *Nonlinear Analysis: Hybrid Systems*, vol. 15, pp. 145–156, 2015.

[13] Z. Wang, G. Wei, and G. Feng, "Reliable H_∞ control for discrete-time piecewise linear systems with infinite distributed delays," *Automatica*, vol. 45, no. 12, pp. 2991–2994, 2009.

[14] O. M. Kwon, M. J. Park, J. H. Park, S. M. Lee, and E. J. Cha, "New criteria on delay-dependent stability for discrete-time neural networks with time-varying delays," *Neurocomputing*, vol. 121, pp. 185–194, 2013.

[15] J. Cheng, H. Zhu, S. Zhong, Q. Zhong, and Y. Zeng, "Finite-time H_∞ estimation for discrete-time Markov jump systems with time-varying transition probabilities subject to average dwell time switching," *Communications in Nonlinear Science and Numerical Simulation*, vol. 20, no. 2, pp. 571–582, 2015.

[16] T. Wang, C. Zhang, S. Fei, and T. Li, "Further stability criteria on discrete-time delayed neural networks with distributeddelay," *Neurocomputing*, vol. 111, pp. 195–203, 2013.

[17] X. Kan, H. Shu, and Z. Li, "Robust state estimation for discrete-time neural networks with mixed time-delays, linear fractional uncertainties and successive packet dropouts," *Neurocomputing*, vol. 135, pp. 130–138, 2014.

[18] R. Lozano, B. Brogliato, O. Egeland, and B. Maschke, *Dissipative Systems Analysis and Control: Theory and Applications*, Springer, London, UK, 2nd edition, 2007.

[19] V. Bevelevich, *Classical Network Synthesis*, Van Nostrand, New York, NY, USA, 1968.

[20] B. Zhang, S. Xu, and J. Lam, "Relaxed passivity conditions for neural networks with time-varying delays," *Neurocomputing*, vol. 142, pp. 299–306, 2014.

[21] D. H. Ji, J. H. Koo, S. C. Won, S. M. Lee, and J. H. Park, "Passivity-based control for Hopfield neural networks using convex representation," *Applied Mathematics and Computation*, vol. 217, no. 13, pp. 6168–6175, 2011.

[22] Z. G. Wu, J. H. Park, H. Su, and J. Chu, "New results on exponential passivity of neural networks with time-varying delays," *Nonlinear Analysis: Real World Applications*, vol. 13, no. 4, pp. 1593–1599, 2012.

[23] T. H. Lee, M.-J. Park, J. H. Park, O.-M. Kwon, and S.-M. Lee, "Extended dissipative analysis for neural networks with time-varying delays," *IEEE Transactions on Neural Networks and Learning Systems*, vol. 25, no. 10, pp. 1936–1941, 2014.

[24] R. Raja, U. K. Raja, R. Samidurai, and A. Leelamani, "Passivity analysis for uncertain discrete-time stochastic BAM neural networks with time-varying delays," *Neural Computing and Applications*, vol. 25, no. 3-4, pp. 751–766, 2014.

[25] Q. Song, J. Liang, and Z. Wang, "Passivity analysis of discrete-time stochastic neural networks with time-varying delays," *Neurocomputing*, vol. 72, no. 7–9, pp. 1782–1788, 2009.

[26] Z.-G. Wu, P. Shi, H. Su, and J. Chu, "Dissipativity analysis for discrete-time stochastic neural networks with time-varying delays," *IEEE Transactions on Neural Networks and Learning Systems*, vol. 24, no. 3, pp. 345–355, 2013.

[27] Z. Wu, P. Shi, H. Su, and J. Chu, "Stability and disspativity analysis of static neural networks with time delay," *IEEE Transactions on Neural Networks and Learning Systems*, vol. 23, no. 2, pp. 199–210, 2012.

Hindawi Publishing Corporation
Mathematical Problems in Engineering
Volume 2015, Article ID 872475, 8 pages
http://dx.doi.org/10.1155/2015/872475

Research Article

A Novel Consensus Protocol for Two-Dimension First-Order Multiagent Systems

Yibo Zhang, Jinfeng Gao, and Jia Ren

Department of Automation, Zhejiang Sci-Tech University, Hangzhou, Zhejiang 310038, China

Correspondence should be addressed to Yibo Zhang; zhangy41@163.com

Received 15 January 2015; Accepted 9 March 2015

Academic Editor: Yun-Bo Zhao

Copyright © 2015 Yibo Zhang et al. This is an open access article distributed under the Creative Commons Attribution License, which permits unrestricted use, distribution, and reproduction in any medium, provided the original work is properly cited.

A novel consensus protocol for two-dimension first-order multiagent systems (MAS) is proposed. After a novel protocol for two-dimension first-order MAS is adopted; consensus and two kinds of possible results are concerned. Then consensus asymptotical conditions and ranges of key parameters are given, and convergence speed is analyzed. Numerical examples illustrate effectiveness of the proposed consensus protocol.

1. Introduction

Networks have been concerned for many years, and it has been researched in many areas such as in sensor networks [1], distribute networks, or wireless networks. Multiagent systems (MAS) have been concerned for many years. It reflects relationships of individuals in a network, such as critical rules or protocols or control of each individual [2]. One common way of pattern is that all agents converge to the same value, which is called consensus or agreement.

Consensus problem is applied in robots, spacecraft, and cooperative multiple vehicles, and it mainly concerns exchange ways of information. For example, reference [3] presented theoretical explanation for characters of continuous and discrete MAS with/without leaders. This classical work showed relations between connection of agents, protocols, and consensus. And [4] researched a new technique based on complex Laplacian to achieve arbitrary formation shape and global stability. Reference [5] mainly researched linear time-varying MAS, a necessary and sufficient condition of consensus ability with a set of admissible protocols. Then some applications are put up; [6] discussed a kind of autonomous scale control of multi-agent in a MAS with shape constrains. It provided a new method for choosing an appropriate geometry and discussed system effect by different parameters. Reference [7] considered MAS with leader of bounded unknown input. After two distributed discontinuous controllers were added, a sufficient condition was applied to ensure stabilization. References [8, 9] researched grouping control and coordinate control of MAS according in different conditions.

Suppose there are n agents in MAS and they are connected by wireless networks, which can be described as a (directed) graph. The graph can be expressed in an adjacency matrix form called Laplacian matrix $L = [l_{ik}]$ $(1 \le i,\ k \le n)$ that satisfies the following conditions:

$$\begin{gathered} l_{ik} \le 0 \quad i \ne k \\ \sum_{k=1}^{n} l_{ik} = 0 \quad i = 1, 2, \ldots, n. \end{gathered} \tag{1}$$

According to [3], the following premise is introduced.

Premise. A first-order MAS should satisfy the condition that exchange topology has a spanning tree or $-L$ has only one zero eigenvalue and all the other nonzero eigenvalues have negative real parts.

The following is based on the fact that the premise is satisfied. In this work, a kind of two-dimension first-order MAS is concerned. Then a novel protocol and its consensus are proposed, and range of key parameter is given. Moreover,

convergence speed is analyzed. Several simulations are shown to ensure the results.

2. Consensus and Convergence Speed

2.1. Consensus for Two-Dimension MAS. Suppose there are n agents in a plat coordinate system, which means each agent has two coordinate positions named as x and y, respectively. Dynamic equations of the ith agent ($i = 1, 2, \ldots, n$) are shown as following:

$$\begin{aligned} \dot{x}_i &= u_{xi} \\ \dot{y}_i &= u_{yi}. \end{aligned} \tag{2}$$

The consensus is that all agents finally converge together, with their positions converging to the same value, or it can be expressed as $|x_i - x_k| \to 0$ and $|y_i - y_k| \to 0$, when $t \to \infty$, where $i, k = 1, 2, \ldots, n$.

Protocol of two-dimension system is introduced as

$$\begin{aligned} u_{xi} &= -\sum_{k=1}^{n} l_{ik} \left[(x_i - x_k) + \gamma (y_i - y_k) \right] \\ u_{yi} &= -\sum_{k=1}^{n} l_{ik} \left[(x_i - x_k) + (y_i - y_k) \right]. \end{aligned} \tag{3}$$

Let $x = \begin{bmatrix} x_1 & x_2 & \cdots & x_n \end{bmatrix}^T$ and $y = \begin{bmatrix} y_1 & y_2 & \cdots & y_n \end{bmatrix}^T$. Equation (2) changes to the following form:

$$\begin{bmatrix} \dot{x} \\ \dot{y} \end{bmatrix} = \begin{bmatrix} u_{xi} \\ u_{yi} \end{bmatrix} = \Gamma \begin{bmatrix} x \\ y \end{bmatrix}, \tag{4}$$

where $\Gamma = \begin{bmatrix} -L & -\gamma L \\ -L & -L \end{bmatrix}$.

Suppose μ_i ($i = 1, 2, \ldots, n$) is the ith eigenvalue of $-L$; then

$$\det(\lambda I_n + L) = \det(\lambda I_n - (-L)) = \prod_{i=1}^{n} (\lambda - \mu_i). \tag{5}$$

Because $-L$ has exactly one zero eigenvalue, and all the other nonzero eigenvalues have negative real parts; without loss of generality, let $\mu_1 = 0$ and the other nonzero eigenvalues $\mu_i = -\alpha_i \pm j\beta_i$, where $\alpha_i > 0$ ($i = 2, 3, \ldots, n$). If μ_i is real, $\beta_i = 0$, and $\beta_i > 0$ if there are conjugate complex eigenvalues.

Let $\overline{\mu}_i$ ($i = 1, 2, \ldots, 2n$) be the ith eigenvalue of Γ; then $\det(\lambda I_{2n} - \Gamma) = \prod_{i=1}^{2n} (\lambda - \overline{\mu}_i)$.

Note that

$$\begin{aligned} \det(\lambda I_{2n} - \Gamma) &= \det\left(\begin{bmatrix} \lambda I_n + L & \gamma L \\ L & \lambda I_n + L \end{bmatrix} \right) \\ &= \det\left(\lambda^2 I_n + 2\lambda L + (1 - \gamma) L^2 \right). \end{aligned} \tag{6}$$

Let λ_1 and λ_2 be roots of the character equation $\lambda^2 + 2\lambda + (1 - \gamma) = 0$; then there are two kinds of possibilities according to different γ.

(1) λ_1 and λ_2 Are Real. If $\gamma \geq 0$, $\lambda_1 = 1 + \sqrt{\gamma}$, and $\lambda_2 = 1 - \sqrt{\gamma}$ are real, then (6) can be decomposed to the following form:

$$\begin{aligned} \det(\lambda I_{2n} - \Gamma) &= \det\left(\lambda^2 I_n + 2\lambda L + (1 - \gamma) L^2 \right) \\ &= \det\left(\lambda I_n + (1 + \sqrt{\gamma}) L \right) \\ &\quad \cdot \det\left(\lambda I_n + (1 - \sqrt{\gamma}) L \right). \end{aligned} \tag{7}$$

Compared with (5), (7) turns to

$$\begin{aligned} \det(\lambda I_{2n} - \Gamma) &= \det\left(\lambda I_n + (1 + \sqrt{\gamma}) L \right) \\ &\quad \cdot \det\left(\lambda I_n + (1 - \sqrt{\gamma}) L \right) \\ &= \prod_{i=1}^{n} \left(\lambda - (1 + \sqrt{\gamma}) \mu_i \right) \prod_{i=1}^{n} \left(\lambda - (1 - \sqrt{\gamma}) \mu_i \right). \end{aligned} \tag{8}$$

Then the following lemma is proposed.

Lemma 1. *When $0 \leq \gamma < 1$, consensus protocol (3) achieves consensus asymptotically, if and only if $-L$ has exactly one zero eigenvalue and the other $n - 1$ eigenvalues have negative real parts, which is equal to the condition if and only if Γ has exactly two zero eigenvalues and the other $2n - 2$ eigenvalues have negative real parts.*

Proof.

Sufficiency. If $0 \leq \gamma < 1$, $1 - \sqrt{\gamma} > 0$, so it is obvious that $\overline{\mu}_1 = (1 - \sqrt{\gamma}) \mu_1 = 0$ and $\mathrm{Re}(\overline{\mu}_i) = -(1 - \sqrt{\gamma}) \alpha_i < 0$ ($i = 2, 3, \ldots, n$). This means that $\overline{\mu}_i$ ($i = 1, 2, \ldots, n$) have the same sign with μ_i ($i = 1, 2, \ldots, n$). The same conclusion can be drawn when $\overline{\mu}_i = (1 + \sqrt{\gamma}) \mu_i$ ($i = 1, 2, \ldots, n$) if $0 \leq \gamma < 1$. Considering (8), the following conclusion is drawn: Γ has exactly two zero eigenvalues and the others have negative real parts, which is equal to $-L$ having exactly one zero eigenvalue and the others have negative real parts.

Let $p = \begin{bmatrix} p_1^T & p_2^T \end{bmatrix}^T$ be an eigenvector of Γ associated with one of zero eigenvalues, where $p_1, p_2 \in R^n$; then

$$\Gamma p = \begin{bmatrix} -L & -\gamma L \\ -L & -L \end{bmatrix} \begin{bmatrix} p_1 \\ p_2 \end{bmatrix} = 0, \tag{9}$$

which implies that $-Lp_1 = 0$ and $-Lp_2 = 0$ if $0 \leq \gamma < 1$. Note that $-L$ has only one linearly independent eigenvector associated with zero eigenvalue, so $p_1 = p_2$. Moreover, Γ has only one linearly independent eigenvector $p = \begin{bmatrix} p_1^T & p_1^T \end{bmatrix}^T$; that is, zero eigenvalue of Γ has geometric multiplicity equal to one.

All of the above show that if $-L$ is chosen as asymptotically, Γ achieves consensus asymptotically also.

Necessity (reduction to absurd). Suppose Γ having exactly two zero eigenvalues and the other eigenvalues having

negative real parts do not hold. From sufficient process, relationships between eigenvalues of Γ and $-L$ are $\overline{\mu}_i = (1 + \sqrt{\gamma})\mu_i$ or $\overline{\mu}_i = (1 - \sqrt{\gamma})\mu_i$, which means zero eigenvalues of Γ are double times those of $-L$. Suppose there are more than two zero eigenvalues of Γ, for example, four zero eigenvalues, so there are at least two zero eigenvalues of $-L$. □

According to [3], consensus cannot be achieved, which is contradicting with the premise, so there must be only two zero eigenvalues of Γ.

Then suppose there is at least one nonzero eigenvalue having positive real part. Note that Γ can be transformed to Jordan canonical form by a nonsingular matrix Q:

$$\Gamma = Q^{-1}JQ. \tag{10}$$

Then

$$\begin{aligned} e^{\Gamma t} &= Q^{-1}e^{Jt}Q \\ &= Q^{-1}\begin{bmatrix} 1 & 0 & 0_{1\times(2n-2)} \\ 0 & 1 & 0_{1\times(2n-2)} \\ 0_{(2n-2)\times 1} & 0_{(2n-2)\times 1} & e^{J't} \end{bmatrix} Q. \end{aligned} \tag{11}$$

It can be seen that if there is at least one eigenvalue with positive real part of Γ, when $t \to \infty$ and $e^{J't} \to \infty$, then $e^{\Gamma t} \to \infty$, which is contradicting with the following condition: "consensus protocol (2) achieves consensus asymptotically."

So the assumption is wrong.

(2) λ_1 and λ_2 Are Conjugate Complex Eigenvalues. If $\gamma < 0$ and $\lambda_{1,2} = 1 \pm j\sqrt{-\gamma}$ are one pair of conjugate complex eigenvalues, then (6) can be decomposed to the following form:

$$\begin{aligned} \det(\lambda I_{2n} - \Gamma) &= \det\left(\lambda I_n + \left(1 - j\sqrt{-\gamma}\right)L\right) \\ &\quad \cdot \det\left(\lambda I_n + \left(1 + j\sqrt{-\gamma}\right)L\right) \\ &= \prod_{i=1}^{n}\left(\lambda - \left(1 - j\sqrt{-\gamma}\right)\mu_i\right) \\ &\quad \cdot \prod_{i=1}^{n}\left(\lambda - \left(1 + j\sqrt{-\gamma}\right)\mu_i\right). \end{aligned} \tag{12}$$

Then the following lemma is proposed.

Lemma 2. *When $-\min_{\mu_i\neq 0}(\alpha_i^2/\beta_i^2) < \gamma < 0$, consensus protocol (3) achieves consensus asymptotically, if and only if $-L$ has exactly one zero eigenvalue and the other $n-1$ eigenvalues have negative real parts, which is equal to the condition if and only if Γ has exactly two zero eigenvalues and the other $2n-2$ eigenvalues have negative real parts.*

The proof is omitted for similarity with Lemma 1. The differenence is range of γ, which is described as follows.

Because $\overline{\mu}_i = (1 + j\sqrt{-\gamma})\mu_i$ or $\overline{\mu}_i = (1 - j\sqrt{-\gamma})\mu_i$, if $\mu_1 \neq 0$, two cases are concerned.

Case 1 (all nonzero eigenvalues μ_i $(i = 2, 3, \ldots, n)$ are real). According to the premise, $\mu_i < 0$, then both $\overline{\mu}_i = (1 + j\sqrt{-\gamma})\mu_i$ and $\overline{\mu}_i = (1 - j\sqrt{-\gamma})\mu_i$ have negative real parts.

Case 2 (there are at least one pair of conjugate complex eigenvalues). Suppose there is only one pair of conjugate complex eigenvalues marked as μ_{i+} and μ_{i-}. Let $\mu_{i\pm} = -\alpha \pm j\beta$, where $\alpha > 0$ and $\beta > 0$. Because $\overline{\mu}_i$ is multiplied by two vectors $1 \pm \sqrt{-\gamma}$ and μ_i, its module is product while phase angle is the sum of them. All possible results are shown in Figure 1.

In Figure 1, θ_i denotes intersection angle between vector $\mu_{i\pm}$ and Y-axis and θ_Γ is abstract phase angle of $1 \pm j\sqrt{-\gamma}$. It can be seen that whether $\overline{\mu}_i = (1 \pm j\sqrt{-\gamma})\mu_{i\pm}$ have negative real parts is decided by angle of $\overline{\mu}_i$. Note that phase angle of μ_{i+} is in $(90^\circ, 180^\circ)$ while that of μ_{i-} is in $(180^\circ, 270^\circ)$, and if $\sqrt{-\gamma} > 0$, then $0 < \theta_\Gamma = \arctan(\sqrt{-\gamma}) < 90^\circ$, so phase angles of $(1 + j\sqrt{-\gamma})\mu_{i+}$ and $(1 - j\sqrt{-\gamma})\mu_{i-}$ are in range of $(90^\circ, 270^\circ)$. In order to ensure all eigenvalues of Γ have negative real parts, phase angles of $(1 - j\sqrt{-\gamma})\mu_{i+}$ and $(1 + j\sqrt{-\gamma})\mu_{i-}$ must be in range of $(90^\circ, 180^\circ)$ and $(180^\circ, 270^\circ)$, respectively, which means $\theta_\Gamma < \theta_i$.

If there are more than one pair of conjugate complex eigenvalues, it is obvious that $\theta_\Gamma < \theta_i$ should satisfied for all pairs of conjugate complexes, so $\theta_\Gamma < \min_{\beta_i\neq 0}\theta_i$. Note that $\theta_\Gamma = \arctan(\sqrt{-\gamma})$ and $\theta_i = \arctan(\alpha_i/\beta_i)$; then,

$$\begin{aligned} &\arctan\left(\sqrt{-\gamma}\right) < \min_{\beta_i\neq 0}\left[\arctan\left(\frac{\alpha_i}{\beta_i}\right)\right] \\ &\Longrightarrow \sqrt{-\gamma} < \min_{\beta_i\neq 0}\left(\frac{\alpha_i}{\beta_i}\right) \\ &\Longrightarrow \gamma > -\min_{\beta_i\neq 0}\left(\frac{\alpha_i^2}{\beta_i^2}\right). \end{aligned} \tag{13}$$

So $-\min_{\beta_i\neq 0}(\alpha_i^2/\beta_i^2) < \gamma < 0$. And for the other real eigenvalues, $\alpha_i^2/\beta_i^2 = \infty$, which means that $\min_{\mu_i\neq 0}(\alpha_i^2/\beta_i^2) = \min_{\beta_i\neq 0}(\alpha_i^2/\beta_i^2)$. Moreover, if all nonzero eigenvalues are real, $-\min_{\mu_i\neq 0}(\alpha_i^2/\beta_i^2) < \gamma < 0$ turns to $-\infty < \gamma < 0$, which is equal to $\gamma < 0$; it is obvious that conditions of Case 1 and Case 2 can be rewritten in the same form as $-\min_{\mu_i\neq 0}(\alpha_i^2/\beta_i^2) < \gamma < 0$.

2.2. Convergence Speed. Convergence speed of system (1) is decided by eigenvalue with the smallest absolute value of real part. Reconsider (12); if all nonzero eigenvalues have negative real parts, then the slowest convergence speed of system (2) is decided by the eigenvalue whose real part is the nearest to Y-axis. Three cases are analyzed according to choice of γ.

Case 1 $(0 \le \gamma < 1)$. From (7), it is obviously that the smallest eigenvalue is one of $((1 - \sqrt{\lambda})\mu_i)$, so smaller $1 - \sqrt{\gamma}$ (or bigger γ) will cause slower convergence speed.

Case 2 $(-\min_{\mu_i\neq 0}(\alpha_i^2/\beta_i^2) < \gamma < 0$ and all nonzero μ_i are real). From (7), it is obvious that $\mathrm{Re}(\overline{\mu}_i) = \mathrm{Re}((1 \pm j\sqrt{-\gamma})\mu_i) = \mu_i$, which means γ has no effect on convergence speed. The bigger

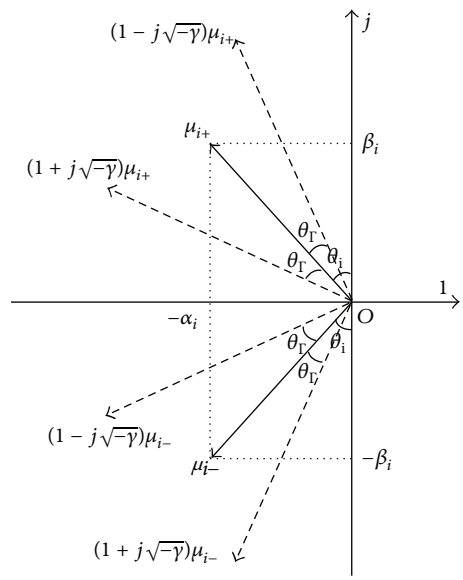

Figure 1: All possible results of $\overline{\mu}_i = (1 \pm j\sqrt{-\gamma})\mu_i$.

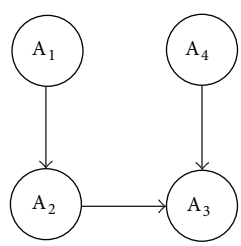

Figure 2: A digraph in [4].

imaginary part $\sqrt{-\gamma}$ of $\overline{\mu}_i$ means bigger $|\gamma|$ will cause larger amplitude of oscillation.

Case 3 ($-\min_{\mu_i \neq 0}(\alpha_i^2/\beta_i^2) < \gamma < 0$ and there are conjugate complex eigenvalues of μ_i). From Figure 1, $\mathrm{Re}(\overline{\mu}_i)$ is given by $\mathrm{Re}(\overline{\mu}_i) = \mathrm{Re}[(1 - j\sqrt{-\gamma})\mu_{i+}] = \mathrm{Re}[(1 - j\sqrt{-\gamma})(-\alpha + j\beta)] = \beta\sqrt{-\gamma} - \alpha$, so bigger $\beta\sqrt{-\gamma} - \alpha$ (or smaller γ) will cause slower convergence.

3. Simulation Results

In this section, examples are illustrated to prove conclusions drawn in Section 2.

3.1. Case 1. A digraph in [4] is shown in Figure 2.

It is obvious that $-L = \begin{bmatrix} -1 & 1 & 0 & 0 \\ 0 & -1 & 1 & 0 \\ 0 & 0 & 0 & 0 \\ 0 & 0 & 1 & -1 \end{bmatrix}$, whose eigenvalues are $\lambda_1 = 0$ and $\lambda_{2,3,4} = -1$. Choose initial coordinate of the four agents as $x_0 = \begin{bmatrix} 0.6 & -0.4 & -0.2 & 0.8 \end{bmatrix}^T$ and $y_0 = \begin{bmatrix} -0.8 & 0.7 & -0.9 & -1 \end{bmatrix}^T$, respectively. All simulation results are shown in Figure 3 according to different $\gamma > 0$.

From Figure 3, asymptotical consensus is achieved when $0 \leq \gamma < 1$, while it is not achieved if $\gamma \geq 1$. And agents stay in fixed positions when $\gamma = 1$ while they reflect in separating trend.

Moreover, asymptotical consensus is achieved in less than 10 seconds when $\gamma = 0$ and in about 20 seconds when $\gamma = 0.5$, which agrees with Case 1 in Section 2.2.

3.2. Case 2. Simulation results with the same system when $\gamma < 0$ are shown in Figure 4.

If all eigenvalues of $-L$ are real, any $\gamma < 0$ can satisfy Lemma 2, so consensuses are achieved when $\gamma = -0.5$ or $\gamma = -3$. There are no obvious differences between their convergence speeds. More oscillation appears when $\gamma = -3$, which agrees with Case 2 in Section 2.2.

3.3. Case 3. Next, $-L$ is chosen as $\begin{bmatrix} -2 & 1 & 0 & 1 \\ 0 & -1 & 1 & 0 \\ 1 & 0 & -1 & 0 \\ 0 & 0 & 0 & 0 \end{bmatrix}$, and other conditions remain the same, so eigenvalues are $\lambda_1 = 0$, $\lambda_2 = -0.2451$, and one pair of conjugate complex eigenvalues $\lambda_{3,4} = -1.8774 \pm j0.7449$. Simulation results are shown in Figure 5.

According to Lemma 2, $-\min_{\mu_i \neq 0}(\alpha_i^2/\beta_i^2) = -6.3521$. When $-\min_{\mu_i \neq 0}(\alpha_i^2/\beta_i^2) < \gamma = -1 < 0$ or $-\min_{\mu_i \neq 0}(\alpha_i^2/\beta_i^2) < \gamma = -3 < 0$, consensus is achieved, while opposite result is obtained when $\gamma = -7 < -\min_{\mu_i \neq 0}(\alpha_i^2/\beta_i^2)$. And the convergence speed is a little faster when $\gamma = -1$, which agrees with Case 3 in Section 2.2.

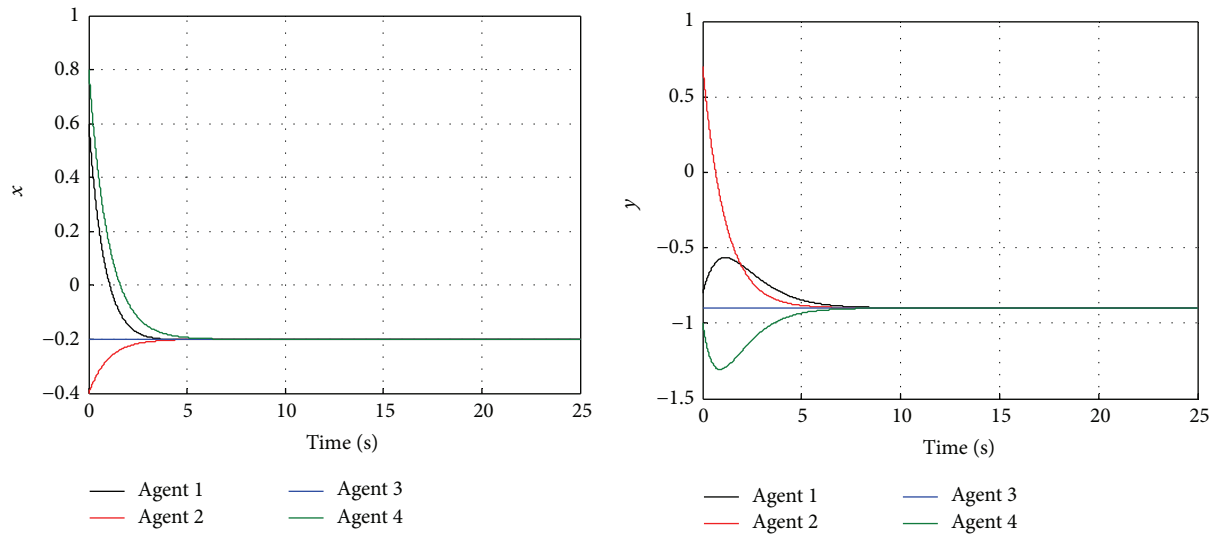

(a) Simulation results ($\gamma = 0$)

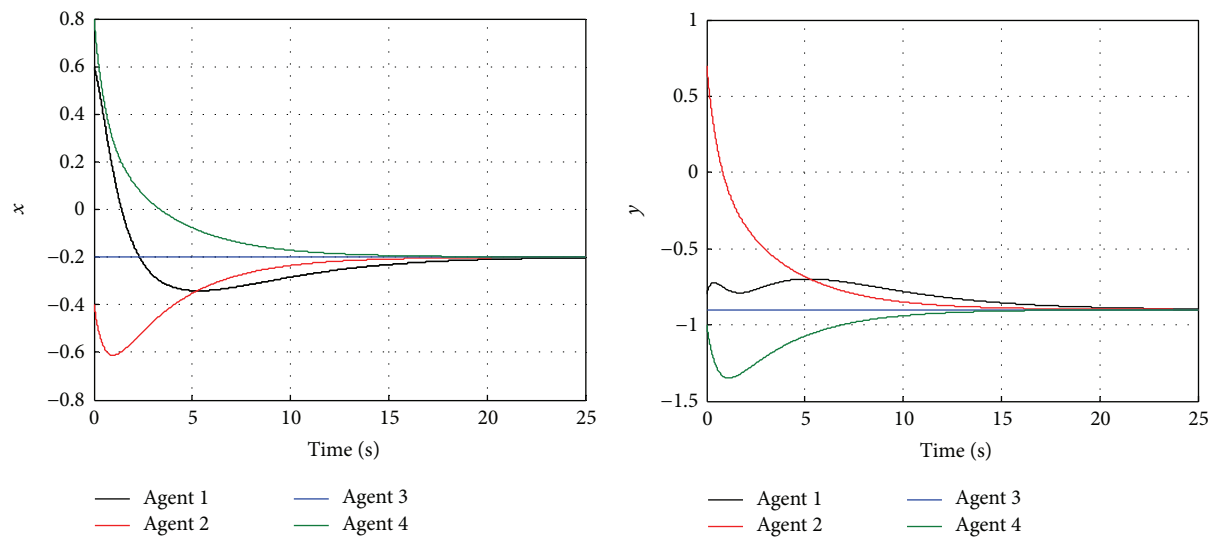

(b) Simulation results ($\gamma = 0.5$)

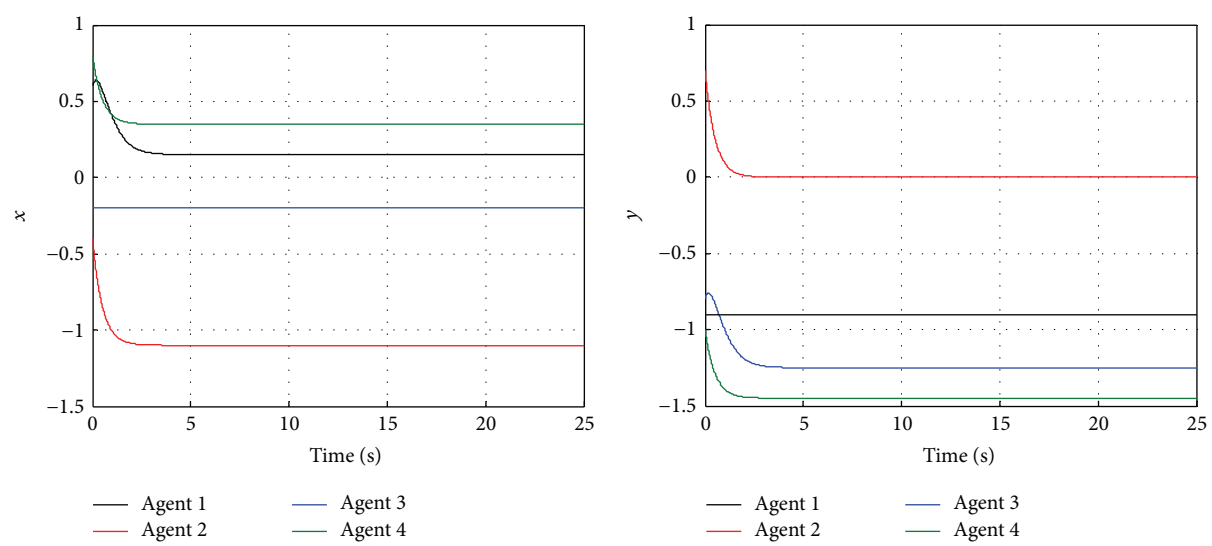

(c) Simulation results ($\gamma = 1$)

Figure 3: Continued.

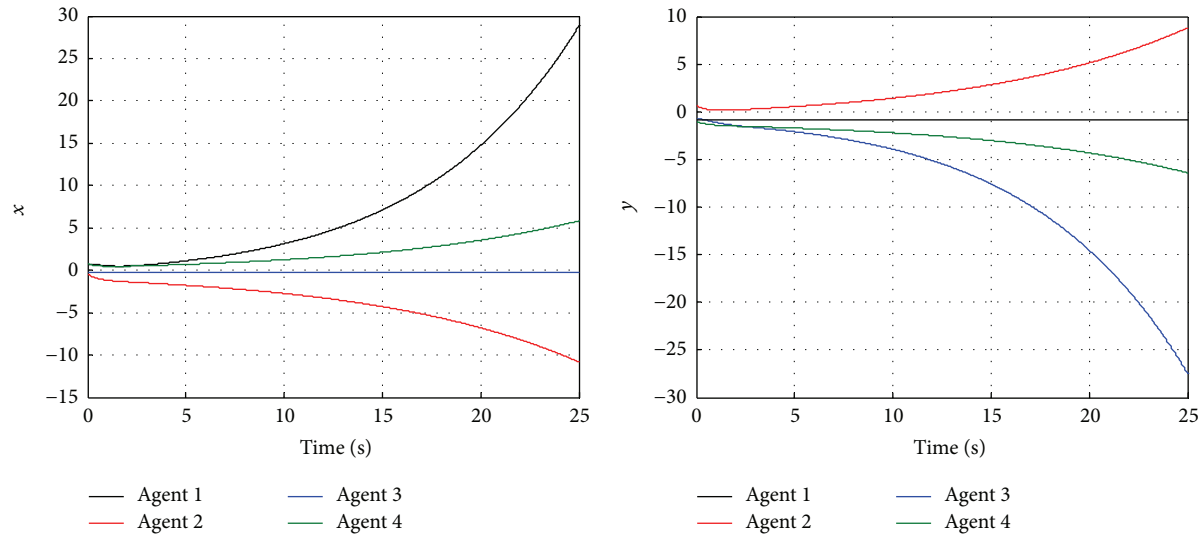

(d) Simulation results ($\gamma = 1.2$)

FIGURE 3: Simulation results with different $\gamma > 0$.

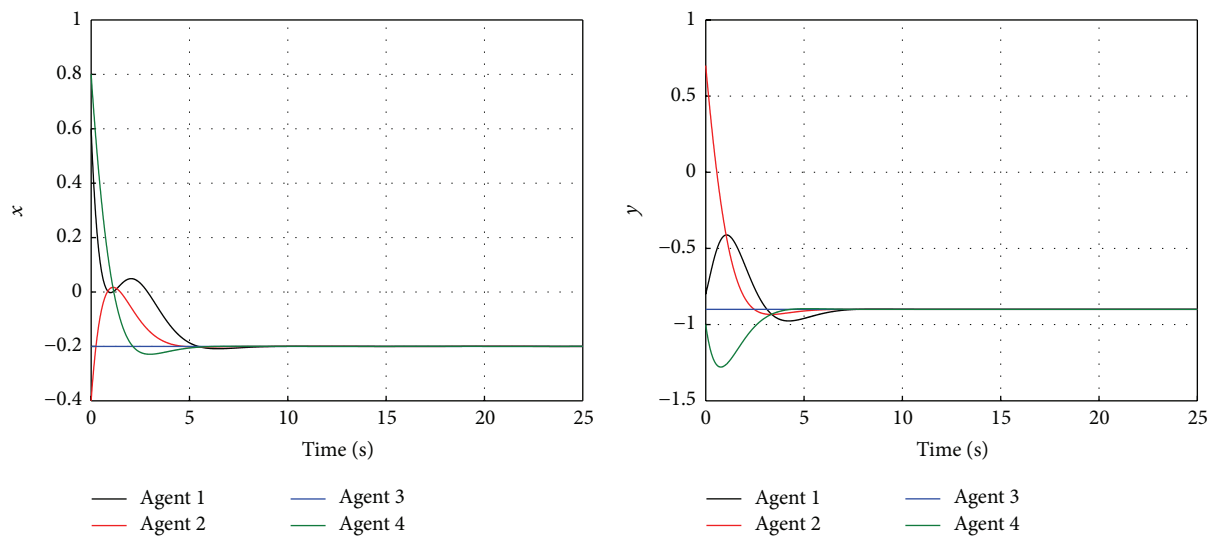

(a) Simulation results ($\gamma = -0.5$)

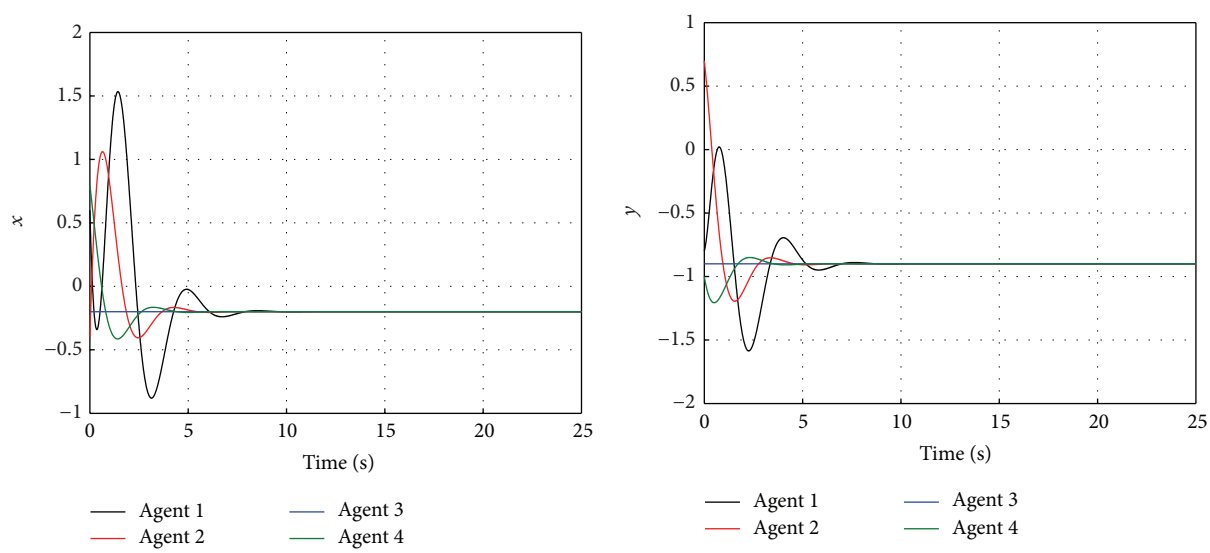

(b) Simulation results ($\gamma = -3$)

FIGURE 4: Simulation results with different $\gamma < 0$ when all eigenvalues of $-L$ is real.

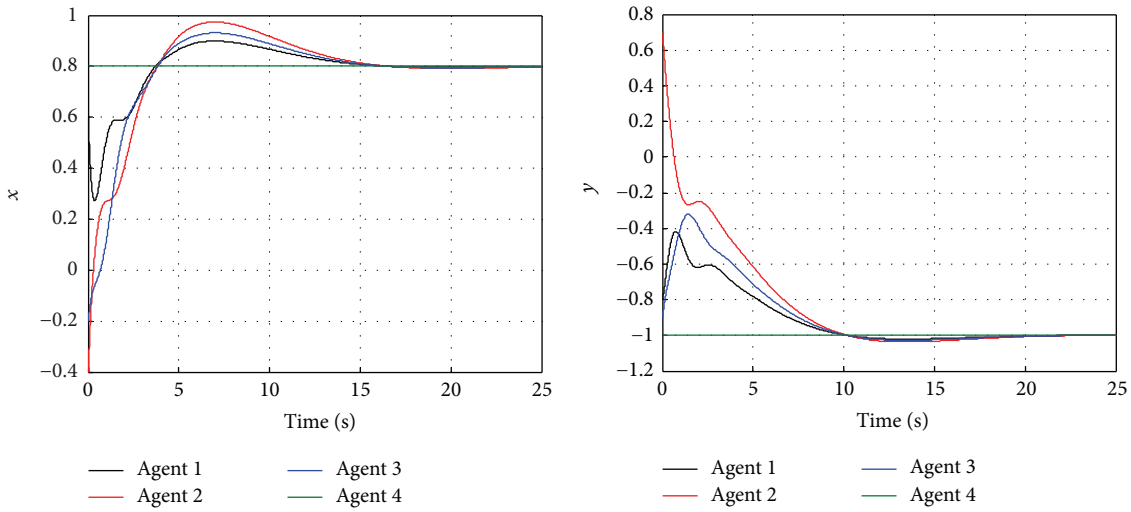

(a) Simulation results ($\gamma = -1$)

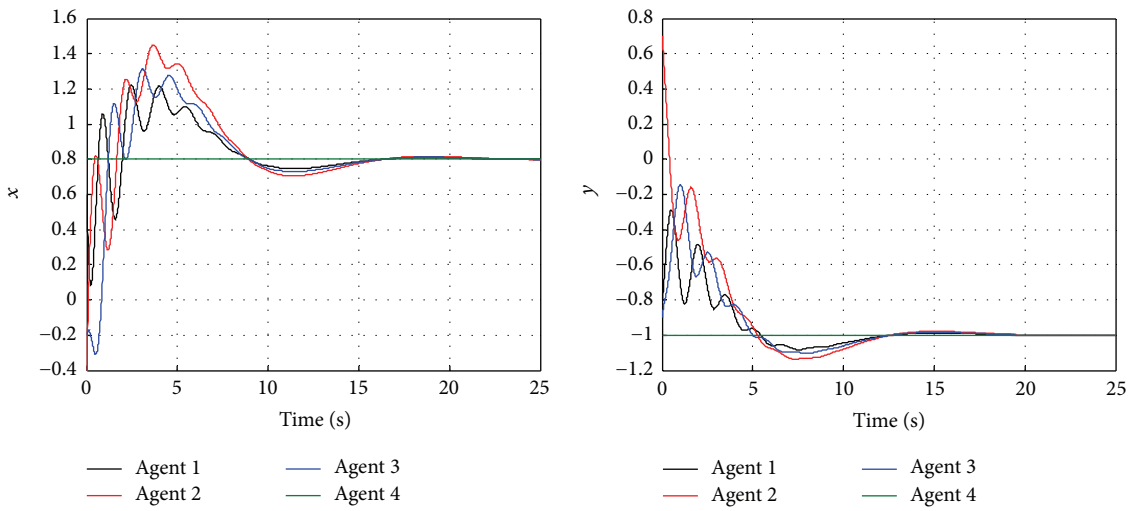

(b) Simulation results ($\gamma = -3$)

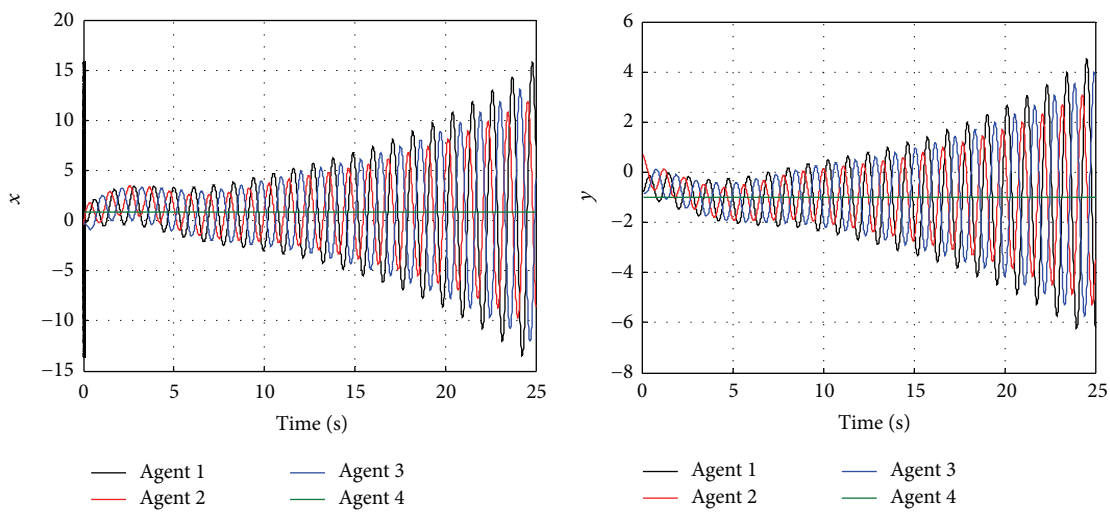

(c) Simulation results ($\gamma = -7$)

FIGURE 5: Simulation results with different $\gamma < 0$ when there are conjugate complex eigenvalues.

4. Conclusion

A novel consensus protocol is presented for the linear two-dimension first-order multiagent systems (MASs). Numerical examples illustrated the effectiveness of the proposed consensus protocol according to different key parameters. Simulation results ensure the relationship between range of key parameter and convergence speed.

Conflict of Interests

The authors declare that there is no conflict of interests regarding the publication of this paper.

Acknowledgments

This work is supported by National Natural Science Foundation of China (nos. 61374083 and 61203177) and Zhejiang Province Key Project of Science and Technology (no. 2014C03027).

References

[1] D. Zhang, W. J. Cai, L. H. Xie, and Q. G. Wang, "Non-fragile distributed filtering for T-S fuzzy systems in sensor networks," *IEEE Transactions on Fuzzy Systems*, 2014.

[2] Y. Yi, Z. Y. Lin, and G. F. Yan, "Variable speed running on kneed biped robot with underactuation degree two," *International Journal of Humanoid Robotics*, vol. 11, Article ID 1450015, 2014.

[3] A. Jadbabaie, J. Lin, and A. S. Morse, "Coordination of groups of mobile autonomous agents using nearest neighbor rules," in *Proceedings of the 41st IEEE Conference on Decision and Control*, pp. 2953–2958, December 2002.

[4] Z. Y. Lin, L. L. Wang, Z. M. Han, and M. Y. Fu, "Distributed formation control of multi-agent systems using complex laplacian," *IEEE Transactions on Automatic Control*, vol. 59, no. 7, pp. 1765–1777, 2014.

[5] C.-Q. Ma and J.-F. Zhang, "Necessary and sufficient conditions for consensusability of linear multi-agent systems," *IEEE Transactions on Automatic Control*, vol. 55, no. 5, pp. 1263–1268, 2010.

[6] H. Huang, C. B. Yu, and Q. H. Wu, "Autonomous scale control of multiagent formations with only shape constraints," *International Journal of Robust and Nonlinear Control*, vol. 23, no. 7, pp. 765–791, 2013.

[7] Z. K. Li, X. D. Liu, W. Ren, and L. H. Xie, "Distributed tracking control for linear multiagent systems with a leader of bounded unknown input," *IEEE Transactions on Automatic Control*, vol. 58, no. 2, pp. 518–523, 2013.

[8] H.-W. Yu and Y.-F. Zheng, "Dynamic behavior of multi-agent systems with distributed sampled control," *Acta Automatica Sinica*, vol. 38, no. 3, pp. 357–365, 2012.

[9] Y.-Y. Chen and Y.-P. Tian, "Directed coordinated control for multi-agent formation motion on a set of given curves," *Acta Automatica Sinica*, vol. 35, no. 12, pp. 1541–1549, 2009.

Hindawi Publishing Corporation
Mathematical Problems in Engineering
Volume 2015, Article ID 573950, 7 pages
http://dx.doi.org/10.1155/2015/573950

Research Article

Passive Control of Switched Singular Systems via Output Feedback

Shuhui Shi,[1] Guoliang Wang,[2] Jianhua Wang,[3] and Hong Li[4]

[1] *Shenyang Institute of Engineering, Shenyang 110136, China*
[2] *Liaoning Shihua University, Fushun 113001, China*
[3] *Shenyang University, Shenyang 110004, China*
[4] *Shenyang Institute of Technology, Fushun 113122, China*

Correspondence should be addressed to Guoliang Wang; gliangwang@aliyun.com

Received 1 January 2015; Accepted 16 February 2015

Academic Editor: Kun Liu

Copyright © 2015 Shuhui Shi et al. This is an open access article distributed under the Creative Commons Attribution License, which permits unrestricted use, distribution, and reproduction in any medium, provided the original work is properly cited.

An instrumental matrix approach to design output feedback passive controller for switched singular systems is proposed in this paper. The nonlinear inequality condition including Lyapunov inverse matrix and controller gain matrix is decoupled by introducing additional instrumental matrix variable. Combined with multiple Lyapunov function method, the nonlinear inequality is transformed into linear matrix inequality (LMI). An LMI condition is presented for switched singular system to be stable and passive via static output feedback under designed switching signal. Moreover, the conditions proposed do not require the decomposition of Lyapunov matrix and its inverse matrix or fixing to a special structure. The theoretical results are verified by means of an example. The method introduced in the paper can be effectively extended to a single singular system and normal switched system.

1. Introduction

The switched singular systems arise from, for instance, power systems, economic systems, and complex networks. As pointed out in [1], when the interrelationships among different industrial sectors are described and the capital and the demand are variable depending on seasons, the dynamic economic systems are modelled as periodically switched singular systems. In some complex hybrid networks, some algebraic constraints have to be considered. The special algebraic constraints that, for example, communication resources are always limited and required to be allocated to different levels of privileged users, are needed in the resource allocation process. Thus, constructing the network model with a set of constraints is reasonable and indispensable. The model can be denoted by a class of singular hybrid systems [2]. There has been increasing interest in analysis and synthesis for switched singular systems. The stability issues are discussed for continuous-time switched singular systems [3], discrete-time switched singular systems [4], linear switched singular systems [5, 6], nonlinear switched singular systems [7], and time-delay switched singular systems [8], respectively. In [9, 10], reachability conditions and admissibility criteria are presented, respectively. Reference [11] studies the initial instantaneous jumps at switching points and a sufficient stability condition is obtained for the switched singular system with both stable and unstable subsystems. At arbitrary switching instant, inconsistent state jump for switched singular systems can be compressed by hybrid impulsive controllers in [12]. Filters and observers are designed for switched singular systems in [13, 14] and [15], respectively.

It has been shown that passivity is a suitable design approach in power systems [16], neural networks [17], network control [18–20], signal processing [21, 22], Markovian jumping systems [23–25], switched systems [26, 27], and singular systems [28, 29]. In [16], the problem of passive control is considered for uncertain singular time-delay systems, and three types of controllers were designed, namely, state feedback controller, observer-based state feedback controller, and

dynamic output feedback controller. Under these controllers, the closed-loop systems are quadratically stable and passive. Contingent failures are possible for a real system, which may cause performance of the system to be degraded and even hazard [30]. The work [17] applies passivity-based fault-tolerant synchronization control to chaotic neural networks against actuator faults by using the semi-Markov jump model approach. The work [27] investigates the problem of robust reliable passive control for a class of uncertain stochastic switched time-delay systems with actuator failures. Sufficient condition for the stochastic switched time-delay systems to be passive and exponentially stable under switching state feedback controller is derived. The work [29] designs a state feedback controller such that, for all possible actuator failures, the closed-loop singular system is exponentially stable and passive.

Up to now, little attention has been paid to passive control problem for switched singular systems. This motivates us to investigate this problem. Furthermore, considering the operational cost and the reliability of systems and the simplicity of implementation, output feedback is always adopted to stabilize a system. Thus, we study passive control of switched singular systems through output feedback.

In this paper, by introducing instrumental matrix variable, the nonlinear inequality including Lyapunov inverse matrix and controller gain matrix is decoupled, which makes the design of output feedback passive controllers for continuous-time switched singular systems easy. Based on multiple Lyapunov functions and variable substitution techniques, a new and simple sufficient condition is presented in terms of LMI, by solving which static output feedback passive controller can be designed. The novelty of the conditions proposed in this paper lies in the following aspect. Decomposition of Lyapunov matrix and its inverse matrix is not required. Moreover, the Lyapunov inverse matrix is not fixed to a special structure.

The rest of this paper is organized as follows. Problem statement and preliminaries are given in Section 2. Output feedback passive control is studied in Section 3. In Section 4, an example shows the efficiency of main results in the paper. Section 5 concludes this paper.

2. Problem Statement and Preliminaries

Consider the following switched singular system:

$$\begin{aligned} E_{ci}\dot{x}(t) &= A_{ci}x(t) + B_{ci}u(t) + G_{ci}\omega(t) \\ z(t) &= H_{ci}x(t) + D_{ci}\omega(t) \\ y(t) &= C_{ci}x(t), \end{aligned} \tag{1}$$

where $i \in \chi = \{1, 2, \ldots, m\}$ is the switching signal. $x(t) \in R^n$ is the state vector, $u(t) \in R^m$ is the control input vector, $\omega(t) \in L_2^r[0, \infty)$ is the external disturbance vector, $z(t) \in R^r$ is the control input vector, and $y(t) \in R^p$ is the measured controlled output vector. $E_{ci}, A_{ci}, B_{ci}, C_{ci}, D_{ci}, G_{ci}, H_{ci}$ are constant matrices with appropriate dimensions. $E_{ci} \in R^{n\times n}$ and rank $E_{ci} = r_i \leq n$. Without loss of generality, we assume that C_{ci} is full row rank.

Let us consider the following static output feedback controller:

$$u(t) = K_i y(t), \tag{2}$$

where K_i is the controller gain matrix to be designed.

Then, the resulting closed-loop system can be described as

$$\begin{aligned} E_{ci}\dot{x}(t) &= \left(A_{ci} + B_{ci}K_iC_{ci}\right)x(t) + G_{ci}\omega(t) \\ z(t) &= H_{ci}x(t) + D_{ci}\omega(t) \\ y(t) &= C_{ci}x(t). \end{aligned} \tag{3}$$

We are now considering the output feedback passive control problem for system (3). In this paper, we aim to design output feedback passive controller such that system (3) simultaneously satisfies the following two requirements.

(i) System (3) with $\omega(t) = 0$ is stable.

(ii) For a give scalar $\eta > 0$, the dissipation inequality

$$\int_0^T \left(\omega^T z - \eta\omega^T\omega\right)dt \geq 0, \quad \forall T > 0, \tag{4}$$

holds for all trajectories with zero initial condition. In this case, the closed-loop switched singular system (3) is said to be stable and passive with dissipation rate η.

To obtain the main results of this paper, the following transformation is introduced.

Since C_{ci} is full row rank, there exists a nonsingular matrix T_i such that $C_{ci}T_i^{-1} = [I_p \quad 0]$. Using the nonsingular T_i as a similarity transformation for system (3), the closed-loop system (3) is equivalent to the following system:

$$\begin{aligned} E_i\dot{x}(t) &= \overline{A}_i x(t) + G_i\omega(t) \\ z(t) &= H_i x(t) + D_i\omega(t) \\ y(t) &= C_i x(t), \end{aligned} \tag{5}$$

where $E_i = T_iE_{ci}T_i^{-1}$, $A_i = T_iA_{ci}T_i^{-1}$, $B_i = T_iB_{ci}$, $C_i = C_{ci}T_i^{-1} = [I_p \quad 0]$, $G_i = T_iG_{ci}$, $H_i = H_{ci}T_i^{-1}$, $D_i = D_{ci}$, and $\overline{A}_i = A_i + B_iK_iC_i$.

3. Output Feedback Passive Control

The following theorem provides a sufficient condition under which system (5) is stable and passive with dissipation rate η.

Theorem 1. *If there exist simultaneously nonnegative real number β_{ij}, η and matrices $X_i > 0$, $X_j > 0$ and matrices K_i such that for any $i, j \in \chi$, $i \neq j$,*

$$X_i^T E_i^T = E_i X_i \geq 0 \tag{6}$$

and inequality

$$\begin{bmatrix} X_i^T\overline{A}_i^T + \overline{A}_iX_i + \sum_{j=1}^{m}\beta_{ij}\left(E_i^TX_i - E_j^TX_j\right) & G_i - X_i^TH_i^T \\ G_i^T - H_iX_i & 2\eta I - D_i - D_i^T \end{bmatrix} < 0 \tag{7}$$

hold, system (5) is stable and passive with dissipation rate η under static output feedback $u(t) = K_iy(t)$ via switching signal

$$i = \arg\max\left\{x^T(t)E_i^TX_ix(t),\ i\in\chi\right\}. \tag{8}$$

Proof. When β_{ij} is simultaneously nonnegative, for $x \in R^n/\{x \mid \prod_{i=1}^m E_ix = 0\}$, there must exist a $i \in \chi = \{1,\dots,m\}$, such that for any $j \neq i$, $j \in \chi$, $x^T(E_i^TX_i - E_j^TX_j)x \geq 0$ holds. Then $\sum_{j=1}^m x^T(E_i^TX_i - E_j^TX_j)x \geq 0$ holds. Let

$$\Omega_i = \left\{x\in R^n \mid x^T\left(E_i^TX_i - E_j^TX_j\right)x \geq 0,\ \prod_{i=1}^m E_ix \neq 0,\ j\neq i,\ j\in\chi\right\}. \tag{9}$$

Clearly, $\bigcup_{i=1}^m \Omega_i = R^n/\{x \mid \prod_{i=1}^m E_ix = 0\}$.

Construct $\overline{\Omega}_1 = \Omega_1,\dots,\overline{\Omega}_i = \Omega_i - \bigcup_{j=1}^{i-1}\overline{\Omega}_j,\dots,\overline{\Omega}_m = \Omega_m - \bigcup_{j=1}^{m-1}\overline{\Omega}_j$. Obviously, $\bigcup_{i=1}^m\overline{\Omega}_i = R^n/\{x \mid \prod_{i=1}^m E_ix = 0\}$ and $\overline{\Omega}_i\bigcap\overline{\Omega}_j = \phi$, $i \neq j$, hold.

Design switching signal as

$$i = \arg\max\left\{x^T(t)E_i^TX_ix(t),\ i\in\chi\right\}. \tag{10}$$

When $x \in \overline{\Omega}_i$, choose Lyapunov function as

$$V(x(t)) = x^T(t)E_i^TX_i^{-1}x(t). \tag{11}$$

Premultiplying X_i^{-T} and postmultiplying X_i^{-1} to $X_i^TE_i^T = E_iX_i$ in (6), respectively, one gets $E_i^TX_i^{-1} = X_i^{-T}E_i$. Then, the derivation of Lyapunov function $V(x(t))$ along the closed-loop system (5) is

$$\begin{aligned}\dot V(x(t)) &= \dot x^T(t)E_i^TX_i^{-1}x(t) + x^T(t)E_i^TX_i^{-1}\dot x(t)\\ &= \left[\overline{A}_ix(t) + G_i\omega(t)\right]^TX_i^{-1}x(t)\\ &\quad + x^T(t)X_i^{-T}\left[\overline{A}_ix(t) + G_i\omega(t)\right].\end{aligned} \tag{12}$$

Therefore

$$\begin{aligned}&\dot V(x(t)) - 2\omega^T(t)z(t) + 2\eta\omega^T(t)\omega(t)\\ &\quad= \left[\overline{A}_ix(t) + G_i\omega(t)\right]^TX_i^{-1}x(t)\\ &\qquad + x^T(t)X_i^{-T}\left[\overline{A}_ix(t) + G_i\omega(t)\right]\\ &\qquad - 2\omega^T(t)\left[H_ix(t) + D_i\omega(t)\right] + 2\eta\omega^T(t)\omega(t)\\ &\quad= \begin{bmatrix}x(t)\\ \omega(t)\end{bmatrix}^T\begin{bmatrix}\overline{A}_i^TX_i^{-1} + X_i^{-T}\overline{A}_i & X_i^{-T}G_i - H_i^T\\ G_i^TX_i^{-1} - H_i & 2\eta I - D_i - D_i^T\end{bmatrix}\begin{bmatrix}x(t)\\ \omega(t)\end{bmatrix}\\ &\quad= \zeta^T(t)\Xi_i\zeta(t),\end{aligned} \tag{13}$$

where $\zeta(t) = \left[\begin{smallmatrix}x(t)\\ \omega(t)\end{smallmatrix}\right]$, $\Xi_i = \left[\begin{smallmatrix}\overline{A}_i^TX_i^{-1}+X_i^{-T}\overline{A}_i & X_i^{-T}G_i-H_i^T\\ G_i^TX_i^{-1}-H_i & 2\eta I-D_i-D_i^T\end{smallmatrix}\right]$. Pre- and postmultiplying Ξ_i by $\left[\begin{smallmatrix}X_i^T & 0\\ 0 & I\end{smallmatrix}\right]$ and $\left[\begin{smallmatrix}X_i & 0\\ 0 & I\end{smallmatrix}\right]$, respectively, we obtain

$$\begin{bmatrix}X_i^T & 0\\ 0 & I\end{bmatrix}\Xi_i\begin{bmatrix}X_i & 0\\ 0 & I\end{bmatrix} = \Phi_i, \tag{14}$$

where $\Phi_i = \left[\begin{smallmatrix}X_i^T\overline{A}_i^T+\overline{A}_iX_i & G_i-X_i^TH_i^T\\ G_i^T-H_iX_i & 2\eta I-D_i-D_i^T\end{smallmatrix}\right]$. Then, $\Xi_i < 0$ is equivalent to $\Phi_i < 0$. Next, we prove that $\Phi_i < 0$ holds.

Suppose that (7) holds. Inequality (7) can be rewritten as

$$\Phi_i + \begin{bmatrix}\sum_{j=1}^m\beta_{ij}\left(E_i^TX_i - E_j^TX_j\right) & 0\\ 0 & 0\end{bmatrix} < 0. \tag{15}$$

According to switching signal (8), $\Phi_i < 0$ when (15) holds, and by (13), we get that the following inequality holds:

$$\dot V(x(t)) - 2\omega^T(t)z(t) + 2\eta\omega^T(t)\omega(t) \leq 0. \tag{16}$$

Taking the integral on the two sides of (16) from 0 to T, we obtain

$$\int_0^T\left[\dot V(x(t)) - 2\omega^T(t)z(t) + 2\eta\omega^T(t)\omega(t)\right]dt \leq 0. \tag{17}$$

To get the result, we introduce

$$S(T) = \int_0^T\left[-2\omega^T(t)z(t) + 2\eta\omega^T(t)\omega(t)\right]dt, \tag{18}$$

where $T > 0$. Noting the zero initial condition, it can be shown that, for any $T > 0$,

$$S(T) \leq \int_0^T\left[\dot V(x(t)) - 2\omega^T(t)z(t) + 2\eta\omega^T(t)\omega(t)\right]dt. \tag{19}$$

It follows from (19) that $S(T) \le 0$, and hence

$$\int_0^T \left[-2\omega^T(t)\, z(t) + 2\eta\omega^T(t)\,\omega(t)\right] dt \le 0 \tag{20}$$

is satisfied for any $T > 0$. The system is passive with dissipation η.

Next, we prove the stability of system (5) with $\omega(t) = 0$. Following the similar procedures as used above, we have

$$\dot{V}(x(t)) = x^T(t)\left(\overline{A}_i^T X_i^{-1} + X_i^{-T}\overline{A}_i\right) x(t). \tag{21}$$

Note that (7) implies $\overline{A}_i^T X_i^{-1} + X_i^{-T}\overline{A}_i < 0$. Therefore, we have $\dot{V}(x(t)) < 0$ when (7) holds. According to Lyapunov theory, system (5) is stable. This completes the proof. □

Condition (7) in Theorem 1 is not linear matrix inequality, which cannot be solved by MATLAB. The controller gains K_i are also difficult to be computed from these conditions. In order to solve output feedback passive controller, we induce the following important lemma.

Lemma 2. *For any $i, j \in \chi$, inequality (7) holds if there exists an instrumental matrix Y_i such that*

$$\begin{bmatrix} \Psi_i & X_i^T - Y_i + \overline{A}_i Y_i^T & G_i - X_i^T H_i^T \\ X_i - Y_i^T + Y_i\overline{A}_i^T & -Y_i - Y_i^T & 0 \\ G_i^T - H_i X_i & 0 & 2\eta I - D_i - D_i^T \end{bmatrix} < 0, \tag{22}$$

where $\Psi_i = Y_i\overline{A}_i^T + \overline{A}_i Y_i^T + \sum_{j=1}^m \beta_{ij}(E_i^T X_i - E_j^T X_j)$.

Proof. Let $\Lambda_i = \begin{bmatrix} I & \overline{A}_i & 0 \\ 0 & 0 & I \end{bmatrix}$; then Λ_i is full row rank. By setting $\Psi_i = Y_i\overline{A}_i^T + \overline{A}_i Y_i^T + \sum_{j=1}^m \beta_{ij}(E_i^T X_i - E_j^T X_j)$, the result of Lemma 2 can be evidently derived from the fact that

$$\begin{aligned} &\Lambda_i \cdot \begin{bmatrix} \Psi_i & X_i^T - Y_i + \overline{A}_i Y_i^T & G_i - X_i^T H_i^T \\ X_i - Y_i^T + Y_i\overline{A}_i^T & -Y_i - Y_i^T & 0 \\ G_i^T - H_i X_i & 0 & 2\eta I - D_i - D_i^T \end{bmatrix} \cdot \Lambda_i^T \\ &= \begin{bmatrix} X_i^T\overline{A}_i^T + \overline{A}_i X_i + \sum_{j=1}^m \beta_{ij}\left(E_i^T X_i - E_j^T X_j\right) & G_i - X_i^T H_i^T \\ G_i^T - H_i X_i & 2\eta I - D_i - D_i^T \end{bmatrix}. \end{aligned} \tag{23}$$

□

Remark 3. The instrumental matrix variable Y_i is introduced to decouple Lyapunov inverse matrix X_i and controller gain matrix K_i, which makes the design of output feedback passive controllers feasible, and, at the same time, X_i and X_i^{-1} do not require decomposition or fixing to a certain structure.

Based on the above lemma, an LMI condition is presented, under which system (5) is stable and passive in the following theorem.

Theorem 4. *If there exist simultaneously nonnegative real number β_{ij}, η and matrices $Z_i > 0$, $Z_j > 0$, Y_i, W_i, U_i, U_j such that for any $i, j \in \chi$, $i \ne j$,*

$$\begin{bmatrix} \Theta_{i11} & \Theta_{i12} & \Theta_{i13} \\ \Theta_{i12}^T & -Y_i - Y_i^T & 0 \\ \Theta_{i13}^T & 0 & 2\eta I - D_i - D_i^T \end{bmatrix} < 0, \tag{24}$$

where $\Theta_{i11} = Y_i A_i^T + A_i Y_i^T + B_i W_i + W_i^T B_i^T + \sum_{j=1}^m \beta_{ij}(E_i^T Z_i E_i^T + E_i^T L_i U_i - E_j^T Z_j E_j^T - E_j^T L_j U_j)$, $\Theta_{i12} = E_i Z_i^T + U_i^T L_i^T - Y_i + A_i Y_i^T + B_i W_i$, $\Theta_{i13} = G_i - E_i Z_i^T H_i^T - U_i^T L_i^T H_i^T$, $Y_i = \begin{bmatrix} Y_{i11} & Y_{i12} \\ 0 & Y_{i22} \end{bmatrix}$, *and* $W_i = \begin{bmatrix} W_{i1} & 0 \end{bmatrix}$, *then, system (5) is stable and passive with dissipation rate η under static output feedback*

$$K_i = W_{i1} Y_{i11}^{-T} \tag{25}$$

via switching signal

$$i = \arg\max\left\{x^T(t)\, E_i^T\left(Z_i E_i^T + L_i U_i\right) x(t),\ i \in \chi\right\}. \tag{26}$$

Proof. Since $C_i = [I_p \quad 0]$ in $\overline{A}_i = A_i + B_i K_i C_i$, then $B_i K_i C_i Y_i^T = B_i[K_i \quad 0] Y_i^T$. Letting $Y_i = \begin{bmatrix} Y_{i11} & Y_{i12} \\ 0 & Y_{i22} \end{bmatrix}$, one gets $Y_i^T = \begin{bmatrix} Y_{i11}^T & 0 \\ Y_{i12}^T & Y_{i22}^T \end{bmatrix}$. Thus, $B_i[K_i \quad 0] Y_i^T = B_i[K_i Y_{i11}^T \quad 0]$. Let $W_i = [W_{i1} \quad 0]$, $W_{i1} = K_i Y_{i11}^T$. A static output feedback gain is denoted by $K_i = W_{i1} Y_{i11}^{-T}$.

By making use of the existent methods (e.g., [31, 32]), we introduce the matrix $L_i \in R^{n\times(n-r_i)}$ with rank $L_i = n - r_i$ satisfying $E_i L_i = 0$. By setting $X_i = Z_i E_i^T + L_i U_i$, one obtains that $X_i^{-T} E_i^T = E_i X_i \ge 0$ holds when $Z_i > 0$. Then, according to Lemma 2, inequality (6) and (7) can be rewritten as inequality (24). Inequality (24) is a linear matrix inequality. This completes the proof. □

Remark 5. If β_{ij} is nonpositive simultaneously, Theorem 4 also holds through choosing the switching signal as $i = \arg\min\{x^T(t) E_i^T (Z_i E_i^T + L_i U_i) x(t),\ i \in \chi\}$.

Remark 6. When switched singular system reduces to a single singular system (i.e., no switching), Theorem 4 also holds by setting $A_i = A$, $B_i = B$, $G_i = G$, and so forth. This will be illustrated in Corollary 7. When switched singular system reduces to a normal switched system (i.e., $E_{ci} = I$), the method introduced in this paper is also available, and, at the same time, Theorem 4 is rewritten as Corollary 8.

Corollary 7. *If there exist a real number $\eta > 0$ and matrices $Z > 0, Y, W, U$ such that*

$$\begin{bmatrix} \Theta_{11} & \Theta_{12} & \Theta_{13} \\ \Theta_{12}^T & -Y - Y^T & 0 \\ \Theta_{13}^T & 0 & 2\eta I - D - D^T \end{bmatrix} < 0, \tag{27}$$

where $\Theta_{11} = YA^T + AY^T + BW + W^T B^T$, $\Theta_{12} = EZ^T + U^T L^T - Y + AY^T + BW$, $\Theta_{13} = G - EZ^T H^T - U^T L^T H^T$, $Y = \begin{bmatrix} Y_{11} & Y_{12} \\ 0 & Y_{22} \end{bmatrix}$, *and* $W = \begin{bmatrix} W_1 & 0 \end{bmatrix}$, *then, the corresponding singular system is*

stable and passive with dissipation rate η under static output feedback

$$K = W_1 Y_{11}^{-T}. \tag{28}$$

Corollary 8. *If there exist simultaneously nonnegative real number β_{ij}, η and matrices $X_i > 0$, $X_j > 0$, Y_i, W_i such that for any $i, j \in \chi$, $i \neq j$,*

$$\begin{bmatrix} \Theta_{i11} & \Theta_{i12} & \Theta_{i13} \\ \Theta_{i12}^T & -Y_i - Y_i^T & 0 \\ \Theta_{i13}^T & 0 & 2\eta I - D_i - D_i^T \end{bmatrix} < 0, \tag{29}$$

where $\Theta_{i11} = Y_i A_i^T + A_i Y_i^T + B_i W_i + W_i^T B_i^T + \sum_{j=1}^m \beta_{ij}(X_i - X_j)$, $\Theta_{i12} = X_i^T - Y_i + A_i Y_i^T + B_i W_i$, $\Theta_{i13} = G_i - X_i^T H_i^T$, $Y_i = \begin{bmatrix} Y_{i11} & Y_{i12} \\ 0 & Y_{i22} \end{bmatrix}$, and $W_i = \begin{bmatrix} W_{i1} & 0 \end{bmatrix}$, then, the corresponding switched system is stable and passive with dissipation rate η under static output feedback

$$K_i = W_{i1} Y_{i11}^{-T} \tag{30}$$

via switching signal

$$i = \arg\max \left\{ x^T(t) X_i x(t),\ i \in \chi \right\}. \tag{31}$$

4. Example

Consider the switched singular system composed of two subsystems

$$\begin{aligned} E_{ci}\dot{x}(t) &= A_{ci}x(t) + B_{ci}u(t) + G_{ci}\omega(t) \\ z(t) &= H_{ci}x(t) + D_{ci}\omega(t) \\ y(t) &= C_{ci}x(t) \\ i &= 1, 2, \end{aligned} \tag{32}$$

where

$$\begin{aligned} E_{c1} &= \begin{bmatrix} 1 & 0 \\ 0 & 0 \end{bmatrix}, & E_{c2} &= \begin{bmatrix} 1 & 0 \\ 0 & 0 \end{bmatrix}, \\ A_{c1} &= \begin{bmatrix} 5 & -2 \\ 10 & -15 \end{bmatrix}, & A_{c2} &= \begin{bmatrix} -6 & -1 \\ -1 & 1.5 \end{bmatrix}, \\ B_{c1} &= \begin{bmatrix} -3 \\ 2.5 \end{bmatrix}, & B_{c2} &= \begin{bmatrix} -4 \\ 2 \end{bmatrix}, \\ C_{c1} &= \begin{bmatrix} 2 & 1 \end{bmatrix}, & C_{c2} &= \begin{bmatrix} -1 & 2 \end{bmatrix}, \\ G_{c1} &= \begin{bmatrix} 0 \\ 1 \end{bmatrix}, & G_{c2} &= \begin{bmatrix} 0 \\ 1 \end{bmatrix}, \\ D_{c1} &= 2, & D_{c2} &= 1, \\ H_{c1} &= \begin{bmatrix} 1 & 1 \end{bmatrix}, & H_{c2} &= \begin{bmatrix} 1 & 2 \end{bmatrix}. \end{aligned} \tag{33}$$

Choose similarity transformation matrices as

$$T_1 = \begin{bmatrix} 2 & 1 \\ -1 & -1 \end{bmatrix}, \qquad T_2 = \begin{bmatrix} -1 & 2 \\ 1 & -1 \end{bmatrix}. \tag{34}$$

Then, we get an equivalent state-space description of the above system:

$$\begin{aligned} E_i\dot{x}(t) &= A_i x(t) + B_i u(t) + G_i\omega(t) \\ z(t) &= H_i x(t) + D_i\omega(t) \\ y(t) &= C_i x(t), \\ i &= 1, 2, \end{aligned} \tag{35}$$

where

$$\begin{aligned} E_1 &= T_1 E_{c1} T_1^{-1} = \begin{bmatrix} 2 & 2 \\ -1 & -1 \end{bmatrix}, \\ E_2 &= T_2 E_{c2} T_2^{-1} = \begin{bmatrix} -1 & -2 \\ 1 & 2 \end{bmatrix}, \\ A_1 &= T_1 A_{c1} T_1^{-1} = \begin{bmatrix} 39 & 58 \\ -32 & -49 \end{bmatrix}, \\ A_2 &= T_2 A_{c2} T_2^{-1} = \begin{bmatrix} 8 & 12 \\ -7.5 & -12.5 \end{bmatrix}, \\ B_1 &= T_1 B_{c1} = \begin{bmatrix} -3.5 \\ 0.5 \end{bmatrix}, \\ B_2 &= T_2 B_{c2} = \begin{bmatrix} 8 \\ -6 \end{bmatrix}, \\ C_1 &= C_{c1} T_1^{-1} = \begin{bmatrix} 1 \\ 0 \end{bmatrix}^T, \\ C_2 &= C_{c2} T_2^{-1} = \begin{bmatrix} 1 \\ 0 \end{bmatrix}^T, \\ D_1 &= D_{c1} = 2, \\ D_2 &= D_{c2} = 1, \\ G_1 &= T_1 G_{c1} = \begin{bmatrix} 1 \\ -1 \end{bmatrix}, \\ G_2 &= T_2 G_{c2} = \begin{bmatrix} 2 \\ -1 \end{bmatrix}, \\ H_1 &= H_{c1} T_1^{-1} = \begin{bmatrix} 0 & -1 \end{bmatrix}, \\ H_2 &= H_{c2} T_2^{-1} = \begin{bmatrix} 3 & 4 \end{bmatrix}. \end{aligned} \tag{36}$$

Choose $\beta_{12} = \beta_{21} = 0.5$, $L_1 = \left[\begin{smallmatrix} 1 \\ -1 \end{smallmatrix}\right]$, $L_2 = \left[\begin{smallmatrix} -2 \\ 1 \end{smallmatrix}\right]$. By solving linear matrix inequality (24) in Theorem 4, we can obtain

$$\begin{aligned} Z_1 &= \begin{bmatrix} 6.1107 & 1.6528 \\ 1.6528 & 0.9175 \end{bmatrix}, \\ Z_2 &= \begin{bmatrix} 2.0404 & -1.1790 \\ -1.1790 & 0.9889 \end{bmatrix}, \\ Y_1 &= \begin{bmatrix} 0.6280 & -0.0791 \\ 0 & 0.0364 \end{bmatrix}, \\ Y_2 &= \begin{bmatrix} 2.7362 & -1.3902 \\ 0 & 0.5073 \end{bmatrix}, \\ W_1 &= \begin{bmatrix} 10.0425 & 0 \end{bmatrix}, \\ W_2 &= \begin{bmatrix} -2.2475 & 0 \end{bmatrix}, \\ X_1 &= \begin{bmatrix} 19.9846 & -6.8114 \\ 0.6831 & -3.5225 \end{bmatrix}, \\ X_2 &= \begin{bmatrix} 7.5201 & -3.3638 \\ -4.4000 & 2.3218 \end{bmatrix}, \\ X_1^{-1} &= \begin{bmatrix} 0.0536 & -0.1036 \\ 0.0104 & -0.3040 \end{bmatrix}, \\ X_2^{-1} &= \begin{bmatrix} 0.8729 & 1.2647 \\ 1.6543 & 2.8273 \end{bmatrix}. \end{aligned} \tag{37}$$

By linear matrix inequality (24), output feedback passive control gains can be obtained:

$$K_1 = 15.9905, \qquad K_2 = -0.8214. \tag{38}$$

The dissipation rate can be obtained:

$$\eta = 0.5. \tag{39}$$

The corresponding switching signal is chosen as

$$\begin{aligned} i &= \begin{cases} 1, & x(t) \in \Omega_1 \\ 2, & x(t) \in \dfrac{\Omega_2}{\Omega_1}, \end{cases} \\ \Omega_1 &= \left\{ x \in R^n \mid x^T \left(E_1^T X_1 - E_2^T X_2 \right) x \geq 0, \right. \\ &\qquad \left. E_1 x \neq 0,\ E_2 x \neq 0 \right\} \\ \Omega_2 &= \left\{ x \in R^n \mid x^T \left(E_2^T X_2 - E_1^T X_1 \right) x \geq 0, \right. \\ &\qquad \left. E_1 x \neq 0,\ E_2 x \neq 0 \right\}. \end{aligned} \tag{40}$$

Under the switching signal, the response curve of the above system is exhibited in Figure 1, where $\omega(t) = \sin t e^{-0.1t}$. From Figure 1, it is obvious that the resulting closed-loop system is stable.

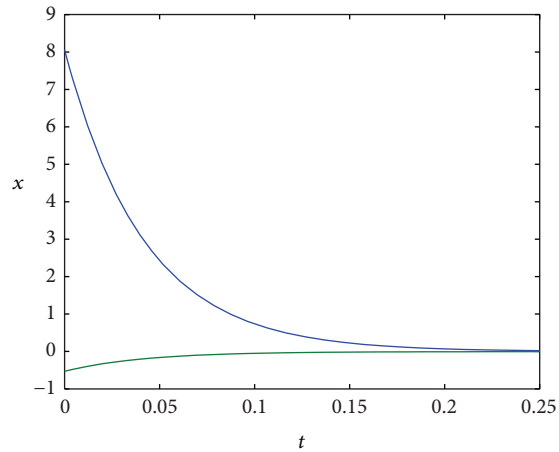

Figure 1: State response of the corresponding closed-loop system.

5. Conclusion

In this paper, the output feedback passive control problem for a class of switched singular systems is investigated. A novel method is proposed to solve static output feedback passive controllers. Sufficient linear matrix inequality condition is presented by means of introducing instrumental matrix variable Y_i and multiple Lyapunov function technique under designed switching law. An example is given to verify the LMI condition proposed for the resulting closed-loop system to be stable and passive with a lower dissipation rate η. Passivity is a suitable design approach in network control. How to extend the results of this paper to network-based control is an interesting problem. This problem deserves a further study and it remains as our future work.

Conflict of Interests

The authors declare that there is no conflict of interests regarding the publication of this paper.

Acknowledgments

This work is supported by the National Natural Science Foundation of China under Grants nos. 61203001, 61104066, and 61473140, Liaoning Educational Committee Foundation under Contract L2014525, and the Natural Science Foundation of Liaoning Province under Grant no. 2014020106.

References

[1] B. Cantó, C. Coll, and E. Sánchez, "Positive N-periodic descriptor control systems," *Systems & Control Letters*, vol. 53, no. 5, pp. 407–414, 2004.

[2] W. Xiong, D. W. C. Ho, and J. Cao, "Synchronization analysis of singular hybrid coupled networks," *Physics Letters, Section A: General, Atomic and Solid State Physics*, vol. 372, no. 44, pp. 6633–6637, 2008.

[3] Y. Q. Xia, E.-K. Boukas, P. Shi, and J. H. Zhang, "Stability and stabilization of continuous-time singular hybrid systems," *Automatica*, vol. 45, no. 6, pp. 1504–1509, 2009.

[4] G. S. Zhai, X. P. Xu, and D. W. C. Ho, "Stability of switched linear discrete-time descriptor systems: a new commutation condition," *International Journal of Control*, vol. 85, no. 11, pp. 1779–1788, 2012.

[5] D. Liberzon and S. Trenn, "On stability of linear switched differential algebraic equations," in *Proceedings of the 48th IEEE Conference on Decision and Control (CDC '09)*, pp. 2156–2161, December 2009.

[6] J. Clotet, J. Ferrer, and M. D. Magret, "Switched singular linear systems," in *Proceedings of the 17th Mediterranean Conference on Control and Automation (MED '09)*, pp. 1343–1347, Thessaloniki, Greece, June 2009.

[7] F. Long, Y. Xiao, X. Chen, and Z. H. Zhang, "Disturbance attenuation for nonlinear switched descriptor systems based on neural network," *Neural Computing and Applications*, vol. 23, no. 7-8, pp. 2211–2219, 2013.

[8] I. Zamani and M. Shafiee, "On the stability issues of switched singular time-delay systems with slow switching based on average dwell-time," *International Journal of Robust and Nonlinear Control*, vol. 24, no. 4, pp. 595–624, 2014.

[9] B. Meng and J.-F. Zhang, "Reachability conditions for switched linear singular systems," *IEEE Transactions on Automatic Control*, vol. 51, no. 3, pp. 482–488, 2006.

[10] X. Y. Ding, X. Liu, and S. M. Zhong, "Delay-independent criteria for exponential admissibility of switched descriptor delayed systems," *Applied Mathematics and Computation*, vol. 228, pp. 432–445, 2014.

[11] L. Zhou, D. W. Ho, and G. Zhai, "Stability analysis of switched linear singular systems," *Automatica*, vol. 49, no. 5, pp. 1481–1487, 2013.

[12] S. H. Shi, Q. L. Zhang, Z. H. Yuan, and W. Q. Liu, "Hybrid impulsive control for switched singular systems," *IET Control Theory & Applications*, vol. 5, no. 1, pp. 103–111, 2011.

[13] J. X. Lin, S. M. Fei, and Q. Wu, "Reliable H_∞ filtering for discrete-time switched singular systems with time-varying delay," *Circuits, Systems, and Signal Processing*, vol. 31, no. 3, pp. 1191–1214, 2012.

[14] D. Zhang, L. Yu, Q.-G. Wang, C.-J. Ong, and Z.-G. Wu, "Exponential H_∞ filtering for discrete-time switched singular systems with time-varying delays," *Journal of the Franklin Institute*, vol. 349, no. 7, pp. 2323–2342, 2012.

[15] D. Koenig, B. Marx, and D. Jacquet, "Unknown input observers for switched nonlinear discrete time descriptor systems," *IEEE Transactions on Automatic Control*, vol. 53, no. 1, pp. 373–379, 2008.

[16] Q. Li, Q. L. Zhang, N. Yi, and Y. H. Yuan, "Robust passive control for uncertain time-delay singular systems," *IEEE Transactions on Circuits and Systems I: Regular Papers*, vol. 56, no. 3, pp. 653–663, 2009.

[17] J. Wang and H. Shen, "Passivity-based fault-tolerant synchronization control of chaotic neural networks against actuator faults using the semi-Markov jump model approach," *Neurocomputing*, vol. 143, pp. 51–56, 2014.

[18] H. J. Gao, T. W. Chen, and T. Y. Chai, "Passivity and passification for networked control systems," *SIAM Journal on Control and Optimization*, vol. 46, no. 4, pp. 1299–1322, 2007.

[19] K. Liu and E. Fridman, "Wirtinger's inequality and Lyapunov-based sampled-data stabilization," *Automatica*, vol. 48, no. 1, pp. 102–108, 2012.

[20] K. Liu, E. Fridman, and L. Hetel, "Stability and L_2-gain analysis of networked control systems under Round-Robin scheduling: a time-delay approach," *Systems & Control Letters*, vol. 61, pp. 666–675, 2012.

[21] Z. Feng and J. Lam, "Robust reliable dissipative filtering for discrete delay singular systems," *Signal Processing*, vol. 92, no. 12, pp. 3010–3025, 2012.

[22] Z.-G. Wu, J. H. Park, H. Su, B. Song, and J. Chu, "Mixed H_∞ and passive filtering for singular systems with time delays," *Signal Processing*, vol. 93, no. 7, pp. 1705–1711, 2013.

[23] Z. L. Xia, J. M. Li, and J. R. Li, "Passivity-based resilient adaptive control for fuzzy stochastic delay systems with Markovian switching," *Journal of the Franklin Institute*, vol. 351, no. 7, pp. 3818–3836, 2014.

[24] S. He and F. Liu, "Optimal finite-time passive controller design for uncertain nonlinear Markovian jumping systems," *Journal of the Franklin Institute: Engineering and Applied Mathematics*, vol. 351, no. 7, pp. 3782–3796, 2014.

[25] X. M. Yao and L. Guo, "Composite disturbance-observer-based output feedback control and passive control for Markovian jump systems with multiple disturbances," *IET Control Theory & Applications*, vol. 8, no. 10, pp. 873–881, 2014.

[26] J. C. Geromel, P. Colaneri, and P. Bolzern, "Passivity of switched linear systems: analysis and control design," *Systems and Control Letters*, vol. 61, no. 4, pp. 549–554, 2012.

[27] H. M. Jia, Z. R. Xiang, and H. R. Karimi, "Robust reliable passive control of uncertain stochastic switched time-delay systems," *Applied Mathematics and Computation*, vol. 231, pp. 254–267, 2014.

[28] G. L. Wang, Q. L. Zhang, and C. Y. Yang, "Dissipative control for singular Markovian jump systems with time delay," *Optimal Control Applications & Methods*, vol. 33, no. 4, pp. 415–432, 2012.

[29] Z.-G. Wu, J. H. Park, H. Su, and J. Chu, "Reliable passive control for singular systems with time-varying delays," *Journal of Process Control*, vol. 23, no. 8, pp. 1217–1228, 2013.

[30] H. Y. Li, H. J. Gao, P. Shi, and X. D. Zhao, "Fault-tolerant control of Markovian jump stochastic systems via the augmented sliding mode observer approach," *Automatica*, vol. 50, no. 7, pp. 1825–1834, 2014.

[31] L. Q. Zhang, B. Huang, and J. Lam, "LMI synthesis of H_2 and mixed H_2/H_∞ controllers for singular systems," *IEEE Transactions on Circuits and Systems II: Analog and Digital Signal Processing*, vol. 50, no. 9, pp. 615–626, 2003.

[32] E. Uezato and M. Ikeda, "Strict LMI conditions for stability, robust stabilization, and H_∞ control of descriptor systems," in *Proceedings of the 38th IEEE Conference on Decision and Control (CDC '99)*, vol. 4, pp. 4092–4097, IEEE, Phoenix, Ariz, USA, December 1999.

Hindawi Publishing Corporation
Mathematical Problems in Engineering
Volume 2015, Article ID 875843, 9 pages
http://dx.doi.org/10.1155/2015/875843

Research Article

Vector Control Algorithm for Electric Vehicle AC Induction Motor Based on Improved Variable Gain PID Controller

Gang Qin,[1] Mushuang Liu,[2] Jianxiao Zou,[1] and Xiaoshuai Xin[1]

[1] *School of Automation Engineering, University of Electronic Science and Technology of China, Chengdu 610023, China*
[2] *School of Microelectronics and Solid-State Electronics, University of Electronic Science and Technology of China, Chengdu 610023, China*

Correspondence should be addressed to Mushuang Liu; lxwgws@163.com

Received 3 December 2014; Revised 28 December 2014; Accepted 28 December 2014

Academic Editor: Hui Zhang

Copyright © 2015 Gang Qin et al. This is an open access article distributed under the Creative Commons Attribution License, which permits unrestricted use, distribution, and reproduction in any medium, provided the original work is properly cited.

The acceleration performance of EV, which affects a lot of performances of EV such as start-up, overtaking, driving safety, and ride comfort, has become increasingly popular in recent researches. An improved variable gain PID control algorithm to improve the acceleration performance is proposed in this paper. The results of simulation with Matlab/Simulink demonstrate the effectiveness of the proposed algorithm through the control performance of motor velocity, motor torque, and three-phase current of motor. Moreover, it is investigated that the proposed controller is valid by comparison with the other PID controllers. Furthermore, the AC induction motor experiment set is constructed to verify the effect of proposed controller.

1. Introduction

With the increased emphasis on saving energy and reducing emission, electric vehicles (EVs) have emerged as very strong candidates to achieve these goals [1–5]. Moreover, the acceleration performance of EV, which affects a lot of performances of EV such as start ability, passing ability, driving safety, and ride comfort, is the key point of EV researches.

Vector control algorithm, which can accurately control the torque and has a wide control range of motor velocity and also has a current loop which can be used for current limiting protection, is widely used in EV driving control. However, the velocity loop controller of vector control algorithm, which uses traditional PID control algorithm generally, limits the dynamic performance of driving system and the acceleration performance of EV. During the last few years, the velocity loop controller of EV AC induction motor (ACIM) controller system is researched and improved unceasingly and many methods are presented. One method is using the fuzzy controller to replace velocity loop traditional PID controller and current loop traditional PID controller of vector control algorithm [6–8], which can make the control system track the different given velocity rapidly and without overshoot in different load and has strong ability against load disturbance, but its steady-state accuracy is not high because of no existing integration element. Another method is using the neutral network PID controller to replace velocity loop traditional PID controller of vector control algorithm [9–11], which has the advantages of adjusting velocity rapidly, zero overshoot, smooth and small-fluctuation control signals, and good system tracking, but it reduces the EV control performance due to learning slowly in learning process and long response time. Literature [12] also presented a method using the fuzzy-PI controller which executes fuzzy control algorithm when velocity deviation is greater than given threshold and executes traditional PID control algorithm when velocity deviation is less instead of velocity loop traditional PID controller [13]. The method can make velocity response rapidly with small overshoot [14], but it is difficult to achieve completely smooth switching and may cause velocity hop when control algorithm switches, thereby affecting the driving safety and ride comfort when EV accelerates.

In this paper, we design a vector control algorithm for vehicle asynchronous motor based on improved variable gain PID controller which can make motor velocity rise rapidly and no overshoot. Moreover, it can satisfy the demands of

EV driving system dynamic performance and acceleration performance no matter whether the EV runs in low velocity, normal velocity, high velocity, or variable velocity.

The sections are organized as follows. In Section 2, asynchronous motor model is studied. In Section 3, improved variable gain PID control algorithm is designed to improve the acceleration performance. In Section 4, vector control algorithm for EV asynchronous motor based on improved variable gain PID controller is proposed. Furthermore the stability condition is given. In Section 5, the effectiveness of controller is demonstrated by simulation with Matlab/Simulink (Figure 4). Section 6 presents some concluding remarks.

2. AC Induction Motor Model

ACIM is widely applied to EV driving system, which has many good characteristics such as robustness, durability, simple structure, reliable operation, low cost, low torque ripple, low noise, no position sensor, and high velocity limit. The design of ACIM for EV which is different from normal ACIM and must satisfy the power performance of EV must have the following characteristics: (1) constant power output and big velocity adjustable range for satisfying the demands for flat road, overtaking, and so on when run in high/low velocity, (2) smaller mass and volume in the condition of certain power level, and (3) robust structure and resistance to vibrations [15].

This paper which takes ACIM for example researches motor mathematical model of EV driving system. The mathematical model of ACIM is a nonlinear, high order, close coupling multivariable system. Ignore these factors such as core loss, space harmonics, the change of frequency, the change of temperature, and the saturation of magnetic circuit on the impact of winding resistances when establishing motor model [16].

A physical model of ACIM is shown in Figure 1. The three-phase winding resistances which are 120° phase different in the space are symmetrical, and the mutual inductance and self-inductance of every winding resistance are constant. The mathematical models of ACIM, which consist of voltage matrix equation, magnetic linkage matrix equation, and torque equation, can be obtained according to the physical model of ACIM.

Based on the voltage balance principle of three-phase stator winding resistances, the voltage matrix equation [17] can be written as

$$\begin{bmatrix} u_A \\ u_B \\ u_C \\ u_a \\ u_b \\ u_c \end{bmatrix} = \begin{bmatrix} R_s & 0 & 0 & 0 & 0 & 0 \\ 0 & R_s & 0 & 0 & 0 & 0 \\ 0 & 0 & R_s & 0 & 0 & 0 \\ 0 & 0 & 0 & R_r & 0 & 0 \\ 0 & 0 & 0 & 0 & R_r & 0 \\ 0 & 0 & 0 & 0 & 0 & R_r \end{bmatrix} \begin{bmatrix} i_A \\ i_B \\ i_C \\ i_a \\ i_b \\ i_c \end{bmatrix} + p \begin{bmatrix} \psi_A \\ \psi_B \\ \psi_C \\ \psi_a \\ \psi_b \\ \psi_c \end{bmatrix}, \quad (1)$$

where u_A, u_B, and u_C are stator phase voltage, u_a, u_b, and u_c are rotor phase voltage, i_A, i_B, and i_C are stator phase current, i_a, i_b, and i_c are rotor phase current, ψ_A, ψ_B, and ψ_C are magnetic linkage of stator winding resistance, ψ_a, ψ_b, and ψ_c are magnetic linkage of rotor winding resistance, R_s is stator resistance, R_r is rotor resistance, and p is differential operator.

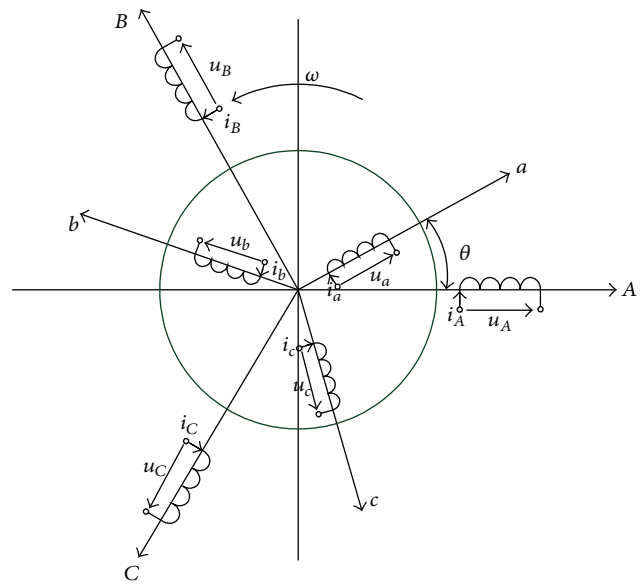

Figure 1: The physical model of ACIM.

Based on the principle that the magnetic linkage of every winding resistance is equal to its self-inductance magnetic linkage plus mutual inductance magnetic linkage with other winding resistances, the magnetic linkage matrix equation can be written as

$$\begin{bmatrix} \psi_A \\ \psi_B \\ \psi_C \\ \psi_a \\ \psi_b \\ \psi_c \end{bmatrix} = \begin{bmatrix} L_{AA} & L_{AB} & L_{AC} & L_{Aa} & L_{Ab} & L_{Ac} \\ L_{BA} & L_{BB} & L_{BC} & L_{Ba} & L_{Bb} & L_{Bc} \\ L_{CA} & L_{CB} & L_{CC} & L_{Ca} & L_{Cb} & L_{Cc} \\ L_{aA} & L_{aB} & L_{aC} & L_{aa} & L_{ab} & L_{ac} \\ L_{bA} & L_{bB} & L_{bC} & L_{ba} & L_{bb} & L_{bc} \\ L_{cA} & L_{cB} & L_{cC} & L_{ca} & L_{cb} & L_{cc} \end{bmatrix} \begin{bmatrix} i_A \\ i_B \\ i_C \\ i_a \\ i_b \\ i_c \end{bmatrix}, \quad (2)$$

where L_{AA} is self-inductance and L_{AB} is mutual inductance.

The torque equation can be expressed as

$$\begin{aligned} T_e = n_p L_m \big[& (i_A i_a + i_B i_b + i_C i_c) \sin\theta \\ & + (i_A i_b + i_B i_c + i_C i_a) \sin(\theta + 120^\circ) \\ & + (i_A i_c + i_B i_a + i_C i_b) \sin(\theta - 120^\circ) \big], \end{aligned} \quad (3)$$

where n_p is pole pairs, L_m is mutual inductance, and θ is electrical degree difference between a axis and A axis.

The ACIM, whose mathematical model is very complex, is very difficult to be controlled in practical application. The vector control algorithm controls ACIM as DC motor through coordinate transformation for the problem that the mathematical model ACIM is very complex so that the governing performance of ACIM can be comparable with DC motor.

3. Improved Variable Gain PID Control Algorithm Design

The fundamental thought of traditional variable gain PID control algorithm is matching the cumulative velocity of integral value with the magnitude of deviation. The integral action reduces to nothing for preventing integral saturation when system deviation is large and is reinforced for improving the stability of velocity when system deviation is small. The more desirable situation is matching the magnitude of proportional coefficient with deviation. The action of proportional part is reinforced for improving the dynamic performance of system when system deviation is large and reduces for preventing overshoot when system deviation is small. This paper designs an improved variable gain PID control algorithm based on improving the variable gain PID control algorithm.

The proportional and integral term of improved variable gain PID control algorithm can be expressed as

$$u(k) = \left(k_p + x[e(k)]\right)e(k) + k_i\left\{\sum_{i=0}^{k-1} e(i) + y[e(k)]\,e(k)\right\}T, \tag{4}$$

where $x[e(k)]$ and $y[e(k)]$ are the functions of deviation $e(k)$. As $e(k)$ increases, $x[e(k)]$ increases and $y[e(k)]$ reduces. As $e(k)$ reduces, $x[e(k)]$ reduces and $y[e(k)]$ increases.

The expression of $x[e(k)]$ can be described as

$$x[e(k)] = \begin{cases} k'_{p1}, & |e(k)| \le e_2, \\ \dfrac{k'_{p2} - k'_{p1}}{e_1}\left(|e(k)| - e_2\right) + k'_{p1}, & e_2 < |e(k)| \le e_1 + e_2, \\ k'_{p2}, & |e(k)| > e_1 + e_2, \end{cases} \tag{5}$$

where parameters e_1, e_2, k'_{p1}, and k'_{p2} are necessary to be ensured, $0 \le k'_{p1} < k'_{p2}$. On one hand, the chosen values of these four parameters must satisfy the condition of system stability. On the other hand, the chosen values of e_1 and k'_{p2} must meet the condition of velocity, and the chosen values of e_2 and k'_{p1} must meet the condition of no velocity overshoot.

The value of $x[e(k)]$ varies in the range of interval $[k'_{p1}, k'_{p2}]$.

When $|e(k)| > e_1 + e_2$, $x[e(k)]$ is equal to k'_{p2} and the proportional coefficient of control algorithm is equal to $k_p + k'_{p2}$, for improving the dynamic performance of system.

When $|e(k)| \le e_2$, $x[e(k)]$ is equal to k'_{p1} and the proportional coefficient of control algorithm is equal to the minimum value $k_p + k'_{p1}$, for preventing overshoot.

When $e_2 < |e(k)| \le e_1 + e_2$, the value of $x[e(k)]$ which is in the range of interval $[k'_{p1}, k'_{p2}]$ and the proportional coefficient of control algorithm which is in the range of interval $[k_p + k'_{p1}, k_p + k'_{p2}]$ vary with the magnitude of $|e(k)|$.

The expression of $x[e(k)]$ can be described as

$$y[e(k)] = \begin{cases} 1, & |e(k)| \le e_4, \\ \dfrac{k'_i - 1}{e_3}\left(|e(k)| - e_4\right) + 1, & e_4 < |e(k)| \le e_3 + e_4, \\ k'_i, & |e(k)| > e_3 + e_4, \end{cases} \tag{6}$$

where parameters e_3, e_4, and k'_i are necessary to be ensured, $0 \le k'_i < 1$. On one hand, the chosen values of these three parameters must satisfy the condition of system stability. On the other hand, the chosen values of e_3 and k'_i must meet the condition of no integral saturation and velocity overshoot, and the chosen value of e_4 must make velocity stability rapidly.

The value of $y[e(k)]$ varies in the range of interval $[k'_i, 1]$.

When $|e(k)| > e_3 + e_4$, the value of $y[e(k)]$ is equal to k'_i, for reducing the integral action to the lowest or not accumulating the current value of $e(k)$.

When $|e(k)| \le e_4$, the integral term is the same as the general, for increasing the integral action to the highest and accumulating the current value of $e(k)$.

When $e_4 < |e(k)| \le e_3 + e_4$, the value of $y[e(k)]$, which is in the range of interval $[k'_i, 1]$, varies with the magnitude of $|e(k)|$ and the integral term accumulates part current value of $e(k)$. Thus, the integral velocity is in the range of $k_i\{\sum_{i=0}^{k-1} e(i) + k'_i e(k)\}T$ to $k_i \sum_{i=0}^{k} e(i)T$.

In order to increase the regulating range of improved variable gain PID control algorithm, the values of parameters e_1, e_2, e_3, and e_4 must be decided by the maximum value of deviation after desired value varies which are not fixed values. Thus, we can get

$$\begin{aligned} e_1 &= |e_{\max}|\, m_1, \\ e_2 &= |e_{\max}|\, m_2, \\ e_3 &= |e_{\max}|\, m_3, \\ e_4 &= |e_{\max}|\, m_4, \end{aligned} \tag{7}$$

where $e_{\max}$ is the maximum value of deviation between desired value and feedback value after the desired value of controller input changes and parameters m_1, m_2, m_3, and m_4 are necessary to be ensured, which must satisfy $0 < m_i < 1$, $i = 1, 2, 3, 4$, $0 < m_1 + m_2 < 1$, and $0 < m_3 + m_4 < 1$. First of all, the chosen values of these four parameters must satisfy the condition of system stability. Secondly, the chosen value of m_1 must make velocity stability rapidly, and the chosen value of m_2 must meet the condition of no velocity overshoot, and the chosen value of m_3 must meet the condition of no integral saturation and velocity overshoot, and the chosen value of m_4 must make velocity stability rapidly.

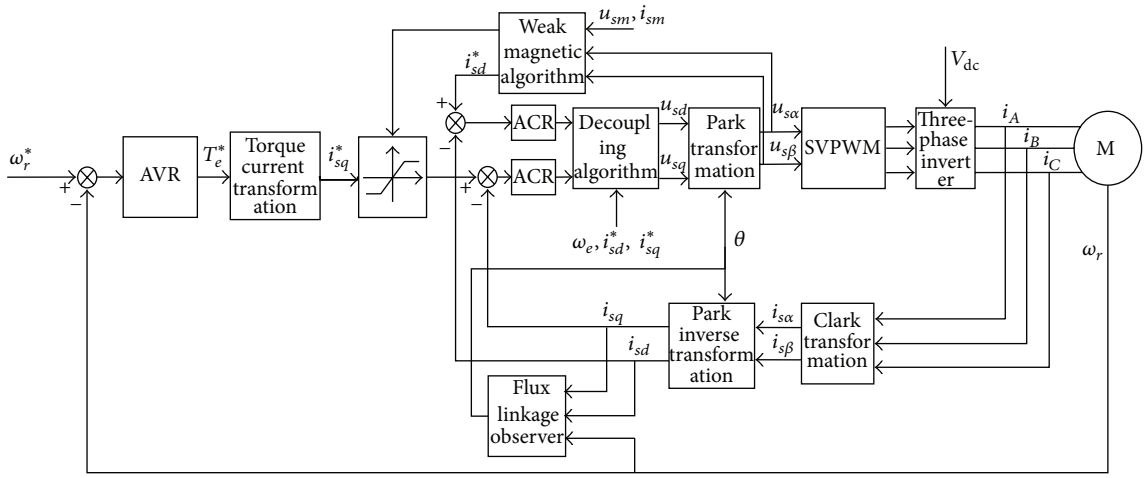

Figure 2: The block diagram of vector control algorithm based on improved variable gain PID controller motor.

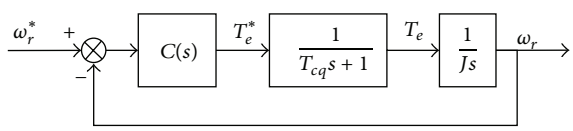

Figure 3: The transfer function block diagram of vector control algorithm based on improved variable gain PID controller.

Finally, the improved variable gain PID control algorithm is obtained as

$$\begin{aligned} u(k) = {} & \left(k_p + x\left[e(k)\right]\right) e(k) \\ & + k_i \left\{ \sum_{i=0}^{k-1} e(i) + y\left[e(k)\right] e(k) \right\} T \\ & + k_d \frac{e(k) - e(k-1)}{T}. \end{aligned} \tag{8}$$

Because requirement of improved variable gain PID control algorithm to the values of parameters m_1, m_2, m_3, m_4, k'_{p1}, k'_{p2}, and k'_i is not accurate, the values are easy to be ensured.

4. Vector Control Algorithm for Vehicle Asynchronous Motor Based on Improved Variable Gain PID Controller

The block diagram of vector control algorithm for EV ACIM based on improved variable gain PID controller is obtained in Figure 2. This algorithm, which uses rotator flux oriented, uses velocity and current double closed-loop control algorithm in control structure.

In outer loop control, collect motor rotor velocity ω_r via revolution velocity transducer from the ACIM side. Then, set the deviation between expected rotor velocity ω_r^* and feedback rotor velocity ω_r as the input of automatic voltage regulator (AVR), and the output is expected electromagnetic torque T_e^*. The expected electromagnetic torque via torque-current transformation and slicing obtains the inner loop expected torque current i_{sq}^*. The requisite parameter θ of Park transformation and Park inverse transformation is provided by flux linkage observer. The inputs of weak magnetic block are $u_{s\alpha}$, $u_{s\beta}$, the maximum output voltage value of inverter is u_{sm}, and the maximum motor current value in safe running is i_{sm}, and the outputs are the slicing values of expected excitation current i_{sd}^* and expected torque current i_{sq}^*.

The transfer function block diagram of vector control algorithm for EV asynchronous motor based on improved variable gain PID controller can be obtained in Figure 2.

In Figure 3, $1/T_{cq}s + 1$ is closed-loop transfer function of torque control system. So the transfer function of controlled object can be expressed as

$$G(s) = \frac{1}{T_{cq}s + 1} * \frac{1}{Js} = \frac{1}{\left(\sigma L_s / k_{iq}\right) s + 1} * \frac{1}{Js}, \tag{9}$$

where k_{iq} is q loop integral coefficient of vector control algorithm current loop, σ is leakage inductance coefficient of ACIM, L_s is stator inductance of ACIM, and J is moment of inertia of ACIM.

The differentiation element of PID control algorithm, which is sensitive to the noise of input signal, is not used in the system which has bigger noise in general. Thus, only PI control in the velocity loop controller of vector control algorithm for EV ACIM in general is used.

The transfer function of velocity loop controller based on improved variable gain PID control algorithm is given as

$$C(s) = \frac{\left(k_p + x\left[e(k)\right]\right) s + k_i y\left[e(k)\right]}{s}, \tag{10}$$

where k_p is proportional coefficient of traditional PID control algorithm, k_i is integral coefficient of PID control algorithm, $k'_{p1} \le x[e(k)] \le k'_{p2}$, and $k'_i \le y[e(k)] \le 1$. Here k'_{p1}, k'_{p2}, and k'_i are parameters of improved variable gain PID control algorithm to be determined.

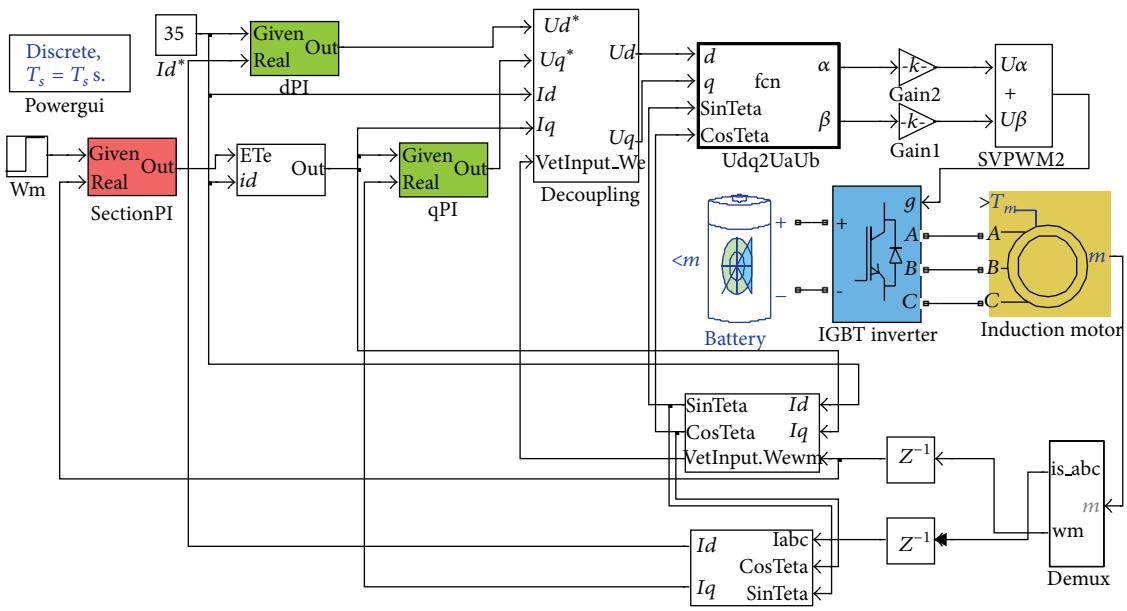

FIGURE 4: Simulation diagram constructed by Matlab/Simulink.

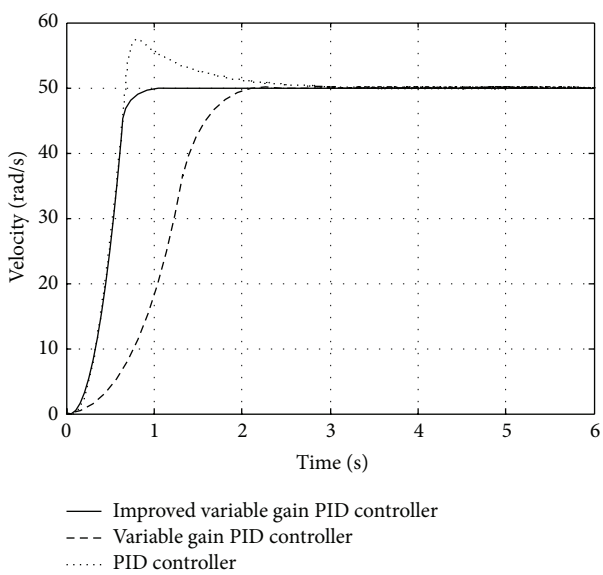

FIGURE 5: The simulation result of motor in low-velocity range.

Therefore, the closed-loop transfer function of system is obtained as

$$\varphi(s) = \frac{C(s)G(s)}{1 + C(s)G(s)}$$

$$= \frac{\left(k_p + x[e(k)]\right)s + k_i y[e(k)]}{\left(\sigma L_s J/k_{iq}\right)s^3 + Js^2 + \left(k_p + x[e(k)]\right)s + k_i y[e(k)]}. \quad (11)$$

Using Routh stability criterion [18] to judge the stability of system can obtain the stability condition of system as

$$k'_{p1} > \frac{\sigma L_s k_i}{k_{iq}} - k_p,$$
$$k'_i > 0. \quad (12)$$

The system can be stable if the values of parameters k'_{p1} and k'_i satisfy the condition of (9) when designing the vector control algorithm for EV ACIM based on improved variable gain PID controller.

5. Simulation and Interpretation of Results

To study the improvements of the improved variable gain PID control algorithm, it is imperative to compare it to classical PID control algorithm through simulation. The motor parameters of 20 kW ACIM which is used in simulation are given in Table 1.

Through debugging the simulation model of specific ACIM described in Table 1, proportional and integral gains as 0.63797 and 30.158, respectively, can be obtained, and the values of parameters of improved variable gain PID control algorithm in the velocity loop controller are $k_p = 2.26$, $k_i = 3.58$, $m_1 = 0.06$, $m_2 = m_3 = 0.04$, $m_4 = 0.16$, $k'_{p1} = 0$, $k'_{p2} = 4$, and $k'_i = 0.01$. $k'_{p1} > \sigma L_s k_i / k_{iq} - k_p = -2.2538$ and $k'_i > 0$; these satisfy the stability condition of system.

As shown in Figure 3, take a PID controller for example for comparison. Sample time T_s is 500 μs which is the sample period of the closed-loop system.

5.1. Low-Velocity Range. EV low running velocity is about 10 km/h, and the corresponding motor velocity is about

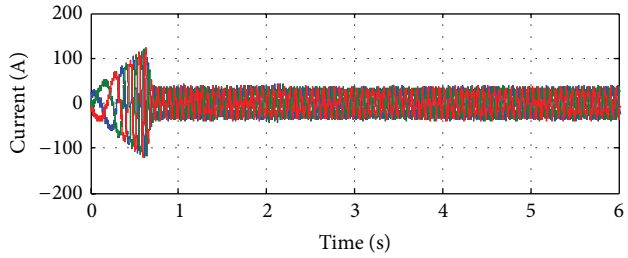

(a) Three-phase current with PID controller

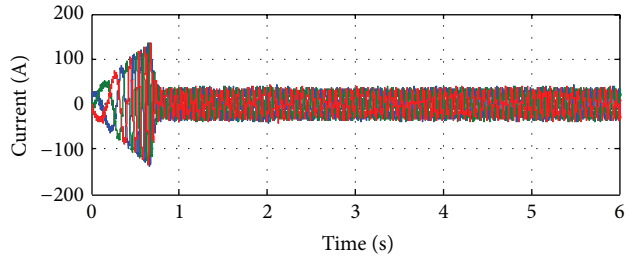

(b) Three-phase current with variable gain PID controller

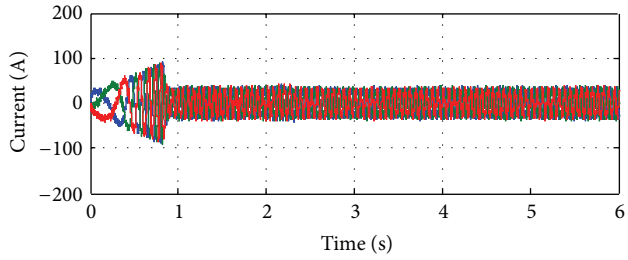

(c) Three-phase current with improved variable gain PID controller

Figure 6: The simulation result of three-phase current.

Table 1: The parameters of ACIM.

Rated line voltage U_N	180 V
Rated torque T_{eN}	53 Nm
Rated velocity n_N	3600 rpm
Stator resistance R_1	0.0205 ohm
Rotor resistance R_2	0.0097 ohm
Stator leakage inductance L_{1s}	$9.2668e-05$ H
Rotor leakage inductance L_{1r}	$10.9033e-07$ H
Mutual inductance L_m	0.0055887 H
Pole pairs	2

50 rad/s. If the expected velocity is motor nominal velocity of 50 rad/s in simulation, the control result is illustrated in Figure 5.

In Figure 5, the response time of the PID controller is about 3 s, and the overshoot is about 14%. The response time of variable gain PID controller is about 2 s, and the overshoot is 0. However, the proposed controller can still track the desired velocity less than 1 s without 0 overshoots.

In Figure 6, compared with PID controller and variable gain PID controller, the peak of three-phase current is less

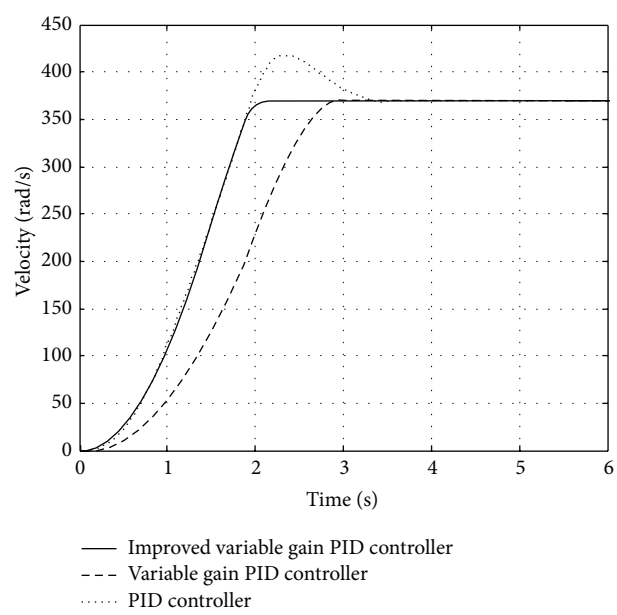

Figure 7: The simulation result of motor in moderate-velocity range.

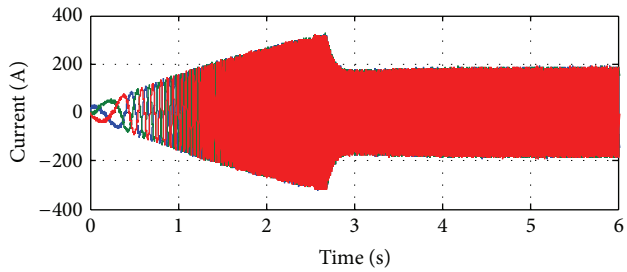

(a) Three-phase current with PID controller

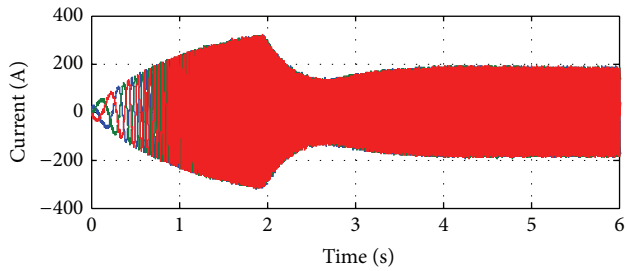

(b) Three-phase current with variable gain PID controller

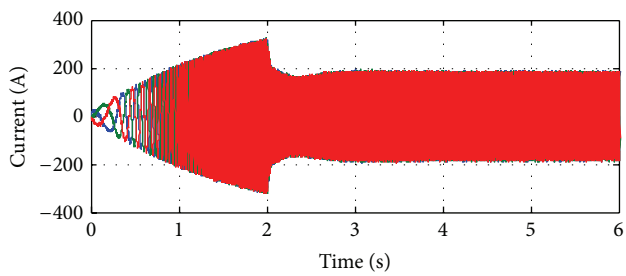

(c) Three-phase current with improved variable gain PID controller

Figure 8: The simulation result of three-phase current.

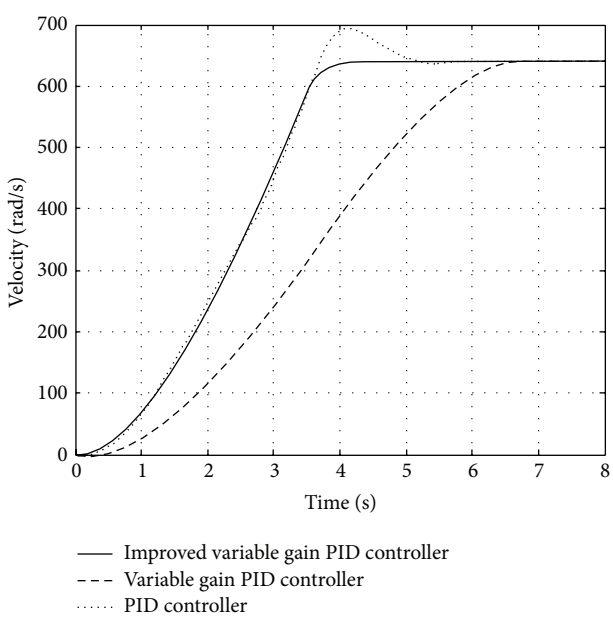

Figure 9: The simulation result of motor in high-velocity range.

than 100 A. In addition, it is investigated that the proposed controller is valid by comparison with the other PID controllers.

5.2. Moderate-Velocity Range. EV normal running velocity is 80 km/h to 100 km/h, and the corresponding motor velocity is about 370 rad/s. If the expected velocity is motor nominal velocity of 370 rad/s in simulation, the control result is illustrated in Figure 7.

In Figure 7, the response time of the PID controller is about 3.5 s, and the overshoot is about 10.8%. The response time of variable gain PID controller is about 3 s, and the overshoot is 0. However, the proposed controller can still track the desired velocity less than 2 s without 0 overshoots.

In Figure 8, compared with PID controller and variable gain PID controller, three-phase current changes slowly and the response time is smaller. In addition, it is investigated that the proposed controller is valid by comparison with the other PID controllers.

5.3. High-Velocity Range. EV high running velocity is about 120 km/h, and the corresponding motor velocity is about

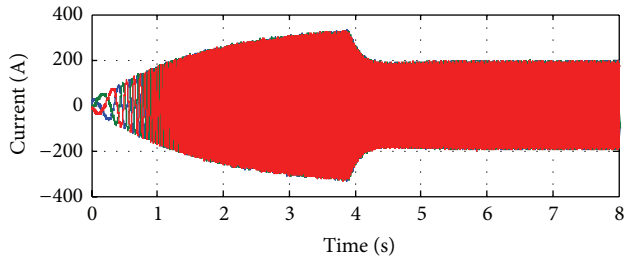

(a) Three-phase current with PID controller

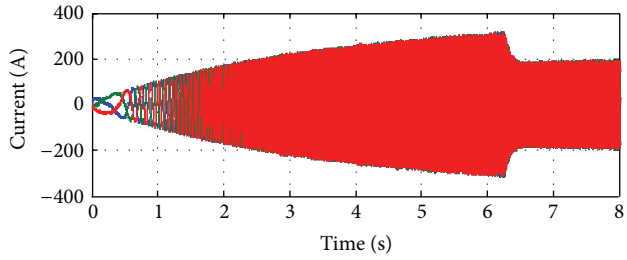

(b) Three-phase current with variable gain PID controller

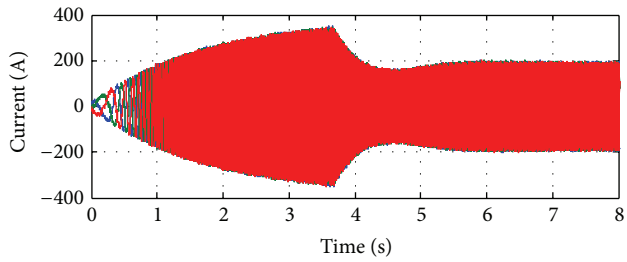

(c) Three-phase current with improved variable gain PID controller

Figure 10: The simulation result of three-phase current.

630 rad/s. If the given expected velocity is motor nominal velocity of 630 rad/s in simulation, the control result is illustrated in Figure 9.

In Figure 9, the response time of the PID controller is about 5 s, and the overshoot is about 11.1%. The response time of variable gain PID controller is about 7 s, and the overshoot is 0. However, the proposed controller can still track the desired velocity less than 4 s without 0 overshoots.

In Figure 10, compared with PID controller and variable gain PID controller, three-phase current changes slowly and the response time is smaller. In addition, it is investigated that the proposed controller is valid by comparison with the other PID controllers.

5.4. Variable Velocity Range. In order to test wheter the method designed in this paper can satisfy the application needs in velocity, we make simulation of motor in variable velocity range with the initial expected velocity as 630 rad/s and turn to 300 rad/s at the 4th second. The control result is illustrated in Figure 11.

As shown in Figure 11, the response time of the PID controller is about 2.5 s, and the overshoot is about 7.9%. The response time of variable gain PID controller is about 3 s, and

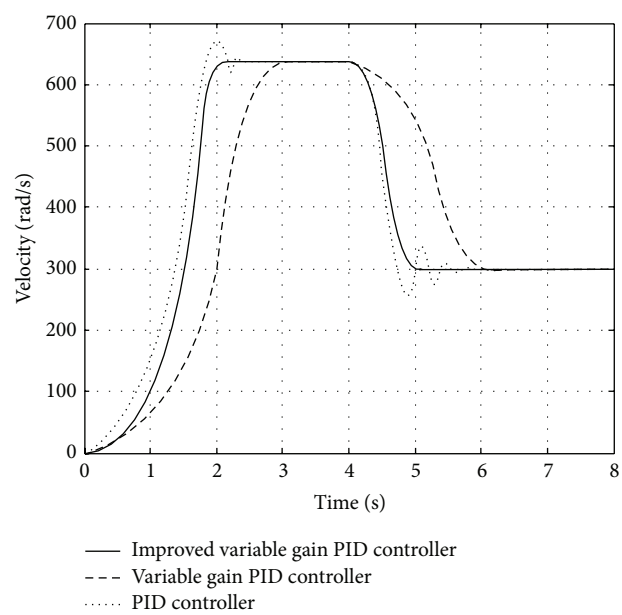

Figure 11: The simulation result of motor in variable velocity range.

the overshoot is 0. However, the proposed controller can still track the desired velocity less than 4 s without 0 overshoots.

6. Conclusion

This paper has presented a novel approach in the automotive field to implement the improved variable gain PID controller to control EV ACIM. In this paper, the design of variable gain PID controller and stability analysis have been presented along with simulation. The simulation results qualitatively demonstrate that the improved variable gain PID controller could improve on the control of motor velocity in the EV versus using the classical PID control method. In addition, this control method can satisfy the demands of EV driving system dynamic performance and acceleration performance when EV runs in low velocity, moderate velocity, high velocity, and variable velocity.

Conflict of Interests

The authors declare that there is no conflict of interests regarding the publication of this paper.

References

[1] C. Larish, D. Piyabongkarn, V. Tsourapas, and R. Rajamani, "A new predictive lateral load transfer ratio for rollover prevention systems," *IEEE Transactions on Vehicular Technology*, vol. 62, no. 7, pp. 2928–2936, 2013.

[2] S.-I. Sakai, H. Sado, and Y. Hori, "Motion control in an electric vehicle with four independently driven in-wheel motors," *IEEE/ASME Transactions on Mechatronics*, vol. 4, no. 1, pp. 9–16, 1999.

[3] Q. Li, Z. Zhang, and W. Zhao, "Dynamic control for four-wheel independent drive electric vehicle," in *Proceedings of the International Conference on Computer Science and Electronics Engineering (ICCSEE '12)*, vol. 3, pp. 252–256, Hangzhou, China, March 2012.

[4] T. Shim and D. Margolis, "Model-based road friction estimation," *Vehicle System Dynamics*, vol. 41, no. 4, pp. 249–276, 2004.

[5] D. Chabrol, C. Aussagues, and V. David, "A spatial and temporal partitioning approach for dependable automotive systems," in *Proceedings of the IEEE Conference on Emerging Technologies & Factory Automation (ETFA '09)*, pp. 1–8, Mallorca, Spain, September 2009.

[6] M. Stecher, N. Jensen, M. Denison et al., "Key technologies for system-integration in the automotive and industrial applications," *IEEE Transactions on Power Electronics*, vol. 20, no. 3, pp. 537–549, 2005.

[7] D. Zhang and L. Yu, "Exponential state estimation for Markovian jumping neural networks with time-varying discrete and distributed delays," *Neural Networks*, vol. 35, pp. 103–111, 2012.

[8] V. P. Petkov, G. K. Balachandran, and J. Beintner, "A fully differential charge-balanced accelerometer for electronic stability control," *IEEE Journal of Solid-State Circuits*, vol. 49, no. 1, pp. 262–269, 2014.

[9] C. F. Caruntu, M. Lazar, R. H. Gielen, P. P. J. van den Bosch, and S. Di Cairano, "Lyapunov based predictive control of vehicle drivetrains over CAN," *Control Engineering Practice*, vol. 21, no. 12, pp. 1884–1898, 2013.

[10] J. Cheng, H. Zhu, S. Zhong, F. Zheng, and Y. Zeng, "Finite-time filtering for switched linear systems with a mode-dependent average dwell time," *Nonlinear Analysis: Hybrid Systems*, vol. 15, pp. 145–156, 2015.

[11] M. B. G. Cloosterman, N. D. van de Wouw, M. P. M. H. Heemels, and H. Nijmeijer, "Robust stability of networked control systems with time-varying network-induced delays," in *Proceedings of the 45th IEEE Conference on Decision and Control*, pp. 4980–4985, December 2006.

[12] S. Olaru and S. Niculescu, "Predictive control for linear systems with delayed input subject to constraints," in *Proceedings of the 17th World Congress the International Federation of Automatic Control (IFAC '08)*, pp. 11208–11213, Seoul, South Korea, July 2008.

[13] L. Hetel, J. Daafouz, and C. Iung, "Stabilization of arbitrary switched linear systems with unknown time-varying delays," *IEEE Transactions on Automatic Control*, vol. 51, no. 10, pp. 1668–1674, 2006.

[14] R. H. Gielen, S. Olaru, M. Lazar, W. P. Heemels, N. van de Wouw, and S.-I. Niculescu, "On polytopic inclusions as a modeling framework for systems with time-varying delays," *Automatica*, vol. 46, no. 3, pp. 615–619, 2010.

[15] X. Yang, Z. Wang, and W. Peng, "Coordinated control of AFS and DYC for vehicle handling and stability based on optimal guaranteed cost theory," *Vehicle System Dynamics*, vol. 47, no. 1, pp. 57–79, 2009.

[16] H. Du, N. Zhang, and G. Dong, "Stabilizing vehicle lateral dynamics with considerations of parameter uncertainties and control saturation through robust yaw control," *IEEE Transactions on Vehicular Technology*, vol. 59, no. 5, pp. 2593–2597, 2010.

[17] G. Zheng, J. D. Wu, M. W. Kuang, D. Zhang, and Y. Yang, "A disturbance rejection strategy for asynchronous motor of the electric vehicle in speed-open-loop operating mode," *Advanced Materials Research*, vol. 479-481, pp. 71–75, 2012.

[18] R. H. Gielen and M. Lazar, "Stabilization of networked control systems via non-monotone control Lyapunov functions," in *Proceedings of the 48th IEEE Conference on Decision and Control Held Jointly with the 28th Chinese Control Conference (CDC/CCC '09)*, pp. 7942–7948, Shanghai, China, December 2009.

Hindawi Publishing Corporation
Mathematical Problems in Engineering
Volume 2015, Article ID 586260, 10 pages
http://dx.doi.org/10.1155/2015/586260

Research Article

Synchronization of Hybrid Microgrids with Communication Latency

Jingang Lai,[1] Hong Zhou,[1] Wenshan Hu,[1] Xiaoqing Lu,[2] and Liang Zhong[1]

[1] *Department of Automation, Wuhan University, Wuhan 430072, China*
[2] *College of Electrical and Information Engineering, Hunan University, Changsha 410082, China*

Correspondence should be addressed to Wenshan Hu; wenshan.hu@whu.edu.cn

Received 11 November 2014; Revised 23 January 2015; Accepted 23 January 2015

Academic Editor: Hui Zhang

Copyright © 2015 Jingang Lai et al. This is an open access article distributed under the Creative Commons Attribution License, which permits unrestricted use, distribution, and reproduction in any medium, provided the original work is properly cited.

A distributed cooperative control scheme is proposed in order to implement a distributed secondary control for hybrid lossy microgrids. The designed distributed control is able to synchronize the frequency of inverse-based distributed generators (DGs) and minisynchronous generators (MSGs/SGs) to the desired state with a virtual leader DG/SG (reference value) in a distribution switching network under the existence of time-varying communication delays. The secondary control stage selects suitable frequencies of each DG/SG such that they can be synchronized at the desired set point. Using the proposed algorithm, each DG/SG only needs to communicate with its neighboring DGs/SGs intermittently even if the communication networks are local, the topology is time-varying, and the communication delays may exist. Therefore, the failure of a single DG/SG will not produce the failing down of the whole system. Sufficient conditions on the requirements for the network connectivity and the delays boundedness which guarantees the stability and synchronization of the controlled hybrid lossy microgrid power systems are presented. The feasibility of the proposed control methodology is verified by the simulation of a given lossy microgrid test system.

1. Introduction

The recent changes in the structure of power generation towards a distributed generation have motivated the increasing interest in the control of so-called microgrids. As the main building blocks of smart grids, microgrids are small-scale power systems that facilitate the effective integration of highly hybrid and heterogeneous DGs and storage devices including solar (photovoltaic array), wind, microturbines, supercapacitor, and batteries [1, 2]. The structure of hybrid microgrid is as shown in Figure 1. Many of these energy sources and storage devices generate or reserve variable frequency AC/DC power and are interfaced with a synchronous AC grid via power electronic DC/AC inverters [3]. Meanwhile, with the rapid growth of power electronics techniques on MSGs or virtual SGs, the increasing application of clear energy sources, including diesel plants, wind plants, and geothermal plants, also makes them possible to be integrated into microgrids. Therefore, new control strategies on how to preserve the synchronization and proportional power sharing in the connected or isolated manner are demanded for the network [4].

Recently, hierarchical control for microgrids has been proposed in order to standardize their operation and functionalities, that is, primary control [5] (droop control maintaining voltage and frequency stability of the microgrid subsequent to the islanding process), secondary control [6] (compensating the voltage and frequency derivations caused by primary control), and tertiary control [7] (optimal operation in both operating modes and power flow control in grid-connected mode).

However, the conventional secondary control of microgrids assumes a centralized control structure which requires a complex communication network and a central controller. A central controller reduces the system reliability [8]. Additionally, some literatures point that physical and communication structures of microgrid can be time-varying because of the desired plug-and-play capability of microgrids [9]. From

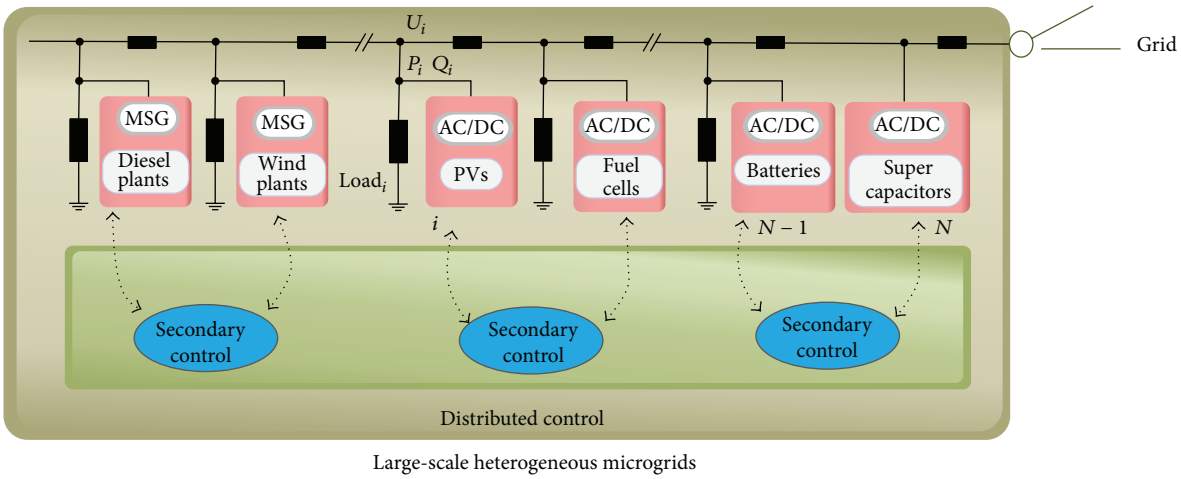

Figure 1: The structure of hybrid microgrid.

this perspective, the distributed control structure provides a robust secondary control framework [10, 11]. It could largely reduce the system reliability [12, 13]. In contrast, decentralised control structures are adopted in [14, 15] to avoid the above drawbacks. Nevertheless, for the large-scale microgrids, it is impossible to determine and maintain a feasible operating condition if all of the DGs are running independently. Alternatively, affected by the idea of cooperation control for multiagent systems [16–21], there are increasing researchers who begin to focus on the distributed control structures which allow all the DGs to communicate with their neighbors and share information among neighboring units via local sparse communication networks [22–26].

Particularly, in paper [27], the authors proposed a secondary voltage and frequency control scheme based on the distributed cooperative control of multiagent systems and thus improved the system reliability. In order to regulate the power output of a microgrid dynamics consisting of a large amount of photovoltaic generators, [28] presented a self-organizing strategy in a distributed time-varying network.

The main common features of the above literatures lie in that a distributed communication network has been taken as a basis for the control strategies designed. In this case, the network variability and communication delays are usually unavoidable. They cannot be neglected for the system stability analysis [29, 30]. In fact, in normal circumstances, the microgrids frequency fluctuation and the amplitudes of each DG unit response to primary frequency control are very small. For the purpose of efficient signal transmission, it is inevitable to induce some disturbance and time-delays during the signal processing. Hence, in [29], decentralized inverter control algorithms for power sharing with nonnegligible constant communication delays are investigated. Also, by using the small-signal analysis method, a distributed secondary voltage and frequency control for reactive power sharing are discussed in [30], in which the constant communication delays are analyzed only in an experimental simulation way.

In view of the above analysis, most research on synchronization and power sharing of microgrids has focused on purely inverter-based systems. However, from a practical consideration, most present and near-future applications involve networks of mixed generation mode including SGs and inverter-based DGs and/or storage devices [31]. This paper aims to develop a distributed cooperative control scheme for hybrid microgrids that is able to synchronize the frequency of DGs/SGs to the desired state with a virtual leader DG/SG (reference value) in a distribution switching network under the existence of time-varying communication delays. Combining with the conventional droop control technique, the distributed cooperative control algorithm is designed and deployed into the secondary control stage, in which manner the control derivation produced during the primary control stage can be well restored. And the secondary control stage selects suitable frequencies of each DG/SG such that they can synchronize to the desired state. With the proposed algorithms, each DG/SG only needs to communicate with its neighboring DGs/SGs intermittently even if the communication networks are local, the topology is time-varying, and the communication delays may exist. Sufficient conditions on the requirements for the network connectivity and the delays boundedness that guarantees the stability and reliability of the controlled microgrid power systems are presented. The effectiveness of the proposed control methodology is verified by the simulation of a lossy microgrid test system.

The main contributions of this paper lie in the following aspects. Firstly, in order to restore the frequency in hybrid lossy microgrids, one first designs a distributed secondary control algorithm to synchronize the frequency of each DG/SG to the desired state (reference value 50 Hz). Secondly, the considered distributed communication network is local and time-varying and with time-varying communication delays. By Lyapunov-Krasovskii stable analysis technique, sufficient conditions on the requirements for the network connectivity and the delays boundedness that guarantees

the stability and synchronization of the controlled microgrid power systems are presented.

The rest of this paper is organized as follows. In Section 2, the droop-based distributed cooperative control for microgrids problem is formulated and several necessary lemmas are then given. The distributed cooperative algorithm is designed for realizing the frequency restoration in Section 3. Section 4 gives some typical examples to verify the effectiveness of the proposed algorithm. Finally, some concluding remarks are drawn in Section 5.

2. Problem Formulation

In normal situation, the microgrid is operating with the nominal frequency and voltage magnitudes. The objective of primary control is to maintain the frequency and/or voltage magnitudes near around its nominal value once user demands and/or power supply changes. Herein our attentions are restricted to the frequency regulation, so the inverters are considered as voltage source with constant voltage amplitude. And we adopt the physically reasonable and widely adopted assumption of an inductive microgrid [26].

The procedure of primary and secondary control is as shown in Figure 2. In the steady state, the load power curve P_L (after linearization processing) and the generator power curve P_G (after linearization processing) have a balance point at a, whose coordinate is $(P^{\text{nom}}, \omega^{\text{nom}})$. The frequency ω will decrease by $\Delta\omega$ in order to make the output power of the DG/SG increase to the point c. Due to the inherent defects of primary control, the increase of the generator power $\Delta P'$ in the above case is smaller than the actual increase in the load power ΔP. In order to compensate the frequency deviation produced by the primary control, secondary frequency control (the green lines in Figure 2) is deployed to regulate the frequency $\Delta\omega$ such that the intersection point c moves to d.

2.1. Droop Characters of SGs in Electrical Networks. For the dynamics of SGs, we consider the conventional expression of a regulated SG by a constant voltage behind transient reactance [24]. The so-called regulated machine is always equipped with a speed governor connected to a governing system. The speed governor is controlled to adjust the output of turbine mechanical power P_i^M and its speed. Droop control is the intrinsic characteristic to maintain system stability. Here, we assume that there is an approximate linear relationship between the valve position and the mechanical power. It is worth noting that the mechanical speed ω^M is different from the electrical speed ω, but their relationship is $\omega = (n/2)\omega^M$, where n is the number of machine poles [31]. Droop control eventually can be expressed as follows:

$$P^M(t) = P^{M,\text{nom}} - \frac{1}{\widehat{k}_P}\omega_i(t), \tag{1}$$

where ω is an input signal, P^M is an output signal, and $1/\widehat{k}_P$ denotes the droop coefficient. The $P^{M,\text{nom}}$ is a constant and the nominal set point for the mechanical power.

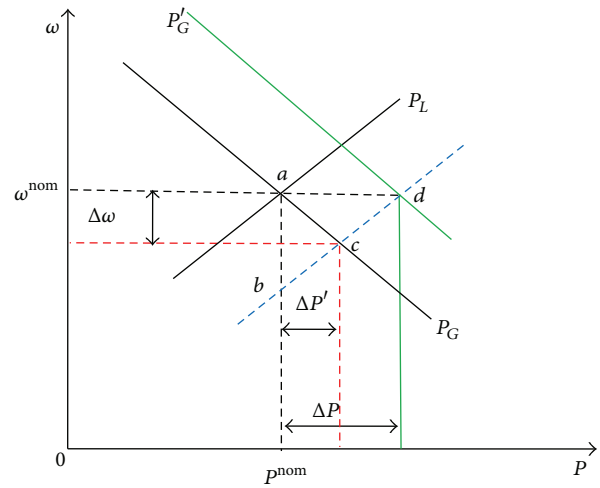

Figure 2: Primary and secondary frequency regulation.

2.2. Droop Control for Inverter-Based DGs Networks. From the above theoretical analysis, the droop technique deployed in primary controller for DGs during the multiple loop control process can be given by

$$\omega = \omega^{\text{nom}} - K^P\left(P - P^{\text{nom}}\right), \tag{2}$$

where ω^{nom} is chosen from the nominal set point of frequency of the DG unit, P is the measured active powers at the DG terminal, K^P is the associated droop coefficient that is usually selected based on the active power rating, and P^{nom} is chosen from the nominal set point of active power of the DG unit.

The control process of each DG generally consists of three control loops (as shown in Figure 3), that is, the power controller, voltage magnitudes controller, and current controller.

The active power P_i and reactive power Q_i of the ith DG are calculated based on the low-pass filter (with cutoff frequency ω_i^c), measured output voltage magnitude, and output current. They can be described by the following equations, respectively:

$$\begin{aligned} P_i &= \frac{\omega_i^c}{\omega_i^c + s}\left(V_i^{\text{od}} I_i^{\text{od}} + V_i^{\text{oq}} I_i^{\text{oq}}\right), \\ Q_i &= \frac{\omega_i^c}{\omega_i^c + s}\left(V_i^{\text{od}} I_i^{\text{oq}} - V_i^{\text{oq}} I_i^{\text{od}}\right). \end{aligned} \tag{3}$$

The nominal value of output frequency ω_i^{nom} of the power controller is used by the sinusoidal pulse width modulation (SPWM) inverter as frequency reference, while the voltage reference of the SPWM inverter needs to be regulated by the following voltage and current controllers. Based on the references provided by the power controller, $V_i^{\text{od,nom}}$ and

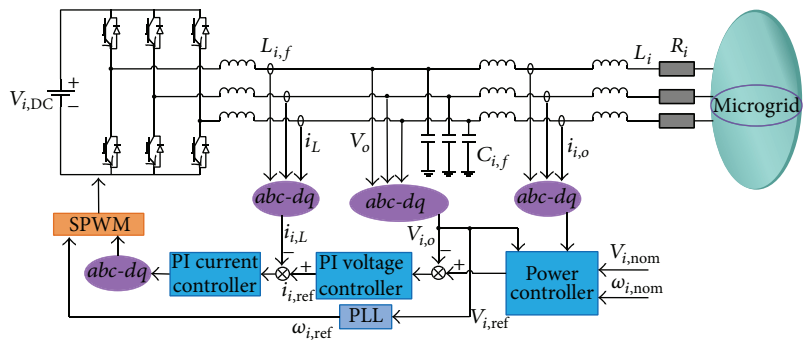

Figure 3: The multiple loop control schematic of the inverter in microgrids.

$V_i^{\mathrm{oq,nom}}$, the output of the voltage magnitude controller is given by

$$\begin{aligned} I_i^{\mathrm{od,nom}} &= k_i^{PV}\left[V_i^{\mathrm{od,nom}} - V_i^{\mathrm{od}}\right] \\ &\quad + k_i^{IV}\int\left[V_i^{\mathrm{od,nom}} - V_i^{\mathrm{od}}\right]\mathrm{d}t - \omega_i^{\mathrm{nom}} C_f V_i^{\mathrm{oq}} \\ &\quad + F I_i^{\mathrm{od}}, \\ I_i^{\mathrm{oq,nom}} &= k_i^{PV}\left[V_i^{\mathrm{oq,nom}} - V_i^{\mathrm{oq}}\right] \\ &\quad + k_i^{IV}\int\left[V_i^{\mathrm{oq,nom}} - V_i^{\mathrm{oq}}\right]\mathrm{d}t - \omega_i^{\mathrm{nom}} C_f V_i^{\mathrm{od}} \\ &\quad + F I_i^{\mathrm{oq}}, \end{aligned} \tag{4}$$

where k_i^{PV} and k_i^{IV} are the proportional and integral gains of the voltage magnitudes controller of ith DG, respectively, while C_f and F are the capacitance of the LC filter and feedforward gain, respectively. On the other hand, based on the references provided by the voltage magnitudes controller, $I_i^{\mathrm{od,nom}}$ and $I_i^{\mathrm{oq,nom}}$, the output of the current controller is given by

$$\begin{aligned} V_i^{\mathrm{od,nom}} &= k_i^{PI}\left[I_i^{\mathrm{od,nom}} - I_i^{\mathrm{od}}\right] + k_i^{II}\int\left[I_i^{\mathrm{od,nom}} - I_i^{\mathrm{od}}\right]\mathrm{d}t \\ &\quad - \omega_i^{\mathrm{nom}} L_f I_{i,L}^{\mathrm{oq}}, \\ V_i^{\mathrm{oq,nom}} &= k_i^{PI}\left[I_i^{\mathrm{oq,nom}} - I_i^{\mathrm{oq}}\right] + k_i^{II}\int\left[I_i^{\mathrm{oq,nom}} - I_i^{\mathrm{oq}}\right]\mathrm{d}t \\ &\quad + \omega_i^{\mathrm{nom}} L_f I_{i,L}^{\mathrm{od}}. \end{aligned} \tag{5}$$

The dynamics of a frequency droop-controlled inverter (2) and a regulated SG (1) are equivalent (see [9] for details on relevant proof). Therefore, next on the analysis of the droop control, DGs and SGs will be considered to be of the same features and deploy the same dynamic model.

Since inverters may connect pure storage devices, for example, batteries, to the network, $P_i^{\mathrm{nom,stor}}$ can also take negative values. In that case, the storage device is charged in dependency of the excess power available in the network and thus functions as a frequency dependent load.

2.3. Secondary Control for Hybrid Microgrid. The conventional secondary control is a kind of centralized control methods, the nominal value ω^{nom} is used in the primary control stage, and it will be regulated gradually in each cycle of secondary control process. Note that the final desired frequency value can be measured from the main grid in the connected mode or obtained by command generator or many forms of DG/SG such as fuel-cells and microturbines in the islanded mode.

Different from the conventional secondary control with centralized mode, this paper in the secondary frequency control stage proposes one distributed cooperative control algorithm for each DG/SG. The basic idea of the proposed distributed control is by incorporating local communication networks that share information among neighboring units.

From this perspective, a microgrid can be considered as a multiagent system, where each DG/SG is an agent. The secondary control design for frequency resembles a tracking synchronization problem while that design for proportional power sharing is carried out. For this purpose, the important network digraph theory is introduced in the following.

2.4. Graph Theory. In this paper, the required communication network for microgrids can be modeled by a digraph $\mathscr{G}(\mathscr{V}, \varepsilon, \mathscr{A})$, where the node set $\mathscr{V} = \{v_1, v_2, \ldots, v_N\}$ denotes the set of DGs/SGs, the set of edges $\varepsilon \subseteq \mathscr{V} \times \mathscr{V}$ denotes the communication links among DGs/SGs, and $\mathscr{A} = (a_{ij})_{N\times N}$ is a weighted adjacency matrix defined as $a_{ii} = 0$ and $a_{ij} \geq 0$. $a_{ij} > 0$ if and only if the edge $(v_i, v_j) \in \varepsilon$. The set of neighbors of the ith DG/SG v_i is given by $N_i = \{v_j \in \mathscr{V} : (v_i, v_j) \in \varepsilon\}$. The degree matrix is defined as $D = \mathrm{diag}\{d_1, \ldots, d_N\}$ with $d_i = \sum_{j\in N_i} a_{ij}$, and then $L = D - A$ is the Laplacian matrix, which has all row sums equal to zero; that is, $L1_N = 0$, with $1_N = (1, \ldots, 1)^T \in R^N$.

In the following, the digraph $\overline{\mathscr{G}}$ is used to describe the interconnection topology of a microgrid consisting of one virtual leader DG/SG, denoted by 0, and followers DGs/SGs, denoted by $1, \ldots, N$. Diagonal matrix $B = \mathrm{diag}\{a_{10}, \ldots, a_{N0}\}$ is called the leader adjacency matrix, where $a_{i0} > 0$ if follower DG/SG v_i is connected to the leader across the communication link (v_0, v_i); otherwise $a_{i0} = 0$. The following lemma plays an important role in the proof of our main results.

Lemma 1 (see [32]). *If the digraph $\mathcal{G}$ corresponding to the Laplacian matrix L is strongly connected, then (i) if $q = (q_1, \ldots, q_N)^T$ is a left eigenvector of L corresponding to eigenvalue 0, then $q_i > 0$ holds for all $i = 1, \ldots, N$, and (ii) all the eigenvalues of $L + B$ have positive real parts, where $B = \mathrm{diag}\{b_1, \ldots, b_N\}$, $\sum_{i=1}^{N} b_i > 0$, and $b_i \geq 0$ for all $i = 1, \ldots, N$.*

3. Main Results

In this section, one will discuss the distributed cooperative control schemes for frequency and power sharing in Sections 3.1 and 3.2, respectively.

It should be noted that the dynamics of the voltage and current control loops are much faster than the dynamics of the power control loop [30]. Therefore, it is necessary and intentional to design a typical inverter system by applying the time separation operation [6]. In order to facilitate our analysis, this paper will focus on the stability of power control loop, while the investigation of current controllers follows traditional proportional-integral (PI) controllers.

3.1. Distributed Cooperative Control for Frequency. In this paper, the d-q reference frame transformation is considered, where the d-axis and q-axis of the reference frame of each inverter are rotating at the common reference frequency. Based on the traditional droop control strategy, the reference of frequency of the ith inverter-based DG or SG is determined by the power control loop and can be abstracted as

$$\omega_i = \omega_i^{\mathrm{nom}} - K_i^P \left(P_i - P_i^{\mathrm{nom}}\right), \tag{6}$$

where ω_i^{nom} is the nominal set point of output frequency and P_i^{nom} is the nominal set point of output active, respectively, while K_i^P is the frequency droop coefficient.

In the following, a distributed pinning control algorithm is designed to pin the frequency ω_i of DGs/SGs to synchronize the reference frequency w^{ref}, respectively.

According to the thought of so-called input-output feedback linearisation [27], differentiating the equations in (6) yields

$$\dot{\omega}_i = \dot{\omega}_i^{\mathrm{nom}} - K_i^P \dot{P}_i = u_i^{\omega}, \tag{7}$$

where u_i^{ω} is the pinning controllers which will be designed later such that $\lim_{t \to +\infty} |\omega_i(t) - \omega^{\mathrm{ref}}(t)| = 0$ for $i = 1, \ldots, N$.

Then the nominal control input ω_i^{nom} used in the droop control procedure can be computed by the following integrator:

$$\omega_i^{\mathrm{nom}} = \int \left(u_i^{\omega} + K_i^P \dot{P}_i\right) \mathrm{d}t. \tag{8}$$

Since it is assumed that each DG/SG only needs to communicate with its neighboring DGs/SGs through a communication network, the pinning controllers u_i^{ω} are designed based on the own information of each DG/SG and the information of its neighbors:

$$u_i^{\omega} = \sum_{j \in N_i(t)} a_{ij}(t) \left[\omega_j(t - \tau(t)) - \omega_i(t - \tau(t))\right] \tag{9}$$

for $i = 1, \ldots, N$, where the time-varying delay $\tau(t) \geq 0$ is a continuously differentiable function and the factors of adjacency matrix $a_{ij}(t)$ are also allowed to be dynamically changing.

In order to facilitate analysis, some denotations are given. Let $B = \mathrm{diag}\{a_{10}, \ldots, a_{N0}\}$, $e_\xi(t) = \xi(t) - \bar{\xi}(t)$ with $\xi = (\omega_1, \ldots, \omega_N)^T \in R^N$ and $\bar{\xi} = (\omega^{\mathrm{ref}} 1_N)^T \in R^N$; then combining (7) and (9) and the fact that $\dot{\omega}^{\mathrm{ref}} = 0$, one can deduce the following error system:

$$\begin{aligned} \dot{e}_\xi(t) &= -\left(H_s \otimes I_2\right) e_\xi(t - \tau(t)), \\ s &= \sigma(t), \end{aligned} \tag{10}$$

where $H_s = L_s + B_s$ with the Laplacian matrix L_s of digraph $\mathcal{G}_s$, $\otimes$ denotes the Kronect product, I_2 denotes the two-dimensional identity matrix, and $\sigma(t) : [0, +\infty) \to \rho_{\mathrm{T}} = \{1, \ldots, m\}$ ($m \in Z^+$ denotes the total number of all possible directed graphs) is a switching signal that determines the communication topology $\mathcal{G}$. If $\sigma(t)$ is a constant function, then the corresponding topology is fixed.

Theorem 2. *Suppose that the digraph $\mathcal{G}_s$ is always strongly connected and there exists at least one $i \in \{1, \ldots, N\}$ such that $a_{i0} > 0$ for any switching signal $s = \sigma(t)$. If the time-varying delays $\tau(t)$ satisfy $\tau(t) < d$ and $\dot{\tau}(t) < d_1 < 1$, then the distributed controllers (9) can pin the DG/SG output frequency ω_i to the reference states ω^{ref} asymptotically.*

Proof. Define a common Lyapunov-Krasovkii function for system (10) as follows:

$$\begin{aligned} V(t) &= e_\xi^T(t) \left(\Xi \otimes I_2\right) e_\xi(t) \\ &\quad + \int_{-d}^{0} \int_{t+\theta}^{t} \dot{e}_\xi^T(r) \dot{e}_\xi(r) \, \mathrm{d}r \, \mathrm{d}\theta \\ &\quad + \gamma \int_{t-\tau(t)}^{t} e_\xi^T(r) \left[\left(H_s^T H_s\right) \otimes I_2\right] e_\xi(r) \, \mathrm{d}r, \end{aligned} \tag{11}$$

where $\Xi = \mathrm{diag}\{q_1, \ldots, q_N\}$ with the positive left eigenvector $q = (q_1, \ldots, q_N)^T$ corresponding to the zero eigenvalue of the Laplacian matrix L_s. Note that since $\mathcal{G}_s$ is strongly connected, one can always choose q such that $\sum_{i=1}^{N} q_i = 1$ and $q_i > 0$ for all $i = 1, \ldots, N$ (by Lemma 1).

Along the trajectory of system (10), we have

$$\begin{aligned} \dot{V}(t) &= -2 e_\xi^T(t) \left[\left(\Xi H_s\right) \otimes I_2\right] e_\xi(t - \tau(t)) + \gamma e_\xi^T(t) \\ &\quad \cdot \left[\left(H_s^T H_s\right) \otimes I_2\right] e_\xi(t) - \int_{t-d}^{t} \dot{e}_\xi^T(r) \dot{e}_\xi(r) \, \mathrm{d}r \\ &\quad - \gamma (1 - \dot{\tau}(t)) e_\xi^T(t - \tau(t)) \left[\left(H_s^T H_s\right) \otimes I_2\right] \\ &\quad \cdot e_\xi(t - \tau(t)) + d e_\xi^T(t - \tau(t)) \left[\left(H_s^T H_s\right) \otimes I_2\right] \\ &\quad \cdot e_\xi(t - \tau(t)). \end{aligned} \tag{12}$$

By Newton-Leibniz formula,

$$e_\xi(t - \tau(t)) = e_\xi(t) - \int_{t-\tau(t)}^{t} \dot{e}_\xi(r) \, \mathrm{d}r \tag{13}$$

and noting that $2x^T y \leq x^T A^{-1} x + y^T A y$ hold for any appropriate positive definite matrix A, we have

$$\begin{aligned} &-2e_\xi^T(t)\left[(\Xi H_s)\otimes I_2\right]e_\xi(t-\tau(t)) \\ &\quad\leq -2e_\xi^T(t)\left[(\Xi H_s)\otimes I_2\right]e_\xi(t) \\ &\qquad+\int_{t-\tau(t)}^{t} 2e_\xi^T(t)\left[(\Xi H_s)\otimes I_2\right]\dot{e}_\xi(r)\,\mathrm{d}r \\ &\quad\leq -e_\xi^T(t)\left[\left(\Xi H_s + H_s^T\Xi\right)\otimes I_2\right]e_\xi(t) \\ &\qquad+ de_\xi^T(t)\left[\left(\Xi H_s H_s^T\Xi\right)\otimes I_2\right]e_\xi(t) \\ &\qquad+\int_{t-\tau(t)}^{t}\dot{e}_\xi^T(r)\,\dot{e}_\xi(r)\,\mathrm{d}r. \end{aligned} \tag{14}$$

Consequently,

$$\begin{aligned} V(t) \leq &-\left[\lambda_{\min}\left(\Xi H_s + H_s^T\Xi\right) - d\lambda_{\max}\left(\Xi H_s H_s^T\Xi\right)\right. \\ &\left.-\gamma\lambda_{\max}\left(H_s^T H_s\right)\right]e_\xi^T(t)\,e_\xi(t) \\ &-\left[\gamma(1-d_1)\lambda_{\min}\left(H_s^T H_s\right)\right. \\ &\left.-d\lambda_{\max}\left(H_s^T H_s\right)\right]e_\xi^T(t-\tau(t))\,e_\xi(t-\tau(t)). \end{aligned} \tag{15}$$

Then, a sufficient condition for $\dot{V}(t) < 0$ is

$$\begin{aligned} &\lambda_{\min}\left(\Xi H_s + H_s^T\Xi\right) - d\lambda_{\max}\left(\Xi H_s H_s^T\Xi\right) \\ &\quad-\gamma\lambda_{\max}\left(H_s^T H_s\right) > 0, \\ &\gamma(1-d_1)\lambda_{\min}\left(H_s^T H_s\right) - d\lambda_{\max}\left(H_s^T H_s\right) > 0, \end{aligned} \tag{16}$$

which leads to

$$\begin{aligned} &\frac{d\lambda_{\max}\left(H_s^T H_s\right)}{(1-d_1)\lambda_{\min}\left(H_s^T H_s\right)} \\ &\quad< \gamma < \frac{\lambda_{\min}\left(\Xi H_s + H_s^T\Xi\right) - d\lambda_{\max}\left(\Xi H_s H_s^T\Xi\right)}{\lambda_{\max}\left(H_s^T H_s\right)}. \end{aligned} \tag{17}$$

Then, one can deduce that

$$d < \frac{(1-d_1)\lambda_{\min}\left(\Xi H_s + H_s^T\Xi\right)}{\lambda_{\max}^2\left(H_s^T H_s\right)/\lambda_{\min}\left(H_s^T H_s\right) + (1-d_1)\lambda_{\max}\left(\Xi H_s H_s^T\Xi\right)} \tag{18}$$

for given $d_1 < 1$. This completes the proof. □

Remark 3. As we all know, the communication latency is a key factor that cannot be ignored in the smart microgrid control problem since many cases have proven that neglect of the communication latency will lead to serious and unpredictable consequences. When analyzing the nonlinear systems containing time-varying communication latency, most existing literatures presented some delay independent stability conditions or just require that the delay is sufficiently small. However, in order to investigate the upper bound of the amount of time-varying delay, this paper constructs a Lyapunov-Krasovskii functional (i.e., $V(x)$) with delay-related parameters. It is worthy pointing out that, for the presented nonlinear system with directed and switching topology, the asymmetry of the adjacency matrix and the nonlinearity of the controlled systems will increase the difficulty to construct $V(x)$ and analyze its stability. By using the special matrix theory, inequality theory, and theory of delay differential equations, this paper solves the above problems.

3.2. Active Power Sharing. It is [26] that has proposed a method on how to choose the frequency droop coefficients and nominal setpoints to keep DGs/SGs realizing the active power sharing according to their power ratings. This control goal is analyzed in many literatures and spread to actual applications [5]. The proposed proportional power sharing method also can guarantee that storage devices in charging mode, that is, $P_i^{\text{nom,stor}}$ for some $i \in N$, are charged proportionally.

In the following, the DGs/SGs proportionally share their power in terms of their power ratings $P_i^{\max}$ if the gains K_i^P and setpoints P_i^{nom} are chosen such that, for all $i = 1, \ldots, N$, the condition $K_i^P P_i = K_j^P P_j$ is standard in the microgrid research:

$$\frac{P_i}{P_i^{\max}} = \frac{P_j}{P_j^{\max}}, \tag{19}$$

where $P_i^{\max}$ and $P_j^{\max}$ are the instantaneous maximum capacity of P_i and P_j and all the $P_i^{\max}$ and $P_j^{\max}$ are assumed to have the same sign. The active powers of DGs/SGs are able to be controlled according to condition (19) and droop control (2) the active power sharing proportionally. Condition (19) that also has a guiding significance achieves the reactive power sharing.

4. Simulation Results and Discussion

In this section, the effectiveness of the proposed distributed control algorithms will be verified by simulating an islanded lossy microgrid in MATLAB. Based on the above analysis for the identity property on dynamics of DGs and SGs, without loss of generality, five DGs have been chosen to the test system. Figure 4 shows the basic diagram of the test system which consists of five DGs. The specifications of the DGs, lines, and loads are summarized in Table 1. Note that its communication topology can be abstracted as digraph $\mathcal{G}_1$ shown in Figure 5. The associated Laplacian matrix of $\mathcal{G}_1$ is

$$L_1 = \begin{pmatrix} 0.005 & 0 & 0 & 0 & -0.005 \\ -0.005 & 0.005 & 0 & 0 & 0 \\ 0 & -0.005 & 0.005 & 0 & 0 \\ 0 & 0 & -0.005 & 0.005 & 0 \\ 0 & 0 & 0 & -0.005 & 0.005 \end{pmatrix}, \tag{20}$$

Table 1: Parameter values for test system.

DG_1		DG_2		DG_3		DG_4		DG_5	
V_{DC}	680 (V)	V_{DC}	1000 (V)	V_{DC}	800 (V)	V_{DC}	750 (V)	V_{DC}	700 (V)
k^P	0.8×10^{-4}	k^P	1.6×10^{-4}	k^P	1.4×10^{-4}	k^P	1.2×10^{-4}	k^P	1.0×10^{-4}
k^Q	1.6×10^{-3}	k^Q	3.7×10^{-3}	k^Q	3.2×10^{-3}	k^Q	2.8×10^{-3}	k^Q	2.1×10^{-3}
R_c	0.001 (Ω)	R_c	0.001 (Ω)	R_c	0.001 (Ω)	R_c	0.001 (Ω)	R_c	0.001 (Ω)
L_c	0.2 (mH)	L_c	0.2 (mH)	L_c	0.2 (mH)	L_c	0.2 (mH)	L_c	0.2 (mH)
$Load_1$	$Load_2$	$Load_3$	$Load_4$	$R_1 + L_1$	$R_2 + L_2$	$R_3 + L_3$	$R_4 + L_4$	V_{MG}	f_{MG}
13.5 (Kw)	18.5 (Kw)	13.5 (Kw)	14 (Kw)	$4 + j1.95$ (Ω)	$2.2 + j1.4$ (Ω)	$1.5 + j0.7$ (Ω)	$1.2 + j0.3$ (Ω)	380 (V)	50 (Hz)
12 (KvAr)	14 (KvAr)	12 (KvAr)	13 (KvAr)						

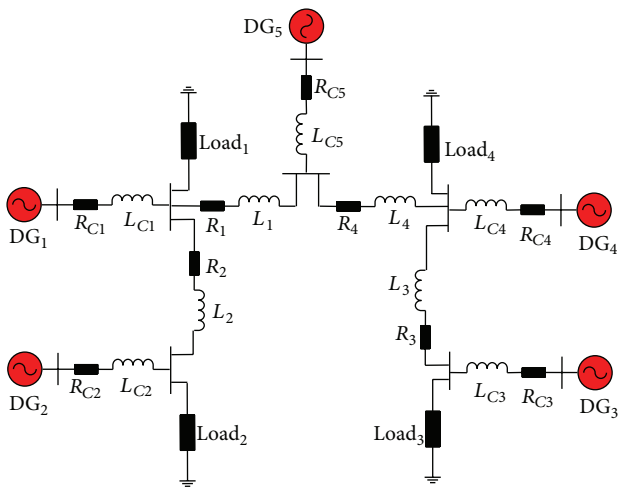

Figure 4: The fixed communication network of DGs.

and the corresponding leader adjacency matrix can be chosen as $B_1 = \mathrm{diag}\{0.005, 0, 0.005, 0, 0\}$.

In the following simulation, the time-varying delay $\tau(t)$ is always taken as $\tau(t) = (1 + 0.1\sin(t))/32$; then $\tau(t) < d = 0.0344$ and $\dot{\tau}(t) < d_1 = 0.0031 < 1$. For the fixed digraph $\mathcal{G}_1$, by simple calculation, one can choose $\Xi = \mathrm{diag}\{0.2, 0.2, 0.2, 0.2, 0.2\}$ and then yield $\lambda_{\min}(\Xi H_1 + H_1^T \Xi) = 5.2717 \times 10^{-4}$, $\lambda_{\max}(\Xi H_1 H_1^T \Xi) = 6.4856 \times 10^{-6}$, $\lambda_{\max}(H_1^T H_1) = 1.6214 \times 10^{-4}$, and $\lambda_{\min}(H_1^T H_1) = 2.1074 \times 10^{-6}$ with $H_1 = L_1 + B_1$. Therefore, the delay constraint condition in Theorem 2 can be verified as

$$\begin{aligned} d &= 0.0031 \\ &< \frac{(1-d_1)\lambda_{\min}\left(\Xi H_1 + H_1^T \Xi\right)}{\lambda_{\max}^2\left(H_1^T H_1\right)/\lambda_{\min}\left(H_1^T H_1\right) + (1-d_1)\lambda_{\max}\left(\Xi H_1 H_1^T \Xi\right)} \\ &= 0.0421. \end{aligned} \tag{21}$$

For the switching digraph Γ shown in Figure 5, one can verify the above conditions similarly.

(1) Case 1 (fixed topology). Consider a directed communication network with five DGs as shown in $\mathcal{G}_1$. Figures 6 and 7 show the state evolution processes of frequency, corresponding to active power with and without delay, respectively. It is assumed that the demands of loads increase suddenly the islanded operation microgrid at $t = 0.4$ s. As seen in Figure 6(a), after islanding, each DG's frequency ω goes to different values less than reference value $\omega^{\mathrm{ref}} = 2\pi f = 314$ rad/s. Then the primary control and secondary control are applied at $t = 0.5$ s and $t = 1$ s, respectively. Due to the droop control technique, each DG's frequency ω converges to stability value still less than reference value. However, the secondary control restores the operating frequency to synchronize their reference value after 1.6 s.

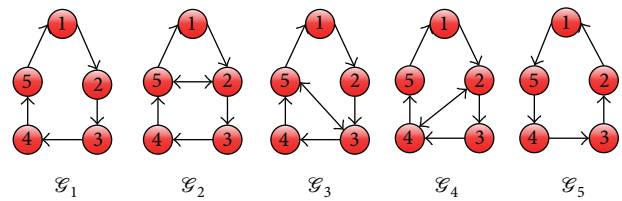

Figure 5: The switching communication digraph topology Γ.

Comparing Figures 6 and 7, respectively, one finds that the existence of communication delay postpones the convergence speed of frequency.

(2) Case 2 (switching topology). Consider a directed network with switching topology $\Gamma = \{\mathcal{G}_1, \ldots, \mathcal{G}_5\}$ as shown in Figure 5. The controlled system begins at the state $\mathcal{G}_1$ and switches at $\Delta t = 0.001$ to the next stage with the following switching order: $\{\mathcal{G}_1, \ldots, \mathcal{G}_5, \mathcal{G}_1, \ldots\}$, where the switching signal $1 \le i \le 5$. All the weights are set to be 0.005, and the corresponding leader adjacency matrix for $\mathcal{G}_2$ to $\mathcal{G}_5$ is chosen as $B_2 = \mathrm{diag}\{0, 0.005, 0, 0.005, 0\}$, $B_3 = \mathrm{diag}\{0, 0, 0.005, 0, 0.005\}$, $B_4 = \mathrm{diag}\{0.005, 0, 0, 0.005, 0\}$, and $B_5 = \mathrm{diag}\{0, 0, 0, 0.005, 0.005\}$. The associated system parameters are similar to the fixed topology case.

Figures 8 and 9 show the state evolution processes of frequency, corresponding to active power with and without delay, respectively. Comparing Figures 6-7 and Figures 8-9, it is not difficult to find that the evolution curves in Figures 8-9 contain some slight oscillation phases. It is because that the controlled system in this case contains frequent switching signals. Similarly, the communication delay also postpones the convergence speed of the whole switching system.

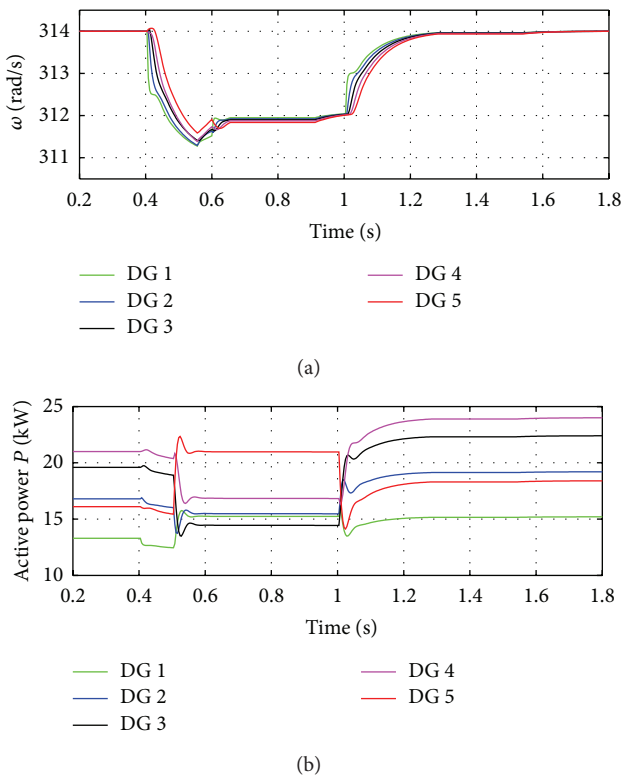

Figure 6: The state evolution processes of frequency, active power with delay under $\mathcal{G}_1$.

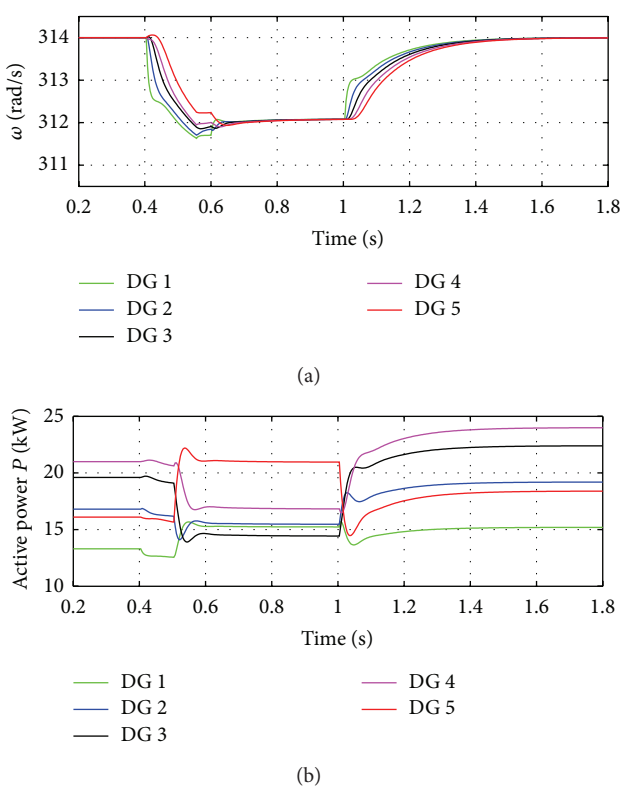

Figure 7: The state evolution processes of frequency, active power without delay under $\mathcal{G}_1$.

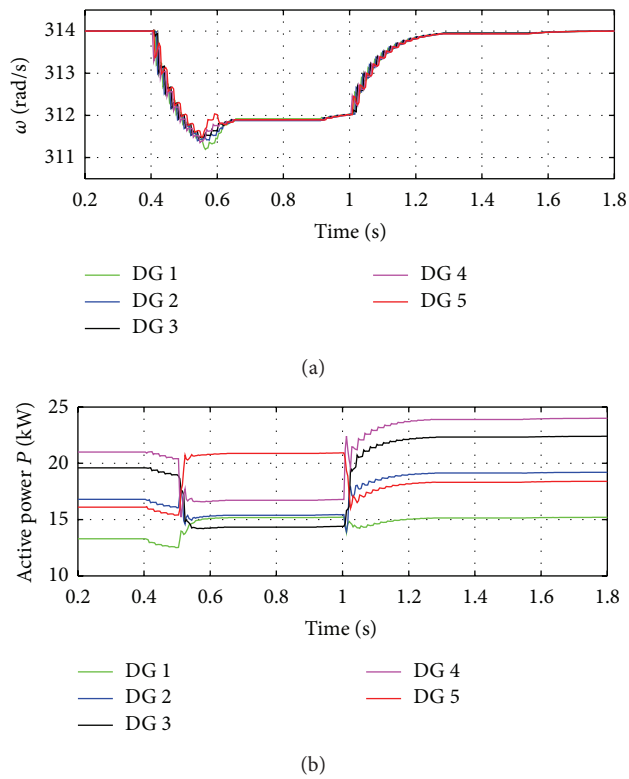

Figure 8: The state evolution processes of frequency, active power with delay under Γ.

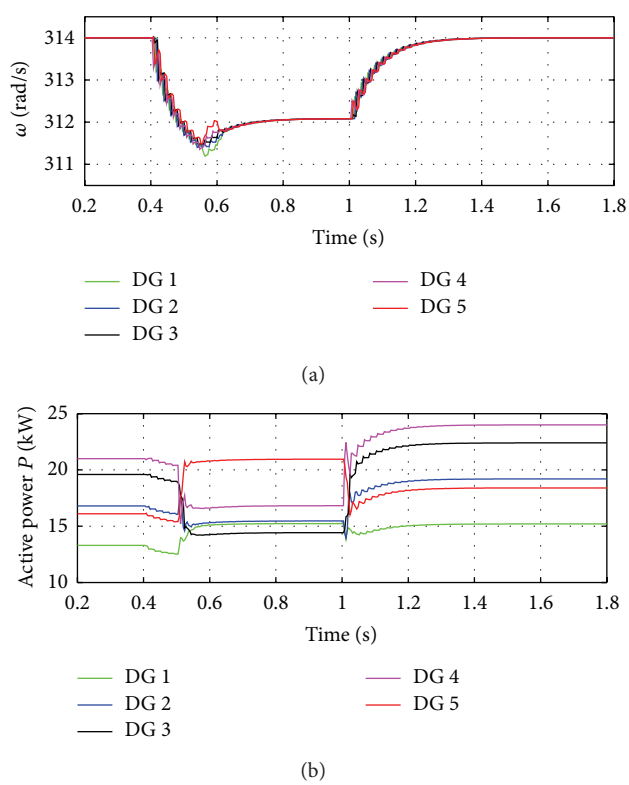

Figure 9: The state evolution processes of frequency, active power without delay under Γ.

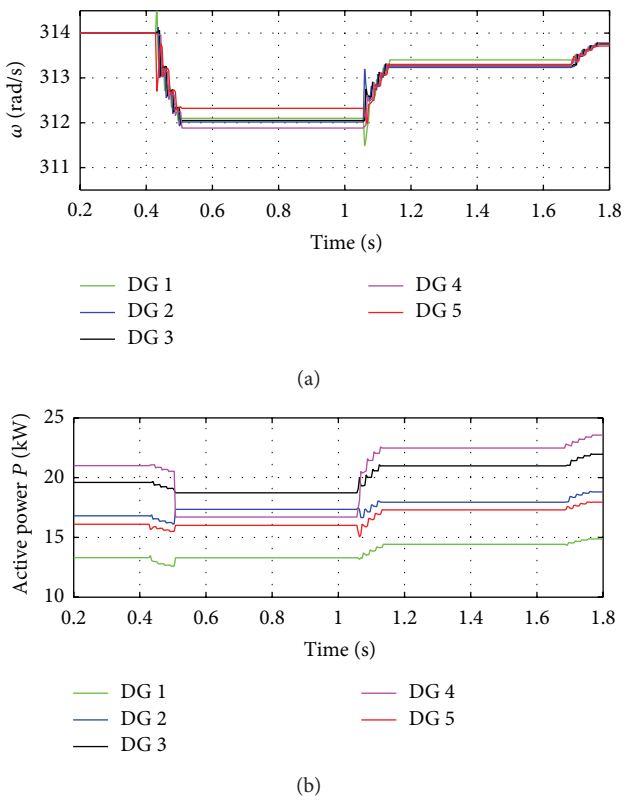

Figure 10: The state evolution processes of frequency, active power with large delay under Γ.

However, if we take the large delay $\tau(t) = (2 + \sin(t))/32$ which does not satisfy the constraint conditions in Theorem 2, the proposed distributed control algorithms may be ineffective. As shown in Figure 10, the state evolution curves do not converge to the desired values in switching case.

5. Conclusion

In this paper, a distributed cooperative control scheme for hybrid lossy microgrids has been proposed. In this method, a distributed secondary control encompasses each DG/SG local controller and the communication system; that is, each DG/SG only needs to communicate with its neighboring DGs/SGs intermittently even though the communication delays may be time-varying. The designed distributed control is able to synchronize the frequency of hybrid lossy microgrids to the desired state (50 Hz) in a distribution switching network under the existence of time-varying communication delays. All the frequency of DGs/SGs can be synchronized to the desired value in both fixed and switching distributed networks. Meanwhile, numerical simulations show higher robustness in front large communication latency.

Conflict of Interests

The authors declare that there is no conflict of interests regarding the publication of this paper.

Acknowledgments

This work was supported by National Key Technology Support Program of China under Grant no. 2013BAA01B01; by the National Natural Science Foundation of China under Grant nos. 61403133, 61374064, and 61304152; by the Young Teachers Growth Plan of Hunan University under Grant no. 531107040651; by the Postdoctoral Foundation of China under Grant no. 2013M540627; by the Postdoctoral Special Foundation of Hunan Province under Grant no. 2013RS4042; by the Natural Science Foundation of Hunan Province under Grant no. 14JJ3051; by the Doctoral Fund of Ministry of Education of China under Grant no. 20130161120016; by the Fundamental Research Funds for the Central Universities no. 2014208020201.

References

[1] N. Pogaku, M. Prodanović, and T. C. Green, "Modeling, analysis and testing of autonomous operation of an inverter-based microgrid," *IEEE Transactions on Power Electronics*, vol. 22, no. 2, pp. 613–625, 2007.

[2] J. G. Lai, H. Zhou, W. S. Hu, D. G. Zhou, and L. Zhong, "Smart demand response based on smart homes," *Mathematical Problems in Engineering*. In press.

[3] H. Farhangi, "The path of the smart grid," *IEEE Power and Energy Magazine*, vol. 8, no. 1, pp. 18–28, 2010.

[4] J. M. Guerrero, J. C. Vasquez, J. Matas, L. G. de Vicuña, and M. Castilla, "Hierarchical control of droop-controlled AC and DC microgrids—a general approach toward standardization," *IEEE Transactions on Industrial Electronics*, vol. 58, no. 1, pp. 158–172, 2011.

[5] Q.-C. Zhong, "Robust droop controller for accurate proportional load sharing among inverters operated in parallel," *IEEE Transactions on Industrial Electronics*, vol. 60, no. 4, pp. 1281–1290, 2013.

[6] Y. A.-R. I. Mohamed and E. F. El-Saadany, "Adaptive decentralized droop controller to preserve power sharing stability of paralleled inverters in distributed generation microgrids," *IEEE Transactions on Power Electronics*, vol. 23, no. 6, pp. 2806–2816, 2008.

[7] M. Savaghebi, A. Jalilian, J. C. Vasquez, and J. M. Guerrero, "Secondary control for voltage quality enhancement in microgrids," *IEEE Transactions on Smart Grid*, vol. 3, no. 4, pp. 1893–1902, 2012.

[8] M. Savaghebi, A. Jalilian, J. C. Vasquez, and J. M. Guerrero, "Secondary control scheme for voltage unbalance compensation in an Islanded droop-controlled microgrid," *IEEE Transactions on Smart Grid*, vol. 3, no. 2, pp. 797–807, 2012.

[9] J. Schiffer, R. Ortegab, A. Astolfic et al., "Conditions for stability of droop-controlled inverter-based microgrids," *Automatica*, vol. 50, no. 10, pp. 2457–2469, 2014.

[10] Q. Shafiee, C. Stefanovic, T. Dragicevic, P. Popovski, J. C. Vasquez, and J. M. Guerrero, "Robust networked control scheme for distributed secondary control of islanded microgrids," *IEEE Transactions on Industrial Electronics*, vol. 61, no. 10, pp. 5363–5374, 2014.

[11] H. Bouattour, J. W. Simpson-Porco, F. Dörfler, and F. Bullo, "Further results on distributed secondary control in microgrids," in *Proceedings of the 52nd IEEE Conference on Decision and Control (CDC '13)*, pp. 1514–1519, December 2013.

[12] P. N. Vovos, A. E. Kiprakis, A. R. Wallace, and G. P. Harrison, "Centralized and distributed voltage control: impact on distributed generation penetration," *IEEE Transactions on Power Systems*, vol. 22, no. 1, pp. 476–483, 2007.

[13] A. G. Tsikalakis and N. D. Hatziargyriou, "Centralized control for optimizing microgrids operation," in *Proceedings of the IEEE PES General Meeting: The Electrification of Transportation and the Grid of the Future*, pp. 1–8, July 2011.

[14] A. Vaccaro, G. Velotto, and A. F. Zobaa, "A decentralized and cooperative architecture for optimal voltage regulation in smart grids," *IEEE Transactions on Industrial Electronics*, vol. 58, no. 10, pp. 4593–4602, 2011.

[15] G. A. Pagani and M. Aiello, "Towards decentralization: a topological investigation of the medium and low voltage grids," *IEEE Transactions on Smart Grid*, vol. 2, no. 3, pp. 538–547, 2011.

[16] J. G. Lai, S. H. Chen, X. Q. Lu, and H. Zhou, "Formation tracking for nonlinear mulit-agent systems with delays and noises disturbance," *Asian Journal of Control*, vol. 17, no. 3, pp. 1–13, 2015.

[17] J. Lai, S. Chen, and X. Lu, "Tracking consensus of nonlinear MASs with asymmetric communication delays in noisy environments," *Communications in Nonlinear Science and Numerical Simulation*, vol. 19, no. 7, pp. 2334–2344, 2014.

[18] Z. H. Guan, Z. W. Liu, G. Feng, and Y. W. Wang, "Synchronization of complex dynamical networks with time-varying delays via impulsive distributed control," *IEEE Transactions on Circuits and Systems. I. Regular Papers*, vol. 57, no. 8, pp. 2182–2195, 2010.

[19] Z.-W. Liu, Z.-H. Guan, X. M. Shen, and G. Feng, "Consensus of multi-agent networks with aperiodic sampled communication via impulsive algorithms using position-only measurements," *IEEE Transactions on Automatic Control*, vol. 57, no. 10, pp. 2639–2643, 2012.

[20] X. Lu, R. Lu, S. Chen, and J. Lu, "Finite-time distributed tracking control for multi-agent systems with a virtual leader," *IEEE Transactions on Circuits and Systems. I. Regular Papers*, vol. 60, no. 2, pp. 352–362, 2013.

[21] X. Q. Lu, S. H. Chen, and J. H. Lü, "Finite-time tracking for double-integrator multi-agent systems with bounded control input," *IET Control Theory & Applications*, vol. 7, no. 11, pp. 1562–1573, 2013.

[22] K. Tanaka, M. Oshiro, S. Toma et al., "Decentralised control of voltage in distribution systems by distributed generators," *IET Generation, Transmission and Distribution*, vol. 4, no. 11, pp. 1251–1260, 2010.

[23] H. Zhou, Z.-H. Wang, Z.-W. Liu, W. S. Hu, and G. P. Liu, "Containment control for multi-agent systems via impulsive algorithms without velocity measurements," *IET Control Theory & Applications*, vol. 8, no. 17, pp. 2033–2044, 2014.

[24] C. H. Zhao, U. Topcu, N. Li, and S. Low, "Design and stability of load-side primary frequency control in power systems," *IEEE Transactions on Automatic Control*, vol. 59, no. 5, pp. 1177–1189, 2014.

[25] H. Bouattour, J. W. Simpson-Porco, F. Dorfler, and F. Bullo, "Further results on distributed secondary control in microgrids," in *Proceedings of the IEEE 52nd Annual Conference on Decision and Control (CDC '13)*, pp. 1514–1519, Firenze, Italy, December 2013.

[26] J. W. Simpson-Porco, F. Dörfler, and F. Bullo, "Synchronization and power sharing for droop-controlled inverters in islanded microgrids," *Automatica*, vol. 49, no. 9, pp. 2603–2611, 2013.

[27] H. Zhang, F. L. Lewis, and A. Das, "Optimal design for synchronization of cooperative systems: state feedback, observer and output feedback," *IEEE Transactions on Automatic Control*, vol. 56, no. 8, pp. 1948–1952, 2011.

[28] H. H. Xin, Z. H. Qu, J. Seuss, and A. Maknouninejad, "A self-organizing strategy for power flow control of photovoltaic generators in a distribution network," *IEEE Transactions on Power Systems*, vol. 26, no. 3, pp. 1462–1473, 2011.

[29] H. Liang, B. J. Choi, W. Zhuang, and X. Shen, "Stability enhancement of decentralized inverter control through wireless communications in microgrids," *IEEE Transactions on Smart Grid*, vol. 4, no. 1, pp. 321–331, 2013.

[30] Q. Shafiee, J. M. Guerrero, and J. C. Vasquez, "Distributed secondary control for islanded microgrids-a novel approach," *IEEE Transactions on Power Electronics*, vol. 29, no. 2, pp. 1018–1031, 2014.

[31] J. Schiffera, D. Goldin, J. Raisch et al., "Synchronization of droop-controlled microgrids with distributed rotational and electronic generation," in *Proceedings of the IEEE 52nd Annual Conference on Decision and Control (CDC '13)*, pp. 2334–2339, 2013.

[32] X. Lu, F. Austin, and S. Chen, "Flocking in multi-agent systems with active virtual leader and time-varying delays coupling," *Communications in Nonlinear Science and Numerical Simulation*, vol. 16, no. 2, pp. 1014–1026, 2011.

Hindawi Publishing Corporation
Mathematical Problems in Engineering
Volume 2015, Article ID 382954, 10 pages
http://dx.doi.org/10.1155/2015/382954

Research Article

One-Step-Ahead Predictive Control for Hydroturbine Governor

Zhihuai Xiao,[1] Suili Meng,[1] Na Lu,[2] and O. P. Malik[3]

[1]*School of Power and Mechanical Engineering, Wuhan University, Wuhan, Hubei 430072, China*
[2]*School of Water Resources and Architectural Engineering, Northwest A&F University, Xi'an, Shaanxi 712100, China*
[3]*Department of Electrical and Computer Engineering, University of Calgary, Calgary, AB, Canada T2N 1N4*

Correspondence should be addressed to Zhihuai Xiao; xiaozhihuai@126.com

Received 24 December 2014; Accepted 23 January 2015

Academic Editor: Yun-Bo Zhao

Copyright © 2015 Zhihuai Xiao et al. This is an open access article distributed under the Creative Commons Attribution License, which permits unrestricted use, distribution, and reproduction in any medium, provided the original work is properly cited.

The hydroturbine generator regulating system can be considered as one system synthetically integrating water, machine, and electricity. It is a complex and nonlinear system, and its configuration and parameters are time-dependent. A one-step-ahead predictive control based on on-line trained neural networks (NNs) for hydroturbine governor with variation in gate position is described in this paper. The proposed control algorithm consists of a one-step-ahead neuropredictor that tracks the dynamic characteristics of the plant and predicts its output and a neurocontroller to generate the optimal control signal. The weights of two NNs, initially trained off-line, are updated on-line according to the scalar error. The proposed controller can thus track operating conditions in real-time and produce the optimal control signal over the wide operating range. Only the inputs and outputs of the generator are measured and there is no need to determine the other states of the generator. Simulations have been performed with varying operating conditions and different disturbances to compare the performance of the proposed controller with that of a conventional PID controller and validate the feasibility of the proposed approach.

1. Introduction

Hydroturbine governor (HTG) provides the basic control in hydropower stations to ensure the reliability and the quality of electricity supply. The conventional hydroturbine governor adopted by most utilities is a proportional, integral, and derivative (PID) type controller based on linear control theory. It has simple structure with flexibility and is easy for implementation, and thus it has made a great contribution in enhancing the quality of electrical supply [1].

The hydroturbine generator regulating system can be considered as one system synthetically integrating water, machine, and electricity. It is a complex and nonlinear system, and its configuration and parameters are time-dependent [2]. Nonlinear models are required when speed and power changes are large during an islanding, load rejection, and system restoration conditions. A nonlinear model should include the effect of water compressibility, that is, inclusion of transmission-line-like reflections which occur in the elastic-walled pipe carrying compressible fluid [3, 4].

This creates discrepancies between the mathematical linear model of the hydroturbine generator regulating system and the physical nonlinear plant. Therefore, with the conventional linear control theory based PID controller, it is difficult to realize the desired control performance over wide operating conditions of the power plant [5]. To yield satisfactory control performance, it is desirable to develop a controller that considers the nonlinear nature of the plant and has the ability to adjust its parameters on-line according to the environment in which it is working, that is, track the plant operating conditions [6].

To meet this requirement, a large amount of research has been conducted on the hydroturbine generator regulating system. Numerous methods for PID tuning have been reported in the literature [7]. For example, to realize the parameter optimization of PID controller, an orthogonal test strategy is adopted in [8, 9] for hydroturbine control application. In this approach, a control performance index that depends on control parameters KP, Ki, and Kd is defined. Each of these parameters is considered under various levels as

a discrete variable. An optimization algorithm is developed to search for better control parameters in the neighbouring space of the present one. However, many of these approaches lack one or more of the three basic and important features that a controller should have, that is, simplicity of structure, fast acting (low computation time), and adaptability.

Neural networks (NNs) have been applied very successfully in the identification and control of dynamic systems. The universal approximation capabilities of the multilayer perceptron make it a popular choice for modeling nonlinear systems and implementing general-purpose nonlinear controllers [10–13]. The concept of intelligent tuning of PID controller is presented in [14, 15]. The use of adaptive learning control schemes is discussed in [14] and the improved dynamic performance of the intelligent PID controller over the conventional PID is presented in [15]. The developed intelligent PID controller is based on anthropomorphic intelligence. Among various types of NNs used in the hydroturbine generator regulating system, the feed-forward multilayer NN is the most commonly used. This is mainly due to the computational efficiency of the back propagation algorithm [12] and the versatility of the three-layer feed-forward NN in approximating an arbitrary static nonlinear function [16]. However, little work has been reported on the use of NNs for hydroturbine generator regulating system for real-time control.

The theory and algorithm of predictive control have achieved great development in the industrial process control after thirty years' application and study. It has been introduced to the optimal control of hydroturbines by lots of experts. Jones and Mansoor [17], for example, applied predictive feed-forward control to the power target signal tracking in part load condition, and the result shows that predictive feed-forward control can achieve a substantial improvement in tracking a power target when a hydroelectric station operates in part load condition mode. However, the power station they used is modeled using linearized transfer function. For systems with strong nonlinear and frequent turbulence or wide range of operating point, the predictive control adopting linear model near operating point can no longer satisfy the requirements of control quality. Therefore, the nonlinear modeled predictive control has aroused wide concern.

A predictive control scheme for hydroturbine governor based on NNs is introduced in this paper. The control architecture consists of two NNs: an adaptive neuroidentifier (ANI) to track the plant and predict its output one-step-ahead and an adaptive neurocontroller (ANC) to produce the control signal. A scalar error is used in each sampling period to update the identifier and controller weights continuously in real-time. With a similar architecture, called indirect adaptive control [12], the use of a reference model is suggested. That is avoided in this work owing to the difficulties in choosing a proper reference model for the complex hydroturbine generator regulating system.

The effect of different amplitude step disturbances and trapezoidal shape reference signal (turbine power) are investigated in this paper. Also, a number of studies are performed to compare the performance of the proposed controller with that of the conventional PID controller under different operating conditions.

2. Basic Plant Equations

A simple layout of a hydropower plant shown in Figure 1 includes a reservoir, a penstock (high pressure), gate, a hydroturbine, and a generator. The function of the reservoir is to store water and thus develop a head. To start the turbine generator unit, water released from the reservoir flows through the penstock and reaches the turbine inlet. From here it enters into the scroll casing of the turbine that distributes the water evenly on the runner blades. The electromechanical power conversion takes place between the turbine runner and the generator mounted on the common shaft. The water flow to the turbine is regulated by the operation of wicket gates that in turn are controlled by the governor. The opening and closing of the gates are a function of the variable electrical load connected to the generator and the shaft speed.

The hydroturbine governing system consisting of the controller and the controlled plant is a complex, nonlinear, time varying, and non-minimum-phase system with fractional distributed parameters and uncertainties. The controlled plant includes a turbine, a penstock, a generator, and a load (Figure 2). In practice, a linearized (or linear) model is used to describe the plant for designing the control system. The dynamic characteristics of the plant are shown in Figure 2 [18].

2.1. Turbine. The characteristic equations of the Francis turbine are [19–21]

$$M_t = M_t(y, h, x),$$
$$Q = Q(y, h, x), \tag{1}$$

where M_t is torque of the turbine, Q is flow rate, y is gate opening, h is head, and x is speed. Taking Taylor series expansion of (1) and omitting the parts containing second- or higher-order derivatives, the linearized model can be expressed as follows in the neighborhood of certain operation:

$$m_t = e_y y + e_x x + e_h h,$$
$$q = e_{qy} y + e_{qx} x + e_{qh} h. \tag{2}$$

The six transmission coefficients (as shown below) change as the gate opening changes:

$$e_y = \frac{\partial m_t}{\partial y}, \qquad e_x = \frac{\partial m_t}{\partial x}, \qquad e_h = \frac{\partial m_t}{\partial h},$$
$$e_{qy} = \frac{\partial q}{\partial y}, \qquad e_{qx} = \frac{\partial q}{\partial x}, \qquad e_{qh} = \frac{\partial q}{\partial h}. \tag{3}$$

2.2. Penstock. The general expression of penstock, taking rigid water hammer, is described as

$$h = -T_w \frac{dq}{dt}, \tag{4}$$

where T_w is the water inertia time constant.

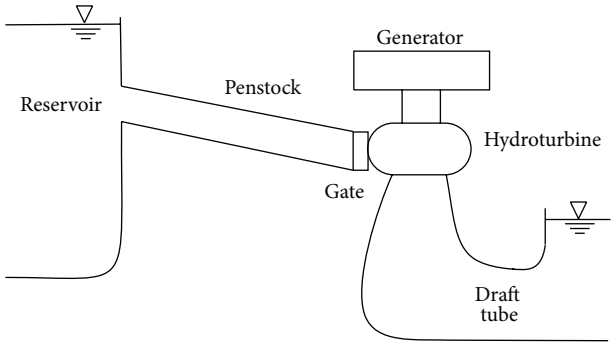

Figure 1: General layout of hydropower plant.

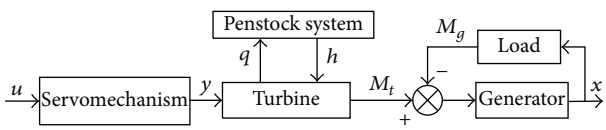

Figure 2: Hydroturbine generator regulating system.

2.3. Generator and Load. The characteristic equation of the generator and the load can be written as

$$T_a \frac{dx}{dt} = m_t - m_g - e_g x, \tag{5}$$

where T_a is the unit inertia time constant, m_g is the load torque, and e_g is the load self-regulation factor, regarding the fluctuation caused by the change of the system frequency.

2.4. Servomechanism. Neglecting small time constants, the servomechanism can be expressed with a first-order equation:

$$T_y \frac{dy}{dt} + y = u, \tag{6}$$

where T_y is the servomotor response time and u is the control signal.

3. Controller Structure

The structure of the controller is shown in Figure 3. It consists of two subnetworks. The first subnetwork is an adaptive one-step-ahead neuroidentifier that tracks the dynamic behaviour of the plant and identifies the plant in terms of its internal weights and the second one is an adaptive neurocontroller to provide the necessary control action in order to minimize certain cost function.

3.1. Adaptive Neuroidentifier. A multilayer perceptron neural network (MLPNN) structure is developed to model the nonlinear dynamic relationship between the gate position and the turbine mechanical power. Considering it is difficult to measure the turbine mechanical power, generator output power is measured instead to obtain the turbine mechanical power by

$$P_e = \frac{P_g}{\eta}, \tag{7}$$

where P_e is turbine mechanical power, P_g is generator output power, and η is generator efficiency.

The network transforms n inputs to m outputs through a nonlinear function $f : R^n \to R^m$. It is shown in [15] that an MLPNN with single hidden layer activated with sigmoid or hyperbolic tangent function can approximate any continuous function. Considering the nature of the dependence of the plant output on a finite number of past inputs, $u(t)$, and outputs, $y(t)$, the nonlinear relationship between the gate position and the turbine power can be represented in the form of predictor/identifier as

$$\begin{aligned} &y_{(k+1)} \\ &\quad = f\left[y_{(k)}, y_{(k-1)}, \ldots, y_{(k-n+1)}, u_{(k)}, u_{(k-1)}, \ldots, u_{(k-m+1)}\right]. \end{aligned} \tag{8}$$

In this case a popular MLPNN with single hidden layer activated with sigmoid function and back propagation learning has been used to develop the predictor of nonlinear relationship model (8). The input vector to the ANI is

$$\begin{aligned} &\left[p_{(k)}, p_{(k-1)}, \ldots, p_{(k-n+1)}, \right. \\ &\quad \left. u_{(k)}, u_{(k-1)}, \ldots, u_{(k-m+1)}\right], \end{aligned} \tag{9}$$

where $p(k)$ is the turbine mechanical power and $u(k)$ is the gate position at the time step k. The output is the predicted turbine mechanical power $\widehat{p}_{(k+1)}$, at time step $(k+1)$. For a finite number of past inputs, $u(t)$, and outputs, $p(t)$, the nonlinear relationship between the control output (gate position) and turbine power can be represented in the form of an identifier as shown in Figure 4.

The input vector to the ANI is scaled in the range of $[-1, +1]$ before being applied to the network. The cost function used for the ANI is

$$J_i(k) = \frac{1}{2} e_i(k)^2 = \frac{1}{2}\left[p(k) - \widehat{p(k)}\right]^2. \tag{10}$$

The weights are updated as

$$w_i(k) = w_i(k-1) - \eta_i \frac{\partial J_i(k)}{\partial w_i(k)}, \tag{11}$$

where w_i is the matrix of identifier weights at time step k and η_i is the learning rate for the ANI. This cost function is minimized by back propagating the scalar error. In each sampling period, the input and the output of the plant are sampled and the input vector to the identifier is formed as in (9). Then the error between the actual and predicted outputs of the plant, a scalar value, is back propagated through the identifier to update the weights of the network ($w_i(k)$). This process is repeated every sampling period that in turn results in an adaptive approach to predict one-step-ahead of the output of the plant. The use of just one error value for back propagation simplifies the training algorithm by reducing computation time.

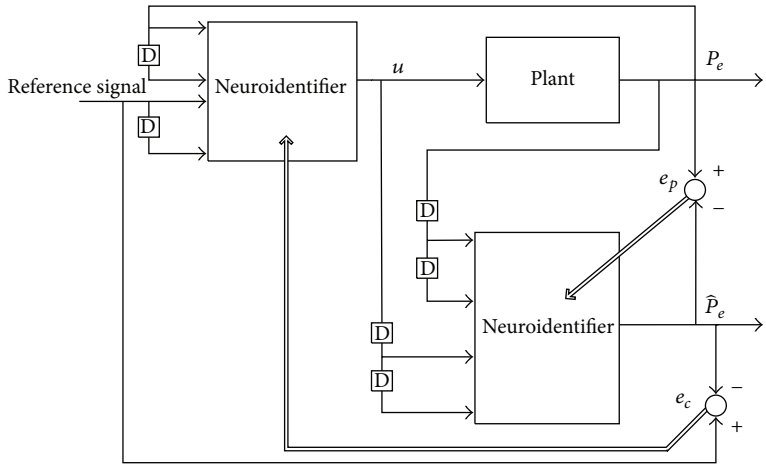

Figure 3: Schematic of control structure.

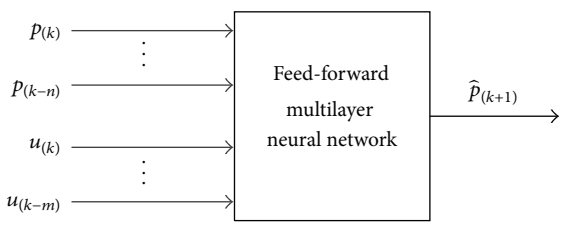

Figure 4: Neuroidentifier.

3.2. Adaptive Neurocontroller. Taking advantage of the recognized universal approximation properties of NN, a nonlinear plant in the MLPNN form is obtained as discussed before. Based on the neural model, a predictive control strategy is implemented by an adaptive neurocontroller. The input vector to the ANC is

$$\begin{aligned}&\left[p_{(k)}, p_{(k-1)}, \ldots, p_{(k-p+1)},\right.\\&\left.r_{(k)}, r_{(k-1)}, \ldots, r_{(k-q+1)}\right],\end{aligned} \tag{12}$$

where $r(k)$ is the reference input signal at time step k. The output of the ANC is the control action $u(k)$ at time step k. The inputs to the ANC are also scaled in the range of $[-l, +l]$. The cost function for the ANC is considered as

$$\begin{aligned}J_c(k) &= \frac{1}{2}\left[e_c(k)^2 + hu(k)\right]^2\\&= \frac{1}{2}\left[r(k) - p(\widehat{k})\right]^2 + \frac{h}{2}u(k)^2,\end{aligned} \tag{13}$$

where $r(k)$ is the reference input signal at time step k and h is a tuning parameter that is used to improve the plant output dynamic characteristics. By taking h larger than zero, a penalty factor is applied to the control operation that helps the tuning of the dynamic trajectory and optimizing the overshoot and the settling time of the response curve. The weights of the controller $w_c(k)$ are updated as

$$w_c(k) = w_c(k-1) - \eta_c \frac{\partial J_c(k)}{\partial w_c(k)}. \tag{14}$$

Using (13) and (14) $J_c(k)$ is minimized in each sampling period. As depicted in (9) and (12), the states of the plant are not required for the implementation of the ANI and ANC, and only input-output data are needed. This greatly simplifies the implementation of the control process.

4. Training Process

The success implementation of the control algorithm presented in Section 3 highly depends on the accuracy of the identifier in tracking dynamic plant. For this reason, the ANI is initially trained off-line before being used in the final configuration. The training is performed over a wide range of operating conditions for the generating unit. After the off-line training stage, the ANI is employed in the system. Further updating of the weights of ANI and ANC is performed in each sampling period by employing the on-line version of the back propagation method. This enables the controller to track the plant variations as they occur to yield the optimum performance. The main steps of the adaptive predictive control algorithm are listed as follows, and the algorithm flowchart is shown in Figure 5.

(1) At time step k, $p(k)$ is sampled.

(2) Compute $\widehat{p}_{(k)}$ using ANI and its input vector (9).

(3) Calculate the error between $p(k)$ and $\widehat{p}_{(k)}$; then update the weights of the ANI to minimize $J_i(k)$ utilizing the back propagation method and the gradient descent algorithm.

(4) The output of the controller $u(k)$ is computed.

(5) Using input vector (9), the predicted $\widehat{p}_{(k+1)}$ is computed by the ANI with weights updated in step (3).

(6) Based on $\widehat{p}_{(k+1)}$ and reference signal, weights of the ANC are updated, minimizing $J_c(k)$ by utilizing the back propagation method and the gradient descent algorithm.

In step (3) above, the training is straightforward since the error at the output of the ANI is obtained. However, in

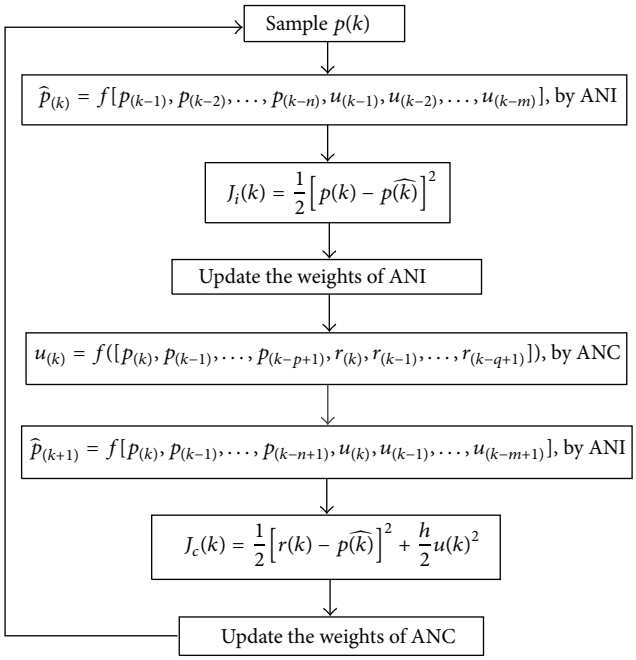

Figure 5: The flowchart of the adaptive predictive control algorithm.

Table 1: Transmission coefficients as a function of gate opening.

Operating point number	Gate opening %	e_y	e_h	e_x	e_{qy}	e_{qh}
1	43.74	2.867	0.526	−0.353	1.674	0.232
2	47.52	2.562	0.679	−0.455	1.541	0.262
3	51.26	2.278	0.814	−0.545	1.416	0.290
4	55	2.016	0.934	−0.626	1.300	0.315
5	58.74	1.766	1.039	−0.696	1.191	0.338
6	62.52	1.654	1.132	−0.759	1.090	0.360
7	66.26	1.333	1.212	−0.813	0.997	0.380
8	70	1.146	1.281	−0.859	0.913	0.397
9	73.74	0.974	1.340	−0.898	0.837	0.414
10	77.52	0.822	1.391	−0.932	0.768	0.429
11	81.26	0.691	1.433	−0.961	0.708	0.443
12	85	0.578	1.468	−0.984	0.655	0.455
13	88.74	0.484	1.498	−1.000	0.611	0.467
14	92.52	0.409	1.523	−1.020	0.574	0.478
15	96.26	0.353	1.544	−1.030	0.546	0.489
16	100	0.317	1.563	−1.047	0.526	0.499

step (6) the training is difficult since the error at the output of the ANC is not provided. In this case, first, the weights of the ANI are frozen and the error between the desired and predicted plant output is back propagated through the ANI. Then, the back propagated signal at the input of the ANI is further propagated through the ANC, making necessary changes to the controller weights. In other words, for adapting weights of the controller, the identifier acts as a channel to convey the error from the output of the identifier to the output of the controller. This evaluates the need to have the identifier. The error is used to train the ANI and the ANC.

5. Simulation Results

The plant model is simulated using the mathematical model given in Section 2. The values of plant parameters used are

$$\begin{aligned} &T_a = 9.06\,\text{s}, \qquad T_w = 1.27\,\text{s}, \qquad T_r = 0.15\,\text{s}, \\ &\xi = 0.2, \qquad T_1 = 0.02\,\text{s}, \qquad T = 0.04\,\text{s}, \\ &s_1 = 0.00167, \qquad i_x = 0.04\%, \end{aligned} \tag{15}$$

where T_r is penstock reflection time, ξ is damping constant-infinite bus tie, T_1 is servomotor response time, T is the sampling period, s_1 is speed limit on control in a governor, and i_x is dead band. The transmission coefficients (except e_{qx} which is usually equal to 0) have different values for the different gate openings. A set of transmission coefficients corresponding to the gate opening for a turbine located in Ouyanghai hydropower plant in China is given in Table 1. The design water head of Ouyanghai hydropower station is 37.6 meters, and design flow is 38.4 m^3/s. Turbine model is chosen as HL123-LJ-225, and rated capacity and voltage of the turbine are 1200 kw and 10.5 kv, respectively.

The Simulation Toolbox SIMULINK of MATLAB is utilized to develop plant model and generate data. The absolute value of pseudorandom binary signal is applied to the input to represent the variation of gate position, and the corresponding turbine mechanical power is obtained. The data collected (input and output) are divided into two sets: one set is for training the NN and the other set is for validation.

An input-output identifier model and control strategy is established and its parameters are set as follows. The number of time delays used for the input of ANI and ANC is set to 3; that is, m, n, p, and q in (8), (9), and (12) are all set to 3. This means that both the ANI and the ANC have 6 inputs. There is one hidden layer of 8 neurons with sigmoid nonlinearity and an output layer with one linear neuron, for both the ANI and the ANC. Initial weights of the ANC lie in $[-0.1, +0.1]$, chosen randomly at the beginning of the process. The initial weights of the ANI are set to those obtained from off-line training stage of the ANI as discussed before. The learning rate for the ANI and the ANC is 0.01 and 0.03, respectively. The value of the penalty factor h is set between 0.1 and 2.0.

The quadratic programming problem in (13) is solved by using the quadprog function in the Optimization Toolbox of MATLAB. The MLP network algorithm is realized by using the functions of Train, Init, and Sim in the Neural Network Toolbox of MATLAB.

As the control parameters have been determined as discussed before, the performance of the proposed adaptive neural predictive control is simulated on a large amplitude step and trapezoidal wave-shape reference signals. These reference signals may represent the nature of load changes. The turbine gate opening and power output are shown in Figures 6–9 on different reference signals and various values of penalty factor h.

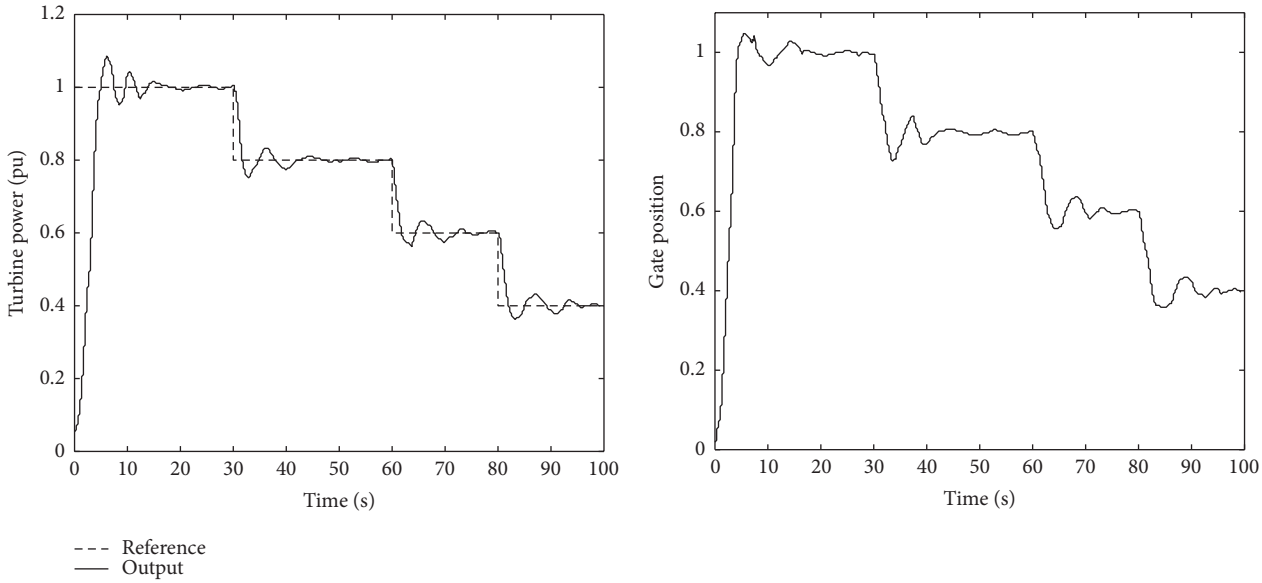

(a) Turbine power output response

(b) Turbine gate opening response

Figure 6: Response to large amplitude step in turbine power reference, $h = 2.0$.

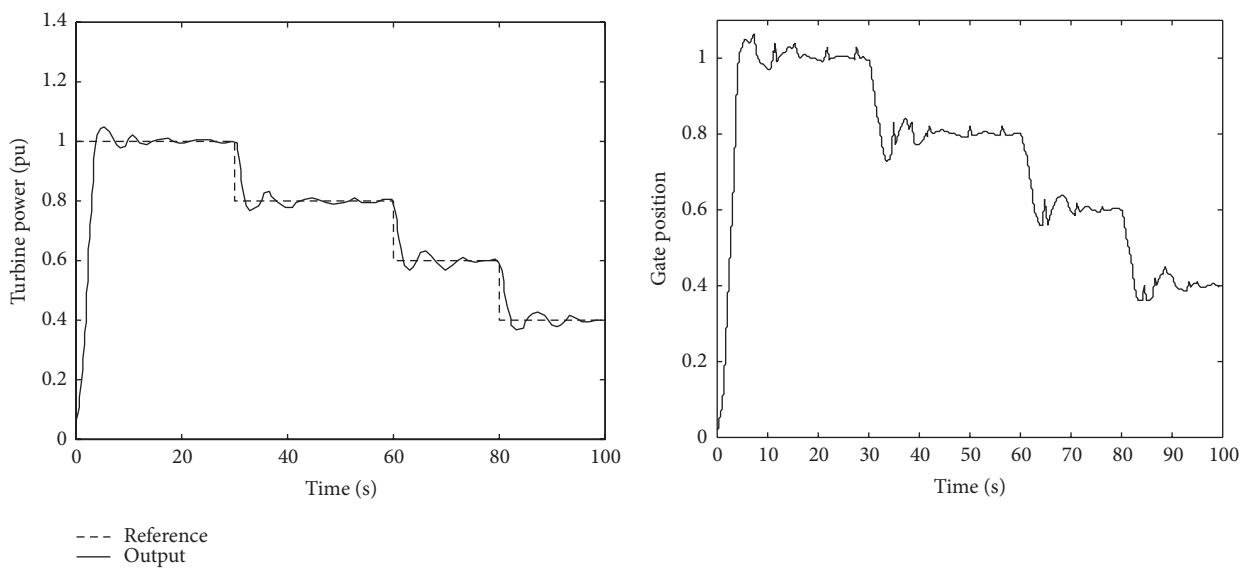

(a) Turbine power output response

(b) Turbine gate opening response

Figure 7: Response to large amplitude step in turbine power reference, $h = 0.18$.

The response shows a non-minimum-phase characteristic. The turbine power response on the large amplitude step signal follows more or less closely. It is evident that despite a large change in the operating conditions the controller still provides good results because of the adaptation process. However, the gate position is observed to exhibit large fluctuation on step change with $h = 0.18$. This would cause undue actuator wear. The optimization seems to be insensitive to variations in control penalty factor. In the case of trapezoidal wave signal, the controlled variable reaches its steady-state value extremely fast with a little offset (i.e., output power overlaps the reference signal) and gate position variation within limits is demonstrated.

A number of studies have been performed to compare the quality of the proposed adaptive predictive controller with those of the conventional PID controller.

Generally, the conventional governors adopt a PI or PID control law. Figure 10 is the illustration of the conventional

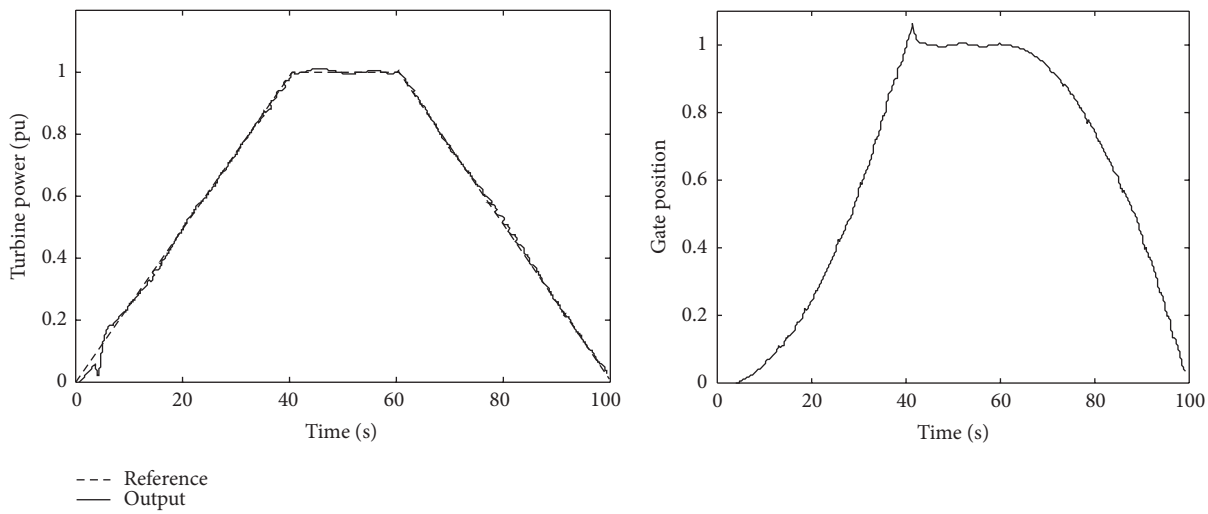

(a) Turbine power output response (b) Turbine gate opening response

Figure 8: Response to trapezoidal wave reference, $h = 2.0$.

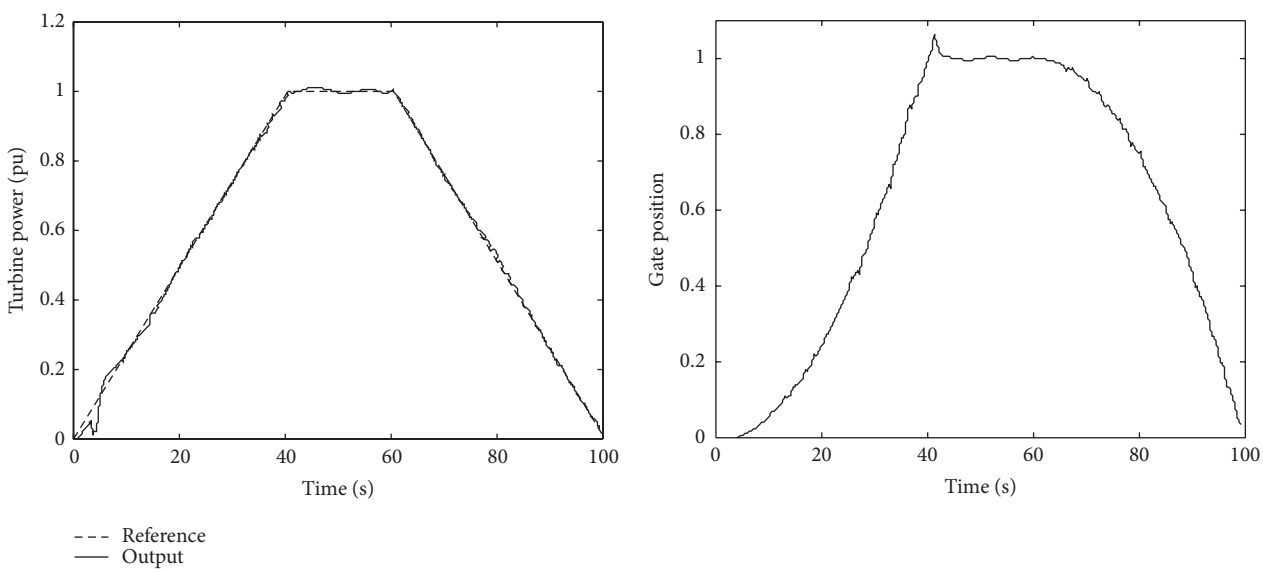

(a) Turbine power output response (b) Turbine gate opening response

Figure 9: Response to trapezoidal wave reference, $h = 0.18$.

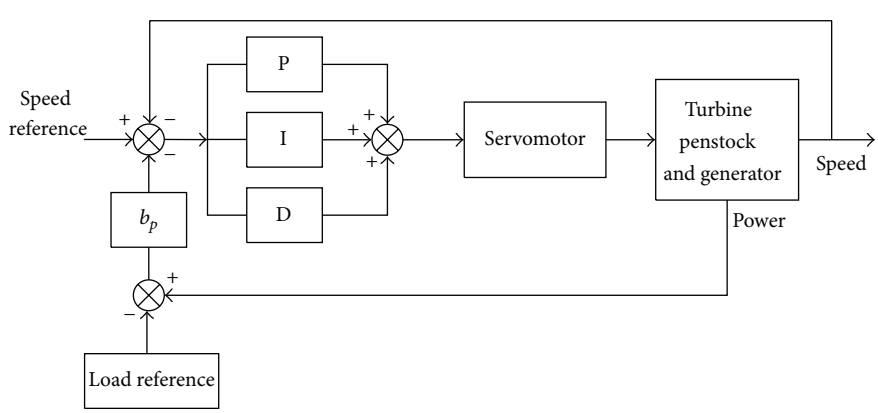

Figure 10: Illustration of the conventional load-change method.

load changing process, where bp is permanent speed droop. It plays an important role in adjusting the load of the unit and the load distribution among all units in the power system.

Regarding the adjustments of PID parameters, the following formulas are often used by experienced engineers.

For PI controller,

$$T_n = 0, \qquad b_t = \frac{2.6T_w}{T_a}, \qquad T_d = 6T_w; \tag{16}$$

for PID controller,

$$T_n = 0.5T_w, \qquad b_t = \frac{1.5T_w}{T_a}, \qquad T_d = 3T_w, \tag{17}$$

where T_n is the derivative time constant, b_t is the transient speed droop, and T_d is the damping time constant. Their relation with proportional, integral, and differential gain coefficients of a continuous PID controller is

$$k_p = \frac{T_d + T_n}{b_t T_d}, \qquad k_i = \frac{1}{b_t T_d}, \qquad k_d = \frac{T_n}{b_t}. \tag{18}$$

According to these empirical formulae, the parameters of the conventional PID controller are chosen as below:

$$k_p = 5.56, \qquad k_i = 1.25, \qquad k_d = 3.03, \qquad b_p = 0. \tag{19}$$

The proposed adaptive neuropredictive controller adopts the parameters determined as discussed above and the value of the penalty factor h is set to 2.0.

Step increases of 10% and 80% in power reference are introduced and the system responses with the conventional PID controller (CPID) and the proposed adaptive neuropredictive controller (PAPC) are shown in Figures 11–14. The dashed curves represent the response of CPID, and the solid lines represent the response of PAPC.

It is observed from Figure 11 that, with the conventional PID controller, the settling time, defined as the moment when the system error is less than 5% of the input reference signal, is 8.9 s and the overshoot is 18.3%, but, with the adaptive predictive controller, the setting time is 7.2 s and overshoot is 13.1%. It can be seen from Figure 12 that the settling time with the conventional PID controller is 28.3 s and the overshoot is 37.4%, but, with the adaptive predictive controller, the setting time is 7.4 s and overshoot is 13.5%.

From the responses for 10% and 80% step changes in power reference, it can be seen that the conventional PID controller only provides acceptable performance for a small disturbance rather than the large disturbance. Even for a small disturbance, the proposed adaptive predictive controller is better than the conventional one regarding the speed and the overshoot of response of the process.

This is logically correct because of the existence of nonlinearities in a hydroturbine governing system. These nonlinearities can be divided into two parts. The first comes from the turbine's nonlinear characteristics that depend on the operating point. It can be clearly seen from (2) of the turbine that the six transmission coefficients change as the gate opening changes. The second part is due to the nonlinear factors such as magnitude limit on control, dead band, and speed limit on control. Therefore, in the conventional PID controller, the regulation parameters that give good performance for small disturbance are no longer optimal for the large disturbance. In the case of a small disturbance, the effect of nonlinearity is negligible and the conventional controller is designed based on the linear control theory, but, in the case of a large disturbance, the effect of nonlinearity cannot be neglected. The plant has changed; however the control parameters of the conventional PID controller have not changed. Therefore, it is unable to maintain adequate performance levels. In contrast, it can be

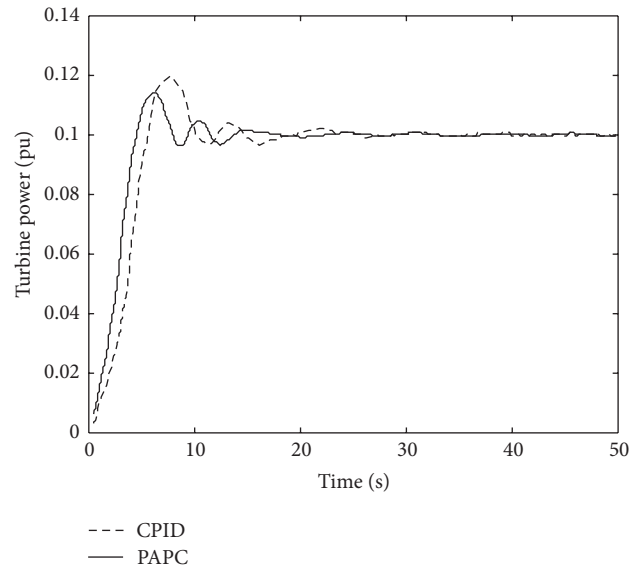

Figure 11: Turbine power output response to a 10% step in reference.

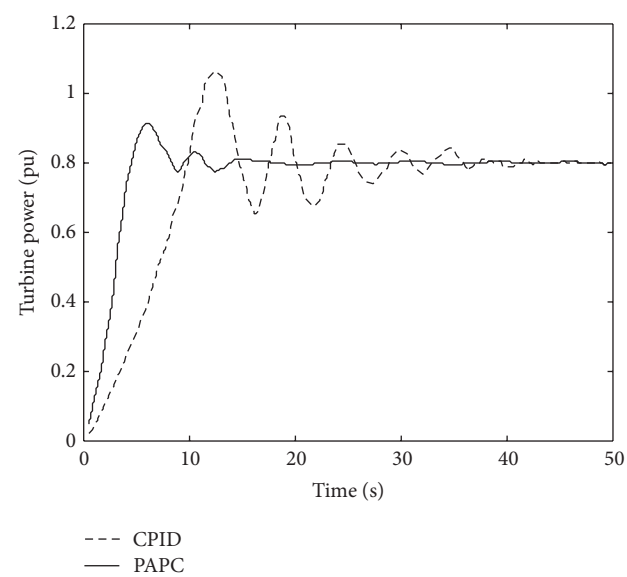

Figure 12: Turbine power output response to an 80% step in reference.

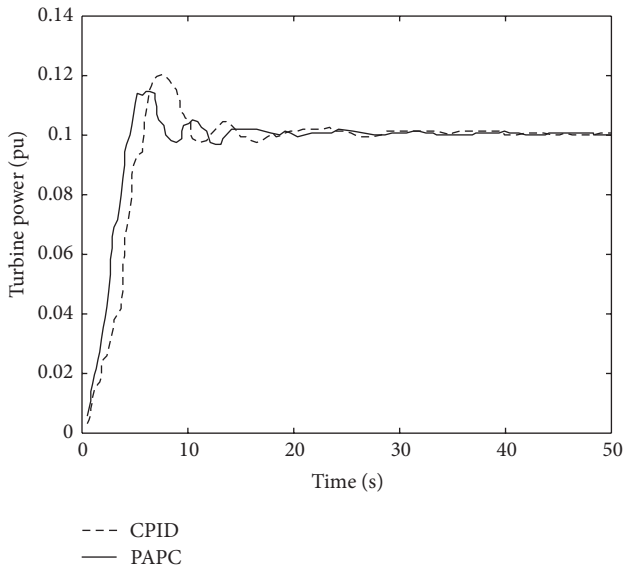

Figure 13: Gate opening response to a 10% step in reference.

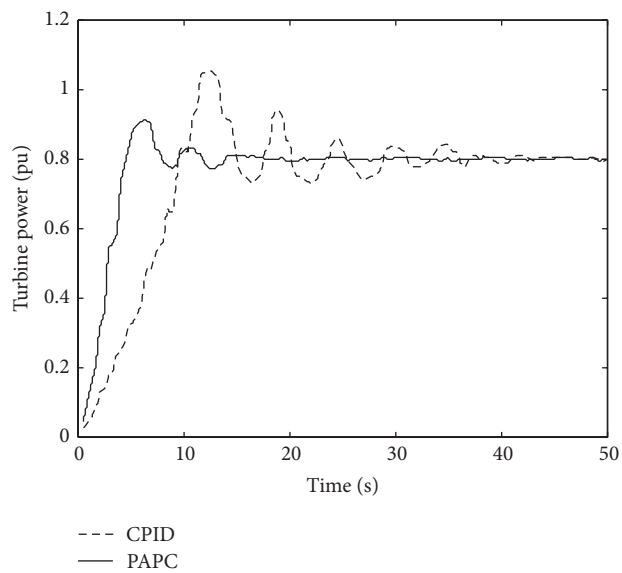

Figure 14: Gate opening response to an 80% step in reference.

seen that the proposed adaptive predictive controller has a good response for both small and large disturbances, because it considers the nonlinear nature of the plant and has the ability to adjust its own parameters on-line according to the working environment. Even for the small disturbance, the proposed adaptive predictive controller considers the plant nonlinearity as well, while it is usually ignored in the conventional PID controller. Therefore, the proposed adaptive predictive controller has better control performance than the conventional one in regard to the speed and the overshoot of the process response.

6. Conclusions

An adaptive neuropredictive control for hydroturbine governor is presented in this paper. The back propagation network with on-line learning is used in the proposed method. The controller introduced in this work inherits the general advantages of neural networks such as high speed, generalization capability, and fault tolerance as well as adaptation (learning) property. This method features the simple structure and the nonrequirement for a large number of neurons in the implementation. The learning algorithm is simplified by employing a single element error vector. The controller weights are updated directly in an on-line mode from the inputs and the outputs of the generator, and the states of the system are not necessarily determined. Simulation results for the large amplitude step and trapezoidal waveshape reference signals show that the proposed adaptive predictive controller can adaptively improve the dynamic performance of the system. By comparing the performance of the proposed adaptive predictive controller with that of the conventional PID controller, it is found that the proposed adaptive predictive controller is not only simple but also robust, and it features strong adaptivity as well.

Conflict of Interests

The authors declare that there is no conflict of interests regarding the publication of this paper.

Acknowledgment

The authors acknowledge the financial supports from the National Natural Science Foundation of China under Grant no. 51379160.

References

[1] N. Kishor, R. P. Saini, and S. P. Singh, "A review on hydropower plant models and control," *Renewable and Sustainable Energy Reviews*, vol. 11, no. 5, pp. 776–796, 2007.

[2] H. Fang, L. Chen, and Z. Shen, "Application of an improved PSO algorithm to optimal tuning of PID gains for water turbine governor," *Energy Conversion and Management*, vol. 52, no. 4, pp. 1763–1770, 2011.

[3] D. G. Ramey and J. W. Skooglund, "Detailed hydro governor representation for system stability studies," *IEEE Transactions on Power Apparatus and Systems*, vol. 89, no. 1, pp. 106–112, 1970.

[4] Q. Chen and Z. Xiao, "Dynamic modeling of hydroturbine generating set," in *Proceedings of the IEEE International Conference on Systems, Man and Cybernetics*, pp. 3427–3430, October 2000.

[5] C. Jiang, Y. Ma, and C. Wang, "PID controller parameters optimization of hydro-turbine governing systems using deterministic-chaotic-mutation evolutionary programming (DCMEP)," *Energy Conversion and Management*, vol. 47, no. 9-10, pp. 1222–1230, 2006.

[6] D. Zhang and L. Yu, "Exponential state estimation for Markovian jumping neural networks with time-varying discrete and distributed delays," *Neural Networks*, vol. 35, pp. 103–111, 2012.

[7] P. Hušek, "PID controller design for hydraulic turbine based on sensitivity margin specifications," *International Journal of Electrical Power and Energy Systems*, vol. 55, pp. 460–466, 2014.

[8] Z. Li and O. P. Malik, "An orthogonal test approach based control parameter optimization and its application to a hydroturbine governor," *IEEE Transactions on Energy Conversion*, vol. 12, no. 4, pp. 388–393, 1997.

[9] A. Soós and O. P. Malik, "An H_2 optimal adaptive power system stabilizer," *IEEE Transactions on Energy Conversion*, vol. 17, no. 1, pp. 143–149, 2002.

[10] H. Fang, L. Chen, N. Dlakavu, and Z. Shen, "Basic modeling and simulation tool for analysis of hydraulic transients in hydroelectric power plants," *IEEE Transactions on Energy Conversion*, vol. 23, no. 3, pp. 834–841, 2008.

[11] M. Mahmoud, K. Dutton, and M. Denman, "Dynamical modelling and simulation of a cascaded reserevoirs hydropower plant," *Electric Power Systems Research*, vol. 70, no. 2, pp. 129–139, 2004.

[12] P. Shamsollahi and O. P. Malik, "An adaptive power system stabilizer using on-line trained neural networks," *IEEE Transactions on Energy Conversion*, vol. 12, no. 4, pp. 382–387, 1997.

[13] I. Eker, "Governors for hydro-turbine speed control in power generation: a SIMO robust design approach," *Energy Conversion and Management*, vol. 45, no. 13-14, pp. 2207–2221, 2004.

[14] Y.-C. Cheng, L.-Q. Ye, F. Chuang, and W.-Y. Cai, "Anthropomorphic intelligent PID control and its application in the hydro turbine governor," in *Proceedings of the International Conference on Machine Learning and Cybernetics*, pp. 391–395, November 2002.

[15] G. Cybenko, "Approximation by superpositions of a sigmoidal function," *Mathematics of Control, Signals, and Systems*, vol. 2, no. 4, pp. 303–314, 1989.

[16] Z. Shen, *Governing of Hydroturbine*, China Water Publishing Press, Beijing, China, 3rd edition, 1998.

[17] D. Jones and S. Mansoor, "Predictive feedforward control for a hydroelectric plant," *IEEE Transactions on Control Systems Technology*, vol. 12, no. 6, pp. 956–965, 2004.

[18] K.-I. Funahashi, "On the approximate realization of continuous mappings by neural networks," *Neural Networks*, vol. 2, no. 3, pp. 183–192, 1989.

[19] C. D. Vournas and A. Zaharakis, "Hydro turbine transfer functions with hydraulic coupling," *IEEE Transactions on Energy Conversion*, vol. 8, no. 3, pp. 527–532, 1993.

[20] Z. Xiao, S. Wang, H. Zeng, and X. Yuan, "Identifying of hydraulic turbine generating unit model based on neural network," in *Proceedings of the 6th International Conference on Intelligent Systems Design and Applications (ISDA '06)*, vol. 1, pp. 113–117, October 2006.

[21] J. Chang, B. Liu, and W. Cai, "Nonlinear simulation of hydroturbine governing system based on neural network," in *Proceedings of the IEEE International Conference on Systems, Man and Cybernetics*, pp. 784–787, October 1996.

Hindawi Publishing Corporation
Mathematical Problems in Engineering
Volume 2015, Article ID 953464, 7 pages
http://dx.doi.org/10.1155/2015/953464

Research Article

Fast Consensus of Networked Multiagent Systems with Two-Hop Network

Jinfeng Gao, Bin Bu, Lihui Feng, and Minming Gu

Department of Automation, Zhejiang Sci-Tech University, Hangzhou 310018, China

Correspondence should be addressed to Jinfeng Gao; gaojf163@163.com

Received 7 January 2015; Accepted 11 March 2015

Academic Editor: Yun-Bo Zhao

Copyright © 2015 Jinfeng Gao et al. This is an open access article distributed under the Creative Commons Attribution License, which permits unrestricted use, distribution, and reproduction in any medium, provided the original work is properly cited.

This paper studies the consensus convergence speed of multiagent systems (MASs) from two aspects including communication topology and the state of agents. Two-hop network is considered in the communication topology. A novel consensus protocol that includes the information of the states motions and their integrals is introduced. And the protocol has much faster convergence speed by choosing some appropriate weight values. The protocol can be applied to distributed control and large-scale systems. A numerical example is presented to illustrate the effectiveness and superiority of the proposed method.

1. Introduction

Consensus problems for networked multiagent systems (MASs) [1–4] attracted lots of researchers in the last decades, due to their broad applications in many areas such as swarms, flock [5], and multivehicle systems. Some researchers began investigating distributed algorithms for MASs in the early 1990s. A group of simulated robots forms approximations to circles [1]. And different networks are discussed, such as time delay network [3, 6], singular network, neural network [7], and random network [8, 9]. Jadbabaie et al. [10] first present the model of MASs. Vicsek et al. [11] propose the way of agents communication whose information is obtained on the average of their neighbors. The original algorithms of MASs are studied by Olfati-Saber and Murray [12]; they also found the convergence speed is related to algebraic correlation, and some works about connected digraph are mentioned [13]. When creating a MASs network or using a MASs network, some other problems must be solved, such as stabilization, packet dropouts [4, 14], finite-time consensus [15], time delay, quantization, and estimation [2, 16, 17].

As we know, when network is given, the MASs consensus depends on the protocol. Different protocols have been proposed for various systems. Lin et al. [18] design the loop chase algorithm to make the system get final convergence. As the topology is varied, Jadbabaie et al. [10] consider switch topology to fit varied topology. Now the switch network extends to the random network. Using Markov tools, You [19, 20] considers the consensus of the random network which includes continuous and discrete system. Li et al. think about the control protocol of MASs which contain more than one leader [21]. Their main idea is distributed control [22]. Yu et al. study the delay network. They find that if current and delay states of agents are given, system can get final convergence [23].

For improving the convergence speed, fast convergence algorithm is obtained under small world network [24]. Xiao and Boyd [25] consider protocol design as optimization problem; they improve the convergence speed through changing the edge value of topology. However, when the edge value changes, the hardware equipment also changes. Jin and Murray [26] figure it out through changing the way of information transmission. Their main idea is that agents can get not only the information of their neighbors but also the information connecting to these neighbors. And another way to improve convergence speed was proposed [27]; they present a fast convergence algorithm based on PI controller. Through the PI controller, system can get consensus in a tolerant range.

Can we design a protocol to make convergence speed much faster? Motivated by existing results, a protocol combining the idea about two-hop network with PI controller is proposed in this paper. Two-hop network deals with the information between agents. And PI controller manages every state of agents. With the two advantages, system will converge much faster. Using this protocol, we do not need to change any hardware equipment; just the algorithm makes the convergence situation better. In this paper, consensus analysis is integrated within a formal framework of graph theory, matrix [28, 29], and stability criterion.

This paper is organized as follows. Section 2 raises the question and gives some fundamental issues of MASs. Section 3 illustrates the main results of consensus analysis for first-order and second-order system. Necessary and sufficient conditions for the convergence of the agent's states to a tolerant range value are presented. A numerical example is given in Section 4. The main conclusions are summarized at last.

Notation. The notations are standard. We use a directed graph $G = (V, \varepsilon, A)$ to represent the interaction topology where V is a set of vertices and $\varepsilon \subseteq V^2$ is a set of edges. Each edge of the graph is denoted by (v_i, v_j) and represents that agent v_i has access to the state of agent v_j. A represents adjacent matrix. The set of neighbors of vertex v_i is denoted by $N(v_i) = \{v_j \in V : (v_i, v_j) \in \varepsilon\}$. L represents Laplace matrix. $\widetilde{\varepsilon}$ represents the state of two-hop agent. In this paper, all the topology structures are concerned with undirected graphs.

2. Preliminaries and Problem Formulation

For systems modeled by

$$\dot{x}_i = u_i, \quad i = 1, 2, \ldots, N, \tag{1}$$

common protocol is described as

$$u_i(t) = \sum_{j \in N_i} a_{ij} \left(x_j(t) - x_i(t) \right), \quad t \geq 0, \ i = 1, 2, \ldots, N, \tag{2}$$

where a_{ij} is weight of agents' communication. When $\lim_{t \to \infty} \| (x_j(t) - x_i(t)) \| = 0$, system approaches consensus. The necessary and sufficient conditions of consensus of system (1) with protocol (2) are presented [30].

For a multiagent system, two-hop network can make convergence speed become much faster [26]. Agents in two-hop network not only get their neighbors' information but also the information by their neighbors. The main idea is that if agents get more information, then system converges much faster. The protocol [26] is

$$u_i(t) = -\sum_{j \in N_i} a_{ij} \left\{ x_i(t) - x_j(t) + \sum_{k \in N_j} a_{ij} \left(x_i(t) - x_k(t) \right) \right\}, \quad t \geq 0, \quad i = 1, 2, \ldots, N. \tag{3}$$

Equation (3) can be simplified to

$$\dot{x} = -Lx - \widetilde{L}x, \tag{4}$$

where $u_i(t)$ is control input and x is variable of agents state, $x = [x_1, x_2, \ldots, x_n]^T$. Laplacian matrix of MASs is donated by L; $\widetilde{L}$ is Laplacian matrix of adjacent matrix $\widetilde{A}$. $\widetilde{A}$ is described as

$$\widetilde{a}_{ik} = \begin{cases} \sum_{j \in V} a_{ij} a_{jk}, & (v_i, v_k) \in \widetilde{\varepsilon}; \\ 0, & \text{other}. \end{cases} \tag{5}$$

Two-hop network has the information of neighbors and passed neighbors. If the network only contains two nodes, then protocol (3) will degenerate to protocol (2).

Except two-hop network, fast control algorithm based on PI controller also can improve convergence speed [27]; the protocol is

$$u_i(t) = \sum_{j \in N_i} a_{ij} \frac{1}{\theta} \left(\int_{-\theta} x_j(t)\, dt - \int_{-\theta} x_i(t)\, dt \right), \quad t \geq 0, \quad i = 1, 2, \ldots, N. \tag{6}$$

θ represents integral time span which is always the same in this paper. Fast convergence algorithm focuses on state of agents and deals with average value of integral time span. The algorithm can improve dynamic property and convergence speed.

For improving convergence speed, the two methods mentioned above deal with two different aspects of MASs. Two-hop network improves information communication of network topology, and fast convergence algorithm changes agents' state. Combining the advantages of these two methods in this paper, a new protocol to make the convergence speed much faster is proposed. The control protocol is

$$\begin{aligned} \overline{u}_i(t) = {} & \alpha u_i(t) \\ & - \beta \sum_{j \in N_i} a_{ij} \left\{ \frac{1}{\theta} \left(\int_{-\theta} x_i(t)\, dt - \int_{-\theta} x_j(t)\, dt \right) \right. \\ & + \sum_{j \in N_j} a_{jk} \frac{1}{\theta} \\ & \left. \cdot \left(\int_{-\theta} x_i(t)\, dt - \int_{-\theta} x_j(t)\, dt \right) \right\}, \\ & t \geq 0, \quad i = 1, 2, \ldots, N, \end{aligned} \tag{7}$$

where $u_i(t)$ is control protocol described in (3), α represents weight value of $u_i(t)$, β represents weight value of integral gain, and θ represents integral time span. Now, first-order model and second-order model will be discussed for the convergence speed in Section 3.

3. Main Results

3.1. First-Order Model. The first-order model can be described as (1). Under two-hop network, (7) can be simplified to

$$\overline{u} = \alpha u - \beta L \frac{1}{\theta} \int_{-\theta} x\, dt - \beta \widetilde{L} \frac{1}{\theta} \int_{-\theta} x\, dt. \tag{8}$$

Theorem 1. *Consider MASs (1) with n agents; if topology is connected and undirected, then network systems which are under protocol (8) will converge if and only if* $\theta < \pi^2/2\beta(\lambda+\widetilde{\lambda})$, *where* $(\lambda + \widetilde{\lambda})$ *represents maximum eigenvalue of Laplacian matrix* $(L + \widetilde{L})$.

Proof. Control protocol u described in (1) can get consensus under two-hop network [26], so we just need to prove

$$\widehat{u} = -\beta L \frac{1}{\theta} \int_{-\theta} x\, dt - \beta \widetilde{L} \frac{1}{\theta} \int_{-\theta} x\, dt. \tag{9}$$

Using protocol (9) into first-order model (1), we can get

$$\dot{x} = -\beta L \frac{1}{\theta} \int_{-\theta} x\, dt - \beta \widetilde{L} \frac{1}{\theta} \int_{-\theta} x\, dt. \tag{10}$$

By Laplace transform it becomes

$$sx - x(0) = -\frac{1}{s\theta} \beta \left(L + \widetilde{L}\right) \left(x - e^{-s\theta} x\right), \tag{11}$$

where $x(0)$ is initial value and the closed-loop poles satisfy

$$\det\left[sI + \frac{1}{s\theta} \beta \left(L + \widetilde{L}\right) \left(1 - e^{-s\theta}\right)\right] = 0. \tag{12}$$

Because $(L + \widetilde{L})$ is Laplace matrix and G is connected and undirected graph, one of the poles is $s = 0$; then we have

$$s \prod_{i=2}^{n} \left\{sI + \frac{1}{s\theta} \beta \left(L + \widetilde{L}\right) \left(1 - e^{-s\theta}\right)\right\} = 0, \quad i = 1, 2, \ldots, n. \tag{13}$$

When $s \neq 0$, we have

$$1 + \frac{1}{s\theta} \beta \left(\lambda_i + \widetilde{\lambda}_i\right) \left(1 - e^{-s\theta}\right) = 0. \tag{14}$$

Because $(\lambda_i + \widetilde{\lambda}_i) \geq 0$ and $s \leq 0$, its open loop frequency characteristic is as follows:

$$\begin{gathered} G(jw) H(jw) = -\frac{1}{w^2\theta} \beta \left(\lambda_i + \widetilde{\lambda}_i\right) \left(1 - e^{-jw\theta}\right), \\ G\left|(jw) H(jw)\right| = -\frac{2}{w^2\theta} \beta \left(\lambda_i + \widetilde{\lambda}_i\right) \left|\sin \frac{w\theta}{2}\right|, \\ \arg\left(G(jw) H(jw)\right) = -\frac{\pi}{2} - \frac{w\theta}{2}. \end{gathered} \tag{15}$$

Now, amplitude-frequency characteristic and phase-frequency characteristics are both diminishing. According to Nyquist criterion, when phase angle first arrives to $-\pi$, $G|(jw)H(jw)|$ in the range of $[-1, 0]$, system is stable. Consider

$$\begin{gathered} w = \frac{\pi}{\theta}, \\ G\left|(jw) H(jw)\right|_{w=\pi/\theta} = \left|\frac{2\beta\theta\left(\lambda + \widetilde{\lambda}\right)}{\pi^2}\right| < 1, \\ \theta < \frac{\pi^2}{2\beta\left(\lambda + \widetilde{\lambda}\right)}, \end{gathered} \tag{16}$$

where $(\lambda + \widetilde{\lambda})$ represents maximum eigenvalue of Laplacian matrix $(L + \widetilde{L})$. □

Lemma 2 (see [28]). *G is an undirected graph; if G is a connected graph, then the eigenvalues are* $0 = \lambda_1 < \lambda_2 \leq \lambda_3 \cdots \leq \lambda_n$; λ_1 *equals 0; convergence speed is determined by the second minimum eigenvalue* λ_2; *if* λ_2 *becomes bigger, then system converges faster.*

Theorem 3. *Multiagent system (1) under fast convergence algorithm (8), when it is with two-hop network, the convergence speed will become faster if and only if system and protocol have the same parameters and conditions in Theorem 1.*

Proof. Consensus algorithm (6) can be simplified to

$$u(t) = -L \frac{1}{\theta} \int_{-\theta} x\, dt. \tag{17}$$

The eigenvalues of Laplacian matrix L are $0 = \lambda_1 < \lambda_2 \leq \lambda_3 \cdots \leq \lambda_n$. When system merges with two-hop network, it can be described as

$$u(t) = -\beta \left(L + \widetilde{L}\right) \frac{1}{\theta} \int_{-\theta} x\, dt. \tag{18}$$

Eigenvalues of Laplacian matrix $(L + \widetilde{L})$ are $0 = \lambda_1 + \widetilde{\lambda}_1 < \lambda_2 + \widetilde{\lambda}_2 \leq \lambda_3 + \widetilde{\lambda}_3 \cdots \leq \lambda_n + \widetilde{\lambda}_n$. According to Lemma 2, two-hop network combined with fast convergence algorithm will improve convergence speed. The proof is thus completed. □

If we choose an appropriate weight value in protocol (8) for α and β, then convergence speed will be satisfied.

3.2. Second-Order Model. The second-order model can be described as

$$\begin{gathered} \dot{m}_i = x_i, \\ \dot{x}_i = u_i, \end{gathered} \tag{19}$$

where m, x are variables of state and u is controller's input. As a second-order model system, every agent has two states. Its common protocol is

$$\begin{gathered} u_i(t) = -\sum_{j \in N} a_{ij} \left\{\beta \left(m_i(t) - m_j(t)\right) + x_i(t) - x_j(t)\right\}, \\ t \geq 0, \quad i = 1, 2, \ldots, N. \end{gathered} \tag{20}$$

In this paper, the protocol combines the fast convergence algorithm with two-hop network, which can be described as

$$\begin{aligned} u_i(t) = {} & -rx_i(t) \\ & - \sum_{j\in N} a_{ij} \Big\{ \beta \left(\widehat{m}_i(t) - \widehat{m}_j(t) \right) \\ & + \beta \sum_{k\in N} w_{jk} \left(\widehat{m}_i(t) - \widehat{m}_k(t) \right) \\ & + \widehat{x}_i(t) - \widehat{x}_j(t) \\ & + \sum_{k\in N} w_{jk} \left(\widehat{x}_i(t) - \widehat{x}_j(t) \right) \Big\}, \\ & t \geq 0, \end{aligned} \tag{21}$$

$$\widehat{m}_i(t) = \frac{1}{\theta} \int_{-\theta} m_i(t)\, dt, \qquad \widehat{m}_j(t) = \frac{1}{\theta} \int_{-\theta} m_j(t)\, dt,$$

$$\widehat{x}_i(t) = \frac{1}{\theta} \int_{-\theta} x_i(t)\, dt, \qquad \widehat{x}_j(t) = \frac{1}{\theta} \int_{-\theta} x_j(t)\, dt,$$

where β and r are weight values and θ is integrating range. It can be simplified to

$$\begin{aligned} u = {} & -rx - \beta L \frac{1}{\theta} \int_{-\theta} m\, dt - \beta \widetilde{L} \frac{1}{\theta} \int_{-\theta} m\, dt \\ & - L \frac{1}{\theta} \int_{-\theta} x\, dt, \quad -\widetilde{L} \frac{1}{\theta} \int_{-\theta} x\, dt. \end{aligned} \tag{22}$$

Theorem 4. *Consider MASs (19) with n agents; if the communication topology is connected and undirected, then network systems which are under protocol (22) will achieve consensus if and only if $\theta < \pi^2/2(\lambda + \widetilde{\lambda})$, where $(\lambda + \widetilde{\lambda})$ represents maximum eigenvalue of Laplacian matrix $(L + \widetilde{L})$.*

Proof. Put control protocol (22) into system (19):

$$\begin{aligned} \ddot{m} = {} & -r\dot{m} - \beta L \frac{1}{\theta} \int_{-\theta} m\, dt - \beta \widetilde{L} \frac{1}{\theta} \int_{-\theta} m\, dt \\ & - L \frac{1}{\theta} \int_{-\theta} \dot{m}\, dt, \quad -\widetilde{L} \frac{1}{\theta} \int_{-\theta} \dot{m}\, dt. \end{aligned} \tag{23}$$

By Laplace transform,

$$\begin{aligned} ms^2 = {} & -\beta ms - \beta \frac{1}{s\theta} \left(L + \widetilde{L} \right) \left(m - e^{-s\theta} m \right) \\ & - s \frac{1}{s\theta} \left(L + \widetilde{L} \right) \left(m - e^{-s\theta} m \right). \end{aligned} \tag{24}$$

Then, the closed-loop poles satisfy

$$\begin{aligned} & \det \Big[s^2 I + \beta s I + \beta \frac{1}{s\theta} \left(L + \widetilde{L} \right) \left(1 - e^{-s\theta} \right) \\ & \quad + s \frac{1}{s\theta} \left(L + \widetilde{L} \right) \left(1 - e^{-s\theta} \right) \Big] = 0, \\ & \det \left[(sI + \beta I) \left(sI + \frac{1 - e^{-s\theta}}{s\theta} \left(L + \widetilde{L} \right) \right) \right] = 0. \end{aligned} \tag{25}$$

Because $\beta > 0$,

$$\det \left[sI + \frac{1 - e^{-s\theta}}{s\theta} \left(L + \widetilde{L} \right) \right] = 0. \tag{26}$$

Comparing (26) and (12), their constructions are similar. So we can get the same result: when $\theta < \pi^2/2(\lambda + \widetilde{\lambda})$, systems converge. $(\lambda + \widetilde{\lambda})$ represents maximum eigenvalue of Laplacian matrix $(L + \widetilde{L})$. The proof is thus completed. □

Theorem 5. *The second-order multiagent system (19) under fast convergence algorithm (22), when it combines with two-hop network, the convergence speed will become faster if and only if system and protocol have the same parameters and conditions in Theorem 4.*

Proof. Consensus algorithm is

$$\begin{aligned} u_i(t) = {} & -rx_i(t) \\ & - \sum_{j\in N} a_{ij} \Big\{ \beta \frac{1}{\theta} \left(\int_{-\theta} m_j(t)\, dt - \int_{-\theta} m_i(t)\, dt \right) \\ & + \frac{1}{\theta} \left(\int_{-\theta} x_j(t)\, dt - \int_{-\theta} x_i(t)\, dt \right) \Big\}. \end{aligned} \tag{27}$$

It can be simplified to

$$u = -rx - \beta L \frac{1}{\theta} \int_{-\theta} m\, dt - L \frac{1}{\theta} \int_{-\theta} x\, dt. \tag{28}$$

Eigenvalues of Laplacian matrix L are $0 = \lambda_1 < \lambda_2 \leq \lambda_3 \cdots \leq \lambda_n$. When merging with two-hop network, protocol is described as

$$u = -rx - \beta \left(L + \widetilde{L} \right) \frac{1}{\theta} \int_{-\theta} m\, dt - \left(L + \widetilde{L} \right) \frac{1}{\theta} \int_{-\theta} x\, dt. \tag{29}$$

Eigenvalues of Laplacian matrix $(L + \widetilde{L})$ are $0 = \lambda_1 + \widetilde{\lambda}_1 < \lambda_2 + \widetilde{\lambda}_2 \leq \lambda_3 + \widetilde{\lambda}_3 \cdots \leq \lambda_n + \widetilde{\lambda}_n$. Except topology, each item is same between (28) and (29), and laplace matrix eigenvalues of topology (29) are bigger than (28). So the system combining the fast convergence algorithm with two-hop network will converge faster. Proof over. □

If we choose an appropriate weight value in protocol (22) for r and β, then convergence speed will be satisfied. We can adjust parameters r and β like a PI controller, regard r as proportion parameter, and regard β as integration parameter.

4. Numerical Simulation

Consider a multiagent system with 4 agents; all agents are first-order model with state x_1, x_2, x_3, x_4. The initial value is $x = [1; 2; -1; -2]$; Figure 1 shows the network topology.

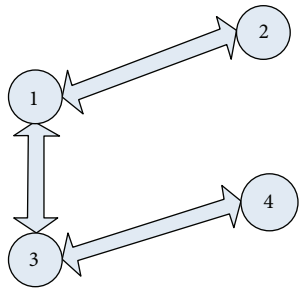

Figure 1: Digraph topology with 4 agents.

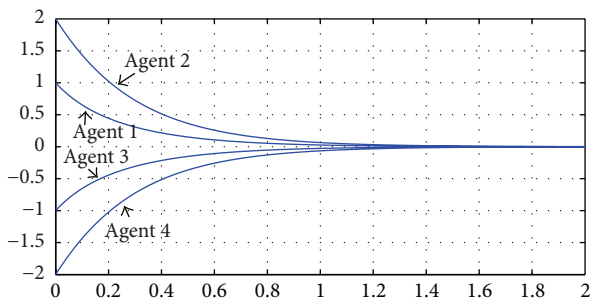

Figure 2: System state curves without fast convergence algorithm and two-hop network protocol.

Network topology is undirected graph; the weight value between every edge is 0.5; then we get laplace matrix L and $\widetilde{L}$:

$$L = \frac{1}{2}\begin{pmatrix} -2 & 1 & 1 & 0 \\ 1 & -1 & 0 & 0 \\ 1 & 0 & -2 & 1 \\ 0 & 0 & 1 & -1 \end{pmatrix},$$
$$\widetilde{L} = \frac{1}{4}\begin{pmatrix} -2 & 1 & 1 & 0 \\ 1 & -1 & 0 & 0 \\ 1 & 0 & -2 & 1 \\ 0 & 0 & 1 & -1 \end{pmatrix}. \tag{30}$$

First, simulation result without fast convergence algorithm and two-hop network protocol is shown in Figure 2.

System without fast convergence algorithm and two-hop network protocol converges around 1.40 s.

Secondly, simulation result with fast convergence algorithm without two-hop network protocol is shown in Figure 3.

System with fast convergence algorithm without two-hop network protocol converges around 1.18 s.

Then, simulation result with fast convergence algorithm and two-hop network protocol is shown in Figure 4 ($\alpha = 7$, $\beta = 0.3$).

System with fast convergence algorithm and two-hop network protocol converges around 0.58 s.

Finally, simulation result with same protocol but different parameter is shown in Figure 5 ($\alpha = 7$, $\beta = 100$).

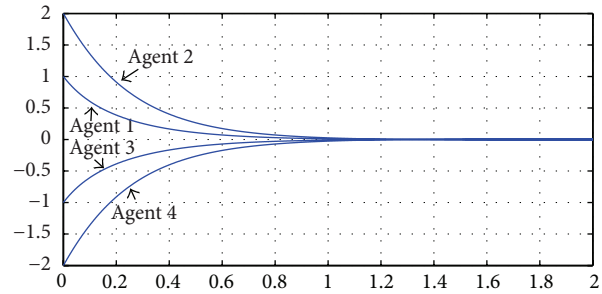

Figure 3: System state curves with fast convergence algorithm without two-hop network protocol.

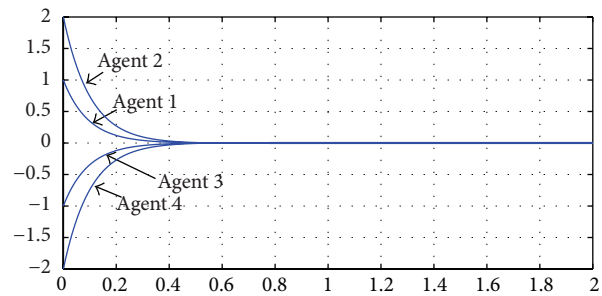

Figure 4: System state curves with fast convergence algorithm and two-hop network protocol $\beta = 0.3$.

System with same protocol but different parameter will have different consensus performance. In Figure 5 too big parameter β gets oscillating curve.

Remark 6. Based on the simulation results showed in Figures 2–4, state curves with fast convergence and two-hop network converge around 0.58 s and are better than others. So we can conclude that the proposed algorithm can achieve a much faster convergence speed. The protocol combining fast convergence algorithm with two-hop network protocol is effective. And this paper just improves the protocol. Through this protocol, we do not need to change the hardware equipment; just the protocol makes the performance of system better.

5. Conclusion

This paper studies consensus convergence speed of MASs. A control protocol is designed to make system consensus convergence speed much faster. The protocol combines the method of information communication in topology with states of every agent. The necessary and sufficient conditions are obtained based on graph theory and stability theorem. Nevertheless, only first-order model and second-order model are discussed. The protocol cannot be applied to the high order model or multihop network. So the future works will focus on the high order model and multihop network.

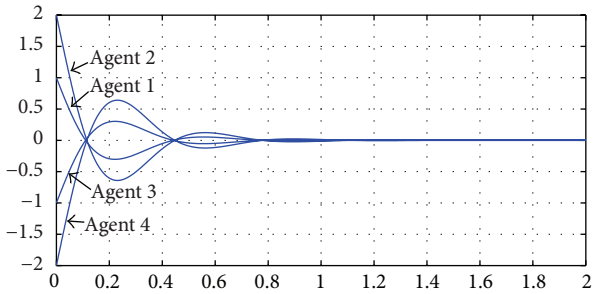

Figure 5: System state curves with fast convergence algorithm and two-hop network protocol $\beta = 100$.

Conflict of Interests

The authors declare that there is no conflict of interests regarding the publication of this paper.

Acknowledgments

This work is supported by National Natural Science Foundation of China under Grant nos. 61374083, 61305135, and 61203177, Science and Technology Department Project of Zhejiang Province under Grant no. 2014C31082, and Natural Science Foundation of Zhejiang Province under Grant no. LQ14F030013, and 521 Talent Project of Zhejiang Sci-Tech University.

References

[1] K. Sugihara and I. Suzuki, "Distributed motion coordination of multiple mobile robots," in *Proceedings of the 5th IEEE International Symposium on Intelligent Control*, vol. 1, pp. 138–143, IEEE, Philadelphia, Pa, USA, September 1990.

[2] D. E. Marelli and M. Fu, "Distributed weighted least-squares estimation with fast convergence for large-scale systems," *Automatica*, vol. 51, no. 1, pp. 27–39, 2015.

[3] D. Zhang, W. Cai, and Q.-G. Wang, "Robust non-fragile filtering for networked systems with distributed variable delays," *Journal of the Franklin Institute*, vol. 351, no. 7, pp. 4009–4022, 2014.

[4] D. Zhang, L. Yu, H. Song, and Q.-G. Wang, "Distributed H_∞ filtering for sensor networks with switching topology," *International Journal of Systems Science*, vol. 44, no. 11, pp. 2104–2118, 2013.

[5] J. A. Fax and R. M. Murray, "Information flow and cooperative control of vehicle formations," *IEEE Transactions on Automatic Control*, vol. 49, no. 9, pp. 1465–1476, 2004.

[6] Y. Chen and W. X. Zheng, "Stability analysis of time-delay neural networks subject to stochastic perturbations," *IEEE Transactions on Cybernetics*, vol. 43, no. 6, pp. 2122–2134, 2013.

[7] Y. Chen and W. X. Zheng, "Stability and L2 performance analysis of stochastic delayed neural networks," *IEEE Transactions on Neural Networks*, vol. 22, no. 10, pp. 1662–1668, 2011.

[8] Z.-G. Wu, P. Shi, H. Su, and J. Chu, "Passivity analysis for discrete-time stochastic markovian jump neural networks with mixed time delays," *IEEE Transactions on Neural Networks*, vol. 22, no. 10, pp. 1566–1575, 2011.

[9] Z.-G. Wu, P. Shi, H. Su, and J. Chu, "Stochastic synchronization of markovian jump neural networks with time-varying delay using sampled data," *IEEE Transactions on Cybernetics*, vol. 43, no. 6, pp. 1796–1806, 2013.

[10] A. Jadbabaie, J. Lin, and A. S. Morse, "Coordination of groups of mobile autonomous agents using nearest neighbor rules," *IEEE Transactions on Automatic Control*, vol. 48, no. 6, pp. 988–1001, 2003.

[11] T. Vicsek, A. Czirók, E. Ben-Jacob, I. Cohen, and O. Shochet, "Novel type of phase transition in a system of self-driven particles," *Physical Review Letters*, vol. 75, no. 6, pp. 1226–1229, 1995.

[12] R. Olfati-Saber and R. M. Murray, "Consensus problems in networks of agents with switching topology and time-delays," *IEEE Transactions on Automatic Control*, vol. 49, no. 9, pp. 1520–1533, 2004.

[13] W. Ren and R. W. Beard, "Consensus seeking in multiagent systems under dynamically changing interaction topologies," *IEEE Transactions on Automatic Control*, vol. 50, no. 5, pp. 655–661, 2005.

[14] Y. Xu, H. Su, and Y.-J. Pan, "Output feedback stabilization for Markov-based nonuniformly sampled-data networked control systems," *Systems and Control Letters*, vol. 62, no. 8, pp. 656–663, 2013.

[15] S. H. Yu and X. J. Long, "Finite-time consensus for second-order multi-agent systems with disturbances by integral sliding mode," *Automatica*, vol. 54, pp. 158–165, 2015.

[16] R. Lu, Y. Xu, A. Xue, and J. Zheng, "Networked control with state reset and quantized measurements: observer-based case," *IEEE Transactions on Industrial Electronics*, vol. 60, no. 11, pp. 5206–5213, 2013.

[17] R. Lu, Z. Li, C.-Y. Su, and A. Xue, "Development and learning control of a human limb with a rehabilitation exoskeleton," *IEEE Transactions on Industrial Electronics*, vol. 61, no. 7, pp. 3776–3785, 2014.

[18] Z. Lin, M. Broucke, and B. Francis, "Local control strategies for groups of mobile autonomous agents," *IEEE Transactions on Automatic Control*, vol. 49, no. 4, pp. 622–629, 2004.

[19] K. You, Z. Li, and L. Xie, "Consensus for general multi-agent systems over random graphs," in *Proceedings of the 9th IEEE International Conference on Control and Automation (ICCA '11)*, pp. 830–835, IEEE, December 2011.

[20] K. You, Z. Li, and L. Xie, "Consensus condition for linear multi-agent systems over randomly switching topologies," *Automatica*, vol. 49, no. 10, pp. 3125–3132, 2013.

[21] Z. Li, Z. Duan, W. Ren, and G. Feng, "Containment control of linear multi-agent systems with multiple leaders of bounded inputs using distributed continuous controllers," *International Journal of Robust and Nonlinear Control*, 2014.

[22] M. P. Fanti, A. M. Mangini, F. Mazzia, and W. Ukovich, "A new class of consensus protocols for agent networks with discrete time dynamics," *Automatica*, vol. 54, pp. 1–7, 2015.

[23] W. Yu, G. Chen, M. Cao, and W. Ren, "Delay-induced consensus and quasi-consensus in multi-agent dynamical systems," *IEEE Transactions on Circuits and Systems*, vol. 60, no. 10, pp. 2679–2687, 2013.

[24] R. Olfati-Saber, "Ultrafast consensus in small-world networks," in *Proceedings of the American Control Conference (ACC '05)*, pp. 2371–2378, IEEE, Portland, Ore, USA, June 2005.

[25] L. Xiao and S. Boyd, "Fast linear iterations for distributed averaging," *Systems & Control Letters*, vol. 53, no. 1, pp. 65–78, 2004.

[26] Z. Jin and R. M. Murray, "Multi-hop relay protocols for fast consensus seeking," in *Proceedings of the 45th IEEE Conference on Decision and Control (CDC '06)*, pp. 1001–1006, San Diego, Calif, USA, December 2006.

[27] Y. Yu, *Research on several problems of consensus in multi-agent systems [Ph.D. thesis]*, Huazhong University of Science and Technology, Wuhan, China, 2010.

[28] R. Horn and C. Johnson, *Matrix Analysis*, Cambridge University Press, Cambridge, UK, 1985.

[29] B. Mohar and Y. Alavi, "The laplacian spectrum of graphs," in *Graph Theory, Combinatorics and Application*, vol. 2, pp. 871–898, 1991.

[30] Y. Liu and K. M. Passino, "Cohesive behaviors of multiagent systems with information flow constraints," *IEEE Transactions on Automatic Control*, vol. 51, no. 11, pp. 1734–1748, 2006.

Hindawi Publishing Corporation
Mathematical Problems in Engineering
Volume 2015, Article ID 535932, 9 pages
http://dx.doi.org/10.1155/2015/535932

Research Article

K-Nearest Neighbor Intervals Based AP Clustering Algorithm for Large Incomplete Data

Cheng Lu,[1,2] Shiji Song,[1] and Cheng Wu[1]

[1] *Department of Automation, Tsinghua University, Beijing 100084, China*
[2] *Army Aviation Institute, Beijing 101123, China*

Correspondence should be addressed to Shiji Song; shijis@mail.tsinghua.edu.cn

Received 15 January 2015; Accepted 2 March 2015

Academic Editor: Hui Zhang

Copyright © 2015 Cheng Lu et al. This is an open access article distributed under the Creative Commons Attribution License, which permits unrestricted use, distribution, and reproduction in any medium, provided the original work is properly cited.

The Affinity Propagation (AP) algorithm is an effective algorithm for clustering analysis, but it can not be directly applicable to the case of incomplete data. In view of the prevalence of missing data and the uncertainty of missing attributes, we put forward a modified AP clustering algorithm based on K-nearest neighbor intervals (KNNI) for incomplete data. Based on an Improved Partial Data Strategy, the proposed algorithm estimates the KNNI representation of missing attributes by using the attribute distribution information of the available data. The similarity function can be changed by dealing with the interval data. Then the improved AP algorithm can be applicable to the case of incomplete data. Experiments on several UCI datasets show that the proposed algorithm achieves impressive clustering results.

1. Introduction

With the developments of sensors and database technology, people get more focus on the Big Data issue [1]. But too often the data is difficult to analyze. Cluster analysis is one of the common methods for analyzing data, which is to partition a set of objects into different groups, so that the data in each cluster share some common traits. Affinity Propagation (AP) is a relatively new clustering algorithm that has been introduced by Frey and Dueck [2], which can handle large datasets in a relatively short period to obtain more satisfactory results. AP algorithm has superiority over other clustering algorithms in terms of processing efficiency and quality of clustering, and AP algorithm does not require the prespecified number of clusters and the initial cluster centers. Thus, AP algorithm has attracted the attention of many scholars, and various improvements have emerged [3–5].

As a common and effective clustering algorithm, the original AP clustering algorithm is only applicable to complete data like other traditional clustering algorithms. However, in practice, many datasets suffer from incompleteness due to various reasons, such as bad sensors, mechanical failures to collect data, illegible images due to low pixels and noises, and unanswered questions in surveys. Therefore, some strategies should be employed to make AP applicable to such incomplete datasets.

In the literature, several approaches to handle incomplete data have been proposed, including listwise deletion (LD), imputation, model-based method, and direct analysis [6]. There is a strong connection between these methods on the concrete implementation algorithm. LD ignores those samples with missing values, which may lose a lot of sample information. Imputation and model-based method are usually based on the assumption that data attributes are missing at random. They substitute the missing values with appropriate estimates and construct a complete dataset. However, it is inefficient to perform imputation, and they usually lead to results far from satisfactory. For incomplete data, many methods have been proposed to reduce the impact of the presence of the missing values on the clustering performance in pattern recognition. An important empirically oriented study was done by Dixon [7]. The expectation-maximization (EM) algorithm [8] is a commonly used iterative algorithm based on maximum likelihood estimation in missing data analysis. Neither statistical methods nor machine learning method for dealing with missing data meets the actual needs of current. Various

methods for handling missing data remain to be further optimized.

Though incomplete data appears everywhere, principled clustering methods for such data still deserve further research. The existing research on improved methods for clustering model is mainly concentrated on the fuzzy C-means clustering (FCM) algorithm (Bezdek, 1981) [9]. In 1998, imputation and discarding/ignoring were proposed by Miyamoto et al. [10] for handling missing values in FCM. In 2001, Hathaway and Bezdek proposed four strategies to improve the FCM clustering of incomplete data and proved the convergence of the algorithms [11]. These strategies are whole data strategy (WDS), partial distance strategy (PDS), optimal completion strategy (OCS), and nearest prototype strategy (NPS). In addition, Hathaway and Bezdek used triangle inequality-based approximation schemes (NERFCM) to cluster incomplete relational data [12]. Li et al. [13] put forward a FCM algorithm based on the nearest neighbor intervals and solved the case of incomplete data. Zhang and Chen [14] introduced a kernel method into the standard FCM algorithm.

However, FCM algorithms are sensitive to the initial centers, which makes the clustering results unstable. In particular when some data are missing, the selection of the initial cluster centers becomes more important. To address this issue, we consider the AP algorithm, which does not require initial cluster centers and the number of clusters. Three strategies for solving AP clustering of incomplete datasets had been proposed in our previous research [15]. These strategies were simple and easy to implement which directly deal with incomplete dataset using AP algorithm. However, the effect of dataset information on missing attributes had not been studied, by which clustering quality would be affected. In this paper, based on Improved Partial Data Strategy (IPDS), a modified AP algorithm for incomplete data based on K-nearest neighbor intervals (KNNI-AP) is proposed. First, missing attributes are represented by KNNI on the basis of IPDS, which are robust. Second, the clustering problems are transformed into clustering problems with interval-valued data, which may provide more accurate clustering results. Third, AP algorithm simultaneously considers all data points as potential centers, which makes the clustering results more stable and accurate.

The remainder of this paper is organized as follows. Section 2 presents a description of AP algorithm and AP clustering algorithm for interval-valued data (IAP) based on clustering objective function minimization. The KNNI representation of missing attributes and the novel KNNI-AP algorithm are introduced in Section 3. Section 4 presents clustering results of several UCI datasets and a comparative study of our proposed algorithm with KNNI-FCM and other methods for handling missing values using AP. We conclude this work and discuss the future work in Section 5.

2. AP Clustering Algorithm for Interval-Valued Data

2.1. AP Clustering Algorithm. AP algorithm and K-means algorithm have similar objective function, but the AP algorithm simultaneously considers all data points as the potential centers.

Let a complete dataset $X = \{x_1, x_2, \ldots, x_N\}$, where $x_i \in \mathbb{R}$. The goal of AP is to find an optimal exemplar set $X_C = \{x_{c1}, x_{c2}, \ldots, x_{ck}\}$, $(1 < k < N)$, by minimizing the clustering error function:

$$J(C) = \sum_{i=1}^{N} d^2\left(x_i, C\left(x_i\right)\right), \tag{1}$$

where $C(x_i)$ represents the exemplar for given x_i. Each data point only corresponds to a cluster, and each exemplar is an actual data point which is the center of the cluster.

First, AP algorithm takes each data point as the candidate exemplar and calculates the attractiveness information between sample points, that is, the similarity between any two sample points. The similarity can be set according to specific applications; similarity measurement mainly includes similarity coefficient function and distance function. Common distance functions are Euclidean distance, Manhattan distance, and Mahalanobis distance. In the traditional clustering problem, similarity is usually set as the negative of squared Euclidean distance:

$$s(i, j) = -d^2\left(x_i, x_j\right) = -\left\|x_i - x_j\right\|_2^2, \quad i \neq j, \tag{2}$$

where $s(i, j)$ is stored in a similarity matrix, representing the suitability that the sample x_i is the exemplar of the sample x_j. $s(i, i)$ is set for each sample, called "preference." The greater the value is, the more possible the corresponding point is selected as the exemplar. Because all samples are equally suitable as centers, the preferences should be set as a common value P. The number of identified exemplars is influenced by P, which can be changeable for different numbers of clusters. Frey and Dueck [2] suggested preference is the median of the input similarities (resulting in a moderate number of clusters) or their minimum (resulting in a small number of clusters). We also employ [5] to measure the preference values to get more accurate clustering results.

To select appropriate clustering centers, AP algorithm searches for two different pieces of information: responsibility ($r(i, j)$) and availability ($a(i, j)$). $r(i, j)$ sent from sample i to sample j reflects how well-suited sample j is to be served as the cluster center for sample i. $a(i, j)$ sent from sample j to sample i reflects how appropriate for sample i to choose sample j as its exemplar. The message-passing procedure terminates after a fixed number of iterations or the changes in the messages fall below a threshold.

2.2. AP Clustering Algorithm for Interval-Valued Data (IAP). AP algorithm should be adjusted to deal with interval data. Let an M-dimensional interval-valued dataset $\overline{X} = \{\overline{x_1}, \overline{x_2}, \ldots, \overline{x_N}\}$, where the ith sample is expressed as $\overline{X_i} = \{\overline{x_{i1}}, \overline{x_{i2}}, \ldots, \overline{x_{iM}}\}$ and $\overline{x_{il}} = [x_{il}^-, x_{il}^+]$, $(1 \leq l \leq M)$. To find the optimal exemplar set $\overline{X_c} = \{\overline{x_{c1}}, \overline{x_{c2}}, \ldots, \overline{x_{ck}}\}$ $(1 < k < N)$, we minimize the following clustering error function:

$$J(C) = \sum_{i=1}^{N} d^2\left(\overline{x_i}, \overline{C(x_i)}\right), \tag{3}$$

where $\overline{C(x_i)}$ represents the exemplar for given $\overline{x_i}$. The similarity is changed as

$$s(i,j) = -d^2\left(\overline{x_i}, \overline{x_j}\right) = -\left\|\overline{x_i} - \overline{x_j}\right\|_2^2, \quad i \neq j. \tag{4}$$

The Euclidean distance can be defined as

$$\begin{aligned}\left\|\overline{x_i} - \overline{x_j}\right\|_2^2 = &\sum_{l=1}^{M}\left|x_{il}^{+} - x_{jl}^{+}\right|^2 + \sum_{l=1}^{M}\left|x_{il}^{-} - x_{jl}^{-}\right|^2 \\ &+ \sum_{l=1}^{M}\left[\frac{\left|x_{il}^{+} - x_{jl}^{+}\right| + \left|x_{il}^{-} - x_{jl}^{-}\right|}{2}\right]^2.\end{aligned} \tag{5}$$

Similarity matrix of $\overline{X}$ can be calculated accordingly. Then the two pieces of information are updated alternately, which are both zero in the initial stage, and the update process is given as follows:

$$\begin{aligned} r(i,j) &\longleftarrow s(i,j) - \max\left[a\left(i,j'\right) + s\left(i,j'\right)\right], \\ a(i,j) &\longleftarrow \begin{cases} \min\limits_{i \neq j}\left\{0, r(j,j) + \sum\limits_{i' \neq i, i' \neq j} \max\left[0, r\left(i',j\right)\right]\right\}, \\ \qquad\qquad i \neq j, \\ \sum\limits_{i' \neq j} \max\left[0, r\left(i',j\right)\right], \quad i = j. \end{cases}\end{aligned} \tag{6}$$

To avoid the numerical oscillation, the damping factor λ is introduced as follows:

$$\begin{aligned} R_i &= (1-\lambda) R_i + \lambda R_{i-1}, \\ A_i &= (1-\lambda) A_i + \lambda A_{i-1}. \end{aligned} \tag{7}$$

The procedure of IAP can be described as follows.

Input is the similarity matrix S and the preference P.

Output is the clustering result.

Step 1. Initialize responsibility ($r(i,j)$) and availability ($a(i,j)$) to zero: $r(i,j) = 0$; $a(i,j) = 0$.

Step 2. Update the responsibilities.

Step 3. Update the availabilities.

Step 4. Terminate the message-passing procedure after a fixed number of iterations or the changes in the messages fall below a threshold. Otherwise go to Step 2.

3. AP Algorithm for Incomplete Data Based on K-Nearest Neighbor Intervals (KNNI-AP)

3.1. K-Nearest Neighbor Intervals of Missing Attributes. As a common method to handle missing data, neighbor imputation has been widely used in many areas [16]. Imputation is the problem of approximating the value of a function for a nongiven point in some space when given the value of that function in points around (neighboring) that point. As a simple imputation, the nearest neighbor algorithm selects the nearest sample and does not consider the neighboring samples at all, which is easy to implement and is commonly used. An improved method is K-nearest neighbor imputation [17], where missing attributes are supplemented by the mean value of the attributes in the K-nearest neighbor values. Subsequently, García-Laencina et al. [18] proposed a K-nearest neighbor interpolation method based on weighted distance characteristics of multiple information. Huang and Zhu [19] introduced a pseudodistance neighbor interpolation method. All the approaches mentioned above developed imputation, which are unsuitable to represent the uncertainty of missing attributes completely.

To produce a robust estimation, K-nearest neighbor intervals (KNNI) of missing attributes are proposed. Let $X = \{x_1, x_2, \ldots, x_N\}$ be an M-dimensional incomplete dataset, which contains at least one incomplete sample with some (but not all) missing attribute values. For an incomplete $X_i = \{x_{i1}, x_{i2}, \ldots, x_{iM}\}$, the K-nearest neighbors should be found first.

On the basis of the Improved Partial Data Strategy (IPDS), the attribute information of both complete sample and incomplete sample (nonmissing attributes) can be fully used. The distance between sample A and sample B can be obtained as follows:

$$\left\|x_a - x_b\right\|_2 = \sqrt{\sum_{j=1}^{M} d_j\left(x_{aj}, x_{bj}\right)^2} \times \frac{M}{\omega}, \tag{8}$$

where

$$\begin{aligned} d_j\left(x_{aj}, x_{bj}\right) &= \begin{cases} 0, & \left(1 - m_{aj}\right)\left(1 - m_{bj}\right) = 0, \\ d_N\left(x_{aj}, x_{bj}\right), & \text{others}, \end{cases} \\ d_N\left(x_{aj}, x_{bj}\right) &= \frac{\left|x_{aj} - x_{bj}\right|}{\max\left(x_j\right) - \min\left(x_j\right)}, \\ m_{ij} &= \begin{cases} 1, & x_{ij} \text{ is missing}, \\ 0, & x_{ij} \text{ is not missing}, \end{cases} \end{aligned} \tag{9}$$

where $1 \leq j \leq M$, $1 \leq i \leq N$. $d_j(x_{aj}, x_{bj})$ represents the distance on the jth attribute between the two samples. ω is the feature dimension in which the two samples are both not missing, and M is the dimensions of all features. $\max(x_j)$ and $\min(x_j)$ are the maximum and minimum of the observation data when the missing attribute exists. m_{ij} is indicator function to explain whether the variable is missing.

According to the principle of the nearest neighbor approach, sample and its nearest neighbor share same or similar attributes. Therefore, for sample A, the ranges of missing attributes are basically between the minimum and maximum values of the corresponding attribute values of its K-nearest neighbors. Then the K-nearest neighbor interval of the sample can be determined, and the dataset can be converted into interval dataset. The missing attribute x_{aj} is represented by its corresponding K-nearest neighbor interval

$\overline{x_{aj}} = [x_{aj}^-, x_{aj}^+]$, and nonmissing attribute x_{cj} can also be rewritten into interval form $\overline{x_{cj}} = [x_{cj}^-, x_{cj}^+]$, where $x_{cj}^- = x_{cj}^+ = x_{cj}$. That is, the original values are unchanged. Then the interval dataset $\overline{X} = \{\overline{x_1}, \overline{x_2}, \ldots, \overline{x_N}\}$ is formed.

The selected K is critical to make the intervals represent the missing attributes effectively. If K is too small, the interval values may not express the missing attribute correctly, which likely leads to a biased estimation. In the extreme situation when K is 1, KNNI is degraded into NNI. However, if K is too large, the interval values also cannot correctly characterize the missing attribute values. In the extreme situation when K is as large as n (the number of samples in the dataset), the missing attribute interval is the range of all samples on the attribute, which is too large to represent the missing attribute properly. This will confuse the attribute characteristics among different clusters and result in unreasonable clustering results. K is not only related with the ratio of the missing attribute, but also related with the distribution of the sample and the relevant clusters. Thus, how to choose an effective K will directly affect the accuracy of clustering.

We randomly selected 3 kinds of three-dimensional data to form a dataset. For example, the number of samples is 900, and the missing rate is 15%. KNNI-AP algorithm is used, respectively, when K is selected from 1 to 50; from the test results we can see that clustering results are basically stabilized when K is more than 10 and there is uncertainty when K is too small. Similar to the above process, for random missing data with different dimensions and different sample numbers, the values of K were tested. It can be found that K selected as the cube root of the sample numbers is more appropriate. Therefore, in this paper, the selected K is the cube root of the sample numbers rounded to the nearest integer.

3.2. AP Algorithm for Incomplete Data Based on KNNI (KNNI-AP). KNNI-AP proposed here deals with clustering problem for incomplete data by transforming the dataset to an interval-valued one. The range of missing attribute interval $\overline{x_{aj}} = [x_{aj}^-, x_{aj}^+]$ will be large if the jth attributes are dispersive in clusters and will be small if the jth attributes are compact in clusters. So the KNNI can represent the uncertainty of missing attributes better. The lower and upper boundaries of missing attributes interval are determined by the distributions of attributes in clusters, that is, by the geometrical structure of clusters which can present to some extent the shape of clusters and sample distribution of the dataset. The proposed KNNI-AP can validate the robustness of clustering pattern.

For an M-dimensional incomplete dataset $X = \{x_1, x_2, \ldots, x_N\}$, the procedure of KNNI-AP can be described as follows.

Step 1. Set K as the cube root of the sample numbers rounded to the nearest integer.

Step 2. The distance between sample A and sample B can be obtained based on the IPDS, and the similarity matrix $S1$ can be constructed.

Step 3. Form the corresponding interval dataset $\overline{X} = \{\overline{x_1}, \overline{x_2}, \ldots, \overline{x_N}\}$. For each missing attribute x_{aj}, find its K-nearest neighbors using $S1$. x_{aj} is represented by $\overline{x_{aj}} = [x_{aj}^-, x_{aj}^+]$, and nonmissing attribute x_{cj} is rewritten into interval form $\overline{x_{cj}} = [x_{cj}^-, x_{cj}^+]$, where $x_{cj}^- = x_{cj}^+ = x_{cj}$.

Step 4. Calculate the similarity matrix S of $\overline{X} = \{\overline{x_1}, \overline{x_2}, \ldots, \overline{x_N}\}$. Choose the parameter of AP: maximum number of iterations performed by AP (default 2000); convergence of the algorithm if the estimated cluster centers stay fixed for convits iterations (default 50); decreasing step of preferences (default 0.01); damping factor (default 0.5).

Step 5. Apply Preference Range algorithm to computing the range of preference. Initialize the preference: $P = P_{\min} - p\text{step}$. Update the preference: $P = P + p\text{step}$.

Step 6. Apply IAP algorithm to generating C clusters. If cluster number is known then judge weather C is equal to the given number of clusters; else a series of Sil values corresponding to the clustering result with different numbers of cluster is calculated.

Step 7. If cluster number is known, algorithm terminates until C is equal to the given number of clusters; else it terminates until Sil is the largest.

4. Simulation Analysis

4.1. Incomplete Datasets. In order to test the proposed clustering algorithm, we use artificially generated incomplete datasets. The scheme for artificially generating an incomplete dataset X is to randomly select a specified percentage of components and designate them as missing. The random selection of missing attribute values should satisfy the following [11]:

(1) each original feature vector x_k retains at least one component;

(2) each attribute has at least one value present in the incomplete dataset X.

At least one-dimensional data exists for each vector data and at least one or more kinds of data exist for each dimension. That is, the data in each row are not empty; each column of data cannot be null. In the following experiments, we test the performance of proposed algorithm on commonly used UCI datasets: Iris, Seeds, Wisconsin Diagnostic Breast Cancer (WDBC), and Wholesale customers, which are taken from the UCI machine repository [20] and are often used as standard databases to test the performance of clustering algorithms.

The Iris dataset contains 150 four-dimensional attribute vectors. The Wine dataset used in this paper contains 178 three-dimensional attribute vectors. The WDBC dataset comprises 569 samples and, for each sample, there are 30 attributes. The Wholesale customers dataset refers to clients of a wholesale distributor containing 440 6-dimensional attribute vectors.

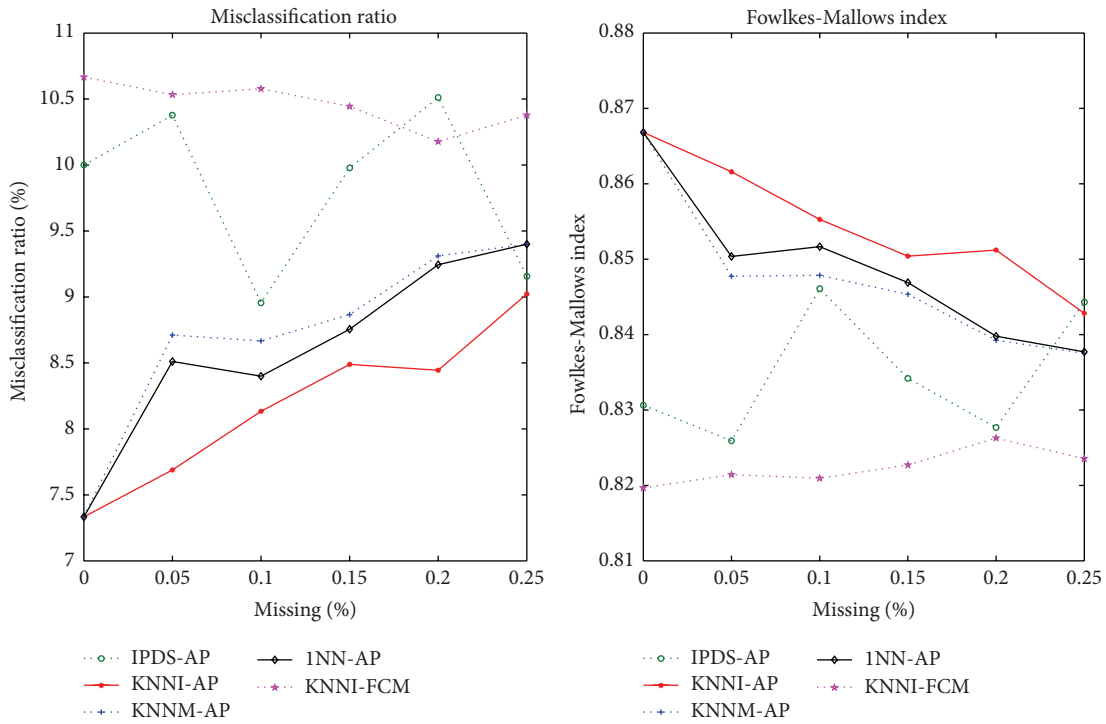

Figure 1: Averaged clustering results of 30 trials using incomplete Iris dataset.

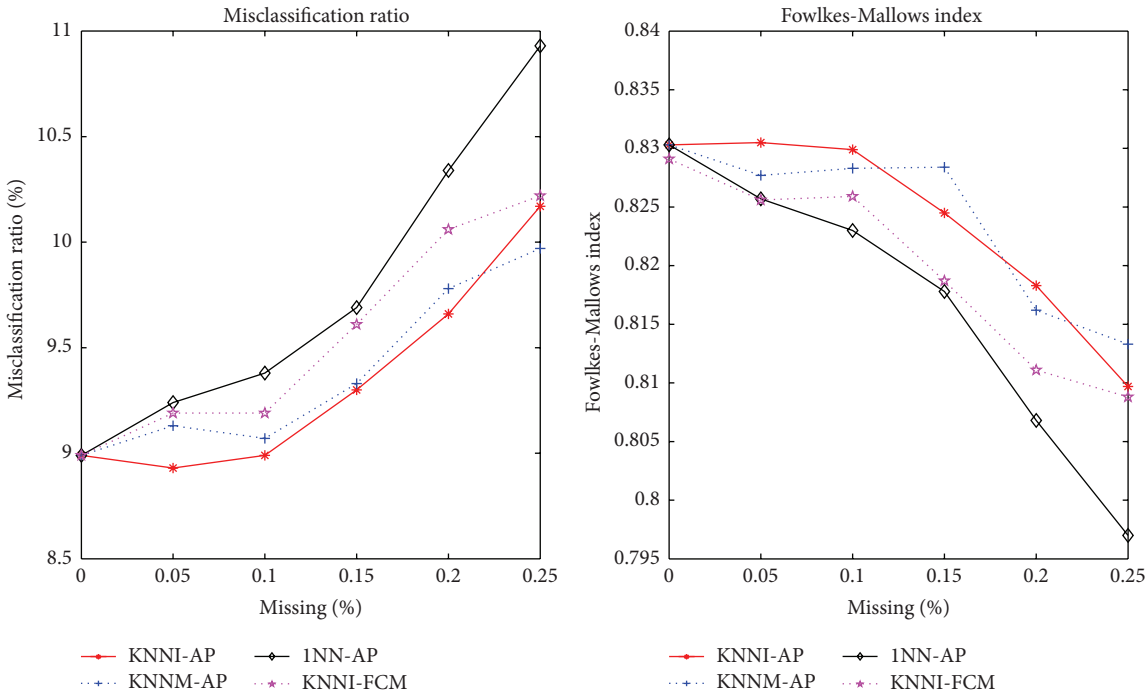

Figure 2: Averaged clustering results of 30 trials using incomplete Wine set.

4.2. Compared Algorithms. To test the clustering performance, we take AP based on the K-nearest neighbor mean (KNNM-AP), AP based on the nearest neighbor (1NN-AP), AP based on IPDS (IPDS-AP), and FCM based on the K-nearest neighbor interval (KNNI-FCM) as compared algorithms. IPDS-AP directly deals with incomplete dataset using AP algorithm, and the others are imputation algorithms using different methods to handle missing values. For KNNM-AP, missing attributes are calculated by the K-nearest neighbor mean; for 1NN-AP, missing attributes are replaced

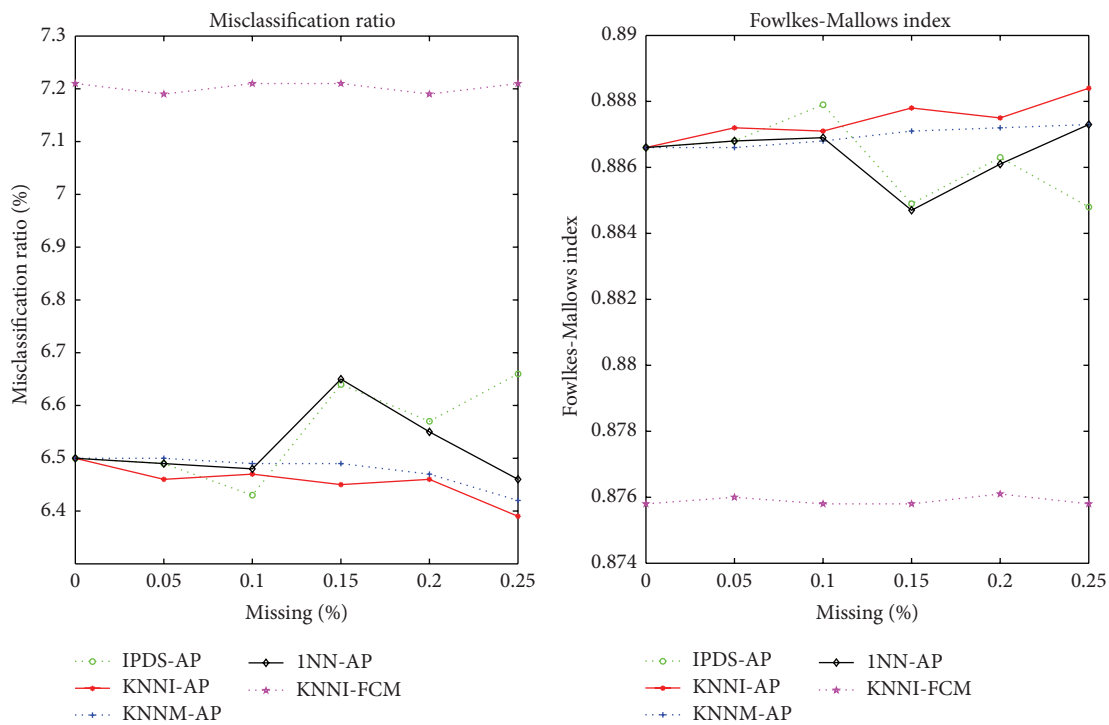

Figure 3: Averaged clustering results of 30 trials using incomplete WDBC dataset.

by the nearest neighbor; for KNNI-FCM, missing attributes are calculated by KNNI similar to KNNM-AP.

4.3. Evaluation Method. To evaluate the quality of clustering results, we use misclassification ratio and Fowlkes-Mallows index [21].

Fowlkes-Mallows (FM) index is used to measure the clustering performance based on external criteria. In general, the larger the FM value is, the better the clustering performance is. The FM index is defined as

$$\mathrm{FM} = \frac{a}{w_1 \cdot w_2} = \sqrt{\frac{a}{a+b} \cdot \frac{a}{a+c}}, \tag{10}$$

where $w_1 = a + b$ and $w_2 = a + c$.

C_1 is a clustering structure of the dataset and C_2 is a defined partition of the data. We refer to a pair of samples (x_u, x_v) from the dataset using the following terms.

SS: if both samples belong to the same cluster of the clustering structure C_1 and to the same group of partition C_2.

SD: if samples belong to the same cluster of C_1 and to different groups of C_2.

DS: if samples belong to different clusters of C_1 and to the same group of C_2.

DD: if both samples belong to different clusters of C_1 and to different groups of C_2.

a, b, c, and d are the number of SS, SD, DS, and DD pairs, respectively. Then $a + b + c + d = W$, which is the maximum number of all pairs in the dataset (meaning, $W = N(N-1)/2$, where N is the total number of samples in the dataset).

The misclassification rate calculates the proportion of an observation being allocated to the incorrect group. It is calculated as follows: the number of incorrect classifications is divided by the total number of samples.

4.4. Experimental Results and Discussion. For the four datasets, damping factor $\lambda = 0.85$, decreasing step of preferences $p$step $= 0.01$, max iteration time $n$run $= 2000$, and convergence condition $n$conv $= 100$. Because missing data was randomly generated, different tests lead to different results, and we noticed significant variation in the results from trial to trial. To eliminate the variation in the results, Figures 1–4 and Tables 1–4 give the averaged results over 30 trials on incomplete Iris, Wine, WDBC, and Wholesale customers datasets. Figures can intuitively reflect the effects of the algorithms and tables can accurately characterize the clustering results of the algorithms. In particular, 30 trials are generated for each row in the table, and the same incomplete dataset is used in each trial for each algorithm, so that the results can be correctly compared. In the tables, the optimal solutions in each row are highlighted in bold, and the suboptimal solutions are italic.

To test the clustering performance, the clustering results of KNNI-AP, 1NN-AP, KNNM-AP, IPDS-AP, and KNNI-FCM are compared. From figures and tables, it can be seen that KNNI-AP, 1NN-AP, and KNNM-AP reduce to regular AP and KNNI-FCM reduces to regular FCM for 0% missing data. For other cases, different methods for handling missing attributes in AP and FCM lead to different clustering results. The different algorithms result in different misclassification ratio and FM index for the different algorithms. With the growth rate of missing data, the uncertainty of dataset

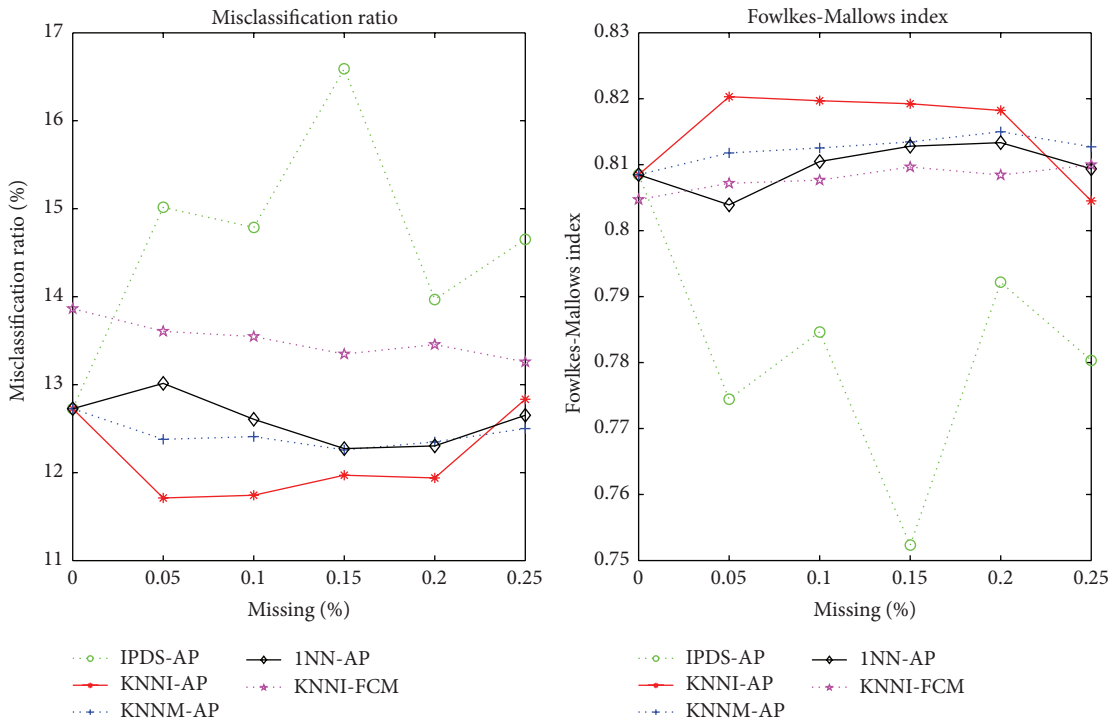

Figure 4: Averaged clustering results of 30 trials using incomplete Wholesale dataset.

increases; therefore, the misclassification ratio increases and FM decreases generally. However, because of handing the missing attributes, the clustering results of algorithms for incomplete data sometimes may be similar to or better than the the results of complete data.

In terms of misclassification ratio, KNNI-AP is always the best performer except for incomplete Wine dataset with 25% missing attributes, incomplete WDBC dataset with 10% missing attributes, and incomplete Wholesale customers dataset with 25% missing attributes. In the three cases, KNNI-AP almost gives suboptimal solutions beside the last case where the result of KNNI-AP is better than the results of IPDS-AP and KNNI-FCM. As for the FM index, KNNI-AP is always the best performer except for incomplete Iris and Wine datasets with 25% missing attributes, incomplete WDBC dataset with 10% missing attributes, and incomplete Wholesale dataset with 25% missing attributes. In the four cases, KNNI-AP almost gives suboptimal solutions beside the last case where the result of KNNI-AP is better than the result of IPDS-AP. From figures and tables, in general, the larger the FM value is, the smaller the misclassification ratio is except for the 25% cases of incomplete Iris and Wholesale datasets. We use misclassification ratio and FM index based on external criteria to accurately evaluate the quality of clustering results.

Comparing KNNI-AP with IPDS-AP, 1NN-AP, and KNNM-AP, the methods are all based on AP algorithm. IPDS-AP ignores missing attributes in incomplete data and scales the partial distances by the reciprocal of the proportion of components used based on the range of feature values, in which the distribution information of missing attributes implicitly embodied in the other data is not taken into account. 1NN-AP substitutes the missing attribute by the corresponding attribute of the nearest neighbor, in which AP algorithm is used to handle the complete dataset. Similarly, missing attributes are supplemented by the mean value of the attributes in the KNNM-AP. Compared with IPDS-AP, KNNI-AP uses the attribute distribution information of datasets sufficiently, including complete data and nonmissing attributes of incomplete data, in which the missing attributes are represented by KNNI on the basis of IPDS. Compared with the other two methods, KNNI-AP achieves interval estimation of missing attributes, taking advantage of the improved IAP, which represents the uncertainty of missing attributes and makes the representation more robust. Furthermore, cluster algorithm with interval data has advantages over cluster with point data, which can present the uncertainty of missing attributes to some degree, thus resulting in more accurate clustering performance.

Comparing KNNI-AP with KNNI-FCM, the methods are both based on KNNI, and the difference between them is the clustering algorithm they use. AP has the advantage that it works for any meaningful measure of similarity between data samples. Unlike most prototype-based clustering algorithms (e.g., K-means), AP does not require a vector space structure and the exemplars are chosen among the observed data samples and are not computed as hypothetical averages of cluster samples. These characteristics make AP clustering particularly suitable for applications in many fields. From our experiments, clustering results of KNNI-AP are far better than those of KNNI-FCM. And in most cases, the methods

Table 1: Averaged results of 30 trials using incomplete Iris dataset.

Missing rate (%)	Misclassification ratio (%)					Fowlkes-Mallows index				
	IPDS	1NN	KNNM	KNNI	KNNI-FCM	IPDS	1NN	KNNM	KNNI	KNNI-FCM
0	10	7.33	7.33	7.33	10.67	0.8306	0.8668	0.8668	0.8668	0.8196
5	10.37	*8.51*	8.71	**7.69**	10.53	0.8259	*0.8504*	0.8477	**0.8616**	0.8214
10	8.96	*8.40*	8.67	**8.13**	10.56	0.8461	*0.8516*	0.8479	**0.8553**	0.8209
15	9.98	*8.76*	8.87	**8.49**	10.56	0.8342	*0.8469*	0.8454	**0.8504**	0.8227
20	10.51	*9.24*	9.31	**8.44**	10.27	0.8277	*0.8397*	0.8392	**0.8512**	0.8262
25	9.16	*9.40*	*9.40*	**9.02**	10.62	**0.8443**	0.8377	0.8375	*0.8428*	0.8235

Table 2: Averaged results of 30 trials using incomplete Wine dataset.

Missing rate (%)	Misclassification ratio (%)					Fowlkes-Mallows index				
	IPDS	1NN	KNNM	KNNI	KNNI-FCM	IPDS	1NN	KNNM	KNNI	KNNI-FCM
0	8.99	8.99	8.99	8.99	8.99	0.8303	0.8303	0.8303	0.8303	0.8291
5	16.94	9.24	*9.13*	**8.93**	9.19	0.7272	0.8257	*0.8277*	**0.8305**	0.8256
10	23.88	9.38	*9.07*	**8.99**	9.19	0.6553	0.8230	*0.8283*	**0.8299**	0.8259
15	24.72	9.69	*9.33*	**9.30**	9.61	0.6417	0.8178	*0.8284*	**0.8245**	0.8187
20	24.80	10.34	*9.78*	**9.66**	10.06	0.6338	0.8068	*0.8162*	**0.8183**	0.8111
25	29.92	10.93	**9.97**	*10.17*	10.22	0.6164	0.7970	**0.8133**	*0.8097*	0.8088

Table 3: Averaged results of 30 trials using incomplete WDBC dataset.

Missing rate (%)	Misclassification ratio (%)					Fowlkes-Mallows index				
	IPDS	1NN	KNNM	KNNI	KNNI-FCM	IPDS	1NN	KNNM	KNNI	KNNI-FCM
0	6.50	6.50	6.50	6.50	7.21	0.8866	0.8866	0.8866	0.8866	0.8758
5	*6.49*	*6.49*	6.50	**6.46**	7.19	*0.8868*	*0.8868*	0.8866	**0.8872**	0.8760
10	**6.43**	6.48	6.49	*6.47*	7.21	**0.8879**	0.8869	0.8868	*0.8871*	0.8758
15	6.64	6.65	*6.49*	**6.45**	7.21	0.8849	0.8847	*0.8871*	**0.8878**	0.8758
20	6.57	6.55	*6.47*	**6.46**	7.19	0.8863	0.8861	*0.8872*	**0.8875**	0.8761
25	6.66	6.46	*6.42*	**6.39**	7.21	0.8848	0.8873	*0.8880*	**0.8884**	0.8758

Table 4: Averaged results of 30 trials using incomplete Wholesale dataset.

Missing rate (%)	Misclassification ratio (%)					Fowlkes-Mallows index				
	IPDS	1NN	KNNM	KNNI	KNNI-FCM	IPDS	1NN	KNNM	KNNI	KNNI-FCM
0	12.73	12.73	12.73	12.73	13.86	0.8084	0.8084	0.8084	0.8084	0.8047
5	15.01	13.02	*12.38*	**11.71**	13.61	0.7745	0.8039	*0.8118*	**0.8203**	0.8071
10	14.79	12.61	*12.41*	**11.74**	13.55	0.7846	0.8105	*0.8125*	**0.8197**	0.8076
15	16.59	12.27	*12.26*	**11.97**	13.35	0.7523	0.8128	*0.8134*	**0.8192**	0.8096
20	13.97	*12.30*	12.35	**11.94**	13.45	0.7922	0.8133	*0.8149*	**0.8182**	0.8084
25	14.65	*12.65*	**12.50**	12.83	13.26	0.7803	0.8094	**0.8127**	0.8045	*0.8099*

based on AP algorithm are also better than KNNI-FCM, which show that AP makes the clustering results more stable and accurate.

5. Conclusion

In this paper, we have studied incomplete data clustering using AP algorithm and presented an AP clustering algorithm based on KNNI for incomplete data. The proposed algorithm is based on the IPDS, estimating the KNNI representation of missing attributes by using K-nearest neighbor interval principle. The proposed algorithm has three main advantages. First, missing attributes are represented by KNNI on the basis of IPDS, which are robust. Second, the interval estimations use the attribute distribution information of datasets sufficiently, which is superior in expressing the uncertainty of missing attributes and enhances the robustness of missing attributes representation. Third, AP algorithm does not require a vector space structure and the exemplars are chosen among the observed data samples and are not computed as hypothetical averages, which makes the clustering results more stable and accurate than other center algorithms.

The results reported in this paper show that our proposed KNNI-AP algorithm is general, simple, and appropriate for the AP clustering with incomplete data. It can be understood that the final clustering results depend on the choice of K and P for KNNI-AP. In the future, our work will focus on the selection of K and P with theoretical basis and the improvement on the similarity measurement of AP when the missing percentage is large, which will be helpful to extend KNNI-AP to solve clustering incomplete data with various missing percentages.

Conflict of Interests

The authors declare that there is no conflict of interests regarding the publication of this paper.

Acknowledgments

This research was partially supported by the National Natural Science Foundation of China under Grant nos. 41427806 and 61273233, the Research Fund for the Doctoral Program of Higher Education under Grant nos. 20120002110035 and 20130002130010, the Project of China Ocean Association under Grant no. DY125-25-02, and Tsinghua University Initiative Scientific Research Program under Grant no. 20131089300.

References

[1] D. Lazer, R. Kennedy, G. King, and A. Vespignani, "The parable of Google flu: traps in big data analysis," *Science*, vol. 343, no. 6176, pp. 1203–1205, 2014.

[2] B. J. Frey and D. Dueck, "Clustering by passing messages between data points," *Science*, vol. 315, no. 5814, pp. 972–976, 2007.

[3] B. J. Frey and D. Dueck, "Response to comment on 'clustering by passing messages between data points'," *Science*, vol. 319, no. 5864, p. 726d, 2008.

[4] K. Wang, J. Zhang, D. Li, X. Zhang, and T. Guo, "Adaptive affinity propagation clustering," *Acta Automatica Sinica*, vol. 33, no. 12, pp. 1242–1246, 2007.

[5] Y. He, Q. Chen, X. Wang, R. Xu, X. Bai, and X. Meng, "An adaptive affinity propagation document clustering," in *Proceedings of the 7th International Conference on Informatics and Systems (INFOS '10)*, pp. 1–7, IEEE, March 2010.

[6] R. J. Little and D. B. Rubin, *Statistical Analysis with Nissing Data*, John Wiley & Sons, New York, NY, USA, 2nd edition, 2002.

[7] J. K. Dixon, "Pattern recognition with partly missing data," *IEEE Transactions on Systems, Man and Cybernetics*, vol. 9, no. 10, pp. 617–621, 1979.

[8] A. P. Dempster, N. M. Laird, and D. B. Rubin, "Maximum likelihood from incomplete data via the EM algorithm," *Journal of the Royal Statistical Society. Series B. Methodological*, vol. 39, no. 1, pp. 1–38, 1977.

[9] J. C. Bezdek, *Pattern Recognition with Fuzzy Objective Function Algorithms*, Kluwer Academic Publishers, 1981.

[10] S. Miyamoto, O. Takata, and K. Umayahara, "Handling missing values in fuzzy c-means," in *Proceedings of the 3rd Asian Fuzzy Systems Symposium*, pp. 139–142, 1998.

[11] R. J. Hathaway and J. C. Bezdek, "Fuzzy c-means clustering of incomplete data," *IEEE Transactions on Systems, Man, and Cybernetics, Part B: Cybernetics*, vol. 31, no. 5, pp. 735–744, 2001.

[12] R. J. Hathaway and J. C. Bezdek, "Clustering incomplete relational data using the non-Euclidean relational fuzzy c-means algorithm," *Pattern Recognition Letters*, vol. 23, no. 1–3, pp. 151–160, 2002.

[13] D. Li, H. Gu, and L. Zhang, "A fuzzy c-means clustering algorithm based on nearest-neighbor intervals for incomplete data," *Expert Systems with Applications*, vol. 37, no. 10, pp. 6942–6947, 2010.

[14] D.-Q. Zhang and S.-C. Chen, "Clustering incomplete data using kernel-based fuzzy C-means algorithm," *Neural Processing Letters*, vol. 18, no. 3, pp. 155–162, 2003.

[15] C. Lu, S. Song, and C. Wu, "Afinity propagation clustering with incomplete data," in *Computational Intelligence, Networked Systems and Their Applications*, pp. 239–248, Springer, Berlin, Germany, 2014.

[16] J. L. Ohmann and M. J. Gregory, "Predictive mapping of forest composition and structure with direct gradient analysis and nearest-neighbor imputation in coastal Oregon, U.S.A.," *Canadian Journal of Forest Research*, vol. 32, no. 4, pp. 725–741, 2002.

[17] E. Acuna and C. Rodriguez, "The treatment of missing values and its effect on classifier accuracy," in *Classification, Clustering, and Data Mining Applications*, pp. 639–647, Springer, Berlin, Germany, 2004.

[18] P. J. García-Laencina, J.-L. Sancho-Gómez, and A. R. Figueiras-Vidal, "Pattern classification with missing data: a review," *Neural Computing and Applications*, vol. 19, no. 2, pp. 263–282, 2010.

[19] X. Huang and Q. Zhu, "A pseudo-nearest-neighbor approach for missing data recovery on Gaussian random data sets," *Pattern Recognition Letters*, vol. 23, no. 13, pp. 1613–1622, 2002.

[20] "UCI machine learning repository," 2014, http://archive.ics.uci.edu/ml/datasets.html.

[21] M. Halkidi, Y. Batistakis, and M. Vazirgiannis, "Cluster validity methods: part I," *ACM SIGMOD Record*, vol. 31, no. 2, pp. 40–45, 2002.

Hindawi Publishing Corporation
Mathematical Problems in Engineering
Volume 2015, Article ID 364138, 9 pages
http://dx.doi.org/10.1155/2015/364138

Research Article

Fault Reconstruction Approach for Distributed Coordinated Spacecraft Attitude Control System

Mingyi Huo,[1] Yanning Guo,[1] and Xing Huo[2]

[1] *Department of Control Science and Engineering, Harbin Institute of Technology, Harbin 150001, China*
[2] *College of Engineering, Bohai University, Jinzhou 121000, China*

Correspondence should be addressed to Xing Huo; hmyi888@163.com

Received 15 January 2015; Accepted 2 March 2015

Academic Editor: Kun Liu

Copyright © 2015 Mingyi Huo et al. This is an open access article distributed under the Creative Commons Attribution License, which permits unrestricted use, distribution, and reproduction in any medium, provided the original work is properly cited.

This work presents a novel fault reconstruction approach for a large-scale system, that is, a distributed coordinated spacecraft attitude control system. The attitude of all the spacecrafts in this distributed system is controlled by using thrusters. All possible faults of thruster including thrust magnitude error and alignment error are investigated. As a stepping stone, the mathematical model of thruster is firstly established based on the thruster configuration. On the basis of this, a sliding mode observer is then proposed to reconstruct faults in each agent of the coordinated control system. A Lyapunov-based analysis shows that the observer asymptotically converges to the actual faults. The key feature of this fault reconstruction approach is that it can achieve a faster reconstruction of the fault in comparison with the conventional fault reconstruction schemes. It can globally reconstruct thruster faults with zero reconstruction error, and this is accomplished within finite time. The effectiveness of the proposed approach is analytically authenticated via simulation study.

1. Introduction

Distributed coordinate spacecraft attitude control system, as a large-scale system, is revolutionizing our way for performing space missions. This brings on several advantages in space mission accomplishment. It usually includes two or more spacecrafts in formation flying. It is to distribute the functionality of a single large/complex spacecraft to a set of smaller, less-expensive cooperative spacecrafts. In recent years, NASA, the U.S. Air Force, and the ESA have shown keen interests in developing reliable autonomous formation strategies to deploy multiple spacecrafts for various space missions [1]. The advantages of multiple-spacecraft formation flying include increasing resolution of scientific observations, reducing cost, enhancing overall system robustness, and adding flexibility to space-based programs. However, it also poses tremendous challenges, such as spacecraft formation initialization to reconfiguration, coordination, and formation trajectory generation. More specifically, distributed coordinate spacecraft attitude control is still an open problem that needs to be further solved.

In the past decades, the problem of distributed coordinated attitude control for spacecraft formation flying has been intensively investigated [2–4]. Classically, the leader-follower [5], the behavioral based approach [6, 7], and the virtual structure [8] are three schemes for the spacecraft formation synchronization. In [9], coordinated control for multiple spacecraft was discussed. In [8], synchronization of spacecraft formation was investigated by using virtual structure technique. Parametric uncertainties and external disturbance were also addressed. In [10], a robust distributed coordinated attitude control law was presented by using behavioral based approach. More specifically, due to its fast convergence rate and its superiority of stabilizing the system within finite time, finite-time controller design for distributed coordinate spacecraft attitude system has attracted more and more attention in recent years. In [11], finite-time attitude synchronization and stabilization problem were investigated for spacecrafts. The designed controller was able to guarantee the finite-time stability of the closed-loop system.

Most of the previous research, however, handles distributed coordinate spacecraft attitude control based on

the assumption that an exact model of the actuator is available. This assumption is rarely satisfied in practice because the actuator parameters may have uncertainties due to installation error, aging and wearing out of the mechanical and electrical parts, and so forth. The first type of uncertainty in actuator that needs to be tackled is actuator faults [12]. Once a spacecraft is launched, it is highly unlikely that its hardware can be repaired. Thus any component or system failure cannot be fixed with replacement parts. These issues can potentially cause a host of economic, environmental, and safety problems. SMC with actuator faults does not seem to have received much attention in the literature. In [13], a SMC based controller was proposed to achieve reliable attitude stabilization, while actuator outage faults were accommodated. An adaptive SMC control approach was proposed in [14] for performing attitude tracking maneuvers in the presence of disturbances and thruster's failures. Another adaptive SMC attitude control was presented in [15] to handle several fault scenarios of rotating solar flaps. The authors in [16] looked at a terminal sliding mode control approach for the satellite formations flying. However, stability analysis of the closed-loop system was not provided when the faults occurred. For a flexible spacecraft with partial loss of control effectiveness fault, a SMC control was developed in [17] to accomplish attitude tracking.

Active FTC relies on the availability of a Fault Detection and Isolation (FDI) block that detects and identifies fault online [18–21] and then reacts to the system fault actively by reconfiguring controller. The application of active FTC to satellite attitude control, especially the FDI design, has attracted considerable interests. A dynamic neural network scheme was presented in [22] to detect and isolate reaction wheel faults. In [23], the problem of detecting reaction wheel faults in a tetrahedron configuration was investigated. An iterative learning observer-based FDI was reported in [24] to estimate time-varying thruster faults. In [25], a two-stage Kalman filtering algorithm was developed to estimate reaction wheel faults; a fault-tolerant controller was then synthesized to accommodate the faults. Two model-based schemes were developed in [26] by using $\mathscr{H}_\infty/\mathscr{H}_2$ filters to address the fault diagnosis problem of micro thrusters. In [27], a set of fault detection filters were presented for deep space satellites to detect and identify faults in sensors or actuators. In [28], the problem of robust FDI design for thruster faults in the Mars Express satellite was discussed. For a benchmark Mars Express satellite, the authors in [29, 30] presented a nonlinear sliding mode observer to identify and isolate faults induced in thruster and sensors.

Another type of uncertainty in actuator that should be addressed is actuator misalignments. Due to finite-manufacturing tolerances or warping of the spacecraft structure during launch, some actuator alignment error will definitely exist. That problem may cause the onboard control algorithm to fail and thus pose significant risk to the successful operation of the spacecraft. It is thus desirable to design a control methodology to handle actuator misalignments. Unfortunately, there has been insufficient research on control in the presence of actuator misalignments. One paper developed an adaptive control law to accomplish attitude maneuver in the presence of relatively small gimbals' alignment error of variable speed control moment gyros [31]. In [32], a nonlinear model reference adaptive control scheme was tested in the presence of alignment errors up to fifteen degrees. Although an extended Kalman filter was used in another approach to develop methods for on-orbit actuator alignment calibration, uncertain inertia properties were not taken into account [33]. In another study [34], an adaptive control approach was proposed for satellite formation flying. The backstepping technique was used to synthesize the controller, and the thrust magnitude error and misalignment were successfully handled.

Based on the above analysis, it is known that if the fault occurring in any spacecraft can not be successfully in real-time, then it may degrade the whole performance of the distributed coordinate spacecraft attitude control system. Sometimes, it would fail the space missions of the spacecraft formation flying. This issue may pose a question for us; that is, if the fault in each spacecraft can be exactly diagnosed or reconstructed, then a fault-tolerant coordinate attitude controller can be designed as follows to guarantee the acceptable performance even in the presence of fault. Motivated by this, this study will investigate the problem of fault reconstruction for each spacecraft of the considered coordinate spacecraft system. In this work, a sliding mode observer-based reconstruction approach will be presented to estimate the faults. This approach can achieve a faster reconstruction in comparison with the conventional fault diagnosis schemes. Moreover, it is able to estimate the occurred fault in finite time with zero reconstruction error.

The remainder of this paper is organized as follows: In Section 2, problem formulation is presented including mathematical model and problem statement. A sliding mode observer-based fault reconstruction approach is developed in Section 3, and also the stability of closed-loop observer error system is provided. In Section 4, simulation results with the application of the designed fault reconstruction scheme to a distributed coordinated spacecraft attitude control system are presented. Section 5 presents some concluding remarks and future work.

2. Problem Formulation

The notation adopted throughout this paper is introduced as follows: Let $\mathbf{I}_n \in \mathfrak{R}^{n\times n}$ denote the n-by-n identity matrix and the symbol $\|\cdot\|$ denotes the Euclidean norm or its induced norm. For vector $\mathbf{x} = [x_1 \;\; x_2 \;\; \cdots \;\; x_n]^{\mathrm{T}} \in \mathfrak{R}^n$, a vector function is defined as $\mathbf{sgn}(\mathbf{x}) = [\mathrm{sign}(x_1) \;\; \mathrm{sign}(x_2) \;\; \cdots \;\; \mathrm{sign}(x_n)]^{\mathrm{T}}$ with $\mathrm{sign}(\cdot)$ the sign function.

2.1. Mathematical Model of Distributed Coordinated Spacecraft Attitude Control System. In this work, each spacecraft in the distributed coordinated system is modeled as a rigid body in a three-dimensional space, and an external disturbance is not considered in the model description. For a distributed coordinate system with n spacecrafts, let $\mathscr{F}_I$ denote the inertial frame and $\mathscr{F}_b^i$ denote the body-fixed frame of the ith

spacecraft. For each spacecraft, given a Euler rotation angle $\phi_i(t) \in \mathfrak{R}$ about the Euler principle axis $\mathbf{n}_i \in \mathfrak{R}^3$, the attitude orientation of the ith spacecraft in $\mathcal{F}_b^i$ with respect to $\mathcal{F}_I$ can be represented by the MRP vector $\boldsymbol{\sigma}_b^i = [\sigma_1^i \ \ \sigma_2^i \ \ \sigma_3^i]^{\mathrm{T}} \in \mathfrak{R}^3$, which is given by [35] $\boldsymbol{\sigma}_b^i = \mathbf{n}_i \tan(\phi_i(t)/4)$, $\phi_i(t) \in [0^\circ, 360^\circ)$.

Let the angular velocity of the ith spacecraft with respect to the inertial reference frame $\mathcal{F}_I$ and expressed in the body-fixed frame $\mathcal{F}_b^i$ be denoted by $\boldsymbol{\omega}_b^i \in \mathfrak{R}^3$. Using the MRPs, the kinematic differential equation of the ith spacecraft can be determined as follows [35]:

$$\begin{aligned}\dot{\boldsymbol{\sigma}}_b^i &= \frac{1}{4}\left[\left(1 - \left(\boldsymbol{\sigma}_b^i\right)^{\mathrm{T}}\boldsymbol{\sigma}_b^i\right)\mathbf{I}_3 + 2\mathbf{S}\left(\boldsymbol{\sigma}_b^i\right) + 2\boldsymbol{\sigma}_b^i\left(\boldsymbol{\sigma}_b^i\right)^{\mathrm{T}}\right]\boldsymbol{\omega}_b^i \\ &= \mathbf{G}_i\left(\boldsymbol{\sigma}_b^i\right)\boldsymbol{\omega}_b^i,\end{aligned} \tag{1}$$

where the matrix $\mathbf{S}(\mathbf{x})$ is the skew-symmetric matrix such that $\mathbf{S}(\mathbf{x})\mathbf{y} = \mathbf{x} \otimes \mathbf{y}$ for any vectors $\mathbf{x}, \mathbf{y} \in \mathfrak{R}^3$, with "$\otimes$" being the vector cross product.

The dynamical model of the ith spacecraft motion can be found from Euler's moment equation, and it is given by [36]

$$\mathbf{J}_i\dot{\boldsymbol{\omega}}_b^i = -\mathbf{S}\left(\boldsymbol{\omega}_b^i\right)\mathbf{J}_i\boldsymbol{\omega}_b^i + \mathbf{u}_i, \tag{2}$$

where $\mathbf{J}_i \in \mathfrak{R}^{3\times 3}$ (positive and definite) is the total inertia matrix of the ith spacecraft and $\mathbf{u}_i = [u_1^i \ \ u_2^i \ \ u_3^i]^{\mathrm{T}} \in \mathfrak{R}^3$ denotes the total control torque generated by all the mounted actuators.

In this work, information exchange among agents can be represented as a graph. Graph $\mathcal{G}$ consists of a node set $\mathcal{V} = \{1, 2, \ldots, n\}$, an edge set $\mathcal{E} \subseteq \mathcal{V} \times \mathcal{V}$, and a weighted adjacency matrix $\boldsymbol{\Lambda} = [a_{jn}] \in \mathfrak{R}^{n\times n}$. To define the communication topology in the network we consider n agent spacecraft as nodes of a graph, called communication graph. The communication links among the agents are considered as the communication graph edge set.

2.2. Thruster Fault of Each Spacecraft. Because thruster can generate larger control torque than reaction wheels, it becomes one type of actuators commonly used in large-angle attitude maneuver. Thus, all the agents in the distributed coordinated spacecraft system considered in this work are controlled by using thrusters. A thruster consists of a flow control valve and a combustion chamber. When propellant passes through the combustion chamber, chemical reaction takes place generating thrust through the nozzle.

Assume that N_i thrusters are mounted in the ith spacecraft. For the jth thruster in the ith spacecraft, $j = 1, 2, \ldots, N_i$, its configuration is shown in Figure 2; the force component can be derived as

$$\mathbf{F}_{ij} = F\begin{bmatrix}\cos\alpha_{ij}\cos\beta_{ij} \\ \cos\alpha_{ij}\sin\beta_{ij} \\ \sin\alpha_{ij}\end{bmatrix}, \tag{3}$$

where $F > 0$ is the constant thrust level, α_{ij} is the elevation angle, and β_{ij} is the azimuth angle. Let $\mathbf{r}_{ij} = r_{xij}\mathbf{X}_{Bi} + r_{yij}\mathbf{Y}_{Bi} + r_{zij}\mathbf{Z}_{Bi}$ be the vector representing the placement of the reaction thruster from the satellite center of mass. Torque component provided by the jth thruster can be calculated as

$$\boldsymbol{\tau}_{ij} = \mathbf{r}_{ij} \times \mathbf{F}_{ij}. \tag{4}$$

Then, the applied control torque $\mathbf{u}_i$ generated by N_i thrusters is

$$\mathbf{u}_i = \sum_{j=1}^{N_i}\boldsymbol{\tau}_{ij} = \sum_{j=1}^{N_i}\mathbf{r}_{ij} \times \mathbf{F}_{ij}. \tag{5}$$

In this study, thruster faults including misalignment error and thrust magnitude error are considered. The nature of those two scenarios is described as follows.

(1) Misalignment Error. In practical aerospace engineering, the configuration of actuators is not perfect. Misalignment error may exist due to space debris or finite-manufacturing technique. As a result, the demanded torque from controller is different from the torque produced by the actuators. For the jth thruster in the ith spacecraft, misalignment error may exist in $\mathbf{r}_{ij}$ and the alignment angles α_{ij}, β_{ij}. Let $\mathbf{r}_{ij}^0$, $\Delta\mathbf{r}_{ij}$ denote the nominal and the alignment error distance between satellite center and the thruster, respectively. Then, $\mathbf{r}_{ij}$ can be rewritten as $\mathbf{r}_{ij} = \mathbf{r}_{ij}^0 + \Delta\mathbf{r}_{ij}$. Assume that the thruster is tilted over nominal direction with small constant angles, $\Delta\alpha_{ij}$ and $\Delta\beta_{ij}$. Then, the alignment angle can be denoted as $\alpha_{ij} = \alpha_{ij}^0 + \Delta\alpha_{ij}$ and $\beta_{ij} = \beta_{ij}^0 + \Delta\beta_{ij}$, where α_{ij}^0 and β_{ij}^0 are the nominal alignment angle.

(2) Thrust Magnitude Error. As discussed in [37], due to reduction in the amount of propellant's mass, the amount of thrust generated is reduced. Moreover, due to wear and tear, the conductivity of the wires, capacitor, and electrodes may decrease. Consequently, the amount of discharge current produced during the generation of pulses is reduced, resulting in the reduction of the amount of thrust produced. Those two issues will inevitably introduce the problem of thrust magnitude error for thruster. For the jth thruster in the ith spacecraft, let F_0 and ΔF_{ij} represent the nominal and error of thrust magnitude, respectively. The actual thrust F can thus be denoted by

$$F = F_0 + \Delta F_{ij}. \tag{6}$$

Taking thruster magnitude error and alignment error into consideration, $\boldsymbol{\tau}_{ij}$ in (4) can be rewritten as

$$\begin{aligned}\boldsymbol{\tau}_{ij} &= \left(F_0 + \Delta F_{ij}\right)\left(\mathbf{r}_{ij}^0 + \Delta\mathbf{r}_{ij}\right) \\ &\quad\times\begin{bmatrix}\cos\left(\alpha_{ij}^0 + \Delta\alpha_{ij}\right)\cos\left(\beta_{ij}^0 + \Delta\beta_{ij}\right) \\ \cos\left(\alpha_{ij}^0 + \Delta\alpha_{ij}\right)\sin\left(\beta_{ij}^0 + \Delta\beta_{ij}\right) \\ \sin\left(\alpha_{ij}^0 + \Delta\alpha_{ij}\right)\end{bmatrix} \\ &= F_0\left(\mathbf{r}_{ij}^0\right) \times \mathbf{D}_{ij}^0 + \Delta F\left(\mathbf{r}_{ij}^0\right) \times \mathbf{D}_{ij}^0 \\ &\quad + \left(F_0 + \Delta F_{ij}\right)\left[\left(\mathbf{r}_{ij}^0\right) \times \Delta\mathbf{D}_{ij} + \Delta\mathbf{r}_{ij} \times \left(\mathbf{D}_{ij}^0 + \Delta\mathbf{D}_{ij}\right)\right],\end{aligned} \tag{7}$$

where

$$\mathbf{D}_{ij}^{0} = \begin{bmatrix} \cos\alpha_{ij}^{0}\cos\beta_{ij}^{0} \\ \cos\alpha_{ij}^{0}\sin\beta_{ij}^{0} \\ \sin\alpha_{ij}^{0} \end{bmatrix}, \tag{8}$$

$$\Delta\mathbf{D}_{ij} = \begin{bmatrix} \cos\left(\alpha_{ij}^{0}+\Delta\alpha_{ij}\right)\cos\left(\beta_{ij}^{0}+\Delta\beta_{ij}\right) \\ \cos\left(\alpha_{ij}^{0}+\Delta\alpha_{ij}\right)\sin\left(\beta_{ij}^{0}+\Delta\beta_{ij}\right) \\ \sin\left(\alpha_{ij}^{0}+\Delta\alpha_{ij}\right) \end{bmatrix} - \begin{bmatrix} \cos\alpha_{ij}^{0}\cos\beta_{ij}^{0} \\ \cos\alpha_{ij}^{0}\sin\beta_{ij}^{0} \\ \sin\alpha_{ij}^{0} \end{bmatrix}. \tag{9}$$

From (5) and (7), the real/total thrust force with magnitude error and misalignment is expressed as the sum of nominal and thrust error terms in the body-fixed frame:

$$\begin{aligned} \mathbf{u}_i &= \underbrace{F_0\sum_{j=1}^{N_i}(\mathbf{r}_{ij}^{0})\times\mathbf{D}_{ij}^{0}}_{\mathbf{u}_{\mathrm{nor}_i}} \\ &\quad + \underbrace{\sum_{j=1}^{N_i}\left\{\Delta F_{ij}\left(\mathbf{r}_{ij}^{0}\right)\times\mathbf{D}_{ij}^{0}+\left(F_0+\Delta F_{ij}\right)\left[\left(\mathbf{r}_{ij}^{0}\right)\times\Delta\mathbf{D}_{ij}+\Delta\mathbf{r}_{ij}\times\left(\mathbf{D}_{ij}^{0}+\Delta\mathbf{D}_{ij}\right)\right]\right\}}_{\mathbf{u}_{\mathrm{fault}_i}}, \end{aligned} \tag{10}$$

where the vector $\mathbf{u}_{\mathrm{nor}_i} \in \mathfrak{R}^3$ is the nominal control torque commanded by the controller of the ith spacecraft and $\mathbf{u}_{\mathrm{fault}_i} \in \mathfrak{R}^3$ denotes the faulty torque induced by misalignment error and thrust magnitude error of thrusters in the ith spacecraft.

2.3. Problem Statement. In this study, our objective to be achieved can be stated as follows: Consider the distributed coordinate spacecraft attitude control system and design an observer-based reconstruction approach to reconstruct all possible faults occurring in thrusters of all the distributed coordinate system. Moreover, the reconstruction error of the faults should be governed to zero in finite time, and a faster reconstruction of thruster fault should be accomplished.

3. Sliding Mode Observer-Based Fault Reconstruction Approach Design

A sliding mode observer-based fault reconstruction approach will be developed for the distributed coordinate system. With application of this approach, the thruster fault occurring in each spacecraft will be reconstructed. The reconstruction error will converge to zero with finite-time convergence. In this section, the upper bound of the thruster faults will be firstly analyzed or estimated. This estimated upper bound will be useful for the choice of the observer gains in the following proposed sliding mode observer.

3.1. Analysis of the Upper Bound of the Thruster Fault. Define a matrix $\mathbf{T}_i(\boldsymbol{\sigma}_b^i) = (\mathbf{G}_i(\boldsymbol{\sigma}_b^i))^{-1}$; combining with the spacecraft kinematics (1) and its dynamics (2), taking thruster fault (10) into consideration, it can establish the following transformed two-order differential equation:

$$\begin{aligned} &\bar{\mathbf{J}}_i\left(\boldsymbol{\sigma}_b^i\right)\ddot{\boldsymbol{\sigma}}_b^i + \mathbf{C}_i\left(\boldsymbol{\sigma}_b^i,\dot{\boldsymbol{\sigma}}_b^i\right)\dot{\boldsymbol{\sigma}}_b^i \\ &\quad = \left(\mathbf{T}_i\left(\boldsymbol{\sigma}_b^i\right)\right)^{\mathrm{T}}\mathbf{u}_{\mathrm{nor}_i} + \left(\mathbf{T}_i\left(\boldsymbol{\sigma}_b^i\right)\right)^{\mathrm{T}}\mathbf{u}_{\mathrm{fault}_i}, \end{aligned} \tag{11}$$

where $\mathbf{C}_i(\boldsymbol{\sigma}_b^i,\dot{\boldsymbol{\sigma}}_b^i) = (\mathbf{T}_i(\boldsymbol{\sigma}_b^i))^{\mathrm{T}}\mathbf{J}_i\dot{\mathbf{T}}_i(\boldsymbol{\sigma}_b^i) + (\mathbf{T}_i(\boldsymbol{\sigma}_b^i))^{\mathrm{T}}\mathbf{S}(\mathbf{T}_i(\boldsymbol{\sigma}_b^i)\dot{\boldsymbol{\sigma}}_b^i)\mathbf{J}_i\mathbf{T}_i(\boldsymbol{\sigma}_b^i)$, $\bar{\mathbf{J}}_i = (\mathbf{T}_i(\boldsymbol{\sigma}_b^i))^{\mathrm{T}}\mathbf{J}_i\mathbf{T}_i(\boldsymbol{\sigma}_b^i)$.

Property 1. The matrix $\mathbf{G}_i(\boldsymbol{\sigma}_b^i)$ is such that [38]

$$\begin{aligned} \mathbf{T}_i\left(\boldsymbol{\sigma}_b^i\right) &= \frac{16}{\left(1+\left(\boldsymbol{\sigma}_b^i\right)^{\mathrm{T}}\boldsymbol{\sigma}_b^i\right)^2}\left(\mathbf{G}_i\left(\boldsymbol{\sigma}_b^i\right)\right)^{\mathrm{T}}, \\ \left(\mathbf{G}_i\left(\boldsymbol{\sigma}_b^i\right)\right)^{\mathrm{T}}\mathbf{G}_i\left(\boldsymbol{\sigma}_b^i\right) &= \left(\frac{1+\left(\boldsymbol{\sigma}_b^i\right)^{\mathrm{T}}\boldsymbol{\sigma}_b^i}{4}\right)^2\mathbf{I}_3. \end{aligned} \tag{12}$$

Property 2. The matrix $\bar{\mathbf{J}}_i(\boldsymbol{\sigma}_b^i)$ is positive-definite and symmetric. There exist two positive scalars $\lambda_{\min_i} \in \mathfrak{R}$ and $\lambda_{\max_i} \in \mathfrak{R}$ such that $\lambda_{\min_i}\|\mathbf{x}\|^2 \le \mathbf{x}^{\mathrm{T}}\bar{\mathbf{J}}_i(\boldsymbol{\sigma}_b^i)\mathbf{x} \le \lambda_{\max_i}\|\mathbf{x}\|^2$ for any vector $\mathbf{x} \in \mathfrak{R}^3$.

Property 3. The matrix $\mathbf{C}_i(\boldsymbol{\sigma}_b^i,\dot{\boldsymbol{\sigma}}_b^i)$ and the time-derivative of $\bar{\mathbf{J}}_i(\boldsymbol{\sigma}_b^i)$ satisfy the skew-symmetric relationship [38] $\mathbf{x}^{\mathrm{T}}(\dot{\bar{\mathbf{J}}}_i(\boldsymbol{\sigma}_b^i) - 2\mathbf{C}_i(\boldsymbol{\sigma}_b^i,\dot{\boldsymbol{\sigma}}_b^i))\mathbf{x} = 0$ for all $\mathbf{x} \in \mathfrak{R}^3$.

Theorem 1. *For the thruster fault $\mathbf{u}_{fault_i}$ in (10), it is bounded by a positive and known constant $\gamma_i \in \mathfrak{R}$. Moreover, if the term $(\mathbf{T}_i(\boldsymbol{\sigma}_b^i))^{\mathrm{T}}\mathbf{u}_{fault_i}$ in (11) is viewed as a lumped fault, then this can be bounded by a positive constant $8\gamma_i$; that is, $\|(\mathbf{T}_i(\boldsymbol{\sigma}_b^i))^{\mathrm{T}}\mathbf{u}_{fault_i}\| \le 8\gamma_i$.*

Proof. As shown in (10), it is known that

$$\begin{aligned} \mathbf{u}_{\mathrm{fault}_i} = \sum_{j=1}^{N_i}&\left\{\Delta F_{ij}\left(\mathbf{r}_{ij}^{0}\right)\times\mathbf{D}_{ij}^{0}+\left(F_0+\Delta F_{ij}\right)\right. \\ &\left.\cdot\left[\left(\mathbf{r}_{ij}^{0}\right)\times\Delta\mathbf{D}_{ij}+\Delta\mathbf{r}_{ij}\times\left(\mathbf{D}_{ij}^{0}+\Delta\mathbf{D}_{ij}\right)\right]\right\}. \end{aligned} \tag{13}$$

According to the physical limitation of thruster, the thrust magnitude error should absolutely satisfy

$$\left|\Delta F_{ij}\right| \le F. \tag{14}$$

On the other hand, although there exists alignment error in each thruster of the ith spacecraft, this misalignment should be finite, and it will be always such that

$$\left\|\Delta\mathbf{r}_{ij}\right\| \le \left\|\mathbf{r}_i^{0}\right\|. \tag{15}$$

From (14) and (15), the following inequality can be obtained:

$$\begin{aligned}\left\|\mathbf{u}_{\text{fault}_i}\right\| &\leq \sum_{j=1}^{N_i}\left\|\Delta F_{ij}\left(\mathbf{r}_{ij}^0\right)\times\mathbf{D}_{ij}^0+\left(F_0+\Delta F_{ij}\right)\right.\\ &\qquad\left.\cdot\left[\left(\mathbf{r}_{ij}^0\right)\times\Delta\mathbf{D}_{ij}+\Delta\mathbf{r}_{ij}\times\left(\mathbf{D}_{ij}^0+\Delta\mathbf{D}_{ij}\right)\right]\right\|\\ &\leq F\sum_{j=1}^{N_i}\left\{\left\|\left(\mathbf{r}_{ij}^0\right)\times\mathbf{D}_{ij}^0\right\|\right.\\ &\qquad\left.+2\left[\left\|\left(\mathbf{r}_{ij}^0\right)\times\Delta\mathbf{D}_{ij}+\Delta\mathbf{r}_{ij}\times\left(\mathbf{D}_{ij}^0+\Delta\mathbf{D}_{ij}\right)\right\|\right]\right\}.\end{aligned} \tag{16}$$

With the definition $\Delta\mathbf{D}_{ij}$ and $\mathbf{D}_{ij}^0$ in (8) and (9), respectively, it follows that $\|\Delta\mathbf{D}_{ij}\|\leq 2\sqrt{3}$ and $\|\mathbf{D}_{ij}^0\|\leq\sqrt{3}$. Then, it leaves inequality (16) as

$$\begin{aligned}\left\|\mathbf{u}_{\text{fault}_i}\right\| &\leq F\sum_{j=1}^{N_i}\left\{\left\|\left(\mathbf{r}_{ij}^0\right)\times\mathbf{D}_{ij}^0\right\|\right.\\ &\qquad\left.+2\left[\left\|\left(\mathbf{r}_{ij}^0\right)\times\mathbf{D}_{ij}^0+\Delta\mathbf{r}_{ij}\times\left(\mathbf{D}_{ij}^0+\Delta\mathbf{D}_{ij}\right)\right\|\right]\right\}\\ &\leq F\sum_{j=1}^{N_i}\left\{\sqrt{3}\left\|\mathbf{r}_{ij}^0\right\|+2\left[2\sqrt{3}\left\|\mathbf{r}_{ij}^0\right\|+3\sqrt{3}\left\|\mathbf{r}_{ij}^0\right\|\right]\right\}\\ &= 11\sqrt{3}F\sum_{j=1}^{N_i}\left\|\mathbf{r}_{ij}^0\right\|.\end{aligned} \tag{17}$$

It can be concluded from (17) that the possible thruster fault $\mathbf{u}_{\text{fault}_i}$ is bounded by $\gamma_i\leq 11\sqrt{3}F\sum_{j=1}^{N_i}\|\mathbf{r}_{ij}^0\|$; that is, $\|\mathbf{u}_{\text{fault}_i}\|\leq\gamma_i$.

In addition, it can be obtained from (12) in Property 1 that

$$\begin{aligned}\left\|\mathbf{T}_i\left(\boldsymbol{\sigma}_b^i\right)\right\| &\leq \left\|\frac{16}{\left(1+\left(\boldsymbol{\sigma}_b^i\right)^{\mathrm{T}}\boldsymbol{\sigma}_b^i\right)^2}\right\|\left\|\left(\mathbf{G}_i\left(\boldsymbol{\sigma}_b^i\right)\right)\right\|\\ &\leq 16\left\|\left(\mathbf{G}_i\left(\boldsymbol{\sigma}_b^i\right)\right)\right\|\leq 8.\end{aligned} \tag{18}$$

Consequently, using inequalities (17) and (18), it yields that the lumped fault $(\mathbf{T}_i(\boldsymbol{\sigma}_b^i))^{\mathrm{T}}\mathbf{u}_{\text{fault}_i}$ in (11) is bounded by

$$\left\|\left(\mathbf{T}_i\left(\boldsymbol{\sigma}_b^i\right)\right)^{\mathrm{T}}\mathbf{u}_{\text{fault}_i}\right\|\leq\left\|\left(\mathbf{T}_i\left(\boldsymbol{\sigma}_b^i\right)\right)^{\mathrm{T}}\right\|\left\|\mathbf{u}_{\text{fault}_i}\right\|\leq 8\gamma_i. \tag{19}$$

To this end, the upper bounds of the thruster fault $\mathbf{u}_{\text{fault}_i}$ and the lumped fault $(\mathbf{T}_i(\boldsymbol{\sigma}_b^i))^{\mathrm{T}}\mathbf{u}_{\text{fault}_i}$ are thus successfully analyzed. Thereby, the proof is completed here. □

3.2. Fault Reconstruction Approach Design. For the transformed attitude dynamics (11), the following change of coordinates will be firstly introduced:

$$\mathbf{x}_{i_1}=\boldsymbol{\sigma}_b^i, \tag{20}$$

$$\mathbf{x}_{i_2}=\dot{\boldsymbol{\sigma}}_b^i, \tag{21}$$

$$\mathbf{y}_{i_1}=\left(\mathbf{T}_i\left(\boldsymbol{\sigma}_b^i\right)\right)^{\mathrm{T}}\mathbf{u}_{\text{fault}_i}. \tag{22}$$

Then, it can rewrite (11) as the following nonlinear system:

$$\dot{\mathbf{x}}_{i_1}=\mathbf{x}_{i_2}, \tag{23}$$

$$\bar{\mathbf{J}}_i\left(\mathbf{x}_{i_1}\right)\dot{\mathbf{x}}_{i_2}=-\mathbf{C}_i\left(\mathbf{x}_{i_1},\mathbf{x}_{i_2}\right)\mathbf{x}_{i_2}+\left(\mathbf{T}_i\left(\boldsymbol{\sigma}_b^i\right)\right)^{\mathrm{T}}\mathbf{u}_{\text{nor}_i}+\mathbf{y}_{i_1}. \tag{24}$$

Before presenting the details of the sliding mode observer-based fault reconstruction approach, the following lemma is firstly presented; it is useful for proving the stability of the proposed observer.

Lemma 2 (see [39]). *Suppose that there exists a continuous positive-definite function $V_1(t)$ satisfying the following inequality:*

$$\dot{V}_1(t)+\alpha_1V_1(t)+\delta_1V_1^{\kappa}(t)\leq 0,\quad\forall t\geq 0. \tag{25}$$

Then, $V_1(t)$ will converge to zero in a finite-time $t_f\in\Re$,

$$t_f\leq\frac{1}{\alpha_1(1+\kappa)}\ln\frac{\alpha_1V_1^{1-\kappa}(0)+\delta_1}{\delta_1}, \tag{26}$$

where $\alpha_1>0$, $\delta_1>0$, and $0<\kappa<1$ are scalars.

To accomplish the reconstruction of thruster fault in finite time, a sliding mode observer will be developed. The sliding surface is given as follows for each spacecraft:

$$\mathbf{M}_i=\mathbf{x}_{i_2}-\boldsymbol{\xi}_i. \tag{27}$$

In (27), $\boldsymbol{\xi}_i$ is designed as follows:

$$\begin{aligned}\dot{\boldsymbol{\xi}}_i=\bar{\mathbf{J}}_i^{-1}\left(\mathbf{x}_{i_1}\right)\Big[&K_i\mathbf{M}_i+\mu_i\mathbf{sgn}\left(\mathbf{M}_i\right)+\varepsilon_i\mathbf{M}_i^{\pi_i/\vartheta_i}\\ &+\left(\mathbf{T}_i\left(\boldsymbol{\sigma}_b^i\right)\right)^{\mathrm{T}}\mathbf{u}_{\text{nor}_i}-\mathbf{C}_i\left(\mathbf{x}_{i_1},\mathbf{x}_{i_2}\right)\boldsymbol{\xi}_i\Big],\end{aligned} \tag{28}$$

where $K_i>0$, $\mu_i>0$, and $\varepsilon_i>0$ are constants. π_i and ϑ_i are odd positive integers such that $\pi_i<\vartheta_i$.

Theorem 3. *Consider the faulty distributed coordinate spacecraft attitude control system; for each spacecraft, design the following sliding mode-base observer $\widehat{\mathbf{y}}_{i_1}$ to reconstruct the lumped fault $\mathbf{y}_{i_1}$:*

$$\widehat{\mathbf{y}}_{i_1}=K_i\mathbf{M}_i+\mu_i\mathbf{sgn}\left(\mathbf{M}_i\right)+\varepsilon_i\mathbf{M}_i^{\pi_i/\vartheta_i}+\mathbf{C}_i\left(\mathbf{x}_{i_1},\mathbf{x}_{i_2}\right)\mathbf{M}_i. \tag{29}$$

If the observer gain μ_i is chosen such that

$$\mu_i > 8\gamma_i \tag{30}$$

then $\hat{\mathbf{y}}_{i_1}$ will converge to $\mathbf{y}_{i_1}$ with finite-time convergence, and its reconstruction error $\tilde{\mathbf{y}}_{i_1} = \hat{\mathbf{y}}_{i_1} - \mathbf{y}_{i_1}$ will converge to zero in finite time.

Proof. Choose a Lyapunov candidate function as $V_i = (1/2)\mathbf{M}_i^{\mathrm{T}}\bar{\mathbf{J}}_i(\mathbf{x}_{i_1})\mathbf{M}_i$. Then, differentiating both sides of V_i, it leads to

$$\begin{aligned}\dot{V}_i &= \frac{1}{2}\mathbf{M}_i^{\mathrm{T}}\dot{\bar{\mathbf{J}}}_i(\mathbf{x}_{i_1})\dot{\mathbf{M}}_i + \mathbf{M}_i^{\mathrm{T}}\bar{\mathbf{J}}_i(\mathbf{x}_{i_1})\dot{\mathbf{M}}_i \\ &= \frac{1}{2}\mathbf{M}_i^{\mathrm{T}}\dot{\bar{\mathbf{J}}}_i(\mathbf{x}_{i_1})\dot{\mathbf{M}}_i + \mathbf{M}_i^{\mathrm{T}}\bar{\mathbf{J}}_i(\mathbf{x}_{i_1})\left(\dot{\mathbf{x}}_{i_2} - \dot{\boldsymbol{\xi}}_i\right).\end{aligned} \tag{31}$$

Using (27) and Property 3, inserting (24) into (31) yields

$$\begin{aligned}\dot{V}_i &= -\mathbf{M}_i^{\mathrm{T}}\Big[K_i\mathbf{M}_i + \mu_i\mathbf{sgn}(\mathbf{M}_i) + \varepsilon_i\mathbf{M}_i^{\pi_i/\vartheta_i} \\ &\qquad + \left(\mathbf{T}_i\left(\boldsymbol{\sigma}_b^i\right)\right)^{\mathrm{T}}\mathbf{u}_{\mathrm{nor}_i} - \mathbf{C}_i(\mathbf{x}_{i_1},\mathbf{x}_{i_2})\boldsymbol{\xi}_i\Big] \\ &\quad + \frac{1}{2}\mathbf{M}_i^{\mathrm{T}}\dot{\bar{\mathbf{J}}}_i(\mathbf{x}_{i_1})\mathbf{M}_i \\ &\quad + \mathbf{M}_i^{\mathrm{T}}\left[-\mathbf{C}_i(\mathbf{x}_{i_1},\mathbf{x}_{i_2})\mathbf{x}_{i_2} + \left(\mathbf{T}_i\left(\boldsymbol{\sigma}_b^i\right)\right)^{\mathrm{T}}\mathbf{u}_{\mathrm{nor}_i} + \mathbf{y}_{i_1}\right] \\ &= -K_i\mathbf{M}_i^{\mathrm{T}}\mathbf{M}_i - \mu_i\mathbf{M}_i^{\mathrm{T}}\mathbf{sgn}(\mathbf{M}_i) \\ &\quad - \varepsilon_i\mathbf{M}_i^{(\pi_i+\vartheta_i)/\vartheta_i} + \mathbf{M}_i^{\mathrm{T}}\mathbf{y}_{i_1}.\end{aligned} \tag{32}$$

From Theorem 1, it is known that $\|(\mathbf{T}_i(\boldsymbol{\sigma}_b^i))^{\mathrm{T}}\mathbf{u}_{\mathrm{fault}_i}\| \le 8\gamma_i$; that is, $\|\mathbf{y}_{i_1}\| \le 8\gamma_i$. Then, with the choice of the observer gain in (30), it leaves (32) as

$$\begin{aligned}\dot{V}_i &\le -K_i\mathbf{M}_i^{\mathrm{T}}\mathbf{M}_i - \varepsilon_i\mathbf{M}_i^{(\pi_i+\vartheta_i)/\vartheta_i} \\ &\le -2K_iV_i - \varepsilon_i 2^{(\pi_i+\vartheta_i)/2\vartheta_i}(V_i)^{(\pi_i+\vartheta_i)/2\vartheta_i}.\end{aligned} \tag{33}$$

Consequently, using Lemma 2, it can be obtained from (33) that $V_i(t) \equiv 0$ for all $t \ge t_{f_i}$:

$$\begin{aligned}t_f &\le \frac{1}{2K_i\left(1 + (\pi_i + \vartheta_i)/2\vartheta_i\right)} \\ &\quad \cdot \ln\frac{2K_iV_i^{(\vartheta_i-\pi_i)/2\vartheta_i}(0) + \varepsilon_i 2^{(\pi_i+\vartheta_i)/2\vartheta_i}}{\varepsilon_i 2^{(\pi_i+\vartheta_i)/2\vartheta_i}}.\end{aligned} \tag{34}$$

At this time, applying the definition of V_i, one has $\mathbf{M}_i(t) \equiv \mathbf{0}$ for all $t \ge t_{f_i}$. Therefore, for all $t \ge t_{f_i}$, it leads to

$$\dot{\mathbf{M}}_i(t) \equiv \mathbf{0}. \tag{35}$$

On the other hand, it follows from the reconstruction error $\tilde{\mathbf{y}}_{i_1}$ that

$$\begin{aligned}\tilde{\mathbf{y}}_{i_1} &= \hat{\mathbf{y}}_{i_1} - \mathbf{y}_{i_1} \\ &= K_i\mathbf{M}_i + \mu_i\mathbf{sgn}(\mathbf{M}_i) + \varepsilon_i\mathbf{M}_i^{\pi_i/\vartheta_i} \\ &\quad + \mathbf{C}_i(\mathbf{x}_{i_1},\mathbf{x}_{i_2})\mathbf{M}_i - \bar{\mathbf{J}}_i(\mathbf{x}_{i_1})\dot{\mathbf{x}}_{i_2} \\ &\quad + \left(\mathbf{T}_i\left(\boldsymbol{\sigma}_b^i\right)\right)^{\mathrm{T}}\mathbf{u}_{\mathrm{nor}_i} - \mathbf{C}_i(\mathbf{x}_{i_1},\mathbf{x}_{i_2})\mathbf{x}_{i_2} \\ &= -\bar{\mathbf{J}}_i(\mathbf{x}_{i_1})\Big[\dot{\mathbf{x}}_{i_2} - \bar{\mathbf{J}}_i^{-1}(\mathbf{x}_{i_1}) \\ &\qquad \cdot \Big(K_i\mathbf{M}_i + \mu_i\mathbf{sgn}(\mathbf{M}_i) + \varepsilon_i\mathbf{M}_i^{\pi_i/\vartheta_i} \\ &\qquad + \left(\mathbf{T}_i\left(\boldsymbol{\sigma}_b^i\right)\right)^{\mathrm{T}}\mathbf{u}_{\mathrm{nor}_i} - \mathbf{C}_i(\mathbf{x}_{i_1},\mathbf{x}_{i_2})\boldsymbol{\xi}_i\Big)\Big] \\ &= -\bar{\mathbf{J}}_i^{-1}(\mathbf{x}_{i_1})\dot{\mathbf{M}}_i.\end{aligned} \tag{36}$$

As a result, it is obtained from (35) and (36) that $\tilde{\mathbf{y}}_{i_1}(t) \equiv 0$ for all $t \ge t_{f_i}$. From this, we can conclude that the lumped fault reconstruction error $\tilde{\mathbf{y}}_{i_1}(t)$ of the proposed sliding mode observer converges to zero within finite time. Thereby the proof is completed here. □

Theorem 4. *For all possible thruster faults in each spacecraft of the considered distributed coordinated attitude system, the fault $\mathbf{u}_{fault_i}$ occurring in the ith spacecraft can be reconstructed by the signal $(\mathbf{G}_i(\boldsymbol{\sigma}_b^i))^{\mathrm{T}}\hat{\mathbf{y}}_{i_1}$ in finite-time t_{f_i}. That is, $\mathbf{u}_{fault_i}(t) \equiv (\mathbf{G}_i(\boldsymbol{\sigma}_b^i))^{\mathrm{T}}\hat{\mathbf{y}}_{i_1}$ for all $t \ge t_{f_i}$.*

Proof. It follows from (22) that

$$\mathbf{u}_{\mathrm{fault}_i} = \left(\mathbf{G}_i\left(\boldsymbol{\sigma}_b^i\right)\right)^{\mathrm{T}}\left(\hat{\mathbf{y}}_{i_1} - \tilde{\mathbf{y}}_{i_1}\right). \tag{37}$$

As stated in Theorem 3, it is seen that $\hat{\mathbf{y}}_{i_1}$ will converge to $\mathbf{y}_{i_1}$ with finite-time convergence. More specifically, it has $\tilde{\mathbf{y}}_{i_1}(t) \equiv 0$ for all $t \ge t_{f_i}$. Hence, it leaves (37)

$$\mathbf{u}_{\mathrm{fault}_i}(t) \equiv \left(\mathbf{G}_i\left(\boldsymbol{\sigma}_b^i\right)\right)^{\mathrm{T}}\hat{\mathbf{y}}_{i_1}, \quad t \ge t_{f_i}, \tag{38}$$

which implies that $\mathbf{u}_{\mathrm{fault}_i}$ can be reconstructed by $(\mathbf{G}_i(\boldsymbol{\sigma}_b^i))^{\mathrm{T}}\hat{\mathbf{y}}_{i_1}$ with zero reconstruction error in a finite-time t_{f_i}. If one defines the reconstruction error between $\mathbf{u}_{\mathrm{fault}_i}$ and $(\mathbf{G}_i(\boldsymbol{\sigma}_b^i))^{\mathrm{T}}\hat{\mathbf{y}}_{i_1}$ as $\mathbf{e}_i(t) = [e_{i1}\ \ e_{i2}\ \ e_{i3}]^{\mathrm{T}}$, then it has $\mathbf{e}_i(t) \equiv 0$ for all $t \ge t_{f_i}$. Hence, the proof of Theorem 3 is completed. □

4. Simulation Results

To illustrate the performance of the proposed fault reconstruction approach, three spacecrafts in a distributed coordinate configuration are considered in the simulation; that is, $n = 3$. Those spacecrafts' inertia are $\mathbf{J}_1 = \mathrm{diag}([20\ \ 17\ \ 15]^{\mathrm{T}})$, $\mathbf{J}_2 = \mathrm{diag}([22.5\ \ 25\ \ 27.5]^{\mathrm{T}})$, and $\mathbf{J}_3 = \mathrm{diag}([27.5\ \ 30\ \ 25.5]^{\mathrm{T}})$, respectively. Each spacecraft mounts

Table 1: Thruster's layout ($i = 1, 2, \ldots, n$ and $j = 1, 2, \ldots, 12$).

Thruster number	Position in $\mathcal{F}_b^i$ of the attitude control system			Orientation in $\mathcal{F}_b^i$	
	r_{xij}^0 (mm)	r_{yij}^0 (mm)	r_{zij}^0 (mm)	α_{ij}^0 (deg)	β_{ij}^0 (deg)
#T_1	700	0	0	0	−90
#T_2	700	0	0	0	90
#T_3	−700	0	0	0	−90
#T_4	−700	0	0	0	90
#T_5	0	800	0	−90	90
#T_6	0	800	0	90	90
#T_7	0	−800	0	−90	90
#T_8	0	−800	0	90	90
#T_9	0	0	−700	0	0
#T_{10}	0	0	−700	0	180
#T_{11}	0	0	700	0	0
#T_{12}	0	0	700	0	180

twelve thrusters to perform large-angle attitude maneuver; that is, $N_i = 12$, $i = 1, 2, \ldots, n$. For the ith spacecraft, those twelve thrusters are assumed to be distributed symmetrically on three axes of $\mathcal{F}_b^i$, and the propulsion force is perpendicular to the corresponding axis such that the distribution matrix can be simply determined by the distance $\mathbf{r}_{ij}^0$, $j = 1, 2, \ldots, 12$. The mechanical configuration of thrusters is illustrated in Figure 3. The thrusters are commanded in pulse delay and duration, providing a nominal force F of 0.8 N. The nominal positions (i.e., the point of application of the main thrust force) and orientation (azimuth and elevation) of thrusters are reported in Table 1.

In simulation, the initial conditions of the ith spacecraft with the quaternion and the angular velocity are $\boldsymbol{\sigma}_b^1(0) = [0.288 \;\; -0.143 \;\; -0.020]^{\mathrm{T}}$, $\boldsymbol{\sigma}_b^2(0) = [0.4 \;\; 0.3 \;\; -0.15]^{\mathrm{T}}$, $\boldsymbol{\sigma}_b^3(0) = [-0.65 \;\; 0.23 \;\; 0.45]^{\mathrm{T}}$, and $\boldsymbol{\omega}_b^i(0) = [0 \;\; 0 \;\; 0]^{\mathrm{T}}$ rad/sec, respectively. The parameters for the proposed reconstruction scheme are chosen as $K_i = 0.75$, $\varepsilon_i = 1.5$, $\mu_i = 14.5$, $\pi_i = 13$, and $\vartheta_i = 19$, $i = 1, 2, \ldots, n$.

4.1. Thruster Faults. To investigate the fault reconstruction performance of the proposed scheme, the following thrust magnitude error scenarios and thruster's misalignments are introduced and simulated.

(i) A random misalignment is added each time the thruster is switched on, which corresponds to a random thrust misalignment. The model for this misalignment is a Gaussian noise on both the azimuth and the elevation angles (i.e., $\Delta\alpha_{ij}$ and $\Delta\beta_{ij}$, resp.; $i = 1, 2, \ldots, n$ and $j = 1, 2, \ldots, 12$), each with standard deviation of 2.5% (Figure 1).

(ii) Supplementary position of thruster $\Delta\mathbf{r}_{ij}$, $i = 1, 2, \ldots, n$, $j = 1, 2, \ldots, 12$, is modeled as a Gaussian noise, each with standard deviation of 4%.

(iii) For all the twelve thrusters in each spacecraft, the force delivered is modeled with a nominal value signal of $F = 0.8$ N corrupted by a zero-mean Gaussian noise with a constant standard deviation of 0.35 N.

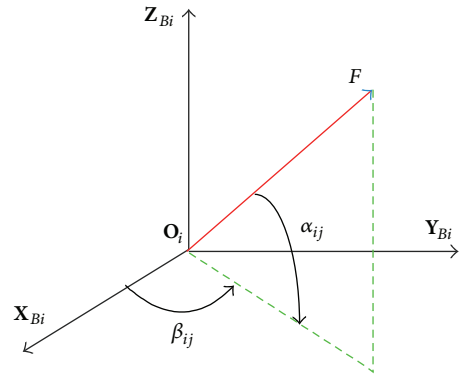

Figure 1: Azimuth and elevation of the jth thruster in the ith spacecraft.

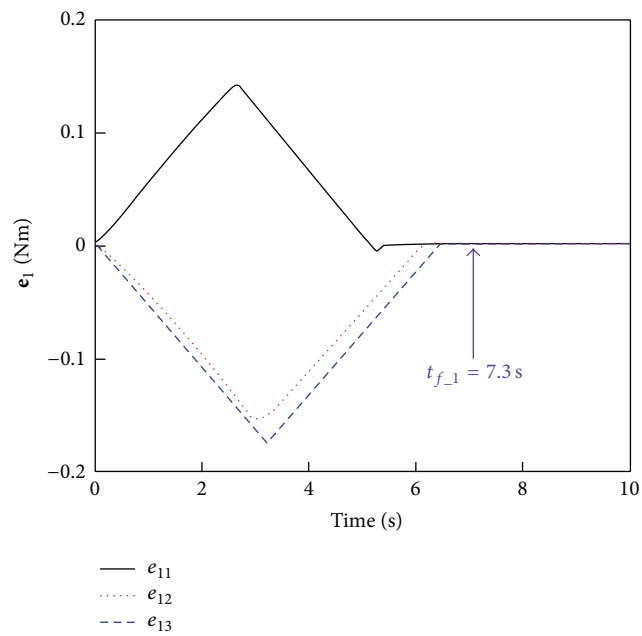

Figure 2: The reconstruction error $\mathbf{e}_1$.

4.2. Control Performance. When the proposed reconstruction approach for thruster faults is applied to each spacecraft of the distributed coordinate attitude system, the sliding mode observer-based reconstruction scheme leads to a good reconstruction performance. Figure 2 illustrates the error between $\mathbf{u}_{\text{fault_1}}$ and its reconstruction value $(\mathbf{G}_1(\boldsymbol{\sigma}_b^1))^{\mathrm{T}}\hat{\mathbf{y}}_{1_1}$. It is seen that the reconstruction error $\mathbf{e}_1(t)$ converges to zero in a finite-time $t_{f_1} = 7.3$ seconds. For the 2nd spacecraft, it is obtained from the reconstruction approach that the reconstruction error $\mathbf{e}_2(t)$ is finite-time stable, and its converging time is $t_{f_2} = 17.5$ seconds, as we can see in Figure 3. Moreover, it is shown in Figure 4 that the reconstruction approach is able to reconstruct the faults occurring in the third spacecraft. This reconstruction is accomplished

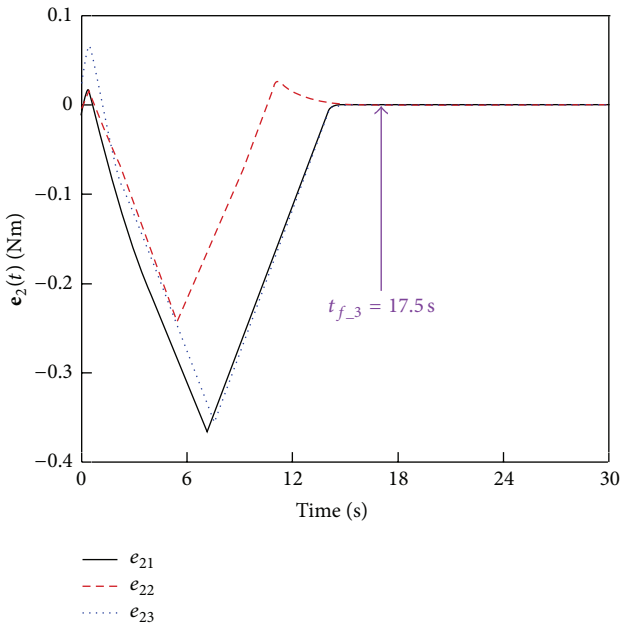

Figure 3: The reconstruction error $\mathbf{e}_2$.

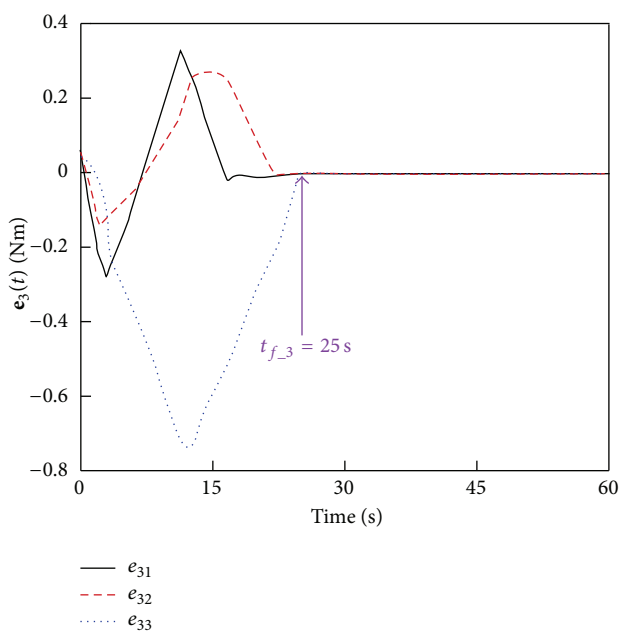

Figure 4: The reconstruction error $\mathbf{e}_3$ for the third spacecraft.

in a finite-time $t_{f_3} = 25$ seconds. From those results, it is seen that a faster reconstruction of the thruster faults in the considered distributed coordinate spacecraft attitude control system is achieved.

5. Conclusions and Future Work

A sliding mode observer-based fault reconstruction scheme was proposed for each agent in a distributed coordinated spacecraft attitude control system. Thruster faults were investigated. The proposed reconstruction approach guaranteed that all possible thruster faults were reconstructed with zero reconstruction error. Moreover, it was able to accomplish a faster fault reconstruction, because it was capable of making the reconstructed signal converge to the actual fault within finite time. By choosing the observer gains, such finite time can be tuned by the designer. If the spacecraft was only under the effect of external disturbance, then this approach can also reconstruct the magnitude of external disturbance with finite-time convergence. This was another feature of this approach. However, this work only carried out fault reconstruction for distributed coordinate spacecraft system; the attitude controller design was not done. As some of future works, reliable attitude controller should be carried out by using the reconstructed fault signals obtained from the reconstruction approach in this work.

Conflict of Interests

The authors declare that there is no conflict of interests regarding the publication of this paper.

References

[1] R. Burns, C. A. McLaughlin, J. Leitner, and M. Martin, "TechSat 21: Formation design, control, and simulation," in *Proceedings of the IEEE Aerospace Conference*, pp. 19–25, March 2000.

[2] H. J. Yang, X. You, Y. Q. Xiu, and H. B. Li, "Adaptive control for attitude synchronisation of spacecraft formation via extended state observer," *IET Control Theory & Applications*, vol. 8, no. 18, pp. 2171–2185, 2014.

[3] L. Zhao and Y. M. Jia, "Decentralized adaptive attitude synchronization control for spacecraft formation using nonsingular fast terminal sliding mode," *Nonlinear Dynamics*, vol. 78, no. 4, pp. 2779–2794, 2014.

[4] H. J. Yang, X. You, Y. Q. Xia, and Z. X. Liu, "Nonlinear attitude tracking control for spacecraft formation with multiple delays," *Advances in Space Research*, vol. 54, pp. 759–769, 2014.

[5] R. Kristiansen, E. I. Grøtli, P. J. Nicklasson, and J. T. Gravdahl, "A model of relative translation and rotation in leader-follower spacecraft formations," *Modeling, Identification and Control*, vol. 28, no. 1, pp. 3–13, 2007.

[6] J. Li and K. D. Kumar, "Decentralized fault-tolerant control for satellite attitude synchronization," *IEEE Transactions on Fuzzy Systems*, vol. 20, no. 3, pp. 572–586, 2012.

[7] B. Wu, D. Wang, and E. K. Poh, "Decentralized sliding-mode control for attitude synchronization in spacecraft formation," *International Journal of Robust and Nonlinear Control*, vol. 23, no. 11, pp. 1183–1197, 2013.

[8] B.-L. Cong, X.-D. Liu, and Z. Chen, "Distributed attitude synchronization of formation flying via consensus-based virtual structure," *Acta Astronautica*, vol. 68, no. 11-12, pp. 1973–1986, 2011.

[9] R. W. Beard, J. Lawton, and F. Y. Hadaegh, "A coordination architecture for spacecraft formation control," *IEEE Transactions on Control Systems Technology*, vol. 9, no. 6, pp. 777–790, 2001.

[10] H. Z. Liang, J. Y. Wang, and Z. W. Sun, "Robust decentralized coordinated attitude control of spacecraft formation," *Acta Astronautica*, vol. 69, no. 5-6, pp. 280–288, 2011.

[11] J. Zhou, Q. Hu, and M. I. Friswell, "Decentralized finite time attitude synchronization control of satellite formation flying," *Journal of Guidance, Control, and Dynamics*, vol. 36, no. 1, pp. 185–195, 2013.

[12] M. Tafazoli, "A study of on-orbit spacecraft failures," *Acta Astronautica*, vol. 64, no. 2-3, pp. 195–205, 2009.

[13] Y. W. Liang, S. D. Xu, and C. L. Tsai, "Study of VSC reliable designs with application to spacecraft attitude stabilization," *IEEE Transactions on Control Systems Technology*, vol. 15, no. 2, pp. 332–338, 2007.

[14] W. C. Cai, X. H. Liao, and Y. D. Song, "Indirect robust adaptive fault-tolerant control for attitude tracking of spacecraft," *Journal of Guidance, Control, and Dynamics*, vol. 31, no. 5, pp. 1456–1463, 2008.

[15] S. Varma and K. D. Kumar, "Fault tolerant satellite attitude control using solar radiation pressure based on nonlinear adaptive sliding mode," *Acta Astronautica*, vol. 66, no. 3-4, pp. 486–500, 2010.

[16] Godard and K. D. Kumar, "Fault tolerant reconfigurable satellite formations using adaptive variable structure techniques," *Journal of Guidance, Control, and Dynamics*, vol. 33, no. 3, pp. 969–984, 2010.

[17] B. Xiao, Q. L. Hu, and Y. M. Zhang, "Adaptive sliding mode fault tolerant attitude tracking control for flexible spacecraft under actuator saturation," *IEEE Transactions on Control Systems Technology*, vol. 20, no. 6, pp. 1605–1612, 2012.

[18] R. Muradore and P. Fiorini, "A PLS-based statistical approach for fault detection and isolation of robotic manipulators," *IEEE Transactions on Industrial Electronics*, vol. 59, no. 8, pp. 3167–3175, 2012.

[19] X.-G. Yan and C. Edwards, "Adaptive sliding-mode-observer-based fault reconstruction for nonlinear systems with parametric uncertainties," *IEEE Transactions on Industrial Electronics*, vol. 55, no. 11, pp. 4029–4036, 2008.

[20] S. Yin, S. Ding, X. Xie, and H. Huo, "A review on basic data-driven approaches for industrial process monitoring," *IEEE Transactions on Industrial Electronics*, vol. 61, no. 11, pp. 6418–6428, 2014.

[21] S. Yin, X. Li, H. Gao, and O. Kaynak, "Data-based techniques focused on modern industry: an 14 overview," *IEEE Transactions on Industrial Electronics*, vol. 62, no. 1, pp. 657–667, 2015.

[22] Z. Q. Li, L. Ma, and K. Khorasani, "A dynamic neural network-based reaction wheel fault diagnosis for satellites," in *Proceedings of the International Joint Conference on Neural Networks (IJCNN '06)*, pp. 3714–3721, Vancouver, BC, Canada, July 2006.

[23] T. Jiang and K. Khorasani, "A fault detection, isolation and reconstruction strategy for a satellite's attitude control subsystem with redundant reaction wheels," in *Proceedings of the IEEE International Conference on Systems, Man, and Cybernetics (SMC '07)*, pp. 3146–3152, Montreal, Canada, October 2007.

[24] B. Chen and S. Nagarajaiah, "Linear-matrix-inequality-based robust fault detection and isolation using the eigenstructure assignment method," *Journal of Guidance, Control, and Dynamics*, vol. 30, no. 6, pp. 1831–1835, 2007.

[25] Q. Hou, Y. H. Cheng, N. Y. Lu, and B. Jiang, "Study on FDD and FTC of satellite attitude control system based on the effectiveness factor," in *Proceedings of the 2nd International Symposium on Systems and Control in Aerospace and Astronautics (ISSCAA '08)*, pp. 1096–1101, Shenzhen, China, December 2008.

[26] D. Henry, "Fault diagnosis of microscope satellite thrusters using H_∞/H_- filters," *Journal of Guidance, Control, and Dynamics*, vol. 31, no. 3, pp. 699–711, 2008.

[27] W. R. Williamson, J. L. Speyer, V. T. Dang, and J. Sharp, "Fault detection and isolation for deep space satellites," *Journal of Guidance, Control, and Dynamics*, vol. 32, no. 5, pp. 1570–1584, 2009.

[28] R. J. Patton, F. J. Uppal, S. Simani, and B. Polle, "Robust FDI applied to thruster faults of a satellite system," *Control Engineering Practice*, vol. 18, no. 9, pp. 1093–1109, 2010.

[29] I. Nagesh and C. Edwards, "A sliding mode observer based FDI scheme for a nonlinear satellite systems," in *Proceedings of the 20th IEEE International Conference on Control Applications (CCA '11)*, pp. 159–164, Denver, Colo, USA, September 2011.

[30] I. Nagesh and C. Edwards, "A sliding mode observer based sensor fault detection and isolation scheme for a nonlinear satellite system," in *Proceedings of the 12th International Workshop on Variable Structure Systems (VSS '12)*, pp. 248–253, Mumbai, India, January 2012.

[31] H. Yoon and P. Tsiotras, "Adaptive spacecraft attitude tracking control with actuator uncertainties," in *Proceedings of the AIAA Guidance, Navigation, and Control Conference*, pp. 6392–6404, San Francisco, Calif, USA, August 2005.

[32] S. K. Scarritt, "Nonlinear model reference adaptive control for satellite attitude tracking," in *Proceedings of the AIAA Guidance, Navigatoin and Control Conference and Exhibit*, Honolulu, Hawaii, USA, August 2008.

[33] A. M. Fosbury and C. K. Nebelecky, "Spacecraft actuator alignment estimation," in *Proceedings of the AIAA Guidance, Navigation, and Control Conference*, Chicago, Ill, USA, August 2009.

[34] H.-C. Lim and H. Bang, "Adaptive control for satellite formation flying under thrust misalignment," *Acta Astronautica*, vol. 65, no. 1-2, pp. 112–122, 2009.

[35] J. L. Crassidis and F. L. Markley, "Sliding mode control using modified Rodrigues parameters," *Journal of Guidance, Control, and Dynamics*, vol. 19, no. 6, pp. 1381–1383, 1996.

[36] M. J. Sidi, *Spacecraft Dynamics and Control*, Cambridge University Press, Cambridge, Mass, USA, 1997.

[37] A. Valdes and K. Khorasani, "A pulsed plasma thruster fault detection and isolation strategy for formation flying of satellites," *Applied Soft Computing Journal*, vol. 10, no. 3, pp. 746–758, 2010.

[38] B. Xiao, Q. Hu, W. Singhose, and X. Huo, "Reaction wheel fault compensation and disturbance rejection for spacecraft attitude tracking," *Journal of Guidance, Control, and Dynamics*, vol. 36, no. 6, pp. 1565–1575, 2013.

[39] M. Chen, Q.-X. Wu, and R.-X. Cui, "Terminal sliding mode tracking control for a class of SISO uncertain nonlinear systems," *ISA Transactions*, vol. 52, no. 2, pp. 198–206, 2013.

Hindawi Publishing Corporation
Mathematical Problems in Engineering
Volume 2015, Article ID 461513, 10 pages
http://dx.doi.org/10.1155/2015/461513

Research Article

A Simulation Perspective: Error Analysis in the Distributed Simulation of Continuous System

Yao-fei Ma and Xiao Song

School of Automation Science and Electrical Engineering, Beihang University, Beijing, China

Correspondence should be addressed to Yao-fei Ma; mayaofeibuaa@163.com

Received 8 January 2015; Revised 8 April 2015; Accepted 15 April 2015

Academic Editor: Yun-Bo Zhao

Copyright © 2015 Y.-f. Ma and X. Song. This is an open access article distributed under the Creative Commons Attribution License, which permits unrestricted use, distribution, and reproduction in any medium, provided the original work is properly cited.

To construct a corresponding distributed system from a continuous system, the most convenient way is to partition the system into parts according to its topology and deploy the parts on separated nodes directly. However, system error will be introduced during this process because the computing pattern is changed from the sequential to the parallel. In this paper, the mathematical expression of the introduced error is studied. A theorem is proposed to prove that a distributed system preserving the stability property of the continuous system can be found if the system error is limited to be small enough. Then, the compositions of the system error are analyzed one by one and the complete expression is deduced, where the advancing step T in distributed environment is one of the key factors associated. At last, the general steps to determine the step T are given. The significance of this study lies in the fact that the maximum T can be calculated without exceeding the expected error threshold, and a larger T can reduce the simulation cost effectively without causing too much performance degradation compared to the original continuous system.

1. Introduction

Engineering problems involve dealing with physical systems. Since most physical laws are described by differential equations, simulation in engineering is in fact related to numerical resolution of differential equations. This is called continuous system simulation and even the components (i.e., the subsystems or submodels) of it are generally described in time discretization manner [1].

The large engineering system has sustained requirement on distributed simulation for two reasons. First, the continuous growth on system scale and complexity results in intense demand on computing capacity, which can be mitigated in distributed environment by scattering the computing load to networked nodes. Second, the system itself is sometimes geographically fragmented; thus, the distributed structure is needed to be consistent with its topology. Except those constructed in distributed manner from scratch, there are still many classic continuous systems that were constructed in the nondistributed way, in that the system was designed and tested without considering the possible scenario of distributed simulation. The demand to transform such system into the distributed one emerges.

The classic continuous system is characterized by computing its components in pipeline, where a computing sequence is set up and the components are computed one by one within a step; the sequence is determined by the component's input/output characteristics and the data dependence. By contrast, the computation on each component in the distributed environment will start simultaneously and advance in a parallel manner; the updating data is exchanged periodically through the network for synchronization.

The difference between two computing patterns can be formulized as follows. Suppose a system containing n components: $M = \{m_1, m_2, \ldots, m_n\}$. A single component can be represented as $m_i = \{x_i, y_i, f_i\}$, where x_i is the input, y_i is the output, and f_i is the model function. We have $y_i = f_i(x_i)$. Assuming a computing sequence $Q = \{q_1, \ldots, q_i, \ldots, q_n\}$ has been determined in the nondistributed environment, the pipeline computing within one step can be described as

$$x_{q_1}^{k\times h} = I^{k\times h},$$

$$y_{q_1}^{k\times h} = f_{q_1}\left(x_{q_1}^{k\times h}\right),$$

$$x_{q_i}^{k\times h} = y_{q_{i-1}}^{k\times h},$$

$$y_{q_i}^{k\times h} = f_{q_i}\left(x_{q_i}^{k\times h}\right) = f_{q_i}\left(y_{q_{i-1}}^{k\times h}\right), \quad i = 2, \ldots, n, \tag{1}$$

where $k = 0, 1, 2, \ldots, h$ is the step size and the subscript q_i refers to the index in Q. In the pipeline computing, the first component is assumed to get the input from a signal source I, and the others get inputs following the data dependence among themselves.

By contrast, the one-step computing in distributed environment can be described as

$$\begin{aligned} x_1^{k\times T} &= I^{k\times T}, \\ y_1^{k\times T} &= f_i\left(x_1^{k\times T}\right), \\ x_i^{k\times T} &= y_{i-1}^{(k-1)\times T}, \\ y_i^{k\times T} &= f_i\left(x_i^{k\times T}\right) = f_i\left(y_{i-1}^{(k-1)\times T}\right), \\ & \qquad i = 2, \ldots, n, \end{aligned} \tag{2}$$

where T is the advancing step of the distributed system. It should be noted that the computing sequence is not held any more in this case.

There are two differences comparing these two computing processes. First, the computing is synchronous in the nondistributed environment. For each component, the input is updated to time step k firstly, and then the output at k is computed (the data dependence among components is assumed to be consistent with the computing sequence). On the other hand, the computation is parallel in the distributed environment and each component starts simultaneously. The input of a component will still hold the value of step $(k - 1)$ when the output at k needs to be computed. Second, the advancing steps of two environments, h and T, may be different. In the nondistributed environment, h is determined by the equation solver; either fixed or variable step is employed. However, the determination of T needs to consider the bandwidth of the underlying network, signal frequency, human perception limitation, and so forth. It is often the case where the whole system advances with a fixed T and $T \geq h$.

A formal approach capable of partitioning a system into parallel parts and properly handling the above two issues is the key to build a distributed simulation from a nondistributed one. This problem, denoted as the *Partitioning Problem*, was early studied in the simulation of complex mechanical systems [2, 3] and then became a research focus in the field of discrete event simulation [2, 4, 5] and the decentralized, large-scale control system [6, 7]. However, the proposed approaches all involved extra efforts to reformulize or reengineer the simulated system and did not consider the possible difference on h and T either. These drawbacks set up barriers to apply these approaches broadly.

In [4], anovel partitioning approach is proposed using the system's topology. This approach is easy to perform since most classic simulations have block-diagram structures, but it is "lossy" because the disorder of the component's input/output data cannot be avoided, thus leading to the error on state trajectory of the resulting distributed system. To reduce the error, a portioning rule was proposed to eliminate the possible cumulative delays caused by improper partitioning, which contribute a lot to the overall error.

This paper will study the mathematical expression of this error. The correlation between the error and the advancing step T in distributed environment is revealed. Then, a maximum T can be calculated according to the error threshold specified by the system engineer. The significance to find the maximum T lies in the fact that a larger T will improve the parallelism of the partitioned system by reducing the synchronization frequency between nodes, without causing too much performance degradation at the same time.

2. Literature Review

The *Partitioning Problem* was early studied in the coupled problem [2, 5] of complex mechanical system simulation, where the fluids, thermal, control, and structure subsystems interacted with each other and formed multi-physical-field system [8]. The partitioning is applied to decompose such system into partitions with physical or computational considerations. The resulting system could separately advance in time over each partition, thus gained high simulation efficiency. However, these studies were focused on the finite element analysis, not for general purpose simulation.

The *Partitioning Problem* is also critical to build the decentralized, large-scale control system [6, 7]. A graph-based approach was employed in that the system states were connected as vertexes and the coupling strength (measured by weight factor) between any two of them was evaluated. Small weight connections were more likely to form the partitioning edge by which the system was split into relative independent parts. Another methodwas to use the delay differential equations [9, 10] to describe the dynamic of the distributed system. Networked control scheme [11] was constructed to obtain the convergence and stability in control of the system. However, this approach focuses on the influence of signal delay associated with network latency, rather than the errors caused by the change of computing pattern. In our opinion, such errors will still exist even though the underlying network is perfect and has no delay.

In the Modeling and Simulation (M&S) domain, DEVS (Discrete Event System Specification) theory casts light into the solving of *Partitioning Problem*. The basic idea was to transform a continuous system into the DEVS form by quantizing the system states. A DEVS system is comprised of a set of connected components (called "atomic model" or "coupled model"). The output of each component will hold unchanged until the values of the states it maintained exceed some predefined quantized level. As a result, the time driving continuous system is transformed into an event driving system; thus, it can be decoupled and partitioned easily [12–14]. The transformed system is suitable for asynchronous, distributed environment in nature; however, the "illegitimacy" phenomenon, where the states may transit for unlimited times within a limited period, often causes the simulation to fail to converge correctly.

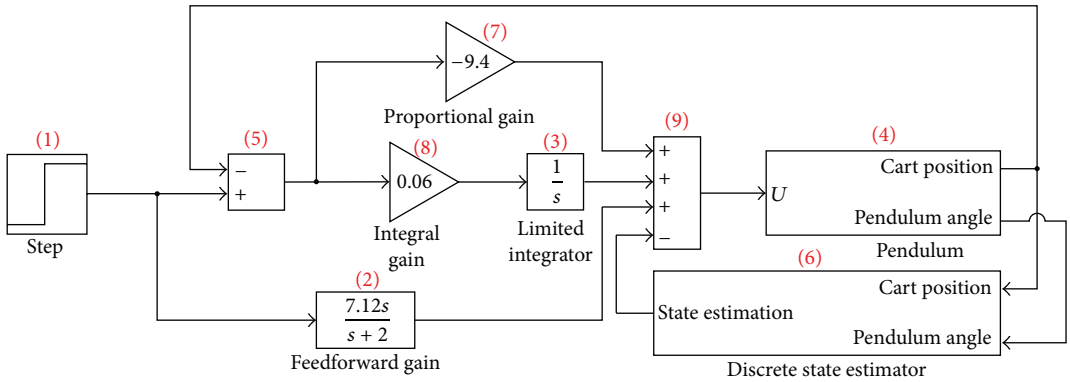

Figure 1: An inverted pendulum system. The states are "cart position" and "pendulum angle." A computing sequence is maintained (indicated by red numbers) in the nondistributed environment.

As an extension of DEVS, the QSS approach [15–17] was proposed to resolve the "illegitimacy" problem by using a special "hysteretic quantization" method, where the output of each component (or model, as called in DEVS system) will not transit to the next quantization level during its descending period until the change has exceeded certain threshold. QSS provides a general approach for the Partitioning Problem since each QSS model interacts with discrete, states updating events. However, the QSS model needs to be particularly designed to allow states transiting between quantization levels. The changes of states are triggered by unpredicted threshold crossing events in QSS. In other words, the advancing "step" of QSS system is unpredicted and time-varying. This characteristic makes QSS unsuitable for applications such as the Hardware-In-the-Loop (HIL) or Man-In-the-Loop (MIL) simulation, where the system has to advance with some fixed step T to align the hardware's working frequency or to take care of the needs of human perception.

The approaches mentioned above all involve extra efforts to reformulize or reengineer the simulated system. For example, in the graph-based approach, the detailed analysis of the coupling strength between system states requests the engineer to have full knowledge of system dynamics. The QSS approach also needs the system components to be modified to follow the DEVS formulation. Additionally, the possible difference between h and T was not considered either. These drawbacks set up barriers to apply these approaches broadly.

By contrast, the partitioning approach proposed in [4] took the advantage of the system's structure characteristics; no extra work is needed except for decomposing the system according to the data transferring route. However, the incurred error needs to be further studied considering the possible correlation with T.

The content of this paper is organized as follows: in Section 3, the previous work is briefly reviewed. In Section 4, the mathematical expression of the errors is given with theorems. In Section 5, a series of steps are concluded to determine the maximum T.

3. Problem Description

Normally, a continuous system can be represented by a block diagram as Figure 1 shows [4]. This assembling approach based on basic components is commonly seen in the construction of complex system.

The components within this system can be classified into two categories: the Direct-Feed-Through (DFT) component and the Non-Direct-Feed-Through (NDFT) component. The output of DFT component is directly associated with its input; that is, the output at time t is determined by the input at the same time. On the other hand, the output of NDFT component is only determined by its current state and has nothing to do with the current input. It implies that, when computing a DFT component, the components it depends on should be computed firstly to maintain the correct data dependence. The NDFT component has no such requirement since its current output does not rely on the current input.

With parallel computing in the distributed environment, more deductions can be deduced from the foregoing. First, if part of the system deployed on a separate node formed a NDFT component (both DFT and NDFT component can have recursive structure), its output would be delayed for T when updating to other nodes. Second, if two or more DFT components were cascaded, they should not be divided into different nodes; otherwise, the output delay would accumulate from the first DFT component. For example, if the components (5), (7), and (9) in Figure 1 were deployed to different nodes, the output of component (9) will be $3T$ delayed compared to the original system, component (7) is $2T$ delayed, and component (5) is T delayed.

These outcomes have been observed in the experiments of [4], and a partitioning rule was proposed to reduce the accumulated delays. The rule is simple: the distributed DFT component should be avoided; each partitioned part should be ensured to form a NDFT component. The system performance was improved by applying this rule, as shown in Figure 2.

Although the partitioning rule made the distributed system more close to the original continuous system, there

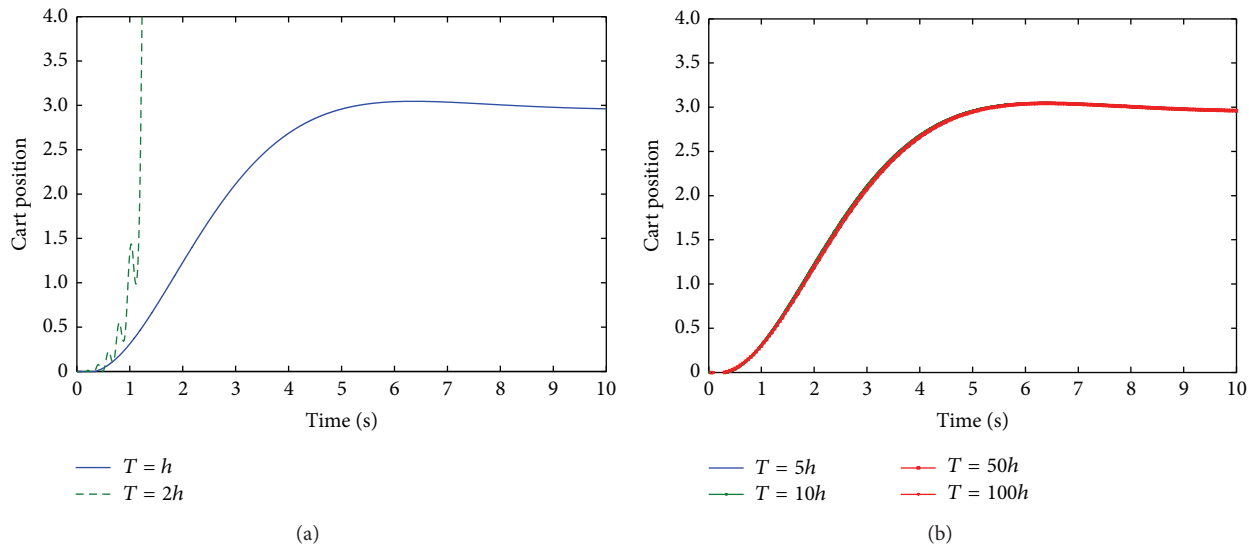

Figure 2: (a) The comparison of the trajectories ("cart position"). (a) The distributed system became unstable when $T = 2h$ without applying the partitioning rule. (b) By applying this rule, the distributed system was stable even when $T = 100h$.

is still one step (T) delay among each node. This delay cannot be eliminated completely because of the parallelism nature of distributed environment, leading to the system error (denoted as ΔE). To understand the influence of T to ΔE, the mathematical expression of ΔE needs to be formulized.

To simplify the analysis of ΔE, an abstract control system containing two components is employed here: one component is the *Controller* and the other is the *Plant*. This system is assumed to be *Asymptotically Stable*. Denoting the original continuous system as CS and the distributed system as DS, the controller and plant can be described as differential equations in CS [15]:

$$\text{Controller (CS)}: \begin{cases} \dot{x_c}(t) = f_c(x_c(t), u_c(t)) \\ y_c(t) = g_c(x_c(t), u_c(t)) \\ u_c = y_p, \end{cases} \tag{3a}$$

$$\text{Plant (CS)}: \begin{cases} \dot{x_p}(t) = f_p(x_p(t), u_p(t)) \\ y_p(t) = g_p(x_p(t)) \\ u_p = y_c, \end{cases} \tag{3b}$$

where $x_c(t)$ and $x_p(t)$ are system states, $y_c(t)$ and $y_p(t)$ are outputs, $u_c(t)$ and $u_p(t)$ are inputs, $f_c(*)$ and $f_p(*)$ are state functions, and $g_c(*)$ and $g_p(*)$ are output functions. In DS, the controller and the plant are described as

$$\text{Controller (DS)}: \begin{cases} \dot{x_c}(t) = f_c(x_c(t), (u_c)_d(t)) \\ y_c(t) = g_c(x_c(t), (u_c)_d(t)) \\ (u_c)_d(t) = (y_p)_d(t-T), \end{cases} \tag{4a}$$

$$\text{Plant (DS)}: \begin{cases} \dot{x_p}(t) = f_p(x_p(t), (u_d)_q(t)) \\ y_p = g_p(x_d(t)) \\ (u_p)_d(t) = (y_c)_d(t-T), \end{cases} \tag{4b}$$

where $(*)_d$ is the discretization operator. This operator indicates the operand updates its value to the external world following the advancing step T, just like being discretized.

Perturbation Analysis is used here to analyze the composition of ΔE. Perturbation analysis treats ΔE as the outcome of disturbances to CS such as the output delay and discretization. The difference between CS and DS can be determined without formulizing the differential equations of both systems and then comparing the eigenvalues. First of all, the DS system is expressed in the form of perturbation equations:

$$\begin{aligned} \dot{x_p} &= f_p(x_p, (g_c)_d(x_c(t-T), g_p(x_p(t-T)))) \\ &= f_p(x_p, g_c(x_c + \Delta x_c, g_p(x_p + \Delta x_p) + \Delta y_p) \\ &\quad + \Delta y_{cd}), \end{aligned} \tag{5a}$$

$$\begin{aligned} \dot{x_c} &= f_c(x_c, (g_p)_d(x_p(t-T))) \\ &= f_c(x_c, g_p(x_p + \Delta x_p) + \Delta y_{pd}), \end{aligned} \tag{5b}$$

where

(i) $\Delta x_c = x_c(t-T) - x_c$, the error of controller state caused by time delay;

(ii) $\Delta x_p = x_p(t-T) - x_p$, the error of plant state caused by time delay;

(iii) $\Delta y_p = g_p(x_p(t-T)) - g_p(x_p)$, the error of plant output caused by time delay;

(iv) $\Delta y_{cd} = (g_c)_d - g_c$, the error of controller output caused by discretization;

(v) $\Delta y_{pd} = (g_p)_d - g_p$, the plant output error caused by discretization.

The system error is represented as

$$\Delta E = \left\| \left(\Delta x_c, \Delta x_p, \Delta y_p, \Delta y_{cd}, \Delta y_{pd} \right) \right\|. \tag{6}$$

To find out the detailed expression of ΔE, a preparation theorem is proposed as follows.

4. The Mathematical Analysis

4.1. A Preparation Theorem. Based on the assumption of *Asymptotically Stable*, the functions of $f_p(*)$, $g_p(*)$, $f_c(*)$, and $g_c(*)$ in (3a), (3b), (4a), and (4b) are further assumed to be *Lipschitz Continuous* over a region D, where D is a nonsaturation region defined by x_p and x_c:

$$\begin{aligned} D = \Big\{ & x_p, x_c \mid x_p \in D_{x_p}, x_c \in D_{x_c}, g_p\left(x_p\right) \\ & \in D_{y_p}, g_c\left(x_c, g_p\left(x_p\right)\right) \in D_{y_c} \Big\}. \end{aligned} \tag{7}$$

For convenience, the time symbol t is omitted unless necessary. D_{x_p} and D_{x_c} are nonsaturation regions for x_p and x_c, respectively, that is, the state spaces of the controller and the plant. D_{y_p} and D_{y_c} are nonsaturation regions for y_p and y_c, respectively, that is, the output spaces of the controller and the plant. With this assumption, a preparation theorem [18] is given.

Theorem 1 (preparation theorem). *For an asymptotically stable CS as shown in (3a) and (3b), if (a) the functions $f(*)$ and $g(*)$ are continuously differentiable and (b) a Lyapunov function V is defined over an open region D containing the original point (assumed to be the equilibrium point), then a DS can be obtained from CS, in that all start positions lying in an arbitrary interior region (denoted as D_1) of D are attracted to another arbitrary interior region (D_2) of D_1 in finite time. D_1 and D_2 are defined by sections of V crossed by two level surfaces.*

This theorem is critical because it guarantees that DS can be derived from a CS given that CS is stable. The assumption that the original point is the equilibrium is easy to be satisfied by translation transformation of the state variables.

Proof. Define an auxiliary function:

$$\begin{aligned} \alpha\left(x, \Delta x_c, \Delta x_p, \Delta y_p, \Delta y_{cd}, \Delta y_{pd}\right) &= \frac{\partial V}{\partial x_p} \\ &\cdot f_p\left(x_p, g_c\left(x_c + \Delta x_c, g_p\left(x_p + \Delta x_p\right) + \Delta y_p\right)\right. \\ &\left. + \Delta y_{cd}\right) + \frac{\partial V}{\partial x_c} \cdot f_c\left(x_c, g_p\left(x_p + \Delta x_p\right) + \Delta y_{pd}\right). \end{aligned} \tag{8}$$

We have

$$\alpha\left(x, 0, 0, 0, 0\right) = \dot{v}(x), \tag{9}$$

where $x = (x_p, x_c)$ and $v(x)$ is the Lyapunov function of CS.

Define the second auxiliary function $\beta(*)$ over a region D_3:

$$\begin{aligned} &\beta\left(\Delta x_c, \Delta x_p, \Delta y_p, \Delta y_{cd}, \Delta y_{pd}\right) \\ &\quad = \sup_{x \in D_3} \left(\alpha\left(x, \Delta x_c, \Delta x_p, \Delta y_p, \Delta y_{cd}, \Delta y_{pd}\right)\right), \end{aligned} \tag{10}$$

where $D_3 = D_2 - D_1$. $\beta(*)$ is continuous since $\alpha(*)$ is continuous. Then, we have

$$\begin{aligned} &\alpha\left(x, \Delta x_c, \Delta x_p, \Delta y_p, \Delta y_{cd}, \Delta y_{pd}\right) \\ &\quad < \beta\left(\Delta x_c, \Delta x_p, \Delta y_p, \Delta y_{cd}, \Delta y_{pd}\right) \end{aligned} \tag{11a}$$

and then

$$\beta\left(0, 0, 0, 0, 0\right) = \sup_{x \in D_3} \left(\alpha\left(x, 0, 0, 0, 0\right)\right) = \sup_{x \in D_3} \left(\dot{v}(x)\right). \tag{11b}$$

A positive real number s can be found since $\dot{v}(x)$ is the negative definition to satisfy:

$$\dot{v}(x) < -s. \tag{12a}$$

Combining (11b), then

$$\beta\left(0, 0, 0, 0, 0\right) < -s. \tag{12b}$$

As a result, a region D_4 can always be found in the vicinity of the origin of $\beta(*)$:

$$\begin{aligned} D_4 = \Big\{ & \left(\Delta x_c, \Delta x_p, \Delta y_p, \Delta y_{cd}, \Delta y_{pd}\right) \mid \\ & \left\| \left(\Delta x_c, \Delta x_p, \Delta y_p, \Delta y_{cd}, \Delta y_{pd}\right) \right\| = \Delta E < \rho \Big\}, \end{aligned} \tag{13}$$

where ρ is a positive real number defining the radius of D_4. Another positive real number s_1 $(0 < s_1 < s)$ can be found to satisfy (14) over D_4:

$$\beta\left(\Delta x_c, \Delta x_p, \Delta y_p, \Delta y_{cd}, \Delta y_{pd}\right) < -s_1. \tag{14}$$

Considering inequality (11a), we have

$$\alpha\left(x, \Delta x_c, \Delta x_p, \Delta y_p, \Delta y_{cd}, \Delta y_{pd}\right) < -s_1, \quad x \in D_3. \tag{15}$$

Consider (9), and we have

$$\dot{v}(x) < -s_1, \quad x \in D_3. \tag{16}$$

To integrate both sides of (16) in $[0, t]$,

$$V\left(x\left(t\right)\right) - V\left(x_0\right) < -s_1 * t, \tag{17a}$$

$$V\left(x\left(t\right)\right) < V\left(x_0\right) - s_1 * t, \tag{17b}$$

where $x_0 \in D_3$ is the start point of state trajectory. Inequation (17b) means the state trajectory in DS is strictly constrained

by a diminishing function in D_3. Considering the fact that $\dot{v}(x) < 0$, we have

$$V(x_0) < V_{D_1}, \tag{18a}$$

$$V(x(t)) < V_{D_1} - s_1 * t, \tag{18b}$$

where V_{D_1} is the value of $V(x)$ where the state trajectory crosses the level surface that defines region D_1. Inequations (18a) and (18b) mean that the state trajectory of DS will stay inside D_1. Considering $\dot{v}(x) < 0$, we also have

$$V(x_0) > V_{D_2}, \tag{19}$$

where V_{D_2} is the value of $V(x)$ where the state trajectory crosses the level surface that defines region D_2. Then, the solution trajectory of DS will go from the start point to D_2 within finite time:

$$\Delta t < \frac{V(x_0) - V_{D_2}}{s_1}. \tag{20}$$

Inequation (20) means a DS can be found, whose trajectory will converge to the equilibrium point of CS eventually within finite time, given CS being asymptotically stable and the system error being constrained as (13) shows. □

4.2. The Mathematical Expression of System Error. The mathematical expression of ΔE is studied by analyzing each component of it.

4.2.1. Δx_c. Δx_c is the variation of the controller's state value within time interval T. According to the definition in (5a) and (5b),

$$\begin{aligned}\Delta x_c &= x_c(t-T) - x_c \\ &= \int_{t-T}^{t} f_c(x_c(\tau), u_c(\tau)) \cdot d\tau,\end{aligned} \tag{21a}$$

$$\|\Delta x_c\| = \left\| \int_{t-T}^{t} f_c(x_c(\tau), u_c(\tau)) \cdot d\tau \right\|. \tag{21b}$$

Integrating both sides of (21b),

$$\begin{aligned}\|\Delta x_c\| &= \left\| \int_{t-T}^{t} f_c(x_c(\tau), u_c(\tau)) \cdot d\tau \right\| \\ &\le \int_{t-T}^{t} \|f_c(x_c(\tau), u_c(\tau))\| \cdot d\tau.\end{aligned} \tag{22}$$

$f_c(*)$ is bounded in $[t-T, t]$ since it is continuously differentiable (one of the conditions in Theorem 1). Then, we have

$$\|\Delta x_c\| \le \int_{t-T}^{t} M_{f_c} \cdot d\tau = M_{f_c} \cdot T, \tag{23}$$

where M_{f_c} is the upper bound of $f_c(*)$ within $[t-T, t]$.

4.2.2. Δx_p. Δx_p is the variation of the plant's state value within time interval T. Following a similar approach in the analysis of Δx_c, we have

$$\|\Delta x_p\| \le M_{f_p} \cdot T, \tag{24}$$

where M_{f_p} is the upper bound of $f_p(*)$ within $[t-T, t]$.

4.2.3. Δy_p. Δy_p is the variation of the plant's output within time interval T. According to (5a) and (5b), we have

$$\begin{aligned}\Delta y_p &= g_p(x_p(t-T)) - g_p(x_p) \\ &= g_p(x_p + \Delta x_p) - g_p(x_p),\end{aligned} \tag{25a}$$

$$\|\Delta y_p\| = \|g_p(x_p + \Delta x_p) - g_p(x_p)\|. \tag{25b}$$

Considering $g_p(*)$ is *Lipschitz Continuous* (Theorem 1), we have

$$\begin{aligned}\|\Delta y_p\| &= \|g_p(x_p + \Delta x_p) - g_p(x_p)\| \\ &\le M_{g_p} \cdot \|(x_p + \Delta x_p) - (x_p)\| \\ &= M_{g_p} \cdot \|\Delta x_p\|.\end{aligned} \tag{26a}$$

Considering (24), we have

$$\|\Delta y_p\| \le M_{g_p} \cdot M_{f_p} \cdot T, \tag{26b}$$

where M_{g_p} is the *Lipschitz Const* of $g_p(*)$.

4.2.4. Δy_{pd}. Δy_{pd} is caused by discretization on the plant's output, where the discrete interval is T. Δy_{pd} is bounded by the changing rate of the output, as shown in Figure 3.

According to the definitions in (5a) and (5b), we have

$$\|\Delta y_{pd}\| = \|(g_p)_d - g_p\| \le \Delta y_p. \tag{27}$$

Considering (26b),

$$\|\Delta y_{pd}\| \le M_{g_p} \cdot M_{f_p} \cdot T. \tag{28}$$

4.2.5. Δy_{cd}. Similarly, we have

$$\|\Delta y_{cd}\| \le M_{g_c} \cdot M_{f_c} \cdot T. \tag{29}$$

Combining (6), (23), (24), (26b), (28), and (29),

$$\begin{aligned}\Delta E &= \|(\Delta x_c, \Delta x_p, \Delta y_p, \Delta y_{cd}, \Delta y_{pd})\| \\ &\le \sqrt{M_{f_c}^2 (1 + M_{g_c}^2) + M_{f_p}^2 \cdot (1 + 2M_{g_p}^2)} \cdot T,\end{aligned} \tag{30}$$

where $\sqrt{M_{f_c}^2 (1 + M_{g_c}^2) + M_{f_p}^2 \cdot (1 + 2M_{g_p}^2)} \cdot T$ defines the upper bound of ΔE. Once an expected ΔE is given (denoted as ΔE^*), $T_{\max}$ can be determined:

$$T_{\max} = \frac{\Delta E^*}{\sqrt{M_{f_c}^2 (1 + M_{g_c}^2) + M_{f_p}^2 \cdot (1 + 2M_{g_p}^2)}} \tag{31}$$

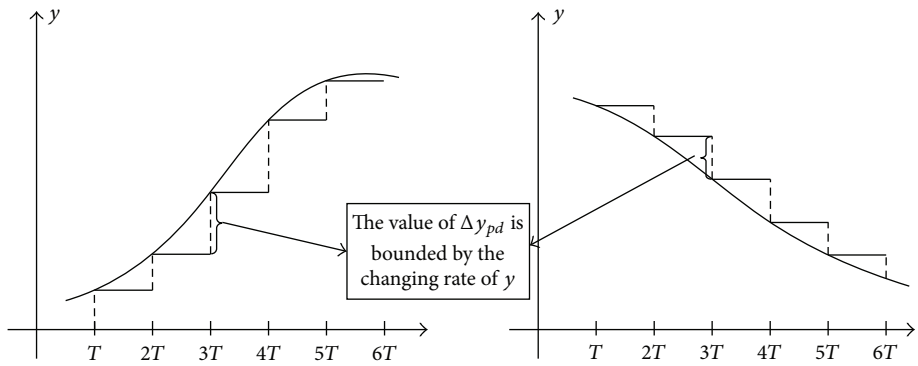

FIGURE 3: Δy_{pd} is bounded by the changing rate of the output value.

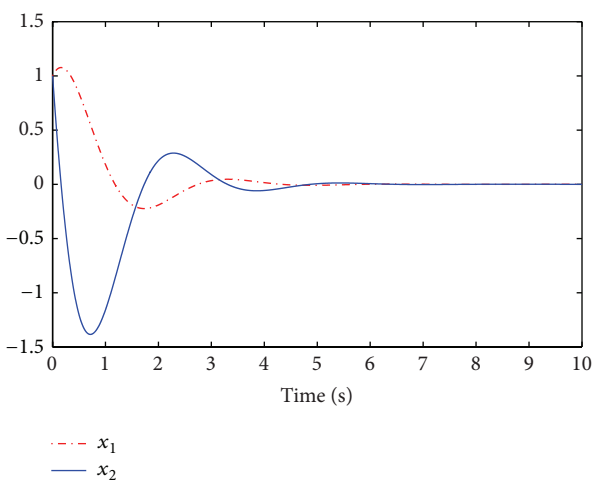

FIGURE 4: The trajectories of x_1, x_2, where $k = 5$, $R = 5$, $m = 1$, and the initial value $x_1^{t=0} = x_2^{t=0} = 1$.

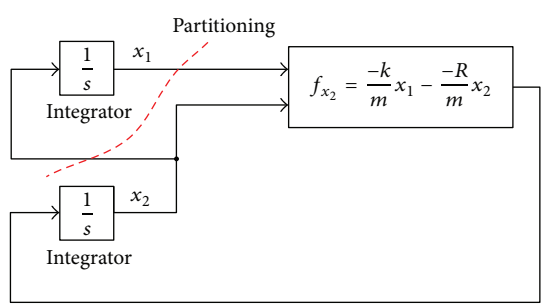

FIGURE 5: This simple system is partitioned into two parts by the dash line to form a distributed system.

for any $T < T_{\max}$, and the overall error will be less than ΔE^*. Equation (31) also indicates the way to partition CS will influence $T_{\max}$: the more the parts partitioned (supposing each part is deployed on a node), the greater the denominator of the right part of (31), thus the smaller that of the allowable $T_{\max}$.

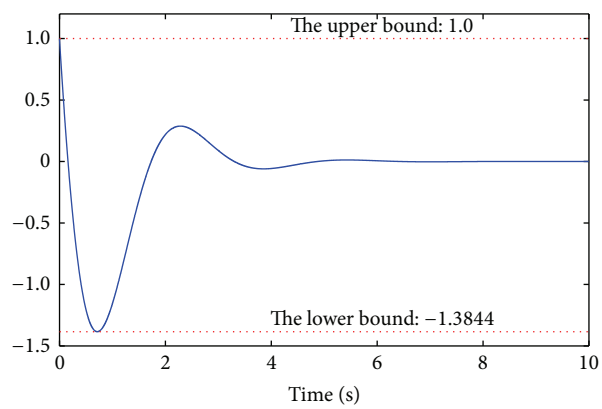

FIGURE 6: The plot of $\dot{x}_1$. $M_{f_{x_1}}$ is determined by the bound of it in this example.

5. Experiment

A distributed simulation is constructed in this section to show the determination of T. The original continuous system is a point mass system with fraction as follows:

$$\begin{aligned} \dot{x}_1 &= x_2, \\ \dot{x}_2 &= \frac{-k}{m}x_1 - \frac{R}{m}x_2, \end{aligned} \tag{32}$$

where k is spring const, m is mass, and R is friction coefficient. This system is asymptotically stable; the trajectories of x_1 and x_2 are shown in Figure 4.

A distributed system can be partitioned from the original system, where the structure has the block-diagram representation (see Figure 5).

The differential equations of these two parts are

$$\text{Component I: } \begin{cases} \dot{x}_1 = f_{x_1} = x_2 \\ y_1 = g_{x_1} = x_1, \end{cases} \tag{33a}$$

$$\text{Component II: } \begin{cases} \dot{x}_2 = f_{x_2} = \dfrac{-k}{m}x_1 - \dfrac{R}{m}x_2 \\ y_2 = g_{x_2} = x_2, \end{cases} \tag{33b}$$

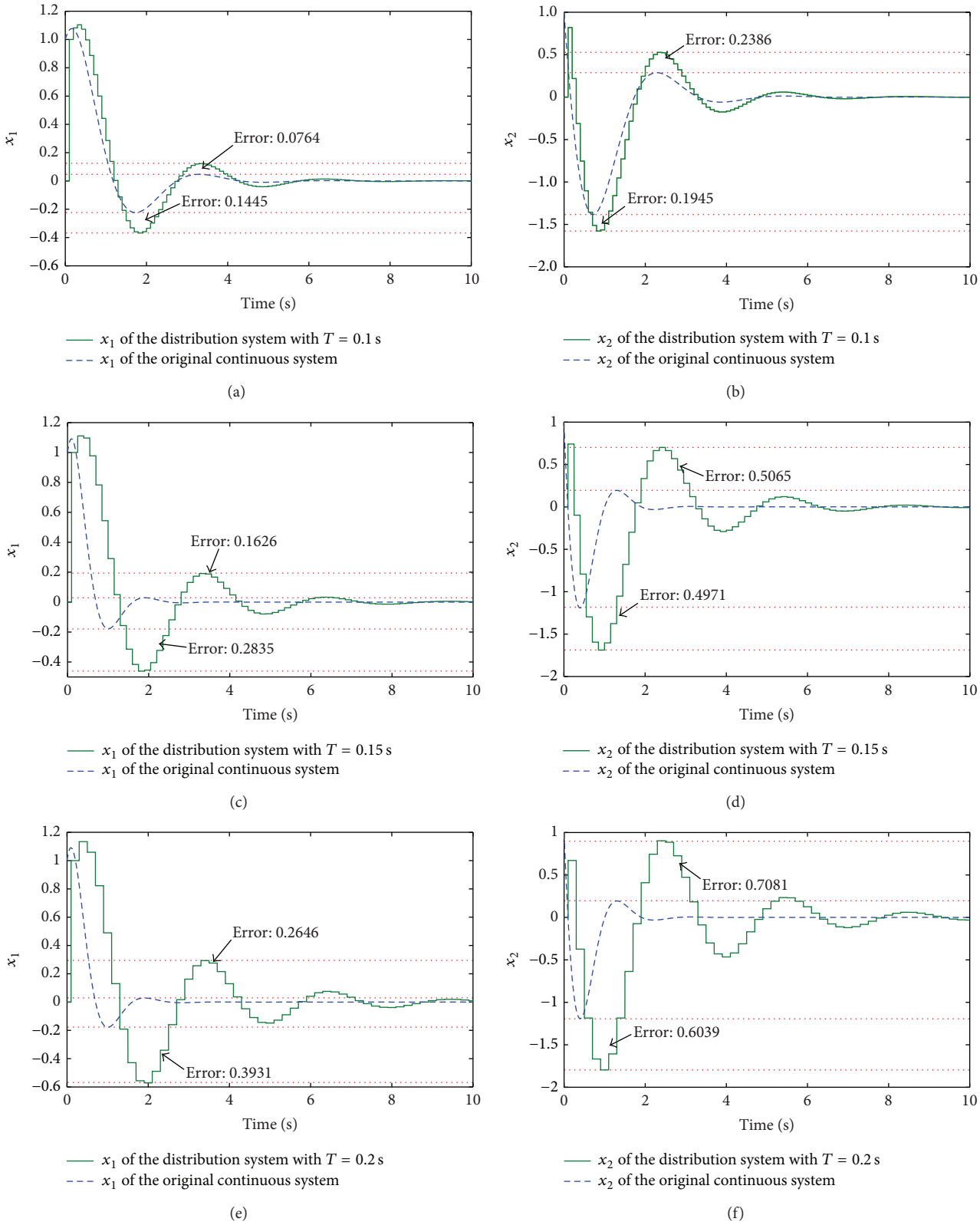

FIGURE 7: The comparison of x_1 and x_2. In the distributed simulation, T is set to be 0.1 s, 0.15 s, and 0.2 s, respectively; the trajectories of x_1 and x_2 are compared in each case.

where y_1, y_2 are the output of components I and II, respectively. These two parts are deployed on two nodes, forming the simple distributed system.

Equation (31) indicates that the parameters reflecting system dynamic need to be determined firstly, which are as follows:

$M_{f_{x_1}}$: the upper bound of function f_{x_1} within any time interval $[t-T, t]$;

$M_{g_{x_1}}$: the *Lipschitz Const* of function g_{x_1};

$M_{f_{x_2}}$: the upper bound of function f_{x_2} within any time interval $[t-T, t]$;

$M_{g_{x_2}}$: the *Lipschitz Const* of function g_{x_2}.

From the engineering perspective, these parameters can be directly observed from the simulation results of the original system. In this case, $M_{f_{x_1}}$ is determined by the lower bound of $\dot{x}_1$ as Figure 6 shows.

As a result, $M_{f_{x_1}} = -1.3844$. According to the definition of *Lipschitz Const*, $M_{g_{x_1}}$ is limited by the upper bound of $\dot{g}_{x_1}$, that is, the upper bound of $\dot{x}_1$ in this case. Then, we have $M_{g_{x_1}} = -1.3844$. Following similar procedures, we have $M_{f_{x_2}} = -1.7796$, $M_{g_{x_2}} = -1.7796$. According to (31), $T_{\max}$ is estimated as follows:

$$\begin{aligned} T_{\max} &\approx \sqrt{M_{f_{x_2}}^2\left(1+M_{g_{x_2}}^2\right)+M_{f_{x_1}}^2\cdot\left(1+2M_{g_{x_1}}^2\right)} \\ &\approx 0.211\cdot\Delta E. \end{aligned} \tag{34}$$

The distributed system described in (33a) and (33b) is simulated. The trajectories of the system states are compared to those of the original continuous system, as Figure 7 shows. The threshold value of ΔE is 0.5, and then $T_{\max}$ is estimated to be 0.1055 s according to (34). Three configurations, where $T = 0.1$ s, $T = 0.15$ s, and $T = 0.2$ s, are tested in the form of distributed simulation. As expected, only the case $T = 0.1$ s satisfies that both x_1 and x_2 do not exceed the threshold value of ΔE.

However, the actual error does not exceed the threshold value immediately when T is configured to be greater than 0.1 s, as shown in Figures 7(c) and 7(d). The reason is that $T_{\max}$ is not strictly estimated since many associated parameters use their boundary values.

6. Conclusion

The mathematical expression of ΔE helps us to gain the insight of system error produced in the construction of the distributed system using the partitioning approach. Giving an expected threshold of ΔE, a proper advancing step T of the distributed system can be determined. A larger T, compared to the integral step in the nondistributed system, will reduce the data-exchange frequency between simulation nodes, leading to the reduction of demands on system timing performance and network bandwidth. Then, the simulation cost is saved eventually. In fact, this approach can also play a role in multicore or multi-CPU parallel computing environments.

However, for systems that may become unstable after system partitioning, this approach is not so convenient since a *Lyapunov function* of the continuous system needs to be found firstly. The parameters defining specific regions satisfying (13)–(15) also need to be determined. More work needs to be done to improve this approach's availability.

Conflict of Interests

The authors declare that there is no conflict of interests regarding the publication of this paper.

References

[1] E. Hairer, S. P. Nørsett, and G. Wanner, *Solving Ordinary Differential Equations I: Nonstiff Problems*, vol. 8 of *Springer Series in Computational Mathematics*, Springer, Berlin, Germany, 2nd edition, 1993.

[2] E. Hinton, P. Bettess, and R. W. Lewis, Eds., *Numerical Methods in Coupled Problems*, Pineridge Press, Swansea, UK, 1981.

[3] R. W. Lewis, Ed., *Numerical Methods in Coupled Problems*, John Wiley & Sons, London, UK, 1984.

[4] Y.-f. Ma, X. Song, J.-y. Wang, and Z. Xiao, "A practical infrastructure for real-time simulation across timing domains," *Mathematical Problems in Engineering*, vol. 2015, Article ID 163845, 12 pages, 2015.

[5] R. W. Lewis, Ed., *Numerical Methods in Coupled Problems*, Wiley, London, UK, 1984.

[6] C. Ocampo-Martinez, S. Bovo, and V. Puig, "Partitioning approach oriented to the decentralised predictive control of large-scale systems," *Journal of Process Control*, vol. 21, no. 5, pp. 775–786, 2011.

[7] K. Salahshoor and S. Kamelian, "A new weighted graph-based partitioning algorithm for decentralized nonlinear model predictive control of large-scale systems," *International Journal of Computer Applications*, vol. 40, no. 14, pp. 7–14, 2012.

[8] C. A. Felippa, K. C. Park, and C. Farhat, "Partitioned analysis of coupled mechanical systems," *Computer Methods in Applied Mechanics and Engineering*, vol. 190, no. 24-25, pp. 3247–3270, 2001.

[9] W. Michiels and S.-I. Niculescu, *Stability and Stabilization of Time-Delay Systems: An Eigenvalue-Based Approach*, vol. 12, SIAM, 2007.

[10] J.-B. Hu, G.-P. Lu, S.-B. Zhang, and L.-D. Zhao, "Lyapunov stability theorem about fractional system without and with delay," *Communications in Nonlinear Science and Numerical Simulation*, vol. 20, no. 3, pp. 905–913, 2015.

[11] S. Kamelian and K. Salahshoor, "A novel graph-based partitioning algorithm for large-scale dynamical systems," *International Journal of Systems Science: Principles and Applications of Systems and Integration*, vol. 46, no. 2, pp. 227–245, 2015.

[12] A. Adegoke, H. Togo, and M. K. Traore, "A unifying framework for specifying DEVS parallel and distributed simulation architectures," *Simulation-Transactions of The Society for Modeling and Simulation International*, vol. 89, no. 11, pp. 1293–1309, 2013.

[13] F. Bergero, E. Kofman, and F. Cellier, "A novel parallelization technique for DEVS simulation of continuous and hybrid systems," *SIMULATION*, vol. 89, no. 6, pp. 663–683, 2013.

[14] S. Jafer, Q. Liu, and G. Wainer, "Synchronization methods in parallel and distributed discrete-event simulation," *Simulation Modelling Practice and Theory*, vol. 30, pp. 54–73, 2013.

[15] E. Kofman, "Quantization-based simulation of differential algebraic equation systems," *Simulation-Transactions of the Society for Modeling and Simulation Internatinal*, vol. 79, no. 9, pp. 363–376, 2003.

[16] E. Kofman, "Discrete event simulation of hybrid systems," *SIAM Journal on Scientific Computing*, vol. 25, no. 5, pp. 1771–1797, 2004.

[17] E. Kofman, J. S. Lee, and B. P. Zeigler, "DEVS representation of differential equation systems: review of recent advances," in *Proceedings of the 13th European Simulation Symposium*, pp. 591–595, October 2001.

[18] E. Kofman, *Discrete event based simulation and control of continuous [Ph.D. thesis]*, Universidad Nacional de Rosario, Santa Fe, Argentina, 2003.

Hindawi Publishing Corporation
Mathematical Problems in Engineering
Volume 2015, Article ID 523424, 10 pages
http://dx.doi.org/10.1155/2015/523424

Research Article

Exponential Cluster Synchronization of Neural Networks with Proportional Delays

Nian Feng, Ye Wu, Weiping Wang, Lin Zhang, and Jinghua Xiao

School of Science, Beijing University of Posts and Telecommunications, Beijing 100876, China

Correspondence should be addressed to Weiping Wang; shiya666888@126.com

Received 15 January 2015; Revised 9 March 2015; Accepted 24 March 2015

Academic Editor: Kun Liu

Copyright © 2015 Nian Feng et al. This is an open access article distributed under the Creative Commons Attribution License, which permits unrestricted use, distribution, and reproduction in any medium, provided the original work is properly cited.

Exponential cluster synchronization of neural networks with proportional delays is studied in this paper. Unlike previous constant delay or bounded time delay, we consider the time-varying proportional delay is unbounded, less conservative, and more widely applied. Furthermore, we designed a novel adaptive controller based on Lyapunov function and inequality technique to achieve exponential cluster synchronization for neural networks and by using a unique way of equivalent system we proved the main conclusions. Finally, an example is given to illustrate the effectiveness of our proposed method.

1. Introduction

In the past most researches focus on the complete synchronization of neural networks, which means that all the nodes of the whole network reach the same synchronization state, and this has achieved significant progress [1–6]. However, in many real world networks, it is to complete several functions at the same time, which implies that the network reaches several different states at last, which is a different synchronization type: cluster synchronization. As a particular synchronization phenomenon, cluster synchronization is achieved when the dynamical nodes realize complete synchronization in each subgroup which is called cluster, but no synchronization appears among the different clusters. Owing to the significant application in biological science and communication engineering, many results have been available for cluster synchronization of complex dynamical networks [7–10]. Ma et al. [9] proposed a coupling scheme with cooperative and competitive weight-couplings to realize cluster synchronization for the connected chaotic networks. In [10], cluster synchronization of complex networks was investigated with centralized adaptive pinning control.

In fact, there exist natural time delays in the operation of systems which are due to the limited communication speed when information transmission exists, extra time required by the sensor to get the measurement information, computation time required for generating the control inputs, and the execution time required for the inputs being acted, and it may cause undesirable dynamic behaviors such as oscillation and instability. Recently, it has been revealed that some types of delayed neural networks (DNNs) exhibit some complicated dynamics and even chaotic behaviors if the parameters and time delays are appropriately chosen. Therefore, dynamic behaviors, especially the cluster synchronization problems of DNNs, have been extensively considered. So far, most studied models of synchronization problem are neural networks (NNs) with constant delays, time-varying and bounded delays, distributed delays, and so on [11–18]. In [17], the authors discuss the synchronization of complex dynamical networks by only designing the adaptive controllers, while we introduce adaptive strategies not only to the coupling strengths but also to the feedback gains. Dahms et al. [18] investigate the stability of synchronized states in delay-coupled networks where synchronization takes place in groups of different local dynamics or in cluster states in networks with identical local dynamics. In addition, delay-dependent stability criteria and synchronization control laws are related to the size of delay so that they can be used to design some better networks according to the allowed time delays of networks. So the cluster synchronization of the neural network with time delay is the right direction for further research.

The proportional delay is one of many delay types and is objectively existent. Unlike previous constant delay or

bounded time delay, the time-varying proportional delay is unbounded, less conservative, and more widely applied. For example, in Web quality of service (QoS) routing decision, the proportional delay is usually required [19–23]. The proportional delay system as an important mathematical model often rises in some fields such as physics, biology systems, and control theory and it has attracted many scholars' interest [24, 25]. If the QoS routing algorithms based on neural networks with proportional delays are proposed, they will be the most suitable algorithms corresponding to the actual situation. Since a neural network usually has a spatial nature due to the presence of an amount of parallel pathways of a variety of axon sizes and lengths, it is reasonable that the proportional delays are introduced in the neural networks according to the topology structure and parameters of neural networks. The proportional delay function $\tau(t) = (1-q)t$ $(0 < q < 1)$ is a monotonically increasing function about the time t, which will be convenient to control the network's running time according to the time delays of network. So far a few results of dynamic behaviors of DNNs with proportional delays have been reported in [26–31]. Zhou [26, 30, 31] has discussed the global exponential stability, asymptotic stability of cellular neural networks (CNNs), and the research of synchronization with proportional delays, by employing matrix theory and constructing Lyapunov function. Dissipativity of a class of CNNs with proportional delays has been investigated by using the inner product properties in [27]. So far, to the best of the author's knowledge, there are few studies with the cluster synchronization of the neural network with proportional delays.

Motivated by the above discussions, we creatively take the element of the proportional delays into the model of neural networks to achieve the exponential cluster synchronization. As an intersection of multibranches of learning, this model will be closer to the reality and much more pertinence for concrete questions. Whether in the study of delays or in the research of cluster synchronizations, the paper has important referring value. The main novelty of our contribution is as follows.

(1) The cluster synchronization model with proportional delay is considered.

(2) The coupling strength of each edge in the system only depends on its local information.

(3) We use a unique way of equivalent system to prove the main results.

This paper is organized as follows. In Section 2, the models and preliminaries are presented. In Section 3, by the application of Lyapunov function, some inequality analysis technique, and the way of equivalent system, the results can be obtained, which is about the cluster synchronization of the delayed neural network. In Section 4, a numerical example and its simulation are given to illustrate the effectiveness of the proposed method. Conclusions are presented in Section 5.

2. Model Description and Preliminaries

Consider a delayed neural network (DNN) with proportional delay of N coupled identical nodes, with each node being an n-dimensional dynamical system, which can be described by the following equations [26]:

$$\begin{aligned}\dot{x}_i(t) &= -Cx_i(t) + Af(x_i(t)) + Bf(x_i(q_i t)) \\ &\quad + \sum_{j=1, j\neq i}^{N} g_{ij}(t)\Gamma\left(x_j(t) - x_i(t)\right), \quad t \geq 1, \\ x_i(s) &= x_{i0}, \quad q \leq s \leq 1,\ i = 1, 2, 3, \ldots, N,\end{aligned} \tag{1}$$

where $N \geq 2$ denotes the number of nodes (neurons) in the network; $x_i(t) = [x_{i1}, x_{i2}, x_{i3}, \ldots, x_{in}]^T \in \mathbb{R}^n$ is the state variable of node i; $C = \operatorname{diag}(c_1, c_2, c_3, \ldots, c_n) \in \mathbb{R}^{n\times n}$ is a diagonal matrix with positive entries. $A = (a_{ij})_{n\times n}$ and $B = (b_{ij})_{n\times n}$ are the corresponding weight and delayed weight matrices; $f(x_i(t)) = (f(x_{i1}, x_{i2}, x_{i3}, \ldots, x_{in}))^T \in \mathbb{R}^n$ denotes a nonlinear activation function of nodes; $G = (g_{ij})_{n\times n}$ is the coupling matrix between nodes. If there is a connection between node i and node j at time t, then $g_{ij}(t) = g_{ji}(t) > 0$ $(i \neq j)$; otherwise $g_{ij}(t) = g_{ji}(t) = 0$ $(i \neq j)$. The diagonal item of the matrix G is $g_{ii}(t) = -\sum_{j=1, j\neq i}^{N} g_{ij}(t)$. In this paper, the network is connected in the sense that there are no isolated clusters in the network, which means that the matrix G is symmetric and irreducible [10]. q_i $(i = 1, 2, 3, \ldots, N)$ are proportional delay coefficient and satisfy $0 < q_i \leq 1$, $q = \min_{1\leq i,j\leq N}\{q_i\}$, and $q_i t = t - (1-q_i)t$ in which $(1-q_i)t$ corresponds to the time delay, and $(1-q_i)t \to \infty$, as $q \neq 1$, $t \to \infty$. Furthermore, the neural networks described in (1) possess initial conditions of $x_i(s) = x_{i0}$, $s \in [q, 1]$, x_{i0} $(i = 1, 2, 3, \ldots, N)$ are constants, and $x_{i0} = [x_{i01}, x_{i02}, \ldots, x_{i0n}]^T$. Γ is inner matrix, and $\Gamma > 0$.

According to the characteristics of the matrix G, system network (1) is easily turned to the following further simplified equations:

$$\begin{aligned}\dot{x}_i(t) &= -Cx_i(t) + Af(x_i(t)) + Bf(x_i(q_i t)) \\ &\quad + \sum_{j=1}^{N} g_{ij}(t)\Gamma x_j(t), \quad t \geq 1, \\ x_i(s) &= x_{i0}, \quad q \leq s \leq 1,\ i = 1, 2, 3, \ldots, N.\end{aligned} \tag{2}$$

Assume the whole N nodes are divided into M clusters. Without loss of generality, the sets of subscripts of these clusters are $C_1 = \{1, 2, 3, \ldots, N_1\}$, $C_2 = \{N_1 + 1, N_1 + 2, \ldots, N_1 + N_2\}, \ldots, C_M = \{N_1 + \cdots + N_{m-1} + 1, \ldots, N\}$, where $N_1 + N_2 + \cdots + N_M = N$. The network is considered to realize

cluster synchronization, when the states of nodes achieve the following states [32]:

$$\begin{aligned} x_1(t) &= x_2(t) = \cdots = x_{N_1}(t) = s_i(t), \quad i = 1, 2, \ldots, N_1, \\ x_{n_1+1}(t) &= x_{N_1+2}(t) = \cdots = x_{N_{1+N_2}}(t) = s_i(t), \\ &\qquad i = N_1 + 1, N_1 + 2, \ldots, N_1 + N_2, \\ &\vdots \\ X_{N_1+\cdots+N_{m-1}+1}(t) &\\ &= x_{N_1+\cdots+N_{m-1}+2}(t) = \cdots = x_N(t) = s_i(t), \\ &\qquad i = N_1 + 1, N_1 + 2, \ldots, N_1 + N_2, \end{aligned} \tag{3}$$

where $s_i(t) = (s_{i1}(t), s_{i2}(t), \ldots, s_{in}(t))^T$ is the desired state of node i at time t and satisfies

$$\dot{s}_i(t) = -Cs_i(t) + Af(s_i(t)) + Bf(s_i(q_i t)). \tag{4}$$

In order to make the network (1) realize cluster synchronization, an input control is added in (1) which is designed as follows:

$$u_i(t) = -\sum_{j=1, j\neq i}^{N} g_{ij}(t)\Gamma\left(x_j(t) - x_i(t)\right). \tag{5}$$

According to the characteristics of the matrix G, the input (5) is easily turned to the following further simplified equation:

$$u_i(t) = -\sum_{j=1}^{N} g_{ij}(t)\Gamma x_j(t), \tag{6}$$

where the coupling strength $g_{ij}(t) = (g_{ij}^1, g_{ij}^2, \ldots, g_{ij}^n)^T$ between nodes adopts the following local adaptive strategy:

$$\begin{aligned} \dot{g}_{ij}(t) = \beta \Big\| &\left[x_j(t) - s_j(t)\right] - \left[x_i(t) - s_i(t)\right] \\ &+ \left[x_j(q_j t) - s_j(q_j t)\right] \\ &- \left[x_i(q_i t) - s_i(q_i t)\right] \Big\|, \end{aligned} \tag{7}$$

where $\beta > 0$ is the adaptive gain.

Before starting to discuss the cluster synchronization, we make the following assumption.

Assumption 1. The activation function $f(x_i(t))$ satisfies that $f: \mathbb{R}^n \to \mathbb{R}^n$, $|f(u) - f(v)| \le L|u - v|$, where $u, v \in \mathbb{R}^n$ and L is positive constant.

Let us consider transformation defined by [27]

$$y_i(t) = x_i\left(e^t\right), \quad i = 1, 2, \ldots, N. \tag{8}$$

Case 1. When $e^t \ge 1$, then $t \ge 0$ and $\dot{y}_i(t) = \dot{x}_i(e^t)e^t$; that is,

$$\dot{x}_i\left(e^t\right) = \dot{y}_i(t)e^{-t}. \tag{9}$$

Let $e^t = z$, $z \ge 1$; then (8) is written as

$$\dot{x}_i(z) = \dot{y}_i(t)z^{-1}. \tag{10}$$

According to the above various formulas one gets

$$\begin{aligned} \dot{y}_i(t)z^{-1} = &-Cx_i(z) + Af(x_i(z)) + Bf(x_i(q_i z)) \\ &+ \sum_{j=1}^{N} g_{ij}(z)\Gamma x_j(z) + u_i(t). \end{aligned} \tag{11}$$

That is to say,

$$\begin{aligned} \dot{x}_i\left(e^t\right) = &-Cx_i\left(e^t\right) + Af\left(x_i\left(e^t\right)\right) + Bf\left(x_i\left(q_i e^t\right)\right) \\ &+ \sum_{j=1}^{N} g_{ij}\left(e^t\right)\Gamma x_j\left(e^t\right) + u_i\left(e^t\right). \end{aligned} \tag{12}$$

According to (8), we have

$$x_i\left(q_i e^t\right) = x_i\left(e^{t+\ln q_i}\right) = y_i(t + \ln q) = y_i(t - \tau_i). \tag{13}$$

Using (8) and (13) in (12) one gets

$$\begin{aligned} \dot{y}_i(t) = e^t \Big\{ &-Cy_i(t) + Af(y_i(t)) + Bf(y_i(t - \tau_i)) \\ &+ \sum_{j=1}^{N} G_{ij}(t)\Gamma u_j(t) \Big\} + U_i(t), \quad t \ge 0. \end{aligned} \tag{14}$$

Case 2. When $e^t \in [q, 1]$, we have

$$x_i\left(e^t\right) = x_{i0}, \quad t \in [-\tau, 0], \tag{15}$$

where $\tau = \max_{1\le i\le N}(\tau_i)$, $\tau_i = -\ln q_i$. Thus, the initial function associated with system (12) is given by

$$Y_i(s) = x_{i0}, \quad -\tau \le s \le 0, \ i = 1, 2, \ldots, N. \tag{16}$$

The analysis is completed.

Remark 2. Conversely, let $\tau_i = -\ln q_i$, $\tau = \max_{1\le i\le N}(\tau_i)$; by (8), (16) and (14) can be turned to (1), which means that the transformation is reversible and equivalent.

Above all, let

$$\begin{aligned} y_i(t) &= x_i\left(e^t\right), \\ w_i(t) &= s_i\left(e^t\right), \\ G_{ij}(t) &= g_{ij}\left(e^t\right), \\ U_i(t) &= u_i\left(e^t\right), \\ i &= 1, 2, 3, \ldots, N. \end{aligned} \tag{17}$$

System (1) with the input control (5) can be equivalently turned to the following neural network with a fixed delay, which can be described as

$$\dot{y}_i(t) = e^t \left\{ -Cy_i(t) + Af(y_i(t)) + Bf(y_i(t-\tau_i)) + \sum_{j=1}^{N} G_{ij}(t)\Gamma y_j(t) \right\} + U_i(t), \tag{18}$$

$$\dot{w}_i(t) = e^t \{-Cw_i(t) + Af(w_i(t)) + Bf(w_i(t-\tau_i))\}, \tag{19}$$

$$U_i(t) = e^t \left\{ -\sum_{j=1, j\neq i}^{N} G_{ij}(t)\Gamma\left(y_j(t) - y_i(t)\right) \right\}, \tag{20}$$

$$\begin{aligned}\dot{G}_{ij}(t) = e^t \{\beta \| [y_j(t) - w_j(t)] - [y_i(t) - w_i(t)] \\ + [y_j(t-\tau_i) - w_j(t-\tau_i)] \\ - [y_i(q_i t) - w_i(q_i t)] \|\},\end{aligned} \tag{21}$$

$$y_i(s) = x_i(s), \quad s \in [-\tau, 0]; \ i = 1, 2, \ldots, N, \tag{22}$$

where $t \geq 0$, $\tau = \max_{1\leq i\leq N}(\tau_i)$, $\tau_i = -\ln q_i > 0$, and $x_i(s) = x_{i0} \in C([-\tau, 0], \mathbb{R}^n)$, $i = 1, 2, \ldots, N$, is constant continuous function.

Remark 3. The translations are to convert the desired cluster synchronization state to another equivalent control system, which is convenient to study the cluster synchronization. Namely, the state when the original system realizes the cluster synchronization means that the control system and the original system realized synchronization.

Definition 4. System (18) and (19) is said to be exponentially synchronized if there exist constants $M \geq 1$ and $\lambda > 0$ such that

$$\sum_{i=1}^{n} |y_i(t) - w_i(t)| \leq M \sum_{i=1}^{n} \sup_{-\tau\leq s\leq 0} |y_i(s) - w_i(s)| e^{-\lambda t}, \quad t \geq 0, \tag{23}$$

where the constant λ is defined as the exponential synchronization rate.

The goal of this paper is to prove that system (1) with adaptive control (5) can achieve the desired cluster synchronization. Now it is equivalently turned to prove that system (18) and (19) can meet the exponential synchronization. In order to prove that it satisfies the exponential synchronization, the following dynamic equations of synchronization error can be obtained:

$$\begin{aligned}\dot{h}_i(t) &= e^t \left\{ -Ch_i(t) + AF(h_i(t)) + BF(h_i(t-\tau_i)) + \sum_{j=1}^{N} G_{ij}(t)\Gamma y_j(t) \right\} + U_i(t) \\ &= e^t \left\{ -Ch_i(t) + AF(h_i(t)) + BF(h_i(t-\tau_i)) + \sum_{j=1}^{N} G_{ij}(t)\Gamma h_j(t) \right\},\end{aligned} \tag{24}$$

where $t \geq 0$, $i = 1, 2, \ldots, N$, and $h_i(t) = y_i(t) - w_i$; $F(h_i(t)) = f(y_i(t)) - f(w_i(t))$; $F(h_i(t-\tau_i)) = f(y_i(t-\tau_i)) - f(w_i(t-\tau_i))$, $\tau_i = -\ln q_i > 0$.

Thus the goal of this paper is further equivalently turned into the proof of the dynamic equations of synchronization error to achieve an exponential stabilization.

3. Main Results

Theorem 5. *Assume that Assumption 1 holds. If $|A|L + |B|Le^{\sigma\tau} + \sigma - 1 < |C|$ is true, system (18) and (19) can achieve exponential stabilization with the synchronization rate $\alpha = \sigma - 1 > 0$, where $L > 0$; $\sigma > 1$; $\tau = \max_{1\leq i\leq N}(\tau_i)$.*

Proof. According to the definition of $\dot{h}_i(t)$ and Assumption 1, we get

$$\begin{aligned}|F(h_i(t))| &\leq L|h_i(t)|, \\ |F(h_i(t-\tau_i))| &\leq L|h_i(t-\tau_i)|.\end{aligned} \tag{25}$$

Consider the following function:

$$H_i(t) = e^{\sigma t}|h_i(t)|, \quad \sigma > 1. \tag{26}$$

From (24) to (26) one gets

$$\begin{aligned}\dot{H}_i(t) &= \sigma e^{\sigma}|h_i(t)| + e^{\sigma t}\frac{d|h_i(t)|}{dt} \\ &= \sigma e^{\sigma}|h_i(t)| + e^{\sigma t}\frac{h_i(t)\dot{h}_i(t)}{|h_i(t)|} \\ &= \sigma e^{\sigma}|h_i(t)| \\ &\quad + e^{\sigma t}\Bigg(\Bigg(h_i(t) * e^t \\ &\quad * \Bigg[-Ch_i(t) + AF(h_i(t)) \\ &\quad + BF(h_i(t-\tau_i)) \\ &\quad + \sum_{j=1}^{N} G_{ij}(t)\Gamma h_j(t)\Bigg]\Bigg) \\ &\quad \cdot |h_i(t)|^{-1}\Bigg)\end{aligned}$$

$$
\begin{aligned}
&\le \sigma e^{\sigma} \left|h_i(t)\right| \\
&\quad + e^{\sigma t} e^{t} \Bigg\{ -|C| \left|h_i(t)\right| \\
&\qquad + |A| L \left|h_i(t)\right| + |B| L \left|h_i(t-\tau_i)\right| \\
&\qquad + \sum_{j=1}^{N} \left|G_{ij}(t)\right| \Gamma \left|h_j(t)\right| \Bigg\} \\
&= \sigma H_i(t) + e^{t} \Bigg\{ -|C| H_i(t) + |A| L H_i(t) \\
&\qquad + |B| L e^{\sigma \tau_i} H_i(t-\tau_i) \\
&\qquad + \sum_{j=1}^{N} \left|G_{ij}(t)\right| \Gamma H_i(t) \Bigg\}.
\end{aligned} \tag{27}
$$

Now construct the following positive Lyapunov functional as follows:

$$
\begin{aligned}
V(t) &= e^{-t} \sum_{i=1}^{N} H_i(t) + |B| \sum_{i=1}^{N} L e^{\sigma \tau_i} \int_{t-\tau_i}^{t} H_i(s)\, ds \\
&\quad + \frac{1}{2\beta} \sum_{\varepsilon} \left(h_{ij} - G_{ij}(t)\right)^{T} \left(h_{ij} - G_{ij}(t)\right),
\end{aligned} \tag{28}
$$

where $t \ge 0$, $\sigma > 1$; ε is the edges' set of the network; h_{ij} is a constant.

Then the differential of $V(t)$ is

$$
\begin{aligned}
\dot{V}(t) &= -e^{-t} \sum_{i=1}^{N} H_i(t) + e^{-t} \sum_{i=1}^{N} \dot{H}_i(t) \\
&\quad + |B| \sum_{i=1}^{N} L e^{\sigma \tau_i} \left(H_i(t) - H_i(t-\tau_i)\right) \varepsilon\varepsilon \\
&\quad - \frac{1}{\beta} \sum_{\varepsilon} \left(h_{ij} - G_{ij}(t)\right)^{T} \dot{G}_{ij}(t).
\end{aligned} \tag{29}
$$

According to (27), we can get

$$
\begin{aligned}
\dot{V}(t) &= -e^{-t} \sum_{i=1}^{N} H_i(t) \\
&\quad + e^{-t} \sum_{i=1}^{N} \Bigg\{ \sigma H_i(t) + e^{t} \Bigg\{ -|C| H_i(t) \\
&\qquad + |A| L H_i(t) \\
&\qquad + |B| L e^{\sigma \tau_i} H_i(t-\tau_i) \\
&\qquad + \sum_{j=1}^{N} \left|G_{ij}(t)\right| \Gamma H_i(t) \Bigg\} \Bigg\} \\
&\quad + |B| \sum_{i=1}^{N} L e^{\sigma \tau_i} \left(H_i(t) - H_i(t-\tau_i)\right) \\
&\quad + \sum_{\varepsilon} \left(h_{ij} - G_{ij}(t)\right)^{T} e^{t} \beta \\
&\qquad \cdot \Big\| \left[y_j(t) - w_j(t)\right] - \left[y_i(t) - w_i(t)\right] \\
&\qquad + \left[y_j(q_j t) - w_j(q_j t)\right] \\
&\qquad - \left[y_i(q_i t) - w_i(q_i t)\right] \Big\| \\
&= \sum_{i=1}^{N} \Bigg\{ (\sigma - 1) e^{-t} - |C| + |A| L \\
&\qquad + |B| L e^{\sigma \tau_i} + \sum_{j=1}^{N} G_{ij}(t) \Gamma \Bigg\} H_i(t) \\
&\quad - \sum_{\varepsilon} \left(h_{ij} - G_{ij}(t)\right)^{T} \\
&\qquad \cdot e^{t} \Big\{ \beta \Big\| \left[y_j(t) - w_j(t)\right] - \left[y_i(t) - w_i(t)\right] \\
&\qquad + \left[y_j(q_j t) - w_j(q_j t)\right] \\
&\qquad - \left[y_i(q_i t) - w_i(q_i t)\right] \Big\| \Big\} \\
&= \sum_{i=1}^{N} e^{\sigma t} \Bigg\{ (\sigma - 1) e^{-t} - |C| + |A| L + |B| L e^{\sigma \tau_i} \\
&\qquad + \sum_{j=1}^{N} \left|G_{ij}(t)\right| \Gamma \Bigg\} \left|h_i(t)\right| \\
&\quad - \sum_{\varepsilon} \left(h_{ij} - G_{ij}(t)\right)^{T} e^{t} \\
&\qquad \cdot \Big\{ \beta \Big\| \left[y_j(t) - w_j(t)\right] - \left[y_i(t) - w_i(t)\right] \\
&\qquad + \left[y_j(q_j t) - w_j(q_j t)\right] \\
&\qquad - \left[y_i(q_i t) - w_i(q_i t)\right] \Big\}.
\end{aligned} \tag{30}
$$

According to Assumption 1 and (25), we can get

$$
\begin{aligned}
\dot{V}(t) &\le \sum_{i=1}^{N} e^{\sigma t} \left\{ (\sigma - 1) - |C| + |A| L + |B| L e^{\sigma \tau} \right\} \left|h_i(t)\right| \\
&\quad + \sum_{i=1}^{N} \sum_{j=1}^{N} e^{\sigma t} \left|G_{ij}(t)\right| \Gamma \left|h_i(t)\right| \\
&\quad + \sum_{\varepsilon} \left(h_{ij} - G_{ij}(t)\right)^{T} \\
&\quad \cdot e^{t} \beta \Big\| \left[y_j(t) - w_j(t)\right] - \left[y_i(t) - w_i(t)\right]
\end{aligned}
$$

$$
\begin{aligned}
&+\left[y_j\left(q_j t\right)-w_j\left(q_j t\right)\right] \\
&-\left[y_i\left(q_i t\right)-w_i\left(q_i t\right)\right]\Big\| \\
\leq & \sum_{i=1}^{N} e^{\sigma t}\left\{(\sigma-1)-|C|+|A| L+|B| L e^{\sigma \tau}\right\}\left|h_i(t)\right| \\
&+\sum_{\varepsilon}\left(h_{ij}-G_{ij}(t)\right)^T \\
&\cdot e^t \beta\Big\|\left[y_j(t)-w_j(t)\right] \\
&-\left[y_i(t)-w_i(t)\right]+\left[y_j\left(q_j t\right)-w_j\left(q_j t\right)\right] \\
&-\left[y_i\left(q_i t\right)-w_i\left(q_i t\right)\right]\Big\| .
\end{aligned} \tag{31}
$$

By the conditions of the theorems $|A|L + |B|Le^{\sigma\tau} + \sigma - 1 < |C|$, and, for any edge $(i, j) \in \varepsilon$, there exists the value h_{ij} which is bigger than or equal to the corresponding edge strength $G_{ij}(t)$, and we get

$$\dot{V}(t) \leq 0, \quad t \geq 0, \tag{32}$$

which means $V(t) \leq V(0)$, for $t \geq 0$. Then, by (25) and (28), one has

$$\sum_{i=1}^{N} e^{\sigma t} e^{-t}\left|h_i(t)\right| \leq V(t) \leq V(0) . \tag{33}$$

It follows from (28) that

$$
\begin{aligned}
V(0) &= \sum_{i=1}^{N}\left|h_i(0)\right|+|B| \sum_{i=1}^{N} L e^{\sigma \tau_i} \int_{-\tau_i}^{0} H_i(s)\, ds \\
&\leq \sum_{i=1}^{N}\left|h_i(0)\right|+|B| \sum_{i=1}^{N} L \tau_i e^{\tau_i} \sup_{-\tau_i \leq s \leq 0} H_i(s) \\
&\leq \sum_{i=1}^{N}\left|h_i(0)\right|+|B| \sum_{i=1}^{N} L \tau e^{\tau} \sup_{-\tau \leq s \leq 0} H_i(s) \\
&\leq \max_{1 \leq i \leq N}\left(1+|B| L \tau e^{\tau}\right) \sum_{i=1}^{N} \sup_{-\tau \leq s \leq 0} H_i(s),
\end{aligned} \tag{34}
$$

where $M = \max_{1\leq i\leq N}(1 + |B|L\tau e^{\tau}) \geq 1$.

All told, one gets

$$\sum_{i=1}^{n}\left|y_i(t)-w_i(t)\right| \leq M \sum_{i=1}^{n} \sup_{-\tau \leq s \leq 0}\left|y_i(s)-w_i(s)\right| e^{-\alpha t}, \tag{35}$$

where $\alpha = \sigma - 1, \sigma > 1$.

The proof is completed. □

Remark 6. System (18) and (19) is asymptotically synchronized if the following conditions are satisfied: (1) the exponential synchronization rate is zero; that is, $\lambda = 0$ and $M > 1$; then $\sum_{i=1}^{n} |y_i(t) - w_i(t)| \leq M \sum_{i=1}^{n} \sup_{-\tau\leq s\leq 0}|y_i(s) - w_i(s)|$, $t \geq 0$; (2) $\lim_{t\to\infty}||h(t)|| = 0$.

According to the foregoing contents $y_i(t) = x_i(e^t)$, $w_i(t) = s_i(e^t)$, one gets

$$\sum_{i=1}^{n}\left|x_i\left(e^t\right)-s_i\left(e^t\right)\right| \leq M \sum_{i=1}^{n} \sup_{-\tau \leq s \leq 0}\left|x_i\left(e^s\right)-s_i\left(e^s\right)\right| e^{-\alpha t}, \quad e^t \geq 1. \tag{36}$$

Let $e^t = \eta$; then $\eta \geq 1$ and $t = \ln\eta \geq 0$; let $e^s = \xi$; then $s = \ln\xi \in [-\tau, 0]$ and $\xi \in [q, 1]$. Thus, it follows from (36) that

$$\sum_{i=1}^{N}\left|x_i(\eta)-s_i(\eta)\right| \leq M \sum_{i=1}^{n} \sup_{q \leq \xi \leq 1}\left|x_i(\xi)-s_i(\xi)\right| e^{-\alpha \ln \eta}, \quad \eta \geq 1. \tag{37}$$

Let $\eta = t$; the following inequality is obtained:

$$\sum_{i=1}^{N}\left|x_i(t)-s_i(t)\right| \leq M \sum_{i=1}^{n} \sup_{q \leq \xi \leq 1}\left|x_{i0}-s_{i0}\right| e^{-\alpha \ln t}, \quad t \geq 1. \tag{38}$$

Thus, control system (4) and original system (1) are considered to be exponentially synchronized, and the exponential synchronization rate is less than α because of $0 < \ln t < t$; that is, $\ln t/t < 1$, as $t \geq 1$.

Thus, the following theorem is derived.

Inference 1. Assume that Assumption 1 holds. If $|A|L + |B|Le^{\sigma\tau} + \sigma - 1 < |C|$ is true, system (1) with the input control (5) can achieve an exponential cluster synchronization for the desired state, with the exponential rate being $\alpha = \sigma - 1 > 0$, where $L > 0$; $\sigma > 1$; $\tau = \max_{1\leq i\leq N}(\tau_i)$, $-\ln q_i > 0$.

The proof is omitted.

4. Illustrative Examples

In the following simulation, the whole neural network is divided into three clusters, which means that $M = 3$. The desired state $s_i(t)$ of node i at time t is chosen as the average states of all the nodes in the same cluster at time t as follows:

$$
\begin{aligned}
s_1(t) &= s_2(t) = \cdots = s_{N_1}(t) \\
&= \frac{x_1(t)+x_2(t)+\cdots+x_{N_1}(t)}{N_1}, \\
s_{N_1+1}(t) &= s_{N_1+2}(t) = \cdots = s_{N_1+N_2}(t) \\
&= \frac{x_{N_1+1}(t)+x_{N_1+2}(t)+\cdots+x_{N_1+N_2}(t)}{N_1},
\end{aligned}
$$

$$\begin{aligned} & s_{N_1+N_2+1}(t) \\ & = s_{N_1+N_2+2}(t) = \cdots = s_{N_1+N_2+N_3}(t) \\ & = \frac{x_{N_1+N_2+1}(t) + x_{N_1+N_2+2}(t) + \cdots + x_{N_1+N_2+N_3}(t)}{N_1}, \end{aligned} \tag{39}$$

where the three clusters are N_1, N_2, and N_3, respectively.

Consider the following delayed neural networks (DCNNs):

$$\dot{y}_i(t) = -Cy_i(t) + Af(y_i(t)) + Bf(y_i(t-\tau_i)), \tag{40}$$

where $y(t) = [y_1(t), y_2(t)]^T$, $f(y) = [\tanh(y_1), \tanh(y_2)]^T$, and the parameters are

$$C = \begin{bmatrix} 1 & 0 \\ 0 & 1 \end{bmatrix}, \quad A = \begin{bmatrix} 2.0 & -0.1 \\ -5.0 & 3.0 \end{bmatrix}, \quad B = \begin{bmatrix} -1.5 & -0.1 \\ -0.2 & -2.5 \end{bmatrix}. \tag{41}$$

The system meets Assumption 1 and Theorem 5 with $L = 1$. The chaotic behavior of system (40) with the initial condition $[y_1(s), y_2(s)]^T = [0.4, 0.6]^T$, $(-1 \le s \le 0)$, has already been reported in the case of $\tau_i = 1s$ [33] (see Figure 1).

Example 1. Referring to the classical model, consider the following improved model with N nodes:

$$\begin{aligned} \dot{y}_i(t) = & -Cy_i(t) + Af(y_i(t)) + Bf(y_i(t-\tau_i)) \\ & + \sum_{j=1}^{N} g_{ij}(t)\Gamma(x_j(t) - s_j(t)). \end{aligned} \tag{42}$$

The system meets Assumption 1 and Theorem 5 with $L = 1$, $\beta = 0.2$,

$$C = \begin{bmatrix} 2 & 0 \\ 0 & 2 \end{bmatrix}, \quad A = \begin{bmatrix} 2.0 & -0.1 \\ -5.0 & 3.0 \end{bmatrix}, \quad B = \begin{bmatrix} -1.5 & -0.1 \\ -0.2 & -2.5 \end{bmatrix}, \quad \Gamma = \begin{bmatrix} 1 & 0 \\ 0 & 1 \end{bmatrix}, \tag{43}$$

$y(t) = [y_1(t), y_2(t)]^T$, and $f(y) = [\tanh(y_1), \tanh(y_2)]^T$, where $q_i = 0.5$ $(i = 1, 2, \ldots, N)$ is constants, which is the proportional delay coefficient.

In the simulation experiment, a BA scale-free neural network is needed, which is constructed with $m = m_0 = 5$ and the neural network size $N = 50$. The construction method of the BA scale-free neural network can refer to [34]. Suppose the whole network will reach three clusters with the cluster size being 14, 8, and 28, respectively. The initial states $y_{i1}(t)$ and $y_{i2}(t)$, $i = 1, 2, \ldots, 50$, are randomly distributed between $[-1, 1]$ and $[-5, 5]$.

As shown in Figure 2(a), for $t > 2$ s, 14 black curves changed into one black curve, 8 red curves changed into one red curve, and the remaining 28 blue curves changed into one blue curve; that is, the 50 state lines of $x_{i1}(t)$, $(i = 1, 2, \ldots, 50)$, in system gradually merged into 3 lines, which means that each node of the neural network realizes the desired cluster synchronization. It reflects that the number of the nodes in the cluster influences the rate of the cluster synchronization. Then in Figure 2(b), for $t > 1.8$ s, it can still be observed that 14 black curves changed into one black curve, 8 red curves changed into one red curve, and the remaining 28 blue curves changed into one blue curve; that is, the 50 state lines of $x_{i1}(t)$, $(i = 1, 2, \ldots, 50)$, in system gradually merged into 3 lines, which means that each node of the neural network realizes the desired cluster synchronization. It reflects that the number of the nodes in the cluster influences the rate of the cluster synchronization. So the conclusion is that the larger the cluster in the delay systems, the slower the rate of the cluster synchronization with the same way of the coupling mode.

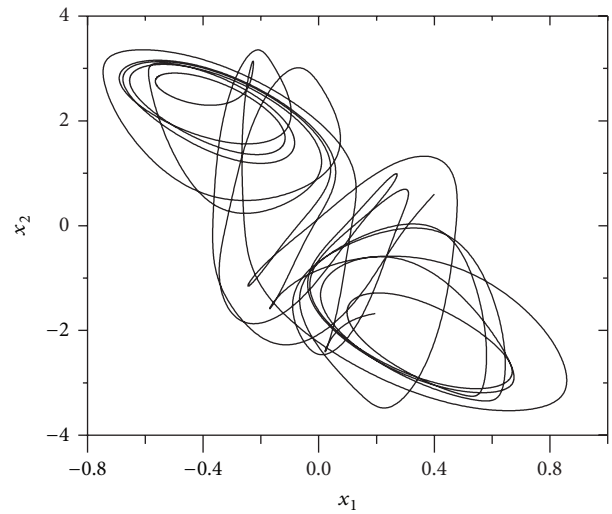

Figure 1: The chaotic DCNNs with $\tau_i = 1s$ in (40).

Figure 3 depicts the synchronization error of the state variables between system (42) and the desired state, which makes it easy to see that the exponential convergence rate of the red curves within all the curves of the 3 cluster's nodes is relatively quick (14 were black, 8 red, and 24 blue classification). And it proves that from another aspect the number of nodes affects the rate of cluster synchronization. Furthermore the shape of the curves indicates that system (42) realizes the cluster synchronization with the exponential synchronization rules, and it is feasible to further study the cluster synchronization of the neural system with proportional delay through the exponential analysis of the synchronization.

In Figure 4, it can be seen that when $t > 2$ s, the edge coupling strength $g_{ij}(t)$ between node i and node j is kept constant in all its dimensions. Combined with Figure 2, it is found that when the neural network realizes cluster synchronization, the edge coupling strengths are fixed, which implies that the left side of (7) will be zero. According to Figure 4, it is shown that most edge coupling strengths are

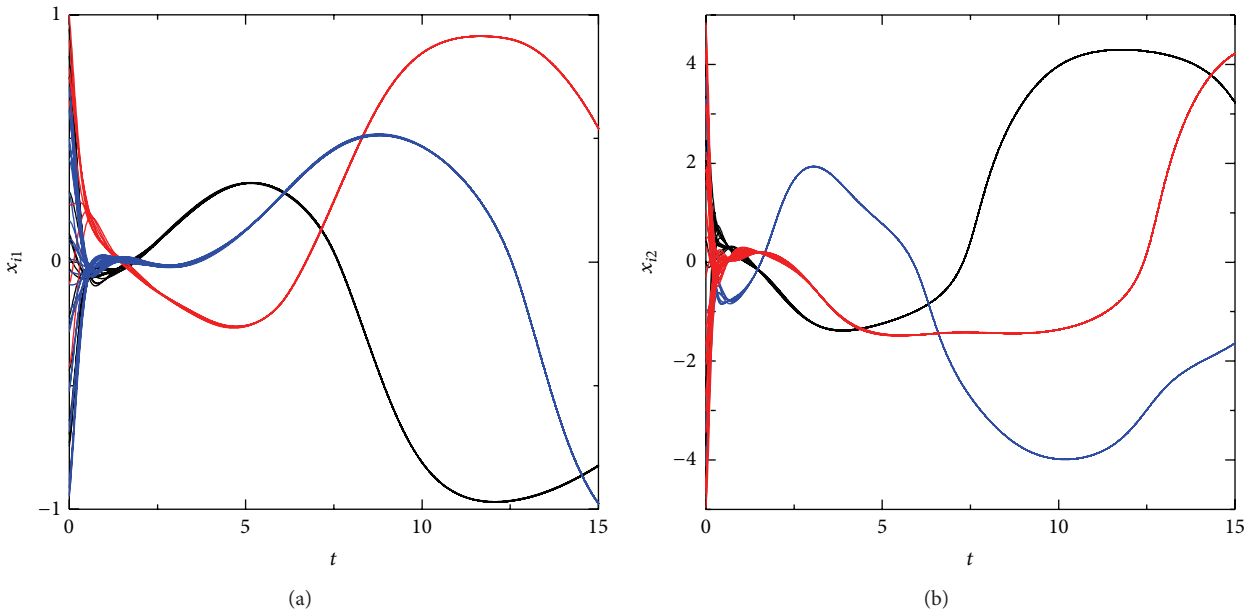

FIGURE 2: Cluster synchronization in the BA scale-free neural network with the proportional delay and the adaptive gain $\beta = 0.2$ and the proportional delay coefficient $q_i = 0.5$. (a) The curve of the state of x_{i1} changing over time; (b) the curve of the state of x_{i2} changing over time.

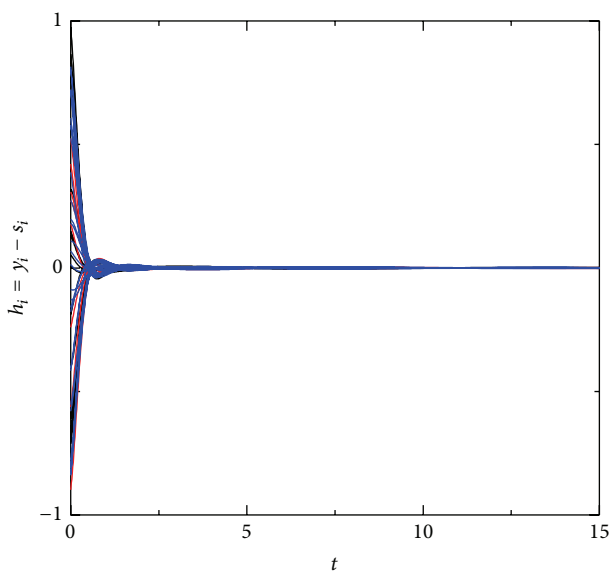

FIGURE 3: The synchronization error between system (42) and the system which the desired state is equivalently turned into.

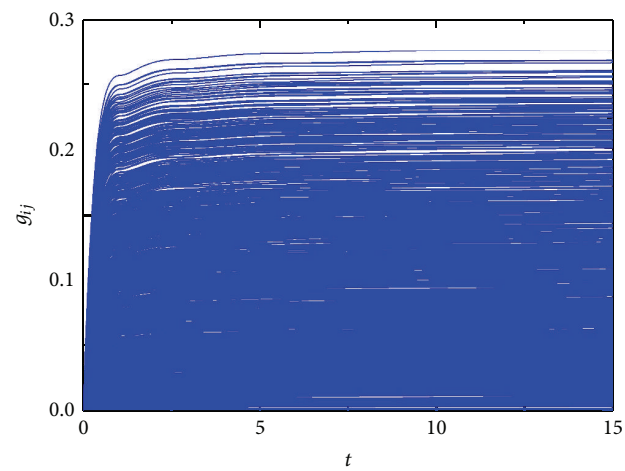

FIGURE 4: Edge strengths' evolution during the interval of the BA scale-free neural network in Figure 2 to realize cluster synchronization.

less than 0.20, and only a small amount of edge coupling strengths is distributed in the interval $[0.2, 0.255]$. If we do not use the adaptive coupling strength in the neural network with the proportional delay, the network will realize the cluster synchronization only when all the edge coupling strengths are greater than 0.20, which means that a lot of unnecessary coupling strengths are wasted. All in all, it is easy to design coupling intensity for each edge by using the adaptive coupling strength, in order to achieve the desired cluster synchronization with faster cluster synchronization rate, which can be implemented in real networks.

5. Conclusions

In this paper, an exponential cluster synchronization control frame of the neural networks with time delay has been established. Different from the prior works, delays in the paper are proportional delays which are unbounded and time-varying, and the coupling strength of each edge in the system only depends on its local information. By constructing the appropriate Lyapunov function and using the inequality

technique, several sufficient conditions were obtained to make the neural network with the proportional delay realize cluster synchronization. Finally, a numerical simulation has been given to verify the theoretical results. Further the example indicates that the cluster synchronization rate is related to the clusters size. This strategy may be extended to study the effects of the rate of the neural system with proportional delay in order to realize cluster synchronization.

Furthermore we can also extend the current result to the Networked Control Systems (NCS) under scheduling protocol [35–37]. Based on this paper, we can provide a stability certificate that takes into account the network imperfections: communication delays (proportional delays), scheduling protocols, and quantization in order to offer several practical advantages: reduced costs, ease of installation and maintenance, and increased flexibility.

Conflict of Interests

The authors declare that there is no conflict of interests regarding the publication of this paper.

Acknowledgments

This work was jointly supported by the National Natural Science Foundation of China (Grants nos. 11375033, 61104152, and 61377067) and the Fundamental Research Funds for the Central Universities (no. 2013XZ02).

References

[1] X. F. Wang, "Complex networks: topology, dynamics and synchronization," *International Journal of Bifurcation and Chaos*, vol. 12, no. 5, pp. 885–916, 2002.

[2] L. M. Pecora and T. L. Carroll, "Synchronization in chaotic systems," *Physical Review Letters*, vol. 64, no. 8, pp. 821–824, 1990.

[3] M. Feki, "An adaptive chaos synchronization scheme applied to secure communication," *Chaos, Solitons & Fractals*, vol. 18, no. 1, pp. 141–148, 2003.

[4] A. Pikovsky, M. Rosenblum, and J. Kurths, *Synchronization: A Universal Concept in Nonlinear Sciences (Paperback)*, Cambridge Nonlinear Science Series, 2003.

[5] P. de Lellis, M. di Bernardo, and F. Garofalo, "Synchronization of complex networks through local adaptive coupling," *Chaos*, vol. 18, no. 3, Article ID 037110, 2008.

[6] W. Ren, "Synchronization of coupled harmonic oscillators with local interaction," *Automatica*, vol. 44, no. 12, pp. 3195–3200, 2008.

[7] W. Lu, B. liu, and T. Chen, "Cluster synchronization in networks of coupled non-identical dynamical systems," *Chaos*, vol. 20, no. 1, Article ID 013120, 2010.

[8] Y. Wang and J. Cao, "Cluster synchronization in nonlinearly coupled delayed networks of non-identical dynamic systems," *Nonlinear Analysis: Real World Applications*, vol. 14, no. 1, pp. 842–851, 2013.

[9] Z. Ma, Z. Liu, and G. Zhang, "A new method to realize cluster synchronization in connected chaotic networks," *Chaos*, vol. 16, no. 2, Article ID 023103, 2006.

[10] W. Wu, W. Zhou, and T. Chen, "Cluster synchronization of linearly coupled complex networks under pinning control," *IEEE Transactions on Circuits and Systems I: Regular Papers*, vol. 56, no. 4, pp. 829–839, 2009.

[11] J. Zhou, T. Chen, and L. Xiang, "Robust synchronization of delayed neural networks based on adaptive control and parameters identification," *Chaos, Solitons and Fractals*, vol. 27, no. 4, pp. 905–913, 2006.

[12] C.-J. Cheng, T.-L. Liao, J.-J. Yan, and C.-C. Hwang, "Exponential synchronization of a class of neural networks with time-varying delays," *IEEE Transactions on Systems, Man, and Cybernetics, Part B: Cybernetics*, vol. 36, no. 1, pp. 209–215, 2006.

[13] J.-S. Lin, M.-L. Hung, J.-J. Yan, and T.-L. Liao, "Decentralized control for synchronization of delayed neural networks subject to dead-zone nonlinearity," *Nonlinear Analysis, Theory, Methods & Applications*, vol. 67, no. 6, pp. 1980–1987, 2007.

[14] X. Li and M. Bohner, "Exponential synchronization of chaotic neural networks with mixed delays and impulsive effects via output coupling with delay feedback," *Mathematical and Computer Modelling*, vol. 52, no. 5-6, pp. 643–653, 2010.

[15] J. Lu, D. W. C. Ho, J. Cao, and J. Kurths, "Exponential synchronization of linearly coupled neural networks with impulsive disturbances," *IEEE Transactions on Neural Networks*, vol. 22, no. 2, pp. 329–335, 2011.

[16] X. Yang, Z. Wu, and J. Cao, "Finite-time synchronization of complex networks with non-identical discontinuous nodes," *Nonlinear Dynamics*, vol. 73, no. 4, pp. 2313–2327, 2013.

[17] W.-T. Miao, T. Yuan, J.-W. Xiao, and Y.-W. Wang, "Adaptive synchronization of complex dynamical networks with two types of time-varying delays," in *Proceedings of the 8th IEEE International Conference on Control and Automation (ICCA '10)*, pp. 1584–1588, IEEE, Xiamen, China, June 2010.

[18] T. Dahms, J. Lehnert, and E. Schöll, "Cluster and group synchronization in delay-coupled networks," *Physical Review E*, vol. 86, no. 1, part 2, Article ID 016202, 2012.

[19] Y. Chen, M. Hamdi, and D. H. K. Tsang, "Proportional QoS over OBS networks," in *Proceedings of the IEEE Global Telecommunicatins Conference (GLOBECOM '01)*, pp. 1510–1514, November 2001.

[20] J. Wei, C.-Z. Xu, X. Zhou, and Q. Li, "A robust packet scheduling algorithm for proportional delay differentiation services," *Computer Communications*, vol. 29, no. 18, pp. 3679–3690, 2006.

[21] S. Kulkarni, R. Sharma, and I. Mishra, "New QoS routing algorithm for MPLS networks using delay and bandwidth constrainst," *International Journal of Information and Communication Technology Research*, vol. 2, no. 3, pp. 285–293, 2012.

[22] J. Liu, D. Yuan, S. Ci, and Y. Zhong, "A new QoS routing optimal algorithm in mobile ad hoc networks based on hopfield neural network," in *Advances in Neural Networks—ISNN 2005*, vol. 3498 of *Lecture Notes in Computer Science*, pp. 343–348, Springer, Berlin, Germany, 2005.

[23] R. Gargi, Y. Chaba, and R. B. Patel, "Improving the performance of dynamic source routing protocol by optimization of neural networks," *International Journal of Computer Science Issues*, vol. 9, Issue 4, no. 3, 2012.

[24] B. van Brunt, J. C. Marshall, and G. C. Wake, "Holomorphic solutions to pantograph type equations with neutral fixed points," *Journal of Mathematical Analysis and Applications*, vol. 295, no. 2, pp. 557–569, 2004.

[25] Y. Liu, "Asymptotic behaviour of functional-differential equations with proportional time delays," *European Journal of Applied Mathematics*, vol. 7, no. 1, pp. 11–30, 1996.

[26] L. Zhou, "Delay-dependent exponential stability of cellular neural networks with multi-proportional delays," *Neural Processing Letters*, vol. 38, no. 3, pp. 347–359, 2013.

[27] L. Zhou, "Dissipativity of a class of cellular neural networks with proportional delays," *Nonlinear Dynamics*, vol. 73, no. 3, pp. 1895–1903, 2013.

[28] A. Iserles and Y. Liu, "On neutral functional–differential equations with proportional delays," *Journal of Mathematical Analysis and Applications*, vol. 207, no. 1, pp. 73–95, 1997.

[29] H. Brunner, Q. Hu, and Q. Lin, "Geometric meshes in collocation methods for Volterra integral equations with proportional delays," *IMA Journal of Numerical Analysis*, vol. 21, no. 4, pp. 783–798, 2001.

[30] L. Zhou, X. Chen, and Y. Yang, "Asymptotic stability of cellular neural networks with multiple proportional delays," *Applied Mathematics and Computation*, vol. 229, no. 5, pp. 457–466, 2014.

[31] L. Zhou, "Global asymptotic stability of cellular neural networks with proportional delays," *Nonlinear Dynamics*, vol. 771, pp. 41–47, 2014.

[32] J. Cao and L. Li, "Cluster synchronization in an array of hybrid coupled neural networks with delay," *Neural Networks*, vol. 22, no. 4, pp. 335–342, 2009.

[33] C.-J. Cheng, T.-L. Liao, J.-J. Yan, and C.-C. Hwang, "Synchronization of neural networks by decentralized feedback control," *Physics Letters A: General, Atomic and Solid State Physics*, vol. 338, no. 1–18, pp. 28–35, 2005.

[34] A.-L. Barabási and R. Albert, "Emergence of scaling in random networks," *Science*, vol. 286, no. 5439, pp. 509–512, 1999.

[35] K. Liu, E. Fridmana, and L. Hetel, "Stability and L2-gain analysis of networked control systems under Round-Robin scheduling: a time-delay approach," *Systems & Control Letters*, vol. 61, no. 8, pp. 666–675, 2012.

[36] W. P. M. H. Heemels, A. R. Teel, N. van de Wouw, and D. Nešić, "Networked control systems with communication constraints: tradeoffs between transmission intervals, delays and performance," *IEEE Transactions on Automatic Control*, vol. 55, no. 8, pp. 1781–1796, 2010.

[37] K. Liu, E. Fridman, and L. Hetel, "Network-based control via a novel analysis of hybrid systems with time-varying delays," in *Proceedings of the IEEE 51st Conference on Decision and Control (CDC '12)*, pp. 3886–3891, December 2012.

Hindawi Publishing Corporation
Mathematical Problems in Engineering
Volume 2015, Article ID 342465, 11 pages
http://dx.doi.org/10.1155/2015/342465

Research Article

Stabilization of Networked Distributed Systems with Partial and Event-Based Couplings

Sufang Zhang, Wei Wang, and Chi Huang

College of Mathematics, Taiyuan University of Technology, Taiyuan 030024, China

Correspondence should be addressed to Chi Huang; huangchima@gmail.com

Received 17 December 2014; Accepted 6 March 2015

Academic Editor: Yun-Bo Zhao

Copyright © 2015 Sufang Zhang et al. This is an open access article distributed under the Creative Commons Attribution License, which permits unrestricted use, distribution, and reproduction in any medium, provided the original work is properly cited.

The stabilization problem of networked distributed systems with partial and event-based couplings is investigated. The channels, which are used to transmit different levels of information of agents, are considered. The channel matrix is introduced to indicate the work state of the channels. An event condition is designed for each channel to govern the sampling instants of the channel. Since the event conditions are separately given for different channels, the sampling instants of channels are mutually independent. To stabilize the system, the state feedback controllers are implemented in the system. The control signals also suffer from the two communication constraints. The sufficient conditions in terms of linear matrix equalities are proposed to ensure the stabilization of the controlled system. Finally, a numerical example is given to demonstrate the advantage of our results.

1. Introduction

Recent years have witnessed a thriving research activity on how to assemble and coordinate networked distributed systems (NDSs) into a coherent whole to perform a common task [1]. NDSs have obvious advantages in practice, such as energy saving, easy installation, and higher reliability [2–6]. Thus, studying stabilization of NDSs is of theoretical and practical importance. To realize the stabilization, a control strategy is needed. However, due to the absence of central data fusion, the classical centralized control scheme is not feasible for NDSs. Accordingly, the cooperative control strategy is a preferred choice. Since an NDS consists of a large number of agents, it is impossible and unnecessary to control every agent. An effective approach is to implement controllers for a fraction of the NDSs to stabilize the whole system, which is referred to as the pinning stabilization problem [7, 8].

To achieve stabilization, the communication in NDSs plays a crucial role. However, due to physical and environmental limitations, communication constraints, such as time delays [9–11] and noise [12, 13], are unavoidable. In fact, incomplete information is universal. As each agent of an NDS has multiple levels of information, the coupling has to be split into multiple channels to transmit the corresponding levels of information. Due to the physical limitatioins, only some parts of the channels can transmit information successfully, which brings the partial-coupling problem. Such a phenomenon can be observed in many real systems. For example, in brain networks, only 5% excitatory synapses sent from a cortical area can be received by another connected cortical area [14]; in sensor networks, the information packet of a target may be partly lost during communication between sensors [5]. Thus, it is highly desirable to analyze NDSs with partial couplings.

The sampling issue has received intense attention, ever since the rapid development of digital technology and intelligent equipment. A traditional sampling protocol is time-based sampling technique [15–17]. Recently, the event-based sampling has been investigated as an alternative to time-based sampling. The distinct feature of event-based sampling is the real-time scheduling algorithm. The information is sampled only when a certain event occurs, for example, when the system state exceeds a predefined threshold. The advantage of the event-based sampling is the capability of fast reacting to sudden events and, therefore, being more efficient [18, 19]. In an NDS, the event conditions are individually designed for each agent. Thus, the agents are sampled at mutually independent instants. This means that the event-based sampling scheme does not require a common sampling schedule, which makes it applicable for a system with large size. For the single system, an event-triggered method was

designed in [20], in which the lower bound of two successive sampling instants was given; in [21, 22], the event-triggered controller was designed for networked control systems with transmission delay. In [23], the event-based control was used in multiagent system drive the agents to average consensus. However, until now, few results have been given for the NDS with partial and event-based couplings. The difficulty of this problem is threefold. Firstly, two communication constraints are considered, both of which make less information available for communication. Secondly, each agent samples information separately; however, they should cooperatively converge. Thus, how to design the event conditions of the agents? Finally, the stabilization conditions should be given to guarantee the stabilization of the NDS.

In this paper, we focus on the stabilization problem of NDSs with partial and event-based couplings. By designing an event condition for each agent, an event-based sampling scheme is proposed for NDSs. Due to the constraint of partial information transmission, the channels are considered in the event condition. Thus, for different channels of one agent, the sampling instants are distinct. The sampled data are used for the communication among agents and building the feedback controllers. The sufficient conditions are given to ensure the stabilization of the controlled NDS with both communication constraints. Finally, a numerical example is given to demonstrate the advantage of our results.

Notations. The standard notations will be used in this paper. Throughout this paper, $\mathbb{R}$ denotes the set of real numbers. $\mathbb{R}^n$ denotes the n dimensional Euclidean space. $\mathbb{R}^{n\times n}$ are the set of $n \times n$ real matrices. $I_n \in \mathbb{R}^{n\times n}$ is the identity matrix. For real symmetric matrices X and Y, the notation $X \leq Y$ (resp., $X < Y$) means that the matrix $X - Y$ is negative semidefinite (resp., negative definite). $\|\cdot\|$ denotes the Euclidean norm for vector or the spectral norm of matrix. $\mathrm{diag}\{\cdots\}$ denotes a diagonal matrix. The superscripts "$\top$" and "-1" represent the matrix transposition and matrix inverse. $*$ in a matrix represents the elements below the main diagonal of a symmetric matrix. Matrices, if not explicitly stated, are assumed to have compatible dimensions.

2. Problem Formulation and Preliminaries

An NDS with N agents can be described by the following:

$$\dot{x}_i(t) = Ax_i(t) + u_{i1}(t), \quad i \in \{1, 2, \ldots, N\}, \tag{1}$$

where $x_i(t) = [x_{i1}(t), x_{i2}(t), \ldots, x_{in}(t)] \in \mathbb{R}^n$ is the state of the ith system; $A = [a_{ij}]_{n\times n}$ is the system matrix. Assuming that each agent can only receive the information of its neighbors, the coupling control $u_{i1}(t)$ can be constructed as follows:

$$u_{i1}(t) = \alpha \sum_{j=1}^{N} g_{ij} R_{ij} \left(x_j(t) - x_i(t)\right), \tag{2}$$

where α is the coupling strength; $G = [g_{ij}]_{N\times N}$ is the Laplacian matrix representing the coupling structure of the NDS. The elements of G are defined as follows: if there is a connection from the jth agent to ith agent, then $g_{ij} > 0$; otherwise, $g_{ij} = 0$, and the diffusive coupling condition $g_{ii} = \sum_{j=1, j\neq i}^{N} g_{ij}$ is satisfied. R_{ij}, named as *channel matrix*, is a diagonal matrix with the diagonal element $r_{ij}^k = 0$ or 1 $(k = 1, 2, \ldots, n)$.

Remark 1. Since the state of each agent consists of n levels of information, the couplings in the NDS have to be divided into n channels to transmit the corresponding levels of information. Due to practical constraints, only part of the n channels can work normally. The diagonal element r_{ij}^k $(k = 1, 2, \ldots, n)$ of the channel matrix R_{ij} is employed to indicate the activity of the kth channel connecting agents j and i. Specifically, $R_{ij}x_j = [r_{ij}^1 x_{j1}, \ldots, r_{ij}^n x_{jn}]^\top$. When $r_{ij}^k = 1$, $r_{ij}^k x_{jk} = x_{jk}$, the kth level of state of agent j can be transmitted to agent i (i.e., the kth channel of the connection is *active*); otherwise, when $r_{ij}^k = 0$, $r_{ij}^k x_{jk} = 0$, the kth level of state of x_j is lost (i.e., the kth channel of the connection fails to transmit the information).

In the coupling control (2), each agent can receive the real-time information of its neighboring agents. However, the real-time information will increase the burden of the communication media. More importantly, it is unnecessary. For the sake of energy saving, the event-based control mechanism has been recently proposed as an effective alternative to the more conventional execution of control tasks. In this paper, the communication of agents will be carried out in an event-based manner; that is, the state of the agent will be sampled, if a given event is triggered.

To realize the event-based sampling, an event condition is designed for each agent. When the event condition is violated, the agent will sample its information and send it to its neighbors. Considering that the information is transmitted through channels, the event condition is given as follows:

$$\begin{gathered}\left|x_{ik}\left(t_m^{ik}\right) - x_{ik}\left(t_m^{ik} + lh\right)\right| \leq \gamma_{ik}\left|x_{ik}\left(t_m^{ik} + lh\right)\right|, \\ i \in \{1, 2, \ldots, N\}, \quad k \in \{1, 2, \ldots, n\},\end{gathered} \tag{3}$$

where $l = 1, 2, \ldots$; γ_{ik} is a positive scalar; $h > 0$ is the sampling period; t_m^{ik} is the latest sampling instant of the kth level of information of the ith agent. Thus, the next event-triggered instant is the time when event condition (3) is violated; that is,

$$\begin{aligned} t_{m+1}^{ik} = t_m^{ik} + h \inf \Big\{ l \in \mathbb{N} : &\left\|x_{ik}\left(t_m^{ik}\right) - x_{ik}\left(t_m^{ik} + lh\right)\right\| \\ &> \gamma_{ik}\left\|x_i\left(t_m^{ik} + lh\right)\right\| \Big\}. \end{aligned} \tag{4}$$

Without loss of generality, $t_0^{ik} = 0$ is the initial sampling time, for all i and k.

Let $\hat{x}_{ik}(t) = x_{ik}(t_m^{ik})$, for $t \in [t_m^{ik}, t_{m+1}^{ik})$ and $\hat{x}_i(t) = [\hat{x}_{i1}(t), \hat{x}_{i2}(t), \ldots, \hat{x}_{in}(t)]$. Thus, NDS (1) with partial and event-based couplings can be described as

$$\dot{x}_i(t) = Ax_i(t) + \alpha \sum_{j=1, j\neq i}^{N} g_{ij} R_{ij} \left(\hat{x}_j(t) - \hat{x}_i(t)\right). \tag{5}$$

Remark 2. Due to the traffic jam and physical characteristics of transmission media, communication constraints, such as

transmission delay [24–26], data packet dropout [27], and noise [28], commonly happen in real systems. In this paper, two kinds of communication constraints including partial information transmission of system and event-based sampled data are simultaneously considered in the couplings of NDS (5). Although both constraints cause information loss, their mechanisms are different. The event-based sampled data makes the real-time information available at the instants when event condition (3) is violated. The constraint of partial information transmission implies that the information sent at every instant is a lack of integrity. When we consider these two communication constraints simultaneously in NDSs, only part of the sampled information can be used for coupling control. Thus, the stabilization of the NDS is much harder to be realized.

Remark 3. Event condition (3) governs the sampling operation of NDS (5). When a subsystem is diverging, that is, the left hand side of the event condition becomes large, the subsystem has to update its state by sampling. In other words, the sampling happens only when it is needed. Thus, the event-based sampling scheme is more flexible and effective. It is able to realize fast reaction to emergency and avoid redundant samplings. Besides energy saving, another advantage of event-based sampling scheme is feasibility for large-scale systems. The sampling instants are independently decided by the event conditions of different subsystems. Thus, the common sampling schedule is unnecessary, which is hardly carried out in a system with large number of components. These two advantages make the event-based sampling scheme more applicable in engineering.

In order to stabilize the NDS, the state feedback controllers will be implemented. Considering that it is difficult and unnecessary to install the controller for every agent, we only choose a small fraction of agents to be controlled. In addition, we also assume that the control signal suffers from the two communication constraints. Thus, the pinning controller of agent i can be constructed as follows:

$$u_{i2}(t) = -d_i H_i \hat{x}_i(t), \tag{6}$$

where $d_i \geq 0$ is the control strength. In particular, when $d_i = 0$, it means that the ith agent will not be controlled. $H_i = \mathrm{diag}\{h_{i1}, h_{i2}, \ldots, h_{in}\}$ with $h_{ik} = 1$ or 0, which indicates that the kth level of the event-based sampled information of $\hat{x}(t)$ can be or cannot be sent from the controller.

Combining (5) and (6), the controlled NDS with partial and event-based couplings can be described by following equation:

$$\dot{x}_i(t) = Ax_i(t) + \alpha \sum_{j=1, j\neq i}^{N} g_{ij} R_{ij} \left(\hat{x}_j(t) - \hat{x}_i(t)\right) - d_i H_i \hat{x}_i(t). \tag{7}$$

Note that, for $t \in [t_m^{ik} + lh, t_m^{ik} + lh + h)$ ($l \geq 0$, $m \geq 0$, $i = 1, 2, \ldots, N$ and $k = 1, 2, \ldots, n$),

$$\begin{aligned}
\hat{x}_{jk}(t) - \hat{x}_{ik}(t) &= x_{jk}\left(t_{m'}^{jk}\right) - x_{ik}\left(t_m^{ik}\right) \\
&= x_{jk}\left(t_{m'}^{jk}\right) - x_{jk}\left(t_m^{ik} + lh\right) - x_{ik}\left(t_m^{ik}\right) \\
&\quad + x_{ik}\left(t_m^{ik} + lh\right) + x_{jk}\left(t_m^{ik} + lh\right) \\
&\quad - x_{ik}\left(t_m^{ik} + lh\right) \\
&= e_{jk}\left(t_m^{ik} + lh\right) - e_{ik}\left(t_m^{ik} + lh\right) \\
&\quad + x_{jk}\left(t_m^{ik} + lh\right) - x_{ik}\left(t_m^{ik} + lh\right),
\end{aligned} \tag{8}$$

where $e_{ik}(t_m^{ik}+lh) = \hat{x}_{ik}(t_m^{ik}+lh) - x_{ik}(t_m^{ik}+lh)$, $t_{m'}^{jk} = \max\{t \mid t \in t_m^{jk}, m = 0, 1, \ldots, t \leq t_m^{ik} + lh\}$, and $x_{jk}(t_{m'}^{jk}) = x_{jk}(t_m^{jk} + lh)$. Let $e_i(t) = [e_{i1}(t), e_{i2}(t), \ldots, e_{in}(t)]^\top$. Thus, for $t \in [mh, (m+1)h)$, (7) can be written as

$$\begin{aligned}
\dot{x}_i(t) = Ax_i(t) &+ \alpha \sum_{j=1, j\neq i}^{N} g_{ij} R_{ij} \left(e_j(mh) + x_j(mh)\right) \\
&- d_i H_i \left(x_i(mh) + e_i(mh)\right).
\end{aligned} \tag{9}$$

Let $C_{ij} = g_{ij} R_{ij}$, for $i, j = 1, 2, \ldots, N$, $i \neq j$ and $C_{ii} = -\sum_{j=1, j\neq i}^{N} C_{ij}$. Thus, C_{ij} are diagonal matrices with diagonal elements $c_{ij}^1, c_{ij}^2, \ldots, c_{ij}^n$ ($c_{ij}^k = g_{ij} \cdot r_{ij}^k$). For each $k = 1, 2, \ldots, n$, it can be followed from (9) that

$$\begin{aligned}
\dot{x}_{ik}(t) = \sum_{j=1}^{n} a_{kj} x_{ij}(t) &+ \alpha \sum_{j=1}^{N} c_{ij}^k \left(e_{jk}(mh) + x_{jk}(mh)\right) \\
&- d_i h_{ik} \left(e_{jk}(mh) + x_{jk}(mh)\right).
\end{aligned} \tag{10}$$

Let $\delta x_k(t) = [x_{1k}(t), x_{2k}(t), \ldots, x_{Nk}(t)]^\top$ and $\delta e_k(t) = [e_{1k}(t), e_{2k}(t), \ldots, e_{Nk}(t)]^\top$. From (10) we can get

$$\delta \dot{x}_k(t) = \sum_{j=1}^{n} a_{kj} \delta x_j(t) + \left(\alpha C_k - D_k\right)\left(\delta e_k(mh) + \delta x_k(mh)\right), \tag{11}$$

where $C_k = [c_{ij}^k]_{N\times N}$ and $D_k = \mathrm{diag}\{d_1 h_{1k}, d_2 h_{2k}, \ldots, d_N h_{Nk}\}$.

The following definition and lemma are needed for the derivation of our main results in this paper.

Definition 4. NDS (7) with partial and event-based couplings is said to achieve globally exponential stabilization, if there exist $M > 0$, $\varepsilon > 0$ such that $\|x_i(t)\|^2 < Me^{-\varepsilon t}$ is satisfied with any initial states $x_i(0)$ for $\forall i \in \{1, 2, \ldots, N\}$.

The purpose of this paper is to propose a set of sufficient conditions for controlled NDS (7) with partial and event-triggered communication to ensure the globally exponential stabilization.

Lemma 5 (see [29]). *For any real vectors a, b and scalar $\varepsilon > 0$, one has*

$$a^\top b + b^\top a \leq \varepsilon a^\top a + \varepsilon^{-1} b^\top b. \tag{12}$$

3. Main Results

In this section, the stabilization conditions will be derived for controlled NDS (7) with partial and event-based couplings.

Theorem 6. *For any $k = 1, 2, \ldots, n$, let $\Gamma_k = \operatorname{diag}\{\gamma_{1k}^2, \gamma_{2k}^2, \ldots, \gamma_{Nk}^2\}$. NDS (7) with partial and event-based couplings can be globally exponentially stabilized, if there exist positive scalars ε_{1k}, ε_{2k} and matrices $P_k > 0$, $Q_k = \operatorname{diag}\{q_{1k}, q_{2k}, \ldots, q_{Nk}\} > 0$, $\mathscr{W}_k = \begin{bmatrix} W_{1k} & W_{2k} & W_{4k} \\ * & W_{3k} & 0 \\ * & * & W_{5k} \end{bmatrix} > 0$, U_{1k}, U_{2k}, U_{3k}, U_{4k}, V_{1k}, V_{2k}, X_k, X_{1k}, such that the following LMIs are satisfied:*

$$\begin{bmatrix} P_k + h\dfrac{X_k + X_k^\top}{2} + W_{1k} & -hX_k + hX_{1k} - W_{1k} & W_{2k} & W_{4k} \\ * & -hX_{1k} - hX_{1k}^\top + h\dfrac{X_k + X_k^\top}{2} + W_{1k} & -W_{2k} & -W_{4k} \\ * & * & W_{3k} & 0 \\ * & * & * & W_{5k} \end{bmatrix} > 0, \tag{13}$$

$$\begin{bmatrix} \Phi_{11}^k & \Phi_{12}^k & \Phi_{13}^k & \Phi_{14}^k & hU_{1k}^\top & nV_{1k}^\top & 0 \\ * & \Phi_{22}^k & \Phi_{23}^k & \Phi_{24}^k & hU_{2k}^\top & 0 & 0 \\ * & * & \Phi_{33}^k & \Phi_{34}^k & hU_{3k}^\top & 0 & nV_{2k}^\top \\ * & * & * & \Phi_{44}^k & hU_{4k}^\top & 0 & 0 \\ * & * & * & * & -hW_{1k} & 0 & 0 \\ * & * & * & * & * & -n\varepsilon_{1k}I_N & 0 \\ * & * & * & * & * & * & -n\varepsilon_{2k}I_N \end{bmatrix} < 0, \tag{14}$$

$$\begin{bmatrix} \Phi_{11}^k & \Phi_{12}^k & \Pi_{13}^k & \Phi_{14}^k & nV_{1k}^\top & 0 \\ * & \Pi_{22}^k & \Pi_{23}^k & \Phi_{24}^k & 0 & 0 \\ * & * & \Pi_{33}^k & \Pi_{34}^k & 0 & nV_{2k}^\top \\ * & * & * & \Pi_{44}^k & 0 & 0 \\ * & * & * & * & -n\varepsilon_{1k}I_N & 0 \\ & * & * & * & * & -n\varepsilon_{2k}I_N \end{bmatrix} < 0, \tag{15}$$

where

$$\begin{aligned}
\Phi_{11}^k &= -\frac{X_k + X_k^\top}{2} - U_{1k} - U_{1k}^\top + \sum_{j=1}^{n} \left(\varepsilon_{1j} + \varepsilon_{2j}\right) a_{jk}^2 I_n, \\
\Phi_{12}^k &= X_k - X_{1k} - W_{2k} + U_{1k}^\top - U_{2k} + V_{1k}^\top \left(\alpha C_k - D_k\right), \\
\Phi_{13}^k &= P_k - U_{3k} - V_{1k}^\top, \\
\Phi_{14}^k &= -W_{4k} - U_{4k} + V_{1k}^\top \left(\alpha C_k - D_k\right), \\
\Phi_{22}^k &= X_{1k} + X_{1k}^\top - \frac{X_k + X_k^\top}{2} + W_{2k} + W_{2k}^\top \\
&\quad + U_{2k} + U_{2k}^\top + Q_k\Gamma_k - hW_{3k}, \\
\Phi_{23}^k &= U_{3k} + \left(\alpha C_k^\top - D_k\right) V_{2k}, \\
\Phi_{24}^k &= W_{4k} + U_{4k}, \\
\Phi_{33}^k &= -V_{2k} - V_{2k}^\top, \\
\Phi_{34}^k &= V_{2k}^\top \left(\alpha C_k - D_k\right), \\
\Phi_{44}^k &= -Q_k - hW_{5k}, \\
\Pi_{13}^k &= h\frac{X_k + X_k^\top}{2} + P_k - U_{3k} - V_{1k}^\top, \\
\Pi_{22}^k &= X_{1k} + X_{1k}^\top - \frac{X_k + X_k^\top}{2} + W_{2k} + W_{2k}^\top \\
&\quad + U_{2k} + U_{2k}^\top + Q_k\Gamma_k + hW_{3k}, \\
\Pi_{23}^k &= hW_{2k}^\top + hX_{1k}^\top - hX_k^\top + U_{3k} + \left(\alpha C_k^\top - D_k\right) V_{2k}, \\
\Pi_{33}^k &= hW_{1k} - V_{2k} - V_{2k}^\top, \\
\Pi_{34}^k &= hW_{4k} + V_{2k}^\top \left(\alpha C_k - D_k\right), \\
\Pi_{44}^k &= -Q_k + hW_{5k}.
\end{aligned} \tag{16}$$

Proof. For $t \in [mh, (m+1)h)$, define the Lyapunov functional $V(t) = \sum_{k=1}^{n} V_k(t)$, where

$$\begin{aligned} V_k(t) &= \delta x_k^\top(t) P_k \delta x_k(t) \\ &\quad + \varsigma(t) \int_{mh}^{t} \begin{bmatrix} \delta \dot{x}_k(s) \\ \delta x_k(mh) \\ \delta e_k(mh) \end{bmatrix}^\top \mathscr{W}_k \begin{bmatrix} \delta \dot{x}_k(s) \\ \delta x_k(mh) \\ \delta e_k(mh) \end{bmatrix} ds \\ &\quad + \varsigma(t) \begin{bmatrix} \delta x_k(t) \\ \delta x_k(mh) \end{bmatrix}^\top \mathscr{X}_k \begin{bmatrix} \delta x_k(t) \\ \delta x_k(mh) \end{bmatrix}, \end{aligned} \tag{17}$$

and $\varsigma(t) = (m+1)h - t$, $\mathscr{X}_k = \begin{bmatrix} (X_k+X_k^\top)/2 & -X_k+X_{1k} \\ * & -X_{1k}-X_{1k}^\top+(X_k+X_k^\top)/2 \end{bmatrix}$.

Before proceeding our proof, it should be pointed out that $V(t)$ is well defined. Based on $\mathscr{W}_k > 0$ and Schur complement [30], we have that

$$\widehat{W}_k \triangleq W_{1k} - W_{2k} W_{3k}^{-1} W_{2k}^\top - W_{4k} W_{5k}^{-1} W_{4k}^\top. \tag{18}$$

Thus, it follows that

$$\begin{aligned} &\mathscr{W}_k - \begin{bmatrix} \widehat{W}_k & 0 & 0 \\ * & 0 & 0 \\ * & * & 0 \end{bmatrix} \\ &= \begin{bmatrix} W_{2k} W_{3k}^{-1} W_{2k}^\top + W_{4k} W_{5k}^{-1} W_{4k}^\top & W_{2k} & W_{4k} \\ * & W_{3k} & 0 \\ * & * & W_{5k} \end{bmatrix} \geq 0, \end{aligned} \tag{19}$$

which implies

$$\mathscr{W}_k \geq \begin{bmatrix} \widehat{W}_k & 0 & 0 \\ * & 0 & 0 \\ * & * & 0 \end{bmatrix}. \tag{20}$$

Based on the above inequality, it can be got that

$$\begin{bmatrix} \delta \dot{x}_k(s) \\ \delta x_k(mh) \\ \delta e_k(mh) \end{bmatrix}^\top \mathscr{W}_k \begin{bmatrix} \delta \dot{x}_k(s) \\ \delta x_k(mh) \\ \delta e_k(mh) \end{bmatrix} \geq \delta \dot{x}_k^\top(s) \widehat{W}_k \delta \dot{x}_k(s). \tag{21}$$

Thus, it follows from (17) and (21) that

$$\begin{aligned} V_k(t) &\geq \delta x_k^\top(t) P_k \delta x_k(t) \\ &\quad + \varsigma(t) \int_{mh}^{t} \delta \dot{x}_k^\top(s) \widehat{W}_k \delta \dot{x}_k(s)\, ds \\ &\quad + \varsigma(t) \begin{bmatrix} \delta x_k(t) \\ \delta x_k(mh) \end{bmatrix}^\top \mathscr{X}_k \begin{bmatrix} \delta x_k(t) \\ \delta x_k(mh) \end{bmatrix}. \end{aligned} \tag{22}$$

By applying the Jensen inequality [31], we have

$$\begin{aligned} &\int_{mh}^{t} \delta \dot{x}_k^\top(s) \widehat{W}_k \delta \dot{x}_k(s)\, ds \\ &\quad \geq \frac{1}{\tau(t)} \int_{mh}^{t} \delta \dot{x}_k^\top(s)\, ds \widehat{W}_k \int_{mh}^{t} \delta \dot{x}_k(s)\, ds \\ &\quad \geq \frac{1}{h} \left[\delta x_k(t) - \delta x_k(mh)\right]^\top \widehat{W}_k \left[\delta x_k(t) - \delta x_k(mh)\right], \end{aligned} \tag{23}$$

where $\tau(t) = t - mh$. From (22) and (23), it can be obtained that

$$V_k(t) \geq \begin{bmatrix} \delta x_k(t) \\ \delta x_k(mh) \end{bmatrix}^\top \mathscr{H}_k \begin{bmatrix} \delta x_k(t) \\ \delta x_k(mh) \end{bmatrix}, \tag{24}$$

where $\mathscr{H}_k = (\varsigma(t)/h)[\mathscr{P}_k + h\mathscr{X}_k + \widehat{\mathscr{W}}_k] + (\tau(t)/h)\mathscr{P}_k$, $\mathscr{P}_k = \begin{bmatrix} P_k & 0 \\ * & 0 \end{bmatrix}$ and $\widehat{\mathscr{W}}_k = \begin{bmatrix} \widehat{W}_k & -\widehat{W}_k \\ * & \widehat{W}_k \end{bmatrix}$. Based on the Schur complement [30], it follows from (13) that $\mathscr{P}_k + h\mathscr{X}_k + \widehat{\mathscr{W}}_k > 0$. Thus, we can always find a positive scalar $\beta < 1$, such that $\mathscr{P}_k + h\mathscr{X}_k + \widehat{\mathscr{W}}_k > \beta \mathscr{P}_k$, which further means that

$$\begin{aligned} V(t) &= \sum_{k=1}^{n} V_k(t) > \sum_{k=1}^{n} \beta \begin{bmatrix} \delta x_k(t) \\ \delta x_k(mh) \end{bmatrix}^\top \mathscr{P}_k \begin{bmatrix} \delta x_k(t) \\ \delta x_k(mh) \end{bmatrix} \\ &= \beta \sum_{i=1}^{N} \left\| x_i(t) \right\|^2. \end{aligned} \tag{25}$$

Therefore, $V(t)$ defined in (17) is a valid Lyapunov functional.

The derivative of $V_k(t)$ can be got that

$$\begin{aligned} \dot{V}_k(t) &= 2\delta \dot{x}_k(t) P_k \delta x_k(t) \\ &\quad - \int_{mh}^{t} \begin{bmatrix} \delta \dot{x}_k(s) \\ \delta x_k(mh) \\ \delta e_k(mh) \end{bmatrix}^\top \widetilde{\mathscr{W}}_k \begin{bmatrix} \delta \dot{x}_k(s) \\ \delta x_k(mh) \\ \delta e_k(mh) \end{bmatrix} ds \\ &\quad + \varsigma(t) \begin{bmatrix} \delta \dot{x}_k(t) \\ \delta x_k(mh) \\ \delta e_k(mh) \end{bmatrix}^\top \mathscr{W}_k \begin{bmatrix} \delta \dot{x}_k(t) \\ \delta x_k(mh) \\ \delta e_k(mh) \end{bmatrix} \\ &\quad - \begin{bmatrix} \delta x_k(t) \\ \delta x_k(mh) \end{bmatrix}^\top \mathscr{X}_k \begin{bmatrix} \delta x_k(t) \\ \delta x_k(mh) \end{bmatrix} \\ &\quad + 2\varsigma(t) \begin{bmatrix} \delta \dot{x}_k(t) \\ 0 \end{bmatrix}^\top \mathscr{X}_k \begin{bmatrix} \delta x_k(t) \\ \delta x_k(mh) \end{bmatrix} \\ &\quad - \chi_1 \int_{mh}^{t} \left\| \delta \dot{x}_k(s) \right\|^2 ds, \end{aligned} \tag{26}$$

where $\widetilde{\mathscr{W}}_k = \mathscr{W}_k - \mathrm{diag}\{\chi_1 I_N, 0, 0\}$ and χ_1 is a positive scalar such that $\widetilde{\mathscr{W}}_k > 0$. By employing the Jensen inequality [31], it follows that

$$\begin{aligned}
&\int_{mh}^{t} \begin{bmatrix} \delta\dot{x}_k(s) \\ \delta x_k(mh) \\ \delta e_k(mh) \end{bmatrix}^{\top} \widetilde{\mathscr{W}}_k \begin{bmatrix} \delta\dot{x}_k(s) \\ \delta x_k(mh) \\ \delta e_k(mh) \end{bmatrix} ds \\
&\quad \geq \tau(t)\,\phi_k^{\top}(t)\left(W_{1k} - \chi_1 I_N\right)\phi_k(t) \\
&\qquad + \tau(t)\,\delta x_k^{\top}(mh)\,W_{3k}\delta x_k(mh) \\
&\qquad + \tau(t)\,\delta e_k^{\top}(mh)\,W_{5k}\delta e_k(mh) \\
&\qquad + 2\left[\delta x_k(t) - \delta x_k(mh)\right]^{\top} W_{2k}\delta x_k(mh) \\
&\qquad + 2\left[\delta x_k(t) + \delta x_k(mh)\right]^{\top} W_{4k}\delta e_k(mh),
\end{aligned} \tag{27}$$

where $\phi(t) = (1/\tau(t))\int_{mh}^{t}\delta\dot{x}_k(s)ds$.

According to the Newton-Leibnitz formula, it can be obtained that

$$\begin{aligned}
0 = {} & 2\left[\delta x_k^{\top}(t)\,U_{1k}^{\top} + \delta x_k^{\top}(mh)\,U_{2k}^{\top} + \delta\dot{x}_k(t)\,U_{3k}^{\top}\right. \\
& \left. + \delta e_k^{\top}(mh)\,U_{4k}^{\top}\right] \\
& \cdot\left[-\delta x_k(t) + \delta x_k(mh) + \tau(t)\,\phi_k(t)\right].
\end{aligned} \tag{28}$$

From (11), one can have that

$$\begin{aligned}
0 = {} & 2\left[\delta x_k^{\top}(t)\,V_{1k}^{\top} + \delta\dot{x}_k(t)\,V_{2k}^{\top}\right] \\
& \cdot\left[-\delta\dot{x}_k(t) + \sum_{j=1}^{n} a_{kj}\delta x_j(t)\right. \\
& \left. + \left(\alpha C_k - D_k\right)\left(\delta e_k(mh) + \delta x_k(mh)\right)\right].
\end{aligned} \tag{29}$$

By employing Lemma 5, it follows that

$$\begin{aligned}
& 2\delta x_k^{\top}(t)\,V_{1k}^{\top}\sum_{j=1}^{n} a_{kj}\delta x_j(t) \\
& \quad \leq n\varepsilon_{1k}^{-1}\delta x_k^{\top}(t)\,V_{1k}^{\top}V_{1k}\delta x_k(t) + \varepsilon_{1k}\sum_{j=1}^{n} a_{kj}^2\delta x_j^{\top}(t)\,\delta x_j(t), \\
& 2\delta\dot{x}_k^{\top}(t)\,V_{2k}^{\top}\sum_{j=1}^{n} a_{kj}\delta x_j(t) \\
& \quad \leq n\varepsilon_{2k}^{-1}\delta\dot{x}_k^{\top}(t)\,V_{2k}^{\top}V_{2k}\delta\dot{x}_k(t) + \varepsilon_{2k}\sum_{j=1}^{n} a_{kj}^2\delta x_j^{\top}(t)\,\delta x_j(t).
\end{aligned} \tag{30}$$

From event condition (3), it can be got that $|e_{ik}(mh)| \leq \gamma_{ik}|x_{ik}(mh)|$, which is equivalent to $\sqrt{q_{ik}}|e_{ik}(mh)| \leq \sqrt{q_{ik}}\gamma_{ik}|x_{ik}(mh)|$. Thus, we have that

$$\delta e_k^{\top}(mh)\,Q_k\delta e_k(mh) \leq \delta x_k^{\top}(mh)\,Q_k\Gamma_k\delta x_k(mh). \tag{31}$$

Combining (26)–(31) yields that

$$\begin{aligned}
\dot{V}(t) = \sum_{k=1}^{n}\Bigg\{ & \eta_k^{\top}(t)\left[\frac{\varsigma(t)}{h}\overline{\Psi}_k + \frac{\tau(t)}{h}\Psi_k\right]\eta_k(t) \\
& -\chi_1\int_{mh}^{t}\left\|\delta\dot{x}_k(s)\right\|^2 ds\Bigg\},
\end{aligned} \tag{32}$$

where $\eta_k(t) = \left[\delta x_k(t)\ \ \delta x_k(mh)\ \ \delta\dot{x}_k(t)\ \ \delta e_k(mh)\ \ \phi_k(t)\right]^{\top}$ and $\overline{\Psi}_k = \left[\begin{smallmatrix} \Psi_k' & 0 \\ * & 0 \end{smallmatrix}\right]$,

$$\Psi_k = \begin{bmatrix} \Phi_{11}^k + n\varepsilon_{1k}^{-1}V_{1k}^{\top}V_{1k} & \Phi_{12}^k & \Phi_{13}^k & \Phi_{14}^k & hU_{1k}^{\top} \\ * & \Phi_{22}^k & \Phi_{23}^k & \Phi_{24}^k & hU_{2k}^{\top} \\ * & * & \Phi_{33}^k + n\varepsilon_{2k}^{-1}V_{2k}^{\top}V_{2k} & \Phi_{34}^k & hU_{3k}^{\top} \\ * & * & * & \Phi_{44}^k & hU_{4k}^{\top} \\ * & * & * & * & -hW_{1k} + h\chi_1 I_N \end{bmatrix},$$
$$\Psi_k' = \begin{bmatrix} \Phi_{11}^k + n\varepsilon_{1k}^{-1}V_{1k}^{\top}V_{1k} & \Phi_{12}^k & \Pi_{13}^k & \Phi_{14}^k \\ * & \Pi_{22}^k & \Phi_{23}^k & \Phi_{24}^k \\ * & * & \Pi_{33}^k + n\varepsilon_{2k}^{-1}V_{2k}^{\top}V_{2k} & \Pi_{34}^k \\ * & * & * & \Pi_{44}^k \end{bmatrix}. \tag{33}$$

By using the Schur complement [30], it follows from (14) and (15) that $\Psi_k|_{\chi_1=0} < 0$ and $\Psi_k' < 0$. Furthermore, we can always choose sufficiently small scalars χ_1, χ_2, χ_3, and χ_4 to ensure $\Psi_k + \mathrm{diag}\{\chi_2 I_N, \chi_3 I_N, 0, \chi_4 I_N, 0\} < 0$ and

$\Psi_k' + \mathrm{diag}\{\chi_2 I_N, \chi_3 I_N, 0, \chi_4 I_N\} < 0$. It follows from (32) that

$$\dot{V}(t) < \sum_{k=1}^{n} \left\{ -\chi_2 \left\|\delta x_k(t)\right\|^2 - \chi_3 \left\|\delta x_k(mh)\right\|^2 - \chi_4 \left\|\delta e_k(mh)\right\|^2 - \chi_1 \int_{mh}^{t} \left\|\dot{\delta x}_k(s)\right\|^2 ds \right\}. \tag{34}$$

From (17), we have that

$$\begin{aligned} &\delta x_k^\top(t) P_k \delta x_k(t) + \varsigma(t) \begin{bmatrix} \delta x_k(t) \\ \delta x_k(mh) \end{bmatrix}^\top \mathscr{X}_k \begin{bmatrix} \delta x_k(t) \\ \delta x_k(mh) \end{bmatrix} \\ &= \begin{bmatrix} \delta x_k(t) \\ \delta x_k(mh) \end{bmatrix}^\top \left\{ \frac{\varsigma(t)}{h} \left[\mathscr{P}_k + h\mathscr{X}_k\right] + \frac{\tau(t)}{h} \mathscr{P}_k \right\} \cdot \begin{bmatrix} \delta x_k(t) \\ \delta x_k(mh) \end{bmatrix} \\ &\le \begin{bmatrix} \delta x_k(t) \\ \delta x_k(mh) \end{bmatrix}^\top \cdot \left\{ \frac{\varsigma(t)}{h} \left[\mathscr{P}_k + h\mathscr{X}_k + \mathscr{U}_k\right] + \frac{\tau(t)}{h} \mathscr{P}_k \right\} \begin{bmatrix} \delta x_k(t) \\ \delta x_k(mh) \end{bmatrix}, \end{aligned} \tag{35}$$

where $\mathscr{U}_k = \begin{bmatrix} W_{1k} & -W_{1k} \\ & W_{1k} \end{bmatrix} \ge 0$. From (13), we have that there exists a positive scalar ρ such that

$$\mathscr{P}_k + h\mathscr{X}_k + \mathscr{U}_k < \rho_1 I_{2N}, \qquad P_k < \rho_1 I_N. \tag{36}$$

Furthermore, a positive number ρ_2 can be chosen such that

$$\begin{aligned} &\varsigma(t) \int_{mh}^{t} \begin{bmatrix} \dot{\delta x}_k(s) \\ \delta x_k(mh) \\ \delta e_k(mh) \end{bmatrix}^\top \mathscr{W}_k \begin{bmatrix} \dot{\delta x}_k(s) \\ \delta x_k(mh) \\ \delta e_k(mh) \end{bmatrix} ds \\ &\le \rho_2 \int_{mh}^{t} \left\|\dot{\delta x}_k(s)\right\|^2 ds + \rho_2 \left\|\delta x_k(mh)\right\|^2 + \rho_2 \left\|\delta e_k(mh)\right\|^2. \end{aligned} \tag{37}$$

Thus, from (35) to (37), it follows that

$$V(t) \le \sum_{k=1}^{n} \left\{ \rho_1 \left\|\delta x_k(t)\right\|^2 + (\rho_1 + \rho_2) \left\|\delta x_k(mh)\right\|^2 + \rho_2 \left\|\delta e_k(mh)\right\|^2 + \rho_2 \int_{mh}^{t} \left\|\dot{\delta x}_k(s)\right\|^2 ds \right\}. \tag{38}$$

Let $\varepsilon > 0$ such that

$$\begin{aligned} &\varepsilon\rho_1 - \chi_2 \le 0, \qquad \varepsilon(\rho_1 + \rho_2) - \chi_3 \le 0, \\ &\varepsilon\rho_2 - \chi_4 \le 0, \qquad \varepsilon\rho_2 - \chi_1 \le 0. \end{aligned} \tag{39}$$

According to (34), (38), and (39), we can get $\dot{V}(t) + \varepsilon V(t) \le 0 \forall t \in [mh, (m+1)h)$. Thus, $V(t) \le e^{-\varepsilon(t-mh)} V(mh)$. By mathematical induction, it can be concluded that $V(t) \le e^{-\varepsilon t} V(0), \forall t > 0$. From (25), we yield that

$$\left\|x_i(t)\right\|^2 \le \sum_{i=1}^{N} \left\|x_i(t)\right\|^2 \le \beta^{-1} V(t) \le \beta^{-1} V(0) e^{-\varepsilon t}, \quad i \in \{1, 2, \ldots, N\}. \tag{40}$$

Hence, from Definition 4, controlled NDS (1) with partial and event-based couplings can achieve globally exponentially stabilization under event condition (3) and pinning controllers (6). This completes the proof. □

When all the channel matrices R_{ij} are identity matrices, that is, $R_{ij} = I_n$ $(i, j = 1, 2, \ldots, N)$, the communication constraint of partial information transmission is removed. Furthermore, we assume that if an agent is controlled, every level of information of the controller can be well transmitted by the controller; that is, H_i $(i = 1, 2, \ldots, N)$ in (6) are also identity matrices. Overall, the controlled NDS with event-based couplings can be constructed by following differential equation:

$$\dot{x}_i(t) = Ax_i(t) + \alpha \sum_{j=1, j\ne i}^{N} g_{ij} \left(\hat{x}_j(t) - \hat{x}_i(t)\right) - d_i \hat{x}_i(t). \tag{41}$$

The main difference between NDS (7) and (41) is that the channels are not considered in (41). Thus, the event condition of each system can be described as

$$\left\|x_i\left(t_m^i\right) - x_i\left(t_m^i + lh\right)\right\| \le \gamma_i \left\|x_i\left(t_m^i + lh\right)\right\|, \quad i \in \{1, 2, \ldots, N\}, \tag{42}$$

where $l = 1, 2, \ldots$, $\gamma_i > 0$. Similarly, the next event-triggered instant is $t_{m+1}^i = t_m^i + h \inf\{l \in \mathbb{N} : \|x_i(t_m^i) - x_i(t_m^i + lh)\| > \gamma_i \|x_i(t_m^i + lh)\|\}$. We also assume that $t_0^i = 0$ for each agent i.

Based on Theorem 6, the stabilization conditions of NDS (41) with event condition (42) can be easily obtained as follows.

Corollary 7. *Let* $\Gamma = \mathrm{diag}\{\gamma_1^2, \gamma_2^2, \ldots, \gamma_N^2\}$ *and* $D = \mathrm{diag}\{d_1, d_2, \ldots, d_N\}$. *NDS (41) with event-based couplings can be exponentially stabilized, if there exist positive scalars* ε_1, ε_2 *and matrices* $P > 0$, $Q = \mathrm{diag}\{q_1, q_2, \ldots, q_N\} > 0$, $\mathscr{W} = \begin{bmatrix} W_1 & W_2 & W_4 \\ * & W_3 & 0 \\ * & * & W_5 \end{bmatrix} > 0$, U_1, U_2, U_3, U_4, V_1, V_2, X, X_1, *such that the following LMIs are satisfied:*

$$\begin{bmatrix} P_k + h\dfrac{X + X^\top}{2} + W_1 & -hX + hX_1 - W_1 & W_2 & W_4 \\ * & -hX_1 - hX_1^\top + h\dfrac{X + X^\top}{2} + W_1 & -W_2 & -W_4 \\ * & * & W_3 & 0 \\ * & * & * & W_5 \end{bmatrix} > 0,$$

$$\begin{bmatrix} \Phi_{11} & \Phi_{12} & \Phi_{13} & \Phi_{14} & hU_1^{\top} & nV_1^{\top} & 0 \\ * & \Phi_{22} & \Phi_{23} & \Phi_{24} & hU_2^{\top} & 0 & 0 \\ * & * & \Phi_{33} & \Phi_{34} & hU_3^{\top} & 0 & nV_2^{\top} \\ * & * & * & \Phi_{44} & hU_4^{\top} & 0 & 0 \\ * & * & * & * & -hW_1 & 0 & 0 \\ * & * & * & * & * & -n\varepsilon_1 I_N & 0 \\ * & * & * & * & * & * & -n\varepsilon_2 I_N \end{bmatrix} < 0,$$

$$\begin{bmatrix} \Phi_{11} & \Phi_{12} & \Pi_{13} & \Phi_{14} & nV_1^{\top} & 0 \\ * & \Pi_{22} & \Pi_{23} & \Phi_{24} & 0 & 0 \\ * & * & \Pi_{33} & \Pi_{34} & 0 & nV_2^{\top} \\ * & * & * & \Pi_{44} & 0 & 0 \\ * & * & * & * & -n\varepsilon_1 I_N & 0 \\ & * & * & * & * & -n\varepsilon_2 I_N \end{bmatrix} < 0, \tag{43}$$

where

$$\begin{aligned}
\Phi_{11} &= -\frac{X+X^{\top}}{2} - U_1 - U_1^{\top} + \sum_{j=1}^{n} \left(\varepsilon_{1j} + \varepsilon_{2j}\right) a_j^2, \\
\Phi_{12} &= X - X_1 - W_2 + U_1^{\top} - U_2 + V_1^{\top} (\alpha G - D), \\
\Phi_{13} &= P - U_3 - V_1^{\top}, \\
\Phi_{14} &= -W_4 - U_4 + V_1^{\top} (\alpha G - D), \\
\Phi_{22} &= X_1 + X_1^{\top} - \frac{X+X^{\top}}{2} + W_2 + W_2^{\top} \\
&\quad + U_2 + U_2^{\top} + Q\Gamma - hW_3, \\
\Phi_{23} &= U_3 + \left(\alpha G^{\top} - D\right) V_2, \\
\Phi_{24} &= W_4 + U_4, \\
\Phi_{33} &= -V_2 - V_2^{\top}, \\
\Phi_{34} &= V_2^{\top} (\alpha G - D), \\
\Phi_{44} &= -Q - hW_5, \\
\Pi_{13} &= h\frac{X+X^{\top}}{2} + P - U_3 - V_1^{\top}, \\
\Pi_{22} &= X_1 + X_1^{\top} - \frac{X+X^{\top}}{2} + W_2 + W_2^{\top} \\
&\quad + U_2 + U_2^{\top} + Q\Gamma + hW_3, \\
\Pi_{23} &= hW_2^{\top} + hX_1^{\top} - hX_k^{\top} + U_3 + \left(\alpha G^{\top} - D\right) V_2, \\
\Pi_{33} &= hW_1 - V_2 - V_2^{\top}, \\
\Pi_{34} &= hW_4 + V_2^{\top} (\alpha G - D), \\
\Pi_{44} &= -Q + hW_5.
\end{aligned} \tag{44}$$

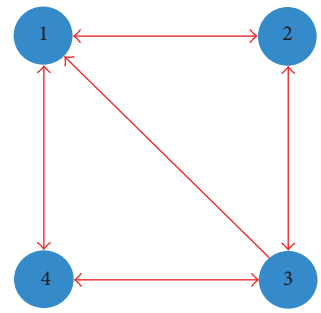

Figure 1: The topological structure of the NDS with 4 subsystems.

4. Numerical Example

In this section, a numerical example will be given to demonstrate the effectiveness of our main results.

An NDS with 4 agents is constructed ($N = 4$), the topological structure of which is depicted in Figure 1. The Laplacian matrix of the NDS is given as $G = \begin{bmatrix} -3 & 1 & 1 & 1 \\ 1 & -2 & 1 & 0 \\ 0 & 1 & -2 & 1 \\ 1 & 0 & 1 & -2 \end{bmatrix}$. The other parameters of the NDS are $\alpha = 0.35$ and $A = \begin{bmatrix} 0.12 & -0.08 \\ -0.06 & 0.12 \end{bmatrix}$. Thus, each agent of the NDS has 2 levels of information ($n = 2$). Due to the constraint of the partial information transmission, the couplings have to be divided into 2 levels of channels to transmit the information. For each coupling of the NDS, a channel matrix is given to reflect the work state of the channels of the coupling. The channel matrices of the couplings are listed as follows:

$$\begin{aligned}
R_{12} &= \operatorname{diag}\{0,1\}, & R_{13} &= \operatorname{diag}\{0,1\}, \\
R_{14} &= \operatorname{diag}\{1,0\}, & R_{21} &= \operatorname{diag}\{1,0\}, \\
R_{23} &= \operatorname{diag}\{0,1\}, & R_{32} &= \operatorname{diag}\{1,0\}, \\
R_{34} &= \operatorname{diag}\{0,1\}, & R_{41} &= \operatorname{diag}\{0,1\}, \\
& & R_{43} &= \operatorname{diag}\{1,0\}.
\end{aligned} \tag{45}$$

Thus, the Laplacian matrices of the channels of the 2 levels can be, respectively, built:

$$C_1 = \begin{bmatrix} -1 & 0 & 0 & 1 \\ 1 & -1 & 0 & 0 \\ 0 & 1 & -1 & 0 \\ 0 & 0 & 1 & -1 \end{bmatrix}, \qquad C_2 = \begin{bmatrix} -2 & 1 & 1 & 0 \\ 0 & -1 & 1 & 0 \\ 0 & 0 & -1 & 1 \\ 1 & 0 & 0 & -1 \end{bmatrix}. \tag{46}$$

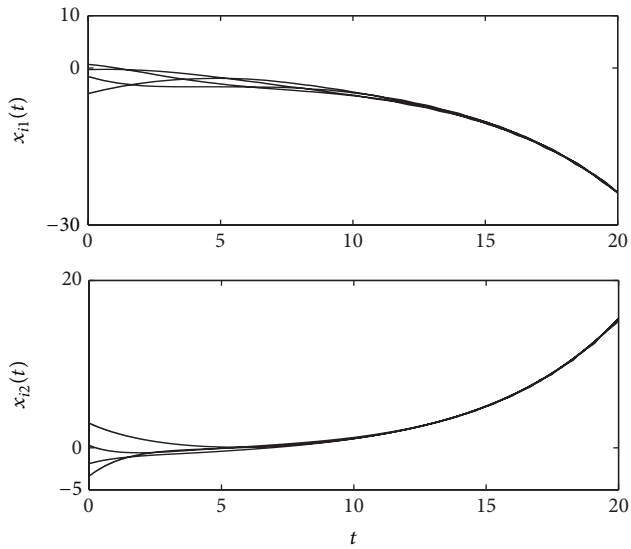

Figure 2: Without controllers, the trajectories of the NDS are divergent.

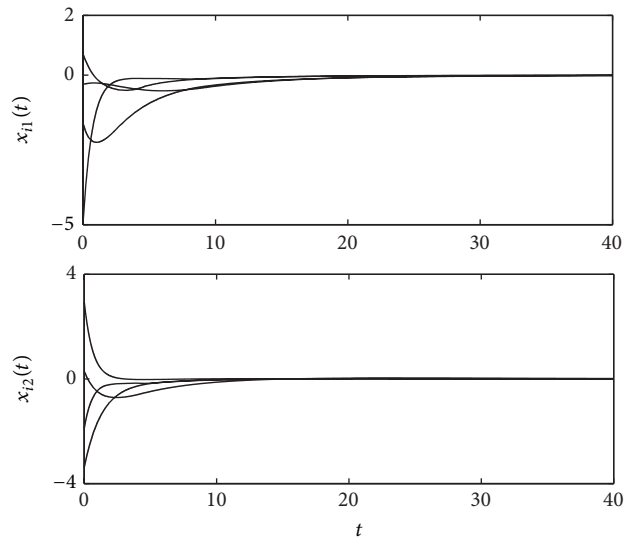

Figure 3: When the NDS is equipped with controllers, the trajectories of NDS tend to zero.

As discussed above, the event-based sampling scheme is used in the communication among agents of the NDS and the control signals. We assume that, in event condition (3), the sampling period $h = 0.1$ and $\gamma_{ik} = 0.15$, for $i = 1, 2, 3, 4$ and $k = 1, 2$. Let the coupling strength $\alpha = 0.35$. Without controllers, the constructed NDS is not stable. The trajectories of the uncontrolled NDS are shown in Figure 2, where $i = 1, 2, 3, 4$.

To achieve stabilization, controllers are distributed, implemented in the NDS with the control strengths: $d_1 = 1$, $d_2 = 1$, $d_3 = 1$, and $d_4 = 0$; that is, except the 4th agent, the other agents are controlled. Furthermore, for the controlled agents, only part of the control signals can be well received. Let $H_1 = \mathrm{diag}\{1, 0\}$, $H_2 = \mathrm{diag}\{0, 1\}$, and $H_3 = \mathrm{diag}\{1, 1\}$. Thus, $D_1 = \mathrm{diag}\{1, 0, 1, 0\}$ and $D_2 = \mathrm{diag}\{0, 1, 1, 0\}$. Based on the above parameters, a feasible solution can be found for conditions (13)–(15). The solution is listed as follows:

$$P_1 = \begin{bmatrix} 6.7804 & 0.9268 & -0.0993 & -1.2156 \\ 0.9268 & 6.5528 & -1.2156 & -1.0043 \\ -0.0993 & -1.2156 & 6.7804 & 0.9268 \\ -1.2156 & -1.0043 & 0.9268 & 6.5528 \end{bmatrix},$$

$$P_2 = \begin{bmatrix} 9.9491 & 0.8285 & 1.4249 & 0.2072 \\ 0.8285 & 10.3109 & 0.9803 & -0.2967 \\ 1.4249 & 0.9803 & 8.2046 & -1.1263 \\ 0.2072 & -0.2967 & -1.1263 & 7.4406 \end{bmatrix}, \tag{47}$$

$$Q_1 = \mathrm{diag}\{12.7657, 8.8809, 12.7657, 8.8809\},$$

$$Q_2 = \mathrm{diag}\{13.1103, 22.4816, 14.3887, 12.1669\}.$$

According to Theorem 6, the controlled NDS can be stabilized by the partial and event-based couplings. To show this fact, the trajectories of the controlled NDS are depicted in Figure 3. It can be found that all the trajectories tend to zero.

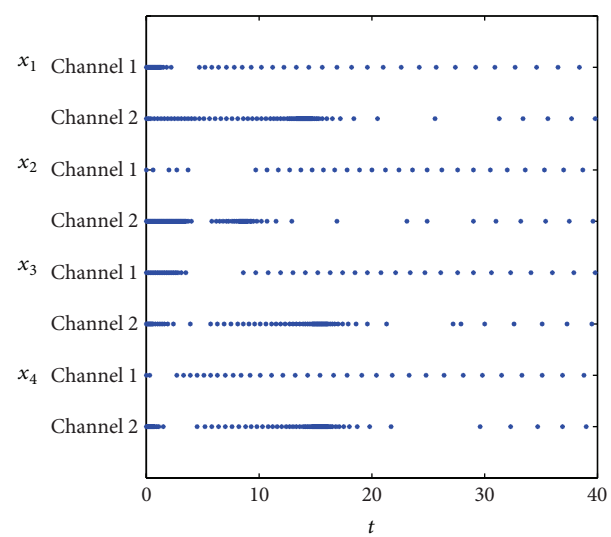

Figure 4: The sampling instants of all the channels of the NDS.

Figure 4 shows the sampling instants of the 2 channels of all the 4 agents of the NDS. The total number of the sampling instants of the NDS is 415. If the NDS employed the time-based sampling scheme with sampling period $h = 0.1$, the sampling number would be 3200. Thus, the sampling number of the event-based sampling scheme is only 12.97% of that of the time-based sampling scheme. In other words, the event-based sampling scheme can save 87% communication resource.

5. Conclusion

The stabilization problem of NDSs with partial and event-based couplings has been investigated. The communication

among the agents has been assumed to suffer from two communication constraints: partial information transmission and event-based sampling. The former constraint leads to the information packet of each agent lack of integrity. However, the constraint of sampling makes the real-time information available at some discrete sampling instants. Furthermore, the sampling instants cannot be figured out in advance. Thus, the two constraints make the stabilization problem much harder. Furthermore, the control signals also suffered from these two constraints. By building the channel Laplacian matrices for different levels of information, the stabilization condition has been derived for the NDS with partial and event-based couplings. The numerical simulation has been given to show the effectiveness of our theoretical results. In this paper, the partial information transmission is considered as the communication constraint. However, some other constraints are also significant, such as the quantization and saturation. When we consider the event-based sampling scheme simultaneously, how would they impact the dynamical behaviour of NDSs? It is an interesting yet challenging problem. We will investigate it in our future work.

Conflict of Interests

The authors declare that there is no conflict of interests regarding the publication of this paper.

Acknowledgments

This work was partially supported by the Tianyuan Special Funds of the NNSF of China under Grant no. 11326126, the Soft Science Funds of Shanxi Province under Grant no. 800104-02040179, and the Qualified Personnel Foundation of Taiyuan University of Technology (QPFT) (no. tyutrc-2030017).

References

[1] F. Bullo, J. Cortés, and S. Martínez, *Distributed Control of Robotic Networks: A Mathematical Approach to Motion Coordination Algorithms*, Princeton University Press, 2009.

[2] J. Lu, J. He, J. Cao, and Z. Gao, "Topology influences performance in the associative memory neural networks," *Physics Letters, Section A: General, Atomic and Solid State Physics*, vol. 354, no. 5-6, pp. 335–343, 2006.

[3] J. Lu and D. W. C. Ho, "Stabilization of complex dynamical networks with noise disturbance under performance constraint," *Nonlinear Analysis: Real World Applications*, vol. 12, no. 4, pp. 1974–1984, 2011.

[4] J. Lu, Z. Wang, J. Cao, D. W. C. Ho, and J. Kurths, "Pinning impulsive stabilization of nonlinear dynamical networks with time-varying delay," *International Journal of Bifurcation and Chaos*, vol. 22, no. 7, Article ID 1250176, 2012.

[5] C. Huang, D. W. C. Ho, and J. Lu, "Partial-information-based distributed filtering in two-targets tracking sensor networks," *IEEE Transactions on Circuits and Systems I: Regular Papers*, vol. 59, no. 4, pp. 820–832, 2012.

[6] J. Lu, D. W. C. Ho, J. Cao, and J. Kurths, "Single impulsive controller for globally exponential synchronization of dynamical networks," *Nonlinear Analysis: Real World Applications*, vol. 14, no. 1, pp. 581–593, 2013.

[7] J. Lu, D. W. C. Ho, and J. Cao, "Synchronization in an array of nonlinearly coupled chaotic neural networks with delay coupling," *International Journal of Bifurcation and Chaos*, vol. 18, no. 10, pp. 3101–3111, 2008.

[8] J. Lu, D. W. C. Ho, J. Cao, and J. Kurths, "Exponential synchronization of linearly coupled neural networks with impulsive disturbances," *IEEE Transactions on Neural Networks*, vol. 22, no. 2, pp. 329–336, 2011.

[9] H. R. Karimi and H. Gao, "New delay-dependent exponential H_∞ synchronization for uncertain neural networks with mixed time delays," *IEEE Transactions on Systems, Man, and Cybernetics. Part B: Cybernetics*, vol. 40, no. 1, pp. 173–185, 2010.

[10] Z. Wang, Y. Wang, and Y. Liu, "Global synchronization for discrete-time stochastic complex networks with randomly occurred nonlinearities and mixed time delays," *IEEE Transactions on Neural Networks*, vol. 21, no. 1, pp. 11–25, 2010.

[11] H. Dong, Z. Wang, and H. Gao, "Distributed H_∞ filtering for a class of markovian jump nonlinear time-delay systems over lossy sensor networks," *IEEE Transactions on Industrial Electronics*, vol. 60, no. 10, pp. 4665–4672, 2013.

[12] H. Dong, Z. Wang, D. W. C. Ho, and H. Gao, "Robust H_∞ fuzzy output-feedback control with multiple probabilistic delays and multiple missing measurements," *IEEE Transactions on Fuzzy Systems*, vol. 18, no. 4, pp. 712–725, 2010.

[13] Y. Tang, H. Gao, and J. Kurths, "Distributed robust synchronization of dynamical networks with stochastic coupling," *IEEE Transactions on Circuits and Systems I: Regular Papers*, vol. 61, no. 5, pp. 1508–1519, 2014.

[14] C. Zhou, L. Zemanová, G. Zamora, C. C. Hilgetag, and J. Kurths, "Hierarchical organization unveiled by functional connectivity in complex brain networks," *Physical Review Letters*, vol. 97, no. 23, Article ID 238103, 2006.

[15] H. Gao, J. Wu, and P. Shi, "Robust sampled-data H_∞ control with stochastic sampling," *Automatica*, vol. 45, no. 7, pp. 1729–1736, 2009.

[16] W. Yu, W. X. Zheng, G. Chen, W. Ren, and J. Cao, "Second-order consensus in multi-agent dynamical systems with sampled position data," *Automatica*, vol. 47, no. 7, pp. 1496–1503, 2011.

[17] B. Shen, Z. Wang, and X. Liu, "Sampled-data synchronization control of dynamical networks with stochastic sampling," *IEEE Transactions on Automatic Control*, vol. 57, no. 10, pp. 2644–2650, 2012.

[18] K. J. Åström and B. M. Bernhardsson, "Comparison of Riemann and Lebesgue sampling for first order stochastic systems," in *Proceedings of the 41st IEEE Conference on Decision and Control*, pp. 2011–2016, December 2002.

[19] X. Meng and T. Chen, "Optimal sampling and performance comparison of periodic and event based impulse control," *IEEE Transactions on Automatic Control*, vol. 57, no. 12, pp. 3252–3259, 2012.

[20] P. Tabuada, "Event-triggered real-time scheduling of stabilizing control tasks," *IEEE Transactions on Automatic Control*, vol. 52, no. 9, pp. 1680–1685, 2007.

[21] S. Hu and D. Yue, "Event-based H_∞ filtering for networked system with communication delay," *Signal Processing*, vol. 92, no. 9, pp. 2029–2039, 2012.

[22] D. Yue, E. Tian, and Q.-L. Han, "A delay system method for designing event-triggered controllers of networked control systems," *IEEE Transactions on Automatic Control*, vol. 58, no. 2, pp. 475–481, 2013.

[23] X. Meng and T. Chen, "Event based agreement protocols for multi-agent networks," *Automatica*, vol. 49, no. 7, pp. 2125–2132, 2013.

[24] Z.-G. Wu, P. Shi, H. Su, and J. Chu, "Passivity analysis for discrete-time stochastic markovian jump neural networks with mixed time delays," *IEEE Transactions on Neural Networks*, vol. 22, no. 10, pp. 1566–1575, 2011.

[25] Z.-G. Wu, P. Shi, H. Su, and J. Chu, "Exponential synchronization of neural networks with discrete and distributed delays under time-varying sampling," *IEEE Transactions on Neural Networks and Learning Systems*, vol. 23, no. 9, pp. 1368–1376, 2012.

[26] Z. G. Wu, P. Shi, H. Su, and J. Chu, "Stochastic synchronization of markovian jump neural networks with time-varying delay using sampled data," *IEEE Transactions on Cybernetics*, vol. 43, no. 6, pp. 1796–1806, 2013.

[27] H. Dong, Z. Wang, and H. Gao, "Distributed filtering for a class of time-varying systems over sensor networks with quantization errors and successive packet dropouts," *IEEE Transactions on Signal Processing*, vol. 60, no. 6, pp. 3164–3173, 2012.

[28] Y. Tang, H. Gao, J. Lu, and J. Kurths, "Pinning distributed synchronization of stochastic dynamical networks: a mixed optimization approach," *IEEE Transactions on Neural Networks and Learning Systems*, vol. 25, no. 10, pp. 1804–1815, 2014.

[29] C. Huang, D. W. C. Ho, and J. Lu, "Synchronization analysis of a complex network family," *Nonlinear Analysis: Real World Applications*, vol. 11, no. 3, pp. 1933–1945, 2010.

[30] S. Boyd, L. Ghaoui, E. Feron, and V. Balakrishnan, *Linear Matrix Inequalities in System and Control Theory*, SIAM, Philadelphia, Pa, USA, 1994.

[31] K. Gu, V. L. Kharitonov, and J. Chen, *Stability of Time-Delay Systems*, Control Engineering, Springer, New York, NY, USA, 2003.

Hindawi Publishing Corporation
Mathematical Problems in Engineering
Volume 2015, Article ID 690578, 13 pages
http://dx.doi.org/10.1155/2015/690578

Research Article

Robust Stabilization and H_∞ Control for Uncertain Neural Networks with Mixed Time Delays

Bin Wen,[1] Hui Li,[1] and Li Liang[2]

[1] *School of Aeronautics and Astronautics, University of Electronic Science and Technology of China, Chengdu, Sichuan 611731, China*
[2] *College of Information Sciences and Technology, Hainan University, Haikou 570228, China*

Correspondence should be addressed to Bin Wen; wenbin_08@126.com

Received 27 October 2014; Revised 5 January 2015; Accepted 7 January 2015

Academic Editor: Hui Zhang

Copyright © 2015 Bin Wen et al. This is an open access article distributed under the Creative Commons Attribution License, which permits unrestricted use, distribution, and reproduction in any medium, provided the original work is properly cited.

This paper is concerned with the problem of robust stabilization and H_∞ control for a class of uncertain neural networks. For the robust stabilization problem, sufficient conditions are derived based on the quadratic convex combination property together with Lyapunov stability theory. The feedback controller we design ensures the robust stability of uncertain neural networks with mixed time delays. We further design a robust H_∞ controller which guarantees the robust stability of the uncertain neural networks with a given H_∞ performance level. The delay-dependent criteria are derived in terms of LMI (linear matrix inequality). Finally, numerical examples are provided to show the effectiveness of the obtained results.

1. Introduction

Neural networks have received a great deal of attention due to their successful applications in various engineering fields such as associative memory [1], pattern recognition [2], adaptive control, and optimization. When designing or implementing a neural network such as Hopfield neural networks and cellular neural networks, the occurrence of time delays is unavoidable in the processing of storage and transmission. Since the existence of time delays is usually one of the main sources of instability and oscillations, the stability problem of neural networks with time delays has been widely considered by many researchers (see [3–13]). Generally speaking, stability criteria of neural networks with time delays are classified into two categories: delay-independent stability criteria and delay-dependent stability criteria. Delay-dependent stability criteria are less conservative than delay-independent ones. Therefore, people always consider the delay-dependent stability criteria. Neural networks usually have a spatial extent due to the presence of many parallel pathways of a variety of axon sizes and lengths [7]. Thus, there will be a distribution of conduction velocities along these pathways and a distribution of propagation delays [14], and both the discrete and the distributed delays should be considered in the neural network model [6, 7, 15–18].

However, in practical application of neural networks, uncertainties are inevitable in neural networks because of the existence of modeling errors and external disturbances. Parameter uncertainties will destroy the stability, so that taking uncertainty into account is important when studying the dynamical behaviors of neural networks (see [12, 19–21]). To facilitate the design of neural networks, it is important to consider neural networks with various activation functions, because the conditions to be imposed on the neural network are determined by the characteristics of various activation functions as well as network parameters [22]. The generalization of activation functions will provide a wider scope for neural network designs and applications [23]. Stability and stabilization results for delayed neural networks with various activation functions can be found in [22–26]. References [24, 25] investigated the stability problem of neural networks with various activation functions. Phat and Trinh [23] dealt with the exponential stabilization problem for neural networks with various activation functions via the Lyapunov-Krasovskii functional. Nevertheless, the results reported therein do not consider the parameter uncertainties

and disturbances. Sakthivel et al. [26] studied the problem of robust stabilization and H_∞ control for a class of uncertain neural networks with various activation functions and mixed time delays by employing the Lyapunov functional method and the matrix inequality technique. In recent years, control of time-delay systems is a subject of both practical and theoretical importance. The performance of a neural control system is influenced by external disturbances. Thus, it is important to use the H_∞ robust technique to eliminate the effect of external disturbances. The H_∞ control problem for time-delay systems has been addressed in [6, 26–34]. However, to the best of our knowledge, the robust stabilization and H_∞ control for uncertain systems with time-varying delays have not yet been fully investigated.

In this paper, we consider the problem of robust stabilization and H_∞ control for a class of uncertain neural networks by employing a new augmented Lyapunov-Krasovskii functional and estimating its derivative from a novel viewpoint. Our aim is to obtain a H_∞ control law to guarantee the robust stability of the closed-loop system with parameter uncertainties and a given disturbance attenuation level $\gamma > 0$. The results employ the quadratic convex combination technique, which is different from the linear convex combination and inverse convex combination techniques extensively used in other literature studies. The criteria are derived with the framework of LMIs, which can be easily calculated by the MATLAb LMI control toolbox. Numerical examples are provided to illustrate the effectiveness of the results.

Notations. The notations used throughout the paper are fairly standard. R^n denotes the n-dimensional Euclidean space; $R^{n\times m}$ is the set of all $n \times m$ real matrices; the notation $A > 0$ (<0) means A is a symmetric positive (negative) definite matrix; A^{-1} and A^T denote the inverse of matrix A and the transpose of matrix A; I represents the identity matrix with proper dimensions, respectively; a symmetric term in a symmetric matrix is denoted by $(*)$; $\mathrm{sym}(A)$ represents $(A+A^T)$; $\mathrm{diag}\{\cdot\}$ stands for a block-diagonal matrix. Matrices, if their dimensions are not explicitly stated, are assumed to be compatible for algebraic operations.

2. Problem Formulation

We consider the following uncertain neural networks with discrete and distributed time-varying delays:

$$\begin{aligned}\dot{x}(t) &= -(A+\Delta A)x(t) + (M_0+\Delta M_0) f(x(t)) \\ &\quad + (M_1+\Delta M_1) g(x(t-d(t))) \\ &\quad + (M_2+\Delta M_2)\int_{t-r(t)}^{t} h(x(s))\,ds \\ &\quad + (B+\Delta B)v(t) + u(t), \\ z(t) &= Cx(t), \\ x(t) &= \phi(t), \quad t\in[-\tau,0],\end{aligned} \tag{1}$$

where $x(t) = [x_1(t), x_2(t), \ldots, x_n(t)]^T \in R^n$ is the state vector of the neural networks, $u(t) \in R^n$ is the control input vector of the neural networks, $v(t) \in R^r$ is the disturbance input vector, and $z(t) \in R^m$ is the output vector; $f(x(t))$, $g(x(t))$, and $h(x(t))$ denote the neuron activation function; $A = \mathrm{diag}\{a_1, a_2, \ldots, a_n\}$ with $a_i > 0$, $i = 1, 2, \ldots, n$ is the positive diagonal matrix; $C \in R^{m\times n}$ represent the output matrix; $M_0, M_1, M_2 \in R^{n\times n}$, and $B \in R^{n\times r}$ denote the connection weights, the delayed connection weights, the distributively connection weights, and the disturbance input weights, respectively. $d(t)$ and $r(t)$ represent the discrete and distributed time-varying delays that satisfy the condition

$$\begin{aligned}0 &\leqslant d(t) \leqslant \overline{\tau}, \\ \dot{d}(t) &\leqslant \mu, \\ 0 &\leqslant r(t) \leqslant \overline{r},\end{aligned} \tag{2}$$

where $\overline{\tau}$, $\overline{r}$, and μ are constants. The function $\phi(t)$ is continuous, defined on $[-\tau, 0]$, $\tau = \max(\overline{r}, \overline{\tau})$.

In order to conduct the analysis, the following assumptions are necessary.

Assumption 1. The parametric uncertainties ΔA, ΔM_0, ΔM_1, ΔM_2, and ΔB are time-varying matrices and satisfy

$$\begin{aligned}&[\Delta A(t), \Delta M_0(t), \Delta M_1(t), \Delta M_2(t), \Delta B(t)] \\ &\quad = NF(t)[J_1, J_2, J_3, J_4, J_5],\end{aligned} \tag{3}$$

where N, J_1, J_2, J_3, J_4, and J_5 are some given constant matrices with appropriate dimensions and $F(t)$ satisfies $F^T(t)F(t) \le I$, for any $t \ge 0$.

Assumption 2. The neuron activation functions are bounded and satisfy

$$\begin{aligned}&F_i^- \leqslant \frac{f_i(x) - f_i(y)}{x-y} \leqslant F_i^+, \quad \forall x, y \in R,\ x \neq y, \\ &f_i(0) = 0, \\ &G_i^- \leqslant \frac{g_i(x) - g_i(y)}{x-y} \leqslant G_i^+, \quad \forall x, y \in R,\ x \neq y, \\ &g_i(0) = 0, \\ &H_i^- \leqslant \frac{h_i(x) - h_i(y)}{x-y} \leqslant H_i^+, \quad \forall x, y \in R,\ x \neq y, \\ &h_i(0) = 0,\end{aligned} \tag{4}$$

where F_i^-, F_i^+, G_i^-, G_i^+, H_i^-, H_i^+, $i = 1, 2, \ldots, n$ are known constants. And we denote

$$\begin{aligned}L_1 &= \mathrm{diag}\{F_1^-F_1^+, F_2^-F_2^+, \ldots, F_n^-F_n^+\}, \\ L_2 &= \mathrm{diag}\left\{\frac{F_1^- + F_1^+}{2}, \frac{F_2^- + F_2^+}{2}, \ldots, \frac{F_n^- + F_n^+}{2}\right\},\end{aligned}$$

$$G_1 = \operatorname{diag}\{G_1^- G_1^+, G_2^- G_2^+, \ldots, G_n^- G_n^+\},$$
$$G_2 = \operatorname{diag}\left\{\frac{G_1^- + G_1^+}{2}, \frac{G_2^- + G_2^+}{2}, \ldots, \frac{G_n^- + G_n^+}{2}\right\},$$
$$H_1 = \operatorname{diag}\{H_1^- H_1^+, H_2^- H_2^+, \ldots, H_n^- H_n^+\},$$
$$H_2 = \operatorname{diag}\left\{\frac{H_1^- + H_1^+}{2}, \frac{H_2^- + H_2^+}{2}, \ldots, \frac{H_n^- + H_n^+}{2}\right\}. \tag{5}$$

Definition 3 (see [26]). Given a prescribed level of disturbance attenuation $\gamma > 0$, the uncertain neural networks are said to be robustly asymptotically stable if they are robustly stable, and the response $z(t)$ under zero initial condition satisfies

$$\int_0^\infty z^T(t) z(t)\, dt \leqslant \gamma^2 \int_0^\infty v^T(t) v(t)\, dt, \tag{6}$$

for every nonzero $v(t) \in L_2[0, \infty)$.

Lemma 4 (see [35]). *For any constant matrix $Z \in R^{n\times n}$, $Z = Z^T > 0$, scalars $h_2 > h_1 > 0$, and vector function x: $[h_1, h_2] \to R^n$ such that the following integrations are well defined; then*

$$\begin{aligned} &-(h_2 - h_1)\int_{t-h_2}^{t-h_1} x^T(s) Z x(s)\, ds \\ &\quad \leqslant -\int_{t-h_2}^{t-h_1} x^T(s)\, ds Z \int_{t-h_2}^{t-h_1} x(s)\, ds. \end{aligned} \tag{7}$$

Lemma 5 (see [36]). *Let $W > 0$, and $\omega(s)$ an appropriate dimensional vector. Then, we have the following facts for any scalar function $\beta(s) \geq 0$, $s \in [t_1, t_2]$:*

$$\begin{aligned} &-\int_{t_1}^{t_2} \omega^T(s) W \omega(s)\, ds \\ &\quad \leqslant (t_2 - t_1)\zeta^T F_1^T W^{-1} F_1 \zeta + 2\zeta^T F_1^T \int_{t_1}^{t_2} \omega(s)\, ds, \\ &-\int_{t_1}^{t_2} \beta(s)\omega^T(s) W \omega(s)\, ds \\ &\quad \leqslant \int_{t_1}^{t_2} \beta(s)\, ds \zeta^T F_2^T W^{-1} F_2 \zeta + 2\zeta^T F_2^T \int_{t_1}^{t_2} \beta(s)\omega(s)\, ds, \\ &-\int_{t_1}^{t_2} \beta^2(s)\omega^T(s) W \omega(s)\, ds \\ &\quad \leqslant (t_2 - t_1)\zeta^T F_3^T W^{-1} F_3 \zeta + 2\zeta^T F_3^T \int_{t_1}^{t_2} \beta(s)\omega(s)\, ds, \end{aligned} \tag{8}$$

and matrices F_i $(i = 1, 2, 3)$ and vector ζ independent of the integral variable are appropriate dimensional arbitrary ones.

Lemma 6 ((Schur complement) [26]). *Given constant symmetric matrices S_1, S_2, and S_3, where $S_1 = S_1^T$ and $S_2 = S_2^T > 0$, then $S_1 + S_3^T S_2^{-1} S_3 < 0$ if and only if*

$$\begin{bmatrix} S_1 & S_3^T \\ S_3 & -S_2 \end{bmatrix} < 0, \quad \text{or} \quad \begin{bmatrix} -S_2 & S_3 \\ S_3^T & S_1 \end{bmatrix} < 0. \tag{9}$$

Lemma 7 (see [36]). *For symmetric matrices Z_0, Z_1, a positive semidefinite matrix $Z_2 \geq 0$ and nonzero vector ζ_t, a necessary and sufficient condition for*

$$f(\alpha) = \zeta_t^T \left(Z_0 + \alpha Z_1 + \alpha^2 Z_2\right)\zeta_t < 0, \quad \alpha \in [\alpha_1, \alpha_2] \tag{10}$$

is that the following set of inequalities hold simultaneously $f(\alpha_1) < 0$, $f(\alpha_2) < 0$.

3. Robust Stabilization

We use the following control law to tackle the robust stabilization problem in this paper:

$$u(t) = K_1 x(t), \tag{11}$$

where K_1 are the gain matrix of the controller.

When the disturbance input $v(t) = 0$, the neural networks (1) can be rewritten in the form

$$\begin{aligned} \dot{x}(t) &= -(A - K_1)x(t) + M_0 f(x(t)) \\ &\quad + M_1 g(x(t - d(t))) \\ &\quad + M_2 \int_{t-r(t)}^{t} h(x(s))\, ds + N\varphi(t), \\ \varphi(t) &= F(t)\Big[-J_1 x(t) + J_2 f(x(t)) \\ &\quad + J_3 g(x(t - d(t))) \\ &\quad + J_4 \int_{t-r(t)}^{t} h(x(s))\, ds\Big], \\ z(t) &= Cx(t). \end{aligned} \tag{12}$$

Theorem 8. *Under Assumptions 1 and 2, for given scalars $\overline{\tau}$, μ, and $\overline{r}$, the system (12) is robustly asymptotically stabilizable via the control law $u(t)$ if there exist positive diagonal matrices $D = \operatorname{diag}\{d_1, d_2, \ldots, d_n\}$, $W_i > 0$, $i = 1, 2, 3, 4$, positive definite matrices $P_1 \in R^{2n\times 2n}$, $S_i \in R^{2n\times 2n}$ $(i = 1, 2, 3, 4, 5)$, $Q_i \in R^{2n\times 2n}$ $(i = 1, 2, 3, 4, 5)$, $R_i \in R^{n\times n}$ $(i = 1, 2)$, scalar*

matrix $U > 0$, and any matrices with appropriate dimensions F_i $(i = 1, 2, \ldots, 6)$, δ such that the following LMIs hold:

$$\Omega_1 = \begin{bmatrix} \Phi_0 & \overline{\tau}F_1^T & \overline{\tau}F_2^T & \sqrt{3}\overline{\tau}F_3^T \\ * & -\overline{\tau}Q_3 & 0 & 0 \\ * & * & -R1 & 0 \\ * & * & * & -\overline{\tau}R_2 \end{bmatrix} < 0,$$
$$\Omega_2 = \begin{bmatrix} \Phi_0 + \overline{\tau}\Phi_1 & \overline{\tau}F_4^T & \overline{\tau}F_5^T & \sqrt{3}\overline{\tau}F_6^T \\ * & -\overline{\tau}Q_3 & 0 & 0 \\ * & * & -R1 & 0 \\ * & * & * & -\overline{\tau}R_2 \end{bmatrix} < 0, \tag{13}$$

where

$$\begin{aligned}
\Phi_1 &= \operatorname{sym}\left(2\mathrm{E}_1\mathrm{F}_5 + 3\mathrm{E}_1\mathrm{F}_6 - 2\mathrm{E}_2\mathrm{F}_2 - 3\mathrm{E}_2\mathrm{F}_3\right) \\
&\quad + \operatorname{sym}\left(\left[E_5, 0\right] Q_1 \left[E_1, 0\right]^T\right), \\
\Phi_0 &= \operatorname{sym}\Big(F_1^T \left[E_8, E_2 - E_3\right]^T + 2\overline{\tau}F_2^T E_2^T - 2F_2^T E_8^T \\
&\qquad + 3\overline{\tau}F_3^T E_2^T - 3F_3^T E_8^T + F_4^T \left[E_9, E_1 - E_2\right]^T \\
&\qquad - 2F_5^T E_9^T - 3F_6^T E_9^T\Big) \\
&\quad + \operatorname{sym}\left(\left[E_1, E_3\right] P_1 \left[E_5, E_{23}\right]^T + E_6 D E_5^T\right) \\
&\quad + \left[E_{10}, E_6\right]\left(S_1 + S_2 + S_5\right)\left[E_{10}, E_6\right]^T \\
&\quad - (1-\mu)\left[E_{11}, E_{14}\right] S_1 \left[E_{11}, E_{14}\right]^T \\
&\quad + \left[E_1, E_1\right]\left(Q_1 + Q_2\right)\left[E_1, E_1\right]^T \\
&\quad + (\mu - 1)\left[E_1, E_2\right] Q_1 \left[E_1, E_2\right]^T \\
&\quad + \operatorname{sym}\left(\left[E_5, 0\right] Q_1 \left[0, E_9\right]^T\right) - \left[E_{19}, E_{20}\right] S_2 \left[E_{19}, E_{20}\right]^T \\
&\quad + \left[E_5, E_7\right]\left(S_3 + S_4\right)\left[E_5, E_7\right]^T \\
&\quad - \left[E_{23}, E_{24}\right] S_3 \left[E_{23}, E_{24}\right]^T - \left[E_1, E_3\right] Q_2 \left[E_1, E_3\right]^T \\
&\quad + \operatorname{sym}\left(\left[E_5, 0\right] Q_2 \left[\overline{\tau}E_1, E_8 + E_9\right]^T\right) \\
&\quad - \left[E_{15}, E_{16}\right] S_4 \left[E_{15}, E_{16}\right]^T - \left[E_{17}, E_{18}\right] S_5 \left[E_{17}, E_{18}\right]^T \\
&\quad + \overline{\tau}\left[E_1, E_5\right] Q_3 \left[E_1, E_5\right]^T + E_5\left(\overline{\tau}^2 R_1 + \overline{\tau}^3 R_2\right) E_5^T \\
&\quad + \overline{r}^2 \left[E_5, E_7\right] Q_4 \left[E_5, E_7\right]^T \\
&\quad - \left[E_1 - E_4, E_{12}\right] Q_4 \left[E_1 - E_4, E_{12}\right]^T \\
&\quad + \overline{r}^2 \left[E_{10}, E_6\right] Q_5 \left[E_{10}, E_6\right]^T - \left[E_{21}, E_{22}\right] Q_5 \left[E_{21}, E_{22}\right]^T \\
&\quad - E_1 L_1 W_1 E_1^T - E_6 W_1 E_6^T \\
&\quad + \operatorname{sym}\left(E_1 L_2 W_1 E_6^T\right) - E_1 G_1 W_2 E_1^T - E_{10} W_2 E_{10}^T \\
&\quad + \operatorname{sym}\left(E_1 G_2 W_2 E_{10}^T\right) - E_1 H_1 W_3 E_1^T - E_7 W_3 E_7^T \\
&\quad + \operatorname{sym}\left(E_1 H_2 W_3 E_7^T\right) - E_2 G_1 W_4 E_2^T - E_{11} W_4 E_{11}^T \\
&\quad + \operatorname{sym}\left(E_2 G_2 W_4 E_{11}^T\right) \\
&\quad + \operatorname{sym}\Big(-\left(E_1 + E_5\right)\left(\delta A - \Lambda_1\right) E_1^T + \left(E_1 + E_5\right)\delta M_0 E_6^T \\
&\qquad + \left(E_1 + E_5\right)\delta M_1 E_{11}^T + \left(E_1 + E_5\right)\delta M_2 E_{12}^T \\
&\qquad + \left(E_1 + E_5\right)\delta N E_{13}^T - \left(E_1 + E_5\right)\delta E_5^T\Big) \\
&\quad + J^T U J - E_{13} U E_{13}^T,
\end{aligned} \tag{14}$$

with

$$\begin{aligned}
E_i &= \left[0_{n\times(i-1)n}, I_n, 0_{n\times(24-i)n}\right]^T, \quad i = 1, 2, \ldots, 24, \\
\Lambda_1 &= \delta K_1, \\
J &= \left[-J_1, 0, 0, 0, 0, J_2, 0, 0, 0, 0, J_3, J_4,\right. \\
&\qquad \left. 0, 0, 0, 0, 0, 0, 0, 0, 0, 0, 0, 0\right].
\end{aligned} \tag{15}$$

Proof. Construct a new class of Lyapunov-Krasovskii functional as follows:

$$V(t, x(t)) = \sum_{i=1}^{6} V_i(x(t)), \tag{16}$$

where

$$\begin{aligned}
V_1(t, x(t)) &= \eta_1^T(t, t-\overline{\tau}) P_1 \eta_1(t, t-\overline{\tau}) \\
&\qquad + 2\sum_{i=1}^{n} d_i \int_0^{x_i(t)} f_i(s)\, ds, \\
V_2(t, x(t)) &= \int_{t-d(t)}^{t} \left[\eta_1^T(t, s) Q_1 \eta_1(t, s) + \eta_4^T(s) S_1 \eta_4(s)\right] ds, \\
V_3(t, x(t)) &= \int_{t-\overline{\tau}}^{t} \Big[\eta_1^T(t, s) Q_2 \eta_1(t, s) \\
&\qquad + \eta_4^T(s) S_2 \eta_4(s) + \eta_3^T(s) S_3 \eta_3(s)\Big] ds, \\
V_4(t, x(t)) &= \int_{t-\overline{r}}^{t} \left[\eta_3^T(s) S_4 \eta_3(s) + \eta_4^T(s) S_5 \eta_4(s)\right] ds, \\
V_5(t, x(t)) &= \int_{t-\overline{\tau}}^{t} \int_{\theta}^{t} \eta_2^T(s) Q_3 \eta_2(s)\, ds\, d\theta \\
&\qquad + 2\int_{t-\overline{\tau}}^{t} \int_{\theta_1}^{t} \int_{\theta_2}^{t} \dot{x}^T(s) R_1 \dot{x}(s)\, ds\, d\theta_1 d\theta_2 \\
&\qquad + 6\int_{t-\overline{\tau}}^{t} \int_{\theta_1}^{t} \int_{\theta_2}^{t} \int_{\theta_3}^{t} \dot{x}^T(s) R_2 \dot{x}(s)\, ds\, d\theta_1 d\theta_2 d\theta_3, \\
V_6(t, x(t)) &= \overline{r} \int_{-\overline{r}}^{0} \int_{t+\theta}^{t} \eta_3^T(s) Q_4 \eta_3(s)\, ds\, d\theta \\
&\qquad + \overline{r} \int_{-\overline{r}}^{0} \int_{t+\theta}^{t} \eta_4^T(s) Q_5 \eta_4(s)\, ds\, d\theta,
\end{aligned} \tag{17}$$

where

$$\begin{aligned}\eta_1^T(t,s) &= \left[x^T(t) \quad x^T(s)\right],\\ \eta_2^T(t) &= \left[x^T(t) \quad \dot{x}^T(t)\right],\\ \eta_3^T(t) &= \left[\dot{x}^T(t) \quad h^T(x(t))\right],\\ \eta_4^T(t) &= \left[g^T(x(t)) \quad f^T(x(t))\right].\end{aligned} \tag{18}$$

We define a vector ζ_t as

$$\begin{aligned}\zeta_t^T = \Big[& x^T(t), x^T(t-d(t)), x^T(t-\overline{\tau}), x^T(t-r(t)),\\ & \dot{x}^T(t), f^T(x(t)), h^T(x(t)), \int_{t-\overline{\tau}}^{t-d(t)} x^T(s)\,ds,\\ & \int_{t-d(t)}^{t} x^T(s)\,ds, g^T(x(t)), g^T(x(t-d(t))),\\ & \int_{t-r(t)}^{t} h^T(x(s))\,ds, \varphi^T(t), f^T(x(t-d(t))),\\ & \dot{x}^T(t-\overline{r}), h^T(x(t-\overline{r})), g^T(x(t-\overline{r})), f^T(x(t-\overline{r})),\\ & g^T(x(t-\overline{\tau})), f^T(x(t-\overline{\tau})), \int_{t-r(t)}^{t} g^T(x(s))\,ds,\\ & \int_{t-r(t)}^{t} f^T(x(s))\,ds, \dot{x}^T(t-\overline{\tau}), h^T(x(t-\overline{\tau}))\Big].\end{aligned} \tag{19}$$

Remark 1. Our paper uses the idea of second-order convex combination, and the property of quadratic convex function is given in Lemma 7.

Remark 2. We fully consider the various activation functions in constructing the Lyapunov-Krasovskii functional. So the augmented vector ζ_t uses more information about $f(x(t))$, $g(x(t))$, and $h(x(t))$ than in [26]. The Lyapunov functional in our paper is more general than that in [26], and the criteria in our paper may be more applicable.

Remark 3. In our paper, the augmented vector ζ_t utilizes more information on state variables than in [26], such as $\dot{x}(t-\overline{\tau})$. This leads to reducing the conservatism of stabilization condition.

The time derivative of $V(t,x(t))$ along the trajectory of system is given by

$$\begin{aligned}\dot{V}_1(t,x(t)) &= 2\eta_1^T(t,t-\overline{\tau})P_1\dot{\eta}_1^T(t,t-\overline{\tau}) + 2f^T(x(t))D\dot{x}(t)\\ &= 2\zeta_t^T[E_1,E_3]P_1[E_5,E_{23}]^T\zeta_t + 2\zeta_t^T E_6 D E_5^T\zeta_t\\ &= \zeta_t^T \operatorname{sym}\left([E_1,E_3]P_1[E_5,E_{23}]^T + E_6 D E_5^T\right)\zeta_t,\end{aligned}$$

$$\begin{aligned}\dot{V}_2(t,x(t)) &= \eta_4^T(t)S_1\eta_4(t) + \eta_1^T(t,t)Q_1\eta_1(t,t)\\ &\quad - \left(1-\dot{d}(t)\right)\eta_4^T(t-d(t))S_1\eta_4(t-d(t))\\ &\quad - \left(1-\dot{d}(t)\right)\eta_1^T(t,t-d(t))Q_1\eta_1(t,t-d(t))\\ &\quad + 2\int_{t-d(t)}^{t}\frac{\partial\eta_1^T(t,s)}{\partial t}Q_1\eta_1(t,s)\,ds\\ &\leqslant \zeta_t^T[E_{10},E_6]S_1[E_{10},E_6]^T\zeta_t\\ &\quad - (1-\mu)\zeta_t^T[E_{11},E_{14}]S_1[E_{11},E_{14}]^T\zeta_t\\ &\quad + \zeta_t^T[E_1,E_1]Q_1[E_1,E_1]^T\zeta_t\\ &\quad + (\mu-1)\zeta_t^T[E_1,E_2]Q_1[E_1,E_2]^T\zeta_t\\ &\quad + 2\zeta_t^T[E_5,0]Q_1[d(t)E_1,E_9]^T\zeta_t,\end{aligned}$$

$$\begin{aligned}\dot{V}_3(t,x(t)) &= \eta_4^T(t)S_2\eta_4(t) - \eta_4^T(t-\overline{\tau})S_2\eta_4(t-\overline{\tau})\\ &\quad + \eta_3^T(t)S_3\eta_3(t) - \eta_3^T(t-\overline{\tau})S_3\eta_3(t-\overline{\tau})\\ &\quad + \eta_1^T(t,t)Q_2\eta_1(t,t)\\ &\quad - \eta_1^T(t,t-\overline{\tau})Q_2\eta_1(t,t-\overline{\tau})\\ &\quad + 2\int_{t-\overline{\tau}}^{t}\frac{\partial\eta_1^T(t,s)}{\partial t}Q_2\eta_1(t,s)\,ds\\ &= \zeta_t^T[E_{10},E_6]S_2[E_{10},E_6]^T\zeta_t\\ &\quad - \zeta_t^T[E_{19},E_{20}]S_2[E_{19},E_{20}]^T\zeta_t\\ &\quad + \zeta_t^T[E_5,E_7]S_3[E_5,E_7]^T\zeta_t\\ &\quad - \zeta_t^T[E_{23},E_{24}]S_3[E_{23},E_{24}]^T\zeta_t\\ &\quad + \zeta_t^T[E_1,E_1]Q_2[E_1,E_1]^T\zeta_t\\ &\quad - \zeta_t^T[E_1,E_3]Q_2[E_1,E_3]^T\zeta_t\\ &\quad + 2\zeta_t^T[E_5,0]Q_2[\overline{\tau}E_1,E_8+E_9]^T\zeta_t,\end{aligned}$$

$$\begin{aligned}\dot{V}_4(t,x(t)) &= \eta_3^T(t)S_4\eta_3(t) - \eta_3^T(t-\overline{r})S_4\eta_3(t-\overline{r})\\ &\quad + \eta_4^T(t)S_5\eta_4(t) - \eta_4^T(t-\overline{r})S_5\eta_4(t-\overline{r})\\ &= \zeta_t^T[E_5,E_7]S_4[E_5,E_7]^T\zeta_t\\ &\quad - \zeta_t^T[E_{15},E_{16}]S_4[E_{15},E_{16}]^T\zeta_t\\ &\quad + \zeta_t^T[E_{10},E_6]S_5[E_{10},E_6]^T\zeta_t\\ &\quad - \zeta_t^T[E_{17},E_{18}]S_5[E_{17},E_{18}]^T\zeta_t,\end{aligned}$$

$$\begin{aligned}
&\dot{V}_5(t,x(t)) \\
&\quad = \bar{\tau}\eta_2^T(t)Q_3\eta_2(t) + \dot{x}^T(t)\left(\bar{\tau}^2R_1 + \bar{\tau}^3R_2\right)\dot{x}(t) \\
&\qquad + V_a(t,x(t)) \\
&\quad = \bar{\tau}\zeta_t^T[E_1,E_5]Q_3[E_1,E_5]^T\zeta_t + \zeta_t^TE_5\left(\bar{\tau}^2R_1 + \bar{\tau}^3R_2\right)E_5^T\zeta_t \\
&\qquad + V_a(t,x(t)),
\end{aligned} \tag{20}$$

where

$$\begin{aligned}
&V_a(t,x(t)) \\
&\quad = -\int_{t-\bar{\tau}}^{t}\left[\eta_2^T(s)Q_3\eta_2(s) + 2(\bar{\tau}-t+s)\dot{x}^T(s)R_1\dot{x}(s)\right. \\
&\qquad\qquad \left. + 3(\bar{\tau}-t+s)^2\dot{x}^T(s)R_2\dot{x}(s)\right]ds, \\
&\dot{V}_6(t,x(t)) \\
&\quad = \bar{r}^2\eta_3^T(t)Q_4\eta_3(t) \\
&\qquad - \bar{r}\int_{t-\bar{r}}^{t}\left[\eta_3^T(s)Q_4\eta_3(s)\right]ds + \bar{r}^2\eta_4^T(t)Q_5\eta_4(t) \\
&\qquad - \bar{r}\int_{t-\bar{r}}^{t}\left[\eta_4^T(s)Q_5\eta_4(s)\right]ds \\
&\quad \leqslant \bar{r}^2\eta_3^T(t)Q_4\eta_3(t) \\
&\qquad - r(t)\int_{t-r(t)}^{t}\left[\eta_3^T(s)Q_4\eta_3(s)\right]ds + \bar{r}^2\eta_4^T(t)Q_5\eta_4(t) \\
&\qquad - r(t)\int_{t-r(t)}^{t}\left[\eta_4^T(s)Q_5\eta_4(s)\right]ds,
\end{aligned} \tag{21}$$

and according to Lemma 4, we can obtain

$$\begin{aligned}
&\dot{V}_6(t,x(t)) \\
&\quad \leqslant \bar{r}^2\eta_3^T(t)Q_4\eta_3(t) \\
&\qquad - \left(\int_{t-r(t)}^{t}\eta_3(s)\,ds\right)^TQ_4\left(\int_{t-r(t)}^{t}\eta_3(s)\,ds\right) \\
&\qquad + \bar{r}^2\eta_4^T(t)Q_5\eta_4(t) \\
&\qquad - \left(\int_{t-r(t)}^{t}\eta_4(s)\,ds\right)^TQ_5\left(\int_{t-r(t)}^{t}\eta_4(s)\,ds\right) \\
&\quad = \bar{r}^2\zeta_t^T[E_5,E_7]Q_4[E_5,E_7]^T\zeta_t \\
&\qquad - \zeta_t^T[E_1-E_4,E_{12}]Q_4[E_1-E_4,E_{12}]^T\zeta_t \\
&\qquad + \bar{r}^2\zeta_t^T[E_{10},E_6]Q_5[E_{10},E_6]^T\zeta_t \\
&\qquad - \zeta_t^T[E_{21},E_{22}]Q_5[E_{21},E_{22}]^T\zeta_t.
\end{aligned} \tag{22}$$

It is easy to obtain the following identities:

$$\begin{aligned}
h-t+s &= [d(t)-t+s] + [h-d(t)], \\
(h-t+s)^2 &= [d(t)-t+s]^2 + \left[h^2-d^2(t)\right] \\
&\quad + 2[h-d(t)](s-t).
\end{aligned} \tag{23}$$

Therefore, we can disassemble the integral into two parts as follows:

$$\begin{aligned}
&V_a(t,x(t)) \\
&\quad = -\int_{t-\bar{\tau}}^{t-d(t)}\left[\eta_2^T(s)Q_3\eta_2(s) + 2(\bar{\tau}-t+s)\dot{x}^T(s)R_1\dot{x}(s)\right. \\
&\qquad\qquad \left. + 3(\bar{\tau}-t+s)^2\dot{x}^T(s)R_2\dot{x}(s)\right]ds \\
&\qquad - \int_{t-d(t)}^{t}\left[\eta_2^T(s)Q_3\eta_2(s) + 2(\bar{\tau}-t+s)\dot{x}^T(s)R_1\dot{x}(s)\right. \\
&\qquad\qquad \left. + 3(\bar{\tau}-t+s)^2\dot{x}^T(s)R_2\dot{x}(s)\right]ds \\
&\quad = -\int_{t-\bar{\tau}}^{t-d(t)}\left[\eta_2^T(s)Q_3\eta_2(s) + 2(\bar{\tau}-t+s)\dot{x}^T(s)R_1\dot{x}(s)\right. \\
&\qquad\qquad \left. + 3(\bar{\tau}-t+s)^2\dot{x}^T(s)R_2\dot{x}(s)\right]ds \\
&\qquad - \int_{t-d(t)}^{t}\left[\eta_2^T(s)Q_3\eta_2(s) + 2(d(t)-t+s)\dot{x}^T(s)R_1\dot{x}(s)\right. \\
&\qquad\qquad \left. + 3(d(t)-t+s)^2\dot{x}^T(s)R_2\dot{x}(s)\right]ds \\
&\qquad - \int_{t-d(t)}^{t}\dot{x}(s)^T\left[2(\bar{\tau}-d(t))R_1 + 3\left(\bar{\tau}^2-d^2(t)\right)R_2\right] \\
&\qquad\qquad \cdot\dot{x}(s)\,ds \\
&\qquad - \int_{t-d(t)}^{t}6(\bar{\tau}-d(t))(s-t)\dot{x}^T(s)R_2\dot{x}(s)\,ds \\
&\quad = V_{a1}(t,x(t)) + V_{a2}(t,x(t)),
\end{aligned} \tag{24}$$

where

$$\begin{aligned}
&V_{a1}(t,x(t)) \\
&\quad = -\int_{t-\bar{\tau}}^{t-d(t)}\left[\eta_2^T(s)Q_3\eta_2(s) + 2(\bar{\tau}-t+s)\dot{x}^T(s)R_1\dot{x}(s)\right. \\
&\qquad\qquad \left. + 3(\bar{\tau}-t+s)^2\dot{x}^T(s)R_2\dot{x}(s)\right]ds \\
&\qquad - \int_{t-d(t)}^{t}\left[\eta_2^T(s)Q_3\eta_2(s) + 2(d(t)-t+s)\dot{x}^T(s)R_1\dot{x}(s)\right. \\
&\qquad\qquad \left. + 3(d(t)-t+s)^2\dot{x}^T(s)R_2\dot{x}(s)\right]ds,
\end{aligned}$$

$$\begin{aligned}
&V_{a2}(t,x(t)) \\
&\quad = -\int_{t-d(t)}^{t} \dot{x}(s)^T \left[2(\overline{\tau}-d(t))R_1 + 3\left(\overline{\tau}^2 - d^2(t)\right)R_2\right] \\
&\qquad\qquad \cdot \dot{x}(s)\,ds \\
&\qquad - \int_{t-d(t)}^{t} 6(\overline{\tau}-d(t))(s-t)\dot{x}^T(s)R_2\dot{x}(s)\,ds.
\end{aligned} \tag{25}$$

It is easy to show the following relation:

$$\begin{aligned}
&V_{a2}(t,x(t)) \\
&\quad = -\int_{t-d(t)}^{t} \dot{x}(s)^T \left[2(\overline{\tau}-d(t))R_1 + 3\left(\overline{\tau}^2 - d^2(t)\right)R_2\right] \\
&\qquad\qquad \cdot \dot{x}(s)\,ds \\
&\qquad - \int_{t-d(t)}^{t} 6(\overline{\tau}-d(t))(s-t)\dot{x}^T(s)R_2\dot{x}(s)\,ds \\
&\quad = -2(\overline{\tau}-d(t))\int_{t-d(t)}^{t} \dot{x}(s)^T R_1\dot{x}(s)\,ds - 3(\overline{\tau}-d(t)) \\
&\qquad \cdot \int_{t-d(t)}^{t} \dot{x}(s)^T\left[(\overline{\tau}+d(t)) + 2(s-t)\right]R_2\dot{x}(s)\,ds \\
&\quad \leqslant -2\int_{t-d(t)}^{t} (\overline{\tau}-d(t))\dot{x}(s)^T R_1\dot{x}(s)\,ds \\
&\qquad - 3\int_{t-d(t)}^{t} (\overline{\tau}-d(t))^2\dot{x}(s)^T R_2\dot{x}(s)\,ds \leqslant 0.
\end{aligned} \tag{26}$$

Applying Lemma 5 to $V_{a1}(t,x(t))$, we get

$$\begin{aligned}
&V_{a1}(t,x(t)) \\
&\quad \leqslant (\overline{\tau}-d(t))\zeta_t^T F_1^T Q_3^{-1} F_1\zeta_t \\
&\qquad + 2\zeta_t^T F_1^T\left[\int_{t-\overline{\tau}}^{t-d(t)} x^T(s)\,ds, x^T(t-d(t)) - x^T(t-\overline{\tau})\right]^T \\
&\qquad + (\overline{\tau}-d(t))^2\zeta_t^T F_2^T R_1^{-1} F_2\zeta_t \\
&\qquad + 4\zeta_t^T F_2^T\left[(\overline{\tau}-d(t))x(t-d(t)) - \int_{t-\overline{\tau}}^{t-d(t)} x(s)\,ds\right] \\
&\qquad + 3(\overline{\tau}-d(t))\zeta_t^T F_3^T R_2^{-1} F_3\zeta_t \\
&\qquad + 6\zeta_t^T F_3^T\left[(\overline{\tau}-d(t))x(t-d(t)) - \int_{t-\overline{\tau}}^{t-d(t)} x(s)\,ds\right] \\
&\qquad + d(t)\zeta_t^T F_4^T Q_3^{-1} F_4\zeta_t \\
&\qquad + 2\zeta_t^T F_4^T\left[\int_{t-d(t)}^{t} x^T(s)\,ds, x^T(t) - x^T(t-d(t))\right]^T \\
&\qquad + d(t)^2\zeta_t^T F_5^T R_1^{-1} F_5\zeta_t \\
&\qquad + 4\zeta_t^T F_5^T\left[d(t)x(t) - \int_{t-d(t)}^{t} x(s)\,ds\right] \\
&\qquad + 3d(t)\zeta_t^T F_6^T R_2^{-1} F_6\zeta_t \\
&\qquad + 6\zeta_t^T F_6^T\left[d(t)x(t) - \int_{t-d(t)}^{t} x(s)\,ds\right] \\
&\quad \leqslant (\overline{\tau}-d(t))\zeta_t^T F_1^T Q_3^{-1} F_1\zeta_t + 2\zeta_t^T F_1^T\left[E_8, E_2 - E_3\right]^T\zeta_t \\
&\qquad + (\overline{\tau}-d(t))^2\zeta_t^T F_2^T R_1^{-1} F_2\zeta_t \\
&\qquad + 4\zeta_t^T F_2^T\left[(\overline{\tau}-d(t))E_2 - E_8\right]^T\zeta_t \\
&\qquad + 3(\overline{\tau}-d(t))\zeta_t^T F_3^T R_2^{-1} F_3\zeta_t \\
&\qquad + 6\zeta_t^T F_3^T\left[(\overline{\tau}-d(t))E_2 - E_8\right]^T\zeta_t \\
&\qquad + d(t)\zeta_t^T F_4^T Q_3^{-1} F_4\zeta_t + 2\zeta_t^T F_4^T\left[E_9, E_1 - E_2\right]^T\zeta_t \\
&\qquad + d(t)^2\zeta_t^T F_5^T R_1^{-1} F_5\zeta_t + 4\zeta_t^T F_5^T\left[d(t)E_1 - E_9\right]^T\zeta_t \\
&\qquad + 3d(t)\zeta_t^T F_6^T R_2^{-1} F_6\zeta_t + 6\zeta_t^T F_6^T\left[d(t)E_1 - E_9\right]^T\zeta_t.
\end{aligned} \tag{27}$$

According to Assumption 2, we have

$$\begin{aligned}
&\left(f_i(x_i(t)) - F_i^- x_i(t)\right)\left(f_i(x_i(t)) - F_i^+ x_i(t)\right) \leqslant 0, \\
&\qquad\qquad i = 1,2,\ldots,n,
\end{aligned} \tag{28}$$

which is equivalent to

$$\begin{aligned}
&\begin{bmatrix} x(t) \\ f(x(t)) \end{bmatrix}^T \begin{bmatrix} F_i^- F_i^+ e_i e_i^T & -\dfrac{F_i^- + F_i^+}{2} e_i e_i^T \\ -\dfrac{F_i^- + F_i^+}{2} e_i e_i^T & e_i e_i^T \end{bmatrix} \\
&\qquad \cdot \begin{bmatrix} x(t) \\ f(x(t)) \end{bmatrix} \leqslant 0, \quad i = 1,2,\ldots,n,
\end{aligned} \tag{29}$$

where e_i is the unit column vector.

Let $W_1 = \operatorname{diag}\{w_{11}, w_{12}, \ldots, w_{1n}\} > 0$, $W_2 = \operatorname{diag}\{w_{21}, w_{22}, \ldots, w_{2n}\} > 0$, $W_3 = \operatorname{diag}\{w_{31}, w_{32}, \ldots, w_{3n}\} > 0$, $W_4 = \operatorname{diag}\{w_{41}, w_{42}, \ldots, w_{4n}\} > 0$; then

$$\begin{aligned}
&\sum_{i=1}^{n} w_{1i}\begin{bmatrix} x(t) \\ f(x(t)) \end{bmatrix}^T \begin{bmatrix} F_i^- F_i^+ e_i e_i^T & -\dfrac{F_i^- + F_i^+}{2} e_i e_i^T \\ -\dfrac{F_i^- + F_i^+}{2} e_i e_i^T & e_i e_i^T \end{bmatrix} \\
&\qquad \cdot \begin{bmatrix} x(t) \\ f(x(t)) \end{bmatrix} \leqslant 0, \quad i = 1,2,\ldots,n,
\end{aligned} \tag{30}$$

and it is equivalent to

$$\begin{bmatrix} x(t) \\ f(x(t)) \end{bmatrix}^T \begin{bmatrix} L_1 W_1 & -L_2 W_1 \\ -L_2 W_1 & W_1 \end{bmatrix} \begin{bmatrix} x(t) \\ f(x(t)) \end{bmatrix} \leqslant 0. \tag{31}$$

Similarly, we obtain

$$\begin{aligned}
&\begin{bmatrix} x(t) \\ g(x(t)) \end{bmatrix}^T \begin{bmatrix} G_1W_2 & -G_2W_2 \\ -G_2W_2 & W_2 \end{bmatrix} \begin{bmatrix} x(t) \\ g(x(t)) \end{bmatrix} \leqslant 0, \\
&\begin{bmatrix} x(t) \\ h(x(t)) \end{bmatrix}^T \begin{bmatrix} H_1W_3 & -H_2W_3 \\ -H_2W_3 & W_3 \end{bmatrix} \begin{bmatrix} x(t) \\ h(x(t)) \end{bmatrix} \leqslant 0, \\
&\begin{bmatrix} x(t-d(t)) \\ g(x(t-d(t))) \end{bmatrix}^T \\
&\quad \cdot \begin{bmatrix} G_1W_4 & -G_2W_4 \\ -G_2W_4 & W_4 \end{bmatrix} \begin{bmatrix} x(t-d(t)) \\ g(x(t-d(t))) \end{bmatrix} \leqslant 0.
\end{aligned} \tag{32}$$

By using (31)-(32), we have

$$\begin{aligned}
&-x(t)^T L_1W_1x(t) - f^T(x(t))W_1f(x(t)) \\
&\quad + x(t)^T L_2W_1f(x(t)) + f^T(x(t))L_2W_1x(t) \\
&\quad - x(t)^T G_1W_2x(t) - g^T(x(t))W_2g(x(t)) \\
&\quad + x(t)^T G_2W_2g(x(t)) + g^T(x(t))G_2W_2x(t) \\
&\quad - x(t)^T H_1W_3x(t) - h^T(x(t))W_3h(x(t)) \\
&\quad + x(t)^T H_2W_3f(x(t)) + h^T(x(t))H_2W_3x(t) \\
&\quad - x(t-d(t))^T G_1W_4x(t-d(t)) - g^T(x(t-d(t))) \\
&\quad \cdot W_4g(x(t-d(t))) + x(t-d(t))^T G_2W_4g(x(t-d(t))) \\
&\quad + g^T(x(t-d(t)))G_2W_4x(t-d(t)) \\
&= \zeta_t^T \left[-E_1L_1W_1E_1^T - E_6W_1E_6^T + E_1L_2W_1E_6^T + E_6L_2W_1E_1^T \right. \\
&\qquad - E_1G_1W_2E_1^T - E_{10}W_2E_{10}^T + E_1G_2W_2E_{10}^T \\
&\qquad + E_{10}G_2W_2E_1^T - E_1H_1W_3E_1^T - E_7W_3E_7^T \\
&\qquad + E_1H_2W_3E_7^T + E_7H_2W_3E_1^T - E_2G_1W_4E_2^T \\
&\qquad \left. - E_{11}W_4E_{11}^T + E_2G_2W_4E_{11}^T + E_{11}G_2W_4E_2^T \right] \zeta_t \\
&\geq 0.
\end{aligned} \tag{33}$$

The following equality holds:

$$\begin{aligned}
&2\left(x^T(t) + \dot{x}^T(t)\right) \\
&\quad \cdot \delta \left\{ -(A-K_1)x(t) + M_0f(x(t)) + M_1g(x(t-d(t))) \right. \\
&\qquad \left. + M_2 \int_{t-r(t)}^{t} h(x(s))\,ds + N\varphi(t) - \dot{x}(t) \right\} = 0,
\end{aligned} \tag{34}$$

which is equivalent to

$$\begin{aligned}
&\zeta_t^T \left[-2(E_1+E_5)\delta(A-K_1)E_1^T + 2(E_1+E_5)\delta M_0E_6^T \right. \\
&\quad + 2(E_1+E_5)\delta M_1E_{11}^T + 2(E_1+E_5)\delta M_2E_{12}^T \\
&\quad \left. + 2(E_1+E_5)\delta NE_{13}^T - 2(E_1+E_5)\delta E_5^T \right] \zeta_t = 0,
\end{aligned} \tag{35}$$

where δ is any matrix.

From Assumption 1, the following inequality holds:

$$\begin{aligned}
&\varphi^T(t)\varphi(t) \leq \zeta_t^T J^T J \zeta_t, \quad \text{where} \\
&J = [-J_1, 0, 0, 0, 0, J_2, 0, 0, 0, 0, J_3, J_4, \\
&\quad 0, 0, 0, 0, 0, 0, 0, 0, 0, 0, 0, 0].
\end{aligned} \tag{36}$$

Furthermore, there exits a positive scalar matrix U, such that the following inequality holds:

$$\zeta_t^T J^T U J \zeta_t - \varphi^T(t) U \varphi(t) \geq 0. \tag{37}$$

Combining (16)–(27) and (33), (35), and (37), we obtain

$$\dot{V}(t, x(t)) \leqslant \zeta_t^T \left[\Phi_0 + d(t)\Phi_1 + \Phi_d\right] \zeta_t, \tag{38}$$

where Φ_0, Φ_1 are defined in the theorem context, and

$$\begin{aligned}
\Phi_d &= (\overline{\tau} - d(t))F_1^T Q_3^{-1} F_1 + (\overline{\tau} - d(t))^2 F_2^T R_1^{-1} F_2 \\
&\quad + 3(\overline{\tau} - d(t))F_3^T R_2^{-1} F_3 + d(t)F_4^T Q_3^{-1} F_4 \\
&\quad + d(t)^2 F_5^T R_1^{-1} F_5 + 3d(t)F_6^T R_2^{-1} F_6.
\end{aligned} \tag{39}$$

Note that $\zeta_t^T[\Phi_0 + d(t)\Phi_1 + \Phi_d]\zeta_t$ is a quadratic function on $d(t)$, and the second-order coefficient is $\zeta_t^T[F_2^T R_1^{-1} F_2 + F_5^T R_1^{-1} F_5]\zeta_t$:

$$\begin{aligned}
&\left[\Phi_0 + d(t)\Phi_1 + \Phi_d\right]_{d(t)=0} \\
&\quad = \left[\Phi_0 + \Phi_d\right]_{d(t)=0} = \Phi_0 + \overline{\tau}F_1^T Q_3^{-1} F_1 + \overline{\tau}^2 F_2^T R_1^{-1} F_2 \\
&\quad + 3\overline{\tau}F_3^T R_2^{-1} F_3 < 0;
\end{aligned} \tag{40}$$

applying Lemma 6, we get $\Omega_1 < 0$:

$$\begin{aligned}
&\left[\Phi_0 + d(t)\Phi_1 + \Phi_d\right]_{d(t)=\overline{\tau}} \\
&\quad = \Phi_0 + \overline{\tau}\Phi_1 + \overline{\tau}F_4^T Q_3^{-1} F_4 + \overline{\tau}^2 F_5^T R_1^{-1} F_5 + 3\overline{\tau}F_6^T R_2^{-1} F_6 \\
&\quad < 0,
\end{aligned} \tag{41}$$

which is equivalent to $\Omega_2 < 0$.

Finally, employing Lemma 7, we get

$$\Phi_0 + d(t)\Phi_1 + \Phi_d < 0, \quad \forall \in [0, \overline{\tau}]. \tag{42}$$

Thus we can obtain from (38) and (42) that

$$\dot{V}(t, x(t)) \leqslant \zeta_t^T \left[\Phi_0 + d(t)\Phi_1 + \Phi_d\right] \zeta_t < 0, \tag{43}$$

which means that the system is asymptotically stable. This completes the proof. □

4. H_∞ Controller Design

In this section, we study the H_∞ control for the considered neural networks with a given disturbance attenuation level $\gamma > 0$. The neural networks (1) can be rewritten in the form

$$\begin{aligned}
\dot{x}(t) &= -(A - K_1)x(t) + M_0 f(x(t)) + M_1 g(x(t-d(t))) \\
&\quad + M_2 \int_{t-r(t)}^{t} h(x(s))\,ds + Bv(t) + N\varphi(t), \\
\varphi(t) &= F(t)\Big[-J_1 x(t) + J_2 f(x(t)) + J_3 g(x(t-d(t))) \\
&\quad + J_4 \int_{t-r(t)}^{t} h(x(s))\,ds + J_5 v(t)\Big], \\
z(t) &= Cx(t).
\end{aligned} \tag{44}$$

Theorem 9. *Under Assumptions 1 and 2, for given disturbance attenuation level $\gamma > 0$, scalars $\overline{\tau}$, μ, and $\overline{r}$, the system (44) is robustly asymptotically stabilizable under the control law $u(t)$ if there exist positive diagonal matrices $D = \operatorname{diag}\{d_1, d_2, \ldots, d_n\}$, $W_i > 0$, $i = 1,2,3,4$, positive definite matrices $P_1 \in R^{2n\times 2n}$, $S_i \in R^{2n\times 2n}$ $(i = 1,2,3,4,5)$, $Q_i \in R^{2n\times 2n}$ $(i = 1,2,3,4,5)$, $R_i \in R^{n\times n}$ $(i = 1,2)$, scalar matrix $U > 0$, and any matrices with appropriate dimensions F_i $(i = 1,2,\ldots,6)$, δ such that the following LMIs hold:*

$$\begin{aligned}
\widetilde{\Omega}_1 &= \begin{bmatrix} \widetilde{\Phi}_0 & \overline{\tau}F_1^T & \overline{\tau}F_2^T & \sqrt{3}\overline{\tau}F_3^T \\ * & -\overline{\tau}Q_3 & 0 & 0 \\ * & * & -R1 & 0 \\ * & * & * & -\overline{\tau}R_2 \end{bmatrix} < 0, \\
\widetilde{\Omega}_2 &= \begin{bmatrix} \widetilde{\Phi}_0 + \overline{\tau}\widetilde{\Phi}_1 & \overline{\tau}F_4^T & \overline{\tau}F_5^T & \sqrt{3}\overline{\tau}F_6^T \\ * & -\overline{\tau}Q_3 & 0 & 0 \\ * & * & -R1 & 0 \\ * & * & * & -\overline{\tau}R_2 \end{bmatrix} < 0,
\end{aligned} \tag{45}$$

where

$$\begin{aligned}
\widetilde{\Phi}_1 &= \operatorname{sym}(2E_1F_5 + 3E_1F_6 - 2E_2F_2 - 3E_2F_3) \\
&\quad + \operatorname{sym}\left([E_5, 0]\, Q_1\, [E_1, 0]^T\right), \\
\widetilde{\Phi}_0 &= \operatorname{sym}\Big(F_1^T [E_8, E_2 - E_3]^T + 2\overline{\tau}F_2^T E_2^T - 2F_2^T E_8^T \\
&\quad + 3\overline{\tau}F_3^T E_2^T - 3F_3^T E_8^T + F_4^T [E_9, E_1 - E_2]^T \\
&\quad - 2F_5^T E_9^T - 3F_6^T E_9^T\Big) \\
&\quad + \operatorname{sym}\left([E_1, E_3]\, P_1\, [E_5, E_{23}]^T + E_6 D E_5^T\right) \\
&\quad + [E_{10}, E_6]\,(S_1 + S_2 + S_5)\,[E_{10}, E_6]^T \\
&\quad - (1-\mu)\,[E_{11}, E_{14}]\, S_1\, [E_{11}, E_{14}]^T \\
&\quad + [E_1, E_1]\,(Q_1 + Q_2)\,[E_1, E_1]^T \\
&\quad + (\mu - 1)\,[E_1, E_2]\, Q_1\, [E_1, E_2]^T \\
&\quad + \operatorname{sym}\left([E_5, 0]\, Q_1\, [0, E_9]^T\right) \\
&\quad - [E_{19}, E_{20}]\, S_2\, [E_{19}, E_{20}]^T \\
&\quad + [E_5, E_7]\,(S_3 + S_4)\,[E_5, E_7]^T \\
&\quad - [E_{23}, E_{24}]\, S_3\, [E_{23}, E_{24}]^T \\
&\quad - [E_1, E_3]\, Q_2\, [E_1, E_3]^T \\
&\quad + \operatorname{sym}\left([E_5, 0]\, Q_2\, [\overline{\tau}E_1, E_8 + E_9]^T\right) \\
&\quad - [E_{15}, E_{16}]\, S_4\, [E_{15}, E_{16}]^T \\
&\quad - [E_{17}, E_{18}]\, S_5\, [E_{17}, E_{18}]^T \\
&\quad + \overline{\tau}\,[E_1, E_5]\, Q_3\, [E_1, E_5]^T + E_5\left(\overline{\tau}^2 R_1 + \overline{\tau}^3 R_2\right) E_5^T \\
&\quad + \overline{r}^2\,[E_5, E_7]\, Q_4\, [E_5, E_7]^T \\
&\quad - [E_1 - E_4, E_{12}]\, Q_4\, [E_1 - E_4, E_{12}]^T \\
&\quad + \overline{r}^2\,[E_{10}, E_6]\, Q_5\, [E_{10}, E_6]^T \\
&\quad - [E_{21}, E_{22}]\, Q_5\, [E_{21}, E_{22}]^T \\
&\quad - E_1 L_1 W_1 E_1^T - E_6 W_1 E_6^T + \operatorname{sym}\left(E_1 L_2 W_1 E_6^T\right) \\
&\quad - E_1 G_1 W_2 E_1^T - E_{10} W_2 E_{10}^T + \operatorname{sym}\left(E_1 G_2 W_2 E_{10}^T\right) \\
&\quad - E_1 H_1 W_3 E_1^T - E_7 W_3 E_7^T + \operatorname{sym}\left(E_1 H_2 W_3 E_7^T\right) \\
&\quad - E_2 G_1 W_4 E_2^T - E_{11} W_4 E_{11}^T + \operatorname{sym}\left(E_2 G_2 W_4 E_{11}^T\right) \\
&\quad + \operatorname{sym}\Big(-(E_1 + E_5)(\delta A - \Lambda_1) E_1^T + (E_1 + E_5)\,\delta M_0 E_6^T \\
&\qquad + (E_1 + E_5)\,\delta M_1 E_{11}^T + (E_1 + E_5)\,\delta M_2 E_{12}^T \\
&\qquad + (E_1 + E_5)\,\delta N E_{13}^T - (E_1 + E_5)\,\delta E_5^T\Big) \\
&\quad + \operatorname{sym}\left((E_1 + E_5)\,\delta B E_{25}^T\right) \\
&\quad + E_1 C^T C E_1^T - \gamma^2 E_{25} E_{25}^T + J^T U J - E_{13} U E_{13}^T,
\end{aligned} \tag{46}$$

with

$$\begin{aligned}
J &= [-J_1, 0, 0, 0, 0, J_2, 0, 0, 0, 0, J_3, J_4, \\
&\qquad 0, 0, 0, 0, 0, 0, 0, 0, 0, 0, 0, 0, J_5], \\
\Lambda_1 &= \delta K_1, \\
E_i &= \left[0_{nx(i-1)n}, I_n, 0_{nx(25-i)n}\right]^T, \quad i = 1, 2, \ldots, 25.
\end{aligned} \tag{47}$$

Proof. By using the $\dot{V}(t, x(t))$ obtained in Theorem 8, we can obtain

$$\begin{aligned} & x^T(t) C^T C x(t) - \gamma^2 v^T(t) v(t) + \dot{V}(t, x(t)) \\ & \quad \leqslant \bar{\zeta}_t^T \left[\widetilde{\Phi}_0 + d(t) \widetilde{\Phi}_1 + \widetilde{\Phi}_d\right] \bar{\zeta}_t, \end{aligned} \tag{48}$$

where

$$\begin{aligned} \bar{\zeta}(t) &= \left[\zeta^T(t), v^T(t)\right]^T, \\ \widetilde{\Phi}_0 &= \Phi_0 + \operatorname{sym}\left((E_1 + E_5) \delta B E_{25}^T\right) + E_1 C^T C E_1^T \\ &\quad - \gamma^2 E_{25} E_{25}^T, \\ \widetilde{\Phi}_1 &= \Phi_1, \\ \widetilde{\Phi}_d &= \Phi_d. \end{aligned} \tag{49}$$

If (45) holds, the inequality $\bar{\zeta}_t^T [\widetilde{\Phi}_0 + d(t)\widetilde{\Phi}_1 + \widetilde{\Phi}_d]\bar{\zeta}_t < 0$ holds, and we can easily obtain

$$\begin{aligned} & \int_0^\infty \left[x^T(t) C^T C x(t) - \gamma^2 v^T(t) v(t) + \dot{V}(t, x(t))\right] dt < 0, \\ & \int_0^\infty \left[z^T(t) z(t) - \gamma^2 v^T(t) v(t) + \dot{V}(t, x(t))\right] dt < 0. \end{aligned} \tag{50}$$

Since $V(t, x(t)) > 0$, we have

$$\int_0^\infty z^T(t) z(t)\, dt < \gamma^2 \int_0^\infty v^T(t) v(t)\, dt. \tag{51}$$

Hence the considered neural networks (44) are robustly stable for a given disturbance attenuation level $\gamma > 0$ according to Definition 3. This completes the proof. □

5. Numerical Examples

In this section, numerical examples are provided to illustrate effectiveness of the developed method for uncertain neural networks with discrete and distributed time-varying delays.

Example 1. We consider the neural networks (12) when the disturbance input $v(t) = 0$. The parameters are as follows:

$$\begin{aligned} A &= \begin{pmatrix} 2 & 0 \\ 0 & 3 \end{pmatrix}, \\ N &= C = \operatorname{diag}\{0.2, 0.2\}, \\ M_0 &= \begin{pmatrix} 0.5 & 0.7 \\ 0.3 & 0.2 \end{pmatrix}, \\ M_1 &= \begin{pmatrix} 0.2 & -0.5 \\ 0.3 & 0.2 \end{pmatrix}, \\ M_2 &= \begin{pmatrix} 0.3 & 0.2 \\ 0.4 & 0.5 \end{pmatrix}, \\ J_1 &= \begin{pmatrix} 0.2 & 0 \\ 0 & 0.5 \end{pmatrix}, \\ J_2 &= \begin{pmatrix} 0.2 & 0.3 \\ 0.5 & 0.1 \end{pmatrix}, \\ J_3 &= \begin{pmatrix} 0.1 & 0 \\ 0.3 & 0.2 \end{pmatrix}, \\ J_4 &= \begin{pmatrix} 0.3 & 0.1 \\ 0.1 & 0.2 \end{pmatrix}, \end{aligned} \tag{52}$$

and the activation functions are

$$\begin{aligned} f(x) &= \begin{pmatrix} \tanh(4x_1) \\ \tanh(4x_2) \end{pmatrix}, \\ g(x) &= \begin{pmatrix} \tanh(2x_1) \\ \tanh(2X_2) \end{pmatrix}, \\ h(x) &= \begin{pmatrix} \tanh(x_1) \\ \tanh(x_2) \end{pmatrix}, \end{aligned} \tag{53}$$

so that

$$\begin{aligned} L_1 &= G_1 = H_1 = \begin{pmatrix} 0 & 0 \\ 0 & 0 \end{pmatrix}, \\ L_2 &= \begin{pmatrix} 2 & 0 \\ 0 & 2 \end{pmatrix}, \\ G_2 &= \begin{pmatrix} 1 & 0 \\ 0 & 1 \end{pmatrix}, \\ H_2 &= \begin{pmatrix} 0.5 & 0 \\ 0 & 0.5 \end{pmatrix}. \end{aligned} \tag{54}$$

If we set $d(t) = 2.5 + 2.5\sin(0.2t)$, the upper bound of time delay $\bar{\tau} = 5$ and $\mu = 0.5$. And we set the upper bounds of time delays $\bar{r} = 5$. By solving through the MATLAB LMI toolbox, we obtain the gain matrix of the stabilization controller:

$$K_1 = \begin{pmatrix} -40.9083 & -38.3622 \\ -36.8673 & -61.2507 \end{pmatrix}. \tag{55}$$

Figures 1 and 2 present the state responses of the considered neural networks. Figure 1 shows the time response of the state variables $x_1(t)$ and $x_2(t)$ of the open-loop system from initial values $(1, -1)$. Figure 2 shows the time response of the state variables $x_1(t)$ and $x_2(t)$ of the closed-loop system from initial values $(1, -1)$. The open-loop system means the system without feedback control, and the closed-loop system means the system with the feedback control. It is clear that $x_1(t)$ and $x_2(t)$ converge rapidly to zero under the feedback control law and they cannot converge to zero without the feedback control. The simulation results reveal that the considered system with discrete and distributed time-varying delays is robustly asymptotically stable under the feedback control law.

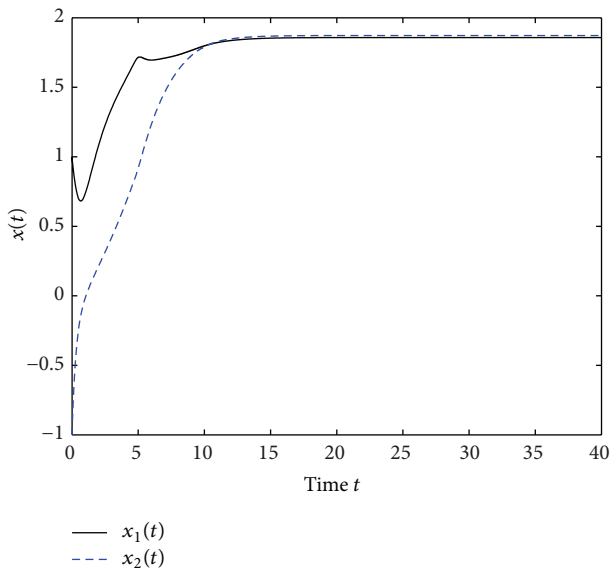

FIGURE 1: State responses of the open-loop system.

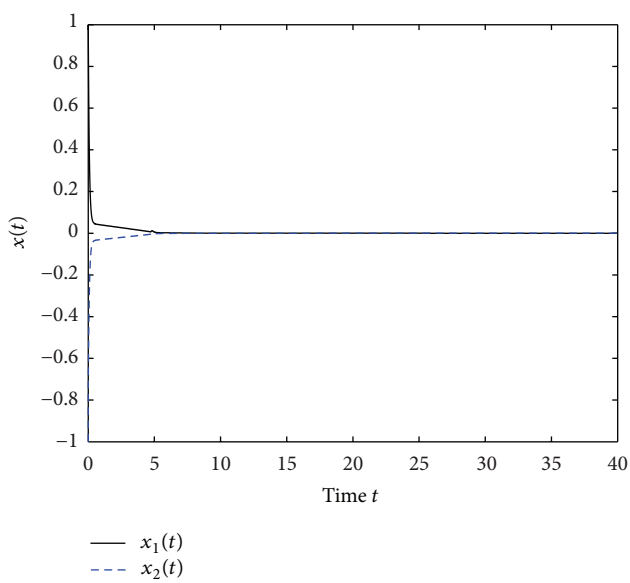

FIGURE 2: State responses of the closed-loop system.

Example 2. We consider the neural networks (44) with the disturbance input. The parameters are as follows:

$$A = \begin{pmatrix} 2 & 0 \\ 0 & 3 \end{pmatrix},$$

$$N = C = \operatorname{diag}\{0.2, 0.2\},$$

$$M_0 = \begin{pmatrix} 1 & 2 \\ 3 & -1 \end{pmatrix},$$

$$M_1 = \begin{pmatrix} 1 & -1 \\ 1 & 1 \end{pmatrix},$$

$$M_2 = \begin{pmatrix} 0.5 & 0.2 \\ 0.3 & 0.5 \end{pmatrix},$$

$$B = \begin{pmatrix} 1 & 0.2 \\ 0.5 & -1 \end{pmatrix},$$

$$J_1 = \begin{pmatrix} 0.2 & 0 \\ 0 & 0.5 \end{pmatrix},$$

$$J_2 = \begin{pmatrix} 0.2 & 0.3 \\ 0.5 & 0.1 \end{pmatrix}, \tag{56}$$

$$J_3 = \begin{pmatrix} 0.1 & 0 \\ 0.3 & 0.2 \end{pmatrix},$$

$$J_4 = \begin{pmatrix} 0.3 & 0.1 \\ 0.1 & 0.2 \end{pmatrix},$$

$$J_5 = \begin{pmatrix} 0.2 & 0 \\ -1 & 0.1 \end{pmatrix},$$

and the activation functions are

$$f(x) = \begin{pmatrix} \tanh(4x_1) \\ \tanh(4x_2) \end{pmatrix},$$

$$g(x) = \begin{pmatrix} \tanh(2x_1) \\ \tanh(2X_2) \end{pmatrix}, \tag{57}$$

$$h(x) = \begin{pmatrix} \tanh(x_1) \\ \tanh(x_2) \end{pmatrix},$$

so that

$$L_1 = G_1 = H_1 = \begin{pmatrix} 0 & 0 \\ 0 & 0 \end{pmatrix},$$

$$L_2 = \begin{pmatrix} 2 & 0 \\ 0 & 2 \end{pmatrix},$$

$$G_2 = \begin{pmatrix} 1 & 0 \\ 0 & 1 \end{pmatrix}, \tag{58}$$

$$H_2 = \begin{pmatrix} 0.5 & 0 \\ 0 & 0.5 \end{pmatrix}.$$

If we set $d(t) = 2 + 2\sin(0.15t)$, the upper bound of time delay $\overline{\tau} = 4$ and $\mu = 0.3$. And we set the upper bounds of time delays $\overline{r} = 4$. By solving through the MATLAB LMI toolbox, we obtain the gain matrix of the stabilization controller with the guaranteed H_∞ performance $\gamma = 0.1$:

$$K_1 = \begin{pmatrix} -410.5111 & -126.6215 \\ -162.0641 & -409.5459 \end{pmatrix}. \tag{59}$$

Figures 3 and 4 present the state responses of the considered neural networks with the disturbance input $v(t) = [1/(0.5 + t), 1/(1 + t^2)]^T$. Figure 3 shows the time response of the state variables $x_1(t)$ and $x_2(t)$ of the open-loop system from initial values $(0.5, -0.5)$. Figure 4 shows the time response of the state variables $x_1(t)$ and $x_2(t)$ of the closed-loop system from initial values $(0.5, -0.5)$. It is clear that $x_1(t)$ and $x_2(t)$ converge rapidly to zero under the feedback control law and

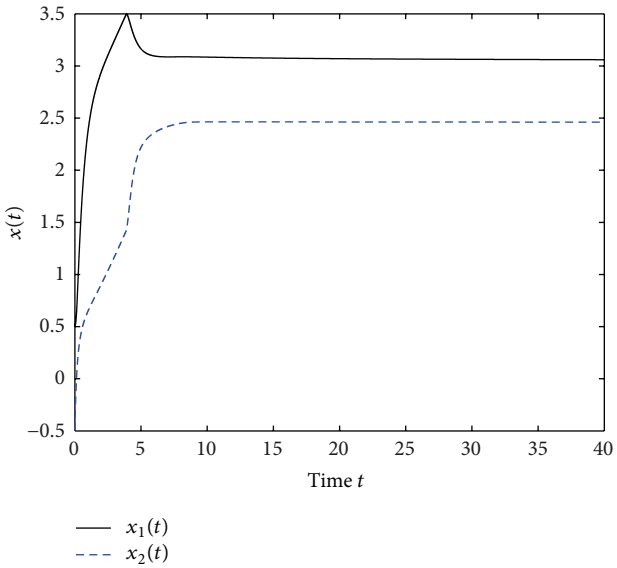

Figure 3: State responses of the open-loop system.

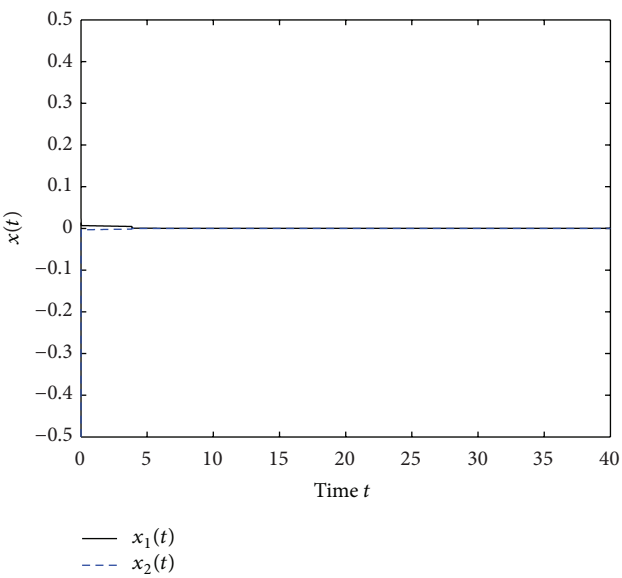

Figure 4: State responses of the closed-loop system.

they cannot converge to zero without the feedback control. The simulation results reveal that the considered system with discrete and distributed time-varying delays is robustly asymptotically stable under the feedback control law.

6. Conclusions

In this paper, we investigated the robust stabilization problem and H_∞ control for a class of uncertain neural networks. By implementing the quadratic convex combination technique together with Lyapunov-Krasovskii functional approach, new delay-dependent conditions were established. The stabilization criterion was derived by the augmented Lyapunov-Krasovskii functional, which ensures the robust stability of the considered uncertain neural networks with various activation functions. Furthermore, our result was extended to the design of a robust H_∞ controller, which guarantees the closed-loop system robustly asymptotically stable with a prescribed H_∞ performance level. The criteria are derived in terms of LMIs, which can be easily calculated by the MATLAB toolbox. Numerical examples are provided to illustrate the effectiveness of the obtained results.

Conflict of Interests

The authors declare that there is no conflict of interests regarding the publication of this paper.

Aknowledgments

This work was supported by the National Basic Research Program of China (2010CB732501) and the Natural Science Foundation of Hainan Province (111002).

References

[1] K. Gopalsamy and X.-Z. He, "Delay-independent stability in bidirectional associative memory networks," *IEEE Transactions on Neural Networks*, vol. 5, no. 6, pp. 998–1002, 1994.

[2] J. B. Hampshire and A. H. Waibel, "Novel objective function for improved phoneme recognition using time-delay neural networks," *IEEE Transactions on Neural Networks*, vol. 1, no. 2, pp. 216–228, 1990.

[3] O. M. Kwon, S. M. Lee, and J. U. H. Park, "Improved results on stability analysis of neural networks with time-varying delays: novel delay-dependent criteria," *Modern Physics Letters B*, vol. 24, no. 8, pp. 775–789, 2010.

[4] A. Arunkumar, R. Sakthivel, K. Mathiyalagan, and J. H. Park, "Robust stochastic stability of discrete-time fuzzy markovian jump neural networks," *ISA Transactions*, vol. 53, no. 4, pp. 1006–1014, 2014.

[5] Y. Liu, S. M. Lee, O. M. Kwon, and J. H. Park, "A study on H_∞ state estimation of static neural networks with time-varying delays," *Applied Mathematics and Computation*, vol. 226, pp. 589–597, 2014.

[6] S. Lakshmanan, K. Mathiyalagan, J. H. Park, R. Sakthivel, and F. A. Rihan, "Delay-dependent H_∞ state estimation of neural networks with mixed time-varying delays," *Neurocomputing*, vol. 129, pp. 392–400, 2014.

[7] K. Shi, H. Zhu, S. Zhong, Y. Zeng, and Y. Zhang, "Less conservative stability criteria for neural networks with discrete and distributed delays using a delay-partitioning approach," *Neurocomputing*, vol. 140, pp. 273–282, 2014.

[8] B. Du and J. Lam, "Stability analysis of static recurrent neural networks using delay-partitioning and projection," *Neural Networks*, vol. 22, no. 4, pp. 343–347, 2009.

[9] M. Luo, S. Zhong, R. Wang, and W. Kang, "Robust stability analysis for discrete-time stochastic neural networks systems with time-varying delays," *Applied Mathematics and Computation*, vol. 209, no. 2, pp. 305–313, 2009.

[10] J. Tian and X. Xie, "New asymptotic stability criteria for neural networks with time-varying delay," *Physics Letters A*, vol. 374, no. 7, pp. 938–943, 2010.

[11] J. Tian and S. Zhong, "Improved delay-dependent stability criterion for neural networks with time-varying delay," *Applied Mathematics and Computation*, vol. 217, no. 24, pp. 10278–10288, 2011.

[12] O. M. Kwon, S. M. Lee, and J. H. Park, "On improved passivity criteria of uncertain neural networks with time-varying delays," *Nonlinear Dynamics*, vol. 67, no. 2, pp. 1261–1271, 2012.

[13] O. M. Kwon, M. J. Park, J. H. Park, S. M. Lee, and E. J. Cha, "Improved approaches to stability criteria for neural networks with time-varying delays," *IEEE Engineering and Applied Mathematics*, vol. 350, no. 9, pp. 2710–2735, 2013.

[14] H. Zhao, "Global asymptotic stability of Hopfield neural network involving distributed delays," *Neural Networks*, vol. 17, no. 1, pp. 47–53, 2004.

[15] S. Lakshmanan, J. H. Park, H. Y. Jung, O. M. Kwon, and R. Rakkiyappan, "A delay partitioning approach to delay-dependent stability analysis for neutral type neural networks with discrete and distributed delays," *Neurocomputing*, vol. 111, pp. 81–89, 2013.

[16] V. N. Phat and H. Trinh, "Exponential stabilization of neural networks with various activation functions and mixed time-varying delays," *IEEE Transactions on Neural Networks*, vol. 21, no. 7, pp. 1180–1184, 2010.

[17] Q. Song, "Design of controller on synchronization of chaotic neural networks with mixed time-varying delays," *Neurocomputing*, vol. 72, no. 13–15, pp. 3288–3295, 2009.

[18] D. Zhang and L. Yu, "Exponential state estimation for Markovian jumping neural networks with time-varying discrete and distributed delays," *Neural Networks*, vol. 35, pp. 103–111, 2012.

[19] O. M. Kwon and J. H. Park, "Exponential stability analysis for uncertain neural networks with interval time-varying delays," *Applied Mathematics and Computation*, vol. 212, no. 2, pp. 530–541, 2009.

[20] R. Sakthivel, K. Mathiyalagan, and S. M. Anthoni, "Design of a passification controller for uncertain fuzzy hopfield neural networks with timevarying delays," *Physica Scripta*, vol. 84, Article ID 045024, 2011.

[21] J. Wang, J. H. Park, H. Shen, and J. Wang, "Delay-dependent robust dissipativity conditions for delayed neural networks with random uncertainties," *Applied Mathematics and Computation*, vol. 221, pp. 710–719, 2013.

[22] K. Mathiyalagan, R. Sakthivel, and S. M. Anthoni, "New stability and stabilization criteria for fuzzy neural networks with various activation functions," *Physica Scripta*, vol. 84, no. 1, Article ID 015007, 2011.

[23] V. N. Phat and H. Trinh, "Exponential stabilization of neural networks with various activation functions and mixed time-varying delays," *IEEE Transactions on Neural Networks*, vol. 21, no. 7, pp. 1180–1184, 2010.

[24] B. Chen and J. Wang, "Global exponential periodicity and global exponential stability of a class of recurrent neural networks with various activation functions and time-varying delays," *Neural Networks*, vol. 20, no. 10, pp. 1067–1080, 2007.

[25] X. Nie and J. Cao, "Stability analysis for the generalized Cohen-Grossberg neural networks with inverse Lipschitz neuron activations," *Computers and Mathematics with Applications*, vol. 57, no. 9, pp. 1522–1536, 2009.

[26] R. Sakthivel, K. Mathiyalagan, and S. M. Anthoni, "Delay-dependent robust stabilization and H_∞ control for neural networks with various activation functions," *Physica Scripta*, vol. 85, Article ID 045801, 2012.

[27] M. Liu, "Robust H_∞ control for uncertain delayed nonlinear systems based on standard neural network models," *Neurocomputing*, vol. 71, no. 16–18, pp. 3469–3492, 2008.

[28] P. Niamsup and V. N. Phat, "H_∞ control for nonlinear time-varying delay systems with convex polytopic uncertainties," *Nonlinear Analysis: Theory, Methods & Applications*, vol. 72, no. 11, pp. 4254–4263, 2010.

[29] V. N. Phat, "Memoryless H_∞ controller design for switched non-linear systems with mixed time-varying delays," *International Journal of Control*, vol. 82, no. 10, pp. 1889–1898, 2009.

[30] Z. Wang, D. W. Ho, Y. Liu, and X. Liu, "Robust H_∞ control for a class of nonlinear discrete time-delay stochastic systems with missing measurements," *Automatica*, vol. 45, no. 3, pp. 684–691, 2009.

[31] Z. Wang, L. Huang, and X. Yang, "H_∞ performance for a class of uncertain stochastic nonlinear Markovian jump systems with time-varying delay via adaptive control method," *Applied Mathematical Modelling*, vol. 35, no. 4, pp. 1983–1993, 2011.

[32] O. M. Kwon, M. J. Park, J. H. Park, S. M. Lee, and E. J. Cha, "Stability and H_∞ performance analysis for Markovian jump systems with time-varying delays," *Journal of the Franklin Institute*, vol. 351, no. 10, pp. 4724–4748, 2014.

[33] J. Cheng, H. Zhu, S. Zhong, Q. Zhong, and Y. Zeng, "Finite-time H_∞ estimation for discrete-time Markov jump systems with time-varying transition probabilities subject to average dwell time switching," *Communications in Nonlinear Science and Numerical Simulation*, vol. 20, no. 2, pp. 571–582, 2015.

[34] J. Cheng, H. Zhu, S. Zhong, F. Zheng, and Y. Zeng, "Finite-time filtering for switched linear systems with a mode-dependent average dwell time," *Nonlinear Analysis: Hybrid Systems*, vol. 15, pp. 145–156, 2015.

[35] S. Boyd, L. El Ghaoui, E. Feron, and V. Balakrishnan, *Linear Matrix Inequalities in System and Control Theory*, vol. 15, SIAM, Philadelphia, Pa, USA, 1994.

[36] H. Zhang, F. Yang, X. Liu, and Q. Zhang, "Stability analysis for neural networks with time-varying delay based on quadratic convex combination," *IEEE Transactions on Neural Networks and Learning Systems*, vol. 24, no. 4, pp. 513–521, 2013.

Hindawi Publishing Corporation
Mathematical Problems in Engineering
Volume 2015, Article ID 604246, 7 pages
http://dx.doi.org/10.1155/2015/604246

Research Article

Design for Nonlinear Networked Control Systems with Time Delay Governed by Markov Chain with Partly Unknown Transition Probabilities

Yan-Feng Wang, Zu-Xin Li, Hui-Ying Chen, Li-Di Quan, and Xiao-Rui Guo

School of Engineering, Huzhou University, Huzhou, Zhejiang 313000, China

Correspondence should be addressed to Yan-Feng Wang; neu2009wyf@163.com

Received 21 October 2014; Accepted 21 November 2014

Academic Editor: Kun Liu

Copyright © 2015 Yan-Feng Wang et al. This is an open access article distributed under the Creative Commons Attribution License, which permits unrestricted use, distribution, and reproduction in any medium, provided the original work is properly cited.

The problem of state feedback control for a class of nonlinear networked control systems with time delay is discussed in this paper. The time delay is modeled as a finite state Markov chain of which transition probabilities are partly unknown. The closed-loop system model is obtained by means of state augmentation. A sufficient condition is given which guarantees the stochastic stability of the closed-loop system in the form of linear matrix inequalities and the maximum bound of the nonlinearity is also obtained. Finally, a simulation example is used to show the validity of the proposed method.

1. Introduction

Networked control systems (NCSs) are feedback control systems with control loops closed via digital communication channels [1]. As is well known, NCSs are widely used in many fields such as remote surgery, mobile sensor networks, and unmanned aerial vehicles especially in a number of emerging engineering applications such as arrays of microactuators and even social-economical systems [2–4]. Compared with the point-to-point wiring, the use of communication channels can reduce the costs of cables and simplify the installation and maintenance of the system. However, the insertion of the network will make system analysis and synthesis more challenging [5–8]. Network-induced delays can degrade the performance of control systems designed without considering them and even destabilize the system [9–11].

Up to now, the effect of time delay on the stability and performance of NCSs has received great attention [12, 13]. The time delay may be constant, time-varying, and, in most cases, random [14–16]. For the random cases, the time delays are commonly modeled as white sequences taking on values of zero and one with certain probability [17, 18] or as finite state Markov chains [19–21]. In the real networks, the current time delays are usually related with the previous delays, so the Markov chain model is proper compared to the white sequence model to describe the time delay.

In [22, 23], the random delays are modeled as Markov chains such that the closed-loop system is a jump linear system. In [24–26], the random time delays are modeled as Markov chains, and output feedback controller design methods for NCSs with random network-induced delays are proposed. In [27], the mixed H_2/H_∞ control issue of NCSs with random time delays has been investigated based on Markov jump linear systems method. In the above literature [22–27], all parts of the elements in the transition probabilities matrix of the time delays are assumed to be completely known. However, in almost all kinds of networks, all parts of the elements in the desired transition probabilities matrix are hard or costly to obtain. In [28–30], the stability issue of discrete-time networked control systems with random Markov delays and uncertain transition probabilities is studied. And the controlled plants in [22–30] are assumed to be linear. However, almost all the practical controlled plants are nonlinear; it is significant and necessary to further study nonlinear NCSs with partly unknown transition probabilities. To the best of the authors' knowledge, up to now, very limited efforts have been devoted to studying the system with uncertain transition probability matrices for nonlinear NCSs, which motivates our investigation.

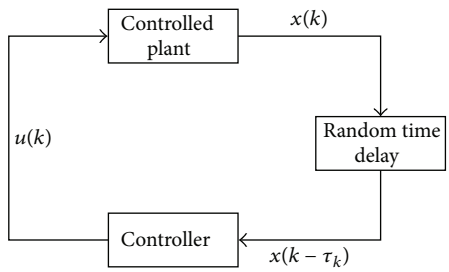

Figure 1: NCSs with random delay.

This paper studies the state feedback problem of a class of nonlinear NCSs. The time delay is modeled as a finite state Markov chain of which transition probabilities are partly unknown. The closed-loop system model is obtained by means of state augmentation and the mode-dependent state feedback controller is designed which guarantees the stochastic stability of the closed-loop system. The state feedback controller is designed which guarantees the stability of the resulting closed-loop systems. The maximum bound of nonlinear disturbance is also obtained.

Notations. The superscript T stands for the transpose of a matrix. R^n and $R^{n\times m}$ denote the n-dimensional Euclidean space and the set of all $n \times m$ real matrices, respectively. diag$\{\cdots\}$ denotes the block diagonal matrix. I and 0 stand for unit matrix and zero matrix with appropriate dimensions, respectively. $*$ denotes the entry of matrices implied by symmetry.

2. Problem Formulation

Consider the NCS setup in Figure 1, in which the controlled plant is a nonlinear time-invariant discrete-time system and $\tau_k > 0$ is the bounded and random time delay from the senor to the controller which takes value in $\Lambda = \{1, 2, \ldots, d\}$ and the transition probability matrix of τ_k is $\Pi = [\pi_{ij}]$.

That is, τ_k jump from mode i to j with probability π_{ij} which is defined by $\pi_{ij} = \Pr(\tau_{k+1} = j \mid \tau_k = i)$, where $\pi_{ij} \geq 0$, $\forall i, j \in \Lambda$, $\sum_{j=1}^{d} \pi_{ij} = 1$. Likewise, the transition probability matrix is defined by

$$\Pi = \begin{bmatrix} \pi_{11} & \pi_{12} & \cdots & \pi_{1d} \\ \pi_{21} & \pi_{22} & \cdots & \pi_{2d} \\ \vdots & \vdots & \ddots & \vdots \\ \pi_{d1} & \pi_{d2} & \cdots & \pi_{dd} \end{bmatrix}. \tag{1}$$

The set Λ contains d modes of τ_k, and the transition probabilities of the jumping process in this paper are considered to be partly accessed; that is, some elements in matrix Π are unknown. For example, for the time delay τ_k with 4 modes, the transition probabilities matrix Π may be as follows:

$$\Pi = \begin{bmatrix} ? & \pi_{12} & ? & ? \\ ? & ? & \pi_{23} & ? \\ \pi_{31} & ? & \pi_{33} & ? \\ ? & ? & ? & \pi_{44} \end{bmatrix}, \tag{2}$$

where "?" represents the inaccessible elements. For notational clarity, $\forall i \in \Lambda$, we denote $\Lambda = \Lambda_k^i + \Lambda_{uk}^i$ by

$$\begin{aligned} \Lambda_k^i &= \left\{ j : \pi_{ij} \text{ is known} \right\}, \\ \Lambda_{uk}^i &= \left\{ j : \pi_{ij} \text{ is unknown} \right\}. \end{aligned} \tag{3}$$

Moreover, if $\Lambda_k^i \neq \emptyset$, it is further described as $\Lambda_k^i = \{k_1^i, k_2^i \cdots k_\mu^i\}$, $1 \leq \mu \leq d$, where k_μ^i represents the μth known element with the index k_μ^i in the ith row of the matrix Π. And Λ_{uk}^i is described as $\Lambda_{uk}^i = \{\bar{k}_1^i, \bar{k}_2^i \ldots \bar{k}_{d-\mu}^i\}$, where $\bar{k}_{d-\mu}^i$ represents the $(d-\mu)$th unknown element with the index $(d-\mu)$th in the ith row of the matrix Π.

Assume that the model of the plant is a nonlinear discrete-time system as follows:

$$x(k+1) = A_p x(k) + B_p u(k) + f(k, x(k)), \tag{4}$$

where $x(k) \in R^n$ is state vector, $u(k) \in R^m$ is the control input, $A_p \in R^{n\times n}$ and $B_p \in R^{n\times m}$ are all real constant matrices, and $f(k, x(k))$ is nonlinear disturbance, satisfying the following Lipschitz condition [31]:

$$f^T(k, x(k)) f(k, x(k)) \leq \alpha^2 x^T(k) H^T H x(k), \tag{5}$$

where H is a real constant matrix and $\alpha \geq 0$ is the bound of the nonlinear disturbance.

It is noticed that when the controller is designed, the exact τ_k is known. Hence, the controller gain can be designed depending on τ_k; that is,

$$\begin{aligned} u(k) &= K(\tau_k) x(k - \tau_k), \\ x(t) &= \eta(t), \quad t \in \{-d, \ldots, 0\}. \end{aligned} \tag{6}$$

Consequently, the closed-loop system from (4) and (6) can be expressed as

$$x(k+1) = A_p x(k) + B_p K(\tau_k) x(k - \tau_k) + f(k, x(k)). \tag{7}$$

At sampling time k, if we augment the state variable as

$$X(k) = \left[x(k)^T \;\; x(k-1)^T \;\; \cdots \;\; x(k-d)^T \right]^T, \tag{8}$$

the closed-loop system (7) can be written as

$$\begin{aligned} X(k+1) &= \left(A + BK(\tau_k) E(\tau_k) \right) X(k) + DF(k, X(k)), \\ X(0) &= \left[\eta(0)^T \;\; \eta(-1)^T \;\; \cdots \;\; \eta(-d)^T \right]^T, \end{aligned} \tag{9}$$

where

$$A = \begin{bmatrix} A_p & 0 & \cdots & 0 & 0 \\ I & 0 & \cdots & 0 & 0 \\ 0 & I & \cdots & 0 & 0 \\ \vdots & \vdots & \ddots & 0 & 0 \\ 0 & 0 & \cdots & I & 0 \end{bmatrix} \in R^{n(1+d)\times n(1+d)},$$

$$B = \begin{bmatrix} B_p \\ 0 \\ 0 \\ \vdots \\ 0 \end{bmatrix} \in R^{n(1+d)\times m},$$

$$D = \begin{bmatrix} I \\ 0 \\ 0 \\ \vdots \\ 0 \end{bmatrix} \in R^{n(1+d)\times n}, \tag{10}$$

$$G = \begin{bmatrix} I & 0 & 0 & \cdots & 0 \end{bmatrix} \in R^{n\times n(1+d)},$$

$$F(k, X(k)) = f(k, GX(k)),$$

$$E(\tau_k) = \begin{bmatrix} 0 & 0 & I & \cdots & 0 \end{bmatrix} \in R^{n\times n(1+d)}$$

has all elements being zeros except for the $(1+\tau_k)$th block being identity. It can be seen that the closed-loop system (9) is a jump linear system with d different modes.

To proceed, we will need the following lemmas.

Lemma 1 (see [2]). *Let $T_1, T_2 \in R^{n\times n}$ be symmetric matrices. The conditions on $x^T T_1 x < 0$, $\forall x \neq 0$ such that $x^T T_2 x \leq 0$ hold if there exists a scalar $\varepsilon \geq 0$ such that $T_1 - \varepsilon T_2 < 0$.*

Lemma 2 (see [32]). *For given scalars $\lambda_i \geq 0$ and matrices $P_i \geq 0$, $\sum_{i=1}^N \lambda_i P_i \leq \sum_{i=1}^N \lambda_i \sum_{i=1}^N P_i$ always holds.*

Lemma 3 (see [18]). *The matrix $E(i)^T$ is of full-array rank; then, there exist two orthogonal matrices $U_i \in R^{n(1+d)\times n(1+d)}$ and $V_i \in R^{g\times g}$, such that $E(i)^T = U_i^T \left[\begin{smallmatrix} \Sigma_i \\ 0 \end{smallmatrix}\right] V_i^T$, where $\Sigma_i = \operatorname{diag}(\sigma_1, \sigma_2, \ldots, \sigma_g)$, where σ_i $(i = 1, 2, \ldots, g)$ are nonzero singular values of E_i^T. If matrix $F(i) \in R^{n(1+d)\times n(1+d)}$ has the following structure,*

$$F(i) = U_i^T \begin{bmatrix} F_{i1} & 0 \\ 0 & F_{i2} \end{bmatrix} U_i, \tag{11}$$

there exists a nonsingular matrix $X_i \in R^{n\times n}$ such that $F(i)E(i)^T = E(i)^T X_i$, where $F_{i1} \in R^{g\times g} > 0$ and $F_{i2} \in R^{n(1+d-g)\times n(1+d-g)} > 0$.

Throughout this paper, we use the following definition.

Definition 4 (see [20]). The system (9) is stochastically stable if, for every finite $X(0)$ and initial mode $\tau_0 \in \Lambda$, there exists a finite matrix $W > 0$ such that the following holds:

$$E\left\{\sum_{k=0}^{\infty} \|X(k)\|^2 \mid X_0, \tau_0\right\} < X_0^T W X_0. \tag{12}$$

Our objective for this paper is to find the controller gain $K(\tau_k)$ such that the closed-loop system (7) is stochastically stable. In the following, if we know that $\tau_k = i$, $K(\tau_k)$ and $E(\tau_k)$ for this paper are denoted by $K(i)$ and $E(i)$, respectively.

3. Controller Design

Theorem 5. *Consider system (9) with partly unknown transition probabilities (3). If there exist matrices $F(i) > 0$, $Y(i)$ and a scalar $\varepsilon > 0$ such that*

$$\begin{bmatrix} -F(i) & 0 & \Omega_{13} & \Omega_{14} & F(i)G^T H^T \\ * & -I & \Omega_{23} & \Omega_{24} & 0 \\ * & * & \Omega_{33} & 0 & 0 \\ * & * & * & \Omega_{44} & 0 \\ * & * & * & * & -\varepsilon I \end{bmatrix} < 0, \tag{13}$$

where

$$\begin{aligned}
\Omega_{13} &= (AF(i) + BY(i)E(i))^T \\
&\quad \times \left[\sqrt{\pi_{ik_1^i}} I \quad \sqrt{\pi_{ik_2^i}} I \quad \cdots \quad \sqrt{\pi_{ik_\mu^i}} I\right], \\
\Omega_{14} &= (AF(i) + BY(i)E(i))^T \\
&\quad \times \left[\sqrt{\lambda_i} I \quad \sqrt{\lambda_i} I \quad \cdots \quad \sqrt{\lambda_i} I\right], \\
\Omega_{23} &= \left[\sqrt{\pi_{ik_1^i}} D \quad \sqrt{\pi_{ik_2^i}} D \quad \cdots \quad \sqrt{\pi_{ik_\mu^i}} D\right], \\
\Omega_{24} &= \left[\sqrt{\lambda_i} D \quad \sqrt{\lambda_i} D \quad \cdots \quad \sqrt{\lambda_i} D\right], \\
\Omega_{33} &= -\operatorname{diag}\left\{F\left(k_1^i\right) \quad F\left(k_2^i\right) \quad \cdots \quad F\left(k_\mu^i\right)\right\}, \\
\Omega_{44} &= -\operatorname{diag}\left\{F\left(\bar{k}_1^i\right) \quad F\left(\bar{k}_2^i\right) \quad \cdots \quad F\left(\bar{k}_{d-\mu}^i\right)\right\}, \\
F(i) &= U_i^T \begin{bmatrix} F_{i1} & 0 \\ 0 & F_{i2} \end{bmatrix} U_i, \\
\lambda_i &= 1 - \sum_{j\in\Lambda_k^i} \pi_{ij}, \\
\varepsilon &= \frac{1}{\alpha^2},
\end{aligned} \tag{14}$$

hold for all $i \in \Lambda$; there exists a mode-dependent controller of the form (6) such that the resulting system (9) is stochastically stable. Furthermore, if the LMI (13) has a solution, an admissible controller is given by

$$K(i) = Y(i) V_i \Sigma_i^{-1} F_{i1}^{-1} \Sigma_i V_i^T. \tag{15}$$

Proof. For the closed-loop system (9), consider the quadratic function which is given by $V(X(k),k) = X^T(k)P(\tau_k)X(k)$. We have

$$\begin{aligned} &E\{\Delta V(X(k),k)\} \\ &\quad = E\left\{X^T(k+1)P(\tau_{k+1})X(k+1) \mid X(k),\tau_k = i\right\} \\ &\qquad - X^T(k)P(\tau_k)X(k) \\ &\quad = \delta^T L(\tau_k)\delta, \end{aligned} \tag{16}$$

where

$$\begin{aligned} L(\tau_k) &= \begin{bmatrix} L_{11} & (A+BK(i)E(i))^T \sum_{j=1}^{d}\pi_{ij}P(j)D \\ * & D^T\sum_{j=1}^{d}\pi_{ij}P(j)D \end{bmatrix}, \\ L_{11} &= (A+BK(i)E(i))^T \\ &\quad \times \sum_{j=1}^{d}\pi_{ij}P(j)(A+BK(i)E(i)) - P(i), \\ \delta &= \left[X(k)^T \quad F(k,X(k))^T\right]^T. \end{aligned} \tag{17}$$

If $L(\tau_k) < 0$, it can be proved that the closed-loop system (9) is stochastically stable which is similar to that of [18] and is omitted here.

From (5), one can get

$$\delta^T \begin{bmatrix} -\alpha^2 G^T H^T HG & 0 \\ * & I \end{bmatrix}\delta \le 0. \tag{18}$$

According to Lemma 1, if there exists a scalar $\varepsilon \ge 0$ such that

$$\begin{aligned} &\begin{bmatrix} L_{11} + \varepsilon\alpha^2 G^T H^T HG & (A+BK(i)E(i))^T \sum_{j=1}^{d}\pi_{ij}P(j)D \\ * & D^T\sum_{j=1}^{d}\pi_{ij}P(j)D - \varepsilon I \end{bmatrix} \\ &\quad < 0, \end{aligned} \tag{19}$$

the inequality (16) subject to (18) holds. Assume that $\varepsilon \ne 0$; inequality (19) can be written as

$$\begin{bmatrix} \widetilde{L}_{11} + \alpha^2 G^T H^T HG & (A+BK(i)E(i))^T \sum_{j=1}^{d}\pi_{ij}\widetilde{P}(j)D \\ * & D^T\sum_{j=1}^{d}\pi_{ij}\widetilde{P}(j)D - I \end{bmatrix} < 0, \tag{20}$$

where

$$\begin{aligned} \widetilde{L}_{11} &= (A+BK(i)E(i))^T \\ &\quad \times \sum_{j=1}^{d}\pi_{ij}\widetilde{P}(j)(A+BK(i)E(i)) - \widetilde{P}(i), \\ \widetilde{P}(j) &= \frac{P(j)}{\varepsilon}, \\ \widetilde{P}(i) &= \frac{P(i)}{\varepsilon}. \end{aligned} \tag{21}$$

According to Lemma 2, one can get

$$\sum_{j=1}^{d}\pi_{ij}\widetilde{P}(j) \le \widetilde{P}\left(\Lambda_k^i\right) + \lambda_i\widetilde{P}\left(\Lambda_{uk}^i\right), \tag{22}$$

where

$$\begin{aligned} \widetilde{P}\left(\Lambda_k^i\right) &= \sum_{j\in\Lambda_k^i}\pi_{ij}\widetilde{P}(j), \\ \widetilde{P}\left(\Lambda_{uk}^i\right) &= \sum_{j\in\Lambda_{uk}^i}\widetilde{P}(j), \\ \lambda_i &= 1 - \sum_{j\in\Lambda_k^i}\pi_{ij}. \end{aligned} \tag{23}$$

By Schur complement, one can obtain

$$\begin{bmatrix} -\widetilde{P}(i) & 0 & \overline{\Omega}_{13} & \overline{\Omega}_{14} & G^T H^T \\ 0 & -I & \Omega_{23} & \Omega_{24} & 0 \\ * & * & \overline{\Omega}_{33} & 0 & 0 \\ * & * & * & \overline{\Omega}_{44} & 0 \\ * & * & * & * & -\varepsilon I \end{bmatrix} < 0, \tag{24}$$

where

$$\begin{aligned} \overline{\Omega}_{13} &= (A+BK(i)E(i))^T \\ &\quad \times \left[\sqrt{\pi_{ik_1^i}}I \quad \sqrt{\pi_{ik_2^i}}I \quad \cdots \quad \sqrt{\pi_{ik_\mu^i}}I\right], \\ \overline{\Omega}_{14} &= (A+BK(i)E(i))^T\left[\sqrt{\lambda_i}I \quad \sqrt{\lambda_i}I \quad \cdots \quad \sqrt{\lambda_i}I\right], \\ \overline{\Omega}_{33} &= -\operatorname{diag}\left\{P^{-1}\left(k_1^i\right) \quad P^{-1}\left(k_2^i\right) \quad \cdots \quad P^{-1}\left(k_\mu^i\right)\right\}, \\ \overline{\Omega}_{44} &= -\operatorname{diag}\left\{P^{-1}\left(\overline{k}_1^i\right) \quad P^{-1}\left(\overline{k}_2^i\right) \quad \cdots \quad P^{-1}\left(\overline{k}_{d-\mu}^i\right)\right\}. \end{aligned} \tag{25}$$

Performing a congruence transformation to (24) by $\operatorname{diag}\{P^{-1}(i) \ I \ I \ I \ I\}$ and letting $\widetilde{P}^{-1}(i) = F(i)$, $\operatorname{diag}\left\{P^{-1}(k_1^i) \ P^{-1}(k_2^i) \ \cdots \ P^{-1}(k_\mu^i)\right\} = \operatorname{diag}\{F(k_1^i) \ F(k_2^i) \ \cdots \ F(k_\mu^i)\}$, $\operatorname{diag}\left\{P^{-1}(\overline{k}_1^i) \ P^{-1}(\overline{k}_2^i) \ \cdots \ P^{-1}(\overline{k}_{d-\mu}^i)\right\} = \operatorname{diag}\left\{F(\overline{k}_1^i) \ F(\overline{k}_2^i) \ \cdots \ F(\overline{k}_{d-\mu}^i)\right\}$, we can get

$$\begin{bmatrix} -F(i) & 0 & \widetilde{\Omega}_{13} & \widetilde{\Omega}_{14} & F(i)G^T H^T \\ * & -I & \Omega_{23} & \Omega_{24} & 0 \\ * & * & \Omega_{33} & 0 & 0 \\ * & * & * & \Omega_{44} & 0 \\ * & * & * & * & -\varepsilon I \end{bmatrix} < 0, \tag{26}$$

where

$$\widetilde{\Omega}_{13} = F(i)(A + BK(i)E(i))^T \times \left[\sqrt{\pi_{ik_1^i}}I \quad \sqrt{\pi_{ik_2^i}}I \quad \cdots \quad \sqrt{\pi_{ik_\mu^i}}I\right],$$
$$\widetilde{\Omega}_{14} = F(i)(A + BK(i)E(i))^T \left[\sqrt{\lambda_i}I \quad \sqrt{\lambda_i}I \quad \cdots \quad \sqrt{\lambda_i}I\right]. \tag{27}$$

For the matrix $E(i)^T$ of full-array rank, there always exist two orthogonal matrices $U_i \in R^{n(1+d)\times n(1+d)}$ and $V_i \in R^{g\times g}$ such that $E_i^T = U_i^T \left[\begin{smallmatrix}\Sigma_i\\ 0\end{smallmatrix}\right] V_i^T$, where $\Sigma_i = \mathrm{diag}(\sigma_1, \sigma_2, \ldots, \sigma_g)$ and σ_i $(i = 1, 2, \ldots, g)$ are nonzero singular values of E_i^T. Assume that the matrix $F(i)$ has the following structure:

$$F(i) = U_i^T \begin{bmatrix} F_{i1} & 0 \\ 0 & F_{i2} \end{bmatrix} U_i; \tag{28}$$

according to Lemma 3, there exists matrix $X_i \in R^{g\times g}$ such that $F(i)E(i)^T = E(i)^T X_i$; setting $X_i K(i)^T = Y(i)^T$, we can obtain (13) from (26). Since $F(i)E(i)^T = E(i)^T X_i$, we can get

$$U_i^T \begin{bmatrix} F_{i1} & 0 \\ 0 & F_{i2} \end{bmatrix} \begin{bmatrix} \Sigma_i \\ 0 \end{bmatrix} V_i^T = U_i^T \begin{bmatrix} \Sigma_i \\ 0 \end{bmatrix} V_i^T X_i; \tag{29}$$

that is, $X_i = V_i \Sigma_i^{-1} F_{i1} \Sigma_i V_i^T$, which implies that $K(i) = Y(i) V_i \Sigma_i^{-1} F_{i1}^{-1} \Sigma_i V_i^T$, which completes the proof. □

Remark 6. When all the elements in the transition probabilities matrix of the time delays are known, then $\lambda_i = 0$, which is a special case.

Remark 7. We introduce some structure restrictions on the matrix variables $F(i)$ which enable us to present the existence conditions of the controller in terms of LMIs. Nevertheless, such restriction will introduce some extents of conservatism into the controller design.

The maximum bound of nonlinear disturbance $\alpha_{\max} = 1/\sqrt{\varepsilon}$ can be found by solving the following optimization problem:

$$\begin{aligned} &\min \quad \varepsilon \\ &\text{s.t.} \quad (13), \quad F(i) > 0, \quad \varepsilon > 0. \end{aligned} \tag{30}$$

4. Numerical Examples

In this section, one numerical example will be given to show the validity and potential of our developed theoretical results. Consider the nonlinear time-invariant discrete-time plant with the following data:

$$A_p = \begin{bmatrix} 0.2 & 0.5 \\ -0.67 & 0.6 \end{bmatrix}, \qquad B_p = \begin{bmatrix} 0.1 \\ 0.2 \end{bmatrix},$$
$$f(k, x(k)) = \begin{bmatrix} 3\sin(x_1(k)) \\ 0.7x_2(k)\cos(x_2(k)) \end{bmatrix}. \tag{31}$$

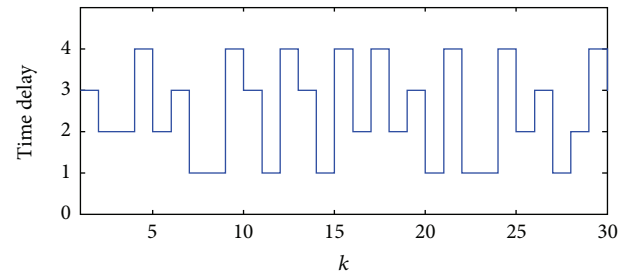

Figure 2: Step of delay τ_k.

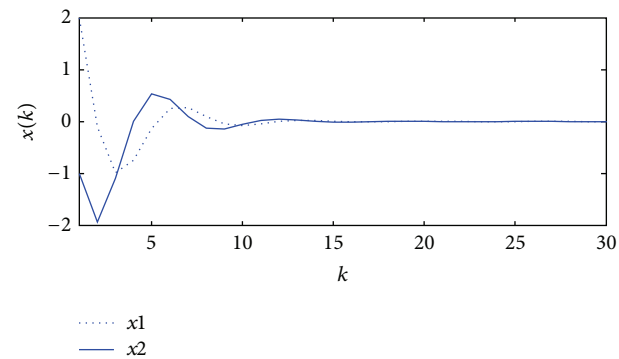

Figure 3: States of the closed-loop system.

Assume that the time delay τ_k from the sensor to the controller takes values from $\Lambda = \{1, 2, 3, 4\}$. Consider the following transition probabilities matrix:

$$\Pi = \begin{bmatrix} 0.4 & 0.2 & 0.3 & 0.1 \\ ? & 0.1 & ? & 0.7 \\ 0.5 & 0.1 & 0.3 & 0.1 \\ ? & 0.6 & 0.2 & ? \end{bmatrix}. \tag{32}$$

Our purpose is to design a mode-dependent controller of the form (6) such that the closed-loop system (9) is stochastically stable with the partly unknown transition probabilities. Let H in (5) be unit matrix; by solving (13) in Theorem 5, the controller gain under the transition probabilities matrix Π is solved as follows:

$$\begin{aligned} K_1 &= [-0.2030 \quad 0.0564], \\ K_2 &= [-0.0834 \quad -0.0229], \\ K_3 &= [0.0086 \quad -0.0301], \\ K_4 &= [0.0022 \quad -0.0015]. \end{aligned} \tag{33}$$

The maximum bound of nonlinear disturbance $\alpha_{\max}$ under the transition probabilities matrix Π is 0.1876.

Figure 2 shows one simulation run of the Markov jump delays under the transition probabilities matrix Π. Figure 3 shows the state response of the closed-loop system using the obtained controller under the transition probabilities matrix Π when $x(0) = [2 \quad -1]^T$.

It can be seen that the closed-loop system with the partly unknown transition probabilities under the designed controller is stochastically stable.

5. Conclusions

In this paper, the state feedback stabilization problem has been considered for a kind of nonlinear networked control systems with random communication delays. A Markov chain is employed to describe the random communication time delay of which transition probabilities are partly unknown. The closed-loop system is established through the state augmentation technique and the state feedback controller is designed which guarantees the stability of the resulting closed-loop systems. It is shown that the controller design problem under consideration is solvable if a set of LMIs is feasible. Simulation results show the validity of the proposed method.

Conflict of Interests

The authors declare that there is no conflict of interests regarding the publication of this paper.

Acknowledgments

This work was supported by the National Natural Science Foundation of China under Grant no. 61174029, the National Natural Science Foundation of China under Grant no.61503136, and the Natural Science Foundation of Huzhou under Grant no. 2014YZ07.

References

[1] W. Zhang, M. S. Branicky, and S. M. Phillips, "Stability of networked control systems," *IEEE Control Systems Magazine*, vol. 21, no. 1, pp. 84–97, 2001.

[2] J. G. Li, J. Q. Yuan, and J. G. Lu, "Observer-based H_∞ control for networked nonlinear systems with random packet losses," *ISA Transactions*, vol. 49, no. 1, pp. 39–46, 2010.

[3] R. Lu, Y. Xu, A. Xue, and J. Zheng, "Networked control with state reset and quantized measurements: observer-based case," *IEEE Transactions on Industrial Electronics*, vol. 60, no. 11, pp. 5206–5213, 2013.

[4] H. Ishii, "H_∞ control with limited communication and message losses," *Systems & Control Letters*, vol. 57, no. 4, pp. 322–331, 2008.

[5] D. Wang, J. Wang, and W. Wang, "H_∞ controller design of networked control systems with markov packet dropouts," *IEEE Transactions on Systems, Man, and Cybernetics Part A: Systems and Humans*, vol. 43, no. 3, pp. 689–697, 2013.

[6] F. L. Qu, Z. H. Guan, T. Li, and F. S. Yuan, "Stabilisation of wireless networked control systems with packet loss," *IET Control Theory and Applications*, vol. 6, no. 15, pp. 2362–2366, 2012.

[7] K. Liu and E. Fridman, "Wirtinger's inequality and Lyapunov-based sampled-data stabilization," *Automatica*, vol. 48, no. 1, pp. 102–108, 2012.

[8] R. Lu, X. Zhou, F. Wu, and A. Xue, "Quantized H_∞ output feedback control for linear discrete-time systems," *Journal of the Franklin Institute*, vol. 350, no. 8, pp. 2096–2108, 2013.

[9] J. Zhang, Y. Xia, and P. Shi, "Design and stability analysis of networked predictive control systems," *IEEE Transactions on Control Systems Technology*, vol. 21, no. 4, pp. 1495–1501, 2013.

[10] R. A. Gupta and M. Y. Chow, "Networked control system: overview and research trends," *IEEE Transactions on Industrial Electronics*, vol. 57, no. 7, pp. 2527–2535, 2010.

[11] F. Xia, S. B. Li, and Y. X. Sun, "A neural network based feedback scheduler for networked control system with flexible workload," in *Advances in Natural Computation*, vol. 3611 of *Lecture Notes in Computer Science*, pp. 242–251, Springer, Berlin, Germany, 2005.

[12] R. Lu, H. Li, and Y. Zhu, "Quantized H_∞ filtering for singular time-varying delay systems with unreliable communication channel," *Circuits, Systems, and Signal Processing*, vol. 31, no. 2, pp. 521–538, 2012.

[13] K. Liu, E. Fridman, and L. Hetel, "Stability and L_2-gain analysis of networked control systems under Round-Robin scheduling: a time-delay approach," *Systems and Control Letters*, vol. 61, no. 5, pp. 666–675, 2012.

[14] R. Lu, F. Wu, and A. Xue, "Networked control with reset quantized state based on bernoulli processing," *IEEE Transactions on Industrial Electronics*, vol. 61, no. 9, pp. 4838–4846, 2014.

[15] M. Yu, L. Wang, T. Chu, and G. Xie, "Stabilization of networked control systems with data packet dropout and network delays via switching system approach," in *Proceedings of the 43rd IEEE Conference on Decision and Control (CDC '04)*, vol. 4, pp. 3539–3544, December 2004.

[16] Y. Shi and B. Yu, "Output feedback stabilization of networked control systems with random delays modeled by Markov chains," *IEEE Transactions on Automatic Control*, vol. 54, no. 7, pp. 1668–1674, 2009.

[17] H. J. Gao, X. Y. Meng, and T. W. Chen, "Stabilization of networked control systems with a new delay characterization," *IEEE Transactions on Automatic Control*, vol. 53, no. 9, pp. 2142–2148, 2008.

[18] F. Yang, Z. Wang, Y. S. Hung, and M. Gani, "H_∞ control for networked systems with random communication delays," *IEEE Transactions on Automatic Control*, vol. 51, no. 3, pp. 511–518, 2006.

[19] X. He, Z. Wang, and D. H. Zhou, "Robust fault detection for networked systems with communication delay and data missing," *Automatica*, vol. 45, no. 11, pp. 2634–2639, 2009.

[20] L. Zhang, Y. Shi, T. Chen, and B. Huang, "A new method for stabilization of networked control systems with random delays," *IEEE Transactions on Automatic Control*, vol. 50, no. 8, pp. 1177–1181, 2005.

[21] F. Li, X. Wang, and P. Shi, "Robust quantized H_∞ control for network control systems with Markovian jumps and time delays," *International Journal of Innovative Computing, Information and Control*, vol. 9, no. 12, pp. 4889–4902, 2013.

[22] R. Krtolica, U. Ozguner, H. Chan, and H. Goktas, "Stability of linear feedback systems with random communication delays," *International Journal of Control*, vol. 59, no. 4, pp. 925–953, 1994.

[23] L. Xiao, A. Hassibi, and J. P. How, "Control with random communication delays via a discrete-time jump system approach," in *Proceedings of the American Control Conference*, vol. 3, pp. 2199–2204, Chicago, Ill, USA, June 2000.

[24] S. W. Gao and G. Y. Tang, "Output feedback stabilization of networked control systems with random delays," in *Proceedings of the 18th IFAC World Congress*, pp. 3250–3255, Milano, Italy, 2011.

[25] Y. Xu, H. Su, and Y. J. Pan, "Output feedback stabilization for Markov-based nonuniformly sampled-data networked control systems," *Systems and Control Letters*, vol. 62, no. 8, pp. 656–663, 2013.

[26] L. Qiu, F. Yao, and X. Zhong, "Stability analysis of networked control systems with random time delays and packet dropouts modeled by markov chains," *Journal of Applied Mathematics*, vol. 2013, Article ID 715072, 10 pages, 2013.

[27] Y. Shi and B. Yu, "Robust mixed H_2/H_∞ control of networked control systems with random time delays in both forward and backward communication links," *Automatica*, vol. 47, no. 4, pp. 754–760, 2011.

[28] S. L. Hu, J. L. Liu, and Z. P. Du, "Stabilization of discrete-time networked control systems with partly known transmission delay: a new augmentation approach," *International Journal of Control, Automation and Systems*, vol. 9, no. 6, pp. 1080–1085, 2011.

[29] Y. Li, Q. Zhang, S. Zhang, and M. Cai, "Stabilization for networked control systems with random sampling periods," *Journal of Applied Mathematics*, vol. 2013, Article ID 252679, 14 pages, 2013.

[30] L. Qiu, C. Liu, F. Yao, and G. Xu, "Analysis and design of networked control systems with random Markovian delays and uncertain transition probabilities," *Abstract and Applied Analysis*, vol. 2014, Article ID 486978, 8 pages, 2014.

[31] Y. Zhang, H. Fang, and Z. Liu, "Fault detection for nonlinear networked control systems with Markov data transmission pattern," *Circuits, Systems, and Signal Processing*, vol. 31, no. 4, pp. 1343–1358, 2012.

[32] G. L. Wang, *Control and filtering for some classes of Markovian jump systems [Doctoral dissertation]*, Northeastern University, 2010.

Hindawi Publishing Corporation
Mathematical Problems in Engineering
Volume 2015, Article ID 785289, 7 pages
http://dx.doi.org/10.1155/2015/785289

Research Article

Fault-Tolerant Control for Networked Control Systems with Limited Information in Case of Actuator Fault

Wang Yan-feng, Wang Pei-liang, Li Zu-xin, and Chen Hui-ying

School of Engineering, Huzhou University, Huzhou, Zhejiang 313000, China

Correspondence should be addressed to Wang Yan-feng; neu2009wyf@163.com

Received 3 January 2015; Revised 17 February 2015; Accepted 25 February 2015

Academic Editor: Hui Zhang

Copyright © 2015 Wang Yan-feng et al. This is an open access article distributed under the Creative Commons Attribution License, which permits unrestricted use, distribution, and reproduction in any medium, provided the original work is properly cited.

This paper is concerned with the problem of designing a fault-tolerant controller for uncertain discrete-time networked control systems against actuator possible fault. The step difference between the running step k and the time stamp of the used plant state is modeled as a finite state Markov chain of which the transition probabilities matrix information is limited. By introducing actuator fault indicator matrix, the closed-loop system model is obtained by means of state augmentation technique. The sufficient conditions on the stochastic stability of the closed-loop system are given and the fault-tolerant controller is designed by solving a linear matrix inequality. A numerical example is presented to illustrate the effectiveness of the proposed method.

1. Introduction

Networked control systems (NCSs) are used in many fields such as remote surgery and unmanned aerial vehicles especially in a number of emerging engineering applications such as arrays of microactuators and even neurobiological and socialeconomical systems [1–3]. Compared with the traditional wiring, the communication channels can simplify the installation and reduce the costs of cables and maintenance of the system. However, the network in the control systems also brings many problems, such as network-induced delay and packet dropout, and makes system analysis more challenging [4, 5]. Network-induced delays can degrade the performance of control systems designed without considering them and even destabilize the system [6, 7].

Because of the complexity caused by network, NCSs are more vulnerable to faults. An effective way to increase the reliability of the NCSs is to introduce fault-tolerant control (FTC). Therefore, the research on fault-tolerant control of NCSs has great theoretical and applied significance; however research on FTC for NCSs is different from that for traditional control systems in many aspects [8, 9]. In [10], a fault estimator was proposed for NCSs with transfer delays, process noise, and model uncertainty. On the basis of the information on fault estimator, a fault-tolerant controller using sliding mode control theory was designed to recover the system performance. In [11], the random packet dropout and the sensor or actuator failure were described as binary random variables; the sufficient condition for asymptotical mean-square stability of the NCSs was derived. By using matrix measure technique, a fault-tolerant controller was designed for NCSs with network-induced delay and model uncertainty in [12]. In [13], a FTC algorithm considering actuator failure of an NCS was presented, and the NCS with data packet dropout was modeled as an asynchronous dynamical system. Based on information scheduling, FTC design methods were proposed for NCSs with communication constrains in [14]. In [15], the problem of fault-tolerant control for NCSs with data packet dropout is studied and the closed-loop system was modeled as Markov jump system. However, elements of transition probabilities matrix are assumed to be completely known and the controller can not be solved by LMIs. To the best of the authors' knowledge, up to now, very limited efforts have been devoted to studying FTC for uncertain NCSs with uncertain transition probability matrices, which motivates our investigation.

Problems of partial sensors inactivation are equal to problems of data pack dropout which can be solved by common technique; we focus on the problems of reliability when actuators are inactivated in this paper.

In this paper, the step difference τ_k between the running step k and the time stamp of the used plant state is modeled as a finite state Markov chain. And the information of the transition probabilities matrix is limited; that is, a part of elements of transition probabilities matrix is unknown. The closed-loop system model is obtained by means of state augmentation technique and the mode-dependent fault-tolerant controller is designed which guarantees the stochastic stability of the closed-loop system.

This paper is organized as follows. In Section 2, we formulate the state feedback controller design problem. In Section 3, the sufficient conditions to guarantee the stochastic stability are presented, and the fault-tolerant controller is also given. A simulation example is used to illustrate the effectiveness of the proposed method in Section 4. The conclusion remarks are addressed in Section 5.

2. Problem Formulation

Consider the NCSs setup in Figure 1, in which the controllers are placed in a remote location, and both sensor measurement data and control data are transmitted through network.

By adding a buffer to the actuator, the delay τ_k^{sc} from sensor to controller and the delay τ_k^{ca} from controller to actuator can be lumped together, and the new variable is described as $\tau_k = \tau_k^{sc} + \tau_k^{ca}$ which is modeled as a Markov chain. And τ_k denotes the step difference between the running step k and the time stamp of the used plant state, and it depends on the random time-delay and the data packet drops on the random communication delay and the data packet dropout [16]. Assume that both time-delay and the data packet dropout are bounded, so τ_k is bounded. The step delay τ_k takes values in $\Lambda = \{1, 2, \ldots, d\}$ and the transition probability matrix of τ_k is $\Pi = [\pi_{ij}]$. That is, τ_k jumps from mode i to j with probability π_{ij} which is defined by $\pi_{ij} = \Pr(\tau_{k+1} = j \mid \tau_k = i)$, where $\pi_{ij} \geq 0$, $\forall i, j \in \Lambda$, $\sum_{j=1}^{d} \pi_{ij} = 1$. The set Λ contains d modes of τ_k, and the transition probabilities of the jumping process in this paper are considered to be partly accessed; that is, some elements in matrix Π are unknown. For example, for the time-delay τ_k with 3 modes, the transition probabilities matrix Π may be as follows:

$$\Pi = \begin{bmatrix} ? & \pi_{12} & ? \\ \pi_{21} & ? & ? \\ ? & \pi_{32} & ? \end{bmatrix}, \tag{1}$$

where "?" represents the inaccessible elements. For notational clarity, $\forall i \in \Lambda$, we denote $\Lambda = \Lambda_k^i + \Lambda_{uk}^i$ with

$$\begin{aligned} \Lambda_k^i &= \left\{ j : \pi_{ij} \text{ is known} \right\}, \\ \Lambda_{uk}^i &= \left\{ j : \pi_{ij} \text{ is unknown} \right\}. \end{aligned} \tag{2}$$

Moreover, if $\Lambda_k^i \neq \emptyset$, it is further described as $\Lambda_k^i = \{k_1^i, k_2^i, \ldots, k_\mu^i\}$, $1 \leq \mu \leq d$, where k_μ^i represents the μth known element with the index k_μ^i in the ith row of the matrix Π.

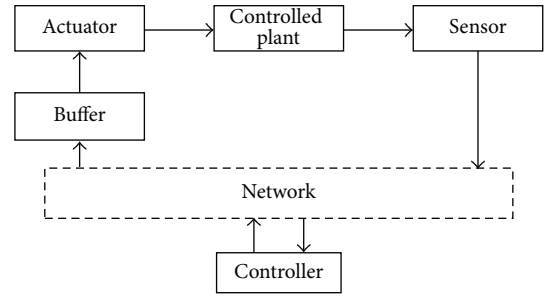

Figure 1: Structure of networked control system.

And Λ_{uk}^i is described as $\Lambda_{uk}^i = \{\bar{k}_1^i, \bar{k}_2^i, \ldots, \bar{k}_{d-\mu}^i\}$, where $\bar{k}_{d-\mu}^i$ represents the $(d-\mu)$th unknown element with the index $(d-\mu)$th in the ith row of the matrix Π.

Assume that the model of the plant is an uncertain discrete-time system as follows:

$$x(k+1) = (A_0 + \Delta A_0)\, x(k) + (B_0 + \Delta B_0)\, u(k), \tag{3}$$

where $x(t) \in R^n$ is state vector and $u(t) \in R^m$ is the control input. $A_0 \in R^{n\times n}$ and $B_0 \in R^{n\times m}$ are all real constant matrices. $[\Delta A_0 \;\; \Delta B_0] = DF(k)\,[E_1 \;\; E_2]$, where $F(k)$ is an uncertain time-varying matrix satisfying the bound $F(k)^T F(k) < I$, where I denotes the identity matrix with appropriate dimension.

Considering the effect of the random communication delay and the data packet dropout, we describe the state feedback control law as

$$\begin{aligned} u(k) &= K(\tau_k)\, x(k - \tau_k), \\ x(0) &= x_0 \in R^n. \end{aligned} \tag{4}$$

The fault indicator matrix L is given by

$$L = \operatorname{diag}\{l_1, \ldots, l_m\} \tag{5}$$

with $l_j \in \{0, 1\}$ for $j = 1, 2, \ldots, m$ and $l_j = 0$ means the jth actuator experiences a total failure, whereas the jth actuator is in healthy state when $l_j = 1$. Since there are m actuators, the set of possible related failure modes is finite and is denoted by $\tilde{L} = \{L^1, \ldots, L^N\}$ with $2^m - 1$ elements, where L^i $(i = 1, 2, \ldots, N)$ is a particular pattern of matrix L.

Consequently, the closed-loop system from (3) and (4) can be expressed as

$$\begin{aligned} x(k+1) = {} & (A_0 + \Delta A_0)\, x(k) \\ & + (B_0 + \Delta B_0)\, LK(\tau_k)\, x(k - \tau_k). \end{aligned} \tag{6}$$

At sampling time k, if we augment the state-variable as $\delta(k) = \left[x(k)^T \;\; x(k-1)^T \;\; \cdots \;\; x(k-d)^T\right]^T$, the closed-loop system (6) can be written as

$$\begin{aligned} \delta(k+1) &= (A + BLK(\tau_k)\, H(\tau_k))\, \delta(k), \\ \delta(0) &= \left[\delta(0)^T \;\; \delta(-1)^T \;\; \cdots \;\; \delta(-d)^T\right]^T, \end{aligned} \tag{7}$$

where

$$A = \begin{bmatrix} A_0 + \Delta A_0 & 0 & \cdots & 0 & 0 \\ I & 0 & \cdots & 0 & 0 \\ 0 & I & \cdots & 0 & 0 \\ \vdots & \vdots & \ddots & 0 & 0 \\ 0 & 0 & \cdots & I & 0 \end{bmatrix} \in R^{n(1+d)\times n(1+d)},$$

$$B = \begin{bmatrix} B_0 + \Delta B_0 \\ 0 \\ 0 \\ \vdots \\ 0 \end{bmatrix} \in R^{n(2+1)\times m}, \tag{8}$$

$$H(\tau_k) = [0 \;\; 0 \;\; I \;\; \cdots \;\; 0] \in R^{n\times n(1+d)}$$

has all elements being zeros except for the $(1+\tau_k)$th block being identity.

It can be seen that the closed-loop system (7) is a jump linear system with d different modes.

It is noticed that $A = \widetilde{A}_0 + \Delta\widetilde{A}_0 = \widetilde{A}_0 + \widetilde{D}F\widetilde{E}_1$ and $B = \widetilde{B}_0 + \Delta\widetilde{B}_0 = \widetilde{B}_0 + \widetilde{D}FE_2$ where

$$\widetilde{A}_0 = \begin{bmatrix} A_0 & 0 & \cdots & 0 & 0 \\ I & 0 & \cdots & 0 & 0 \\ 0 & I & \cdots & 0 & 0 \\ \vdots & \vdots & \ddots & 0 & 0 \\ 0 & 0 & \cdots & I & 0 \end{bmatrix}, \quad \Delta\widetilde{A}_0 = \begin{bmatrix} DFE_1 & 0 & \cdots & 0 & 0 \\ 0 & 0 & \cdots & 0 & 0 \\ 0 & 0 & \cdots & 0 & 0 \\ \vdots & \vdots & \ddots & 0 & 0 \\ 0 & 0 & \cdots & 0 & 0 \end{bmatrix},$$

$$\widetilde{D} = \begin{bmatrix} D \\ 0 \\ 0 \\ \vdots \\ 0 \end{bmatrix}, \quad \widetilde{B}_0 = \begin{bmatrix} B_0 \\ 0 \\ 0 \\ \vdots \\ 0 \end{bmatrix}, \quad \Delta\widetilde{B}_0 = \begin{bmatrix} DFE_2 \\ 0 \\ 0 \\ \vdots \\ 0 \end{bmatrix},$$

$$\widetilde{E}_1 = [E_1 \;\; 0 \;\; 0 \;\; \cdots \;\; 0]. \tag{9}$$

Throughout this paper, we use the following definition.

Definition 1. System (7) is stochastically stable if for every finite $\delta(0)$ and initial mode $\tau_0 \in \Lambda$ there exists a finite $W > 0$ such that the following holds:

$$E\left\{\sum_{k=0}^{\infty} \|\delta(k)\|^2 \mid \delta_0, \tau_0\right\} < \delta_0^T W \delta_0. \tag{10}$$

The object of this paper is to construct a fault-tolerant controller with structure as given by (4) which achieves that the closed-loop system (7) is stochastically stable under all actuator failure modes. In the following, $K(\tau_k)$ and $H(\tau_k)$ for this paper are denoted as $K(i)$ and $E(i)$, respectively.

To proceed, we will need the following two lemmas.

Lemma 2 (see [17]). *Given matrices W, M, and N of appropriate dimensions and W is symmetric, $W + N^T F(k)^T M^T + MF(k)N < 0$ holds for all $F(k)$ satisfying $F(k)^T F(k) \le I$ if and only if there exists a scalar $\varepsilon > 0$ such that $W + \varepsilon MM^T + \varepsilon^{-1} N^T N < 0$.*

Lemma 3 (see [18]). *The matrix $E(i)^T$ is of full-array rank; then there exist two orthogonal matrices $U_i \in R^{n(1+d)\times n(1+d)}$ and $V_i \in R^{g\times g}$, such that $E(i)^T = U_i^T \left[\begin{smallmatrix} \Sigma_i \\ 0 \end{smallmatrix}\right] V_i^T$, where $\Sigma_i = \mathrm{diag}(\sigma_1, \sigma_2, \ldots \sigma_g)$, where σ_i $(i = 1, 2, \ldots, g)$ are nonzero singular values of $E(i)^T$. If matrix $Q(i) \in R^{n(1+d)\times n(1+d)}$ has the following structure*

$$Q(i) = U_i^T \begin{bmatrix} Q_{i1} & 0 \\ 0 & Q_{i2} \end{bmatrix} U_i, \tag{11}$$

there exists a nonsingular matrix $X_i \in R^{n\times n}$ such that $Q(i)E(i)^T = E(i)^T X_i$, where $Q_{i1} \in R^{g\times g} > 0$, $Q_{i2} \in R^{n(1+d-g)\times n(1+d-g)} > 0$.

3. Controller Design

With Definition 1, the sufficient conditions on the stochastic stability of the closed-loop system (7) can be obtained.

Theorem 4. *The closed-loop system (7) with partly unknown transition probabilities (2) is stochastically stable if there exists matrix $P(i) > 0$, $i \in \Lambda$ such that*

$$A(i)^T \sum_{j\in\Lambda_k^i} \pi_{ij} P(j) A(i) - \sum_{j\in\Lambda_k^i} \pi_{ij} P(i) < 0, \tag{12}$$

$$A(i)^T P(j) A(i) - P(i) < 0, \quad \forall j \in \Lambda_{uk}^i, \tag{13}$$

where $A(i) = A + BLK(i)H(i)$.

Proof. For the closed-loop system (7), consider the quadratic function which is given by

$$V(\delta(k), k) = \delta^T(k) P(\tau_k) \delta(k). \tag{14}$$

Then,

$$\begin{aligned} &E\{\Delta V(\delta(k), k)\} \\ &\quad = E\left\{\delta^T(k+1) P(\tau_{k+1}) \delta(k+1) \mid \delta(k), \tau_k = i\right\} \\ &\qquad - \delta^T(k) P(\tau_k) \delta(k) \\ &\quad = \delta(k)^T (A + BLK(i) H(i))^T \\ &\qquad \cdot \sum_{j=1}^{d} \pi_{ij} P(j) (A + BLK(i) H(i)) \\ &\qquad - \delta^T(k) P(i) \delta(k) \end{aligned}$$

$$
\begin{aligned}
&= \delta(k)^T \left(A(i)^T \sum_{j\in\Lambda_k^i} \pi_{ij} P(j) A(i) - \sum_{j\in\Lambda_k^i} \pi_{ij} P(i) \right) \\
&\quad \cdot \delta(k) + \delta(k)^T \\
&\quad \cdot \left(A(i)^T \sum_{j\in\Lambda_{uk}^i} \pi_{ij} P(j) A(i) - \sum_{j\in\Lambda_{uk}^i} \pi_{ij} P(i) \right) \delta(k) \\
&= \delta(k)^T \left(A(i)^T \sum_{j\in\Lambda_k^i} \pi_{ij} P(j) A(i) - \sum_{j\in\Lambda_k^i} \pi_{ij} P(i) \right) \delta(k) \\
&\quad + \delta(k)^T \left(\sum_{j\in\Lambda_{uk}^i} \pi_{ij} A(i)^T P(j) A(i) - P(i) \right) \delta(k).
\end{aligned} \tag{15}
$$

Hence, if (12) and (13) hold, $\Delta V(\delta(k), k) < 0$. One has

$$
\begin{aligned}
&E\{V(\delta(k), k) - V(\delta(0), 0)\} \\
&\quad = E\left\{ \sum_{k=0}^{k} \Delta V(k) \right\} \le \beta E\left\{ \sum_{k=0}^{k} \|\delta(k)\|^2 \right\},
\end{aligned} \tag{16}
$$

where $\beta = \lambda_{\min}(A + BLK(i)H(i))^T \sum_{j=1}^{d} \pi_{ij} P(j)(A + BLK(i)H(i)) - P(i)$; hence one can get $\lim_{k\to\infty} E\{\sum_{k=0}^{k} \|\delta(k)\|^2\} \le (1/\beta) E\{V(0)\}$. According to Definition 1, system (7) is stochastically stable.

Clearly, no knowledge on π_{ij}, $\forall j \in \Lambda_{uk}^i$ is needed in (12) and (13), which completes the proof. □

Theorem 5. *Consider system (7) with partly unknown transition probabilities (2). If there exist matrices $Q(i) > 0$, $Y(i)$ and positive scalars μ_1, μ_2, μ_3, and μ_4 such that*

$$
\begin{bmatrix}
-\sum_{j\in\Lambda_k^i} \pi_{ij} Q(i) & * & * & * \\
\Lambda_k^i \left(\widetilde{A}_0 + \widetilde{B}_0 LY(i) H(i) \right) & \Gamma + \Xi_k^i & * & * \\
E_2 LY(i) H(i) & 0 & -\mu_1 I & * \\
\widetilde{E}_1 & 0 & 0 & -\mu_2 I
\end{bmatrix} < 0,
$$

$$
\begin{bmatrix}
-Q(i) & * & * & * \\
\widetilde{A}_0 + \widetilde{B}_0 LY(i) H(i) & -Q(j) + (\mu_3 + \mu_4) \widetilde{D}\widetilde{D}^T & * & * \\
E_2 LY(i) H(i) & 0 & -\mu_3 I & * \\
\widetilde{E}_1 Q(i) & 0 & 0 & -\mu_4 I
\end{bmatrix}
< 0, \quad \forall j \in \Lambda_{uk}^i, \tag{17}
$$

where

$$
\Lambda_k^i = \left[\sqrt{\pi_{ik_1^i}} I \quad \sqrt{\pi_{ik_2^i}} I \quad \cdots \quad \sqrt{\pi_{ik_\mu^i}} I \right]^T,
$$

$$
\Xi_k^i = -\operatorname{diag}\left\{ Q(k_1^i) \quad Q(k_2^i) \quad \cdots \quad Q(k_\mu^i) \right\},
$$

$$
\Gamma = \begin{bmatrix}
(\mu_1 + \mu_2) \widetilde{D}\widetilde{D}^T & * & * & * \\
(\mu_1 + \mu_2) \widetilde{D}\widetilde{D}^T & (\mu_1 + \mu_2) \widetilde{D}\widetilde{D}^T & * & * \\
\vdots & \vdots & \ddots & * \\
(\mu_1 + \mu_2) \widetilde{D}\widetilde{D}^T & (\mu_1 + \mu_2) \widetilde{D}\widetilde{D}^T & \cdots & (\mu_1 + \mu_2) \widetilde{D}\widetilde{D}^T
\end{bmatrix}, \tag{18}
$$

then there exists a mode-dependent controller of the form (4) such that the resulting system (7) is stochastically stable. Furthermore, an admissible controller is given by

$$
K(i) = Y(i) V_i \Sigma_i^{-1} Q_{i1}^{-1} \Sigma_i V_i^T. \tag{19}
$$

Proof. According to Theorem 4, we know that the system (7) is stochastically stable with the partly unknown transition probabilities (2) if inequalities (12) and (13) hold. By Schur complement, inequality (12) is equivalent to

$$
\begin{bmatrix}
-\sum_{j\in\Lambda_k^i} \pi_{ij} P(i) & * \\
\Lambda_k^i \left(A + \widetilde{B}_0 LK(i) H(i) \right) & \Omega_k^i
\end{bmatrix} + \Psi F \Theta + \Psi^T F^T \Theta^T < 0, \tag{20}
$$

where $\Psi = \begin{bmatrix} 0 & \widetilde{D}^T & \cdots & \widetilde{D}^T & \widetilde{D}^T \end{bmatrix}^T$, $\Theta = \begin{bmatrix} E_2 LK(i) & 0 & \cdots & 0 & 0 \end{bmatrix}^T$.

By Lemma 2, there exists a scalar $\mu_1 > 0$ such that

$$
\begin{bmatrix}
-\sum_{j\in\Lambda_k^i} \pi_{ij} P(i) & * & * \\
\Lambda_k^i \left(\widetilde{A}_0 + BLK(i) H(i) \right) & \widetilde{\Gamma} + \widetilde{\Xi}_k^i & * \\
E_2 LK(i) H(i) & 0 & -\mu_1
\end{bmatrix} < 0, \tag{21}
$$

where

$$
\widetilde{\Xi}_k^i = -\operatorname{diag}\left\{ P(k_1^i)^{-1} \quad P(k_2^i)^{-1} \quad \cdots \quad P(k_\mu^i)^{-1} \right\},
$$

$$
\widetilde{\Gamma} = \begin{bmatrix}
\mu_1 \widetilde{D}\widetilde{D}^T & * & * & * \\
\mu_1 \widetilde{D}\widetilde{D}^T & \mu_1 \widetilde{D}\widetilde{D}^T & * & * \\
\vdots & \vdots & \ddots & * \\
\mu_1 \widetilde{D}\widetilde{D}^T & \mu_1 \widetilde{D}\widetilde{D}^T & \cdots & \mu_1 \widetilde{D}\widetilde{D}^T
\end{bmatrix}. \tag{22}
$$

Using Schur complement and Lemma 2 again, one can get

$$
\begin{bmatrix}
-\sum_{j\in\Lambda_k^i} \pi_{ij} P(i) & * & * & * \\
\Lambda_k^i \left(\widetilde{A}_0 + \widetilde{B}_0 LK(i) H(i) \right) & \Gamma + \widetilde{\Xi}_k^i & * & * \\
E_2 LK(i) H(i) & 0 & -\mu_1 I & * \\
\widetilde{E}_1 & 0 & 0 & -\mu_2 I
\end{bmatrix} < 0. \tag{23}
$$

Similarly, from (13) one can obtain

$$\begin{bmatrix} -P(i) & * & * & * \\ \widetilde{A}_0 + \widetilde{B}_0 LK(i) H(i) & -P(j) + (\mu_3 + \mu_4) \widetilde{D}\widetilde{D}^T & * & * \\ E_2 LK(i) H(i) & 0 & -\mu_3 I & * \\ \widetilde{E}_1 & 0 & 0 & -\mu_4 I \end{bmatrix} < 0, \quad \forall j \in \Lambda_{uk}^i. \tag{24}$$

Performing a congruence transformation to (23) and (24) by $\operatorname{diag}\left\{P(i)^{-1} \;\; I \;\; I \;\; I\right\}$, setting $Q(i) = P(i)^{-1}$, one can obtain (25) and (26), respectively. One has

$$\begin{bmatrix} -\sum_{j\in\Lambda_k^i} \pi_{ij} Q(i) & * & * & * \\ \Lambda_k^i \left(\widetilde{A}_0 + \widetilde{B}_0 LK(i) H(i)\right) Q(i) & \Gamma + \Xi_k^i & * & * \\ E_2 LK(i) H(i) Q(i) & 0 & -\mu_1 I & * \\ \widetilde{E}_1 Q(i) & 0 & 0 & -\mu_2 I \end{bmatrix} < 0, \tag{25}$$

$$\begin{bmatrix} -Q(i) & * & * & * \\ \left(\widetilde{A}_0 + \widetilde{B}_0 LK(i) H(i)\right) Q(i) & -Q(j) + (\mu_3 + \mu_4) \widetilde{D}\widetilde{D}^T & * & * \\ E_2 LK(i) H(i) Q(i) & 0 & -\mu_3 I & * \\ \widetilde{E}_1 Q(i) & 0 & 0 & -\mu_4 I \end{bmatrix} < 0, \quad \forall j \in \Lambda_{uk}^i. \tag{26}$$

For the matrix $E(i)^T$ of full-column rank, there always exist two orthogonal matrices $U_i \in R^{n(1+d)\times n(1+d)}$ and $V_i \in R^{g\times g}$ such that

$$E(i)^T = U_i^T \begin{bmatrix} \Sigma_i \\ 0 \end{bmatrix} V_i^T, \tag{27}$$

where $\Sigma_i = \operatorname{diag}(\sigma_1, \sigma_2, \ldots \sigma_g)$, σ_i $(i = 1, 2, \ldots, g)$ are nonzero singular values of $E(i)^T$. Assume that the matrix $Q(i)$ has the following structure:

$$Q(i) = U_i^T \begin{bmatrix} Q_{i1} & 0 \\ 0 & Q_{i2} \end{bmatrix} U_i; \tag{28}$$

according to Lemma 3, there exists matrix $X_i \in R^{n\times n}$ such that $F(i)E(i)^T = E(i)^T X_i$, setting

$$X_i K(i)^T = Y(i)^T. \tag{29}$$

Since $F(i)E(i)^T = E(i)^T X_i$, one can get

$$\begin{bmatrix} \Sigma_i \\ 0 \end{bmatrix} V_i^T = U_i^T \begin{bmatrix} \Sigma_i \\ 0 \end{bmatrix} V_i^T X_i, \tag{30}$$

which implies that

$$X_i = V_i \Sigma_i^{-1} F_{i1} \Sigma_i V_i^T. \tag{31}$$

Thus, (19) is obtained from (29) and (31), which completes the proof. □

4. Numerical Example

In this section, a numerical example is given to show the validity and potential of our developed theoretical results. The dynamics are described as follows:

$$A_0 = \begin{bmatrix} 0.7 & -0.1 \\ 0.1 & 0.3 \end{bmatrix}, \quad B_0 = \begin{bmatrix} 0.9 & 0.6 \\ 0.7 & 1 \end{bmatrix},$$
$$D = \begin{bmatrix} 0.01 & 0 \\ 0 & 0.02 \end{bmatrix}, \quad E_1 = \begin{bmatrix} 0.02 & 0 \\ 0 & 0.03 \end{bmatrix}, \tag{32}$$
$$E_2 = \begin{bmatrix} 0.01 & 0 \\ 0 & 0.03 \end{bmatrix}.$$

Assume the time-delay τ_k takes values from $\Lambda = \{1, 2, 3\}$ and the transition probabilities matrix is $\Pi = \begin{bmatrix} 0.6 & ? & ? \\ ? & ? & 0.7 \\ ? & 0.8 & ? \end{bmatrix}$. When the first actuator experiences a total failure, that is, the fault indicator matrix $L = \begin{bmatrix} 0 & 0 \\ 0 & 1 \end{bmatrix}$, the fault-tolerant and delay-dependent controller gain is solved from Theorem 5 as follows:

$$K_1 = \begin{bmatrix} 0.0109 & -0.002 \\ 0 & 0 \end{bmatrix}, \quad K_2 = \begin{bmatrix} 0.0026 & -0.004 \\ 0 & 0 \end{bmatrix},$$
$$K_3 = \begin{bmatrix} 0.0100 & -0.0020 \\ 0 & 0 \end{bmatrix}. \tag{33}$$

When the second actuator experiences a total failure while the first actuator works normally, that is, the fault indicator matrix $L = \begin{bmatrix} 1 & 0 \\ 0 & 0 \end{bmatrix}$, the controller gain is solved as follows:

$$K_1 = \begin{bmatrix} 0 & 0 \\ 0.0091 & 0.0013 \end{bmatrix}, \quad K_2 = \begin{bmatrix} 0 & 0 \\ 0.0022 & -0.0010 \end{bmatrix},$$
$$K_3 = \begin{bmatrix} 0 & 0 \\ 0.0080 & -0.0010 \end{bmatrix}. \tag{34}$$

When both actuators work normally, that is, the fault indicator matrix $L = \begin{bmatrix} 1 & 0 \\ 0 & 1 \end{bmatrix}$, the controller gain is solved as

$$K_1 = \begin{bmatrix} 0.0204 & -0.0098 \\ -0.0108 & 0.0108 \end{bmatrix}, \quad K_2 = \begin{bmatrix} 0.0048 & -0.0020 \\ -0.0024 & 0.0018 \end{bmatrix},$$
$$K_3 = \begin{bmatrix} 0.0018 & -0.0007 \\ -0.0009 & -0.0005 \end{bmatrix}. \tag{35}$$

Zero-input responses of states x_1, x_2 are shown in Figures 2 and 3 when $x(0) = \begin{bmatrix} -0.02 & 0.01 \end{bmatrix}^T$.

The curves of zero-input response states x_1, x_2 show that the NCS with partly unknown transition probabilities is stochastically stable against actuator possible fault.

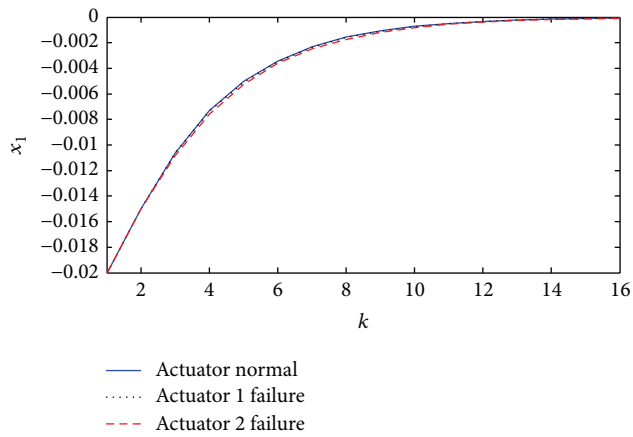

Figure 2: Zero-input response of x_1.

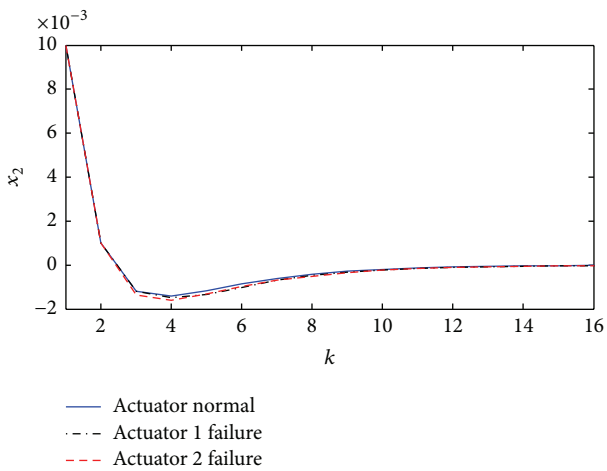

Figure 3: Zero-input response of x_2.

5. Conclusions

This paper is concerned with the problem of fault-tolerant control for uncertain discrete-time networked systems against actuator possible fault. The time-delay is modeled as a finite state Markov chain and the Markov chain's transition probabilities the information is limited. The closed-loop system is established through the state augmentation technique and the state feedback controller is designed which guarantees the stability of the resulting closed-loop systems. It is shown that the controller design problem under consideration is solvable if a set of LMIs is feasible. Simulation results show that the closed-loop systems are stochastically stable against actuator fault.

Conflict of Interests

The authors declare that there is no conflict of interests regarding the publication of this paper.

Acknowledgments

This study is supported by the National Natural Science Foundation of China under Grant no. 61174029, the National Natural Science Foundation of China under Grant no. 61503136, the Zhejiang Provincial Natural Science Foundation of China under Grant no. LY12F03008, and the Huzhou Natural Science Foundation of China under Grant no. 2014YZ07.

References

[1] W. Zhang, M. S. Branicky, and S. M. Phillips, "Stability of networked control systems," *IEEE Control Systems Magazine*, vol. 21, no. 1, pp. 84–97, 2001.

[2] H. Ishii, "H_∞ control with limited communication and message losses," *Systems & Control Letters*, vol. 57, no. 4, pp. 322–331, 2008.

[3] J. Wu, H. R. Karimi, and P. Shi, "Network-based H_∞ output feedback control for uncertain stochastic systems," *Information Sciences*, vol. 232, pp. 397–410, 2013.

[4] D. Wang, J. Wang, and W. Wang, "H_∞ controller design of networked control systems with markov packet dropouts," *IEEE Transactions on Systems, Man, and Cybernetics Part A: Systems*, vol. 43, no. 3, pp. 689–697, 2013.

[5] L. X. Zhang, H. J. Gao, and O. Kaynak, "Network-induced constraints in networked control systems—a survey," *IEEE Transactions on Industrial Informatics*, vol. 9, no. 1, pp. 403–416, 2013.

[6] J. Zhang, Y. Xia, and P. Shi, "Design and stability analysis of networked predictive control systems," *IEEE Transactions on Control Systems Technology*, vol. 21, no. 4, pp. 1495–1501, 2013.

[7] X. Li and X. B. Wu, "Guaranteed cost fault-tolerant controller design of networked control systems under variable-period sampling," *Information Technology Journal*, vol. 8, no. 4, pp. 537–543, 2009.

[8] Y. Zhang and J. Jiang, "Bibliographical review on reconfigurable fault-tolerant control systems," *Annual Reviews in Control*, vol. 32, no. 2, pp. 229–252, 2008.

[9] S. X. Ding, P. Zhang, C. I. Chihaia, W. Li, Y. Wang, and E. L. Ding, "Advanced design scheme for fault tolerant distributed networked control systems," in *Proceedings of the 17th IFAC World Congress*, pp. 13569–13574, Seoul, Republic of Korea, 2008.

[10] Z. H. Mao and B. Jiang, "Fault estimation and accommodation for networked control systems with transfer delay," *Acta Automatica Sinica*, vol. 33, no. 7, pp. 738–743, 2007.

[11] X. Qi, C. Zhang, and J. Gu, "Robust fault-tolerant control for uncertain networked control systems with state-delay and random data packet dropout," *Journal of Control Science and Engineering*, vol. 2012, Article ID 734758, 7 pages, 2012.

[12] D. M. Kong and H. J. Fang, "Stable fault-tolerance control for a class of networked control systems," *Acta Automatica Sinica*, vol. 31, no. 2, pp. 267–273, 2005.

[13] Z. H. Huo and Z. X. Zhang, "Research on fault-tolerant control for NCS with data packet dropout," in *Proceedings of the 2nd International Symposium on Systems and Control in Aerospace and Astronautics (ISSCAA '08)*, pp. 1–4, IEEE, Shenzhen, China, December 2008.

[14] S. Klinkhieo, C. Kambhampati, and R. J. Patton, "Fault tolerant control in NCS medium access constraints," in *Proceedings of the IEEE International Conference on Networking, Sensing and*

Control (ICNSC '07), pp. 416–423, IEEE, London, UK, April 2007.

[15] D. X. Xie, D. F. Zhang, G. Huang, and Z. H. Wang, "Robust fault-tolerant control for a class of uncertain networked control systems," *Information and Control*, vol. 39, no. 4, pp. 472–478, 2010.

[16] H. Gao, X. Meng, and T. Chen, "Stabilization of networked control systems with a new delay characterization," *IEEE Transactions on Automatic Control*, vol. 53, no. 9, pp. 2142–2148, 2008.

[17] Y. Wang, L. Xie, and C. E. de Souza, "Robust control of a class of uncertain nonlinear systems," *Systems & Control Letters*, vol. 19, no. 2, pp. 139–149, 1992.

[18] F. Yang, Z. Wang, Y. S. Hung, and M. Gani, "H_∞ control for networked systems with random communication delays," *IEEE Transactions on Automatic Control*, vol. 51, no. 3, pp. 511–518, 2006.

Hindawi Publishing Corporation
Mathematical Problems in Engineering
Volume 2015, Article ID 197215, 10 pages
http://dx.doi.org/10.1155/2015/197215

Research Article

An Improved Information Hiding Method Based on Sparse Representation

Minghai Yao,[1,2,3] Miao Qi,[1] Yugen Yi,[1] Yanjiao Shi,[1] and Jun Kong[1,2]

[1] *School of Computer Science and Information Technology, Northeast Normal University, Changchun 130017, China*
[2] *School of Mathematics and Statistics, Northeast Normal University, Changchun 130017, China*
[3] *College of Information Science and Technology, Bohai University, Jinzhou 121013, China*

Correspondence should be addressed to Miao Qi; qim801@nenu.edu.cn and Jun Kong; kongj435@nenu.edu.cn

Received 5 November 2014; Revised 9 December 2014; Accepted 9 December 2014

Academic Editor: Hui Zhang

Copyright © 2015 Minghai Yao et al. This is an open access article distributed under the Creative Commons Attribution License, which permits unrestricted use, distribution, and reproduction in any medium, provided the original work is properly cited.

A novel biometric authentication information hiding method based on the sparse representation is proposed for enhancing the security of biometric information transmitted in the network. In order to make good use of abundant information of the cover image, the sparse representation method is adopted to exploit the correlation between the cover and biometric images. Thus, the biometric image is divided into two parts. The first part is the reconstructed image, and the other part is the residual image. The biometric authentication image cannot be restored by any one part. The residual image and sparse representation coefficients are embedded into the cover image. Then, for the sake of causing much less attention of attackers, the visual attention mechanism is employed to select embedding location and embedding sequence of secret information. Finally, the reversible watermarking algorithm based on histogram is utilized for embedding the secret information. For verifying the validity of the algorithm, the PolyU multispectral palmprint and the CASIA iris databases are used as biometric information. The experimental results show that the proposed method exhibits good security, invisibility, and high capacity.

1. Introduction

In recent years, with the rapid development of the information technology, Internet has become an indispensable part of people's lives. In the meantime, Internet fraud and network attack have become a major problem to Internet users. Network service system puts forward higher requirements for the accuracy, security, and reliability of identity recognition. The traditional identity recognition methods, such as smart card, ID, and password, have been unable to meet the need of people. Biometric characteristics of the human body, such as palmprint, iris, and face, have the properties of uniqueness and invariability, which have become an important foundation for identity recognition.

The biometrics is a new identification technique. An individual is identified by their distinct physiological or behavioral characteristics. The identification method based on biometric technology is better than traditional methods. However, biometric data itself has no confidentiality and security. Therefore, the security problem of biometric data has already become an urgent and important problem. Information hiding is an effective solution to protect security and integrity of biometric data. Many researchers have proposed various methods for protecting biometric data.

Bedi et al. presented the multimodal biometric authentication method using PSO based watermarking [1]. The key idea is that the multimodal biometric image was used as the watermark image. PSO was used to select best DCT coefficient in the face image. Vatsa et al. presented a three-level RDWT biometric watermarking algorithm for embedding the voice biometric MFC coefficient into a color face image [2]. The watermarking algorithm used adaptive user-specific parameters for improving performance. A novel method of empirical mode decomposition and gene expression programming together was used to embed biometric information in the literature [3]. The singular value decomposition and lifting based discrete wavelet transform were employed in the watermarking algorithm. Li et al. proposed Tamper

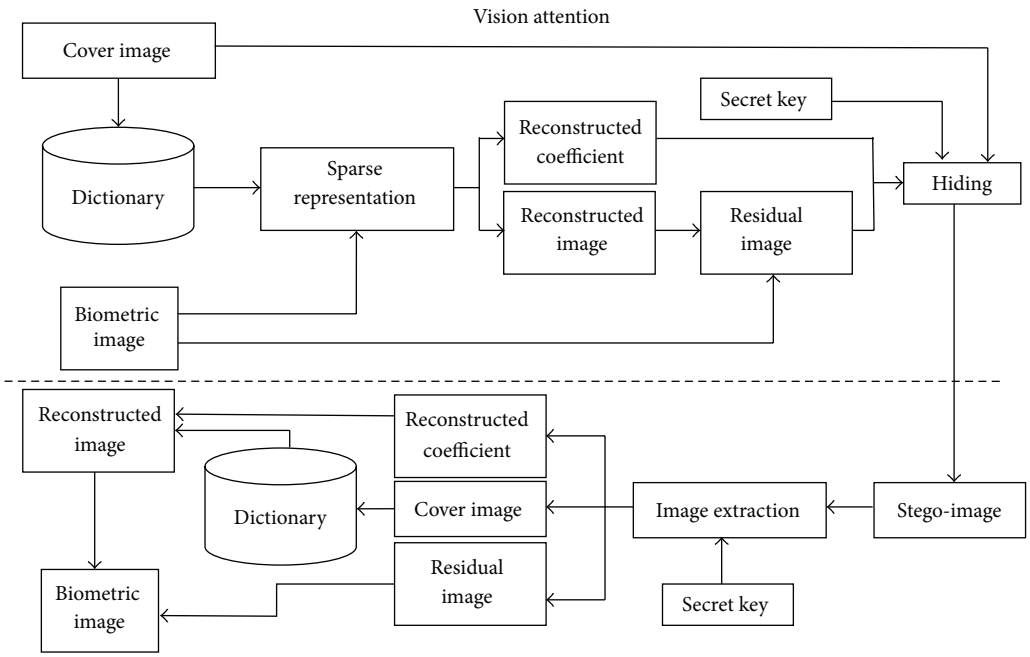

Figure 1: The flowchart of biometric information hiding method.

detection and self-recovery of biometric images using salient region-based authentication watermarking scheme [4]. Che et al. took into account the content relevance of the cover image and the watermarked image; they proposed content-based image hiding method [5]. The biometric information hiding methods based on correlation analysis were proposed in the literature [6]. For the video data, the dual video watermark authentication method has been proposed by Shi et al. [7].

Through analyzing existing biometric information hiding methods, we found almost all of hiding methods adopt digital watermarking and hide one or more biometric images or their features into another biometric image directly based on transform domain for verification. These methods are robust against some types of attacks, but the hiding capacity is low. At the same time, the existing methods rarely consider the content correlation between the biometric image and the cover image. The cover image is only used as a hidden carrier and their rich content cannot be fully utilized. Therefore, a novel biometric authentication image hiding method based on the sparse representation is proposed in this paper, which considers the content correlation between the biometric image and the cover image adequately.

2. The Proposed Method

The sparse representation and visual attention model are used in the biometric hiding method, which uses the sparse representation theory to analyze the content correlation between the cover image and the biometric image. First, the dictionary is built by the cover images for calculating the sparse representation coefficients of a biometric image. The biometric image is reconstructed by the dictionary and sparse representation coefficients. The difference between the original biometric image and the reconstructed biometric image is used as one part of the secret information. The sparse representation coefficients are another part of the secret information. The two parts of secret information are embedded into the cover image. In order to facilitate the embedding of secret information, the secret information is converted into a binary sequence. Through statistical analysis of a large number of experimental data, we found that the absolute value of each pixel value in the residual image is less than 31. Therefore, each pixel value of residual image can be represented by six binary bits, where the first one represents the sign bit and the other five are the pixel values. The amount of embedded information is greatly reduced compared with the original image. Besides, the embedding region of secret information is selected by the saliency image of cover image. At last, the reversible watermarking algorithm based on histogram is used to embed secret information, where the embedded order is determined by the saliency image of the cover image.

When we extract the secret information, the binary sequence in stego-image is firstly extracted by the secret key. Then, the binary sequence is converted to residual image and sparse representation coefficients. The dictionary is built by recovered stego-image. Finally, the biometric image is restored by the residual image and the reconstructed biometric image.

The flowchart of hiding method is described in Figure 1. The method is divided into three stages of sparse representation, vision attention, and image hiding.

2.1. Sparse Representation. With the rapid development of computer technology, abundant signal processing methods

have been proposed. As a branch of signal processing, sparse representation has been wildly applied in image denoising, image restoration, feature extraction, image compression, pattern recognition, machine learning, compressed sensing, and other fields. Nevertheless, the sparse representation theory is rarely used in the information hiding field. Jost et al. applied the sparse representation theory to the information security field; the secret information was embedded into the decomposition path of the sparse decomposition image. The receiver extracts the secret information by decomposition path of the cover image [8]. Cencelli and his colleagues embedded information by modifying the sparse representation coefficients of image [9–11]. These methods only use a sparse representation coefficient and decomposition path to achieve information hiding. They do not analyze the correlation between the secret information and the cover image by sparse representation method. Therefore, this paper uses sparse representation method to analyze the correlation between secret information and the cover image for reducing the number of secret information.

The element of decomposition signal is called the atom in the sparse representation theory. Suppose $y \in R^n$ is an image block representation vector, $D \in R^{n\times L}$ represents redundant dictionary, L represents the number of atoms, and sparse representation process can be described as

$$\widehat{\alpha} = \arg\min_{\alpha} \left\| y - D\alpha \right\|_2^2 \quad \text{s.t.} \ \ \|\alpha\|_0 \le S, \tag{1}$$

where $\|*\|_2$ represents the l_2-norm, $\|*\|_0$ represents the l_0-norm, S represents sparse degree, D is the redundant dictionary, $D = [d_1, d_2, \ldots, d_L]$, α represents sparse representation coefficient, and $\|\alpha\|_0$ represents the number of non-zero coefficients in α. Figure 2 is schematic diagram of the sparse representation theory.

Two of the most critical problems need to be solved using the sparse representation for information hiding. One is how to build an effective dictionary D, and the other is how to obtain sparse representation coefficient. Taking into account the characteristics of the cover image and biometric image, we use the integer value dictionary. In order to reduce the difficulty and the complexity of building dictionary, data sampling method is used to build the redundant dictionary by the cover image. Palmprint images and iris images are divided into blocks for improving the computational efficiency of the algorithm in this paper. Palmprint image is divided into 16 blocks with the size of 32×32; iris image is divided into 8 blocks with the size of 32×32. The dictionary is built by data sampling methods with size of 1024×6561. Orthogonal matching pursuit algorithm (OMP) is used to calculate the sparse representation coefficient [12] which is an improved algorithm based on matching pursuit algorithm [13]. The original image, reconstructed image and residual image are shown in Figures 3 and 4.

2.2. Vision Attention. Visual attention mechanism is an emerging research field, which contains neurobiology psychology, computer vision, pattern recognition, artificial intelligence, and many other disciplines. It is one kind of mechanism of human visual systems in selecting regions of interest

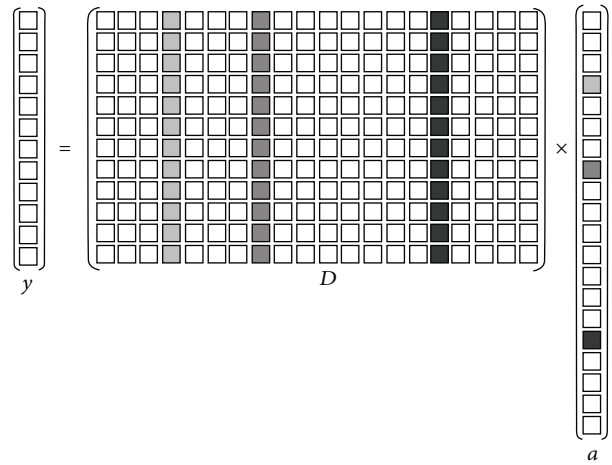

Figure 2: The schematic diagram of the sparse representation theory.

from complex scenes. Recently, it has become the focus of research in computer vision, due to its applications for object detection [14–16] and digital image processing field [17–20]. Visual attention model is divided into two categories by visual information processing method in computer vision system. The first one is a bottom-up visual attention model method, which is directed by the data. But it is not dependent on the specific task. The second one is a top-down visual attention model method, which is affected by subjective consciousness. It depends on the specific task. In this paper, we use the method of literature [21]. The saliency of object is detected by the unified approach, which integrates bottom-up for lower-level features and top-down for higher-level priors.

After multiscale feature extraction, we decompose an image into small regions by image segmentation. Then the mean of the feature vectors in a segment is treated as the feature. The matrix representation of the image is formed by stacking them. By this means, even when the object size is large, the number of segments in a salient object is still small, due to the fact that salient objects usually have spatial and appearance-wise coherence. At the same time, in order to ensure that the matrix representing the background has a low rank, we train a linear feature transformation using labeled data. This method can achieve good performance on saliency detection, even without higher-level knowledge. Figures 5 and 6 show the illustration of the method.

In order to ensure the consistency of the saliency image from the cover image and the stego-image, the saliency image is computed by the reference subsampling image. The reference subsampling image is computed by (3) and (4).

2.3. Information Hiding. One target of information hiding is to hide secret information into another nonsecret cover image for avoiding the attacker's attention. The information hiding technique requires that the secret information cannot be found in digital media. At the same time, if the attacker does not get the secret key, anyone cannot extract the secret information from the digital media.

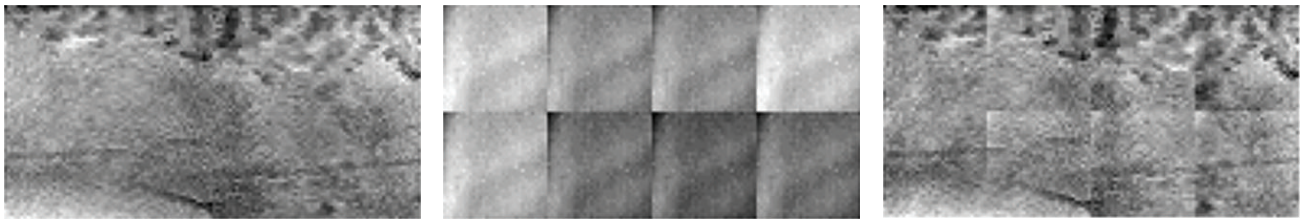

Original image Sparse representation results Residual image

Figure 3: Iris image reconstruction result.

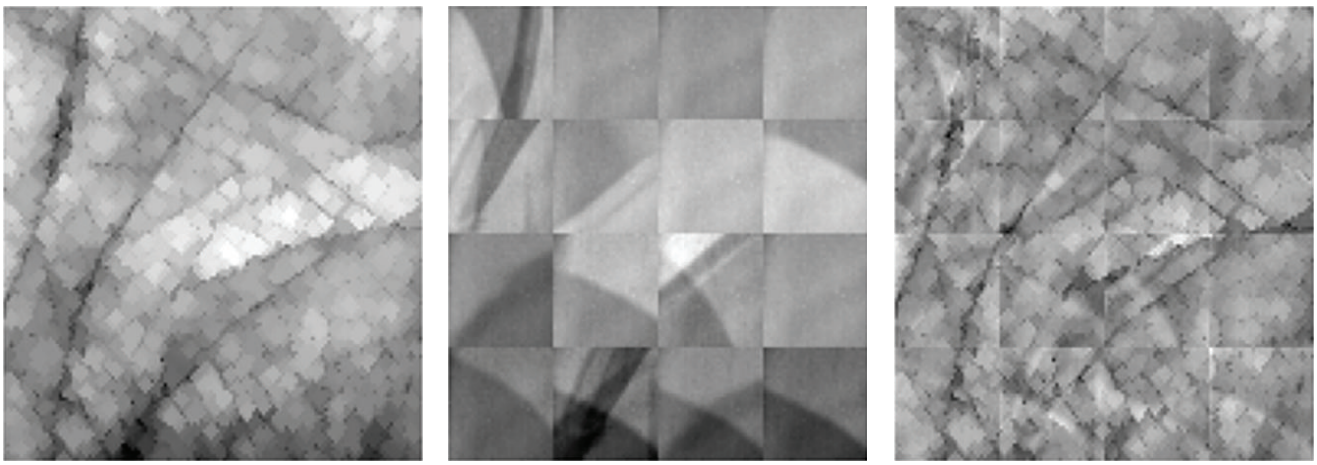

Original image Sparse representation results Residual image

Figure 4: Palmprint image reconstruction result.

Cover image Image saliency

Figure 5: Lena image and its saliency image.

The histogram is the most basic statistical characteristics of the image. A digital image has L gray-level in the range $[0, G]$, and the discrete function of the histogram is defined as

$$h(k) = n_k, \tag{2}$$

where k represents the gray value of the image, n_k represents the number of the pixel that the gray value is k, and the value of G is 255 in the gray image.

Histogram analysis is an important tool for digital image processing. Thus, the reversible watermarking algorithm based on histogram is used in the process of embedding secret

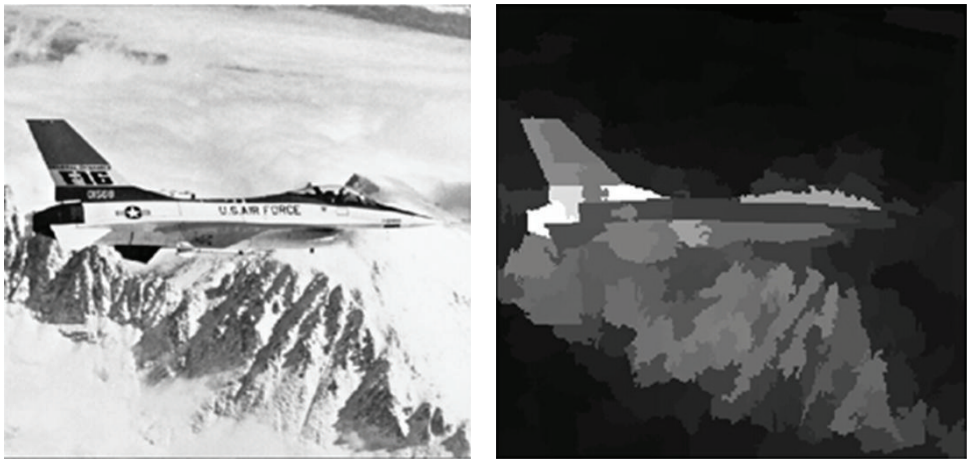

Cover image

Image saliency

Figure 6: Airplane image and its saliency image.

information. The research focus of the traditional hiding algorithm based on histogram is how to determine the peak-value point and zero-value point, which results in that the watermark embedding capacity is too small and random. The application scope of the algorithm is limited because of these problems. A large number of statistical results show that the embedding capacity can be increased by segmenting the image into blocks. Since the pixel value is relatively concentrated in the image block, more embedded space can be got from the image [22].

The watermark embedding method of literature [23] is used in this paper, meanwhile the division block method of cover image and embedding sequence of watermark are improved. The cover image is divided into small pieces by saliency image, each of which is a small cover image. All image blocks are sorted by significance. The secret information is segmented according to the embedding capacity of each small cover image and embedded in the corresponding cover image block until all the secret information is embedded.

The embedding method of secret information can be described as follows.

Step 1. According to the significance, the block of cover image I is selected, and the values of sampling coefficients u and v are 2, respectively. All the subsampled images I_1, I_2, I_3, I_4 are generated by (3)

$$I_m(i,j) = I\left(i \cdot v + \text{floor}\left(\frac{m-1}{u}\right), j \cdot u + (m-1) \bmod u\right). \tag{3}$$

Step 2. I_{Ref} represents the reference subsampled image. I_{Des} represents the target subsampled image. $I_{\text{Ref–Des}}$ represents the difference of I_{Ref} and I_{Des}. All $I_{\text{Ref–Des}}$ are calculated by (5):

$$I_{\text{Ref}} = \left(\text{Round}\left(\frac{u}{2} - 1\right)\right) \times v + \text{Round}\left(\frac{v}{2}\right), \tag{4}$$

$$I_{\text{Ref–Des}}(i,j) = I_{\text{Ref}}(i,j) - I_{\text{Des}}(i,j), \tag{5}$$

where $0 \le i \le M/(v-1)$, $0 \le j \le N/(u-1)$.

Step 3. The embedding position of secret information is determined by moving the histogram based on the embedded level L. In order to adaptively embed secret information, the histogram is moved around according to embedding level L. When the histogram is modified, the secret information is embedded in the range of $[-L, L]$. The moving method of the histogram is shown in the following:

$$H_S = \begin{cases} H + L + 1 & H \ge L + 1 \\ H - L - 1 & H \le -L - 1, \end{cases} \tag{6}$$

where H represents the gray values and L represents embedding level.

The pixel value of the reference subsampling image cannot be changed in order to ensure reversibility of the method. Therefore, we can only modify the pixel value of the target subsampled image. The modification method of the pixel value is shown in the following:

$$I'_{\text{Des}}(i,j) = \begin{cases} I_{\text{Des}}(i,j) - (L+1) & H \ge L + 1 \\ I_{\text{Des}}(i,j) + (L+1) & H \le -L - 1. \end{cases} \tag{7}$$

Step 4. The secret information is embedded by moving the histogram. We scan the pixel value of $I_{\text{Ref–Des}}$. When the size of the pixel value is L or $-L$, the secret information is embedded. The scanning process is repeated until all the pixel values are not equal to L or $-L$. In this case, the embedded level L is -1, and repeat the above process until $L < 0$. The embedding method is shown in (8). The moving process of the histogram is shown in Figure 7:

$$L > 0,$$

$$I''_{\text{Des}}(i,j) = \begin{cases} I'_{\text{Des}}(i,j) - (L+1) & P' = L,\ w(n) = 1 \\ I'_{\text{Des}}(i,j) + (L+1) & P' = -L,\ w(n) = 1 \\ I'_{\text{Des}}(i,j) + L & P' = -L,\ w(n) = 0 \\ I'_{\text{Des}}(i,j) - L & P' = L,\ w(n) = 0, \end{cases}$$

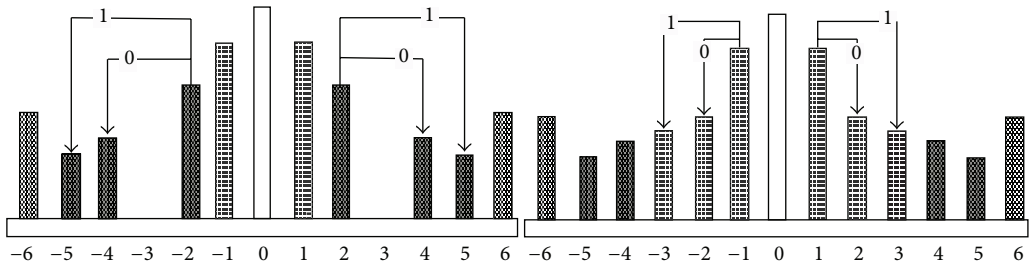

Figure 7: The moving process of histogram.

Cover image Stego-image

Figure 8: The cover images and the stego-images contain iris information.

$$L = 0,$$

$$I''_{\mathrm{Des}}(i,j) = \begin{cases} I'_{\mathrm{Des}}(i,j) & P' = 0,\ w(n) = 1 \\ I'_{\mathrm{Des}}(i,j) - 1 & P' = 0,\ w(n) = 0. \end{cases} \tag{8}$$

The original image and the stego-image are shown in Figures 8 and 9. The extraction of secret information is an inverse process of the embedding process. First, the reference subsampled image is extracted from stego-image for computing the saliency image. Then, the stego-image is divided into blocks. The image blocks are sorted by the significance of image block. The reference subsampled image of image block is extracted by (3) and (4). The secret information is extracted by the secret key and the reference subsampled image. Finally, the biometric authentication image is reconstructed by residual image, dictionary, and sparse representation coefficients.

3. Experiment and Analysis

The proposed method is verified by the biometric authentication data in this paper, and the performance of the method is tested from security, invisibility, and embedding capacity.

3.1. Experimental Data. The PolyU multispectral palmprint database and the CASIA iris database of Chinese Academy of Sciences are used as biometric information [24, 25]. We select 100 images from each database. The size of palmprint image

Cover image Stego-image

Figure 9: The cover images and the stego-images contain palmprint information.

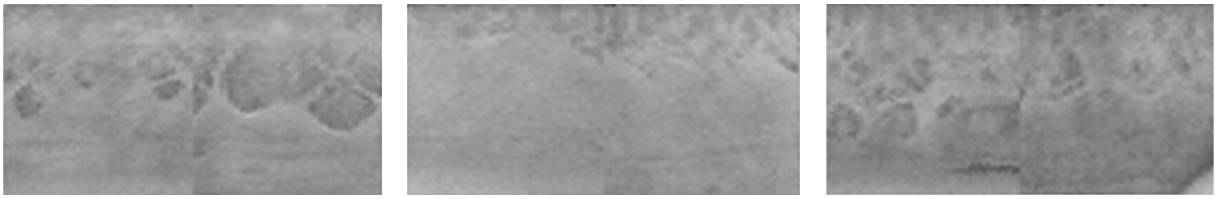

Figure 10: The iris images.

is 128 × 128; the size of iris image is 128 × 64. Some images in the database are shown in Figures 10 and 11. The cover images contain rich texture information and are unrelated with the biometric image. The cover images are shown in Figure 12.

3.2. Performance Analysis. Firstly, from the security point of view, the biometric information is hidden into the unnoticed cover image, which reduces the attacker's attention. Secondly, the main part of the biometric image is reconstructed by the sparse representation method, and the other part is embedded into the cover image. Even if the embedded information is intercepted, the attacker cannot restore the entire biometric image. Finally, the visual attention mechanism is used to select embedding location and embedding sequence of secret information. The visual attention mechanism increases the confidentiality of embedded information.

Peak Signal to Noise Ratio (PSNR) is an effective way to evaluate invisibility of information hiding. The PSNR of an image is calculated by the following:

$$\mathrm{PSNR} = 10 \times \log_{10}\left(\frac{255 \times 255 \times M \times N}{\sum_{i=1}^{M}\sum_{j=1}^{N}\left[C(i,j) - S(i,j)\right]^2}\right), \quad (9)$$

where C represents the cover image and S represents the stego-image. When PSNR is higher than 30 dB, we believe that the stego-image holds good invisibility. The proposed method and the method of literature [26] are compared and the comparison results are shown in Table 1.

From Table 1 we can see that the invisibility of our method is better than the other. Because the correlation analysis method based on sparse representation is used in the information hiding, the PSNR value of our method is higher

Table 1: PSNR comparison results.

Cover image	Cover image (pixel)	Database	PSNR (dB)	
			Literature [26]	The proposed method
Lena	512 × 512	CASIA	36.52	41.97
Lena	512 × 512	PolyU	34.26	37.62
Airplane	512 × 512	CASIA	38.5	44.90
Airplane	512 × 512	PolyU	34.42	39.42
Barbara	512 × 512	CASIA	36.12	40.50
Barbara	512 × 512	PolyU	33.05	36.05

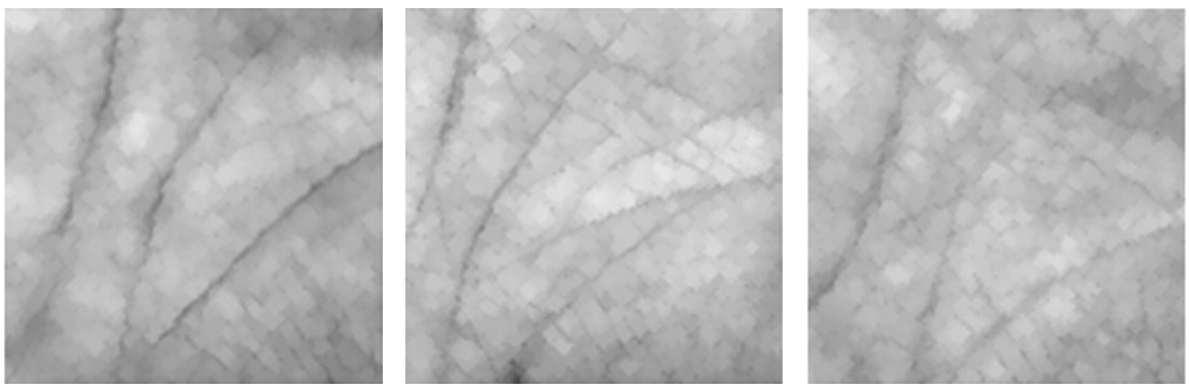

Figure 11: The palmprint images.

Figure 12: The cover images.

than the other method. At the same time, the cover image is changed very little in the embedding process due to the fact that the pixel value of the residual image is very small. The embedding information has a minor effect on cover image.

The embedding capacity is a main evaluation criterion for information hiding algorithm. The embedding capacity is calculated by the following:

$$\text{bpp} = \frac{N_s}{M_c \times N_c}, \tag{10}$$

where N_s represents the number of binary bits of secret information and $M_c \times N_c$ represents the size of the cover image. The proposed method and the method of literature [27–29] are compared to embedding capacity, and the comparison results are shown in Table 2.

Table 2 shows the embedding capacity comparison results of different methods. The embedding capacity of our method is higher than other methods. Relatively speaking, Vatsa et al. get the worst results.

4. Conclusions

A novel biometric image hiding method based on the sparse representation is proposed in this paper. The transmission security of biometric information is improved in the network. The biometric image is divided into the reconstructed image with high energy and the residual image with low energy.

Table 2: Embedding capacity comparison results.

Algorithm	Cover image (pixel)	Secret information (bit)	bpp
Vatsa et al. [27]	1024×768	1000	0.0013
Vatsa et al. [28]	512×512	16384	0.0625
Shih and Wu [29]	$512 \times 512 \times 3$	86016	0.1094
Our method	512×512	142084	0.5420

Residual image is embedded into the cover image. In order to reduce the attacker's attention to stego-image, visual attention mechanism is used in the secret information embedding process. At the same time, the hiding strategy is modified in the information hiding algorithm, where the secret information embedding process is guided by the saliency image. Since the reconstruction method has a certain complexity, the secret key has high secrecy and is difficult to decipher. Because the biometric image is divided into two parts, the attacker cannot restore biometric authentication images with any part. A large number of experimental results show that the proposed method can protect the biometric authentication information effectively. Currently, our approach can only process the gray-scale image. How to hide biometric information into color image is an important problem in future research.

Conflict of Interests

The authors declare that there is no conflict of interests regarding the publication of this paper.

Acknowledgments

This work is supported by the Science and Technology Research Project of Liaoning Province Education Department (no. L2014450), Social Science Planning Foundation Project of Liaoning Province (no. L13BXW006), Fund of Jilin Provincial Science & Technology Department (nos. 20130206042GX and 20130522115JH), and National Natural Science Foundation of China (no. 61403078).

References

[1] P. Bedi, R. Bansal, and P. Sehgal, "Mulitimodal biometric authentication using PSO based watermarking," *Procedia Technology*, vol. 4, pp. 612–618, 2012.

[2] M. Vatsa, R. Singh, and A. Noore, "Feature based RDWT watermarking for multimodal biometric system," *Image and Vision Computing*, vol. 27, no. 3, pp. 293–304, 2009.

[3] A. K. Shaw, S. Majumder, S. Sarkar, and S. K. Sarkar, "A novel EMD based watermarking of fingerprint biometric using GEP," *Procedia Technology*, vol. 10, pp. 172–183, 2013.

[4] C. Li, Y. Wang, B. Ma, and Z. Zhang, "Tamper detection and self-recovery of biometric images using salient region-based authentication watermarking scheme," *Computer Standards and Interfaces*, vol. 34, no. 4, pp. 367–379, 2012.

[5] X. Che, J. Kong, J. Dai, Z. Gao, and M. Qi, "Content-based image hiding method for secure network biometric verification," *International Journal of Computational Intelligence Systems*, vol. 4, no. 4, pp. 596–605, 2011.

[6] M. Qi, Y. Lu, N. Du, Y. Zhang, C. Wang, and J. Kong, "A novel image hiding approach based on correlation analysis for secure multimodal biometrics," *Journal of Network and Computer Applications*, vol. 33, no. 3, pp. 247–257, 2010.

[7] Y. Shi, M. Qi, Y. Yi, M. Zhang, and J. Kong, "Object based dual watermarking for video authentication," *Optik*, vol. 124, no. 19, pp. 3827–3834, 2013.

[8] P. Jost, P. Vandergheynst, and P. Frossard, "Redundant image representations in security applications," in *Proceedings of the International Conference on Image Processing (ICIP '04)*, pp. 2151–2154, October 2004.

[9] G. Cancelli, M. Barni, and G. Menegaz, "MPSteg: hiding a message in the matching pursuit domain," in *Security, Steganography, and Watermarking of Multimedia Contents VIII*, vol. 6072 of *Proceedings of SPIE*, pp. 1–9, 2006.

[10] G. Cancelli and M. Barni, "MPSteg-color: a new steganographic technique for color images," in *Information Hiding: 9th International Workshop (IH '07), Saint Malo, France, June 11–13, 2007*, vol. 4567 of *Lecture Notes in Computer Science*, pp. 1–15, Springer, Berlin, Germany, 2007.

[11] G. Cancelli and M. Barni, "MPSteg-color: data hiding through redundant basis decomposition," *IEEE Transactions on Information Forensics and Security*, vol. 4, no. 3, pp. 346–358, 2009.

[12] Y. C. Pati, R. Rezaiifar, and P. S. Krishnaprasad, "Orthogonal matching pursuit: recursive function approximation with applications to wavelet decomposition," in *Proceedings of the 27th Annul Asilomar Conference on Signals, Systems and Computers*, pp. 40–44, Pacific Grove, Calif, USA, 1993.

[13] S. G. Mallat and Z. Zhang, "Matching pursuits with time-frequency dictionaries," *IEEE Transactions on Signal Processing*, vol. 41, no. 12, pp. 3397–3415, 1993.

[14] M. W. Guo, Y. Z. Zhao, C. B. Zhang, and Z. H. Chen, "Fast object detection based on selective visual attention," *Neurocomputing*, vol. 144, no. 20, pp. 184–197, 2014.

[15] H. P. Yu, Y. X. Chang, P. Lu, Z. Y. Xu, C. Y. Fu, and Y. F. Wang, "Efficient object detection based on selective attention," *Computers and Electrical Engineering*, vol. 40, no. 3, pp. 907–919, 2014.

[16] Q. Liu, Q. Z. Zhang, W. B. Chen, and Z. C. Huang, "Pedestrian detection based on modeling computation of visual attention," *Journal of Beijing Information Science & Technology University*, vol. 29, no. 2, pp. 59–65, 2014.

[17] C. Guo and L. Zhang, "A novel multiresolution spatiotemporal saliency detection model and its applications in image and video compression," *IEEE Transactions on Image Processing*, vol. 19, no. 1, pp. 185–198, 2010.

[18] C. Yang, L. H. Zhang, H. C. Lu, X. Ruan, and M.-H. Yang, "Saliency detection via graph-based manifold ranking," in *Proceedings of the 26th IEEE Conference on Computer Vision and Pattern Recognition (CVPR '13)*, pp. 3166–3173, Portland, Ore, USA, June 2013.

[19] B. Yang and S. T. Li, "Visual attention guided image fusion with sparse representation," *Optik*, vol. 125, no. 17, pp. 4881–4888, 2014.

[20] H.-Y. Yang, Y.-W. Li, W.-Y. Li, X.-Y. Wang, and F.-Y. Yang, "Content-based image retrieval using local visual attention feature," *Journal of Visual Communication and Image Representation*, vol. 25, no. 6, pp. 1308–1323, 2014.

[21] X. H. Shen, Y. Wu, and Evanston, "A unified approach to salient object detection via low rank matrix recovery," in *Proceedings of the IEEE Conference on Computer Vision and Pattern Recognition (CVPR '12)*, pp. 853–860, Providence, RI, USA, June 2012.

[22] K.-S. Kim, M.-J. Lee, H.-Y. Lee, and H.-K. Lee, "Reversible data hiding exploiting spatial correlation between sub-sampled images," *Pattern Recognition*, vol. 42, no. 11, pp. 3083–3096, 2009.

[23] J. H. Hwang, J. W. Kim, and J. U. Choi, "A reversible watermarking based on histogram shifting," in *Digital Watermarking: 5th International Workshop (IWDW '06), Jeju Island, Republic of Korea, November 8–10, 2006*, vol. 4283 of *Lecture Notes in Computer Science*, pp. 348–361, Springer, Berlin, Germany, 2006.

[24] PolyU multispectral palmprint Database, http://www.comp.polyu.edu.hk/~biometrics/MultispectralPalmprint/MSP.htm.

[25] CASIA-IrisV1[DB/OL], 2004, http://www.cbsr.ia.ac.cn/IrisDatabase.htm.

[26] M. Qi, J. Y. Dai, J. Z. Wang, X. X. Yu, and M. Zhang, "Content-based reversible steganographic method for multimodal biometrics," *Computer Science*, vol. 39, no. 11, pp. 70–74, 2012.

[27] M. Vatsa, R. Singh, P. Mitra et al., "Comparing robustness of watermarking algorithms on biometrics data," in *Proceedings of the Workshop on Biometric Challenges from Theory to Practice (ICPR Workshop '04)*, pp. 5–8, August 2004.

[28] M. Vatsa, R. Singh, A. Noore, M. M. Houck, and K. Morris, "Robust biometric image watermarking for fingerprint and face template protection," *IEICE Electronics Express*, vol. 3, no. 2, pp. 23–28, 2006.

[29] F. Y. Shih and S. Y. T. Wu, "Combinational image watermaking in the spatial and frequency domains," *Pattern Recognition*, vol. 36, no. 4, pp. 969–975, 2002.

Hindawi Publishing Corporation
Mathematical Problems in Engineering
Volume 2015, Article ID 580289, 7 pages
http://dx.doi.org/10.1155/2015/580289

Research Article

Optimal Power Constrained Distributed Detection over a Noisy Multiaccess Channel

Zhiwen Hu[1] and Zhenhua Xu[2]

[1] *School of New Media, Zhejiang University of Media and Communications, Hangzhou 310018, China*
[2] *No. 38 Research Institute, China Electronics Technology Group Corporation, Hefei 230000, China*

Correspondence should be addressed to Zhiwen Hu; sunneyhu@gmail.com

Received 26 November 2014; Revised 28 December 2014; Accepted 28 December 2014

Academic Editor: Hui Zhang

Copyright © 2015 Z. Hu and Z. Xu. This is an open access article distributed under the Creative Commons Attribution License, which permits unrestricted use, distribution, and reproduction in any medium, provided the original work is properly cited.

The problem of optimal power constrained distributed detection over a noisy multiaccess channel (MAC) is addressed. Under local power constraints, we define the transformation function for sensor to realize the mapping from local decision to transmitted waveform. The deflection coefficient maximization (DCM) is used to optimize the performance of power constrained fusion system. Using optimality conditions, we derive the closed-form solution to the considered problem. Monte Carlo simulations are carried out to evaluate the performance of the proposed new method. Simulation results show that the proposed method could significantly improve the detection performance of the fusion system with low signal-to-noise ratio (SNR). We also show that the proposed new method has a robust detection performance for broad SNR region.

1. Introduction

Distributed detection of phenomenon of interest constitutes an important application of wireless sensor networks. Usually, a distributed detection system consists of multiple sensors and a fusion center (FC) [1].

As we know, distributed detection using multiple sensors has become a fast-growing research area [2]. Current and future applications of distributed detection range from data acquisition, health care, and environment monitoring to battlefield surveillance and disaster warning [3, 4]. Compared to a centralized scheme where all raw observation data are communicated to the fusion center, distributed detection scheme could dramatically reduce the communication bandwidth and thus are very competitive candidates to be implemented in wireless sensor networks. However, to implement distributed detection in networking, we meet some new challenges. One challenge is the stringent power constraint. Normally, local sensors are powered by small batteries and it is difficult or not economic to replace those batteries when they run out. Therefore, power management is considered to be an important issue in detection fusion.

Traditionally, numerous researches focus on the usual parallel topology which assumes that each sensor transmits through a parallel access channel (PAC). In that case, the target detection system is made up of a large number of sensors, which are deployed in the environment to collect observations. Each sensor could give the local detection decision independently, and then the sensor node has the ability to communicate with the fusion center via wireless channels. For this scheme, a dedicated channel will be established for each sensor that wishes to communicate with the fusion center [1, 2]. In practical applications, since the wireless medium is naturally a broadcast medium, the PAC has to be realized through time division multiple access (TDMA), frequency division multiple access (FDMA), or code division multiple access (CDMA) [5].

Recently, distributed detection over multiple access channels (MAC) has received much attention; it has been verified that in some cases the MAC schemes could offer high efficiency in bandwidth usage and achieve a significant improvement in performance compared to the PAC scheme when a large number of sensors are deployed [6–8]. The problem of distributed detection under power constraints has been studied by many researchers [9–16].

Using the PAC, in [9], it was shown that the performance is asymptotically optimal for binary decentralized detection using identical sensor nodes under joint power constraint. In [10], the optimal power scheduling for distributed detection has been considered, where an optimal power allocation scheme was developed with respect to the so-called J-divergence performance index. In [11], when the whole system is subjected to a total average power constraint in noisy and band-limited channels, it showed that it is better to combine as many local decisions as possible rather than only relying on a few very good local decisions in the case of deterministic signal detection. They have shown that the optimal power allocation is determined by the qualities of the local decisions of the sensors and the communication channels. In [12], the problem of optimal power allocation in the cases of both independent and correlated observations has been addressed by using constrained particle swarm optimization; however, the algorithm is not economic to realize in engineering. Using the MAC, in [13], the optimal quantization function has been studied under the total power constraint which assumed that the sensors are homogeneous. Under the local power constraints of sensors, in [14], it was shown that the optimal fusion rule can be reduced to a simple threshold test on the signal received by the fusion center. In [15], a new method for detection fusion over multiple-access channel based on deflection coefficient maximization (DCM) and Neyman-Pearson (NP) rule has been proposed. However, all the above authors assumed that the local sensors are homogeneous. In [16], it was shown that, in addition to vastly improved bandwidth efficiency, MAC fusion with optimal local mapping rules yields better detection performance as measured by error exponents compared with PAC fusion under the same transmission power constraint. In reality, the stringent power constraint of local sensor is also an important issue; therefore we are motivated to study the distributed detection fusion problem under power constraints of local sensors over noisy multiaccess channel.

2. System Model

The model of the distributed detection system considered here is illustrated in Figure 1, where the system consists of N sensors and a fusion center (FC). Here, H_0 denotes the null hypothesis (e.g., the target is absent), and H_1 denotes the alternative hypothesis (e.g., the target is present). The prior probabilities for both hypotheses (denoted by P_0 and P_1, resp.) are assumed known. v_i $(i = 1, 2, \ldots, N)$ denotes the observation of the ith sensor, where n is the Gaussian noise with zero mean and variance σ^2.

We do not assume any determined distribution for observations but do assume that the observations are all conditionally independent of any hypothesis. Based on its observation, the ith sensor makes a local decision u_i $(i = 1, 2, \ldots, N)$. We adopt the OOK mode in this paper, which means that $u_i = 1$ is sent if H_1 is decided and $u_i = 0$ is sent otherwise. The detection performance of the ith local sensor

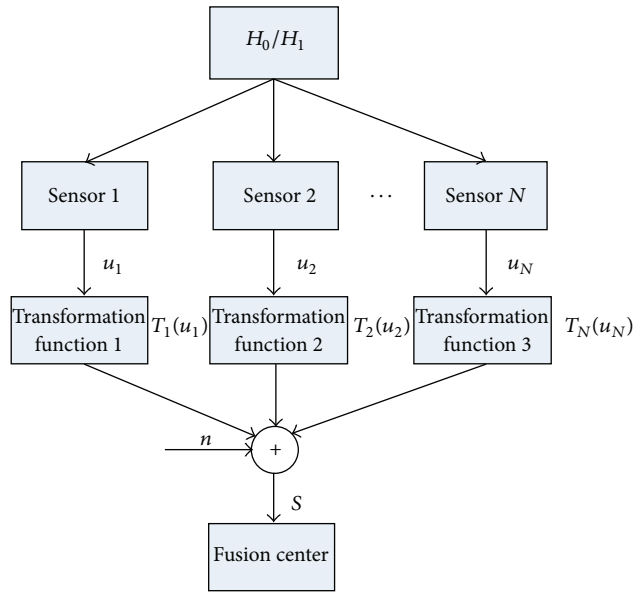

Figure 1: Model of underwater distributed detection fusion.

node can be characterized by its corresponding probability of false alarm P_{fi} and detection P_{di}, denoted by

$$P_{fi} = p\left(u_i = 1 \mid H_0\right),$$
$$P_{di} = p\left(u_i = 1 \mid H_1\right). \tag{1}$$

The ith sensor will inform the fusion center by transmitting a waveform. We use a local transformation function $T_i(u_i)$ to realize such a mapping from the local decision to a particular waveform. Under the power constraint of local sensors, the same as [14], we define the transformation function of the ith local sensor as follows:

$$T_i\left(u_i\right) = \begin{cases} \sqrt{\omega_i}\left(1 - \beta_i\right), & u_i = 1, \\ \sqrt{\omega_i}\left(0 - \beta_i\right), & u_i = 0, \end{cases} \tag{2}$$

where ω_i is a nonnegative multiplication weight coefficient and β_i is an offset. We model the channel between local sensor and fusion center as a noisy multiple access. Although perfect synchronization on MAC is a strong assumption, synchronization error often cannot be completely removed in practical sensor networks; many authors have developed effective synchronization schemes to solve this problem [8, 16]. In addition, we consider the case when the number of the sensors is not large in this paper; thus, we make the same assumption as in [6, 7, 14] that all the sensors are fully synchronized and are allowed to communicate with the fusion center simultaneously over a multiaccess channel. Then, the data received from the fusion center can be expressed as

$$S = \sum_{i=1}^{N} T_i\left(u_i\right) + n. \tag{3}$$

After receiving the information S, the global decision is made based on the NP rule that involves the comparison of S with

a threshold. The fusion center will give a final decision about the presence or absence of a target according to a certain fusion rule.

3. Distributed Detection via Deflection Coefficient Maximization

The deflection coefficient could reflect the output signal-to-noise ratio and has been widely used in optimizing detectors [17, 18]. The larger the deflection coefficient is, the better the performance of the system will be. We therefore are motivated to optimize the fusion system via maximizing the deflection coefficient. The deflection coefficient is defined as

$$D(S) = \frac{\left(E(S \mid H_1) - E(S \mid H_0)\right)^2}{\operatorname{Var}(S \mid H_0)}, \tag{4}$$

where $E(\cdot \mid H_j)$ and $\operatorname{Var}(\cdot \mid H_j)$ $(j = 0, 1)$ denote the expected value and variance, respectively. $E(S \mid H_j)$ and $\operatorname{Var}(S \mid H_0)$ are given by

$$E(S \mid H_j) = \sum_{i=1}^{N} \sqrt{\omega_i}\left[E(u_i \mid H_j) - \beta_i\right], \tag{5}$$

$$\begin{aligned} E(u_i \mid H_j) &= \begin{cases} P_{di}, & \mid j = 1, \\ P_{fi}, & \mid j = 0, \end{cases} \\ \operatorname{Var}(S \mid H_0) &= \sum_{i=1}^{N} \omega_i \left[\operatorname{Var}(u_i \mid H_0)\right] + \sigma^2, \\ \operatorname{Var}(u_i \mid H_0) &= E(u_i^2 \mid H_0) - E^2(u_i \mid H_0) = P_{fi} - P_{fi}^2. \end{aligned} \tag{6}$$

Based on (6), we have

$$D(S) = \frac{\left[\sum_{i=1}^{N} \sqrt{\omega_i}(P_{di} - \beta_i) - \sum_{i=1}^{N} \sqrt{\omega_i}(P_{fi} - \beta_i)\right]^2}{\sum_{i=1}^{N} \omega_i \left(P_{fi} - P_{fi}^2\right) + \sigma^2}. \tag{7}$$

Under the power constraints of local sensors, we can formulate the deflection coefficient maximization problem as

$$\begin{aligned} &\max \quad D(S) \\ &\text{s.t.} \quad E\left[T_i^2(u_i)\right] \le Q_i, \end{aligned} \tag{8}$$

where Q_i is the maximum transmission power of the ith local sensor. Moreover, we can obtain the explicit expression of the power constraint

$$E\left[T_i^2(u_i)\right] = \omega_i \left[E(u_i^2) + \beta_i^2 - 2E(u_i)\beta_i\right] \le Q_i, \tag{9}$$

with $E(u_i^2) = E(u_i) = P_0 P_{fi} + P_1 P_{di}$. Then, the constraint (9) is rewritten as

$$\begin{aligned} E\left[T_i^2(u_i)\right] = \omega_i \big[&\beta_i^2 - 2\beta_i\left(P_0 P_{fi} + P_1 P_{di}\right) \\ &+ P_0 P_{fi} + P_1 P_{di}\big] \le Q_i. \end{aligned} \tag{10}$$

Since the minimum of $[\beta_i^2 - 2\beta_i(P_0 P_{fi} + P_1 P_{di}) + P_0 P_{fi} + P_1 P_{di}]$ is

$$C_i = \left(P_0 P_{fi} + P_1 P_{di}\right) - \left(P_0 P_{fi} + P_1 P_{di}\right)^2 > 0, \tag{11}$$

we have

$$0 \le \omega_i \le \frac{Q_i}{C_i}. \tag{12}$$

Denoting a vector

$$\mathbf{a} = (a_1, a_2, \ldots, a_i, \ldots, a_N)^T, \tag{13}$$

with $a_i = P_{di} - P_{fi} > 0$, and a diagonal matrix

$$\mathbf{B} = \operatorname{diag}(b_1, b_2, \ldots, b_i, \ldots, b_N), \tag{14}$$

with $b_i = P_{fi} - P_{fi}^2 > 0$, and defining $x_i = \sqrt{\omega_i}$ and $y_i = x_i / \sqrt{Q_i / C_i}$, then the constraint (12) is converted into

$$0 \le y_i = \frac{x_i}{\sqrt{Q_i / C_i}} \le 1. \tag{15}$$

Then (7) is equivalently rewritten as

$$D(S) = \frac{\left(\sum_{i=1}^{N} \sqrt{Q_i / C_i}\, y_i a_i\right)^2}{\sum_{i=1}^{N} (Q_i / C_i)\, y_i^2 b_i + \sigma^2}. \tag{16}$$

Further, assuming that

$$\begin{aligned} \tilde{\mathbf{a}} &= \left(a_1\sqrt{\frac{Q_1}{C_1}}, a_2\sqrt{\frac{Q_2}{C_2}}, \ldots, a_i\sqrt{\frac{Q_i}{C_i}}, \ldots, a_N\sqrt{\frac{Q_N}{C_N}}\right)^T, \\ \tilde{\mathbf{B}} &= \operatorname{diag}\left(Q_1\frac{b_1}{C_1}, Q_2\frac{b_2}{C_2}, \ldots, Q_i\frac{b_i}{C_i}, \ldots, Q_N\frac{b_N}{C_N}\right), \\ \mathbf{y} &= (y_1, y_2, \ldots, y_i, \ldots, y_N)^T, \end{aligned} \tag{17}$$

then the optimization problem (8) is converted into

$$\begin{aligned} &\max \quad f(\mathbf{y}) = \frac{\mathbf{y}^T \tilde{\mathbf{a}} \tilde{\mathbf{a}}^T \mathbf{y}}{\mathbf{y}^T \tilde{\mathbf{B}} \mathbf{y} + \sigma^2} \\ &\text{s.t.} \quad 0 \le y_i \le 1, \quad i = 1, 2, \ldots, N. \end{aligned} \tag{18}$$

The gradient of $f(\mathbf{y})$ is

$$g(\mathbf{y}) = \nabla f(\mathbf{y}) = \frac{2\left(\tilde{\mathbf{a}}^T \mathbf{y}\right)^2 \left[\left(\left(\mathbf{y}^T \tilde{\mathbf{B}} \mathbf{y} + \sigma^2\right) / \tilde{a}^T y\right) \tilde{a} - \tilde{\mathbf{B}} \mathbf{y}\right]}{\left(\mathbf{y}^T \tilde{\mathbf{B}} \mathbf{y} + \sigma^2\right)^2}. \tag{19}$$

Assume that $\mathbf{y}^*$ is the optimal solution of the problem (18), y_i^* is the ith component of $\mathbf{y}^*$, and $g_i(\mathbf{y})$ is the ith component of $g(\mathbf{y})$. Obviously, we know that $y_i^* \neq 0$, as if $y_i^* = 0$, then $g_i(\mathbf{y}^*) > 0$; thus we can find another $y_i^* > 0$ which will maximize the objective function. Then, the optimality conditions are

$$\begin{aligned} &g_i(\mathbf{y}^*) = 0, \quad y_i^* \epsilon (0, 1] \\ &g_i(\mathbf{y}^*) > 0, \quad y_i^* = 0. \end{aligned} \tag{20}$$

We claim that there is no local maximizer for $f(\mathbf{y})$, which means that the maximizer is global.

The proof is as follows. Assuming that y^* is the global maximizer and $\mathbf{l}^*$ is the local maximizer, we define $\widetilde{\mathbf{y}}^* = \begin{pmatrix} \mathbf{y}^* \\ 1 \end{pmatrix}$, $\widetilde{\mathbf{l}}^* = \begin{pmatrix} \mathbf{l}^* \\ 1 \end{pmatrix}$, $\widehat{\mathbf{a}} = \begin{pmatrix} \widetilde{\mathbf{a}} \\ 0 \end{pmatrix}$, and $\widehat{\mathbf{B}} = \begin{pmatrix} \widetilde{\mathbf{B}} & \mathbf{0} \\ \mathbf{0} & \sigma^2 \end{pmatrix}$. There $\exists 0 < \lambda < 1$ that satisfies $y_\lambda = \lambda \mathbf{y}^* + (1-\lambda)\mathbf{l}^*$; then

$$\begin{aligned}
\sqrt{f(y_\lambda)} &= \sqrt{f(\lambda \mathbf{y}^* + (1-\lambda)\mathbf{l}^*)} \\
&= \frac{\widehat{\mathbf{a}}^T \left[\lambda \widetilde{\mathbf{y}}^* + (1-\lambda)\widetilde{\mathbf{l}}^*\right]}{\left\| \begin{pmatrix} \sqrt{\widetilde{\mathbf{B}}} & \mathbf{0} \\ \mathbf{0} & \sigma \end{pmatrix} \left[\lambda \widetilde{\mathbf{y}}^* + (1-\lambda)\widetilde{\mathbf{l}}^*\right] \right\|} \\
&\geq \frac{\widehat{\mathbf{a}}^T \left[\lambda \widetilde{\mathbf{y}}^* + (1-\lambda)\widetilde{\mathbf{l}}^*\right]}{\lambda \left\| \begin{pmatrix} \sqrt{\widetilde{\mathbf{B}}} & \mathbf{0} \\ \mathbf{0} & \sigma \end{pmatrix} \widetilde{\mathbf{y}}^* \right\| + (1-\lambda) \left\| \begin{pmatrix} \sqrt{\widetilde{\mathbf{B}}} & \mathbf{0} \\ \mathbf{0} & \sigma \end{pmatrix} \widetilde{\mathbf{l}}^* \right\|} \\
&> \frac{\widehat{a}^T \widetilde{\mathbf{l}}^*}{\left\| \begin{pmatrix} \sqrt{\widetilde{\mathbf{B}}} & \mathbf{0} \\ \mathbf{0} & \sigma \end{pmatrix} \widetilde{\mathbf{l}}^* \right\|} = \sqrt{f(\mathbf{l}^*)}.
\end{aligned} \tag{21}$$

This is a contradiction.

We also claim that if

$$\frac{\widetilde{a_1}}{\widetilde{b_1}} \geq \frac{\widetilde{a_2}}{\widetilde{b_2}} \geq \cdots \frac{\widetilde{a_k}}{\widetilde{b_k}} \geq \cdots \frac{\widetilde{a_N}}{\widetilde{b_N}}, \tag{22}$$

then

$$y_1^* \geq y_2^* \geq \cdots y_i^* \geq y_N^*. \tag{23}$$

The proof is as follows. Without loss of generality, we assume that $\widetilde{a_i}/\widetilde{b_i} \geq \widetilde{a_j}/\widetilde{b_j}$; then there are four cases of comparison for y_i^* and y_j^* which are (1) $y_i^* = y_j^* = 1$, (2) $y_i^* = 1$, $0 < y_j^* < 1$, (3) $0 < y_i^* < 1$, $0 < y_j^* < 1$, and (4) $0 < y_i^* < 1$, $y_j^* = 1$. Cases (1) and (2) are so obvious that are needless to prove. For case (3), we have $g_i(\mathbf{y}^*) = g_j(\mathbf{y}^*) = 0$. Let

$$\begin{aligned}
k_1 &= \frac{2\left(\widetilde{\mathbf{a}}^T \mathbf{y}^*\right)^2}{\left(\mathbf{y}^{*T} \widetilde{\mathbf{B}} \mathbf{y}^* + \sigma^2\right)^2} > 0, \\
k_2 &= \frac{\mathbf{y}^{*T} \widetilde{\mathbf{B}} \mathbf{y}^* + \sigma^2}{\widetilde{\mathbf{a}}^T \mathbf{y}^*} > 0,
\end{aligned} \tag{24}$$

and thus we have

$$\begin{aligned}
g_i(\mathbf{y}^*) &= k_1\left(k_2 \widetilde{a_i} - \widetilde{b_i} y_i^*\right) = 0, \\
g_j(\mathbf{y}^*) &= k_1\left(k_2 \widetilde{a_j} - \widetilde{b_j} y_j^*\right) = 0.
\end{aligned} \tag{25}$$

Since $\widetilde{a_i}/\widetilde{b_i} \geq \widetilde{a_j}/\widetilde{b_j}$, then $y_i^* \geq y_j^*$. For case (4), we claim that it is impossible to happen. Because there exist $g_i(\mathbf{y}^*) = 0$ and $g_j(\mathbf{y}^*) \geq 0$ based on the optimality conditions, which induce $y_i^* = k_2(\widetilde{a_i}/\widetilde{b_i}) \leq 1$ and $y_j^* = 1 \leq k_2(\widetilde{a_j}/\widetilde{b_j})$, and $\widetilde{a_i}/\widetilde{b_i} \geq \widetilde{a_j}/\widetilde{b_j}$, it is noted that $y_i^* = k_2(\widetilde{a_i}/\widetilde{b_i}) \geq k_2(\widetilde{a_j}/\widetilde{b_j}) \geq 1$ which is a contradiction. So far, we have proved the second claim.

Based on the above claim, we rearrange the components of $\mathbf{y}^*$ in descending order. Without loss of generality, we assume that

$$\begin{aligned}
&y_1^* = y_2^* = \cdots = y_k^* = 1, \\
&1 > y_{k+1}^* \geq \cdots \geq y_N^* > 0, \\
&z^* = \frac{\mathbf{y}^{*T} \widetilde{\mathbf{B}} \mathbf{y}^* + \sigma^2}{\widetilde{\mathbf{a}}^T \mathbf{y}^*}.
\end{aligned} \tag{26}$$

From the optimality conditions, we have

$$y_i^* = \frac{\widetilde{a_i}}{\widetilde{b_i}} z^*, \quad k+1 \leq i \leq N. \tag{27}$$

Then, we have

$$\begin{aligned}
&\mathbf{y}^{*T} \widetilde{\mathbf{B}} \mathbf{y}^* = \sum_{i=1}^{k} \widetilde{b_i} + \sum_{i=k+1}^{N} \widetilde{b_i} y_i^{*2} = \sum_{i=1}^{k} \widetilde{b_i} + \sum_{i=k+1}^{N} \frac{\widetilde{a_i}^2}{\widetilde{b_i}} (z^*)^2, \\
&\widetilde{\mathbf{a}}^T \mathbf{y}^* = \sum_{i=1}^{k} \widetilde{a_i} + \sum_{i=k+1}^{N} \widetilde{a_i} y_i^* = \sum_{i=1}^{k} \widetilde{a_i} + \sum_{i=k+1}^{N} \frac{\widetilde{a_i}^2}{\widetilde{b_i}} z^*, \\
&\sum_{i=1}^{k} \widetilde{b_i} + \sum_{i=k+1}^{N} \frac{\widetilde{a_i}^2}{\widetilde{b_i}} (z^*)^2 + \sigma^2 = z^* \left(\sum_{i=1}^{k} \widetilde{a_i} + \sum_{i=k+1}^{N} \frac{\widetilde{a_i}^2}{\widetilde{b_i}} z^* \right), \\
&z^* = \frac{\sum_{i=1}^{k} \widetilde{b_i} + \sigma^2}{\sum_{i=1}^{k} \widetilde{a_i}}, \\
&y_i^* = \frac{\widetilde{a_i}}{\widetilde{b_i}} \frac{\sum_{i=1}^{k} \widetilde{b_i} + \sigma^2}{\sum_{i=1}^{k} \widetilde{a_i}}, \quad k+1 \leq i \leq N.
\end{aligned} \tag{28}$$

By using the above linear equations, we can derive all feasible solutions $\mathbf{y}^*$'s for all k $(1 \leq k \leq N)$ and calculate $f(\mathbf{y})$ for every feasible solution. Then, the optimal solution to the problem (18) is the $\mathbf{y}^*$ corresponding to the largest value of $f(\mathbf{y})$. This is a one-dimensional search process. Moreover, we know that $x_i = \sqrt{\omega_i}$ and $y_i = x_i/\sqrt{Q_i/C_i}$; then

$$w_i^* = \frac{Q_i (y_i^*)^2}{C_i}, \quad (1 \leq i \leq N). \tag{29}$$

By plugging (29) into constraint (10), we get the quadratic inequality about β_i; that is,

$$\beta_i^2 - 2\beta_i \left(P_0 P_{fi} + P_1 P_{di}\right) + P_0 P_{fi} + P_1 P_{di} - \frac{Q_i}{\omega_i} \leq 0. \tag{30}$$

The discriminant is as follows:

$$\Delta = 4\left(P_0 P_{fi} + P_1 P_{di}\right)^2 - 4\left(P_0 P_{fi} + P_1 P_{di} - \frac{Q_i}{\omega_i}\right). \tag{31}$$

Since $Q_i/\omega_i = C_i/(y_i^*)^2$, $C_i = (P_0 P_{fi} + P_1 P_{di}) - (P_0 P_{fi} + P_1 P_{di})^2$, and $(y_i^*)^2 \leq 1$, then $\Delta \geq 0$.

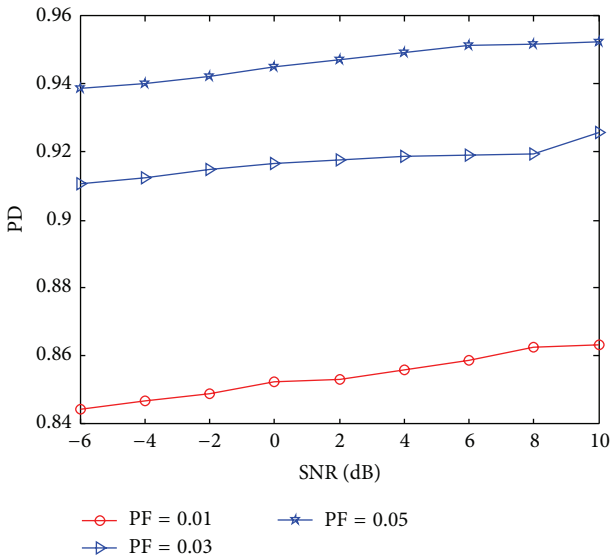

Figure 2: The relationship between SNR and PD ($P_0 = 0.3$).

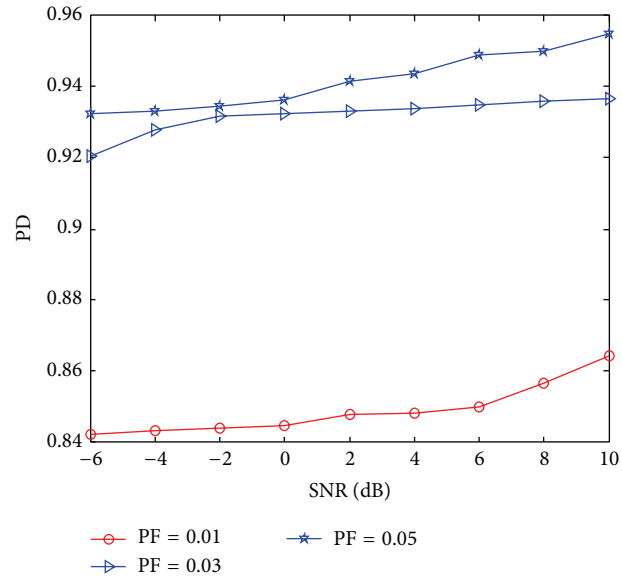

Figure 3: The relationship between SNR and PD ($P_0 = 0.5$).

Assuming that $\beta_i \in R_{\beta_i}$, under the power constraints, we could derive the optimal β_i by solving the following optimization problem:

$$\begin{aligned} &\min \quad E\left[T_i^2(u_i)\right] \\ &\text{s.t.} \quad \beta_i \in R_{\beta_i}, \quad i = 1, 2, \ldots, N. \end{aligned} \tag{32}$$

We note that problem (32) is an easy quadratic extremum problem of β_i.

4. Numerical Simulation and Analysis

To evaluate the performance of the proposed method for power constrained distributed detection fusion using multiple sensors, we do the following numerical simulation. Assume that the detection fusion system is composed of N local sensors and one fusion center, while the parameters are defined as $N = 8$, $\{P_{fi}\} = \{0.05\}$, $Q_i = 100$, and $\{P_{di}\} = \{0.5, 0.3, 0.4, 0.35, 0.5, 0.45, 0.6, 0.7\}$. The signal-to-noise ratio is defined to be $\text{SNR} = 10\log_{10}(1/\sigma^2)$ dB. Each curve is obtained by 10^6 Monte Carlo runs.

Under given prior probability $P_0 = 0.3$ and 0.5, respectively, Figures 2 and 3 illustrate the relationship between SNR and detection probability (PD) corresponding to different probabilities of false alarm (PF). In order to compare the performance with other methods, Figure 4 gives the detection performance of existing likelihood ratio test (LRT) approach which is applied under noisy channel in this paper; as we know, the LRT has the best performance among all the rules under the parallel access channel [19]. When the prior probability $P_0 = 0.3$, Figures 5 and 6 show the receiving operation characteristic (ROC) curves for the proposed method and LRT method at different values of SNR, respectively. Figures 7 and 8 illustrate the relationship between SNR and error detection probability (Pe) corresponding to different PF.

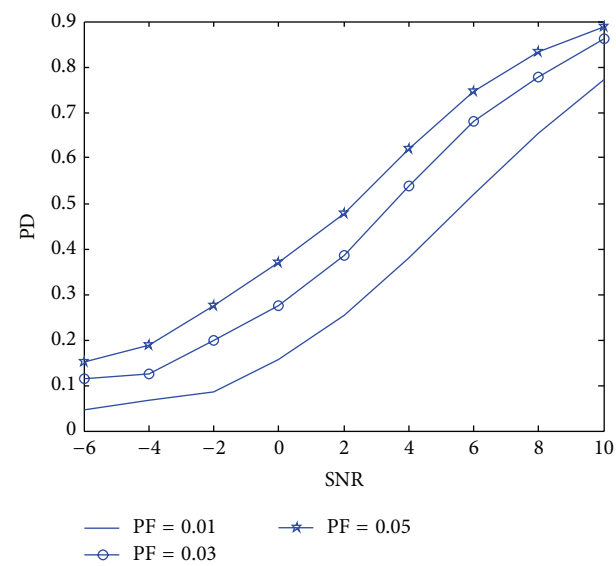

Figure 4: The relationship between SNR and PD (LRT-PAC).

From the simulation results, we can see that the proposed method could significantly improve the detection performance of the fusion system especially in low SNR. From Figures 2–4, we note that the performance of the proposed method is superior to LRT's; moreover, there is a big performance gap between the two kinds of methods. Figures 2 and 3 also indicate that the performance of the proposed method is robust to SNR and prior probability.

From Figures 5 and 6, we can see that under given PF, as the SNR increases, the ROC curves become more convex, which conforms to the traditional detection theory. Figures 5 and 6 also verify that the performance of the proposed method has big superiority to LRT. Figures 7 and 8 show that as the SNR increases, the error detection probability

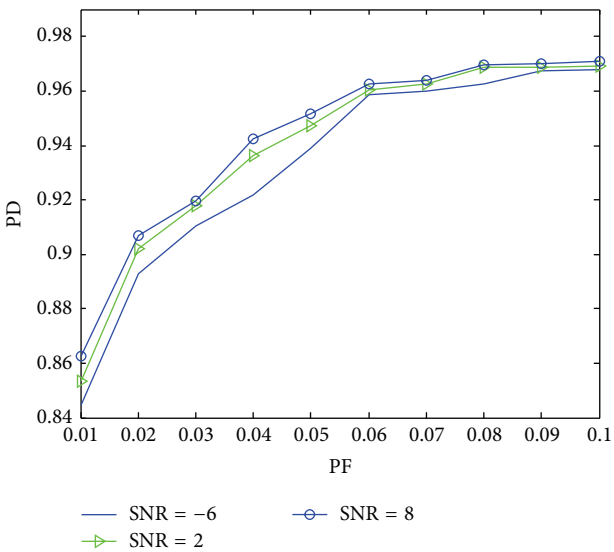

Figure 5: ROC curves ($P_0 = 0.3$).

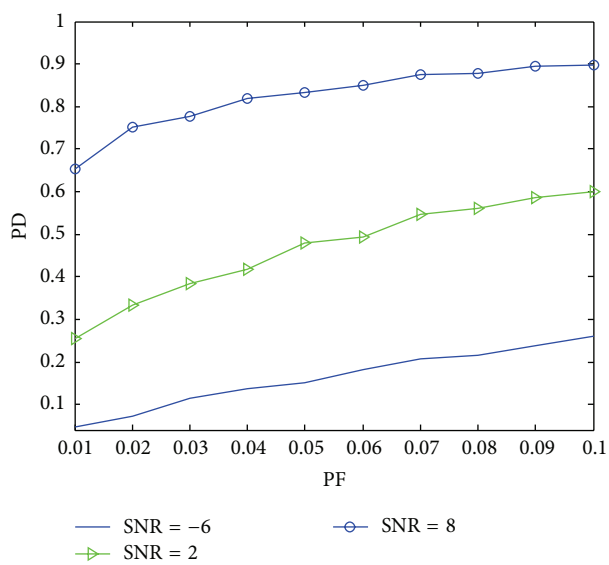

Figure 6: ROC curves (LRT-PAC).

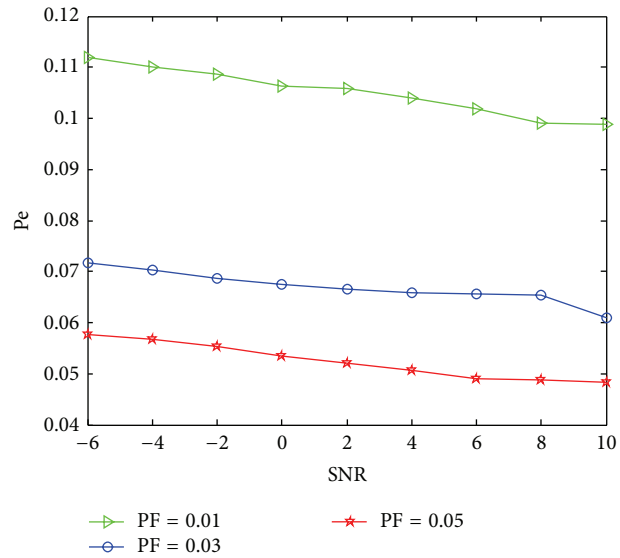

Figure 7: Comparison of error detection probability ($P_0 = 0.3$).

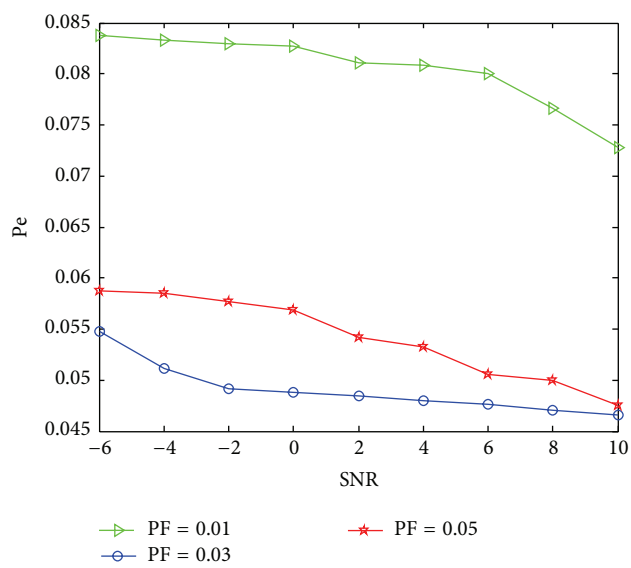

Figure 8: Comparison of error detection probability ($P_0 = 0.5$).

decreases; under given PF, the larger the SNR is, the smaller the Pe will be.

5. Conclusions

The problem of optimal power constrained distributed detection over a noisy multiaccess channel has been studied in this paper. Under the local power constraint, the criterion of deflection coefficient maximization has been used to optimize the performance of fusion system. The closed-form solution to the considered optimization problem has been obtained. Numerical simulation has been carried out to verify the performance of the proposed new method, which shows that, under the local power constraints, the detection performance could be improved and the error probability could be decreased effectively for a given low false alarm probability. We also showed that the proposed new method has a robust detection performance for broad SNR region and outperforms LRT which is utilized for the parallel access channel.

Conflict of Interests

The authors declare that there is no conflict of interests regarding the publication of this paper.

Acknowledgments

This work is supported by the Zhejiang Provincial Natural Science Foundation of China under Grant no. LY13F010006,

the Natural Science Foundation of China under Grant no. 61202171, the Program for Zhejiang Leading Team of Science and Technology Innovation under Grant no. 2011R50019, and the Zhejiang Provincial International Science and Technology Cooperation Program of China under Grant no. 2012C24019. The authors gratefully acknowledge the anonymous reviewers for their helpful comments and suggestions that improved the presentation of this work.

References

[1] G. Fabeck and R. Mathar, "Chernoff information-based optimization of sensor networks for distributed detection," in *Proceedings of the 9th IEEE International Symposium on Signal Processing and Information Technology (ISSPIT '09)*, pp. 606–611, 2009.

[2] L. Shu, J. Lloret, J. J. P. C. Rodrigues, and M. Chen, "Editorial: distributed intelligence and data fusion for sensor systems," *IET Communications*, vol. 5, no. 12, pp. 1633–1636, 2011.

[3] X. Zhu, H. Zhang, D. Cao, and Z. Fang, "Robust control of integrated motor-transmission powertrain system over controller area network for automotive applications," *Mechanical Systems and Signal Processing*, 2014.

[4] H. Zhang, X. Liu, J. Wang, and H. R. Karimi, "Robust H_∞ sliding mode control with pole placement for a fluid power electrohydraulic actuator (EHA) system," *The International Journal of Advanced Manufacturing Technology*, vol. 73, no. 5–8, pp. 1095–1104, 2014.

[5] C. R. Berger, M. Guerriero, P. Willett, and S. Zhou, "PAC vs. MAC for decentralized detection using noncoherent modulation," *IEEE Transactions on Signal Processing*, vol. 57, no. 9, pp. 3562–3575, 2009.

[6] K. Liu and A. M. Sayeed, "Type-based decentralized detection in wireless sensor networks," *IEEE Transactions on Signal Processing*, vol. 55, no. 5, pp. 1899–1910, 2007.

[7] G. Mergen, V. Naware, and L. Tong, "Asymptotic detection performance of type-based multiple access over multiaccess fading channels," *IEEE Transactions on Signal Processing*, vol. 55, no. 3, pp. 1081–1092, 2007.

[8] Y. Lin, B. Chen, and L. Tong, "Distributed detection over multiple access channels," in *Proceedings of the IEEE International Conference on Acoustics, Speech and Signal Processing (ICASSP '07)*, pp. 541–544, April 2007.

[9] J.-F. Chamberland and V. V. Veeravalli, "Asymptotic results for decentralized detection in power constrained wireless sensor networks," *IEEE Journal on Selected Areas in Communications*, vol. 22, no. 6, pp. 1007–1015, 2004.

[10] X. Zhang, H. V. Poor, and M. Chiang, "Optimal power allocation for distributed detection over MIMO channels in wireless sensor networks," *IEEE Transactions on Signal Processing*, vol. 56, no. 9, pp. 4124–4140, 2008.

[11] S. K. Jayaweera, "Large sensor system performance of decentralized detection in noisy, bandlimited channels," in *Proceedings of the IEEE 61st Vehicular Technology Conference (VTC '05)*, vol. 2, pp. 1096–1100, June 2005.

[12] T. Wimalajeewa and S. K. Jayaweera, "Optimal power scheduling for correlated data fusion in wireless sensor networks via constrained PSO," *IEEE Transactions on Wireless Communications*, vol. 7, no. 9, pp. 3608–3618, 2008.

[13] C. R. Berger, P. Willett, S. Zhou, and P. F. Swaszek, "Deflection-optimal data forwarding over a Gaussian multiaccess channel," *IEEE Communications Letters*, vol. 11, no. 1, pp. 1–3, 2007.

[14] F. Li and J. S. Evans, "Optimal strategies for distributed detection over multiaccess channels," in *Proceedings of the IEEE International Conference on Acoustics, Speech and Signal Processing (ICASSP '08)*, pp. 2417–2420, Las Vegas, Nev, USA, April 2008.

[15] Z. Xu, J. Huang, and Q. Zhang, "New method for detection fusion of MAC based on DCM and NP rule," *Journal of Systems Engineering and Electronics*, vol. 23, no. 4, pp. 612–617, 2012.

[16] W. Li and H. Dai, "Distributed detection in wireless sensor networks using a multiple access channel," *IEEE Transactions on Signal Processing*, vol. 55, no. 3, pp. 822–833, 2007.

[17] M. K. Steven, *Fundamentals of Statistical Signal Processing: Detection Theory*, Prentice Hall, Englewood Cliffs, NJ, USA, 1998.

[18] H. Sadeghi, P. Azmi, and H. Arezumand, "Cyclostationarity-based soft cooperative spectrum sensing for cognitive radio networks," *IET Communications*, vol. 6, no. 1, pp. 29–38, 2012.

[19] B. Chen, L. Tong, and P. K. Varshney, "Channel-aware distributed detection in wireless sensor networks," *IEEE Signal Processing Magazine*, vol. 23, no. 4, pp. 16–26, 2006.

Hindawi Publishing Corporation
Mathematical Problems in Engineering
Volume 2015, Article ID 195390, 13 pages
http://dx.doi.org/10.1155/2015/195390

Research Article

Distributed Modeling and Control of Large-Scale Highly Flexible Solar-Powered UAV

Rui Wang,[1] Zhou Zhou,[1] Xiaoping Zhu,[2] and Xiaoping Xu[1]

[1] *School of Aeronautics, Northwestern Polytechnical University, Xi'an 710072, China*
[2] *Institute of UAV, Northwestern Polytechnical University, Xi'an 710072, China*

Correspondence should be addressed to Rui Wang; wangrui@nwpu.edu.cn

Received 16 January 2015; Revised 27 March 2015; Accepted 16 April 2015

Academic Editor: Jaromir Horacek

Copyright © 2015 Rui Wang et al. This is an open access article distributed under the Creative Commons Attribution License, which permits unrestricted use, distribution, and reproduction in any medium, provided the original work is properly cited.

The modeling, stability, and control characteristics of a large scale highly flexible solar-powered UAV with distributed all-span multielevons were presented. A geometrically nonlinear intrinsic beam model was introduced to establish the structural/flight dynamics coupled equation of motion (EOM); based on it, the explicit decoupled linear flight dynamics and structural dynamics EOM were derived through mean axis theory. Undeformed, deformed, and flexible models were compared through trimming and modal analysis. Since the deformation of wing has increased the UAV's moment of inertia about the pitch axis, the frequency of short period mode has obviously decreased for the deformed model. The serious coupling between short period mode and 1st bending mode also significantly influences the roots of short period mode of flexible model. So flexible model was the only one which is able to accurately estimate the flight dynamics behaviors and was selected as the later control model. Forty distributed elevons and LQG/LTR controller were employed to control the attitude and suppress the aeroelastic deformation of the UAV simultaneously. The dynamics performance, robustness, and simulation results show that they were suitable for large scale highly flexible solar-powered UAV.

1. Introduction

The wing of high aspect-ratio solar-powered UAV is highly flexible and the surface density of structure is much lower than other kinds of aircraft, which may lead to the huge scale of solar-powered UAV in order to carry sufficient payload. These characteristics will lead to significant geometrically nonlinear aeroelastic deformation during flight and strong coupling between aeroelasticity and flight dynamics. If these issues have not been taken into full account, large error will occur. One of the key recommendations from the flight mishap investigation of the most famous solar-powered UAV "Helios" was to "develop more advanced, multidisciplinary (structures, aeroelastic, aerodynamics, atmospheric, materials, propulsion, controls, etc) "time-domain" analysis methods appropriate to highly flexible, "morphing" vehicles" [1].

In the modeling of "morphing" vehicles, fruitful works have been presented by Hodges, Cesnik, and their coworkers. The analysis method of Hodges et al. underlying NATASHA (Nonlinear Aeroelastic Trim And Stability of HALE Aircraft), a computer program that is based on geometrically exact, fully intrinsic beam equations and a finite-state induced flow model [2–4]. The University of Michigan's Nonlinear Aeroelastic Simulation Toolbox (UM/NAST) is developed by Cesnik and his coworkers [5, 6], which includes nonlinear strain-based beam model, unsteady aerodynamics with simplified stall models, and a six-degrees-of-freedom flight dynamic formulation.

In the study of flight dynamics of highly flexible UAV, [2] found that the behavior is distinctly different from that of a rigid aircraft while taking into account the flexibility effects. Because the low-frequency modes of structure are completely coupled to the flight dynamics mode, the phugoid as well as the short period mode is affected by wing flexibility significantly. Reference [3] furthered the study, the paper presented a theoretical basis for the flight dynamic response estimation of a highly flexible flying wing, multiple engines, and multiple control surfaces are taken into account. The results show that the phugoid mode may become unstable during large

dihedral angles caused by large mass of payload pod. The pair of complex-conjugate short period roots merges to become two real roots. This is because the deformed "U"-shape leads to an order-of-magnitude increase in the pitch moment of inertia and so there is corresponding decrease in the frequency. Thus, this highly flexible aircraft does not show a classical short-period mode in its deformed state. Similar studies by Raghavan and Patil [4] and Su and Cesnik [5] confirmed this result. All the references paid attention to the nonlinear model and the results analysis, but the modeling of linear dynamics was ignored.

In [7], an optimal Static Output Feedback controller was designed for flutter suppression and gust load alleviation. However, only an elevon on the wing tip was employed in the controller, and the performance was highly dependent on sensor selection and placement.

In [8, 9], dynamic inversion control laws were presented for the trajectory control for Very Flexible Aircraft (VFA). However, in the use of dynamic inversion, there is an assumption that the stability and control derivatives remain fairly constant during the flight. This is not the case with highly flexible UAV.

In [10], a reduced-order H_∞ controller was employed to control a high speed civil transport aircraft, and the results implied that the reduced-order H_∞ controller was robust in the presence of unstructured uncertainty arising due to the model reduction error. However, the reduced order controller is weakly robust when employed to control the full-order model with parametric uncertainty.

LQG/LTR is another popular robust control method. The primary objective of LQG/LTR is to recover the robustness of LQG, an excellent full-state feedback robust controller. The procedure of LQG/LTR method is as follows: firstly, design a target feedback loop, which satisfies desired frequency performance, such as disturbance rejection and uncertainty deviation of the unmodeled dynamics, and then design a model based compensator to recover the properties of the target feedback loop [11]. LQG/LTR has been used widely in flight control, but only a few references are concentrated on the highly flexible aircraft.

In [12], an adaptive LQG/LTR controller was employed to control a very flexible aircraft, but the dynamics model was greatly simplified to capture only the unstable phugoid mode, and there were only 3 traditional control effectors, throttle, elevator, and aileron, available for the controller.

The large scale highly flexible UAV discussed in this paper is shown in Figure 1. It is equipped with 8 propulsion system nacelles (including secondary batteries, electrical motor, and propeller) and 5 vertical tails. The span is 70 m and the mean aerodynamics chord is 2.44 m. In order to enhance the control ability, trailing-edge elevon spans the entire wing. Similar to the Helios [1], the elevon is divided into 40 distributed parts to release the notable aeroelastic deformation caused by large scale highly flexible wing.

For the aeroelastic flight dynamics analysis of such a UAV, most papers ignored the aerodynamics force distribution characteristic along the span and assumed the center of gravity (CG), elastic center (EC), and aerodynamics center (AC) to be coincident for simplification. In this paper, a more practical UAV model is proposed, in which the AC and EC is separated, the 3D quasisteady aerodynamics force is considered, and aerodynamics derivatives in every wing sections are derived for accuracy. In order to get a more accurate characteristic of solar-powered UAV, the mass parameters derived from conceptual design are employed, shown in Table 1.

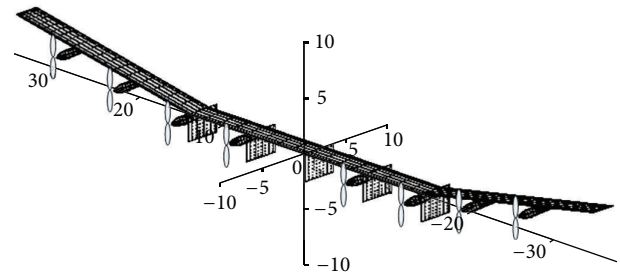

Figure 1: High aspect-ratio highly flexible solar-powered UAV.

Table 1: The mass parameters of high aspect-ratio solar-powered UAV.

	Coefficient of mass	CG (from leading edge)	Elastic center
Structure	0.3	35%	35%
Solar array	0.15	45%	/
Propulsion system	0.5	0%	/
Payload	0.05	(at the CG of UAV)	/

In this paper, a nonlinear coupled structural and flight dynamics model based on geometrically nonlinear intrinsic beam was established first, and then its explicit linear dynamics model is derived for decoupled dynamics modal analysis by mean axis theory. At last, a LQG/LTR controller is designed with distributed 40 elevons for attitude control and aeroelastic deformation suppression for the large-scale highly flexible solar-powered UAV.

2. Modeling of Nonlinear Structural/Flight Dynamics

2.1. Structural Dynamics Model. The geometrically nonlinear structural dynamics and flight dynamics equations are based on the intrinsic beam equation derived by Hodges et al. shown as follows [3, 13]:

$$\dot{\overline{P}} + \widetilde{\overline{\Omega}}\,\overline{P} = F' + \widetilde{\overline{K}}\,\overline{F} + \overline{f},$$

$$\dot{\overline{H}} + \widetilde{\overline{\Omega}}\,\overline{H} + \widetilde{\overline{V}}\,\overline{P} = M' + \widetilde{\overline{K}}\,\overline{M} + \left(\widetilde{e}_2 + \widetilde{\overline{\gamma}}\right)\overline{F} + \overline{m},$$

$$\dot{\overline{\gamma}} = V' + \widetilde{\overline{K}}\,\overline{V} + \left(\widetilde{e}_2 + \widetilde{\overline{\gamma}}\right)\overline{\Omega},$$

$$\dot{\overline{\kappa}} = \Omega' + \widetilde{\overline{K}}\,\overline{\Omega},$$

$$\dot{\hat{P}} + \widetilde{\widehat{\Omega}}\widehat{P} = \widehat{f},$$
$$\dot{\hat{H}} + \widetilde{\widehat{\Omega}}\widehat{H} = \widehat{m}. \tag{1}$$

The equations above are the core of structural dynamics, but they still cannot be used for the analysis of aerodynamics and flight dynamics without the relationship between displacements and rotations. Hence, the kinematics motion must be established to obtain the relationship between strain and displacement. The position vector of the origin of the deformed beam frame (B-) in the root frame (R-) and their rotational relationship are [14]:

$$\{r_B\}_R = C_{RB}(\gamma + e_2),$$
$$C'_{BR} = -\left(\widetilde{\kappa} + \widetilde{k}\right) C_{BR}. \tag{2}$$

The spatial derivatives can be replaced by the following equations, namely, central difference method [15]:

$$x'_i = \frac{1}{2h}(x_{i+1} - x_{i-1}),$$
$$x''_i = \frac{1}{h^2}(x_{i+1} - 2x_i + x_{i-1}),$$
$$x'''_i = \frac{1}{2h^3}(x_{i+2} - 2x_{i+1} + 2x_{i-1} - x_{i-2}),$$
$$x''''_i = \frac{1}{h^4}(x_{i+2} - 4x_{i+1} + 6x_i - 4x_{i-1} + x_{i-2}), \tag{3}$$

where h is the distance between two points.

The mean axis is applied to simplify and linearize the equation of motion. In the mean axis (M-) frame, the linear and angular momentums due to elastic deformation are zero at every instant, which eliminates the coupling between the rigid body modes and the structural mode and results in a reduced-order system with only six degrees-of-freedom.

Since the equations in (1) are written in the B-frame, the equations of motion of rigid mode can be derived by premultiplying all terms by C_{MB} to obtain components in the M- frame and integrating in it along the beam axis as follows [16]:

$$M_{\text{tot}}\left(\left\{\dot{V}_{cg}\right\}_M + \{\Omega_M\}_M \times \left\{V_{cg}\right\}_M\right) = \sum C_{MB_i}\{f_n\}_{B_i}, \tag{4}$$

$$\begin{aligned}&\left\{I_{cg}\right\}_M\left\{\dot{\Omega}_M\right\}_M + \left\{\dot{I}_{cg}\right\}_M\{\Omega_M\}_M + \{\Omega_M\}_M \\ &\quad\times\left(\left\{I_{cg}\right\}_M\{\Omega_M\}_M\right) = \sum\{r\}_M \times C_{MB_i}\{f_n\}_{B_i} \\ &\quad+\sum C_{MB_i}\{m_i\}_{B_i} - \sum C_{MB_n}\{I_i\}_B\left\{\dot{\Omega}_i\right\}_B \\ &\quad-\sum \dot{C}_{MB_n}\{I_i\}_B\{\Omega_i\}_B,\end{aligned} \tag{5}$$

where the linear and angular velocities are defined as

$$\left\{V_{cg}\right\}_M = \frac{1}{M_{\text{tot}}}\sum \mu_i C_{MB_i} V_i,$$
$$\{\Omega_M\}_M = \left\{I_{cg}\right\}_M^{-1}\sum\left\{r_{B_iM}\right\}_M \times \mu_i C_{MB_i} V_i. \tag{6}$$

The relationship of coordinate transformation is

$$C_{MB} = C_{Mg}C_{gB}. \tag{7}$$

The total moment of inertia of the UAV is solved as follows:

$$\left\{I_{cg}\right\}_M = \sum\left[C_{MB_i}I_iC_{MB_i}^T + \left(r_i^T r_i E - r_i r_i^T\right)m_i\right]. \tag{8}$$

If the relative position of the rigid body does not vary significantly, $\{\dot{I}_{cg}\}_M$ can be approximated to be zero. If the motion of the UAV is limited to longitudinal only, the last two terms at the right hand of (5) can also be equal to zero.

2.2. Force and Moment Model

2.2.1. Internal Forces and Moments Model. The wing of solar-powered UAV may undergo large deformations during normal flight, while the strain is small, exhibiting geometrically nonlinear behaviors. Therefore, the small-strain assumption is suitable for this problem. The internal forces and moments are linearly related to the strains and curvatures, shown in (9) [17]:

$$\begin{bmatrix} F \\ M \end{bmatrix} = \begin{bmatrix} R & S \\ S^T & T \end{bmatrix}^{-1}\begin{bmatrix} \gamma \\ \kappa \end{bmatrix}. \tag{9}$$

The wing is assumed to be a prismatic and isotropic beam with the shear center and tension axis coincident with the reference axis, by which the above equation can be derived as follows:

$$\begin{bmatrix} F_x \\ F_y \\ F_z \end{bmatrix} = \begin{bmatrix} GA_x & & \\ & EA & \\ & & GA_z \end{bmatrix}\begin{bmatrix} \gamma_x \\ \gamma_y \\ \gamma_z \end{bmatrix},$$
$$\begin{bmatrix} M_x \\ M_y \\ M_z \end{bmatrix} = \begin{bmatrix} EI_x & & \\ & GJ & \\ & & EI_z \end{bmatrix}\begin{bmatrix} \kappa_x \\ \kappa_y \\ \kappa_z \end{bmatrix}, \tag{10}$$

where G represents the shear modulus; E represents Young's modulus; J represents the torsional constant; I_x and I_z represent the area moment of inertia along the x and z direction.

2.2.2. Aerodynamics Model. In order to analyze the motion of the flexible UAV exactly, the aerodynamic force of vibrating-wings should be analyzed. Unsteady aerodynamics models that are useful for aeroelastic analysis are usually Theodorsen unsteady aerodynamic model and finite state induced flow model of Peters and Cao [18]. The Theodorsen model is derived in frequency domain, but it can be converted into time domain by rational function approximation. The finite state induced flow model is derived in time domain, and it can be used in a state-space model easily. These two types of aerodynamics are equivalent and can be derived from one another through Laplace and Fourier transforms.

In this paper, the Theodorsen unsteady aerodynamics model is adopted, which has been used widely for airfoil or

large aspect ratio wings, and its quasisteady form is relative to the traditional aerodynamics derivatives used in rigid aircraft.

For the Theodorsen model, the wing section is described in Figure 2, where the definitions of points are as follows: LE: leading edge, G: center of gravity of the wing section, g: center of gravity of the UAV, A: aerodynamics center, M: middle point of chord, E: elastic center, the position in x direction of s-frame is $\bar{a}b$, C: control point of unsteady aerodynamics, and D: aerodynamics center of control surface.

The definitions of variables are as follows: α: angle of attack, b: length of 1/2 chord, u: deformation defined in B-frame, and s-frame: the origin is at LE, x along the chord and pointing to the trailing edge, z perpendicular to x and point up.

The formulation of Theodorsen unsteady aerodynamics force and its moment to the elastic center are

$$\begin{aligned} C_L &= \pi b\left(\frac{\dot{\alpha}}{V}+\frac{\ddot{h}}{V^2}-\frac{b\bar{a}\ddot{\alpha}}{V^2}\right)+2\pi C(k)\left(\frac{\dot{h}}{V}+\alpha\right.\\ &\quad\left.+b\left(\frac{1}{2}-\bar{a}\right)\frac{\dot{\alpha}}{V}\right),\\ C_{M,E} &= \frac{\pi}{2}\left(\frac{b\bar{a}\ddot{h}}{V^2}-\frac{b^2}{V^2}\left(\frac{1}{8}+\bar{a}^2\right)\ddot{\alpha}-\left(\frac{1}{2}-\bar{a}\right)\frac{b\dot{\alpha}}{V}\right)\\ &\quad+\pi\left(\bar{a}+\frac{1}{2}\right)C(k)\left(\frac{\dot{h}}{V}+\alpha+b\left(\frac{1}{2}-\bar{a}\right)\frac{\dot{\alpha}}{V}\right)\\ &= \pi b\left(\frac{\dot{\alpha}}{V}\left[-\left(\frac{1}{4}-\frac{1}{2}\bar{a}\right)\right]+\frac{\ddot{h}}{V^2}\left[\frac{1}{2}\bar{a}\right]\right.\\ &\quad\left.-\frac{b\bar{a}\ddot{\alpha}}{V^2}\left[\left(\frac{1}{8}+\bar{a}^2\right)\frac{1}{2}b\right]\right)+\left[\left(\frac{1}{4}+\frac{1}{2}\bar{a}\right)\right]2\pi C(k)\\ &\quad\cdot\left(\frac{\dot{h}}{V}+\alpha+b\left(\frac{1}{2}-\bar{a}\right)\frac{\dot{\alpha}}{V}\right), \end{aligned} \tag{11}$$

where 2π is the theoretic lift slope of airfoil, the steady aerodynamics center is at 1/4 chord and unsteady aerodynamics center and its control point is at 3/4 chord. All these variables can be replaced by the actual airfoil data. $C(k)$ is the Theodorsen function, produced by circulation. $k = \omega b/V$ is the reduced frequency. If k is low enough and $C(k) = 0$, the flow will become quasisteady. As the flight dynamics and control of solar-powered UAV on low frequency is more concerned, quasisteady flow assumption is adopted for analysis in this paper.

By applying the quasisteady flow assumption and ignoring the terms in high orders, (11) becomes

$$\begin{aligned} C_L &= C_{L\alpha}\left(\alpha+\frac{\dot{u}_z}{V}+(1-\bar{a})\frac{b\dot{\alpha}}{V}\right),\\ C_{M,E} &= C_{L\alpha}\left(\frac{1}{4}+\frac{1}{2}\bar{a}\right)\left(\alpha+\frac{\dot{u}_z}{V}\right)\\ &\quad+C_{L\alpha}\left(\frac{1}{4}\bar{a}-\frac{1}{2}\bar{a}^2\right)\frac{b\dot{\alpha}}{V}, \end{aligned} \tag{12}$$

where the airfoil data have been replaced by the actual ones.

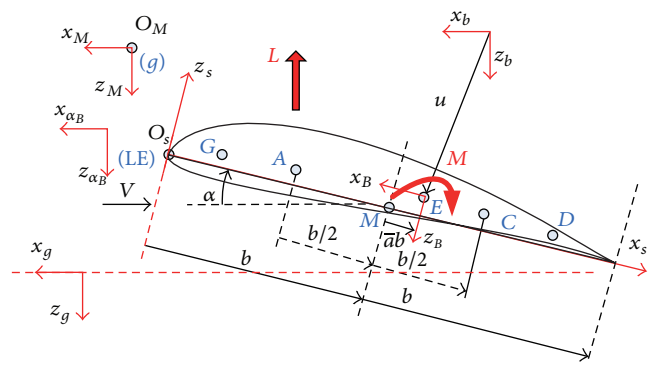

Figure 2: Illustration of wing section, coordinate systems, and variables.

The physical meaning of the above equations is that the lift of wing section is produced by steady and quasisteady flow together, and the steady part is produced by the angle of attack α of the section and its increment $\dot{u}_z/V_0$ caused by relative elastic deformation. The quasisteady part is caused by $\dot{\alpha}$.

It should be noted that, in most cases, the angles of attack in every sections (denoted as α_B) are not easy to be measured directly. Hence, the relationship between α_B and incident angle at the CG of UAV expressed in a_M-frame (notated as α_M and β_M) can be calculated as

$$\begin{aligned} -\sin\alpha_B &= C_{a_BB}(3,1) = [0,0,1]\\ &\quad\cdot C_{a_Ba_M}C_{a_MM}C_{MB}[1,0,0]^T\\ &= (\cos\alpha_M\sin\beta_M\sin\varphi_{BM,x}-\sin\alpha_M\cos\varphi_{BM,x})\\ &\quad\cdot(\cos\varphi_{BM,y}\cos\varphi_{BM,z})+(\cos\beta_M\sin\varphi_{BM,x})\\ &\quad\cdot(\cos\varphi_{BM,y}\sin\varphi_{BM,z})\\ &\quad-(\sin\alpha_M\sin\beta_M\sin\varphi_{BM,x}+\cos\alpha_M\cos\varphi_{BM,x})\\ &\quad\cdot\sin\varphi_{BM,y}, \end{aligned} \tag{13}$$

where φ_{BM} is the Euler angle from B-frame to M-frame and the subscripts x, y, and z represent the 3 components of Euler angle, which correspond to the roll, pitch, and yaw angle of the aircraft, respectively.

If the wing rotates along the x axis only, (13) can be simplified as

$$\begin{aligned} \sin\alpha_B &= -\cos\alpha_M\sin\beta_M\sin\varphi_{BM,x}\\ &\quad+\sin\alpha_M\cos\varphi_{BM,x}. \end{aligned} \tag{14}$$

The magnitude of drag is small, and its influence on the flight dynamics characteristics is limited, so the drag on every wing section can be divided from the total drag. The expression of total drag is

$$C_D = C_{D0}+a_{\text{induce}}C_L^2. \tag{15}$$

The aerodynamics force expressed in a_M-frame can be derived by the following axis conversion:

$$\{f_a\}_{a_M} = C_{a_M a_B} \{f_a\}_{a_B}, \tag{16}$$

where

$$C_{a_M a_B} = \begin{bmatrix} 1 & 0 & 0 \\ 0 & \cos\varphi_{BM,x} & -\sin\varphi_{BM,x} \\ 0 & \sin\varphi_{BM,x} & \cos\varphi_{BM,x} \end{bmatrix}. \tag{17}$$

Substituting (17) into (16), the nondimensional force coefficients at the a_M-coordinate are derived as follows:

$$\begin{aligned} \{C_D\}_{a_M} &= \{C_D\}_{a_B}, \\ \{C_C\}_{a_M} &= \{C_L\}_{a_B} \sin\varphi_{BM,x}, \\ \{C_L\}_{a_M} &= \{C_L\}_{a_B} \cos\varphi_{BM,x}. \end{aligned} \tag{18}$$

Changing the reference point of moment into CG, the aerodynamics moment to CG of UAV is

$$\{m_a\}_M = \{m_{a,0}\}_M + \{r\}_M \times \left(C_{Ma_M} \{f_a\}_{a_M}\right). \tag{19}$$

It should be noted that the method proposed in this section can be used to calculate either the aerodynamics force or the moment of vertical tails, although the incident angle and Euler angle may vary significantly.

2.2.3. 3D Effect Correction of Aerodynamics. In the analysis of the aeroelastic flight dynamics of solar-powered UAV, most papers ignored the aerodynamics force distribution characteristics along the wing span and considered the flow condition to be same as the airfoils. Actually, the wing span is finite, which will make the flow of each section affect each other; that is to say, 3D effect must be considered for precision. In this paper, 3D effect is corrected based on lifting-line theory, and it applies well to wings that have aspect ratio greater than 5 and sweep angle less than 20 degrees.

According to lifting-line theory, the lift of airfoil is determined by effective angle of attack α_{eff}, which is formulated as follows:

$$\alpha_{\text{eff}} = \alpha_{\text{geo}} - \alpha_{\text{ind}}, \tag{20}$$

where α_{geo} and α_{ind} represent geometric and induced angle of attack, respectively.

According to the relationship of trailing vortex and circulation, the equation above becomes

$$\begin{aligned} \alpha_{\text{geo}}(y_0) = {} & \frac{\Gamma(y_0)}{\pi V_\infty c(y_0)} + \alpha_{L=0} \\ & + \frac{1}{4\pi V_\infty} \int_0^l \frac{(d\Gamma/dy)\, dy}{y_0 - y}, \end{aligned} \tag{21}$$

where y_0 is an arbitrary spanwise position on the wing and 2π refers to theoretical lift slope of airfoil, which can be substituted by true airfoil value in the actual computation. Since (21) is a nonlinear integral-differential equation, coordinate transformation method should be applied before solving it for simplification [19].

After solving the circulation distribution $\Gamma(y)$ from (21), the lift distribution can be obtained from the Kutta-Joukowski theorem:

$$L(y_0) = \rho V_\infty \Gamma(y_0). \tag{22}$$

By repeating the above steps for different geometric angles of attack and taking a derivative, one can obtain the lift slope of each cross section of the wing considering 3D effect correction.

3. Model Linearization

3.1. Linearized Aerodynamics. The movement of wing section is separated into two parts: the rigid movement of UAV and the elastic movement of structure. Then, the lift coefficients applied on the wing section can be deployed in the a_B-frame as follows:

$$\begin{aligned} & C_{L\alpha}, \\ & C_{Lq} = 0.5C_{L\alpha} + 2C_{L\alpha}\left(\frac{3}{4} - \{\overline{x}_g\}_s\right), \\ & C_{Lp} = -2C_{L\alpha}\frac{\{y_g\}_s}{l}, \\ & C_{L\varphi_y} = C_{L\alpha}, \\ & C_{L\dot{u}_z} = C_{L\alpha}\frac{1}{V}, \\ & C_{L\dot{\varphi}_y} = C_{L\alpha}(1 - \overline{a})\frac{c}{2V}. \end{aligned} \tag{23}$$

It should be noted that the variables in the above equations are measured in the a_B-frame and B-frame.

According to the 2nd equation of (12), the aerodynamics moment to the elastic center (EC) is

$$\begin{aligned} & C_{m\alpha,E} = -C_{L\alpha}\{\overline{x}_{AE}\}_B \approx C_{L\alpha}\left(\frac{1}{4} + \frac{1}{2}\overline{a}\right), \\ & C_{mq,E} = 0.5C_{L\alpha}\{\overline{x}_{CE}\}_B + 2C_{L\alpha}\{\overline{x}_{Cg}\}_s\{\overline{x}_{AE}\}_B, \\ & C_{mp,E} = -2C_{L\alpha}\frac{\{y_g\}_s}{l}\{\overline{x}_{AE}\}_B, \\ & C_{m\varphi_y,E} = C_{m\alpha,E}, \\ & C_{m\dot{u}_z,E} = C_{m\alpha,E}\frac{1}{V}, \\ & C_{m\dot{\varphi}_y,E} = C_{L\alpha}\left(\frac{1}{4}\overline{a} - \frac{1}{2}\overline{a}^2\right)\frac{c}{2V}. \end{aligned} \tag{24}$$

From the 2nd equation of (18), the difference of lift expressed in the a_M-frame and a_B-frame is only $\cos\varphi_{BM,x}$. Hence, by replacing $C_{L\alpha}$ in (23) with $C_{L\alpha}\cos\varphi_{BM,x}$, the lift expressed in the a_B-frame will be derived.

Substituting the expression of lift at a_M-frame into (19), the pitch moment about the center of gravity of the UAV can be obtained as follows:

$$\begin{aligned}
C_{m\alpha,g} &= -C_{L\alpha}\cos\varphi_{MB,x}\left(\{\overline{x}_A\}_s - \{\overline{x}_g\}_s\right),\\
C_{mq,g} &= C_{L\alpha}\cos\varphi_{MB,x}\left(0.5\{\overline{x}_{Cg}\}_B - 2\{\overline{x}_{Cg}\}_B^{\ 2}\right),\\
C_{mp,g} &= -2C_{L\alpha}\frac{\{y_g\}_s}{l}\{\overline{x}_{Cg}\}_B,\\
C_{m\varphi_y,g} &= C_{m\alpha,g},\\
C_{m\dot{u}_z,g} &= C_{m\alpha,g}\frac{1}{V},\\
C_{m\dot{\varphi}_y,g} &= -2C_{L\alpha}\cos\varphi_{MB,x}\left(\frac{1}{2} - \{\overline{x}_g\}_s\right)^2\frac{b}{V}.
\end{aligned} \tag{25}$$

3.2. Linearized Flight Dynamics Equation. It can be found that the form of (4) and (5) is similar to that of flight dynamics equations of normal rigid vehicles. Hence, they can also be linearized by small disturbance method and written into two sets of equations: longitudinal and lateral-directional. Different from the normal rigid vehicle, the external force such as aerodynamics, thrust, and gravity are related to rigid motion and elastic motion for elastic model. The linear equation of flight dynamics for elastic UAV is

$$\dot{\mathbf{x}}_r = \mathbf{A}_r\mathbf{x}_r + \mathbf{B}_r\mathbf{u}_r + \mathbf{A}_{re}\mathbf{x}_e, \tag{26}$$

where $\mathbf{x}_r$ is the independent variable of rigid motion, with $\mathbf{x}_r = [v, \alpha, q, \theta]^T$ in longitudinal equations; $\mathbf{x}_e = [\dot{u}_x^{\ T}, \dot{u}_z^{\ T}, \dot{\varphi}_y^{\ T}, u_x^{\ T}, u_z^{\ T}, \varphi_y^{\ T}]^T$ is the independent variable of elastic motion; $\mathbf{u}_r$ is the control variable of rigid motion, $\mathbf{u}_r = [\delta_{e,1}\cdots\delta_{e,40}, \delta_t]^T$; that is, all the elevons can be controlled independently, but all throttles act conformably again for simplification; $\mathbf{A}_r$ is the same as conventional rigid vehicles as shown in [20]; and $\mathbf{B}_r$ is similar to the rigid model also, but the column is equal to the length of $\mathbf{u}_r$; $\mathbf{A}_{re}$ is the influence matrix of elastic motion to rigid motion, for longitudinal motion:

$$\mathbf{A}_{re} = \begin{bmatrix} 0_{1\times n} & 0_{1\times n} & 0_{1\times n} & 0_{1\times n} & 0_{1\times n} & 0_{1\times n}\\ 0_{1\times n} & Z_{\dot{u}_z,1}\cdots Z_{\dot{u}_z,n} & Z_{\dot{\varphi}_y,1}\cdots Z_{\dot{\varphi}_y,n} & 0_{1\times n} & 0_{1\times n} & Z_{\varphi_y,1}\cdots Z_{\varphi_y,n}\\ 0_{1\times n} & M_{\dot{u}_z,1}\cdots M_{\dot{u}_z,n} & M_{\dot{\varphi}_y,1}\cdots M_{\dot{\varphi}_y,n} & 0_{1\times n} & 0_{1\times n} & M_{\varphi_y,1}\cdots M_{\varphi_y,n}\\ 0_{1\times n} & 0_{1\times n} & 0_{1\times n} & 0_{1\times n} & 0_{1\times n} & 0_{1\times n} \end{bmatrix}. \tag{27}$$

The details of $\mathbf{A}_{re}$ can be found in [21].

3.3. Linearized Structural Dynamics Equation. Ignoring nonlinear coupling terms in (1), and assuming that the translational strain is small and the external moment and the moment of inertia of x and z direction are equal to zero, (1) can be reduced into

$$\begin{aligned}
\mu\dot{V}_x &= EI_z\kappa_z'' + f_x,\\
\mu\dot{V}_z &= -EI_x\kappa_x'' + f_z,\\
I_{yy}\dot{\Omega}_y &= EI_y\kappa_y' + m_z,\\
\dot{\kappa}_x &= V_z'',\\
\dot{\kappa}_y &= \Omega_y',\\
\dot{\kappa}_z &= -V_x',\\
\mu\dot{V}_y &= f_y.
\end{aligned} \tag{28}$$

The equations above can be rearranged into a compact form as follows:

$$\begin{aligned}
\mu\ddot{x} + EI_z x'''' &= f_x,\\
\mu\ddot{z} + EI_x z'''' &= f_z,\\
I_{yy}\ddot{\varphi}_{Bg,y} - GJ_z\varphi_{Bg,y}'' &= m_y,\\
\mu\dot{V}_y &= f_y.
\end{aligned} \tag{29}$$

Since the focus of this paper is the flight dynamics characteristics of the total UAV, the structural dynamics characteristics are used to derive the increment of aerodynamics force caused by aeroelasticity only and many assumptions can be introduced to linearize the equations above for simplification.

Equation (29) can be simplified to the form as in (30) by rewriting in M-frame and assuming that the structural elastic vibrations are small perturbations near the static trim state and the elastic motion in x direction is ignorable. In the case of geometry, it is assumed that the M-frame is parallel to R-frame and the sweep angle of wing is zero. Besides, in mean axis system, the elastic motion is influenced by rigid motion through aerodynamics force only:

$$\begin{aligned}
\mu\{\ddot{u}_x\}_{M,x} + EI_z\{u_x\}_{M,x}'''' &= \cos\varphi_{BM,z}\{f\}_{B,x},\\
\mu\{\ddot{u}_z\}_{M,z} + EI_x\{u_z\}_{M,z}'''' &= \cos\varphi_{BM,x}\{f\}_{B,z},\\
I_{yy}\ddot{\varphi}_{BM,y} - GJ_z\varphi_{BM,y}'' &= \{m\}_{B,y},
\end{aligned} \tag{30}$$

where $\varphi_{BM,y}$ represents the angle between x-axis of B-frame and the oxy plane of M-frame. All variables in (30) are in incremental form and the notation Δ has been neglected for simplification.

Replacing the spatial derivatives by (3), and knowing the fact that the wing tip is free, the boundary conditions can be defined that the bending moments and shear forces at the first and last nodes are zero for the 2nd equation in (30); that is [15],

$$u''_{z,1} = 0,$$
$$u''_{z,n} = 0, \tag{31}$$
$$u'''_{z,1} = 0,$$
$$u'''_{z,n} = 0. \tag{32}$$

Thus, the structural dynamics equation can be derived as follows:

$$M_{u_z}\ddot{u}_z + K_{u_z}u_z = Q_{u_z}, \tag{33}$$

where

$$u_z = \left[u_1 \ \cdots \ u_n\right]^T,$$
$$M_{u_z} = \begin{bmatrix} \mu_1 & & \\ & \ddots & \\ & & \mu_n \end{bmatrix},$$
$$K_{u_z} = \begin{bmatrix} 2 & -4 & 2 & & & & \\ -2 & 5 & -4 & 1 & & & \\ 1 & -4 & 6 & -4 & 1 & & \\ & \ddots & \ddots & \ddots & \ddots & \ddots & \\ & & 1 & -4 & 6 & -4 & 1 \\ & & & 1 & -4 & 5 & -2 \\ & & & & 2 & -4 & 2 \end{bmatrix} * \frac{1}{\Delta l^4}\operatorname{diag}\left(EI_{z,i}\right). \tag{34}$$

For the 2nd equation in (30), it is the same as (33); that is,

$$M_{u_x}\ddot{u}_x + K_{u_x}u_x = Q_{u_x}. \tag{35}$$

For the 3rd equation in (30), the boundary conditions are [15]

$$\varphi'_{BM,y,1} = 0,$$
$$\varphi'_{BM,y,n} = 0. \tag{36}$$

Then, the structural dynamics equation becomes

$$M_{\varphi_y}\ddot{\varphi}_y + K_{\varphi_y}\varphi_y = Q_{\varphi_y}, \tag{37}$$

where

$$\varphi_y = \left[\varphi_{BM,y,1} \ \cdots \ \varphi_{BM,y,n}\right]^T,$$
$$M_{\varphi_y} = \begin{bmatrix} I_1 & & \\ & \ddots & \\ & & I_n \end{bmatrix},$$
$$K_{\varphi_y} = -\begin{bmatrix} -2 & 2 & & & & \\ 1 & -2 & 1 & & & \\ & \ddots & \ddots & \ddots & & \\ & & 1 & -2 & 1 & \\ & & & 2 & -2 & \end{bmatrix} * \frac{1}{\Delta l^2}\operatorname{diag}\left(GJ_i\right). \tag{38}$$

In order to further simplify the linear structural dynamics equations, (33), (35), and (37) can be expanded in the modal coordinate system, and the final form can be derived as follows:

$$\dot{\mathbf{x}}_{ne} = \mathbf{A}_{ne}\mathbf{x}_{ne} + \mathbf{A}_{ner}\mathbf{x}_r + \mathbf{B}_{ne}\mathbf{u}_r, \tag{39}$$

where the independent variables are

$$\mathbf{x}_{ne} = \begin{bmatrix} \dot{\mathbf{x}}_n \\ \mathbf{x}_n \end{bmatrix},$$
$$\mathbf{x}_e = \mu\mathbf{x}_n, \tag{40}$$
$$\mathbf{x}_e = \left[u_x^T, u_z^T, \varphi_y^T\right]^T,$$

where $\mathbf{x}_n$ is the modal displacements of structural elastic motion, which is the symmetric modes for longitudinal motion; μ is the transfer matrix from modal coordinate to physical coordinate.

For longitudinal motion, the coefficient matrices in (39) are

$$A_{ne} = \begin{bmatrix} M_n^{-1}Q_{n1} & M_n^{-1}\left(Q_{n2} - K_n\right) \\ I & 0 \end{bmatrix},$$
$$A_{ner} = \begin{bmatrix} M_n^{-1}Q_{n0} \\ 0 \end{bmatrix},$$
$$B_{ne} = \begin{bmatrix} M_n^{-1}Q_{n3} \\ 0 \end{bmatrix},$$
$$M_n = \mu^T M\mu,$$
$$K_n = \mu^T K\mu,$$
$$Q_{ni} = \mu^T Q_i,$$

$$
\begin{aligned}
Q_{n0} &= \mu^T Q_0, \\
Q_{n1} &= \mu^T Q_1 \mu, \\
Q_{n2} &= \mu^T Q_2 \mu, \\
Q_{n3} &= \mu^T Q_3 \mu,
\end{aligned}
$$

$$
Q_0 = \begin{bmatrix}
X_{v,1} & X_{\alpha,1} & & \\
\vdots & \vdots & 0_{n\times 1} & 0_{n\times 1} \\
X_{v,n} & X_{\alpha,n} & & \\
Z_{v,1} & Z_{\alpha,1} & Z_{q,1} & \\
\vdots & \vdots & \vdots & 0_{n\times 1} \\
Z_{v,n} & Z_{\alpha,n} & Z_{q,n} & \\
M_{v,1} & M_{\alpha,1} & M_{q,1} & \\
\vdots & \vdots & \vdots & 0_{n\times 1} \\
M_{v,n} & M_{\alpha,n} & M_{q,n} &
\end{bmatrix},
$$

$$
Q_1 = \begin{bmatrix}
X_{\dot{u}_x,1} \cdots X_{\dot{u}_x,n} & X_{\dot{u}_z,1} \cdots X_{\dot{u}_z,n} & 0_{n\times 1} \\
Z_{\dot{u}_x,1} \cdots Z_{\dot{u}_x,n} & Z_{\dot{u}_z,1} \cdots Z_{\dot{u}_z,n} & Z_{\dot{\varphi}_y,1} \cdots Z_{\dot{\varphi}_y,n} \\
0_{n\times 1} & M_{\dot{u}_z,1} \cdots M_{\dot{u}_z,n} & M_{\dot{\varphi}_y,1} \cdots M_{\dot{\varphi}_y,n}
\end{bmatrix},
$$

$$
Q_2 = \begin{bmatrix}
0_{1\times n} & 0_{1\times n} & X_{\varphi_y,1} \cdots X_{\varphi_y,n} \\
0_{1\times n} & 0_{1\times n} & Z_{\varphi_y,1} \cdots Z_{\varphi_y,n} \\
0_{1\times n} & 0_{1\times n} & M_{\varphi_y,1} \cdots M_{\varphi_y,n}
\end{bmatrix},
$$

$$
Q_3 = \begin{bmatrix}
X_{\delta_{e,1}} & \cdots & X_{\delta_{e,n}} & X_{\delta_t} \\
Z_{\delta_{e,1}} & \cdots & Z_{\delta_{e,n}} & Z_{\delta_t} \\
M_{\delta_{e,1}} & \cdots & M_{\delta_{e,n}} & M_{\delta_t}
\end{bmatrix}, \tag{41}
$$

where $Z_{\dot{u}_z}$ is related to some derivatives (e.g., $C_{L\dot{u}_z}$). The exact expressions are the same as the derivatives of general flight dynamics equations. More details about them can be referred to [21].

3.4. Total Linearized Equation. Combining (26) and (39), the final total linear equations can be derived as follows:

$$
\begin{aligned}
\dot{\mathbf{x}}_r &= \mathbf{A}_r \mathbf{x}_r + \mathbf{A}_{rne} \mathbf{x}_{ne} + \mathbf{B}_r \mathbf{u}_r, \\
\dot{\mathbf{x}}_{ne} &= \mathbf{A}_{ner} \mathbf{x}_r + \mathbf{A}_{ne} \mathbf{x}_{ne} + \mathbf{B}_{ne} \mathbf{u}_r.
\end{aligned} \tag{42}
$$

The independent variable is

$$
\mathbf{x} = \left[\mathbf{x}_r^T, \mathbf{x}_{ne}^T\right]^T \tag{43}
$$

and the state matrix is

$$
A = \begin{bmatrix} A_r & A_{rne} \\ A_{ner} & A_{ne} \end{bmatrix}. \tag{44}
$$

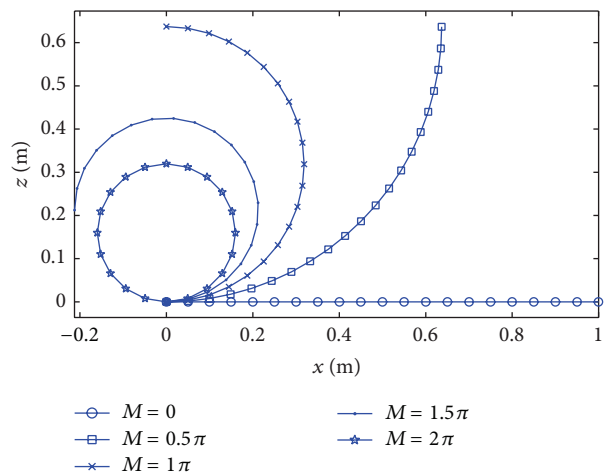

Figure 3: Beam deformation with increasing tip moment.

And the control matrix is:

$$
B = \begin{bmatrix} B_r \\ B_{ne} \end{bmatrix}. \tag{45}
$$

The eigenvalues of the above state matrix are the modal eigenvalues of the elastic UAV considering the coupling of aeroelastic and flight dynamics:

$$
\dot{\mathbf{x}} = \mathbf{A}\mathbf{x} + \mathbf{B}\mathbf{u}. \tag{46}
$$

4. Model Verification

4.1. Geometrically Nonlinear Deformation. In order to validate the effectiveness of the geometrically nonlinear structural model and central difference method proposed in this paper, a cantilever beam with bending rigidity $EI = 1$ and length $l = 1\,\mathrm{m}$ is employed. While applying increasing moment M at the tip of the beam, the deformation of the beam is shown in Figure 3. It can be seen that while $M = 2\pi$, the angular displacement is 2π, the tip coincides with the root and the beam is deformed into a circle, which is consistent with the analytical results [16]. The effectiveness of structural model is validated.

4.2. Aerodynamics Model. Aerodynamics model is the most complex and important external force model in the problem of flight dynamics and control, so it must be checked carefully before further studies. The lift coefficient distribution along the wing span obtained from two methods are compared in Figure 4; one is derived from the Thin-Strip lifting-line theory proposed in Section 3.1 in this paper, and the other is the Vortex-Lattice method from AVL software. It can be seen that the precision of Thin-Strip lifting-line theory model can satisfy the application requirements of this paper.

4.3. Linear Structural Model. In order to investigate the error of different modal truncation, 4 linear structural models of the wing are compared with the geometrically nonlinear

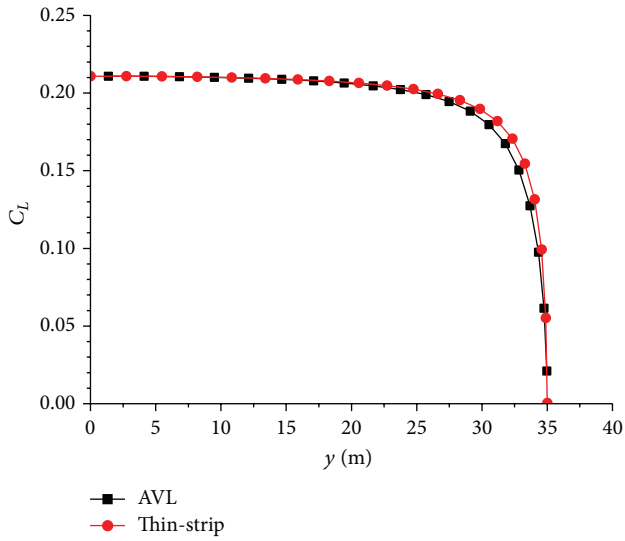

Figure 4: Comparison of spanwise lift coefficient distribution.

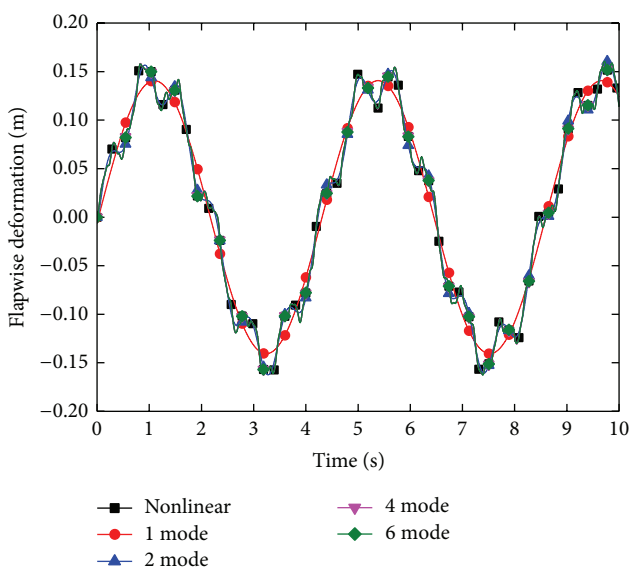

Figure 5: Time domain responses of the wing tip of different truncated linear wing models.

one: truncating at the 1st, 2nd, 4th, and 6th bending mode, respectively, and then applying a flapwise impulse force to the tip of the wing. The time domain responses of the wing tip of different models are shown in Figure 5.

It can be seen that, if the deformation is not large enough, for the flapwise deformation, if we employ the first 6 bending modes to constitute the linear structural model, the responses of the wing tip are coincident with the nonlinear one well. Similarly, it can be found from simulation that the first 4 twist modes and 2 chordwise modes are precise enough. So, the first 6 flapwise bending, 4 twist and 2 chordwise bending modes are adopted to constitute the linear structural model of the wing in the following of this paper.

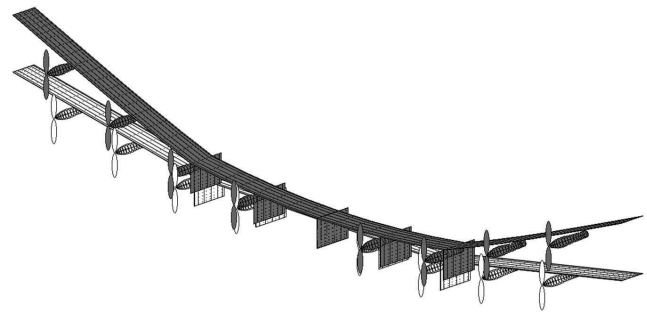

Figure 6: Deformed UAV in trimming.

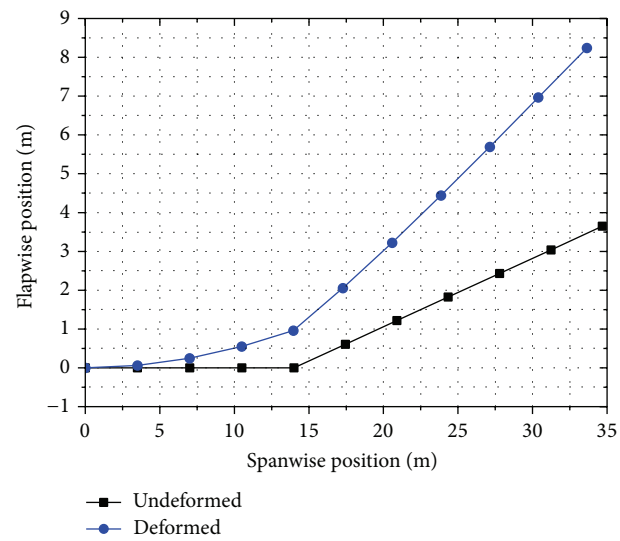

Figure 7: Flapwise position of UAV of different calculation model.

5. Flight Dynamics of Highly Flexible UAV

5.1. Trimming. Two kinetics models are employed for trimming: the "Undeformed" model represents the common rigid flight dynamics model; the "Deformed" model corresponding to (1) represents the flexible flight dynamics model.

In level flight, assuming that all the 40 distributed elevons deflect conformably for trimming for simplification, the highly flexible UAV will deform under the aeroelastic effect. In fact, the deformed UAV in trimming is shown in Figure 6, are the flapwise position and pitch angle of the UAV are shown in Figures 7 and 8.

It can be seen that the maximum wing deformation is 4.58 m at the wing tip, and the pitch angle at wing tip is larger than the root for about 3°. Larger pitch angle brings larger lift, and larger lift at wing tip will bring larger deformation. So, all the distributed elevons deflecting conformably is not the optimal control case while considering aeroelasticity.

5.2. Modal Analysis. The "Underformed" and "Deformed" models are corresponding to conventional rigid vehicles, and the linear "Flexible" model is based on (42). The longitudinal modes of different calculation models are shown in Table 2.

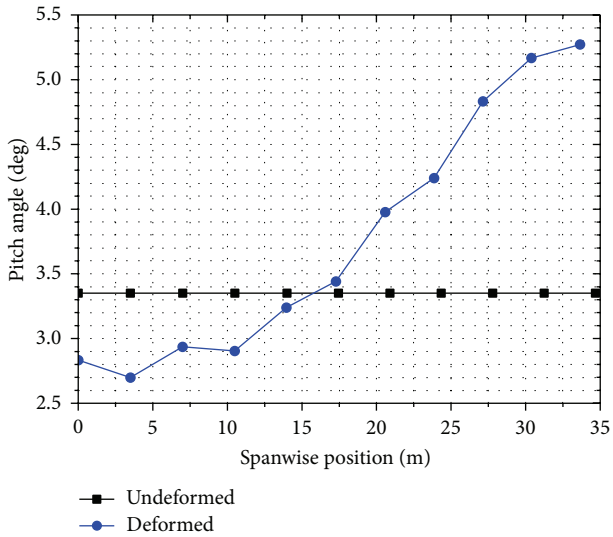

Figure 8: Pitch angle of UAV of different calculation model.

Table 2: Roots of longitudinal mode of different calculation models.

	Short period	Phugoid	1st bending
Undeformed	$-6.710 \pm 3.925i$	$-0.046 \pm 1.003i$	/
Deformed	$-5.985 \pm 3.100i$	$-0.002 \pm 1.063i$	/
Flexible	$-0.394 \pm 1.707i$	$0.002 \pm 1.031i$	$-3.819 \pm 1.459i$

The results showed that the difference of these models is huge in longitudinal mode. Since the deformation of wing has increased the UAV's moment of inertia about the pitch axis, the frequency of short period mode has obviously decreased for the deformed model. The serious coupling between short period mode and 1st bending mode also significantly influences the roots of short period mode, which then results in the phugoid changing from stable to unstable. These tendencies are similar to the results presented by Hodges et al. Through these analyses, it is clear that the flexible model is the only one which is able to accurately estimate the longitudinal flight dynamics behaviors.

6. Distributed LQG/LTR Controller Design

6.1. Statement of LQG/LTR Control. For a standard state space system described in (46), the design procedure of LQG/LTR controller in the output port is as follows:

(1) Design a LQR regulator F, which ensures that the singular value of open loop system $FG(s)$ on a certain frequency satisfies the robustness requirement.

(2) Design a target loop: select appropriate Ξ and Θ, so as to the singular value of full-state feedback loop transfer function $G_c(s)G(s)$ on the considering frequency close to that of $FG(s)$ adequately.

Where, the controlled plant $G(s)$ is

$$G(s) = C(sI - A)^{-1} B \tag{47}$$

and the derived LQG/LTR controller plant $G_c(s)$ is

$$G_c(s) = F(sI - A + BF + LC)^{-1} L. \tag{48}$$

The methodology of LQR is searching a full state feedback controller $u = -Fx$ to minimize the quadratic cost function:

$$J = \min\left(\int_0^\infty \left(x^T Q x + u^T R u\right) dt\right) \tag{49}$$

subject to the system dynamics described in (46).

The expression of F can be calculated by

$$F = R^{-1} B^T P, \tag{50}$$

where P is the solution of the following algebraic Riccati equation:

$$A^T P + PA - PBR^{-1} B^T P + Q = 0. \tag{51}$$

The solution of L in (48) is similar to F; one just needs to replace the matrix A, B, Q, R in (49)–(51) to $A^T, C^T, \Xi + \rho BB^T, \Theta$, respectively, where $\Xi + \rho BB^T$ represents the noise intensity; different noise intensity can be adjusted by ρ; Θ represents the sensor noise intensity. A well-designed LQG/LTR controller should be that, when $\rho \to \infty$, the singular value of $G_c(s)G(s)$ on the considering frequency close to that of $FG(s)$ adequately. But it should be noted that larger ρ will derive larger gain of $G_c(s)$.

6.2. Designing LQG/LTR Pitch Angle Controller. Before designing LQG/LTR control law, one shall augment the plant to satisfy the specific performance requirement. For example, adding integrators will assure the zero steady-state errors to step inputs. So, in order to control the pitch angle precisely, the integrator of pitch angle θ_i and velocity V_i should be included in the control plant. Then, the control plant in (46) becomes

$$\begin{bmatrix} \dot{\mathbf{x}} \\ \dot{\theta}_i \\ \dot{V}_i \end{bmatrix} = \begin{bmatrix} \mathbf{A} & 0_{4\times1} & 0_{4\times1} \\ [0\ 0\ 0\ 1\ 0_{1\times2n}] & 0 & 0 \\ [1\ 0\ 0\ 0\ 0_{1\times2n}] & 0 & 0 \end{bmatrix} \begin{bmatrix} \mathbf{x} \\ \theta_i \\ V_i \end{bmatrix} + \begin{bmatrix} \mathbf{B} \\ 0 \\ 0 \end{bmatrix} \mathbf{u}. \tag{52}$$

The critical factor for a practical controller is that not all the state variables are easy to be measured in engineering. So only a part of variables can be used to implement the output feedback control. Because the LTR technology can recover the stable margin of LQR, which is known as an excellent state feedback robust controller, the robustness of LQG/LTR output feedback controller can be guaranteed.

Because the flapwise bending motion of the wing is easy to be measured, so u_z together with $V, \alpha, q, \theta, \theta_i, V_i$ are selected to be the measured variables for the controller. Then, we can apply the LQG/LTR method described above in (52).

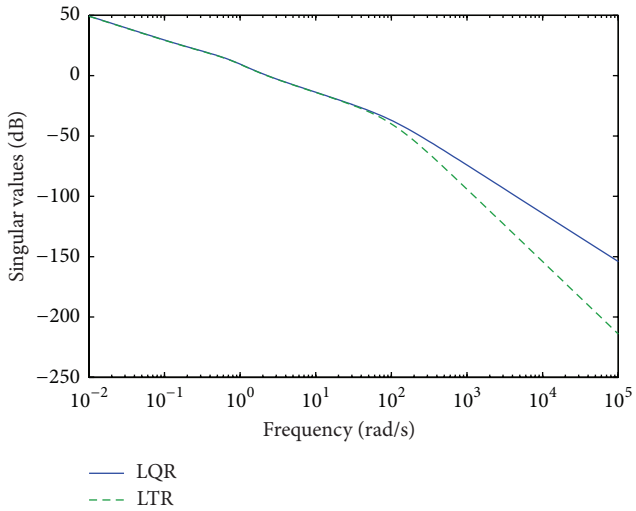

Figure 9: Singular values of pitch angle loop.

If we select $\rho = 1 \times 10^6$, the singular values of pitch angle loop of $FG(s)$ denoted by LQR and $G_c(s)G(s)$ denoted by LTR are compared in Figure 9.

It can be seen from Figure 9 that, after the loop transfer recovery, the two singular values coincide perfectly on low frequency band, which indicates that the response of the close loop system to common control such as step input is quick and the tracking error is small even with model deviation. On high frequency band, the singular value of LTR decreases more quickly than that of LQR, which will provide excellent robustness to the high frequency disturbance such as unmodeled high frequency structural dynamics and unsteady aerodynamics. So, the LTR satisfies the required performance well.

6.3. Flight Simulation. There are 40 distributed elevons in the large scale highly flexible solar-powered UAV. The details about control actuator are omitted temporally for brief while designing the LQG/LTR controller. But in the stage of flight simulation, two kinds of actuators are employed to verify the robustness of the controller. The model of the elevons actuator is

$$\delta_{\text{ea}} = \frac{1}{0.05s + 1} u. \tag{53}$$

The model of the throttles is

$$\delta_t = \frac{1}{0.5s + 1} u. \tag{54}$$

Their bandwidths are 20 and 2 rad/s, respectively.

Applying the LQG/LTR controller proposed above to the linear structural and flight dynamics model described in (52), when given a desired pitch angle $\theta_c = 5^\circ$, the longitudinal response of solar aircraft is shown in Figures 10–14. As shown in Figure 10, the adjust time of pitch angle is about 3 seconds; because of the use of integrator, steady-state error is eliminated. Seen from Figure 11, the variation

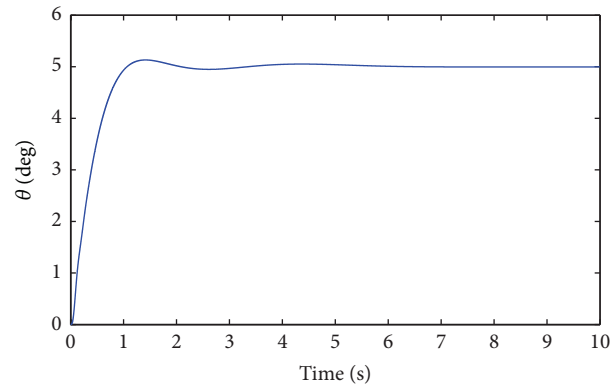

Figure 10: Response of pitch angle.

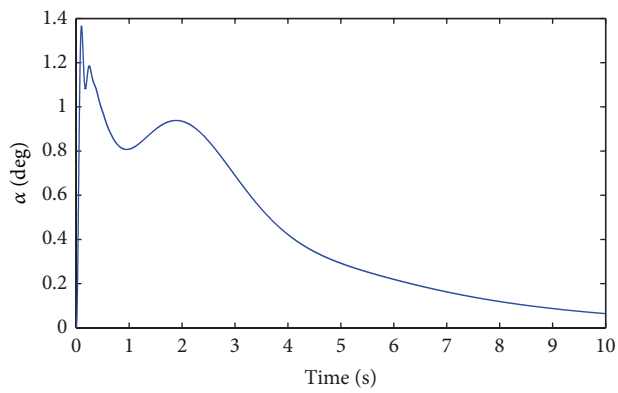

Figure 11: Response of angle of attack.

of angle of attack in the whole process does not exceed 1.4°, so the additional load it brings is very small, indicating that the overall movement of the highly-flexible UAV is relatively stable. Seen from Figure 12, the largest deflection angle of elevons is less than 20 degrees, and it occurs in the initial phase only, and when approaching a steady state, the deflections are no more than 5 degrees, far less than the limitation. It must be noted that the deflection angle of the 40 elevons are all different, because in addition to providing pitch angle control, distributed elevons also need to suppress the elastic deformation movement of the highly-flexible wing in the LQG/LTR controller. Seen from Figure 13, the maximum deformation of the wing occurs in the tip and the maximum magnitude of wing deformation is only about 0.09 m, far less than the deformation of 4.58 m in trimming, reminding that all the elevons deflect conformably in trimming. Seen from Figure 14, the max rate of twist angle is only 0.26 rad/s, corresponding to the reduced frequency of 0.0144. In a word, with distributed elevons, the use of LQG/LTR control method allows faster attitude control of the large scale highly flexible UAV while good aeroelastic deformation suppression is achieved simultaneously.

In addition, reminding that the linear structural model coincide with the nonlinear one perfectly on the condition of small deformation (shown in Figure 5). Since the LQG/LTR controller has restrained the structural deformation and

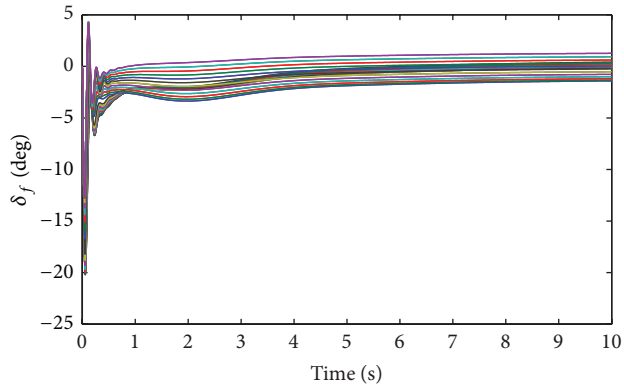

Figure 12: Response of elevons at different stations.

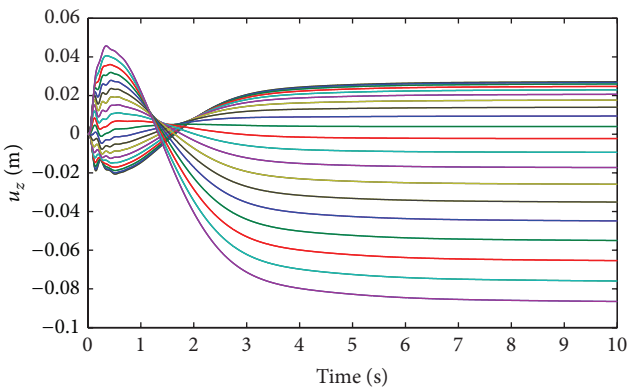

Figure 13: Response of vertical displacements of wing at different stations.

incident angle in a relative small range, it can be deduced that the simulation results in this section are reliable.

7. Conclusions

In this paper, the modeling, stability, and control characteristics of a highly flexible large scale solar-powered UAV with distributed all-span multi elevons were presented.

A geometrically nonlinear intrinsic beam model is introduced to establish the equation of motion of flexible solar-powered UAV. Based on it, the decoupled linear flight dynamics and structural dynamics equations of motions are derived in mean axis frame. Steady aerodynamics model is derived by theoretical airfoil data and corrected for 3D effect by lifting-line theory, quasisteady aerodynamics model is derived by Theodorsen unsteady aerodynamics model, and the aerodynamics derivatives of every wing sections are derived and transferred to different frames for the multirole in linear equations of flight dynamics or structural dynamics.

The nonlinear coupled structural and flight dynamics model was employed to trim the large scale flexible UAV, under the assumption that all the 40 distributed elevons deflect conformably. The maximum aeroelastic defection of wingtip is 4.58 m in flapwise, about 13% to the halfspan. The pitch angle at wing tip is larger than the root for about 3°.

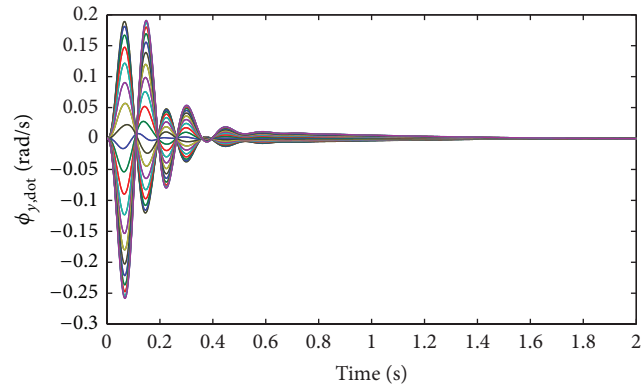

Figure 14: Response of rate of twist angle of wing at different stations.

Larger pitch angle brings larger lift and leads to larger deformation. So all the distributed elevons deflecting conformably are not the optimal control case while considering aeroelastic effects.

Three different linear dynamics models, undeformed, deformed, and elastic, were compared for longitudinal mode analysis. The results showed that the difference of three models is huge. Since the deformation of wing has increased the UAV's moment of inertia about the pitch axis, the frequency of short period mode has obviously decreased for the deformed model. The serious coupling between short period mode and 1st bending mode also significantly influences the roots of short period mode, which then results in the phugoid changing from stable to unstable. So, it is clear that the flexible model is the only one which is able to accurately estimate the longitudinal flight dynamics behaviors and control the large scale highly flexible UAV exactly.

Forty distributed all-span elevons were employed to control the attitude and suppress the aeroelastic deformation. LQG/LTR methodology was employed to accomplish the dynamics performance and robustness requirement. The flight simulation showed that the designed LQG/LTR controller can provide the adjust time of pitch angle in 3 seconds without steady-state error, and the maximum magnitude of wing deformation is only about 0.09 m, far less than the deformation of 4.58 m in trimming. So, LQG/LTR control method with distributed elevons is suitable for large scale highly flexible solar-powered UAV.

Nomenclature

P: Linear momentum
H: Angular momentum
M: Mass or moment
I: Moment of inertia
V: Linear velocity
Ω: Angular velocity
γ: Strain
κ: Curvature
f: External force
m: External moment

c: Chord
l: Wing span
C_{ab}: Direction cosine matrix from b to a
α: Angle of attack
β: Angle of side slip
x, y, z: Distance from the origin at x, y, and z directions.

Subscripts and Superscripts

g: Ground axis frame
R: Deformed beam axis frame at wing root
B: Deformed beam axis frame
b: Undeformed beam axis frame
M: Mean axis frame
s: Structure axis frame
a_B: Aero axis frame at deformed beam
a_R: Aero axis frame at wing root
a_M: Aero axis frame at mean axis frame
$\{x\}_y$: Vector x expressed in y-frame
$\{x\}_{y,z}$: Z part of vector x expressed in y-frame
x': Spatial derivative of variable x
$\dot{x}$: Temporal derivative of variable x
$\overline{x}$: Mean value over the beam element
$\widehat{x}$: Nodal value.

Conflict of Interests

The authors declare that there is no conflict of interests regarding the publication of this paper.

Acknowledgments

This study is supported by the National Natural Science Foundation of China (Grant no. 11202162) and the Scientific and Technology Foundation of State Key Laboratory on UAV (Grant no. 9140C390103130C39142).

References

[1] T. E. Noll, S. D. Ishmael, B. Henwood, M. E. Perez-Davis, G. C. Tiffany, and J. Madura, "Technical findings, lessons learned, and recommendations resulting from the helios prototype vehicle mishap," Meeting Proceedings RTO-MP-AVT-145, 2007.

[2] M. J. Patil, *Nonlinear aeroelastic analysis, flight dynamics, and control of a complete aircraft [Ph.D. thesis]*, Georgia Institute of Technology, Atlanta, Ga, USA, 1999.

[3] M. J. Patil and D. H. Hodges, "Flight dynamics of highly flexible flying wings," *Journal of Aircraft*, vol. 43, no. 6, pp. 1790–1798, 2006.

[4] B. Raghavan and M. J. Patil, "Flight dynamics of high aspect-ratio flying wings: effect of large trim deformation," AIAA 2007–6386, The American Institute of Aeronautics and Astronautics, 2007.

[5] W. Su and C. E. S. Cesnik, "Dynamic response of highly flexible flying wings," *AIAA Journal*, vol. 49, no. 2, pp. 324–339, 2011.

[6] C. M. Shearer and C. E. S. Cesnik, "Nonlinear flight dynamics of very flexible aircraft," *Journal of Aircraft*, vol. 44, no. 5, pp. 1528–1545, 2007.

[7] M. J. Patil and D. H. Hodges, "Output feedback control of the nonlinear aeroelastic response of a slender wing," *Journal of Guidance, Control, and Dynamics*, vol. 25, no. 2, pp. 302–308, 2002.

[8] C. M. Shearer and C. E. S. Cesnik, "Trajectory control for very flexible aircraft," AIAA 2006-6316, 2006.

[9] B. Raghavan and M. J. Patil, "Flight control for flexible, high-aspect-ratio flying wings," *Journal of Guidance, Control, and Dynamics*, vol. 33, no. 1, pp. 64–74, 2010.

[10] X. Li and R. K. Agarwal, "Application of eeduced-order-models to robust control of the dynamics of a flexible aircraft," AIAA 2003-5504, 2003.

[11] M. Athans, "A tutorial on LQG/LTR method," in *Proceedings of the American Control Conference*, Seattle, Wash, USA, June 1986.

[12] T. E. Gibson, A. M. Annaswamy, and E. Lavretsky, "Modeling for control of very flexible aircraft," in *Proceedings of the AIAA Guidance, Navigation, and Control Conference*, AIAA 2011-6202, Portland, Ore, USA, August 2011.

[13] D. H. Hodges, "A mixed variational formulation based on exact intrinsic equations for dynamics of moving beams," *International Journal of Solids and Structures*, vol. 26, no. 11, pp. 1253–1273, 1990.

[14] R. Palacios, J. Murua, and R. Cook, "Structural and aerodynamic models in nonlinear flight dynamics of very flexible aircraft," *AIAA Journal*, vol. 48, no. 11, pp. 2648–2659, 2010.

[15] S. S. Rao, *Mechanical Vibrations*, Pearson Education, Upper Saddle River, NJ, USA, 4th edition, 2004.

[16] B. Raghavan, *Flight dynamics and control of highly flexible flying-wing [Ph.D. thesis]*, Virginia Polytechnic Institute and State University, 2009.

[17] D. H. Hodges, "Geometrically exact, intrinsic theory for dynamics of curved and twisted anisotropic beams," *AIAA Journal*, vol. 41, no. 6, pp. 1131–1137, 2003.

[18] D. A. Peters and W.-M. Cao, "Finite state induced flow models part I: two-dimensional thin airfoil," *Journal of Aircraft*, vol. 32, no. 2, pp. 313–322, 1995.

[19] J. D. Anderson, *Fundamentals of Aerodynamics*, McGraw-Hill, 4th edition, 2007.

[20] Z. Fang, W. Chen, and S. Zhang, *Aeronautic Vehicle Flight Dynamics*, Beihang University Press, 1st edition, 2005 (Chinese).

[21] R. Wang, "Research on dynamics and control of highly flexible solar-powered UAV," Postdoctoral Report, Northwestern Polytechnology University, Xi'an, China, 2011 (Chinese).

Hindawi Publishing Corporation
Mathematical Problems in Engineering
Volume 2015, Article ID 601782, 13 pages
http://dx.doi.org/10.1155/2015/601782

Research Article

Novel Degree Constrained Minimum Spanning Tree Algorithm Based on an Improved Multicolony Ant Algorithm

Xuemei Sun, Cheng Chang, Hua Su, and Chuitian Rong

School of Computer Science and Software, Tianjin Polytechnic University, Tianjin 300387, China

Correspondence should be addressed to Xuemei Sun; seesea_sun@163.com

Received 22 October 2014; Accepted 12 January 2015

Academic Editor: Kun Liu

Copyright © 2015 Xuemei Sun et al. This is an open access article distributed under the Creative Commons Attribution License, which permits unrestricted use, distribution, and reproduction in any medium, provided the original work is properly cited.

Degree constrained minimum spanning tree (DCMST) refers to constructing a spanning tree of minimum weight in a complete graph with weights on edges while the degree of each node in the spanning tree is no more than d ($d \geq 2$). The paper proposes an improved multicolony ant algorithm for degree constrained minimum spanning tree searching which enables independent search for optimal solutions among various colonies and achieving information exchanges between different colonies by information entropy. Local optimal algorithm is introduced to improve constructed spanning tree. Meanwhile, algorithm strategies in dynamic ant, random perturbations ant colony, and max-min ant system are adapted in this paper to optimize the proposed algorithm. Finally, multiple groups of experimental data show the superiority of the improved algorithm in solving the problems of degree constrained minimum spanning tree.

1. Introduction

Minimum spanning tree (MST) is a classic combinatorial optimization problem. Many engineering problems in common cases, for example, pipeline, circuit design, and transportation network, can be transformed into minimum spanning tree. Minimum spanning tree means to construct a minimum cost spanning tree with weight graph by adapting proven algorithms like avoid cycle method, tear cycle method, and so forth. However, things will be different when values, which bring about restrictions to degree of each vertex in a tree, are given in advance. It is in fact a problem of so-called degree-constrained minimum spanning tree (DCMST). As a matter of fact, it means to find out the minimum spanning tree with minimum weight while complying with the vertex constraints in all spanning trees. With the development of science and society, there is a growing need for solving the problems of DCMST in different fields such as computer communication, telephone communication, transportation, and allocation of resources, thus making DCMST optimization a problem worth studying.

As NP hard problem, various algorithms with high time complexity such as branch and bound method, approximate algorithm, iterative method, and multistart hill-climbing are exploited in DCMST in previous study. Heuristic algorithms, for instance, genetic algorithms, simulated annealing algorithm, and ant colony algorithm, have been a research focus to generate acceptable solutions in a valid time. Among these modern optimization algorithms, ant colony algorithm comes as a novel bionics algorithm and converges to the shortest path by information transferring and updating among ants. It combines distributed computation, positive feedback mechanism, and greedy search which enables fast approaching of better solutions.

Many DCNST problems are solved by ant colony algorithm [1–5]; these applications adopt ant colony algorithm with single colony. It comes with shortcomings of long search time and stagnation. Ant colony operates through organized cooperation and task-sharing in nature and their pheromone regulation mechanisms differ from one colony to another. These corporations show great significance when ant colony deals with complex tasks. Algorithms that employ multicolony ant algorithm will converge in a shorter period of time compared to those applied with single colony but feature the same ant population in total especially when the problem is in large scale. Taking all these factors into account,

the paper proposes a degree-constrained minimum spanning tree based on improved multiant colonies. The proposed algorithm features multipaths search through multiant colonies under setting conditions. Moreover, the thinking of dynamic ant colony is utilized here to dynamically adjust volatilization factor and enhancement factor during the running process in order to increase the diversity of solutions. Upper and lower bounds of pheromone are configured on the basis of the thinking of max-min ant system during its updating process. What is more, the tabu list is applied in case of local circling while random disturbance factor is set here to increase the possibility of selection among different paths so as to promote objective and diverse solutions.

2. Background

Providing G is a connected complete graph with weights on edges while the values of the weight are not negative, supposing T is the spanning tree of G, $w(T)$ means the sum of weights of T. Then construct a spanning tree with a minimum $w(T)$ under the condition that the degree of each node is no more than d, where $d \geq 2$. Spanning trees meeting the above description are named degree-constrained minimum spanning tree (DCMST).

DCMST was first proposed by Narula and Ho in 1980. Then branch and bound algorithm [6, 7], which enables optimal solutions search for DCMST with less nodes, was given at the same time. After that, a branch and cut algorithm [8] that promoted a more objective construction when searching for optimal solutions was raised by Caccetta and Hill, and so forth. In particular, Volgenant presented double solution information based Lagrangian algorithm [9] for DCMST. Soon after that, Behle et al. further optimized this problem by presenting preferential branch and cut algorithm [10] by adopting separation standards and principles of 0/1 integer programming.

With further exploration of DCMST, evolutionary algorithm [11–13] taking genetic immune thinking as a main representative emerged. During that period of time Japanese scholar Zhou and Gen achieved a major breakthrough by solving DCMST using evolutionary algorithm and encoding spanning tree by Prufe. Nevertheless, the information of degree cannot be reflected in Prufe coding and infeasible solutions generated in this procession. Since then, many evolutionary thinking based algorithms have been proposed to solve the problem of DCMST. These algorithms mainly focused on bringing improvements in evolutionary coding and these improvements are insufficient for a DCMST task. In addition, randomized primal method (RPM) [12], which is a dynamic table structure, integrated multistart hill-climbing (MHC) [14], stimulated annealing (SA), and genetic algorithm (GA) [12, 13] and the node weight information as a whole was presented by Knowles to find the optimal solutions of DCMST. Many heuristic algorithms, for instance, ant colony algorithm [3, 15–17] and particle swarm optimization algorithm [18, 19], have been applied to study DCMST from different ways and have gained positive effects.

A typical example was given in [2] to solve DCMST by an improved ant colony algorithm. In this example, a group of ants were asked to explore the given graph; then a group of signed edge set which is related to the pheromone on paths was selected as a candidate set. Afterwards, Kruskal's algorithm was adopted to construct a DCMST according to the candidate set. Finally, local optimization was carried out in DCMST to better improve the spanning tree. The algorithm proposed in this paper is basically based on ant colony algorithm and further optimizes the solutions by introducing multiant colonies.

3. Mathematical Model of DCMST

In the mathematical model of DCMST, graph $G = (V, E, W)$ means a connected undirected graph, wherein $V = \{v_1, v_2, \ldots, v_n\}$ is the vertex set, the edge set is $E = \{e_1, e_2, \ldots, e_m\}$, and $W = (\omega_{ij})_{n\times n}$ is the weight matrix. Supposing $\omega_{ij} = \omega_{ji}$, $\omega_{ii} = \infty$, $i, j = 1, 2, \ldots, n$, if $(v_i, v_j) \in E(G)$, then $\omega_{ij} = W(v_i, v_j)$; if $(v_i, v_j) \notin E(G)$, then $\omega_{ij} = \infty$. The mathematical model of DCMST can be described as

$$\min \quad Z = \sum_{i=1}^{n}\sum_{j=1}^{n}\omega_{ij}X_{ij} \tag{1}$$

$$\text{s.t.} \quad \sum_{i=1}^{n}X_{ij} \leq b_i \tag{2}$$

$$\sum_{i,j\in S}^{n}X_{ij} \leq |S| - 1, \quad \forall S \subset V,\ S \neq \varnothing \tag{3}$$

$$\sum_{i=1}^{n}\sum_{j=1}^{n}X_{ij} = n - 1 \tag{4}$$

$$X_{ij} \in \{0, 1\}, \quad i, j \in V, \tag{5}$$

wherein variable

$$X_{ij} = \begin{cases} 1, & \text{edge } (i, j) \text{ lies on the optimal tree} \\ 0, & \text{other.} \end{cases} \tag{6}$$

Condition (2) limits the number of edges that connected to node I which ensures the restrictions of degree constraint. Condition (3) makes sure that the obtained subgraph is a spanning tree of graph G. Condition (4) ensures that there are $n - 1$ edges in the final subgraph.

4. Degree-Constrained Minimum Spanning Tree Based on Multiant Colonies

In this paper, multiple ant colonies are arranged to search multiple paths following given conditions. They are supposed to search for optimal solutions independently and to communicate with each other through information entropy. Entropy is mainly used for description of the disordered relation in thermodynamics. In here, information entropy which can be expressed as $s = -k\sum_{i=1}^{n} p_i \ln p_i$ is employed to display the diversity of solutions, wherein p_i is the possibility that condition i can be determined while $p_i \geq 0$, $\sum_{i=1}^{n} p_i = 1$. The size of information entropy dominates the diversity of

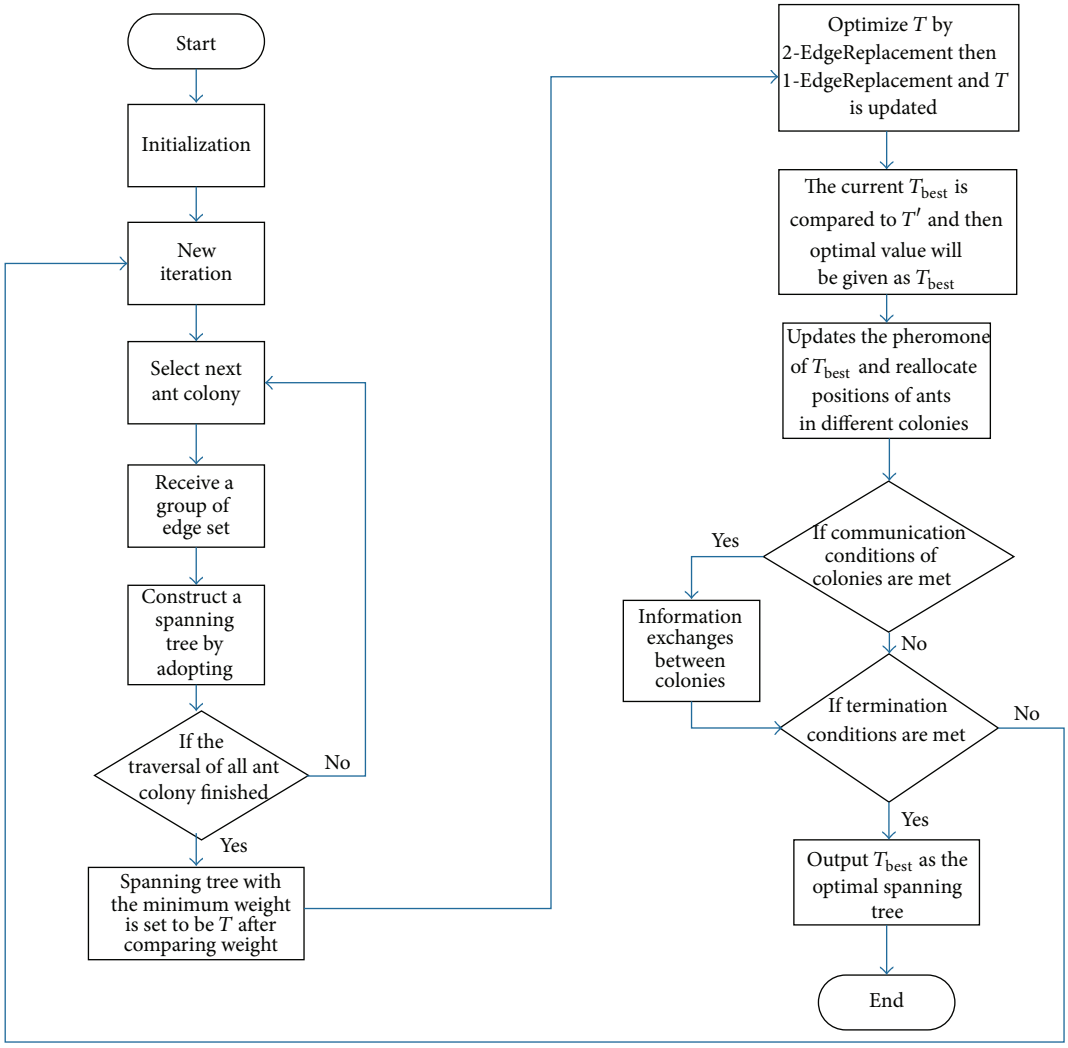

Figure 1: Flow chart of the algorithm.

solutions and it is also an important basis for pheromone updating between ant colonies.

Besides, the improved algorithm enlarged search area of ant and added to the diversity of solutions by dynamically adjusting volatilization factor and enhancement factor to affect the distribution of pheromone. By introducing adaptive optimization strategy in case of local circling and random disturbance factor to increase the possibility that each path is being selected, the obtained solutions are supposed to be objective and diverse.

At the beginning of the experiment, each ant is allocated with an initial position; then initial values of pheromone of edges are given. After DCMST T_{best} is constructed, ant colonies start the search process and a set of edge set TE will be obtained. Kruskal algorithm then will be applied to construct a spanning tree according to TE. After all rge spanning trees are constructed by each colony, all these spanning trees will be compared with each other and the optimal spanning tree with the least weight will be note into T_{better}. Algorithms 2-EdgeReplacement and 1-EdgeRepalcement will be exploited to optimize T_{better}. Then, comparing T_{better} with T_{best} after iteration, the one that features the smaller weight is set to be T_{best}. Next, globally update the pheromone of T_{best} and reallocate positions of each ant. If communication requirements are met between colonies, then pheromone updating will be conducted between colonies, or next iteration will be conducted. Final solution T_{best} will not be obtained until all the iterations are complete. See Algorithm 1.

The flow chart is as shown in Figure 1.

4.1. The Initialization Stage. The edge weight will be computed according to the distances between node sets when initialization begins. Maximum weight M and minimum weight m will be recorded. Then the initial pheromone concentration of each edge is acquired by analyzing obtained weight. Assuming the range of weight lies between $(M - m)/3$ and $4(M - m)/3$, the initial edge set will be obtained according to initial pheromone matrix. After that, each ant will be allocated with an initial position. See Algorithm 2.

```
Input:
  G = (V, E): a complete graph with weight;
  ω: function to calculate weight;
  d: degree constraint of vertex, d ≥ 2;
  MA: the amount of ant colonies
Output:
  A degree constrained minimum spanning tree T
Begin
  //Initialization
  i ← 1; i_best ← 0; i_restart ← 0
  Create the Multiple set of ants A[MA] of size |V| with the number of colonies k
  InitAntsEdges(V, E, ω)
  T_best ← ConstructSpanningTree(E, d)
  while i < i_max and i − i_best < i_stop do
    for ma = 1 to MA do
      AntsMove(A[ma], E) //Exploration
      s ← Calculation Entropy
      T ← ConstructSpanningTree(E, d)
      If ω(T) < ω(T_better) then
        T_better ← T
        ma_better ← ma
      //local optimization
      T_better ← 2-EdgeReplacement(T_better, E, V, ω)
      T_better ← 1-EdgeReplacement(T_better, E, V, ω)
    If ω(T_better) < ω(T_best) then
      T_best ← T_better
      i_best ← i
    foreach e ∈ T_best do //enhance
      e·phm ← γ · e·phm
    if i_max(i_best, i_restart) > R then
      i_restart ← i
      Restart(T_best)
    if i mod gap(s) = 0 then
      ExchangePheromone()
    i ← i + 1
    ResetAnts(A)
    Update parameters γ and η
  return T_best
```

Algorithm 1

```
InitAntsEdges(V, E, ω)
begin
  for i = 0 to |V| − 1 do
    Ant[i]·location ← V[i]
    Ant[i]·tabuList ← ∅
  foreach e ∈ E do
    e·initPhm ← (M − ω(e)) + (M − m)/3
    e·phm ← e·initPhm
    e·nVisited ← 0
```

Algorithm 2

4.2. The Search Stage. The transfer rule of an improved ant colony algorithm is employed when ants start their search for next target position in the search stage.

The algorithm integrates the characteristics of optimized algorithms like dynamic ant colony algorithm and random disturbance ant colony algorithm as a whole and each ant is allocated with its own tabu list. Ants will select next target according to transfer rule in

$$C_{ij}^{k} = \begin{cases} sp_{ij}^{k} & q \le q_0 \\ p_{ij}^{k} & q > q_0 \\ 0 & \text{other.} \end{cases} \tag{7}$$

In this formula, q is a random number within 0~1. q_0 is a constant; it is set to be 0.5 in here. When q is less than or equal to q_0, according to random disturbance strategy, the next target position will be the node when sp_{ij}^{k} takes the largest value. Consider

$$sp_{ij}^{k} = \frac{\left(\tau_{ij}{}^{\alpha} \cdot \eta_{ij}{}^{\beta}\right)^{\gamma}}{\sum \tau_{ij}{}^{\alpha} \cdot \eta_{ij}{}^{\beta}}, \tag{8}$$

```
AntsMove(A[ma], E)
begin
  for i = 1 to maxSteps do
    if i mod updatePeriod = 0 then
      UpdatePheromone(E)
    foreach a ∈ A[ma] do
      nAttempts ← 0
      moved ← False
      while not moved and nAttempts < 5 do
        v1 ← a·location
        Select an edge (v1, v2) at random and proportional to (v1, v2)·phm
        if v2 ∉ a·tabuList then
          add v2 into a·tabuList
          a·location ← v2
          (v1, v2)·nVisited++
          moved ← True
        else nAttempts++
  s ← Calculation Entropy of the current colony
```

Algorithm 3

wherein α is equal to 1 and β changes with the number of iterations, recorded as mn, by a kind of dynamic ant colony strategy. $\beta = 5$ when the number of iterations lies in $1 \sim mn/3$. When it comes to be in $mn/3 \sim mn/2$, $\beta = 4$. $\beta = 3$ when the number lies in $mn/2 \sim mn2/3$. Similarly, $\beta = 2$ when this number lies in $mn2/3 \sim mn$.

Γ calculated by $\gamma = a \cdot e^{b/k}$ is the disturbance factor. a is a random number within 0~2. b is equal to 4 and k is the number of iterations.

When q is larger than q_0,

$$p_{ij}^k = \frac{{\tau_{ij}}^{\alpha} \cdot {\eta_{ij}}^{\beta}}{\sum {\tau_{ij}}^{\alpha} \cdot {\eta_{ij}}^{\beta}}. \tag{9}$$

p_{ij}^k means the possibility that j is being selected; the possibility increases as p_{ij}^k grows rather than forcing sp_{ij}^k to be the maximum node. Then next target position will be determined and add this position to tabu list of this ant in case of being selected again; then add 1 to the number of visits.

Information entropy of a colony will be calculated as (10) according to obtained p_{ij}^k of each ant after a colony completes searching:

$$s = -k \sum_{i=1}^{m} p_i \ln p_i. \tag{10}$$

m represents the number of ants in a colony. The calculated information entropy of colonies will be a basis for colonies selection when pheromone exchanges. See Algorithm 3.

4.3. Updating of Pheromone. All ant colonies search for edges following a given step length. All ants will not stop moving in parallel in each step and updating pheromone on edges that have been searched until all the steps have been finished. Pheromone updating is set to be operated after finishing a group of specific steps instead of updating pheromone concentration after each step in order to promote more effective search. Pheromone is supposed to be updated when an ant has finished 1/3 of its maximum step.

```
UpdatePheromone(E)
begin
  foreach e ∈ E do
    e·phm ← (1 − η) × e·phm + e·nVisited × e·initPhm
    e·nVisited ← 0
    if e·phm > maxPhm then
      e·phm ← maxPhm − e·initPhm
    if e·phm < minPhm then
      e·phm ← minPhm + e·initPhm
```

Algorithm 4

Pheromone on each path ranges between minPhm and maxPhm. It is similar to max-min ant system, which will be of help to prevent the solution from falling into local optimal:

$$\begin{aligned} \text{maxPhm} &= 1000 \cdot (M - m) + \frac{(M - m)}{3}, \\ \text{minPhm} &= \frac{(M - m)}{3}. \end{aligned} \tag{11}$$

M and m are maximum weight and minimum weight referred to at the beginning.

A counter will be set on each edge to know how many times it has been visited after an update is complete. Local update of pheromone is arranged as the formula lists as follows:

$$\text{phm} = (1 - \eta) \cdot \text{phm} + n\text{Visited} \cdot \text{initPhm}. \tag{12}$$

```
ConstructSpanningTree(E, d)
begin
  T_n ← ∅
  Sort E in order of descreasing pheromone level
  C ← top nCandidates edges from E
  Sort C in order of increasing edges cost
    while |T_n| < |V| − 1 do
      if C ≠ ∅ then
        Let e be the next edge in C
        Remove e from C
        if adding e into T_n with meet the degree constraint then
          T_n = T_n ∪ {e}
        else
        C ← next nCandidates edges from E
        Sort C in order of increasing edges cost
return T_n
```

Algorithm 5

η means the volatilization factor and it is updating with the operating of algorithm. Consider

$$\eta = \eta \cdot \left(\frac{n\text{Visited}}{\text{phm}}\right)^k. \tag{13}$$

initPhm is the initial pheromone value of edge and nVisited implies the number on edges being visited. k is a constant and, in here, it is set to be 0.5. It should be noted that when the value of pheromone on a path exceeds threshold value, the value of pheromone will be adjusted by adjusting initial pheromone values of edges for better solution. See Algorithm 4.

4.4. Constructing Spanning Tree. A group of edges will be obtained after an ant colony completes searching. Pheromone matrix is adopted to construct a corresponding DCMST due to the absolute connectivity of obtained edge sets and they are all labeled with high pheromone values.

Sort edges sets by pheromone values, from largest to smallest. Construct a candidate set by choosing the top nCandidates edges and arrange them from smallest to largest by weight values. Next, a spanning tree in which the degrees of nodes meet constraints will be constructed. If the selected nCandidates set does not meet the requirements to construct a spanning tree, another nCandidates set will be selected to construct a spanning tree until a degree constrained spanning tree was constructed. After all ant colonies constructed their own spanning tree, the one that owns the smallest weight will be selected as the optimal spanning tree in this iteration, labeled as T. Then its pheromone matrix and colony number will be recorded. See Algorithm 5.

4.5. Local Optimization Stage. Spanning tree T will be processed by two local optimization algorithms of 2-EdgeReplacement and 1-EdgeReplacement. 2-EdgeReplacement means to replace any two edges of spanning tree with two other edges, wherein the weights of two other edges are smaller than two previous edges being replaced. Furthermore, spanning tree has to meet degree constraints after two edges being replaced. What makes 1-EdgeReplacement different from 2-EdgeReplacement is that only one edge rather than two edges is replaced in a spanning tree in 1-EdgeReplacement. Finally, optimized spanning tree is noted as T'. See Algorithms 6 and 7.

4.6. Global Optimization Stage. Spanning tree T' after iterative optimization is compared with optimal spanning tree T_{best} generated in latest iteration; the one that gets the smaller weight will be noted as T_{best}. Then pheromone will be updated globally in T_{best} and ants will be allocated with new positions. Only if communication requirements between colonies are met will pheromone be updated between colonies, or a new iteration will be conducted.

4.7. Information Exchanges between Colonies. Information exchanges between colonies are conducted at certain time intervals, which is determined according to information entropy of all colonies; in other words, it changes by the convergence of all colonies. Time intervals gap of information exchanges between colonies is in accordance with the following formula:

$$\text{gap} = k_1 \cdot e^{\sum_{i=1}^{h} s_i / h}, \tag{14}$$

wherein k_1 is a constant, h is the number of subcolonies, and s_i is the information entropy of the ith subcolony.

Selection criteria of colonies, where information exchanges existed between colonies, are determined by information entropies of each colony. Provided that colony j is the selected colony of colony i for information exchanging, then j is determined by the following formula:

$$j = \arg\max_{1 \le j \le h} \left(\left|s_i - s_j\right|\right), \tag{15}$$

in which s_i and s_j are information entropies of colonies i and j, respectively. Colonies with greater entropy will choose colonies with smaller entropy as objects to exchange information. Then colonies with small information entropy are

```
2-EdgeReplacement(T_better, E, V, ω)
begin
  T_n ← T_better
  nTries ← 0
  while nTries < |V|/2 do
    e_1 ← a random edge in T_n
    e_b ← e_1; c_b ← 0
    foreach e_2 ∈ T_better and e_1, e_2 are not adjacent do
      {e_r1, e_r2} ← rep2Opt(e_1, e_2)
      if ω(e_1) + ω(e_2) − ω(e_r1) − ω(e_r2) > c_b then
      c_b ← ω(e_1) + ω(e_2) − ω(e_r1) − ω(e_r2)
      e_b ← e_2
    if c_b > 0 then
      T_n ← (T_n − {e_1, e_b}) ∪ rep2Opt(e_1, e_b)
      nTries ← 0
    else
      nTries ← nTries + 1
  return T_n
```

Algorithm 6

```
1-EdgeReplacement(T_better, E, V, ω)
begin
  T_n ← T_better
  Sort E in order of increasing edges cost
  repeat
    changed ← False
    Sort T_n in order of increasing edges cost
    j ← |V| − 1
    while j ≥ 0 do
      k ← 0
      while ω(T_n[j]) > ω(E[k]) do
        if swapping E[k] and T_n[j] creates no cycle in T_n and satisfies degree constraint then
          T_n ← T_n ∪ {E[k]} − {T_n[j]}
          changed ← True
          break
        k ← k + 1
      j ← j + 1
  until not changed
  return T_n
```

Algorithm 7

concentratedly distributed and information exchanges with high entropy colonies will help to improve their pheromone amount. Similarly, colonies with high information entropy will be distributed scatteredly to help to improve colonies with small information entropy.

Pheromone updates will be conducted depending on formula (16) when colony i selects colony j as an object to exchange information. Consider

$$\tau_{uv}^{i} = \tau_{uv}^{i} + \lambda \Delta \tau_{uv}^{i}. \tag{16}$$

$\lambda = s_i - s_j$, $\lambda_{\min} < \lambda < \lambda_{\max}$, and $\lambda_{\min}$ and $\lambda_{\max}$ are constants and present the minimum and maximum update coefficient, respectively. $\Delta\tau_{uv}^{i}$ is the pheromone of colony j on path (u, v). See Algorithm 8.

5. Simulation and Analysis

5.1. Experimental Data. The data in Table 1 was selected as experimental subjects. Single colony ant algorithm was compared with multicolony ant algorithm. Experimental parameters were set as follows: maximum number of loop iterations $i_{\max} = 100$, $i_{\text{stop}} = 25$. The number of ant colonies is 3, the maximum search step of ant $m_{\text{Steps}} = 75$, update cycle of local pheromone updatePeriod $= m_{\text{Steps}}/3$, and the degree of vertex $d = 2, 3, 4, 5$.

5.2. Experimental Platform. The algorithm is coded with standard Java and has been compiled and debugged on the platform of Eclipse. A computer installed with 32-bit Windows 7 operating system and equipped with 3 G RAM

```
ExchangePheromone(A, E)
begin
  λ ← 0
  for i = 0 to |MA| − 1 do
    for j = 0 to |MA| − 1 do
      if |s_i − s_j| > λ then
        λ ← |s_i − s_j|
        mj ← j
    for k = 0 to |E| − 1 do
      E_i[k]·phm ← E_i[k]·phm + λ × Emj[k]·phm
```

Algorithm 8

Table 1

Sample graph (G)	Number of vertexes $\lvert V\rvert$	Sample graph (G)	Number of vertexes $\lvert V\rvert$
att48	20	rand100	100
bier127	127	rat99	99
eil51	51	pr107	107
eil76	76	pr136	136
eil101	101	pr152	152
ulysses16	16	ulysses22	22
kroA100	100	chn31	31
kroA200	200	ch130	130
kroA150	150	ch150	150
rand50	50	st70	70
rand75	75	overil30	30
danzig42	42	bayg29	29
gr96	96	burma14	14
gr120	120	berlin52	52
gr137	137		

and 2.20 GHz CPU was used to operate the algorithm. Experimental results are obtained by operating the proposed algorithm 20 times for each sample data set.

5.3. Parameters Configuration. Parameters are configured as Table 2 in experiment.

5.4. Evaluation Index. In experiment, the optimal value, average value, standard deviation, coefficient of variation CV, and mean deviation value Gap were selected as evaluation indexes of experimental results, wherein coefficient of variation CV reflects the robustness of the algorithm: $\mathrm{CV} = \sigma/\mu \times 100$. The proposed algorithm tends to be more stable as the value of CV gets smaller. Mean deviation value Gap illustrates the possibility of better solution obtaining $\mathrm{Gap} = (C_{\mathrm{mean}} - C_{\mathrm{opt}})/C_{\mathrm{opt}} \times 100$.

5.5. Experimental Results and Analysis. Experiment was conducted when degree of vertex d was set to be 2, 3, 4, 5, respectively. Each sample graph run 20 times; then a minimum spanning tree and its weight was gained. If the value d of the minimum spanning tree is not within the scope of the above set, the output answer is invalid.

Table 2

Parameters	Values	Notes
$i_{\max}$	100	Maximum number of iterations
i_{stop}	30	Maximum iterations without improvement
maxSteps	75	Number of steps that an ant traverses each iteration
nCandidates	$5\lvert V\rvert$	Candidate set cardinality
η	0.5	Initial pheromone evaporation factor
γ	1.5	Initial pheromone enhancement factor
updatePeriod	maxSteps/3	Pheromone update period
R	10	Number of iterations without improvement before escaping

Tables 3–6 provide the statistical results of optimal value, average value, standard deviation, coefficient of variation CV, and mean deviation value Gap after 20 times of operation for all the sample graphs under various conditions.

According to the deviation coefficient CV and mean deviation value Gap listed in the table, these values are large when $d = 2$. Significant changes can be observed comparing to optimal solution and the changes in optimal search are obvious.

With the increase of d, the restrictions of spanning tree construction will not be tightly controlled. It can be drawn from the table that optimal solution, taking graph att48 as an example, tends to be stable while changes in deviation coefficient and mean deviation value approach zero. Optimal tree weight tends to be stable and algorithm optimization gets improved with changes of d by adopting improved algorithm. With the increase of degree in sample graph, variation ranges of deviation coefficient and standard deviation value were kept within 0.00%–6.00%, even close to 0.00%. The above results show advantages of improved ant colony algorithm in solving DCMST of dense graph and advantages of ant colony algorithm in solving combinatorial optimization problem in minimum spanning tree.

When d is equal to 4 or 5, obtained solutions optimized by ant colony algorithm are basically stable in a certain range and optimized performance of algorithm and optimized values of results tend to be constant. The results imply that there are no more promotions on solution searching when degree constraints go over a certain range. Therefore, in practical applications, the degree of limitation on the spanning tree should be more considered. Excessive restrictions on spanning tree will not result in an expected optimization effect.

Table 3: Experimental results when $d = 2$.

Sample graph (G)	Optimal value (best)	Average value (μ)	Standard deviation (σ)	Coefficient of variation (CV)	Mean deviation value (Gap)
att48	32699.57	32865.26	193.35	1.00	1.00
bier127	117484.46	118228.23	0.00	1.00	1.00
eil51	402.00	413.50	9.19	2.00	4.00
eil76	524.00	537.50	0.71	0.00	3.00
eil101	519.00	534.50	2.12	0.00	3.00
ulysses16	43.00	45.50	2.12	5.00	6.00
ulysses22	43.00	45.00	2.83	6.00	5.00
kroA100	21802.88	22214.5	89.54	0.00	2.00
kroA200	32001.91	32139.63	145.86	0.00	0.00
rand50	5450.00	5450.00	0.00	0.00	0.00
rand75	7329.46	7384.14	0.00	0.00	1.00
rand100	8212.65	8398.32	262.58	3.00	2.00
rat99	1203.00	1250.00	41.01	3.00	4.00
pr107	38405.70	38943.71	59.19	0.00	1.00
pr136	105046.60	105417.40	405.11	0.00	0.00
pr152	67577.00	67880.68	312.56	0.00	0.00
chn31	13870.83	14041.91	175.49	1.00	1.00
ch130	6268.00	6389.03	171.16	3.00	2.00
ch150	6787.99	6875.00	0.00	0.00	1.00
overil30	367.23	372.11	6.91	2.00	1.00

Table 4: Experimental results when $d = 3$.

Sample graph (G)	Optimal value (best)	Average value (μ)	Standard deviation (σ)	Coefficient of variation (CV)	Mean deviation value (Gap)
att48	27855.00	27855.00	0.00	0.00	0.00
bier127	94680.00	94680.00	0.00	0.00	0.00
eil51	362.00	363.50	0.71	0.00	0.00
eil76	456.00	459.00	2.83	1.00	1.00
eil101	455.00	458.00	0.00	0.00	1.00
ulysses16	43.00	45.50	2.12	5.00	6.00
ulysses22	43.00	45.00	2.83	6.00	5.00
kroA100	18731.00	18731.00	0.00	0.00	0.00
kroA200	15853.00	25853.00	0.00	0.00	0.00
rand50	4967.00	4967.00	0.00	0.00	0.00
rand75	5996.00	5996.00	0.00	0.00	0.00
rand100	6907.00	6907.00	0.00	0.00	0.00
rat99	1082.00	1082.00	0.00	0.00	0.00
pr107	34890.00	34890.00	0.00	0.00	0.00
pr136	88940.00	88940.00	0.00	0.00	0.00
pr152	59105.00	59105.00	0.00	0.00	0.00
chn31	12111.00	12111.00	0.00	0.00	0.00
ch130	5102.00	5102.50	0.71	0.00	0.00
ch150	5812.00	5812.00	0.00	0.00	0.00
overil30	334.00	334.50	0.71	0.00	0.00

Table 5: Experimental results when $d = 4$.

Sample graph (G)	Optimal value (best)	Average value (μ)	Standard deviation (σ)	Coefficient of variation (CV)	Mean deviation value (Gap)
att48	27623.00	27623.00	0.00	0.00	0.00
bier127	94680.00	94680.00	0.00	0.00	0.00
eil76	456.00	457.50	2.12	0.00	0.00
eil51	359.00	359.00	0.00	0.00	0.00
eil101	456.00	458.00	1.41	0.00	0.00
ulysses16	41.00	42.00	0.00	0.00	2.00
ulysses22	41.00	43.00	0.00	0.00	0.00
kroA100	18731.00	18731.00	0.00	0.00	0.00
kroA200	25844.00	25844.00	0.00	0.00	0.00
rand50	4665.00	4665.00	0.00	0.00	0.00
rand75	5996.00	5996.00	0.00	0.00	0.00
rand100	6889.00	6889.00	0.00	0.00	0.00
rat99	1082.00	1082.00	0.00	0.00	0.00
pr107	34756.00	34756.00	0.00	0.00	0.00
pr136	88940.00	88940.00	0.00	0.00	0.00
pr152	59105.00	59105.00	0.00	0.00	0.00
chn31	12111.00	12111.00	0.00	0.00	0.00
ch130	5103.00	5103.50	0.00	0.00	0.00
ch150	5809.00	5809.00	0.00	0.00	0.00
overil30	334.00	334.50	0.71	0.00	0.00

Table 6: Experimental results when $d = 5$.

Sample graph (G)	Optimal value (best)	Average value (μ)	Standard deviation (σ)	Coefficient of variation (CV)	Mean deviation value (Gap)
att48	27623.00	27623.00	0.00	0.00	0.00
bier127	94680.00	94680.00	0.00	0.00	0.00
eil76	455.00	460	0.00	0.00	1.00
eil51	360.00	360.00	0.00	0.00	0.00
eil101	456.00	458.50	2.12	0.00	1.00
ulysses16	41.00	41.50	0.71	2.00	1.00
ulysses22	41.00	42.50	0.71	2.00	4.00
kroA100	18731.00	18731.00	0.00	0.00	0.00
kroA200	25844.00	25844.00	0.00	0.00	0.00
rand50	4665.00	4665.00	0.00	0.00	0.00
rand75	5996.00	5996.00	0.00	0.00	0.00
rand100	6889.00	6889.00	0.00	0.00	0.00
rat99	1082.00	1082.00	0.00	0.00	0.00
pr107	34756.00	34756.00	0.00	0.00	0.00
pr136	88940.00	88940.00	0.00	0.00	0.00
pr152	59105.00	59105.00	0.00	0.00	0.00
chn31	12111.00	12111.00	0.00	0.00	0.00
ch130	5102.00	5102.50	0.71	0.00	0.00
ch150	5809.00	5809.00	0.00	0.00	0.00
overil30	334.00	334.50	0.71	0.00	0.00

Table 7: Results of comparison for multiple and single colony ant algorithm.

Sample graph	$d = 2$			
	Average solution (μ)		Optimal solution (best)	
	Multiple	Single	Multiple	Single
eil51	374.43	413.50	398.00	402.00
eil76	534.98	537.50	519.00	524.00
chn31	14012.02	14041.91	13870.86	13870.83
overil30	371.92	372.11	365.00	367.23
ulysses16	45.00	45.50	43.00	44.00
ulysses22	46.50	45.00	43.00	44.00
rand75	7390.14	7384.14	7326.04	7329.46
rand100	8248.18	8398.32	8166.56	8212.65
gr96	462.50	463.70	445.00	449.00
gr120	1678.90	1692.41	1631.00	1663.00
gr137	686.80	690.30	682.00	683.00
bayg29	8107.22	8597.52	8432.44	8439.00
beilin52	7702.51	7761.52	7442.58	7627.00
burma14	19.70	19.90	18.00	19.00
danzig42	647.16	656.39	640.65	642.92
st70	662.73	663.90	643.00	650.00
kroA150	27446.79	27611.06	27363.01	27471.08

Table 8: Results of comparison for multiple and single colony ant algorithm.

Sample graph	$d = 3$			
	Average solution (μ)		Optimal solution (best)	
	Multiple	Single	Multiple	Single
eil51	363.25	363.50	362.00	363.00
eil76	459.00	460.00	454.00	456.00
gr96	398.40	399.75	395.00	397.00
bayg29	7456.81	7459.00	7415.16	7459.00
danzig42	565.75	566.15	565.00	566.00
ulysses22	42.60	45.00	41.00	43.00
st70	544.50	544.65	542.00	543.00

By comparing multicolony ant algorithm with single colony ant algorithm [2], multicolony ant algorithm is obviously more effective in solution optimization which proves that multicolony ant algorithm shows greater advantages in DCMST optimal searching. Conditions under $d = 2$ and $d = 3$ are selected here to illustrate the proposed opinion. Solution assessment of these two algorithms is evaluated by average solution (μ) and optimal solution (best). Solution comparisons of multicolony ant algorithm and single colony ant algorithm under $d = 2$ and $d = 3$ are listed in Tables 7 and 8.

Experimental data as shown in Tables 7 and 8 show that average weight and optimal weight of DCMST obtained by multicolony ant algorithm are obviously smaller than those solved by single colony ant algorithm. Multicolony ant algorithm yields better optimization results than single colony ant algorithm which implies that coordination and cooperation through information entropy in multiant colonies promotes better convergence of algorithm and expands search space which adds to the diversity of solution. By comparing experimental results of $d = 2$ and $d = 3$, it can be seen that the tougher the degree constraints of minimum spanning tree are, the more accurate the solution searched by multicolony ant algorithm is. The above analysis proved that the algorithm has strong search ability.

It can be drawn from the above analysis that multicolony ant algorithm shows greater superiority in solving DCMST. It features outstanding ability of optimal solution finding and also it will extensively distribute the solutions and obtain new optimal solutions, thus making it a better algorithm for searching DCMST with smallest weight.

6. Conclusion

The paper carried out studies on applications of ant colony algorithm in DCMST optimization. Many problems remain

unresolved in this study since researches on swarm intelligence of ant colony algorithm are still in a primary stage. Works to be carried out next are as follows: to find out links among genetic algorithm, hill-climbing algorithm, and particle swarm optimization algorithm and integrate them into a novel improved algorithm. By adopting it to optimizations like DCMST, practical application demands can be met.

Another work to be done is to improve parameters selection criteria of algorithm optimization and assessment standard of algorithm stability on account of the lack of related study in depth while ant colony algorithm is a heuristic search algorithm and also due to few works being carried out in this field to perfectly prove its correctness.

Owing to the complexity and diversity of practical problems and variations in working environment, multilayered algorithms have not been reached in this paper. In addition, complex theory has become a powerful framework to deal with the complexity problems in real-world systems [20–23]. Thus, concurrent collaborations of multiant colonies will be a key emphasis in work so as to increase the speed and efficiency of solving tasks.

In a word, related works presented in this paper reflect smart features of intelligent computing and dynamic execution in parallel, and significant achievements have been made by it in DCMST.

Conflict of Interests

The authors declare that there is no conflict of interests regarding the publication of this paper.

Acknowledgments

The project is supported by the National Natural Science Foundation of China (Grant no. 61173032), the Young Scientists Fund of the National Natural Science Foundation of China (Grant no. 61402329), and the Natural Science Foundation of Tianjin, China (Grant nos. 13JCYBJC15500 and 12JCYBJC31900).

References

[1] M. N. Doan, "An effective ant-based algorithm for the degree-constrained minimum spanning tree problem," in *Proceedings of the IEEE Congress on Evolutionary Computation (CEC '07)*, pp. 485–491, IEEE, September 2007.

[2] T. N. Bui, X. Deng, and C. M. Zrncic, "An improved ant-based algorithm for the degree-constrained minimum spanning tree problem," *IEEE Transactions on Evolutionary Computation*, vol. 16, no. 2, pp. 266–278, 2012.

[3] F. Neumann and C. Witt, "Ant colony optimization and the minimum spanning tree problem," *Theoretical Computer Science*, vol. 411, no. 25, pp. 2406–2413, 2010.

[4] T. N. Bui and C. M. Zrncic, "An ant-based algorithm for finding degree-constrained minimum spanning tree," in *Proceedings of the 8th Annual Genetic and Evolutionary Computation Conference*, pp. 11–18, ACM, July 2006.

[5] Y.-T. Bau, C.-K. Ho, and H.-T. Ewe, "Ant colony optimization approaches to the degree-constrained minimum spanning tree problem," *Journal of Information Science and Engineering*, vol. 24, no. 4, pp. 1081–1094, 2008.

[6] S. C. Narula and C. A. Ho, "Degree-constrained minimum spanning tree," *Computers and Operations Research*, vol. 7, no. 4, pp. 239–249, 1980.

[7] M. Savelsbergh and T. Volgenant, "Edge exchanges in the degree-constrained minimum spanning tree problem," *Computers and Operations Research*, vol. 12, no. 4, pp. 341–348, 1985.

[8] L. Caccetta and S. P. Hill, "A branch and cut method for the degree-constrained minimum spanning tree problem," *Networks*, vol. 37, no. 2, pp. 74–83, 2001.

[9] A. Volgenant, "A Lagrangean approach to the degree-constrained minimum spanning tree problem," *European Journal of Operational Research*, vol. 39, no. 3, pp. 325–331, 1989.

[10] M. Behle, M. Jünger, and F. Liers, "A primal branch-and-cut algorithm for the degree-constrained minimum spanning tree problem," in *Experimental Algorithms*, vol. 4525 of *Lecture Notes in Computer Science*, pp. 379–392, Springer, Berlin, Germany, 2007.

[11] G. R. Raidl, "An efficient evolutionary algorithm for the degree-constrained minimum spanning tree problem," in *Proceedings of the Congress on Evolutionary Computation*, vol. 1, pp. 104–111, La Jolla, Calif, USA, 2000.

[12] G. R. Raidl and B. A. Julstrom, "A weighted coding in a genetic algorithm for the degree-constrained minimum spanning tree problem," in *Proceedings of the ACM Symposium on Applied Computing (SAC '00)*, vol. 1, pp. 440–445, ACM, March 2000.

[13] J. Knowles and D. Corne, "A new evolutionary approach to the degree-constrained minimum spanning tree problem," *IEEE Transactions on Evolutionary Computation*, vol. 4, no. 2, pp. 125–134, 2000.

[14] M. Dorigo and C. Blum, "Ant colony optimization theory: a survey," *Theoretical Computer Science*, vol. 344, no. 2-3, pp. 243–278, 2005.

[15] T. Stützle and H. H. Hoos, "MAX-MIN ant system," *Future Generation Computer Systems*, vol. 16, no. 8, pp. 889–914, 2000.

[16] B. Doerr and D. Johannsen, "Refined runtime analysis of a basic ant colony optimization algorithm," in *Proceedings of the IEEE Congress on Evolutionary Computation (CEC '07)*, pp. 501–507, Singapore, September 2007.

[17] M. Krishnamoorthy, A. T. Ernst, and Y. M. Sharaiha, "Comparison of algorithms for the degree constrained minimum spanning tree," *Journal of Heuristics*, vol. 7, no. 6, pp. 587–611, 2001.

[18] H. T. T. Binh and T. B. Nguyen, "New particle swarm optimization algorithm for solving degree constrained minimum spanning tree problem," in *PRICAI 2008: Trends in Artificial Intelligence*, vol. 5351 of *Lecture Notes in Computer Science*, pp. 1077–1085, Springer, Berlin, Germany, 2008.

[19] A. T. Ernst, "A hybrid Lagrangian particle swarm optimization algorithm for the degree-constrained minimum spanning tree problem," in *Proceedings of the IEEE Congress on Evolutionary Computation (CEC '10)*, IEEE, 2010.

[20] Z.-Q. Ma, C.-Y. Xia, S.-W. Sun, L. Wang, H.-B. Wang, and J. Wang, "Heterogeneous link weight promotes the cooperation in spatial prisoner's dilemma," *International Journal of Modern Physics C*, vol. 22, no. 11, pp. 1257–1268, 2011.

[21] J.-J. Zhang, H.-Y. Ning, Z.-Y. Yin et al., "A novel snowdrift game model with edge weighting mechanism on the square lattice," *Frontiers of Physics*, vol. 7, no. 3, pp. 366–372, 2012.

[22] C. Y. Xia, S. W. Sun, Z. X. Liu, Z. Q. Chen, and Z. Z. Yuan, "Epidemics of sirs model with nonuniform transmission on scale-free networks," *International Journal of Modern Physics B*, vol. 23, no. 9, pp. 2203–2213, 2009.

[23] C. Y. Xia, Z. X. Liu, Z. Q. Chen, and Z. Z. Yuan, "SIRS epidemic model with direct immunization on complex networks," *Control and Decision*, vol. 23, no. 4, pp. 468–472, 2008.

Hindawi Publishing Corporation
Mathematical Problems in Engineering
Volume 2015, Article ID 720523, 15 pages
http://dx.doi.org/10.1155/2015/720523

Research Article

A Method for Signal Coordination in Large-Scale Urban Road Networks

Bao-Lin Ye, Weimin Wu, and Weijie Mao

National Laboratory of Industrial Control Technology, Institute of Cyber-Systems and Control, Zhejiang University, Yuquan Campus, Hangzhou, Zhejiang 310027, China

Correspondence should be addressed to Weimin Wu; wmwu@iipc.zju.edu.cn

Received 28 October 2014; Accepted 5 January 2015

Academic Editor: Kun Liu

Copyright © 2015 Bao-Lin Ye et al. This is an open access article distributed under the Creative Commons Attribution License, which permits unrestricted use, distribution, and reproduction in any medium, provided the original work is properly cited.

Signal coordination methods have been widely investigated to improve the performance of traffic control system in urban road networks. Due to the large-scale of road networks and numerous time-varying parameters, a basic challenge faced by these methods is the high computational complexity. In this research, a method to optimize and coordinate the traffic signal in urban road networks is developed, which deals with this challenge by decomposing the network into several arterial roads and scattered intersections. As a result, an area coordination problem has been solved by coordinating several principal arterial roads and isolated intersections. Firstly, we propose a bandwidth oriented two-way arterial coordination approach. In contrast to previous methods, one important feature of the proposed approach is that not only the phases which provide right of way to the coordinated directions but the phases which provide right of way to the uncoordinated directions are considered. Secondly, to reduce the computational complexity a network decomposition approach is designed, in which a priority level index is defined to quantify the priority level of each road. Then, a coordination algorithm for the whole road network is developed. Finally, effectiveness and efficiency of the proposed method are validated by simulations on VISSIM.

1. Introduction

Aterial traffic congestion and the associated time-consuming, traffic jams, and noise and air pollution are a hard nut to crack to traffic administration organs of both the developed and developing countries. Consequently, the researches on reducing urban traffic congestion with advanced control and information technologies have long been a hot research topic. It is generally recognized that traffic signal control is one of the most effective and efficient manners to alleviate traffic congestion. As a result, many traffic signal control strategies have been developed [1–25].

As one of the earliest signal control strategies, isolated intersection control strategies mainly focused on the optimization of an isolated intersection. In general, it includes fixed-time control and traffic-responsive control [1]. The former one is based on the statistics of history traffic flow patterns. The latter one is an online process that utilizes real time traffic data to optimize the green time of a traffic light. As pointed out in [2], with a strong optimization capability, the isolated intersection control strategies can provide a strong basis for implicit coordination with the adjacent intersections. Hence, several new signal control strategies for isolated intersection have been proposed. For example, a new approach for controlling the traffic at isolated intersections is developed, whereby the dynamic behavior of the traffic is considered and modeled with Petrinets [3]. In [4], inspired by the observation of self-organized oscillations of pedestrian flows at bottlenecks, Lämmer and Helbing proposed a self-organization approach to traffic light control. Xie et al. [5] reported on a schedule-driven intersection control strategy, whereby the main characteristic is an alternative formulation of intersection control optimization as a scheduling problem to reduce the state space.

Then, to improve the performance of isolated intersection control, coordinated control strategies were proposed. In general, coordinated control mainly falls into two categories, fixed-time coordinated control and coordinated traffic-responsive strategies. For example, bandwidth oriented signal timing approaches MAXBAND [6] and MULTIBAND [7]

and traffic network study tool TRANSYT [8] are well known fixed-time coordination control methods. SCOOT [9] and SCATS [10] are regarded as the earliest and leading examples of the coordinated traffic-responsive control approaches. After that, lots of model-based traffic-responsive control strategies with rolling time horizon emerged in 1990s, for example, OPCA [11], PRODYN [12], and CRONOS [13]. However, the performance of these strategies is limited due to the fact that the computational complexity grows exponentially with the size of the urban traffic network. Moreover, based on store-and-forward strategy, a traffic-responsive urban control (TUC) framework was proposed in [14]. Despite the simplicity and the efficiency of the proposed TUC, such a framework does not allow for immediate consideration of modifications and expansions of the controlled traffic network.

Owing to the fact that the predominant traffic flow in urban traffic networks is mainly along arterials, coordination of traffic signals along arterials usually provides numerous advantages [15]. For example, (1) higher level of traffic service is provided in terms of higher overall speed and reduced number of stops; (2) there are few accidents because the platoons of vehicles arrive at each signal when it is green, thereby reducing the possibility of red signal violations and rear-end collisions; (3) greater obedience to the signal commands is obtained from both motorists and pedestrians. The motorists try to keep being within the green interval, and the pedestrian stays at the curb because the vehicles are more tightly spaced. Hence, coordinating the traffic signals along these arterial roads is essential for the effective operation of the urban traffic networks. Some early results can be found in [6, 7]. In [15], Stamatiadis and Gartner proposed a bandwidth oriented progression model and designed the MULTIBAND-96 program, which can produce variable-width progression along arterial road in traffic networks. In [16], Tian and Urbanik reported a signal coordination approach based on a system partition technique to optimize the progression bandwidths for continuous signals along a signalized arterial. Later, Tian et al. [17] developed a computer program which aims to provide maximum bandwidth solutions for randomly generated multiple signal system scenarios. In [18], Kong et al. proposed a bidirection green wave intelligent control technology to solve the coordinate control problems of urban arterial traffic, whereby a two-level control structure was developed. In [19], to optimize the bandwidth for continuous signal along arterial road, Lin et al. developed a new mixed-integer nonlinear programming model with the objection of allowing vehicles to pass through the maximum number of downstream intersections without a stop. In [20], Lu et al. developed an improved two-way bandwidth maximization model for arterial roads with unbalanced bandwidth demands. In their model, a proration impact factor was defined to allow engineers to assign the importance of satisfying the target bandwidth demand rate.

It is noted that all the above progression models and results [16–20] are main focus on arterial signal coordination. It seems that the corresponding results on coordinating urban road networks with green wave coordination strategies are very few. In [21] arterial progression models were first introduced by Gartner and Stamatiadis to deal with the coordination and optimization of traffic signal in urban grid networks. It was shown that the computational efficiency of the optimization model was improved by introducing a heuristic network decomposition procedure. Then, in [22], Gartner and Stamatiadis extended their previous work [21] and developed a network multiband progression model. This model was based on selecting and optimizing an arterial priority network or a route priority network. It should be noted that one of the key aspects of the network decomposition presented in [21, 22] was the definition of a priority subnetwork. However, only two simple criteria were presented in [21, 22]; the details of the selection of a priority subnetwork were not clearly discussed. In addition, coordination control of a large-scale road network should take into account numerous time-varying parameters, such as cycle time, splits, and offset. Although it is technically feasible, it may not always be practical in implementation for real time signal control. It means that a coordination method, which allows simple implementation and nonexcessive data communication, while pointing toward the general direction of alleviating congestion, is needed.

Motivated by the above discussion, in this paper we propose an arterial progression based approach for signal coordination in urban road networks. Simulations on VISSIM have been presented to demonstrate the effectiveness and efficiency of the proposed approach. The main contribution of this paper can be summarized as follows. (1) A bandwidth oriented two-way arterial coordination approach is developed. Different from the typical MAXBAND model [6] and MULTIBAND model [7], one important feature of the proposed method is that not only the phases which provide right of way to the coordinated directions but the phases which provide right of way to uncoordinated directions are also taken into account during the process of optimization of phase sequences; (2) to deal with computational complexity in large-scale road networks, an economical and practical network decomposition strategy is proposed, whereby a novel priority level index is employed to quantify the priority level of each road; (3) the problem of coordinating a large-scale urban road network has been solved by coordinating the principal arterial and several isolated intersections on the boundary of the area, and a novel coordination methodology is proposed.

The reminder of this paper is organized as follows. In Section 2, we propose a new arterial signal coordination model, whereby the phase sequences are optimized. Section 3 presents a novel priority level index and a network decomposition method. A coordination framework of traffic signal control for urban road networks is developed in Section 4. Section 5 reports the results of numerical simulation. Finally, Section 6 concludes this paper with a summary of work.

2. Coordination of Arterial Road

Figure 1 illustrates an urban arterial road A that comprises n intersections that are controlled by traffic lights. For each intersection, there are a set of entry and exit links

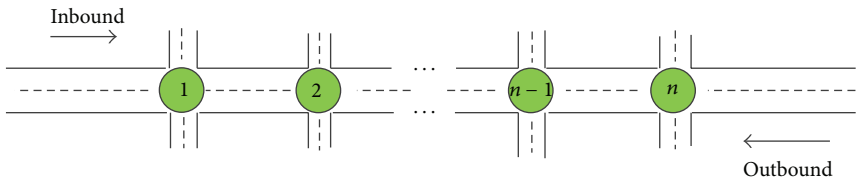

Figure 1: An arterial road A with n intersections.

(approaches), where each link has a fixed length and a set of lanes. For each lane, the "First In and First Out (FIFO)" discipline is used to discharge the vehicle platoons and lane changing or overtaking will not be allowed if vehicles enter a study section [19]. To facilitate the model description, the variables used hereafter are summarized as follows:

(i) C_A: the cycle time of all intersections along the arterial road A;

(ii) g_j^p: the green time of phase p of intersection j;

(iii) $l_{j,j+1}$: the distance between intersection j and intersection $j+1$;

(iv) $v_{j,j+1}$: the travelling speed between intersection j and intersection $j+1$;

(v) $O_{j,j+1}^{p_1}$: the inbound offset of phase p_1 between two successive intersections j and $j+1$;

(vi) $O_{j+1,j}^{p_2}$: the outbound offset of coordinated phase p_2 between two successive intersections j and $j+1$;

(vii) $t_j^{p_1}$: the start time of phase p_1 of intersection j along the inbound direction;

(viii) $t_j^{p_2}$: the start time of phase p_2 of intersection j along the outbound direction;

(ix) F_j: the phase set of intersection j, that is, $\{p_1, \ldots, p_{|F_j|}\}$.

Figure 2 shows the time space diagram between intersection j and $j+1$. It is shown that, by optimizing the green time of coordinated phase p_1 and phase p_2, travel speed $v_{j,j+1}$ and $v_{j+1,j}$, offset $O_{j,j+1}^{p_1}$ and $O_{j,j+1}^{p_2}$ between intersection, and vehicles along inbound and outbound directions can cross intersection j and $j+1$ without stops simultaneously. The key idea of the proposed arterial road coordination method is to construct a two-way green wave band along two coordinated directions by optimizing and coordinating the green start time of two coordinated phase p_1 and phase p_2. Different from previous studies [15–23], in our proposed coordination framework not only the coordinated phase p_1 and phase p_2 but the phase p_3 has been optimized during the process of optimization of phase sequences.

2.1. Cycle Time. First of all, according to the well-known approach known as Websters formula [1], the optimal cycle time of intersection can be expressed as follows:

$$C_j = \frac{1.5L_j + 5}{1 - \sum_{i \in I_j} q_i / S_j^i}, \tag{1}$$

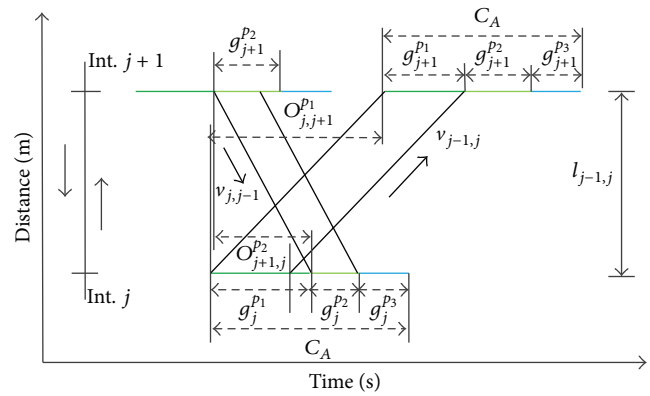

Figure 2: The time space diagram between intersections $j-1$ and j.

where L_j is lost time of intersection j, q_i is the nominal inflow to link i in vehicles per hour, S_i is the saturation flow of link i, and I_j denotes the set of all links which belong to intersection j.

In order to facilitate the coordination of an arterial road, each coordinated intersection along the arterial should be associated with an identical cycle time. The intersection with the biggest cycle time is defined as the key intersection of the arterial. The biggest cycle time is usually selected as the common cycle for all intersections along the arterial. For example, the common cycle time C_A of the arterial A is defined as

$$C_A = \max_{j \in A} C_j. \tag{2}$$

2.2. Signal Splits. For each phase p of intersection j, the optimal green splits can be calculated by the Websters formula [1] as

$$g_j^p = \frac{\max \hbar}{\sum_{p \in F_j} \max \hbar} \cdot \left(C_A - L_j\right), \tag{3}$$

where $\hbar = \{q_{j,1}^p / S_{j,1}^p, \ldots, q_{j,i}^p / S_{j,i}^p, \ldots, q_{j,n}^p / S_{j,n}^p\}$, $q_{j,i}$ is the inflow to link i of intersection j, $S_{j,i}^p$ is the saturation flow of link i, and phase p provides the right of way to link i.

In general, to guarantee the safety of pedestrians and cyclists, there usually exists a green constraint for each phase p of intersection j. Hence, if the green time calculated by (3) is not satisfied by the following constraint:

$$g_{j,\min}^p \le g_j^p \le g_{j,\max}^p, \tag{4}$$

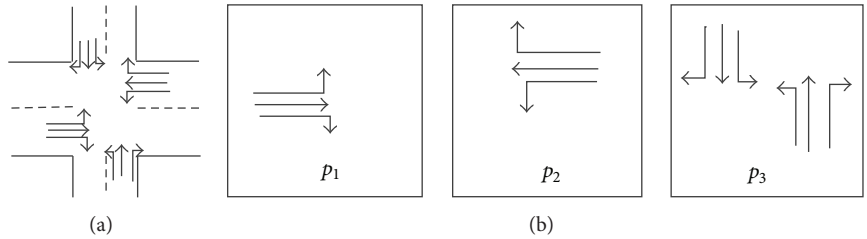

Figure 3: (a) Intersection layout, (b) phase setting.

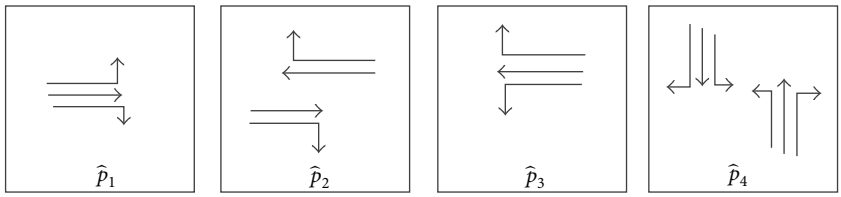

Figure 4: Lead/lag left-turn phase.

then we need to regulate g_j^p. Unfortunately, when there are several phases of an intersection which do not satisfy constraint (4), the regulating process will be a tedious work. Therefore, we propose a new method to calculate and regulate the green time g_j^p, as it is shown in the following two equations:

$$\widehat{g}_j^p = g_{j,\min}^p + \frac{\max \hbar}{\sum_{p\in F_j} \max \hbar} \cdot \left(C_A - \sum_{p=1} g_{j,\min}^p \right),$$
$$g_j^p = \begin{cases} \widehat{g}_j^p, & \text{if } \widehat{g}_j^p < g_{j,\max}^p, \\ g_{j,\max}^p, & \text{else}, \end{cases} \tag{5}$$

where $g_{j,\min}^p$ and $g_{j,\max}^p$ are the predefined minimum and maximum green time.

2.3. Phase Setting. As one of the most critical and creative parts of traffic signal coordination, the establishment of a phase scheme has great impact on intersection capacity and efficiency. Note that if left-turn vehicle flows are not controlled, it will severely disturb straight-go vehicles and have big impact on the safety of pedestrians, even if left-turn vehicle flows on arterial road are not heavy [18]. Hence, herein a left-turn phase is designed for the left-turn vehicle flows along arterial road. Consider a typical four-legged intersection shown in Figure 3(a). Regularly, an idyllic phase combination is developed in Figure 3(b) for bidirection arterial signal coordination. It means that phase p_2 starts just when phase p_1 completes.

However, in practice to obtain a bidirection green wave band along the arterial road, phase p_1 and phase p_2 usually overlap. Assume that phase p_1 and phase p_2 provide the right of way for the inbound and outbound traffic flows as shown in Figure 1, respectively. To prevent left-turn traffic flows disturbing the straight-go traffic flows, the advance-close and lag-open strategies are introduced to deal with left-turn phases [18]. Therefore, the phase combination shown in Figure 3(b) can be extended to the phase combination illustrated in Figure 4. It is clear that the phase $\widehat{p}_2$ in Figure 4 is the combination of phase p_1 and phase p_2 in Figure 3(b). Herein, the advance-close strategy and the lag-open strategies are applied to the left-turn of phase and that of phase, respectively. Figure 5 shows another phase sequences.

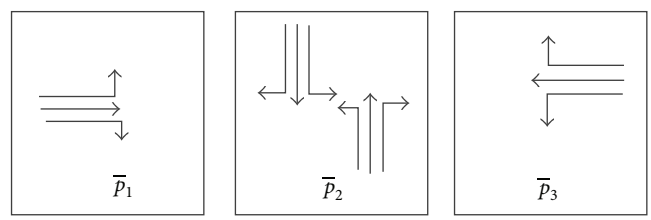

Figure 5: Regulated phase sequence.

2.4. Speed Constraints. As shown in previous studies [19], to provide smooth traffic flows to users and design adequate signal offsets along an arterial road, the range of link travel time under different traffic conditions should be calculated first. On the other hand, the length of each link is known. Therefore, the following two speed limit constraints (6) are introduced to determine the lower and upper speed limits when the model of maximum progression bandwidth is applied:

$$\begin{aligned} v_{\min} &\le v_{j,j+1} \le v_{\max}, \\ \overline{v}_{\min} &\le v_{j+1,j} \le \overline{v}_{\max}. \end{aligned} \tag{6}$$

In addition, the following constraints (7) are used to ensure that the speed changes between two adjacent links fall into a reasonable range:

$$\begin{aligned} \tilde{v}_{\min} &\le \left| v_{j-1,j} - v_{j,j+1} \right| \le \tilde{v}_{\max}, \\ \hat{v}_{\min} &\le \left| v_{j-1,j} - v_{j,j+1} \right| \le \hat{v}_{\max}, \end{aligned} \tag{7}$$

where $v_{\min}$ ($\bar{v}_{\min}, \tilde{v}_{\min}, \hat{v}_{\min}$) and $v_{\max}$ ($\bar{v}_{\max}, \tilde{v}_{\max}, \hat{v}_{\max}$) are predefined constants.

2.5. Calculation of Offsets. The offset between two intersections is defined as the duration from the beginning of a green phase at one intersection to the start of the following nearest green phase at another intersection. In order to obtain a green wave band and allow uninterrupted flows of traffic pass through the entire arterial without stop, the offset between two adjacent intersections can be approximated by the travelling time between the two intersections. Thus, the inbound and outbound offset can be calculated as follows:

$$O_{j,j+1}^{p_1} = \frac{l_{j,j+1}}{v_{j,j+1}}, \tag{8a}$$

$$O_{j+1,j}^{p_2} = \frac{l_{j,j+1}}{v_{j+1,j}}. \tag{8b}$$

2.6. Start Time of Coordination Phases. As discussed above, the phase p_1 and phase p_2 shown in Figure 3(b) govern the right of way of the inbound and outbound traffic flow, respectively. Take the arterial road A shown in Figure 1 as an example, assume that the start time of phase p_1 at intersection 1 along the inbound direction is t_0; then the start time of phase p_1 at the jth intersection can be updated by the following equation:

$$t_j^{p_1} = t_0 + \sum_{k=2}^{j} O_{k-1,k}^{p_1}, \quad j = 2, \ldots, n. \tag{9}$$

Similarly, if we assume that the start time of phase p_2 at intersection n along the outbound direction is $\hat{t}_0$, then the start time of phase p_2 at the jth intersection can be calculated as

$$t_j^{p_2} = \hat{t}_0 + \sum_{k=j}^{n-1} O_{k+1,k}^{p_2}, \quad j = n-1, \ldots, 1. \tag{10}$$

2.7. Objective Function. It is shown in Figure 6(a), corresponding to the phase combination illustrated in Figure 3(b), the ideal case is that when the green time of phase p_1 (or phase p_2) ends then the green time of phase p_2 (or phase p_1) starts immediately. However, in practice the length of downstream and upstream road sections is regularly not the same and the travel speed on road sections is heterogeneous. Thus, the ideal case is less likely to happen. There usually exist another two cases. One case shown in Figure 6(b) is that phase p_1 and phase p_2 are overlapped. Meanwhile, the phase combination shown in Figure 3(b) is extended to the one illustrated in Figure 4. Another case shown in Figure 6(c) is that, before the start of the green time of phase p_2 (or phase p_1), the green time of phase p_1 (or phase p_2) has already ended. In real-world application, Case 3 shown in Figure 6(c) must be avoided.

In [18], to avoid the occurrence of case 3 shown in Figure 6(c) and obtain the maximal progression band, Kong et al. formulated the problem of arterial signal coordination as a biobjective optimization model. In addition, Ye et al. [23] extend the biobjective model to the signal control and coordination for a simple road network constituted by two crossed arterial roads. Since the two objective functions of the biobjective model have different priority level, the problem-solving process is tedious and time-consuming especially for large size problems. Aiming at dealing with this difficultly, we have improved the biobjective model and developed a single objective model. The equation of the objective function is defined as follows:

$$\min J_A = \min \sum_{j=1}^{n} \left| \Delta t_j \right|, \tag{11}$$

subject to (1)–(10) and

$$\Delta t_j = \begin{cases} t_j^{p_2} - t_j^{p_2} - g_j^{p_1}, & \text{if } t_j^{p_1} \le t_j^{p_2} \\ t_j^{p_1} - t_j^{p_2} - g_j^{p_2}, & \text{else.} \end{cases} \tag{12}$$

Remark 1. Although according to the presented optimization model Case 3 shown in Figure 6(c) only has a small chance of occurring, the occurrence of it can not be completely eliminated. Therefore, to deal with this problem we propose a regulate scheme as a part of model correction.

2.8. Regulate Schemes. Consider Case 2 shown in Figure 6(b); assume that the optimal green time of phase p_1 and phase p_2 at the jth intersection is $g_j^{p_1}$ and $g_j^{p_2}$, respectively, and the overlapping time is Δt_j. Under this situation, it is naturally to define the overlap interval as a new phase. In other words, the phase setting shown in Figure 3(b) should be extended to that illustrated in Figure 4. It is shown in Figure 7 that the start time and the green time of phase $\hat{p}_1$, phase $\hat{p}_2$, phase $\hat{p}_3$, and phase $\hat{p}_4$ (shown in Figure 4) can be derived by (13). For simplicity, herein we assume that $t_j^{p_1} \le t_j^{p_2}$:

$$\begin{aligned} t_j^{\hat{p}_1} &= t_j^{p_1}, & t_j^{\hat{p}_2} &= t_j^{p_2}, \\ t_j^{\hat{p}_3} &= t_j^{p_2} + g_j^{\hat{p}_2}, & t_j^{\hat{p}_4} &= t_j^{p_3} + g_j^{\hat{p}_3}, \end{aligned}$$

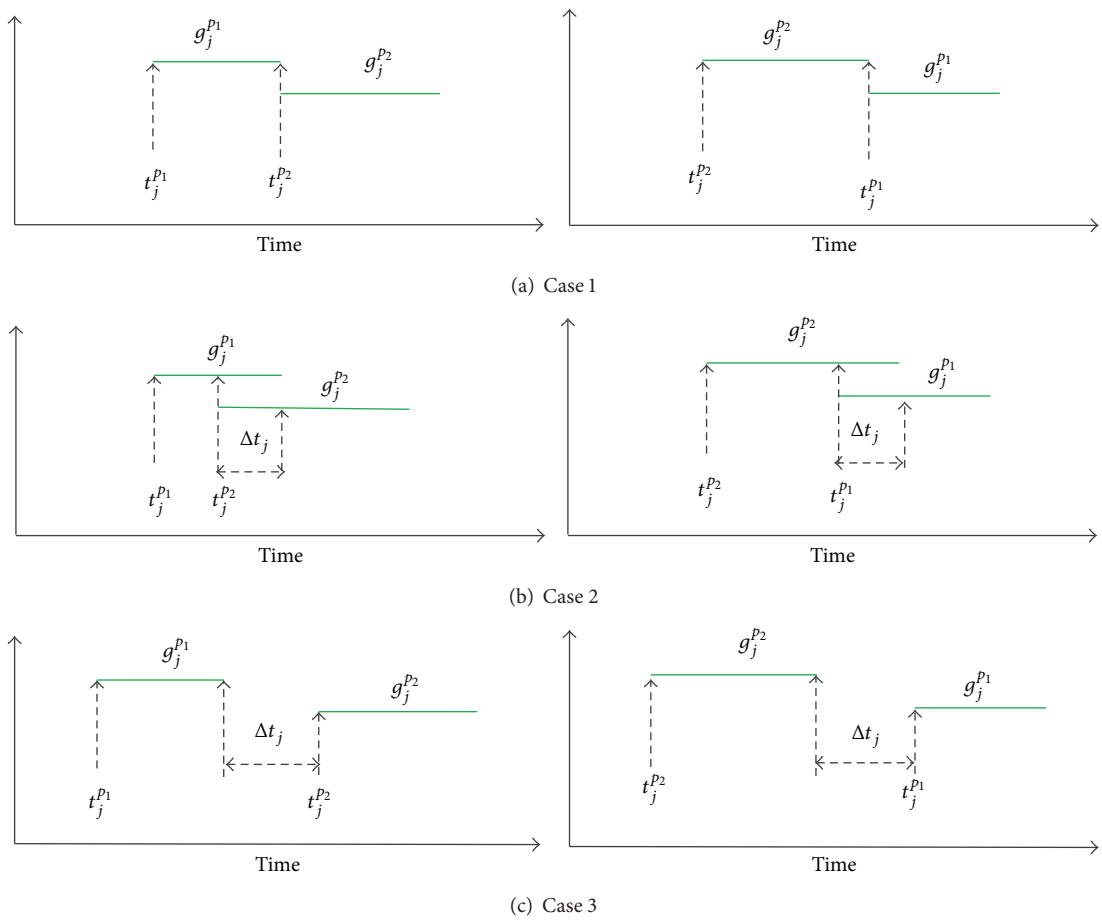

FIGURE 6: The relations between the start time of phase p_1 and phase p_2.

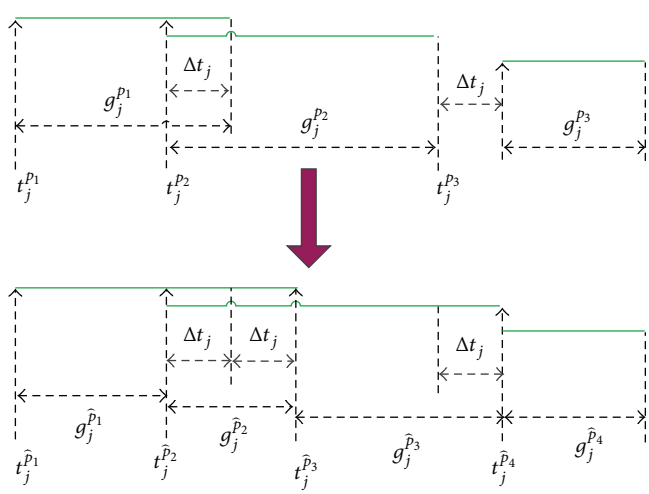

FIGURE 7: Adjustments for Case 2.

$$g_j^{\hat{p}_1} = g_j^{p_1} - \Delta t_j, \qquad g_j^{\hat{p}_2} = 2 \cdot \Delta t_j,$$
$$g_j^{\hat{p}_3} = g_j^{p_2}, \qquad g_j^{\hat{p}_4} = g_j^{p_3}. \tag{13}$$

It should be noted that, for the case $t_j^{p_1} > t_j^{p_2}$, similar results can also be derived with the same method. Furthermore, since the length of the cycle time C_A is kept unchanged, the overlap time Δt_j should be assigned to phase $\hat{p}_1$ (or $\hat{p}_2$

or $\widehat{p}_3$). Herein, Δt_j is assigned to phase $\widehat{p}_2$ to maximize the bandwidth.

As mentioned previously, although Case 3 shown in Figure 6(c) should be avoided as much as possible, it might be encountered in real-world traffic conditions. Since the length of overlap time Δt_j has a significant effect on the length of green time for left-turn traffic of phase p_1 and that of phase p_2, we proposed the following three different regulate strategies to respond to the situations that the overlap time Δt_j falls into different ranges.

Subcase 1 ($0 \le \Delta t_j < \delta_1 \cdot g_j^{p_3}$). In this scenario, Δt_j is a small proportion of the green time of phase p_3. It is argued that one of the simplest ways to eliminate the gap is to prolong the green time of phase p_1 and advance the green start time of phase p_2. At the same time, due to the length of the cycle time C_A was kept unchanged and the green time of phase p_3 must be reduced by Δt_j. The result of the regulation is illustrated in Figure 8. Then, we have

$$\begin{aligned}
\widetilde{t}_j^{p_1} &= t_j^{p_1}, \qquad \widetilde{t}_j^{p_3} = t_j^{p_3}, \\
\widetilde{t}_j^{p_2} &= t_j^{p_2} - \frac{\Delta t_j \cdot g_j^{p_2}}{\left(g_j^{p_1} + g_j^{p_2}\right)}, \\
\widetilde{g}_j^{p_1} &= g_j^{p_1} + \frac{\Delta t_j \cdot g_j^{p_1}}{\left(g_j^{p_1} + g_j^{p_2}\right)}, \\
\widetilde{g}_j^{p_2} &= g_j^{p_2} + \frac{\Delta t_j \cdot g_j^{p_2}}{\left(g_j^{p_1} + g_j^{p_2}\right)}, \\
\widetilde{g}_j^{p_3} &= g_j^{p_3} - \Delta t_j,
\end{aligned} \tag{14}$$

where δ_1 is a regulator parameter and $\widetilde{t}_j^{p_1}$ and $\widetilde{t}_j^{p_2}$ are the start time corresponding to phase p_1 and phase p_2 after the regulating strategy is implemented. The phase setting shown in Figure 3(b) is implemented. The start time of phase p_1 remains unchanged, and that of phase p_2 would be advanced by $\Delta t_j \cdot g_j^{p_2}/(g_j^{p_1} + g_j^{p_2})$. In addition, the green time of p_1 and phase p_2 is extended, and the sum of them equals the reduction of the green time of phase p_3.

Subcase 2 ($\delta_1 \cdot g_j^{p_3} < \Delta t_j < \delta_2 \cdot g_j^{p_3}$). Under the current situation, the gap Δt_j is not a small proportion of the green time of phase p_3. The approach for eliminating the gap used in previous strategy cannot be adopted. Because if we eliminate the gap by reducing equal amount of green time of phase p_3, the remaining part of the green time of phase p_3 will be not sufficient to dissipate all the traffic flows of northbound and southbound at intersection j in one cycle. As a result, extra queuing delay will be imposed on part of the traffic flows of the minor streets whose right of way is controlled by phase p_3.

Herein, to eliminate the gap Δt_j, on one hand we advance the start time of phase p_1 and that of phase p_2. Simultaneously, to reduce the influences of these regulations imposed on coordinated directions, we also regulate the length of

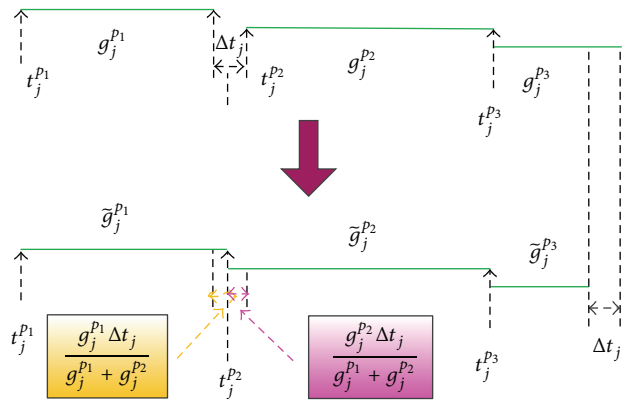

Figure 8: Adjustments for Subcase 1.

the green time of phase p_1 and that of phase p_2. As shown in Figure 9, the start time and green time of phase p_1, phase p_2, and phase p_3 are calculated as

$$\begin{aligned}
\widetilde{t}_j^{p_1} &= t_j^{p_1} + \frac{\Delta t_j \cdot g_j^{p_1}}{\left(g_j^{p_1} + g_j^{p_2} + g_j^{p_3}\right)}, \\
\widetilde{t}_j^{p_2} &= t_j^{p_2} - \frac{\Delta t_j \cdot g_j^{p_2} \cdot g_j^{p_3}}{\left(g_j^{p_2} + g_j^{p_2}\right)\left(g_j^{p_2} + g_j^{p_2} + g_j^{p_3}\right)} \\
&\quad - \frac{\Delta t_j \cdot g_j^{p_2}}{\left(g_j^{p_2} + g_j^{p_2} + g_j^{p_3}\right)}, \\
\widetilde{t}_j^{p_3} &= t_j^{p_3} - \frac{\Delta t_j \cdot g_j^{p_2}}{\left(g_j^{p_2} + g_j^{p_2} + g_j^{p_3}\right)}, \\
\widetilde{g}_j^{p_1} &= g_j^{p_1} + \frac{\Delta t_j \cdot g_j^{p_1} \cdot g_j^{p_3}}{\left(g_j^{p_2} + g_j^{p_2}\right)\left(g_j^{p_2} + g_j^{p_2} + g_j^{p_3}\right)}, \\
\widetilde{g}_j^{p_2} &= g_j^{p_2} + \frac{\Delta t_j \cdot g_j^{p_2} \cdot g_j^{p_3}}{\left(g_j^{p_2} + g_j^{p_2}\right)\left(g_j^{p_2} + g_j^{p_2} + g_j^{p_3}\right)}, \\
\widetilde{g}_j^{p_3} &= g_j^{p_3} - \frac{\Delta t_j \cdot g_j^{p_3}}{\left(g_j^{p_1} + g_j^{p_2} + g_j^{p_3}\right)},
\end{aligned} \tag{15}$$

where δ_2 is a regulator parameter. The phase setting shown in Figure 3(b) is implemented.

Subcase 3 ($\delta_2 \cdot g_j^{p_3} < \Delta t_j < g_j^{p_3}$). Different from the previous subcase 1 and subcase 2, for the current condition the gap Δt_j is close to the length of green time of phase p_3. In other words, compared with the length of green time of phase p_1 and phase p_2, $g_j^{p_3} - \Delta t_j$ is small. As a result, phase p_3 can be inserted between phase p_1 and phase p_2 to eliminate the gap. Meanwhile, the start time of phase p_1 should be advanced, and the start time of phase should be lagged. As illustrated in

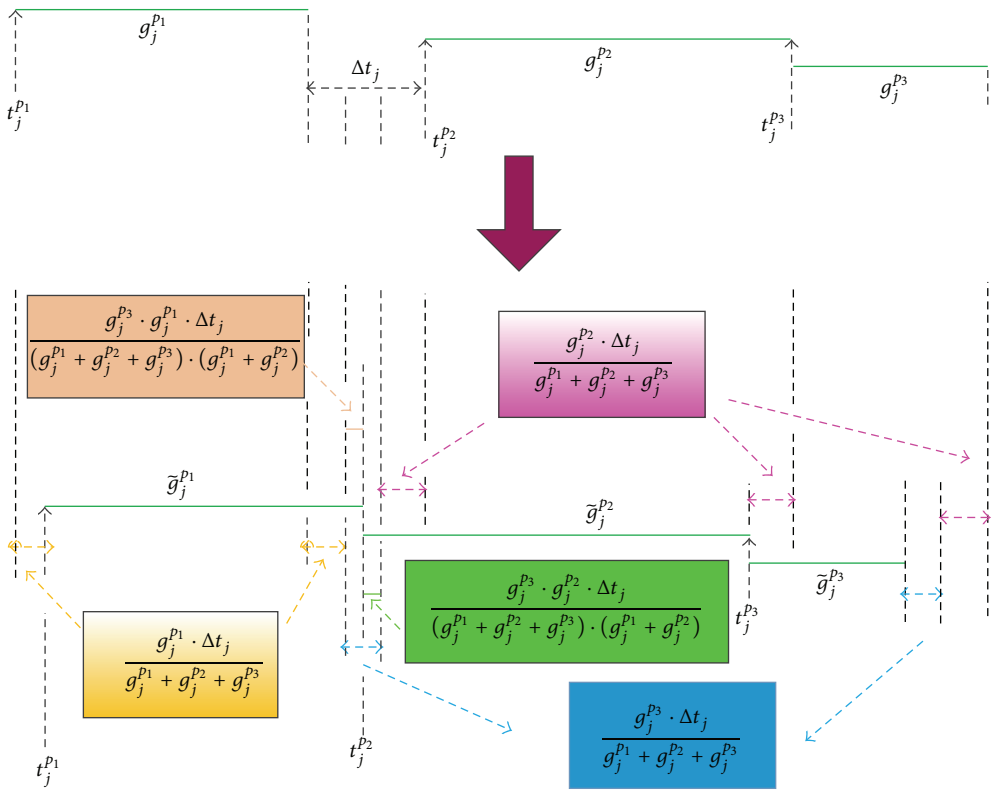

Figure 9: Adjustments for Subcase 2.

Figure 10, the start time and the length of green time can be regulated with the following equations:

$$
\begin{gathered}
t_j^{\bar{p}_1} = t_j^{p_1} - \frac{\left(g_j^{p_3} - \Delta t_j\right) \cdot g_j^{p_1}}{\left(g_j^{p_1} + g_j^{p_2}\right)}, \\
t_j^{\bar{p}_2} = t_j^{\bar{p}_1} + g_j^{\bar{p}_1}, \qquad t_j^{\bar{p}_3} = t_j^{\bar{p}_2} + g_j^{\bar{p}_2}, \\
g_j^{\bar{p}_1} = g_j^{p_1}, \qquad g_j^{\bar{p}_2} = g_j^{p_2}, \\
g_j^{\bar{p}_3} = g_j^{p_3}.
\end{gathered} \tag{16}
$$

Under this condition, the phase sequence defined in Figure 3(b) is extended as a new one shown in Figure 5. Compared with the phase setting in Figure 3(b), the phase which provides right of way for minor roads is in advance.

Remark 2. On one hand, the common cycle time C_A of all intersections on the arterial road A is kept unchanged during the coordination process. On the other hand, phase p_1, phase p_2, and phase p_3 are periodically implemented. Therefore, the gap Δt_j between phase p_1 and phase p_2 is always limited in the interval $[k_1 \cdot C_A, k_2 \cdot C_A + g_j^{p_3}]$, $k_1, k_2 \in \mathbb{Z}^+$. As a result, herein only the upper three conditions were discussed.

3. Network Decomposition

On one hand, decomposition of system structures or models is a prerequisite in coordination and control of large-scale complex systems. On the other hand, as a large-scale complex system, urban traffic system is usually composed by numerous interconnected subsystems. It is difficult to be controlled with centralized control structure due to the high computational burden, communication bandwidth limitations, and robustness and reliability problem [26]. Therefore, many decomposition strategies have been proposed in previous literatures [16, 22, 24, 25].

In [16], Tian and Urbanik proposed a system partition technology for signal timing of large signalized arterial, whereby the decomposition strategy is purely heuristic and defines three to five intersections as a subsystem. In [24], Zhou and Lu defined each intersection and its connected roads as a subsystem and developed a neighbor-based distributed coordination scheme to enhance the computational efficiency. In [22], Gartner and Stamatiadis proposed an iterative heuristic network decomposition framework, in which a priority subnetwork would be defined firstly in each iteration. The priority network was chosen so that it contained only a tree of arterials, eliminating any network loops. However, Gartner et al. only presented two simple criteria to select a priority subnetwork, without details of the operation and definition of a priority subnetwork. For this reason, in this paper we define a priority level index first and then develop a novel netowork decomposition approach.

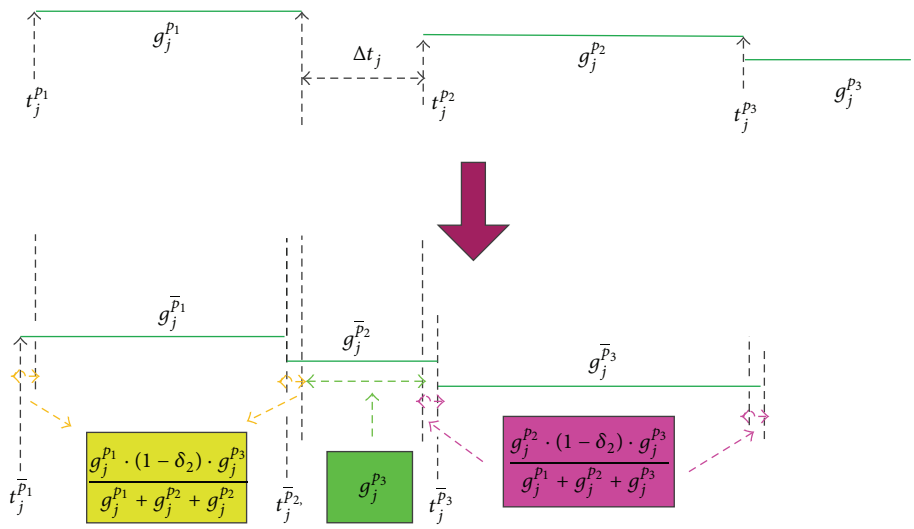

Figure 10: Adjustments for Subcase 3.

3.1. Priority Level Index. In order to quantify the priority level of each road (including arterial and minor roads) in road networks, we develop a priority level index which is defined as

$$\mathrm{PL}_A = w_1 * X_A + w_2 * Q_A + w_3 * E_A, \tag{17}$$

$$w_1 + w_2 + w_3 = 1, \tag{18}$$

where PL_A denotes the value of the priority level index of road A and X_A and Q_A are the saturation degree and throughput of road A, respectively. E_A is the score decided by experts or engineers. w_1, w_2, and w_3 are the weights.

The saturation X_A of road i is calculated by

$$X_A = \frac{1}{n_A} \cdot \sum_{j \in A} \sum_{p \in F_j} \max_{i \in I_j^p} \left\{ \frac{q_{j,i}^p}{g_{j,i}^p \cdot S_{j,i}} \right\}, \tag{19}$$

where F_j is the phase set of intersection j, $q_{j,i}^p$ and $S_{j,i}$ are the nominal inflow and saturation flow of link i in vehicles per hour, respectively, and n_A is the number of intersections on arterial road A.

The throughput of road A is calculated by

$$Q_A = \sum_{j \in A} \sum_{p \in F_j^{co}} q_j^p, \tag{20}$$

where F_j^{co} is the phase set which governs the right of way of the traffic flow along the inbound and outbound directions and q_j^p is the traffic flow corresponding to phase p of intersection j.

Instead of designing a heuristic scheme, herein we introduce a score index E_A to quantify the expert knowledge. Furthermore, based on the specific network topology and the history volumes of traffic flow of each road, the score E_A is estimated by experts or engineers.

Remark 3. Note that when we use (17) to calculate the priority level index PL_A, X_A, Q_A, and E_A should be normalized into the interval $[0, 1]$ first. In addition, since the proposed method is a fixed-time control strategy and the traffic flows in road networks can be assumed to be steady-state, the vehicular traffic flow data used in (19)-(20) can be estimated by history traffic data collected by inductive loop detectors or magnetic sensors.

3.2. Decomposition Algorithm. The decomposition algorithm described herein does not merely use some heuristic schemes, as most previous method do, but rather it is based on the priority level index. Central to our decomposition algorithm is to order the principle arterial roads of the network according to the priority index. The arterial roads with higher priority index PL are picked out firstly, and then a threshold $\tilde{n} = \gamma \cdot n$ is set to guarantee that the key intersections insider the network will be selected. It should be noted that the parameter $\gamma \in (0, 1]$ can be dynamically regulated according to the coordination performance of the road networks. Finally, we summarized the network decomposition approach in the following.

Algorithm 4.

Step 1. Collect the topology information and the traffic flow characteristics of the studied road network. Set R as an empty set and the iteration index $\ell = 1$.

Step 2. Calculate the priority level of each arterial (or minor) road with (17), sort them in decreasing order, and store them in a set B.

Step 3. Pick out the road A with the highest priority level in the set $B - R$ and place it into the set C.

Step 4. Count the number of intersections that belong to the roads of set C and mark it as n^{co}; denote the total number of intersections in the network as n.

Step 5. Update the result set $R = B(1 : \ell)$ that is a set constituted by the first ℓ elements in the set B.

Step 6. Check if the termination iteration condition $n^{co} \geq \gamma \cdot n$ is satisfied. If the termination condition is satisfied, then end the iteration and return R.

Step 7. Let $\ell = \ell + 1$; go back to Step 3.

4. Coordination of Urban Traffic Networks

It is common knowledge that the predominant traffic flows in urban traffic networks are along arterial roads. Coordination of traffic signals along arterial roads offers numerous benefits as indicated in previous literatures [15–23]. Therefore, coordinating the traffic signals along these arterial roads is essential for the effective operation of the urban traffic networks. In this section, we propose a novel coordination approach for urban traffic networks, which is abbreviated as CoA in the remainder of this paper. The basic idea of our coordination approach is that the problem of coordinating an urban traffic network can be transformed into that of coordinating the principal arterial roads and scattered isolated intersections on the boundary of the road networks.

In general, based on the coordination model of an arterial road, the objective function of an urban traffic network can be defined as

$$\min \sum_{A \in N} J_A = \min \sum_{A \in N} \sum_{j=1}^{n_A} \left| \Delta t_j \right|, \tag{21}$$

subject to the constraints (1)–(10) and (12), where N denotes a traffic network. It indicates that the objective function is to maximize the width of the green wave band of the whole network which includes not only the arterial roads but the minor roads.

However, in real-life traffic conditions and applications, the minor roads are not suitable to be coordinated with green wave coordination technology due to lower traffic demands and physical topology of minor roads. In addition, traffic flows are mainly concentrated in principle arterial roads. Hence, herein based on the network decomposition approach proposed in previous section, we define an objective function as follows:

$$\min \sum_{A \in R} \omega_A \cdot J_A = \min \sum_{A \in R} \omega_A \cdot \sum_{j=1}^{n_A} \left| \Delta t_j \right|, \tag{22}$$

where ω_A is the weight coefficient which reflects the priority level of arterial road A and R is the road set with higher priority level and is calculated by Algorithm 4. It means that only the intersections which belong to the key arterial roads set are coordinated.

In addition, it should be noted that if an intersection belongs to two coordinate arterials, it means that there are two major coordination directions. Therefore, the phase setting shown in Figure 4 should be regulated. As shown in Figure 11, another phase setting is presented. For example, intersection 6 and intersection 12 (shown in Figure 12) have six phases.

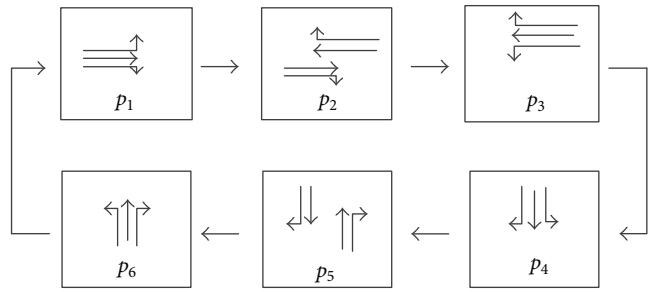

Figure 11: A phase sequence for two-crossed arterial roads.

Based on the arterial signal coordination and network decomposition approach presented in previous sections, our proposed coordination approach CoA for the whole road network is described in Algorithm 6.

Remark 5. As shown in Figure 7, the grid network consisted of eight arterial (or minor) roads and fifteen intersections. Assume that according to (17) we have the set $B = \{A_1, A_2, \ldots, A_8\}$, which implies that arterial road A_1 has the highest priority level while A_8 has the smallest priority level. Setting $\gamma = 0.65$, then utilizing Algorithm 4, we can get the decomposition result set $B = \{A_1, A_2, A_3\}$. It means that only the three principal arterial roads are coordinated, while the remaining intersections 1, 4, 9, 12, and 13 are controlled by fixed-time control strategy.

Algorithm 6.

Step 1 (Initialization). Based on the network decomposition Algorithm 4 a given traffic road network can be decomposed into a set of arterials R. Each arterial can be seen as a subnetwork which contains the bulk traffic flows of the network. Coordinate the signals along the arterial with the highest priority level in R that is $R(1)$ with the proposed arterial coordination approach in Section 2; then let $\ell = 2$.

Step 2 (check). If arterial $R(\ell)$ will form a loop with the previous coordinated arterials, then go to Step 4; else go to Step 3.

Step 3 (coordination). Coordinate the arterial $R(\ell)$ with the proposed arterial coordination approach in Section 2.

Step 4 (loop). If $\ell < |R|$, let $\ell = \ell + 1$ and go back to Step 2; else terminate the iteration.

Step 5 (complementary). Fixed-time control strategy or actuated control strategy is implemented to the intersections of the network except those along the coordinated arterials.

Step 6 (finish). Stop the coordination process.

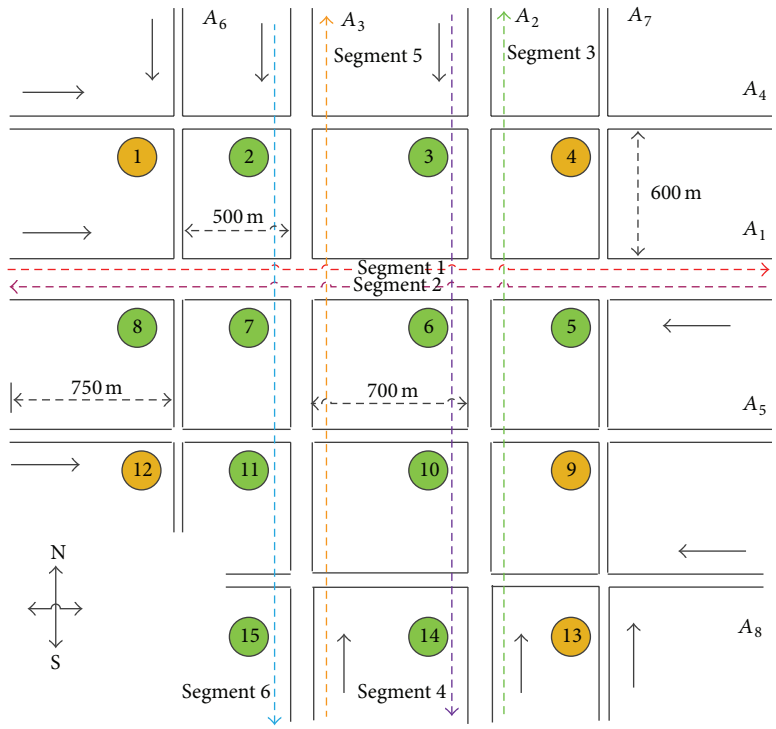

FIGURE 12: Simulation road network.

5. Simulation Results

In this section, to demonstrate the effectiveness and efficiency of the proposed signal coordination approach, measures of effectiveness (MOE) acquired by VISSIM, including average delay, average travel time, average queue length, and stops per vehicle on each travel segment, are introduced.

The simulation network is created as shown in Figure 12, and the road network includes eight arterial roads and fifteen signalized intersections. A_1 is a bidirection arterial road with six lanes and A_2 and A_3 are bidirection arterial road with four lanes. One direction and one lane are defined for the other roads. The width of each lane is 3.5 meters. As marked in Figure 12, to evaluate the coordination performance, we define six travel segments, which undertake the main traffic demand of the road network. The input flow and tuning rates of the road network are presented in Tables 1 and 2, respectively. We assume the average vehicle length is 5 meters, and the minimum and maximum free vehicle speed is 40 km/h and 50 km/h, respectively.

Moreover, as we choose the default traffic configuration, which contains 98% cars and 2% heavy good cars, herein the saturated rate of each link is set as 2000 veh/h (refer to the manual of Vissim 3.7). All other parameters, such as lane-change distance, minimum headway, and waiting time before diffusion, are using the default settings.

The proposed model is simulated by VISSIM 3.7. A fixed-time control (FC) strategy is used as a reference to the proposed coordination (CoA) method. In order to evaluate the performance of CoA under different traffic demands, the simulations are implemented under three scenarios, according to different input traffic flow rates supplied to the network as shown in Table 2. Firstly, the simulation results are compared for these different scenarios. The average travel time along each segment is shown in Figure 13. According to it, we can clearly see that CoA performs better than that of FC on all travel segments under different scenarios, and the average travel time is reduced by around 9.27%–11.68%. The travel time of segments 1, 3, and 5 is much bigger than that of segments 1, 3, and 5. This is mainly due to the input traffic flows of segments 1, 3, and 5 which are high and the traffic condition is more crowded.

Figure 14 illustrates the delay time per vehicle on each travel segment under different traffic demands. Compared with FC, the average delay time of CoA is reduced by about 27.5%–33.81%. Moreover, with the increase of traffic demand, the rate of decrease of delay time is greater. Under the FC control strategy, for Case 1 and Case 2 the maximum delay time is 140 (s/veh), while it is increased quickly to 260 (s/veh) for Case 3. However, with the proposed control strategy CoA, the increase of delay time under different traffic demand is relatively flat. It illustrates that the robustness of CoA is better than that of FC.

Figure 15 shows that the average number of stops per vehicle on each travel segment increases remarkably with the traffic demand increase. It can be seen that CoA achieves better performance than that of FC under all traffic scenarios. Compared with the FC strategy, CoA obtains much less stops (per vehicle), particularly for Case 3 which has much higher traffic demand. The reason is that with bidirection green

Table 1: Turning rates.

Int.	Northbound			Westbound			Southbound			Eastbound		
	LT	TH	RT	LT	TH	RT	LT	TH	RT	LT	TH	RT
1		0.8	0.2				0.15	0.85				
2	0.15	0.75	0.1				0.15	0.85			0.8	0.2
3	0.15	0.7	0.15				0.15	0.85			0.85	0.15
4	0.15	0.85									0.7	0.3
5	0.1	0.9			0.87	0.13				0.05	0.75	0.2
6	0.07	0.83	0.10	0.07	0.81	0.12	0.05	0.79	0.16	0.09	0.73	0.18
7	0.05	0.85	0.10	0.05	0.84	0.11	0.05	0.80	0.15	0.05	0.76	0.19
8		0.9	0.1	0.08	0.92		0.2	0.7	0.1			
9	0.2	0.8									0.8	0.2
10	0.06	0.84	0.1				0.1	0.9			0.83	0.17
11	0.05	0.83	0.12				0.11	0.89			0.85	0.15
12		0.8	0.2				0.08	0.92				
13					0.9	0.1				0.1	0.9	
14				0.18	0.75	0.07		0.9	0.1	0.05	0.95	
15				0.15	0.8	0.05		0.85	0.15	0.07	0.93	

Table 2: Input traffic flow (veh/h).

Scenarios	Entrance	Input traffic flow of each arterial road							
		A_1	A_2	A_3	A_4	A_5	A_6	A_7	A_8
Case 1	Eastbound	1200			300	500			
	Westbound	1000							300
	Southbound		800	900			350		
	Northbound		1000	950				300	
Case 2	Eastbound	1800			400	450			
	Westbound	1500							350
	Southbound		1200	1350			400		
	Northbound		1500	1450				400	
Case 3	Eastbound	2400			450	500			
	Westbound	2000							400
	Southbound		1500	1600			450		
	Northbound		1800	1750				450	

wave coordination the traffic flows along arterial roads are smoothed. Many vehicles can cross two or more adjacent intersections without stops.

The average queue length on each travel segment is reported in Figure 16; we can find that there are a few queued vehicles for both control strategies CoA and FC under Case 1 which has the lowest traffic demand. However, as the traffic demand increases from Case 1 to Case 3, the queue length grows quickly. In comparison with FC, the average queue length of CoA is greatly reduced.

Another observation on the performance curves of queue length shown in Figure 11 is that the queue length of the travel segments 1, 3, and 5 is much bigger than that of 2, 4, and 6. This is mainly due to the input traffic flows for segments 1, 3, and 5 are bigger than that of the remaining three segments. As shown in Figure 13 to Figure 16, it should be noted that CoA performs much better on segments 1, 3, and 5 than that of on segments 2, 4, and 6. The reason for this phenomenon is that, during the process of regulating the start time of inbound and outbound, we prefer to guarantee the coordination efficiency of the direction with higher traffic demand.

The performance index of the whole network is presented in Table 3 and Figure 17. According to it, we can find that the proposed method CoA performance is much better than that of FC. In particularly, compared with FC, the average delay time, stops per vehicle, and average queue length are greatly reduced at least by about 27.5%–33.88% under different traffic scenarios.

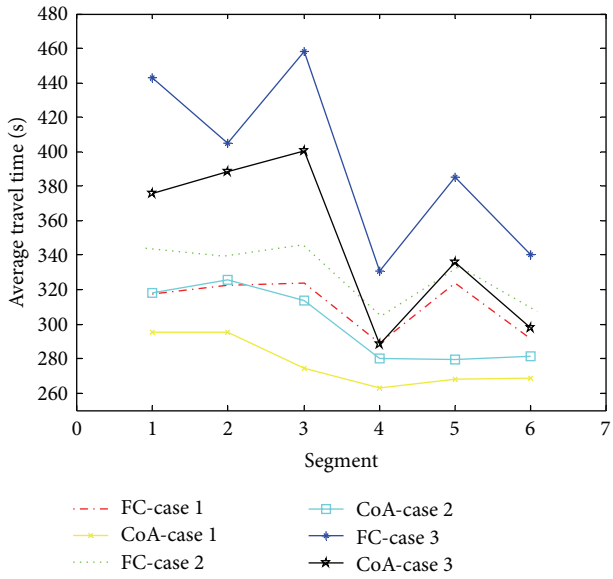

Figure 13: Comparison of average travel time on different travel segment.

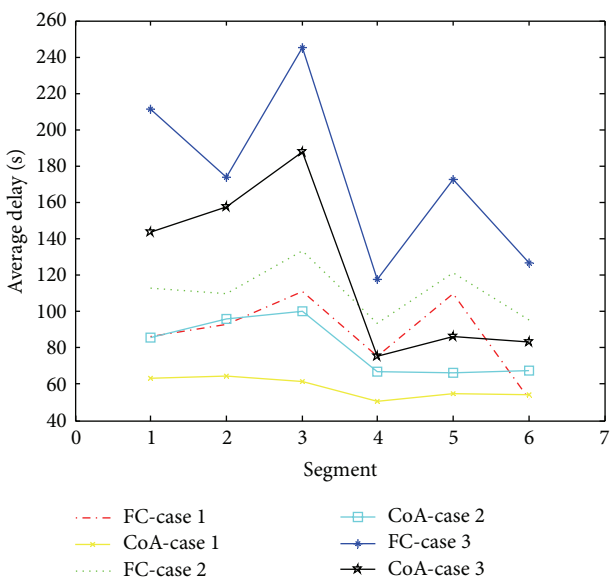

Figure 14: Comparison of average delay time on different travel segment.

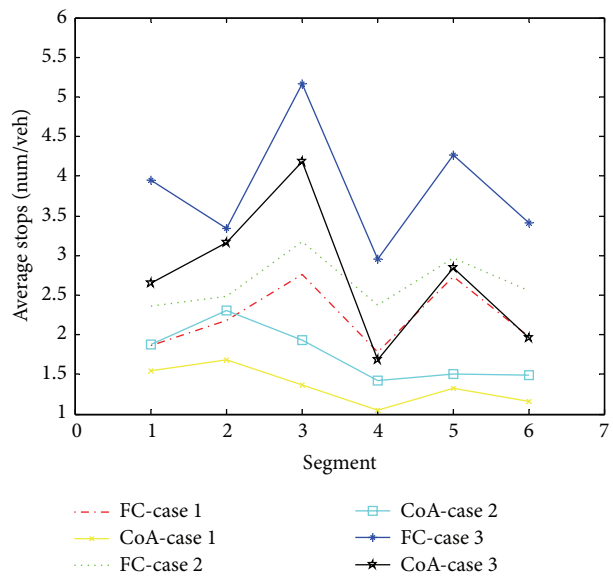

Figure 15: Comparison of average stops per vehicle on different travel segment.

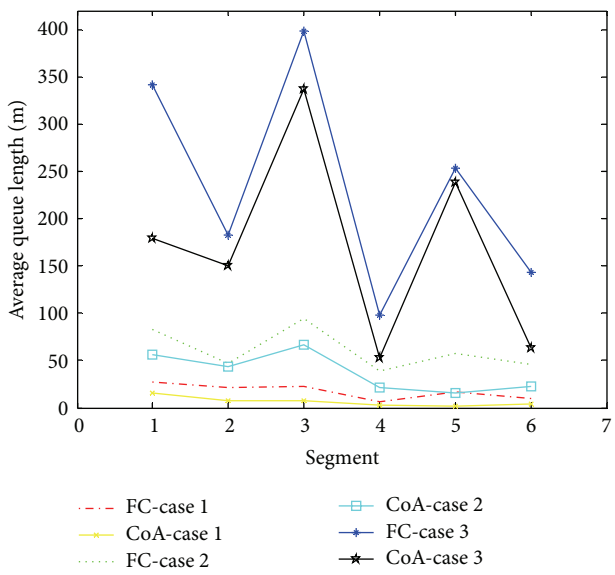

Figure 16: Comparison of average queue length on different travel segment.

6. Conclusion

This paper investigates the optimization and coordination of signal splits in large-scale urban road networks. To reduce the high computational complexity and improve the applicability of signal coordination methods, a novel method based on a system decomposition strategy was proposed. The key idea of the proposed method is that a large-scale network coordination problem has been solved by coordinating several principle arterial roads and several isolated intersections on the boundary of the area. In this study, to satisfy the minimum (maximum) green time constraints, which are used to guarantee the safety of pedestrians and cyclists, we propose a strategy to regulate the calculated green time. In addition, a new two-way arterial signal coordination model is developed. Different from previous studies, not only the phases which provide right of way to the coordinated directions but also the phases which provide right of way to uncoordinated directions were optimized in our proposed arterial coordination method. Moreover, a system decomposition strategy was reported, whereby a novel priority level index is defined to quantify the priority level of each road. The performance of the proposed method CoA has been validated by VISSIM under various traffic conditions. Simulation results show that

Table 3: Measurements of effectiveness.

Scenarios	Control strategy	Travel time (s)	Delay (s/veh)	Stops (num/veh)	Queue (m)
Case 1	FC	1867.7	527.3	13.29	104
	CoA	1664.2	349	8.14	39
	Improved	10.9%	33.81%	38.75%	62.5%
Case 2	FC	1981.8	666.2	15.94	366
	CoA	1798	483	10.54	227
	Improved	9.27%	27.5%	33.88%	37.98%
Case 3	FC	2362.5	1047.5	23.1	1419
	CoA	2086.6	733.9	16.48	1020
	Improved	11.68%	29.94%	28.66%	28.12%

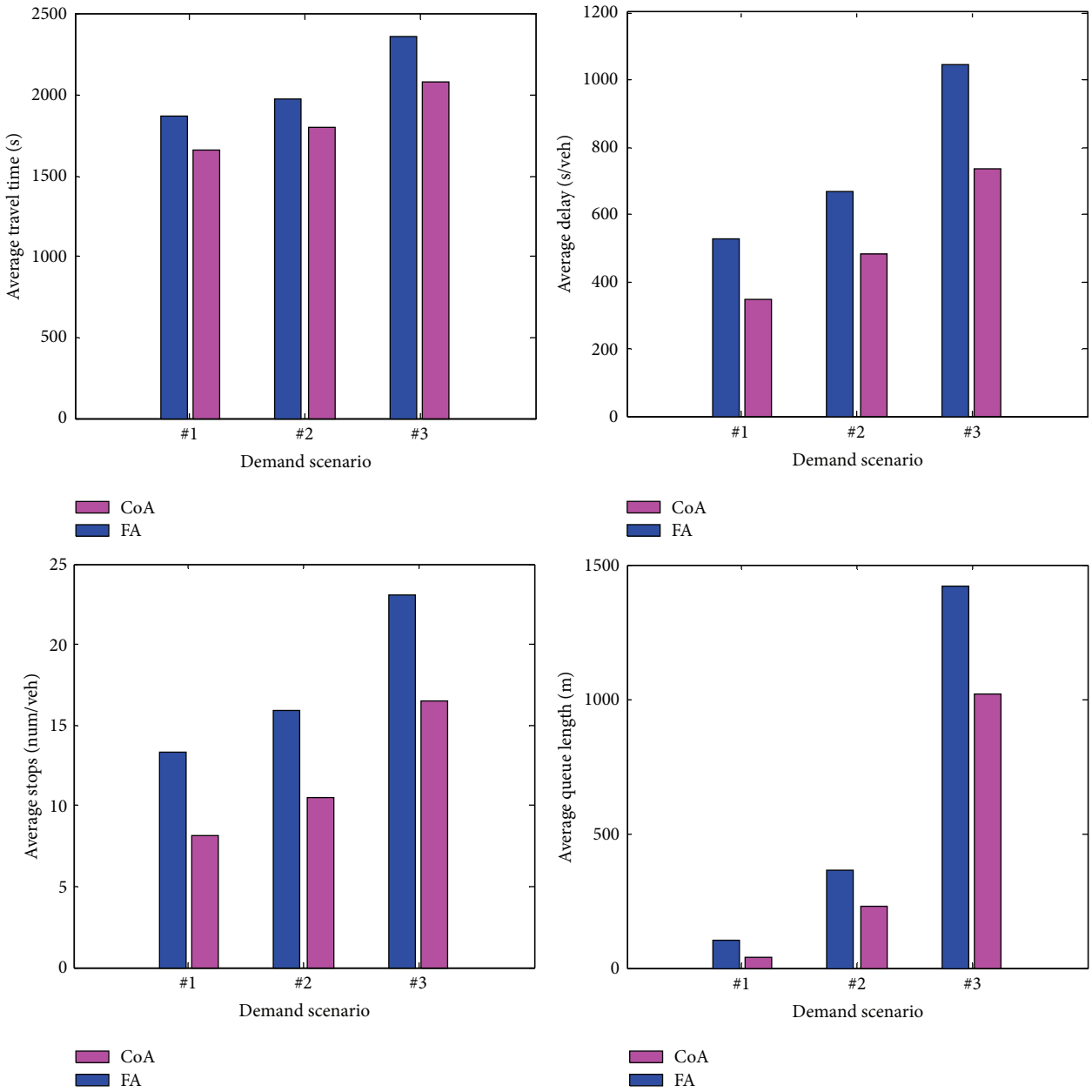

Figure 17: Comparison of network performance.

CoA can greatly reduce the average delay, stops, and queue length.

In future, we will do further numerical and simulation studies with more complex and large-scale urban road networks aims to confirm the potential of the proposed method. For practical application purpose, research will continue on addressing the signal coordination of road networks under more realistic traffic conditions, such as transit signal priority; uncertainty traffic flow will be considered.

Conflict of Interests

The authors declare that there is no conflict of interests regarding the publication of this paper.

Acknowledgments

The work described in this study was supported by the National Natural Science Foundation of China under Grants no. 61374066 and no. 61473252 and the Fundamental Research Funds for the Central Universities of China.

References

[1] M. Papageorgiou, C. Diakaki, V. Dinopoulou, A. Kotsialos, and Y. Wang, "Review of road traffic control strategies," *Proceedings of the IEEE*, vol. 91, no. 12, pp. 2043–2065, 2003.

[2] I. Porche and S. Lafortune, "Adaptive look-ahead optimization of traffic signals," *Journal of Intelligent Transportation System*, vol. 4, no. 3-4, pp. 209–254, 1998.

[3] M. Ahmane, A. Abbas-Turki, F. Perronnet et al., "Modeling and controlling an isolated urban intersection based on cooperative vehicles," *Transportation Research Part C: Emerging Technologies*, vol. 28, pp. 44–62, 2013.

[4] S. Lämmer and D. Helbing, "Self-control of traffic lights and vehicle flows in urban road networks," *Journal of Statistical Mechanics: Theory and Experiment*, vol. 2008, Article ID P04019, 2008.

[5] X.-F. Xie, S. F. Smith, L. Lu, and G. J. Barlow, "Schedule-driven intersection control," *Transportation Research Part C: Emerging Technologies*, vol. 24, pp. 168–189, 2012.

[6] J. D. C. Little, "The synchronization of traffic signals by mixedintegerlinearprogramming," *Operations Research*, vol. 14, no. 4, pp. 568–594, 1966.

[7] N. H. Gartner, S. F. Assman, F. Lasaga, and D. L. Hou, "A multi-band approach to arterial traffic signal optimization," *Transportation Research Part B: Methodological*, vol. 25, no. 1, pp. 55–74, 1991.

[8] D. I. Robertson, "TRANSYT: a traffic network study tool," Report LR253, Road Research Laboratory, Crowthorne, UK, 1969.

[9] D. I. Robertson and R. D. Bretherton, "Optimizing networks of traffic signals in real time—the SCOOT method," *IEEE Transactions on Vehicular Technology*, vol. 40, no. 1, pp. 11–15, 1991.

[10] P. Lowrie, *SCATS: A Traffic Responsive Method of Controlling Urban Traffic*, Roads and Traffic Authority, Sydney, Australia, 1992.

[11] N. H. Gartner, "OPAC: a demand-responsive strategy for traffic signal control," *Transportation Research Record*, no. 906, pp. 75–81, 1983.

[12] J. J. Henry, J. L. Farges, and J. Tufal, "The PRODYN real time traffic algorithm," in *Proceedings of the IFAC Conference on Control in Transportation System*, pp. 305–310, 1983.

[13] F. Boillot, S. Midenet, and J.-C. Pierrelée, "The real-time urban traffic control system CRONOS: algorithm and experiments," *Transportation Research Part C: Emerging Technologies*, vol. 14, no. 1, pp. 18–38, 2006.

[14] C. Diakaki, M. Papageorgiou, and K. Aboudolas, "A multivariable regulator approach to traffic-responsive network-wide signal control," *Control Engineering Practice*, vol. 10, no. 2, pp. 183–195, 2002.

[15] C. Stamatiadis and N. H. Gartner, "MULTIBAND-96: a program for variable-bandwidth progression optimization of multiarterial traffic networks," *Transportation Research Record*, vol. 1554, no. 1, pp. 9–17, 1996.

[16] Z. Tian and T. Urbanik, "System partition technique to improve signal coordination and traffic progression," *Journal of Transportation Engineering*, vol. 133, no. 2, pp. 119–128, 2007.

[17] Z. Tian, V. Mangal, and H. Liu, "Effectiveness of lead-lag phasing on progression bandwidth," *Transportation Research Record: Journal of the Transportation Research Board*, no. 2080, pp. 22–27, 2008.

[18] X. Kong, G. Shen, F. Xia, and C. Lin, "Urban arterial traffic two-direction green wave intelligent coordination control technique and its application," *International Journal of Control, Automation and Systems*, vol. 9, no. 1, pp. 60–68, 2011.

[19] L.-T. Lin, L.-W. C. Tung, and H.-C. Ku, "Synchronized signal control model for maximizing progression along an arterial," *Journal of Transportation Engineering*, vol. 136, no. 8, pp. 727–735, 2010.

[20] K. Lu, X. Zeng, L. Li, and J. Xu, "Two-way bandwidth maximization model with proration impact factor for unbalanced bandwidth demands," *Journal of Transportation Engineering*, vol. 138, no. 5, pp. 527–534, 2012.

[21] N. H. Gartner and C. Stamatiadis, "Arterial-based control of traffic flow in urban grid networks," *Mathematical and Computer Modelling*, vol. 35, no. 5-6, pp. 657–671, 2002.

[22] N. H. Gartner and C. Stamatiadis, "Progression optimization featuring arterial- and route-based priority signal networks," *Journal of Intelligent Transportation Systems: Technology, Planning, and Operations*, vol. 8, no. 2, pp. 77–86, 2004.

[23] B.-L. Ye, W. Wu, X. Zhou, W. Mao, and Y.-S. Huang, "A green wave band based method for arterial signal control," in *Proceedings of the 11th IEEE International Conference on Networking, Sensing and Control (ICNSC '14)*, pp. 126–131, Miami, Fla, USA, April 2014.

[24] X. Zhou and Y. Lu, "Coordinate model predictive control with neighbourhood optimisation for a signal split in urban traffic networks," *IET Intelligent Transport Systems*, vol. 6, no. 4, pp. 372–379, 2012.

[25] B.-L. Ye, W. Wu, and W. Mao, "Distributed model predictive control method for optimal coordination of signal splits in urban traffic networks," *Asian Journal of Control*, 2014.

[26] R. Scattolini, "Architectures for distributed and hierarchical model predictive control—a review," *Journal of Process Control*, vol. 19, no. 5, pp. 723–731, 2009.

Hindawi Publishing Corporation
Mathematical Problems in Engineering
Volume 2015, Article ID 658153, 8 pages
http://dx.doi.org/10.1155/2015/658153

Research Article

On Fixed-Point Smoothing for Descriptor Systems with Multiplicative Noise and Single Delayed Observations

Xiao Lu, Xin Dong, Haixia Wang, and Baoye Song

Key Laboratory for Robot & Intelligent Technology of Shandong Province, Shandong University of Science and Technology, Qingdao 266590, China

Correspondence should be addressed to Xiao Lu; luxiao98@163.com

Received 9 January 2015; Revised 5 February 2015; Accepted 5 February 2015

Academic Editor: Kun Liu

Copyright © 2015 Xiao Lu et al. This is an open access article distributed under the Creative Commons Attribution License, which permits unrestricted use, distribution, and reproduction in any medium, provided the original work is properly cited.

Optimal fixed-point smoothing problem for the descriptor systems with multiplicative noises is considered, where instantaneous and delayed observations are available. Standard singular value decomposition is used to give the restricted equivalent delayed system, where the observations also include two different types of measurements. Reorganized innovation lemma and projection theorem are used to give the fixed-point smoother for the restricted equivalent delayed system. The fixed-point smoother is given in terms of recursive Riccati equations.

1. Introduction

The optimal estimation problem has long been one of the important problems in control theory and signal processing [1–4], and it is the dual problem of control [5–8]. Estimation includes three cases: prediction, filter, and smoothing [9–11], and smoothing problem is the most difficult among three problems. Smoothing problem is to estimate the past state or signal based on the observations in future, which mainly includes fixed-point smoothing, fixed-interval smoother, and fixed-lag smoother, where fixed-point is to estimate the fixed-point state or signal in past based on its future observations, which can reveal the development trend of estimation with the increase of observations [9, 12, 13]. Under the optimal performance, estimation (prediction, filter, and smoothing) problem for normal system without multiplicative noises and delayed measurements has been studied well in recent years [12, 13].

The optimal smoothing problem has received much attention these years [9, 10, 12, 13]. For the optimal smoothing of descriptor systems with multiplicatives, some researchers have given some important results [14–16], where Kalman filtering and standard decomposition are to study the optimal estimation of the descriptor systems.

As is well known, the measured output may be with delay in practical applications such as engineering, biological, and economic systems [8]. However, the above descriptor systems are without delay in observation; for the systems with delayed measurement, the classic approach is system or variable augmentation [11, 17], which may lead to much computation burden. In this paper, the optimal fixed-point smoothing problems for descriptor systems with multiplicative noises and delayed measured output will be studied. Being different from the classic system augmentation, the reorganized innovation lemma developed in our previous works [17, 18] will be proposed. Standard singular value decomposition will be used to change the system into the restricted equivalent delayed system.

The presented approach is very efficient and important for estimation on descriptor system with multiplicative noise, and reorganized innovation lemma is used to decrease much computation burden compared to traditional system augmentation [17]. The proposed result extends the optimal filter and multistep predictor [19].

The rest of the paper is organized as follows. The fixed-point smoothing problem will be proposed in Section 2. Substate fixed-point smoother will be given for the restricted equivalent delayed system in Section 3. Fixed-point smoother for the delayed descriptor systems with multiplicative noise will be given in Section 4. Some concluding remarks will be drawn in Section 5.

2. Problem Statement

In this paper, we will deal with the following linear discrete-time descriptor system:

$$\begin{aligned} F\mathbf{x}(t+1) &= A\mathbf{x}(t) + B\mathbf{u}(t), \\ \mathbf{y}(t) &= C\mathbf{x}(t) + D\mathbf{w}(t)\mathbf{x}(t) + \mathbf{v}(t), \\ \mathbf{y}_d(t) &= C_d\mathbf{x}(t_d) + D_d\mathbf{w}(t)\mathbf{x}(t_d) + \mathbf{v}_d(t), \quad t_d = t - d, \end{aligned} \tag{1}$$

where A, B, C, D, C_d, and D_d are known matrices and the information of other parameters can be listed as

$d \to R^1 \to$ delay,

$\mathbf{x}(t) \to R^n \to$ state,

$\mathbf{y}(t), \mathbf{v}(t) \to R^q \to$ observation and its noise,

$\mathbf{y}_d(t), \mathbf{v}_d(t) \to R^{q_d} \to$ delayed observation and its noise,

$\mathbf{u}(t) \to R^p \to$ input disturbance,

$\mathbf{w}(t) \to R^1 \to$ multiplicative noise.

We first give two assumptions as follows.

Assumption 1. $\mathbf{u}(t)$, $\mathbf{v}(t)$, $\mathbf{v}_d(t)$, and $\mathbf{w}(t)$ are uncorrelated white noises of zero means and uncorrelated with $\mathbf{x}(0)$, and the corresponding variance is $\langle \boldsymbol{\xi}(t), \boldsymbol{\xi}(s)\rangle = Q_\xi \delta_{t,s}$, and $\xi(t)$ can be $\mathbf{u}(t)$, $\mathbf{v}(t)$, $\mathbf{v}_d(t)$, and $\mathbf{w}(t)$; in addition, $\langle \mathbf{x}(0), \mathbf{x}(0)\rangle = \Pi(0)$.

Assumption 2. F is known and singular, and the system is regular, that is, $\operatorname{rank} F = n_1 < n$, and there exists s that satisfies $\det(sF - A) \neq 0$.

Remark 3. Assumption 1 is given for general optimal or H_2 estimation problem. Assumption 2 is standard assumption for general descriptor system, since the regularity is very important for the existence of solution which is dependent on the initial value for descriptor system [14, 20].

Optimal fixed-point smoothing (FPS) problem for the above descriptor system model (1) can be described as follows.

Problem FPS. Consider the system model (1) with the instantaneous and delayed observations $\{\mathbf{y}(0), \ldots, \mathbf{y}(k); \mathbf{y}_d(d), \ldots, \mathbf{y}_d(k)\}$, a fixed time t and $t \le k \le N$; find the linear least square error smoother $\hat{\mathbf{x}}(t \mid k)$ of $\mathbf{x}(t)$, where $0 \le t \le N$.

Under Assumption 2, according to the classical result of descriptor system [11, 14, 20], there exist nonsingular matrices $\{J_1, J_2\} \in R^{n\times n}$, $\mathbf{x}(t) = J_2 \left[\begin{smallmatrix} \mathbf{x}_1(t) \\ \mathbf{x}_2(t) \end{smallmatrix}\right]$, and we can give the following lemma.

Lemma 4 (see [19]). *System (1) under Assumptions 1 and 2 can be restricted equivalent to*

$$\mathbf{x}_1(t+1) = A_1\mathbf{x}_1(t) + B_1\mathbf{u}(t), \tag{2}$$

$$F_1\mathbf{x}_2(t+1) = \mathbf{x}_2(t) + B_2\mathbf{u}(t), \tag{3}$$

$$\begin{aligned} \mathbf{y}(t) &= C_1\mathbf{x}_1(t) + C_2\mathbf{x}_2(t) + D_1\mathbf{w}(t)\mathbf{x}_1(t) \\ &\quad + D_2\mathbf{w}(t)\mathbf{x}_2(t) + \mathbf{v}(t), \end{aligned} \tag{4}$$

$$\begin{aligned} \mathbf{y}_d(t) &= C_{1d}\mathbf{x}_1(t_d) + C_{2d}\mathbf{x}_2(t_d) + D_{1d}\mathbf{w}(t)\mathbf{x}_1(t_d) \\ &\quad + D_{2d}\mathbf{w}(t)\mathbf{x}_2(t_d) + \mathbf{v}_d(t), \end{aligned} \tag{5}$$

where

$$\begin{gathered} J_1FJ_2 = \begin{bmatrix} I_{n_1} & 0 \\ 0 & F_1 \end{bmatrix}, \qquad J_1AJ_2 = \begin{bmatrix} A_1 & 0 \\ 0 & I_{n-n_1} \end{bmatrix}, \\ J_1B = \begin{bmatrix} B_1 \\ B_2 \end{bmatrix}, \qquad \begin{bmatrix} C \\ C_d \\ D \\ D_d \end{bmatrix} J_2 = \begin{bmatrix} C_1 & C_2 \\ C_{1d} & C_{2d} \\ D_1 & D_2 \\ D_{1d} & D_{2d} \end{bmatrix}, \end{gathered} \tag{6}$$

$\mathbf{x}_1 \in R^{n_1}$, $\mathbf{x}_2 \in R^{n-n_1}$, *and* F_1 *is a* λ*-nilpotent matrix; that is,* $F_1^\lambda = 0$, $F_1^{\lambda-1} \neq 0$.

3. Optimal Fixed-Point Smoother $\hat{\mathbf{x}}_1(t \mid k)$

From Lemma 4, in order to give the fixed-point smoother of *Problem FPS*, we first give the fixed-point smoother of the restricted equivalent system (2)–(5).

3.1. Riccati Equation $P_1(t+1, i)$. The Riccati equation will be given mainly by using reorganized innovation analysis [17], the corresponding definitions $\mathbf{e}_1(t,i)$, $\widetilde{\mathscr{Y}}_i(t)$, $\Pi_1(t)$, $P_1(t,i)$, $P_1(t,s,i)$, $L(t,s,i)$, $Q_{\overline{\mathscr{Y}}_i}(t)$, $T(t,s,i)$, $R(t,s,i)$, and $R(t,s,12)$ in [19], and the following denotations:

$$\begin{aligned} &\begin{bmatrix} G(t,s,i) & G_1(t,s,i) & G_2(t,s \mid l,i) & G_3(t,s \mid l,i) \\ H(t,s,i) & H_1(t,s,i) & H_2(t,s \mid l,i) & H_3(t,s \mid l,i) \end{bmatrix} \\ &\triangleq \left\langle \begin{bmatrix} \mathbf{u}(t) \\ \overline{\mathscr{V}}_i(t) \end{bmatrix}, \begin{bmatrix} \widetilde{\mathscr{Y}}_i^T(s) \\ \mathbf{e}_1^T(s,i) \\ \widehat{\overline{\mathscr{V}}}_i^T(s \mid l,i) \\ \hat{\mathbf{u}}^T(s \mid l,i) \end{bmatrix}^T \right\rangle, \end{aligned} \tag{7}$$

$$\begin{aligned} &\begin{bmatrix} H(t,s,12) & H_1(t,s,12) & H_2(t,s \mid l,12) & H_3(t,s \mid l,12) \end{bmatrix} \\ &\triangleq \left\langle \overline{\mathscr{V}}_1(t), \begin{bmatrix} \widetilde{\mathscr{Y}}_2^T(s) \\ \mathbf{e}_1^T(s,2) \\ \widehat{\overline{\mathscr{V}}}_2^T(s \mid l,2) \\ \hat{\mathbf{u}}^T(s \mid l,2) \end{bmatrix}^T \right\rangle. \end{aligned} \tag{8}$$

$P_1(t+1, 1)$ can be given in the following lemma.

Lemma 5 (see [19]). *Consider the restricted equivalent delayed descriptor system (2)–(5) under Assumptions 1 and 2; the error covariance matrix $P_1(t+1,1)$ of $\mathbf{x}_1(t+1)$ can be given as*

$$\begin{aligned} P_1(t+1,1) &= A_1 P_1(t,1) A_1^T + B_1 \left[Q_u - G_3(t,t \mid t,1)\right] B_1^T \\ &\quad + A_1 \left[G_1^T(t,t,1) - K(t,t,1) G^T(t,t,1)\right] B_1^T \\ &\quad + B_1 \left[G_1(t,t,1) - G(t,t,1) K^T(t,t,1)\right] A_1^T \\ &\quad - A_1 K(t,t,1) Q_{\overline{\mathscr{Y}}_1}(t) K^T(t,t,1) A_1^T, \\ P_1(t_d+1,1) &= P_1(t_d+1,2), \quad t \geq d, \end{aligned} \tag{9}$$

where

$$K(t,t,1) = L(t,t,1) Q_{\overline{\mathscr{Y}}_1}^{-}(t), \tag{10}$$

with

$$L(t,t,1) = P_1(t,1) \mathscr{C}_{11}^T + H_1^T(t,t,1), \tag{11}$$

$$\begin{aligned} Q_{\overline{\mathscr{Y}}_1}(t) &= \mathscr{C}_{11} P_1(t,1) \mathscr{C}_{11}^T + D_1 M \Pi_1(t) D_1^T + R(t,t,1) \\ &\quad - H_2(t,t \mid t-1,1) + \mathscr{C}_{11} H_1^T(t,t,1) \\ &\quad + H_1(t,t,1) \mathscr{C}_{11}^T, \end{aligned} \tag{12}$$

where

$$\begin{aligned} R(t,t,1) &= Q_v + \sum_{j=0}^{\lambda-1} \mathscr{C}_{21} F_1^j B_2 Q_u B_2^T \left(F_1^j\right)^T \mathscr{C}_{21}^T \\ &\quad + M \sum_{j=0}^{\lambda-1} D_2 F_1^j B_2 Q_u B_2^T \left(F_1^j\right)^T D_2^T, \end{aligned} \tag{13}$$

$G(t,t,1)$, $G_1(t,t,1)$, $G_3(t,t \mid t,1)$, $H_1(t,t,1)$, and $H_2(t,t \mid t-1,1)$ are defined in (7) and given in [19], and $\Pi_1(t) = A_1 \Pi_1(t) A_1^T + B_1 Q_u B_1^T$.

3.2. Fixed-Point Smoother $\hat{\mathbf{x}}_1(t \mid k)$. In this subsection, we will give the optimal fixed-point smoother for $\mathbf{x}_1(t)$ ($k = t+1, \ldots, N$) based on the above lemmas.

Theorem 6. *For a fixed t, consider the presented restricted equivalent delayed system (2)–(5) under Assumptions 1 and 2; the fixed-point smoother $\hat{\mathbf{x}}_1(t \mid k)$ can be given as*

$$\begin{aligned} \hat{\mathbf{x}}_1(t \mid k) &= \hat{\mathbf{x}}_1(t \mid t,1) + \sum_{j=1}^{k-t} L(t,t+j,1) Q_{\overline{\mathscr{Y}}_1}^{-}(t+j) \\ &\quad \times \left[\mathscr{Y}_1(t+j) - \mathscr{C}_{11} \hat{\mathbf{x}}_1(t+j,1) - \widehat{\overline{\mathscr{V}}}_1(t+j,1)\right], \\ &\quad k = t+1, \ldots, N, \quad t \geq d, \end{aligned} \tag{14}$$

where

$$\begin{aligned} &\hat{\mathbf{x}}_1(t \mid t,1) \\ &\quad = \hat{\mathbf{x}}_1(t,1) \\ &\qquad + L(t,t,1) Q_{\overline{\mathscr{Y}}_1}^{-}(t) \left[\mathscr{Y}_1(t) - \mathscr{C}_{11} \hat{\mathbf{x}}_1(t,1) - \widehat{\overline{\mathscr{V}}}_1(t,1)\right], \end{aligned} \tag{15}$$

$$\begin{aligned} &L(t,t+j,1) \\ &\quad = P_1(t,t+j,1) \mathscr{C}_{11}^T + H_1^T(t+j,t,1) \\ &\qquad - \sum_{i=0}^{j-1} L(t,t+i,1) Q_{\overline{\mathscr{Y}}_1}^{-}(t+i) H^T(t+j,t+i,1), \\ &\qquad j = 1, \ldots, k-t, \end{aligned} \tag{16}$$

with

$$\begin{aligned} P_1(t,t+j,1) &\triangleq \langle \mathbf{e}_1(t,1), \mathbf{e}_1(t+j,1) \rangle = P_1(t,1) \left(A_1^j\right)^T \\ &\quad + \sum_{i=0}^{j-1} G_1^T(t+i,t,1) B_1^T \left(A_1^{j-1-i}\right)^T \\ &\quad - \sum_{i=0}^{j-1} \sum_{m=0}^{i} L(t,t+m,1) Q_{\overline{\mathscr{Y}}_1}^{-}(t+m) G^T \\ &\qquad \cdot (t+i,t+m,1) B_1^T \left(A_1^{j-1-i}\right)^T \\ &\quad - \sum_{i=0}^{j-1} L(t,t+j-1-i,1) Q_{\overline{\mathscr{Y}}_1}^{-}(t+j-1-i) \\ &\quad \times L^T(t,t+j-1-i,1) \left(A_1^{i+1}\right)^T. \end{aligned} \tag{17}$$

$L(t,t,1)$ is as in (11); $P_1(t,1)$ is as in (9); $\hat{\mathbf{x}}_1(t,1)$ and $\hat{\mathbf{x}}_1(t+j,1)$ ($j = 1, \ldots, k-t$) can be given as

$$\begin{aligned} &\hat{\mathbf{x}}_1(t+1,1) \\ &\quad = A_1 \hat{\mathbf{x}}_1(t,1) + A_1 L(t,t,1) Q_{\overline{\mathscr{Y}}_1}^{-}(t) \\ &\qquad \cdot \left[\mathscr{Y}_1(t) - \mathscr{C}_{11} \hat{\mathbf{x}}_1(t,1) - \widehat{\overline{\mathscr{V}}}_1(t,1)\right] \\ &\qquad + B_1 \hat{\mathbf{u}}(t \mid t,1), \\ &\hat{\mathbf{x}}_1(t_d+1,1) = \hat{\mathbf{x}}_1(t_d+1,2), \\ &\qquad t \geq d, \end{aligned} \tag{18}$$

and $\hat{\mathbf{x}}_1(t_d+1,2)$ *can be given by*

$$\begin{aligned}\hat{\mathbf{x}}_1(t_d+1,2) &= A_1\hat{\mathbf{x}}_1(t_d,2)+A_1L(t_d,t_d,2)Q^{-}_{\widetilde{\mathcal{Y}}_2}(t_d)\\ &\quad\cdot\left[\mathcal{Y}_2(t_d)-\mathcal{C}_{12}\hat{\mathbf{x}}_1(t_d,2)-\widehat{\widetilde{\mathcal{V}}}_2(t_d,2)\right]\\ &\quad+B_1\hat{\mathbf{u}}(t_d\mid t_d,2),\\ \hat{\mathbf{x}}_1(0,2) &= \hat{\mathbf{x}}_1(0\mid -1,2)=0.\end{aligned}\tag{19}$$

In the above,

$$\begin{aligned}\hat{\mathbf{u}}(t\mid t,1) &= \hat{\mathbf{u}}(t\mid t-1,1)+G(t,t,1)Q^{-}_{\widetilde{\mathcal{Y}}_1}(t)\\ &\quad\cdot\left[\mathcal{Y}_1(t)-\mathcal{C}_{11}\hat{\mathbf{x}}_1(t,1)-\widehat{\widetilde{\mathcal{V}}}_1(t,1)\right],\end{aligned}\tag{20}$$

$$\begin{aligned}\hat{\mathbf{u}}(t_d\mid t_d,2) &= \hat{\mathbf{u}}(t_d\mid t_d-1,2)+G(t_d,t_d,2)Q^{-}_{\widetilde{\mathcal{Y}}_2}(t_d)\\ &\quad\cdot\left[\mathcal{Y}_2(t_d)-\mathcal{C}_{12}\hat{\mathbf{x}}_1(t_d,2)-\widehat{\widetilde{\mathcal{V}}}_2(t_d,2)\right],\end{aligned}\tag{21}$$

where

$$\begin{aligned}\widehat{\widetilde{\mathcal{V}}}_1(t,1) &= \widehat{\widetilde{\mathcal{V}}}_1(t\mid t-2,1)+H(t,t-1,1)Q^{-}_{\widetilde{\mathcal{Y}}_1}(t-1)\\ &\quad\times\left[\mathcal{Y}_1(t-1)-\mathcal{C}_{11}\hat{\mathbf{x}}_1(t-1,1)-\widehat{\widetilde{\mathcal{V}}}_1(t-1,1)\right],\\ \widehat{\widetilde{\mathcal{V}}}_1(t_d+1,1) &= \widehat{\widetilde{\mathcal{V}}}_1(t_d+1,2),\end{aligned}\tag{22}$$

$$\begin{aligned}\widehat{\widetilde{\mathcal{V}}}_2(t_d,2) &= \widehat{\widetilde{\mathcal{V}}}_2(t_d\mid t_d-2,2)+H(t_d,t_d-1,2)Q^{-}_{\widetilde{\mathcal{Y}}_2}(t_d-1)\\ &\quad\times\left[\mathcal{Y}_2(t_d-1)-\mathcal{C}_{12}\hat{\mathbf{x}}_1(t_d-1,2)-\widehat{\widetilde{\mathcal{V}}}_2(t_d-1,2)\right],\\ \widehat{\widetilde{\mathcal{V}}}_2(0,2) &= 0,\end{aligned}\tag{23}$$

with $\widehat{\widetilde{\mathcal{V}}}_1(t_d+1,2)$ *being given as*

$$\begin{aligned}\widehat{\widetilde{\mathcal{V}}}_1(t_d+1,2) &= \widehat{\widetilde{\mathcal{V}}}_1(t_d+1\mid t_d-1,2)+H(t_d+1,t_d,12)Q^{-}_{\widetilde{\mathcal{Y}}_2}(t_d)\\ &\quad\times\left[\mathcal{Y}_2(t_d)-\mathcal{C}_{12}\hat{\mathbf{x}}_1(t_d,2)-\widehat{\widetilde{\mathcal{V}}}_2(t_d,2)\right];\end{aligned}\tag{24}$$

$G(t,s,2)$, $G(t,s,1)$, *and* $H(t_d+1,t_d,12)$ *are in [19].*

Proof. According to the projection theorem, we have

$$\begin{aligned}\hat{\mathbf{x}}_1(t\mid N) &= \operatorname{Proj}\left\{\mathbf{x}_1(t)\mid\widetilde{\mathcal{Y}}_2(0),\ldots,\widetilde{\mathcal{Y}}_2(t_d);\right.\\ &\qquad\left.\widetilde{\mathcal{Y}}_1(t_d+1),\ldots,\widetilde{\mathcal{Y}}_1(t),\ldots,\widetilde{\mathcal{Y}}_1(N)\right\}\\ &= \hat{\mathbf{x}}_1(t\mid t)+\sum_{j=1}^{N-t}\operatorname{Proj}\left\{\mathbf{x}_1(t)\mid\widetilde{\mathcal{Y}}_1(t+j)\right\}\\ &= \hat{\mathbf{x}}_1(t\mid t)+\sum_{j=1}^{N-t}L(t,t+j,1)Q^{-}_{\widetilde{\mathcal{Y}}_1}(t+j)\widetilde{\mathcal{Y}}_1(t+j),\end{aligned}\tag{25}$$

which is (14).

Since $\hat{\mathbf{x}}_1(t,1)\perp\widetilde{\mathcal{Y}}_1(t+1)$, then

$$\begin{aligned}L(t,t+1,1) &= \left\langle\mathbf{x}_1(t),\widetilde{\mathcal{Y}}_1(t+1)\right\rangle\\ &= \left\langle\mathbf{e}_1(t,1),\widetilde{\mathcal{Y}}_1(t+1)\right\rangle\\ &= P_1(t,t+1,1)\mathcal{C}_{11}^T+H_1^T(t+1,t,1)\\ &\quad-\left\langle\mathbf{e}_1(t,1),\widehat{\widetilde{\mathcal{V}}}_1(t+1,1)\right\rangle.\end{aligned}\tag{26}$$

According to the projection theorem, we have

$$\begin{aligned}\widehat{\widetilde{\mathcal{V}}}_1(t+1,1) &= \operatorname{Proj}\left\{\overline{\mathcal{V}}_1(t+1)\mid\widetilde{\mathcal{Y}}_2(0),\ldots,\widetilde{\mathcal{Y}}_2(t_d);\right.\\ &\qquad\left.\widetilde{\mathcal{Y}}_1(t_d+1),\ldots,\widetilde{\mathcal{Y}}_1(t)\right\}\\ &= \operatorname{Proj}\left\{\overline{\mathcal{V}}_1(t+1)\mid\widetilde{\mathcal{Y}}_2(0),\ldots,\widetilde{\mathcal{Y}}_2(t_d);\right.\\ &\qquad\left.\widetilde{\mathcal{Y}}_1(t_d+1),\ldots,\widetilde{\mathcal{Y}}_1(t-1)\right\}\\ &\quad+\operatorname{Proj}\left\{\overline{\mathcal{V}}_1(t+1)\mid\widetilde{\mathcal{Y}}_1(t)\right\}\\ &= \widehat{\widetilde{\mathcal{V}}}_1(t+1\mid t-1,1)+H(t+1,t,1)Q^{-}_{\widetilde{\mathcal{Y}}_1}(t)\widetilde{\mathcal{Y}}_1(t),\end{aligned}\tag{27}$$

which is (22). By considering $\mathbf{e}_1(t,1)\perp\widehat{\widetilde{\mathcal{V}}}_1(t+1\mid t-1,1)$ and (27), (26) can be rewritten as

$$\begin{aligned}L(t,t+1,1) &= P_1(t,t+1,1)\mathcal{C}_{11}^T+H_1^T(t+1,t,1)\\ &\quad-L(t,t,1)Q^{-}_{\widetilde{\mathcal{Y}}_1}(t)H^T(t+1,t,1).\end{aligned}\tag{28}$$

Similarly,

$$\begin{aligned}L(t,t+2,1) &= \left\langle\mathbf{e}_1(t,1),\widetilde{\mathcal{Y}}_1(t+2)\right\rangle\\ &= P_1(t,t+2,1)\mathcal{C}_{11}^T+H_1^T(t+2,t,1)\\ &\quad-\left\langle\mathbf{e}_1(t,1),\widehat{\widetilde{\mathcal{V}}}_1(t+2,1)\right\rangle,\end{aligned}\tag{29}$$

while

$$\begin{aligned}\widehat{\mathscr{V}}_1(t+2,1) &= \widehat{\mathscr{V}}_1(t+2\mid t,1)\\ &\quad + H(t+2,t+1,1)\,Q^{-}_{\widetilde{\mathscr{Y}}_1}(t+1)\,\widetilde{\mathscr{Y}}_1(t+1)\\ &= \widehat{\mathscr{V}}_1(t+2\mid t-1,1)\\ &\quad + H(t+2,t,1)\,Q^{-}_{\widetilde{\mathscr{Y}}_1}(t)\,\widetilde{\mathscr{Y}}_1(t)\\ &\quad + H(t+2,t+1,1)\,Q^{-}_{\widetilde{\mathscr{Y}}_1}(t+1)\,\widetilde{\mathscr{Y}}_1(t+1),\end{aligned} \tag{30}$$

since $\mathbf{e}_1(t,1)\perp\widehat{\mathscr{V}}_1(t+2\mid t-1,1)$, so from (29) and (30),

$$\begin{aligned}L(t,t+2,1) &= P_1(t,t+2,1)\,\mathscr{C}_{11}^T + H_1^T(t+2,t,1)\\ &\quad - L(t,t,1)\,Q^{-}_{\widetilde{\mathscr{Y}}_1}(t)\,H^T(t+2,t,1)\\ &\quad - L(t,t+1,1)\,Q^{-}_{\widetilde{\mathscr{Y}}_1}(t+1)\,H^T\\ &\quad \cdot(t+2,t+1,1).\end{aligned} \tag{31}$$

Then by inductive method, we have

$$\begin{aligned}&L(t,t+j,1)\\ &\quad = P_1(t,t+j,1)\,\mathscr{C}_{11}^T + H_1^T(t+j,t,1)\\ &\qquad - \sum_{i=0}^{j-1} L(t,t+i,1)\,Q^{-}_{\widetilde{\mathscr{Y}}_1}(t+i)\,H^T(t+j,t+i,1),\\ &\qquad\qquad j=1,\ldots,k-t,\end{aligned} \tag{32}$$

which is (16).

According to the projection theorem, we have

$$\begin{aligned}&\widehat{\mathbf{x}}_1(t\mid t,1)\\ &\quad = \operatorname{Proj}\{\mathbf{x}_1(t)\mid \widetilde{\mathscr{Y}}_2(0),\ldots,\widetilde{\mathscr{Y}}_2(t_d);\\ &\qquad\qquad \widetilde{\mathscr{Y}}_1(t_d+1),\ldots,\widetilde{\mathscr{Y}}_1(t)\}\\ &\quad = \widehat{\mathbf{x}}_1(t\mid t-1,1) + \operatorname{Proj}\{\mathbf{x}_1(t)\mid \widetilde{\mathscr{Y}}_1(t)\}\\ &\quad = \widehat{\mathbf{x}}_1(t\mid t-1,1) + L(t,t,1)\,Q^{-}_{\widetilde{\mathscr{Y}}_1}(t)\,\widetilde{\mathscr{Y}}_1(t);\end{aligned} \tag{33}$$

then (15) can be given.

Similarly, we have

$$\begin{aligned}&\widehat{\mathbf{x}}_1(t+1,1)\\ &\quad = \operatorname{Proj}\{\mathbf{x}_1(t+1)\mid \widetilde{\mathscr{Y}}_2(0),\ldots,\widetilde{\mathscr{Y}}_2(t_d);\\ &\qquad\qquad \widetilde{\mathscr{Y}}_1(t_d+1),\ldots,\widetilde{\mathscr{Y}}_1(t)\}\\ &\quad = \operatorname{Proj}\{A_1\mathbf{x}_1(t) + B_1\mathbf{u}(t)\mid \widetilde{\mathscr{Y}}_1(t)\}\\ &\quad = A_1\widehat{\mathbf{x}}_1(t,1) + A_1L(t,t,1)\,Q^{-}_{\widetilde{\mathscr{Y}}_1}(t)\,\widetilde{\mathscr{Y}}_1(t) + B_1\widehat{\mathbf{u}}(t\mid t,1),\end{aligned} \tag{34}$$

which is (18). Then combining (34) with (2) yields

$$\begin{aligned}\mathbf{e}_1(t+1,1) &= A_1\mathbf{e}_1(t,1) + B_1\mathbf{u}(t) - B_1\widehat{\mathbf{u}}(t\mid t,1)\\ &\quad - A_1L(t,t,1)\,Q^{-}_{\widetilde{\mathscr{Y}}_1}(t)\,\widetilde{\mathscr{Y}}_1(t).\end{aligned} \tag{35}$$

We have

$$\begin{aligned}\mathbf{e}_1(t+j,1) &= A_1^j\mathbf{e}_1(t,1) + \sum_{i=0}^{j-1} A_1^{j-1-i}B_1\mathbf{u}(t+i)\\ &\quad - \sum_{i=0}^{j-1} A_1^{j-1-i}B_1\widehat{\mathbf{u}}(t+i\mid t+i,1)\\ &\quad - \sum_{i=0}^{j-1} A_1^{i+1}L(t,t+j-1-i,1)\,Q^{-}_{\widetilde{\mathscr{Y}}_1}\\ &\qquad \cdot(t+j-1-i)\,\widetilde{\mathscr{Y}}_1(t+j-1-i).\end{aligned} \tag{36}$$

According to the projection theorem, we have

$$\begin{aligned}&\widehat{\mathbf{u}}(t\mid t,1)\\ &\quad = \operatorname{Proj}\{\mathbf{u}(t)\mid \widetilde{\mathscr{Y}}_2(0),\ldots,\widetilde{\mathscr{Y}}_2(t_d);\\ &\qquad\qquad \widetilde{\mathscr{Y}}_1(t_d+1),\ldots,\widetilde{\mathscr{Y}}_1(t)\}\\ &\quad = \operatorname{Proj}\{\mathbf{u}(t)\mid \widetilde{\mathscr{Y}}_2(0),\ldots,\widetilde{\mathscr{Y}}_2(t_d);\\ &\qquad\qquad \widetilde{\mathscr{Y}}_1(t_d+1),\ldots,\widetilde{\mathscr{Y}}_1(t-1)\}\\ &\qquad + \operatorname{Proj}\{\mathbf{u}(t)\mid \widetilde{\mathscr{Y}}_1(t)\}\\ &\quad = \widehat{\mathbf{u}}(t\mid t-1,1) + \langle \mathbf{u}(t),\widetilde{\mathscr{Y}}_1(t)\rangle\,Q^{-}_{\widetilde{\mathscr{Y}}_1}(t)\,\widetilde{\mathscr{Y}}_1(t)\\ &\quad = \widehat{\mathbf{u}}(t\mid t-1,1) + G(t,t,1)\,Q^{-}_{\widetilde{\mathscr{Y}}_1}(t)\,\widetilde{\mathscr{Y}}_1(t);\end{aligned} \tag{37}$$

then (20) can be given.

Similarly,

$$\begin{aligned}&\widehat{\mathbf{u}}(t+i\mid t+i,1)\\ &\quad = \widehat{\mathbf{u}}(t+i\mid t-1,1)\\ &\qquad + \sum_{m=0}^{i} G(t+i,t+m,1)\,Q^{-}_{\widetilde{\mathscr{Y}}_1}(t+m)\,\widetilde{\mathscr{Y}}_1(t+m),\end{aligned} \tag{38}$$

since $\mathbf{e}_1(t,1) \perp \hat{\mathbf{u}}(t+i \mid t-1,1)$, so from (36) and (38), we have

$$\begin{aligned}
&P_1(t,t+j,1)\\
&\quad=\langle \mathbf{e}_1(t,1), \mathbf{e}_1(t+j,1)\rangle\\
&\quad=\Bigg\langle \mathbf{e}_1(t,1), A_1^j\mathbf{e}_1(t,1)+\sum_{i=0}^{j-1}A_1^{j-1-i}B_1\mathbf{u}(t+i)\\
&\qquad-\sum_{i=0}^{j-1}A_1^{j-1-i}B_1\hat{\mathbf{u}}(t+i\mid t+i,1)\\
&\qquad-\sum_{i=0}^{j-1}A_1^{i+1}L(t,t+j-1-i,1)Q^{-}_{\widetilde{\mathscr{Y}}_1}\\
&\qquad\cdot(t+j-1-i)\widetilde{\mathscr{Y}}_1(t+j-1-i)\Bigg\rangle \qquad (39)\\
&\quad=P_1(t,1)\left(A_1^j\right)^T+\sum_{i=0}^{j-1}G_1^T(t+i,t,1)B_1^T\left(A_1^{j-1-i}\right)^T\\
&\qquad-\sum_{i=0}^{j-1}\sum_{m=0}^{i}L(t,t+m,1)Q^{-}_{\widetilde{\mathscr{Y}}_1}(t+m)G^T\\
&\qquad\cdot(t+i,t+m,1)B_1^T\left(A_1^{j-1-i}\right)^T\\
&\qquad-\sum_{i=0}^{j-1}L(t,t+j-1-i,1)Q^{-}_{\widetilde{\mathscr{Y}}_1}(t+j-1-i)L^T\\
&\qquad\cdot(t,t+j-1-i,1)\left(A_1^{i+1}\right)^T,
\end{aligned}$$

which is (17).

Equations (19) and (21) can also be given similar to (18) and (20). Equation (23) can be given similar to (22) in (27).

According to the projection theorem, we have

$$\begin{aligned}
&\widehat{\widetilde{\mathscr{V}}}_1(t_d+1,2)\\
&\quad=\operatorname{Proj}\left\{\widetilde{\mathscr{V}}_1(t_d+1)\mid\widetilde{\mathscr{Y}}_2(0),\ldots,\widetilde{\mathscr{Y}}_2(t_d)\right\}\\
&\quad=\operatorname{Proj}\left\{\widetilde{\mathscr{V}}_1(t_d+1)\mid\widetilde{\mathscr{Y}}_2(0),\ldots,\widetilde{\mathscr{Y}}_2(t_d-1)\right\}\\
&\qquad+\operatorname{Proj}\left\{\widetilde{\mathscr{V}}_1(t_d+1)\mid\widetilde{\mathscr{Y}}_2(t_d)\right\} \qquad (40)\\
&\quad=\widehat{\widetilde{\mathscr{V}}}_1(t_d+1\mid t_d-1,2)\\
&\qquad+H(t_d+1,t_d,12)Q^{-}_{\widetilde{\mathscr{Y}}_2}(t_d)\widetilde{\mathscr{Y}}_2(t_d);
\end{aligned}$$

then (24) can be given. □

4. Fixed-Point Smoother $\hat{\mathbf{x}}(t \mid k)$

By using projection theorem and reorganized innovation, the fixed-point smoother $\hat{\mathbf{x}}_1(t \mid k,1)$ $(k=t+1,\ldots,N)$ has been given, then it is time to give the main result of fixed-point smoother $\hat{\mathbf{x}}(t \mid k)$.

Theorem 7. *Consider the descriptor system (1) under Assumptions 1 and 2 and* $[0\ \ I]J_2^{-1}\mathbf{x}(0) = -\sum_{j=0}^{\lambda-1}F_1^jB_2\mathbf{u}(j)$*; then the optimal fixed-point smoother* $\hat{\mathbf{x}}(t \mid k)=\hat{\mathbf{x}}(t \mid k,1)$ *can be given by*

$$\hat{\mathbf{x}}(t \mid k)=J_2\begin{bmatrix}\hat{\mathbf{x}}_1(t \mid k,1)\\ \hat{\mathbf{x}}_2(t \mid k,1)\end{bmatrix},\quad k=t+1,\ldots,N,\ t\geq d. \qquad (41)$$

In the above, $\hat{\mathbf{x}}_1(t \mid k,1)$ *is from (14);* $\hat{\mathbf{x}}_2(t \mid k,1)$ *is given as*

$$\begin{aligned}
&\hat{\mathbf{x}}_2(t \mid k,1)\\
&\quad=\begin{cases}-\sum_{j=0}^{\lambda-1}F_1^jB_2\hat{\mathbf{u}}(t+j \mid k,1), & k>t+\lambda-1,\\ -\sum_{j=0}^{k-t}F_1^jB_2\hat{\mathbf{u}}(t+j \mid k,1), & t<k\leq t+\lambda-1,\end{cases} \qquad (42)\\
&\hat{\mathbf{u}}(t+j \mid k,1)\\
&\quad=\hat{\mathbf{u}}(t+j \mid t+j,1)\\
&\qquad+\sum_{i=1}^{k-t-j}\Big[G_1(t+j,t+j+i,1)\mathscr{C}_{11}^T+T(t+j,t+j+i,1)\\
&\qquad\qquad-G_2(t+j,t+j+i \mid t+j+i-1,1)\Big]\\
&\qquad\cdot Q^{-}_{\widetilde{\mathscr{Y}}_1}(t+j+i)\widetilde{\mathscr{Y}}_1(t+j+i), \qquad (43)
\end{aligned}$$

where

$$\begin{aligned}
&\hat{\mathbf{u}}(t+j \mid t+j,1)\\
&\quad=\hat{\mathbf{u}}(t+j \mid t+j-1,1) \qquad (44)\\
&\qquad+G(t+j,t+j,1)Q^{-}_{\widetilde{\mathscr{Y}}_1}(t+j)\widetilde{\mathscr{Y}}_1(t+j),
\end{aligned}$$

with $\hat{\mathbf{u}}(t+j \mid t_d,1)=\hat{\mathbf{u}}(t+j \mid t_d,2)$ *being given as*

$$\begin{aligned}
\hat{\mathbf{u}}(t+j \mid t_d,2)&=\hat{\mathbf{u}}(t+j \mid t_d-1,2)\\
&\quad+G(t+j,t_d,2)Q^{-}_{\widetilde{\mathscr{Y}}_2}(t_d)\widetilde{\mathscr{Y}}_2(t_d),
\end{aligned} \qquad (45)$$

with

$$\widetilde{\mathscr{Y}}_i(t)=\mathscr{Y}_i(t)-\mathscr{C}_{1i}\hat{\mathbf{x}}_1(t,i)+\widehat{\widetilde{\mathscr{V}}}_i(t,i),\quad i=1,2, \qquad (46)$$

and $G(t+j,t+j,1)$, $G_1(t+j,t+j+i,1)$, $G_2(t+j,t+j+i,1)$, $G(t+j,t_d,2)$, *and* $T(t+j,t+j+i,1)$ *can be referred to [19];* $\hat{\mathbf{x}}_1(t,1)$ *is from (18);* $\widehat{\widetilde{\mathscr{V}}}_1(t,1)$ *is from (22).*

Proof. Equation (41) can be given easily by considering Lemma 4.

According to the projection theorem, when $k > t + \lambda - 1$, we have

$$\begin{aligned}
&\hat{\mathbf{x}}_2(t \mid k, 1) \\
&\quad = \operatorname{Proj}\left\{\mathbf{x}_2(t) \mid \widetilde{\mathcal{Y}}_2(0), \ldots, \widetilde{\mathcal{Y}}_2(t_d); \right. \\
&\qquad\qquad \left. \widetilde{\mathcal{Y}}_1(t_d+1), \ldots, \widetilde{\mathcal{Y}}_1(k)\right\} \\
&\quad = \operatorname{Proj}\left\{-\sum_{j=0}^{\lambda-1} F_1^j B_2 \mathbf{u}(t+j) \mid \widetilde{\mathcal{Y}}_2(0), \ldots, \widetilde{\mathcal{Y}}_2(t_d); \right. \\
&\qquad\qquad \left. \widetilde{\mathcal{Y}}_1(t_d+1), \ldots, \widetilde{\mathcal{Y}}_1(k)\right\} \\
&\quad = -\sum_{j=0}^{\lambda-1} F_1^j B_2 \hat{\mathbf{u}}(t+j \mid k, 1).
\end{aligned} \tag{47}$$

When $t < k \le t + \lambda - 1$, we have

$$\begin{aligned}
&\hat{\mathbf{x}}_2(t \mid k, 1) \\
&\quad = \operatorname{Proj}\left\{\mathbf{x}_2(t) \mid \widetilde{\mathcal{Y}}_2(0), \ldots, \widetilde{\mathcal{Y}}_2(t_d); \right. \\
&\qquad\qquad \left. \widetilde{\mathcal{Y}}_1(t_d+1), \ldots, \widetilde{\mathcal{Y}}_1(k)\right\} \\
&\quad = \operatorname{Proj}\left\{-\sum_{j=0}^{k-t} F_1^j B_2 \mathbf{u}(t+j) \mid \widetilde{\mathcal{Y}}_2(0), \ldots, \widetilde{\mathcal{Y}}_2(t_d); \right. \\
&\qquad\qquad \left. \widetilde{\mathcal{Y}}_1(t_d+1), \ldots, \widetilde{\mathcal{Y}}_1(k)\right\} \\
&\quad = -\sum_{j=0}^{k-t} F_1^j B_2 \hat{\mathbf{u}}(t+j \mid k, 1);
\end{aligned} \tag{48}$$

then (47) and (48) yield (42).

According to the projection theorem, we have

$$\begin{aligned}
&\hat{\mathbf{u}}(t+j \mid k, 1) \\
&\quad = \operatorname{Proj}\left\{\mathbf{u}(t+j) \mid \widetilde{\mathcal{Y}}_2(0), \ldots, \widetilde{\mathcal{Y}}_2(t_d); \right. \\
&\qquad\qquad \left. \widetilde{\mathcal{Y}}_1(t_d+1), \ldots, \widetilde{\mathcal{Y}}_1(k)\right\} \\
&\quad = \operatorname{Proj}\left\{\mathbf{u}(t+j) \mid \widetilde{\mathcal{Y}}_2(0), \ldots, \widetilde{\mathcal{Y}}_2(t_d); \right. \\
&\qquad\qquad \left. \widetilde{\mathcal{Y}}_1(t_d+1), \ldots, \widetilde{\mathcal{Y}}_1(t+j)\right\} \\
&\qquad + \sum_{i=1}^{k-t-j} \operatorname{Proj}\left\{\mathbf{u}(t+j) \mid \widetilde{\mathcal{Y}}_1(t+j+i)\right\} \\
&\quad = \hat{\mathbf{u}}(t+j \mid t+j, 1) \\
&\qquad + \sum_{i=1}^{k-t-j} \left\langle \mathbf{u}(t+j), \widetilde{\mathcal{Y}}_1(t+j+i)\right\rangle \\
&\qquad\qquad \cdot Q_{\widetilde{\mathcal{Y}}_1}^{-}(t+j+i)\, \widetilde{\mathcal{Y}}_1(t+j+i) \\
&\quad = \hat{\mathbf{u}}(t+j \mid t+j, 1) \\
&\qquad + \sum_{i=1}^{k-t-j} \left[G_1(t+j, t+j+i, 1)\, \mathcal{C}_{11}^T + T(t+j, t+j+i, 1)\right. \\
&\qquad\qquad \left. - G_2(t+j, t+j+i \mid t+j+i-1, 1)\right] \\
&\qquad\qquad \cdot Q_{\widetilde{\mathcal{Y}}_1}^{-}(t+j+i)\, \widetilde{\mathcal{Y}}_1(t+j+i),
\end{aligned} \tag{49}$$

which is (43).

Equations (44) and (45) can be given similar to (20). □

5. Conclusion

The optimal fixed-point smoother for the descriptor system has been proposed, where the system model is corrupted by multiplicative noise, and the system is observed by instantaneous and single delayed observations. By using standard singular value decomposition, the origin system has been changed into the restricted system, fixed-point smoother is given based on reorganized innovation analysis [17] and projection theorem for the restricted system model, and then the fixed-point smoother for the origin system has been given based on the above result. The fixed-point smoother is given in terms of recursive Riccati equation and can be computed easily [21].

Conflict of Interests

The authors declare that there is no conflict of interests regarding the publication of this paper.

Acknowledgments

This paper is supported by the National Nature Science Foundation of China (61273197), Nature Science Foundation of Shandong Province (ZR2013FM018), the Science Research Foundation for the Excellent Middle-Aged and Youth Scientists of Shandong Province (BS2013DX012), the Applied Fundamental Research of Qingdao (14-2-4-19-jch), Huangdao District Science and Technology Project (2014-1-33), and "Taishan Scholarship" Construction Engineering.

References

[1] N. Wiener, *Extrapolation Interpolation, and Smoothing of Stationary Time Series*, The Technology Press and Wiley, New York, NY, USA, 1949.

[2] R. E. Kalman, "A new approach to linear filtering and prediction problems," *Journal of Basic Engineering*, vol. 82, no. 1, pp. 35–45, 1960.

[3] T. Kailath, A. H. Sayed, and B. Hassibi, *Linear Estimation*, Prentice Hall, Englewood Cliffs, NJ, USA, 1999.

[4] B. D. O. Anderson and J. B. Moore, *Optimal Filtering*, Prentice Hall, Englewood Cliffs, NJ, USA, 1979.

[5] Y. J. Liu, C. L. P. Chen, G. X. Wen, and S. Tong, "Adaptive neural output feedback tracking control for a class of uncertain discrete-time nonlinear systems," *IEEE Transactions on Neural Networks*, vol. 22, no. 7, pp. 1162–1167, 2011.

[6] Y. Liu and S. Tong, "Adaptive neural network tracking control of uncertain nonlinear discrete-time systems with nonaffine dead-zone input," *IEEE Transactions on Cybernetics*, vol. 45, no. 3, pp. 497–505, 2015.

[7] Y.-J. Liu, L. Tang, S. Tong, C. L. P. Chen, and D.-J. Li, "Reinforcement learning design-based adaptive tracking control with less learning parameters for nonlinear discrete-time MIMO systems," *IEEE Transactions on Neural Networks and Learning Systems*, vol. 26, no. 1, pp. 165–176, 2015.

[8] H. Gao, T. Chen, and T. Chai, "Passivity and passification for networked control systems," *SIAM Journal on Control and Optimization*, vol. 46, no. 4, pp. 1299–1322, 2007.

[9] H. Zhang, L. Xie, and Y. C. Soh, "Risk-sensitive filtering, prediction and smoothing for discrete-time singular systems," *Automatica*, vol. 39, no. 1, pp. 57–66, 2003.

[10] H. S. Zhang, T. Y. Chai, and X. J. Liu, "A unified approach to optimal state estimation for stochastic singular systems," *Automatica*, vol. 34, no. 6, pp. 777–781, 1998.

[11] L. Y. Dai, "Filtering and LQG problems for discrete-time stochastic singular systems," *IEEE Transactions on Automatic Control*, vol. 34, no. 10, pp. 1105–1108, 1989.

[12] S. Nakamori, R. Caballero-guila, A. Hermoso-Carazo, and J. Linares-Prez, "Design of recursive Wiener fixed-point smoothers based on innovations approach in linear discrete-time stochastic systems," *Applied Mathematics and Computation*, vol. 165, no. 3, pp. 731–747, 2005.

[13] S. Nakamori, "Design of extended recursive Wiener fixed-point smoother and filter in discrete-time stochastic systems," *Digital Signal Processing*, vol. 17, no. 1, pp. 360–370, 2007.

[14] D. Chu and S. Gao, "State optimal estimation algorithm for singular systems with multiplicative noise," *Periodical of Ocean University of China*, vol. 38, no. 9, pp. 814–818, 2008.

[15] D. Chu, S. Gao, and L. Guo, "State estimation for multi-channel stochastic singular systems with multiplicative noise," *Asian Journal of Control*, vol. 12, no. 6, pp. 725–733, 2010.

[16] S. Gao, *Study of optimal estimation algorithm for singular systems with multiplicative noise [M.S. thesis]*, Ocean University of China, 2010.

[17] X. Lu, X. Dong, and H. Wang, "Optimal fixed-point smoothing for delayed descriptor systems with multiplicative noise," in *Proceedings of the 27th Chinese Control and Decision Conference*, Qingdao, China, 2015.

[18] H. Zhang, L. Xie, D. Zhang, and Y. C. Soh, "A reorganized innovation approach to linear estimation," *IEEE Transactions on Automatic Control*, vol. 49, no. 10, pp. 1810–1814, 2004.

[19] X. Lu, H. Wang, and F. Wu, "Optimal multiple-step predictor for singular systems with multiplicative noise and delayed measurement," *Control Theory & Applications*. Revised.

[20] H.-Q. Wang, H.-S. Zhang, G.-R. Duan, and G.-C. Wang, "Design of H-infinity multi-step predictor for descriptor systems," *Journal of Control Theory & Applications*, vol. 24, no. 5, pp. 693–700, 2007.

[21] K. M. Nagpal and P. P. Khargonekar, "Filtering and smoothing in an H_∞ setting," *IEEE Transactions on Automatic Control*, vol. 36, no. 2, pp. 152–166, 1991.

Hindawi Publishing Corporation
Mathematical Problems in Engineering
Volume 2015, Article ID 606048, 8 pages
http://dx.doi.org/10.1155/2015/606048

Research Article

Robust Stability and Stabilization of Interval Uncertain Descriptor Fractional-Order Systems with the Fractional-Order α: The $1 \leq \alpha < 2$ Case

Yuanhua Li, Heng Liu, and Hongxing Wang

School of Finance, Huainan Normal University, Huainan 232038, China

Correspondence should be addressed to Hongxing Wang; winghongxing0902@163.com

Received 16 January 2015; Revised 28 May 2015; Accepted 30 May 2015

Academic Editor: Anna Pandolfi

Copyright © 2015 Yuanhua Li et al. This is an open access article distributed under the Creative Commons Attribution License, which permits unrestricted use, distribution, and reproduction in any medium, provided the original work is properly cited.

Stability and stabilization of fractional-order interval system is investigated. By adding parameters to linear matrix inequalities, necessary and sufficient conditions for stability and stabilization of the system are obtained. The results on stability check for uncertain FO-LTI systems with interval coefficients of dimension n only need to solve one $4n$-by-$4n$ LMI. Numerical examples are presented to shown the effectiveness of our results.

1. Introduction

During the last two decades, the study of fractional-order control systems has received more and more attention. As a generalization of the traditional calculus, the fractional calculus have found many applications in viscoelastic systems, robotics, finance, and so on ([1–4], etc.). Studying on fractional-order calculus has become an active research field.

Stability analysis is a basic problem in control theory. For Caputo fractional derivative-based linear systems, the stability results were formulated with the fractional-order α belonging to $0 < \alpha < 1$ and $1 \leq \alpha < 2$, in [5–7] and so on. In [8], the stability issue of interval fractional-order linear time-invariant (FO-LTI) systems was first presented and discussed. The stability of single-input single-output FO-LTI systems was further discussed based on an experimentally verified Kharitonov-like procedure [9].

Robust stability analysis was carried out for FO-LTI interval system with fractional commensurate order $1 \leq \alpha < 2$ based on the maximum eigenvalue of a Hermitian matrix by applying Lyapunov inequality in [10] and then further discussed in [7].

The uncertain FO-LTI systems have been wildly studied. In [11], the robust stability problem was discussed based on the ranges of the corresponding interval eigenvalues by applying the matrix perturbation theory. In [12], a new and effectively robust stability checking method was first proposed for FO-LTI interval uncertain systems in terms of LMIs, and an analytical design of the stabilizing controllers for fractional-order dynamic interval systems was given. Note that the above-mentioned results on stability check for uncertain FO-LTI systems with interval coefficients of dimension n need to solve one $(n^2 + 2n) \times (n^2 + 2n)$ LMI. Therefore, it is valuable to seek some simple necessary and sufficient conditions for checking robust stability of uncertain FO-LTI systems with interval coefficients. With the above motivation, based on the results of [12], the robust stability and stabilization problems of uncertain FO-LTI interval systems with the fractional-order α belonging to $1 \leq \alpha < 2$ are further investigated in this paper.

This paper is organized as follows: in Section 2, we present some preliminaries results on the fractional derivative, the linear algebra and the matrix theory. In Section 3, we study the problems of the stability and stabilization of uncertain FO-LTI systems with interval coefficients in terms of LMIs. In Section 4, numerical examples are presented to illustrate our proposed results. Finally, Section 5 concludes this work.

Notations. Throughout this paper, $\mathbf{R}^{m\times n}$ stands for the set of m by n matrices with real entries. The symbols M^T, $\mathrm{Sym}\{M\}$,

and I_n stand for the transpose of M, the expression $M^T + M$, and the identity matrix of order n, respectively. The symbol $e_n \in \mathbf{R}^n$ is used to denote the row vector with the kth element being 1, $i = 1, \ldots, n$; that is,

$$e_n = (1, 1, \ldots, 1) \in \mathbf{R}^n. \tag{1}$$

The symbol $\otimes$ is the Kronecker product of two matrices and

$$(A \otimes C)^T = A^T \otimes C^T. \tag{2}$$

The symbol $\cdot$ will be used in some matrix expressions to indicate a symmetric structure; that is, if matrices $H_1 = H_1^H \in \mathbf{R}^{m\times m}$ and $H_2 = H_2^H \in \mathbf{R}^{n\times n}$ were given, then

$$\begin{pmatrix} H_1 & \cdot \\ L & H_2 \end{pmatrix} = \begin{pmatrix} H_1 & L^T \\ L & H_2 \end{pmatrix}. \tag{3}$$

Let $N = \operatorname{diag}(a_1, a_2, \ldots, a_n)$; consider the symbol

$$N^{1/2} = \operatorname{diag}\left(\sqrt{a_1}, \sqrt{a_2}, \ldots, \sqrt{a_n}\right), \tag{4}$$

in which $a_i \geq 0$, $i = 1, \ldots, n$.

2. Preliminaries

Throughout the paper, only the Caputo definition is used. The following Caputo definition is adopted for fractional derivatives of order α of function $f(t)$ [13]:

$$D^\alpha f(t) = \frac{1}{\Gamma(\alpha - m)} \int_0^t \frac{f^{(m)}(\tau)}{(t-\tau)^{(\alpha-m+1)}} d\tau, \quad m - 1 \leq \alpha < m \tag{5}$$

with $m \in \mathbf{Z}$, $\alpha \in \mathbf{R}^+$, where $\Gamma(\cdot)$ is the Gamma function:

$$\Gamma(z) = \int_0^\infty e^{-t} t^{z-1}\, dt. \tag{6}$$

Consider the following FO-LTI interval system:

$$D^\alpha x(t) = Ax(t) + Bu(t), \tag{7}$$

where α is the fractional commensurate order, $x(t) \in \mathbf{R}^n$ and $u(t) \in \mathbf{R}^p$ stand for the state vector and control input, respectively, and the system matrices A and B are interval uncertain in the sense that

$$\begin{aligned} A \in A_I &= \left[\underline{A}, \overline{A}\right] \\ &= \left\{\left(a_{ij}\right)_{n\times n} : \underline{a}_{ij} \leq a_{ij} \leq \overline{a}_{ij},\ 1 \leq i, j \leq n\right\}, \\ B \in B_I &= \left[\underline{B}, \overline{B}\right] \\ &= \left\{\left(b_{ij}\right)_{n\times p} : \underline{b}_{ij} \leq b_{ij} \leq \overline{b}_{ij},\ 1 \leq i \leq n,\ 1 \leq j \leq p\right\}, \end{aligned} \tag{8}$$

where $\underline{A}$, $\overline{A}$, $\underline{B}$, and $\overline{B}$ are given matrices.

To take into account the stability [14], we introduce the following definition.

Definition 1. The fractional-order interval system (7) is said to be asymptotically stabilizable via linear state-feedback control if there exists a state-feedback controller $u(t) = Kx(t)$ such that the closed-loop system

$$D^\alpha f(t) = (A + BK)\, x(t) \tag{9}$$

is asymptotically stable.

Denote

$$\begin{aligned} A_0 &= \frac{1}{2}\left(\underline{A} + \overline{A}\right), \\ \Delta A &= \frac{1}{2}\left(\overline{A} - \underline{A}\right) = \left(\gamma_{ij}\right)_{n\times n}, \\ B_0 &= \frac{1}{2}\left(\underline{B} + \overline{B}\right), \\ \Delta B &= \frac{1}{2}\left(\overline{B} - \underline{B}\right) = \left(\beta_{ij}\right)_{n\times p}. \end{aligned} \tag{10}$$

To handle the interval uncertain, the following notations are introduced:

$$\begin{aligned} D_A &= \operatorname{diag}\left(\gamma_{11}, \ldots, \gamma_{1n}, \ldots, \gamma_{n1}, \ldots, \gamma_{nn}\right)_{n^2\times n^2}, \\ H_A &= \Big\{\operatorname{diag}\left(\delta_{11}, \ldots, \delta_{1n}, \ldots, \delta_{n1}, \ldots, \delta_{nn}\right) \in \mathbf{R}^{n^2\times n^2}, \\ &\quad \left|\delta_{ij}\right| \leq 1,\ i, j = 1, \ldots, n\Big\}, \\ D_B &= \operatorname{diag}\left(\beta_{11}, \ldots, \beta_{1p}, \ldots, \beta_{n1}, \ldots, \beta_{np}\right)_{(np)\times(np)}, \\ H_B &= \Big\{\operatorname{diag}\left(\eta_{11}, \ldots, \eta_{1p}, \ldots, \eta_{n1}, \ldots, \eta_{np}\right) \\ &\quad \in \mathbf{R}^{(np)\times(np)},\ \left|\eta_{ij}\right| \leq 1,\ i = 1, \ldots, n,\ j = 1, \ldots, p\Big\}. \end{aligned} \tag{11}$$

Lemma 2. *Let $t_{ij} > 0$, $i, j = 1, \ldots, n$:*

$$\begin{aligned} T_{A1} &= \operatorname{diag}\left(t_{11}, \ldots, t_{1n}, \ldots, t_{n1}, \ldots, t_{nn}\right)_{n^2\times n^2}, \\ T_{A2} &= T_{A1}^{-1}, \\ \tau_{ij} &> 0, \quad i = 1, \ldots, n,\ j = 1, \ldots, p, \\ T_{B1} &= \operatorname{diag}\left(\tau_{11}, \ldots, \tau_{1p}, \ldots, \tau_{n1}, \ldots, \tau_{np}\right)_{(np)\times(np)}, \\ T_{B2} &= T_{B1}^{-1}, \end{aligned} \tag{12}$$

$$\begin{aligned} A_J &= \Big\{A = A_0 \\ &\quad + \left(I_n \otimes e_n\right) T_{A1} D_A F_A T_{A2} \left(e_n^T \otimes I_n\right),\ F_A \in H_A\Big\}, \end{aligned} \tag{13}$$

$$\begin{aligned} B_J &= \Big\{B = B_0 + \left(I_n \otimes e_p\right) T_{B1} D_B F_B T_{B2} \left(e_n^T \otimes I_p\right),\ F_B \\ &\quad \in H_B\Big\}. \end{aligned} \tag{14}$$

Then $A_J = A_I$, $B_J = B_I$.

Proof. Since T_{A1}, F_A, D_A, and T_{A2} are all diagonal, it is easy to check that

$$\begin{aligned}
&T_{A1}D_AF_AT_{A2} = D_AF_A,\\
&I_n \otimes e_n = \begin{pmatrix} e_n & 0 & \cdots & 0\\ 0 & e_n & \cdots & 0\\ \vdots & \vdots & \ddots & \vdots\\ 0 & 0 & \cdots & e_n \end{pmatrix},\\
&T_{A1}D_AF_AT_{A2}\left(e_n^T \otimes E_n\right) = D_AF_A \begin{pmatrix} I_n\\ I_n\\ \vdots\\ I_n \end{pmatrix}\\
&\quad = \begin{pmatrix} \operatorname{diag}\left(\delta_{11}\gamma_{11},\ldots,\delta_{1n}\gamma_{1n}\right)\\ \operatorname{diag}\left(\delta_{21}\gamma_{21},\ldots,\delta_{2n}\gamma_{2n}\right)\\ \vdots\\ \operatorname{diag}\left(\delta_{n1}\gamma_{n1},\ldots,\delta_{nn}\gamma_{nn}\right) \end{pmatrix},\\
&e_n \operatorname{diag}\left(\delta_{i1}\gamma_{i1},\ldots,\delta_{in}\gamma_{in}\right)\\
&\quad = \left(\delta_{i1}\gamma_{i1} \quad \delta_{i2}\gamma_{i2} \quad \cdots \quad \delta_{i2}\gamma_{in}\right)_{1\times n}, \quad i = 1,\ldots,n.
\end{aligned} \tag{15}$$

It follows that

$$\begin{aligned}
&\left(I_n \otimes e_n\right) D_AF_A\left(e_n^T \otimes E_n\right)\\
&= \begin{pmatrix} e_n & 0 & \cdots & 0\\ 0 & e_n & \cdots & 0\\ \vdots & \vdots & \ddots & \vdots\\ 0 & 0 & \cdots & e_n \end{pmatrix} \begin{pmatrix} \operatorname{diag}\left(\delta_{11}\gamma_{11},\ldots,\delta_{1n}\gamma_{1n}\right)\\ \operatorname{diag}\left(\delta_{21}\gamma_{21},\ldots,\delta_{2n}\gamma_{2n}\right)\\ \vdots\\ \operatorname{diag}\left(\delta_{n1}\gamma_{n1},\ldots,\delta_{nn}\gamma_{nm}\right) \end{pmatrix}\\
&= \begin{pmatrix} e_n \operatorname{diag}\left(\delta_{11}\gamma_{11},\ldots,\delta_{1n}\gamma_{1n}\right)\\ e_n \operatorname{diag}\left(\delta_{21}\gamma_{21},\ldots,\delta_{2n}\gamma_{2n}\right)\\ \vdots\\ e_n \operatorname{diag}\left(\delta_{n1}\gamma_{n1},\ldots,\delta_{nn}\gamma_{nn}\right) \end{pmatrix}\\
&= \begin{pmatrix} \delta_{11}\gamma_{11} & \delta_{12}\gamma_{12} & \cdots & \delta_{1n}\gamma_{1n}\\ \delta_{21}\gamma_{21} & \delta_{22}\gamma_{22} & \cdots & \delta_{2n}\gamma_{2n}\\ \vdots & \vdots & \ddots & \vdots\\ \delta_{n1}\gamma_{n1} & \delta_{n2}\gamma_{n2} & \cdots & \delta_{nn}\gamma_{nn} \end{pmatrix}.
\end{aligned} \tag{16}$$

Thus, $A_I \subseteq A_J$.

Noting that the above proof is reversible, it is easy to know that $A_J \subseteq A_I$. Therefore, $A_J = A_I$.

In the same way, we have $B_J = B_I$. □

Lemma 3 (see [7, 15]). *Let $A \in \mathbf{R}^{n\times n}$ be a deterministic real matrix without uncertainty. Then, a necessary and sufficient condition for the asymptotical stability of $D^\alpha x(t) = Ax(t)$ is*

$$\left|\arg\left(\operatorname{spec}(A)\right)\right| > \frac{\pi}{2}\alpha, \tag{17}$$

where $\operatorname{spec}(A)$ *is the spectrum of all eigenvalues of A.*

Lemma 4 (see [16]). *Let $A \in \mathbf{R}^{n\times n}$ be a real matrix. Then $|\arg(\operatorname{spec}(A))| > (\pi/2)\alpha$ where $1 \le \alpha < 2$, if and only if there exists $P > 0$ such that*

$$\begin{pmatrix} \left(AP + PA^T\right)\sin\theta & \cdot\\ \left(PA^T - AP\right)\cos\theta & \left(AP + PA^T\right)\sin\theta \end{pmatrix} < 0, \tag{18}$$

where $\theta = \pi - \alpha(\pi/2)$.

Lemma 5 (see [17]). *For any matrices X and Y with appropriate dimensions, we have*

$$X^TY + Y^TX \le \varepsilon X^TX + \varepsilon^{-1}Y^TY, \quad \forall\varepsilon > 0. \tag{19}$$

Lemma 6 (see [18]). *Let X, Y, and Z be real matrices of suitable dimensions. Then, for any $x \in \mathbf{R}^n$,*

$$\begin{aligned}
&\max\left\{\left(x^TXFYx\right)^2 : F^TF \le I\right\}\\
&\quad = \left(x^TXX^Tx\right)\left(x^TY^TYx\right).
\end{aligned} \tag{20}$$

Lemma 7 (see [18]). *Let X, Y, and Z be $n \times n$ symmetric matrices such that $X \ge 0$, $Y < 0$, and $Z \ge 0$. Furthermore, assume that $(x^TYx)^2 - 4(x^TXx)(x^TZx) > 0$ for all nonzero $x \in \mathbf{R}^n$. Then, there exists a constant $\lambda > 0$ such that*

$$\lambda^2X + \lambda Y + Z < 0. \tag{21}$$

3. Main Results

In this section, by adding parameters into linear matrix inequalities, necessary and sufficient conditions for stability and stabilization of the system are obtained. Those results are generalization of the main theorems in [12].

Theorem 8. *Let $1 \le \alpha < 2$. The uncertain FO-LTI interval system (7) with controller $u(t)$ is asymptotically stable if and*

only if there exist some symmetric positive definite matrix $P \in \mathbf{R}^{n\times n}$ and a real scalar constant $\varepsilon > 0$ such that

$$\Gamma = \begin{pmatrix} \Gamma_{11} & \cdot & \cdot & \cdot \\ \Gamma_{21} & \Gamma_{22} & \cdot & \cdot \\ \Omega_2 P & 0 & -\varepsilon I_n & \cdot \\ 0 & \Omega_2 P & 0 & -\varepsilon I_n \end{pmatrix} < 0, \tag{22}$$

where

$$\begin{aligned} \theta &= \pi - \alpha\left(\frac{\pi}{2}\right), \\ \Gamma_{11} &= \Gamma_{22} = \left(A_0 P + P A_0^T\right)\sin\theta + \varepsilon\Omega_1, \\ \Gamma_{21} &= \left(P A_0^T - A_0 P\right)\cos\theta, \\ \Omega_1 &= \operatorname{diag}\left(\sum_{i=1}^{n} t_{1i}^2 \gamma_{1i}^2, \ldots, \sum_{i=1}^{n} t_{ni}^2 \gamma_{ni}^2\right)_{n\times n}, \\ \Omega_2 &= \operatorname{diag}\left(\sqrt{\sum_{i=1}^{n} t_{i1}^{-2}}, \ldots, \sqrt{\sum_{i=1}^{n} t_{in}^{-2}}\right)_{n\times n}. \end{aligned} \tag{23}$$

Proof. It is easy to check that

$$\begin{aligned} &\left(I_n \otimes e_n\right) T_{A1} D_A \left(\left(I_n \otimes e_n\right) T_{A1} D_A\right)^T \\ &\quad = \operatorname{diag}\left(\sum_{i=1}^{n} t_{1i}^2 \gamma_{1i}^2, \ldots, \sum_{i=1}^{n} t_{ni}^2 \gamma_{ni}^2\right). \end{aligned} \tag{24}$$

Denote $\Pi = T_{A2}(e_n^T \otimes I_n)$; then we see that

$$\begin{aligned} \Pi &= \operatorname{diag}\left(t_{11}^{-1}, \ldots, t_{1n}^{-1}, \ldots, t_{n1}^{-1}, \ldots, t_{nn}^{-1}\right) \begin{pmatrix} I_n \\ \vdots \\ I_n \end{pmatrix} \\ &= \begin{pmatrix} \operatorname{diag}\left(t_{11}^{-1}, \ldots, t_{1n}^{-1}\right) \\ \vdots \\ \operatorname{diag}\left(t_{n1}^{-1}, \ldots, t_{nn}^{-1}\right) \end{pmatrix}, \end{aligned} \tag{25}$$

$$\begin{aligned} \Pi^T \Pi &= \operatorname{diag}\left(\sum_{i=1}^{n} t_{i1}^{-2}, \ldots, \sum_{i=1}^{n} t_{in}^{-2}\right)_{n\times n}, \\ \begin{pmatrix} \Pi P & 0 \\ 0 & \Pi P \end{pmatrix}^T \begin{pmatrix} \Pi P & 0 \\ 0 & \Pi P \end{pmatrix} &= \begin{pmatrix} P\Pi^T \Pi P & 0 \\ 0 & P\Pi^T \Pi P \end{pmatrix} \\ &= \begin{pmatrix} P\left(\Pi^T\Pi\right)^{1/2}\left(\Pi^T\Pi\right)^{1/2} P & 0 \\ 0 & P\left(\Pi^T\Pi\right)^{1/2}\left(\Pi^T\Pi\right)^{1/2} P \end{pmatrix} \\ &= \begin{pmatrix} \left(\Pi^T\Pi\right)^{1/2} P & 0 \\ 0 & \left(\Pi^T\Pi\right)^{1/2} P \end{pmatrix}^T \\ &\quad \cdot \begin{pmatrix} \left(\Pi^T\Pi\right)^{1/2} P & 0 \\ 0 & \left(\Pi^T\Pi\right)^{1/2} P \end{pmatrix}, \end{aligned} \tag{26}$$

where $P \in \mathbf{R}^{n\times n}$ is an arbitrary positive define matrix.

By applying (13), we have

$$\begin{aligned} &\begin{pmatrix} \left(AP + PA^T\right)\sin\theta & \cdot \\ \left(PA^T - AP\right)\cos\theta & \left(AP + PA^T\right)\sin\theta \end{pmatrix} \\ &\quad = \begin{pmatrix} \left(A_0 P + P A_0^T\right)\sin\theta & \cdot \\ \left(P A_0^T - A_0 P\right)\cos\theta & \left(A_0 P + P A_0^T\right)\sin\theta \end{pmatrix} \\ &\qquad + \operatorname{Sym}\left\{\begin{pmatrix} \left(I_n \otimes e_n\right) T_{A1} D_A F_A T_{A2}\left(e_n^T \otimes I_n\right) P\sin\theta & \left(I_n \otimes e_n\right) T_{A1} D_A F_A T_{A2}\left(e_n^T \otimes I_n\right) P\cos\theta \\ -\left(I_n \otimes e_n\right) T_{A1} D_A F_A T_{A2}\left(e_n^T \otimes I_n\right) P\cos\theta & \left(I_n \otimes e_n\right) T_{A1} D_A F_A T_{A2}\left(e_n^T \otimes I_n\right) P\sin\theta \end{pmatrix}\right\} \\ &\quad = \begin{pmatrix} \left(A_0 P + P A_0^T\right)\sin\theta & \cdot \\ \left(P A_0^T - A_0 P\right)\cos\theta & \left(A_0 P + P A_0^T\right)\sin\theta \end{pmatrix} \\ &\qquad + \operatorname{Sym}\left\{\begin{pmatrix} \left(I_n \otimes e_n\right) T_{A1} D_A \sin\theta & \left(I_n \otimes e_n\right) T_{A1} D_A \cos\theta \\ -\left(I_n \otimes e_n\right) T_{A1} D_A \cos\theta & \left(I_n \otimes e_n\right) T_{A1} D_A \sin\theta \end{pmatrix} \begin{pmatrix} F_A & 0 \\ 0 & F_A \end{pmatrix} \begin{pmatrix} T_{A2}\left(e_n^T \otimes I_n\right) P & 0 \\ 0 & T_{A2}\left(e_n^T \otimes I_n\right) P \end{pmatrix}\right\} \\ &\quad = Z + \operatorname{Sym}\left\{M\widehat{F_A}N\right\}, \end{aligned} \tag{27}$$

in which

$$Z = \begin{pmatrix} \left(A_0P + PA_0^T\right)\sin\theta & \cdot \\ \left(PA_0^T - A_0P\right)\cos\theta & \left(A_0P + PA_0^T\right)\sin\theta \end{pmatrix},$$

$$M = \begin{pmatrix} (I_n \otimes e_n)\, T_{A1} D_A \sin\theta & (I_n \otimes e_n)\, T_{A1} D_A \cos\theta \\ -(I_n \otimes e_n)\, T_{A1} D_A \cos\theta & (I_n \otimes e_n)\, T_{A1} D_A \sin\theta \end{pmatrix}, \quad (28)$$

$$\widehat{F_A} = \begin{pmatrix} F_A & 0 \\ 0 & F_A \end{pmatrix},$$

$$N = \begin{pmatrix} T_{A2}\left(e_n^T \otimes I_n\right)P & 0 \\ 0 & T_{A2}\left(e_n^T \otimes I_n\right)P \end{pmatrix}.$$

Sufficiency. Suppose that there exists a symmetric positive definite matrix $P \in \mathbf{R}^{n\times n}$ such that (22) holds. By applying (26), (27), and Lemma 5, we have

$$\begin{aligned} Z + \mathrm{Sym}\left\{M\widehat{F_A}N\right\} &\le Z + \varepsilon MM^T + \varepsilon^{-1}N^TN \\ &= \begin{pmatrix} \Gamma_{11} & \cdot \\ \Gamma_{21} & \Gamma_{22} \end{pmatrix} + \frac{1}{\varepsilon}\begin{pmatrix} \left(\Pi^T\Pi\right)^{1/2}P & 0 \\ 0 & \left(\Pi^T\Pi\right)^{1/2}P \end{pmatrix}^T \\ &\quad \cdot \begin{pmatrix} \left(\Pi^T\Pi\right)^{1/2}P & 0 \\ 0 & \left(\Pi^T\Pi\right)^{1/2}P \end{pmatrix} < 0. \end{aligned} \quad (29)$$

By using the Schur complement of (22), one obtains

$$\begin{pmatrix} \left(AP + PA^T\right)\sin\theta & \cdot \\ \left(PA^T - AP\right)\cos\theta & \left(AP + PA^T\right)\sin\theta \end{pmatrix} < 0. \quad (30)$$

It follows from Lemma 4 that $|\arg(\mathrm{spec}(A))| > \pi/2$. Therefore, by Lemma 3, the uncertain FO-LTI interval system (7) is asymptotically stable.

Necessity. Suppose that the uncertain FO-LTI interval system (7) is asymptotically stable. Then, $|\arg(\mathrm{spec}(A))| > \pi/2$. It follows from Lemma 4 that there exists a symmetric positive definite matrix P such that

$$\begin{pmatrix} \left(AP + PA^T\right)\sin\theta & \cdot \\ \left(PA^T - AP\right)\cos\theta & \left(AP + PA^T\right)\sin\theta \end{pmatrix} < 0. \quad (31)$$

By using Lemma 2 and after some calculations, one can obtain from (27) that

$$Z + \mathrm{Sym}\left\{M\widehat{F_A}N\right\} < 0. \quad (32)$$

Therefore, for all $\varsigma_1, \varsigma_2 \in \mathbf{R}^n$, $\varsigma = \left(\varsigma_1^T \;\; \varsigma_2^T\right)^T \neq 0$,

$$\varsigma^T Z\varsigma < -2\varsigma^T M\widehat{F_A}N\varsigma; \quad (33)$$

that is,

$$\varsigma^T Z\varsigma < -2\max\left\{\varsigma^T M\widehat{F_A}N\varsigma \,\middle|\, \widehat{F_A}^T\widehat{F_A} \le I\right\} \le 0. \quad (34)$$

Consequently, given any $\varsigma \in \mathbf{R}^{2n}$ and $\varsigma \neq 0$, we have

$$\left(\varsigma^T Z\varsigma\right)^2 > 4\max\left\{\varsigma^T M\widehat{F_A}N\varsigma \,\middle|\, \widehat{F_A}^T\widehat{F_A} \le I\right\}. \quad (35)$$

Applying Lemma 6, we obtain

$$\left(\varsigma^T Z\varsigma\right)^2 > 4\left(\varsigma^T MM^T\varsigma\right)\left(\varsigma^T N^T N\varsigma\right). \quad (36)$$

It follows by Lemma 7 that there exists a constant $\varepsilon > 0$ such that

$$Z + \varepsilon^{-1}N^TN + \varepsilon MM^T < 0. \quad (37)$$

So we derive that

$$\begin{aligned} Z + \varepsilon MM^T + \varepsilon^{-1}N^TN &= \begin{pmatrix} \Gamma_{11} & \cdot \\ \Gamma_{21} & \Gamma_{22} \end{pmatrix} \\ &\quad + \frac{1}{\varepsilon}\begin{pmatrix} \left(\Pi^T\Pi\right)^{1/2}P & 0 \\ 0 & \left(\Pi^T\Pi\right)^{1/2}P \end{pmatrix}^T \\ &\quad \cdot \begin{pmatrix} \left(\Pi^T\Pi\right)^{1/2}P & 0 \\ 0 & \left(\Pi^T\Pi\right)^{1/2}P \end{pmatrix} < 0. \end{aligned} \quad (38)$$

Applying the well-known Schur complement yields (22). This ends the proof. □

Next, let us establish a stabilization result.

Theorem 9. *Let $1 \le \alpha < 2$. The uncertain FO-LTI interval system (7) is asymptotically stable if and only if there are a matrix $X \in \mathbf{R}^{p\times n}$, a symmetric positive definite matrix $P \in \mathbf{R}^{n\times n}$, and two real scalars $\varepsilon_i > 0$ $(i = 1, 2)$, such that*

$$\Gamma^1 = \begin{pmatrix} \Gamma_{11}^1 & \cdot & \cdot & \cdot & \cdot & \cdot \\ \Gamma_{21}^1 & \Gamma_{22}^1 & \cdot & \cdot & \cdot & \cdot \\ \Omega_2P & 0 & -\varepsilon_1 I_n & \cdot & \cdot & \cdot \\ 0 & \Omega_2P & 0 & -\varepsilon_1 I_n & \cdot & \cdot \\ \Omega_4X & 0 & 0 & 0 & -\varepsilon_2 I_p & \cdot \\ 0 & \Omega_4X & 0 & 0 & 0 & -\varepsilon_2 I_p \end{pmatrix} < 0, \quad (39)$$

where

$$\begin{aligned}
\theta &= \pi - \alpha\left(\frac{\pi}{2}\right),\\
\Gamma_{11}^{1} &= \Gamma_{22}^{1}\\
&= \left(A_0P + PA_0^T + B_0X + (B_0X)^T\right)\sin\theta + \varepsilon_1\Omega_1\\
&\quad + \varepsilon_2\Omega_3,\\
\Gamma_{21}^{1} &= \left(PA_0^T - A_0P + (B_0X)^T - B_0X\right)\cos\theta,\\
\Omega_1 &= \operatorname{diag}\left(\sum_{i=1}^{n} t_{1i}^2\gamma_{1i}^2, \ldots, \sum_{i=1}^{n} t_{ni}^2\gamma_{ni}^2\right)_{n\times n},\\
\Omega_2 &= \operatorname{diag}\left(\sqrt{\sum_{i=1}^{n} t_{i1}^{-2}}, \ldots, \sqrt{\sum_{i=1}^{n} t_{in}^{-2}}\right)_{n\times n},\\
\Omega_3 &= \operatorname{diag}\left(\sum_{i=1}^{p} \tau_{1i}^2\eta_{1i}^2, \ldots, \sum_{i=1}^{p} \tau_{ni}^2\eta_{ni}^2\right)_{n\times n},\\
\Omega_4 &= \operatorname{diag}\left(\sqrt{\sum_{i=1}^{n} \tau_{i1}^{-2}}, \ldots, \sqrt{\sum_{i=1}^{n} \tau_{ip}^{-2}}\right)_{p\times p}.
\end{aligned} \tag{40}$$

Moreover, the robustly asymptotically stabilizing state-feedback gain matrix is given by

$$K = XP^{-1}. \tag{41}$$

Remark 10. When one takes $T_{A1} = I_{n^2}$ and $T_{A2} = I_{np}$, it is easy to obtain equivalence of Theorem 8 and [12, Theorem 1] and Theorem 9 and [12, Theorem 2], respectively.

4. Numerical Examples

Example 1 (see [12]). Consider the robust stability of the following uncertain FO-LTI interval system:

$$D^{\alpha}x(t) = Ax(t), \tag{42}$$

where $\alpha = 1.6$ and $A \in A_I = [\underline{A}, \overline{A}]$:

$$\begin{aligned}
\underline{A} &= \begin{pmatrix} -1.5 & 0.5 & 1.0\\ 0.4 & -2.5 & 0.9\\ 0.2 & -1.3 & -2.0 \end{pmatrix},\\
\overline{A} &= \begin{pmatrix} -1.05 & 0.65 & 1.3\\ 0.7 & -2.1 & 1.3\\ 0.35 & -1.05 & -1.75 \end{pmatrix}.
\end{aligned} \tag{43}$$

Taking $T_{A1}^2 = 0.001 * I_9$, a feasible solution of (22) is as follows:

$$\begin{aligned}
P &= \begin{pmatrix} 0.1709 & 0.0299 & -0.0501\\ 0.0299 & 0.1070 & 0.0050\\ -0.0501 & 0.0050 & 0.0872 \end{pmatrix},\\
\varepsilon &= 4.8484.
\end{aligned} \tag{44}$$

Let

$$A = \begin{pmatrix} -1.25 & 0.55 & 1.15\\ 0.55 & -2.25 & 1\\ 0.27 & -1.18 & -1.85 \end{pmatrix} \tag{45}$$

and let the initial conditions be $x_1(0) = 2$, $x_2(0) = -1$, and $x_3(0) = 1$. Time response of the state variables is depicted in Figure 1.

In the following example, we have shown the effectiveness of our results by choosing different parameters.

Example 2 (see [12]). Consider the robust stability of the following uncertain FO-LTI interval system:

$$D^{\alpha}x(t) = Ax(t) + Bu(t), \tag{46}$$

where $\alpha = 1.8$ and $A \in A_I = [\underline{A}, \overline{A}]$, $B \in B_I = [\underline{B}, \overline{B}]$ with

$$\begin{aligned}
\underline{A} &= \begin{pmatrix} -1.95 & 0.35 & 0.7\\ -1.3 & -3.9 & 0.7\\ -0.65 & -1.95 & -3.25 \end{pmatrix},\\
\underline{B} &= \begin{pmatrix} 0.4\\ 0.5\\ 0.9 \end{pmatrix},\\
\overline{A} &= \begin{pmatrix} -1.05 & 0.65 & 1.3\\ -0.7 & -2.1 & 1.3\\ -0.35 & -1.05 & -1.75 \end{pmatrix},\\
\overline{B} &= \begin{pmatrix} 0.5\\ 0.6\\ 1 \end{pmatrix}.
\end{aligned} \tag{47}$$

(I) Taking $T_{A1}^2 = 0.1 \times I_9$ and $T_{B1}^2 = 0.1 \times I_3$, a feasible solution of (39) is as follows:

$$\begin{aligned}
P &= \begin{pmatrix} 19.0307 & -4.8726 & 3.6969\\ -4.8726 & 9.9174 & -4.4783\\ 3.6969 & -4.4783 & 9.8415 \end{pmatrix},\\
\varepsilon_1 &= 23.2647,\\
X &= \begin{pmatrix} 4.4393 & 0.1546 & -27.5631 \end{pmatrix},\\
\varepsilon_2 &= 23.4538.
\end{aligned} \tag{48}$$

Finally, the asymptotically stabilizing state-feedback gain matrix is obtained as

$$K = \begin{pmatrix} 0.5980 & -1.3300 & -3.6306 \end{pmatrix}. \tag{49}$$

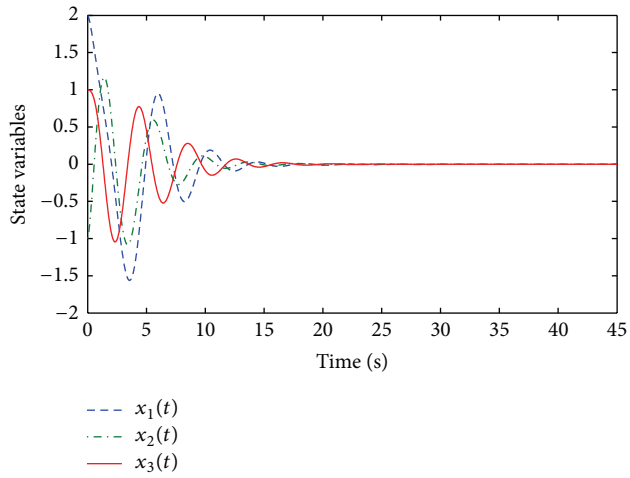

FIGURE 1: Time response of the state variables.

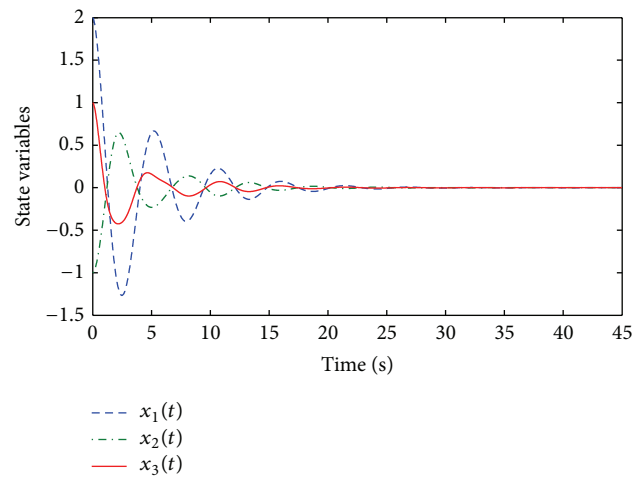

FIGURE 2: Time response of the state variables when K is as in (49).

(II) Taking $T_{A1}^2 = I_9$ and $T_{B1}^2 = I_3$, we have

$$P = 10^{-10} \times \begin{pmatrix} 0.0509 & -0.0334 & 0.0506 \\ -0.0334 & 0.1002 & 0.0405 \\ 0.0506 & 0.0405 & 0.3195 \end{pmatrix},$$
$$\varepsilon_1 = 8.5956 \times 10^{-10}, \tag{50}$$

$$X = 10^{-9} \times \begin{pmatrix} -0.2978 & -0.3742 & -0.7021 \end{pmatrix},$$
$$\varepsilon_2 = 2.7808 \times 10^{-10},$$
$$K = \begin{pmatrix} -116.5937 & -78.8292 & 6.4958 \end{pmatrix}. \tag{51}$$

(III) Taking $T_{A1}^2 = 4 \times I_9$ and $T_{B1}^2 = 4 \times I_3$, we have

$$P = 10^{-11} \times \begin{pmatrix} 0.0374 & -0.0091 & 0.0146 \\ -0.0091 & 0.0664 & 0.0264 \\ 0.0146 & 0.0264 & 0.1502 \end{pmatrix},$$
$$\varepsilon_1 = -2.7962 \times 10^{-12}, \tag{52}$$

$$X = 10^{-10} \times \begin{pmatrix} -0.2460 & -0.3091 & -0.5579 \end{pmatrix},$$
$$\varepsilon_2 = 8.3122 \times 10^{-11},$$
$$K = \begin{pmatrix} -68.4565 & -47.1044 & -22.2054 \end{pmatrix}. \tag{53}$$

Let

$$A = \begin{pmatrix} -1.5 & 0.45 & 1 \\ -1 & -3 & 1 \\ -0.5 & -1.5 & -2 \end{pmatrix} \in A_I,$$
$$B = \begin{pmatrix} 0.45 \\ 0.55 \\ 0.95 \end{pmatrix} \in B_I, \tag{54}$$

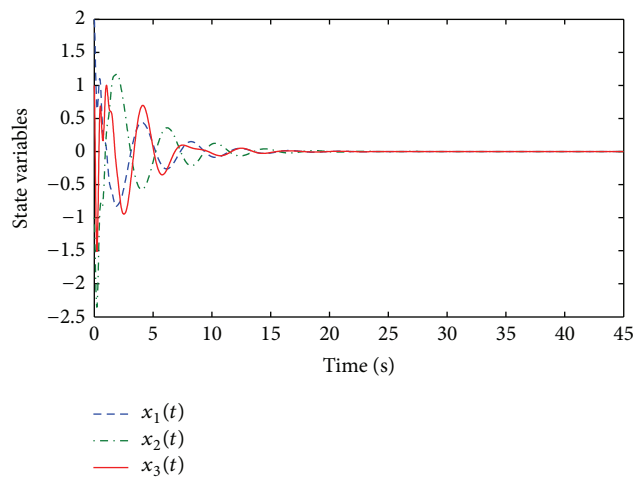

FIGURE 3: Time response of the state variables when K is as in (51).

and let the initial conditions be $x_1(0) = 2$, $x_2(0) = -1$, and $x_3(0) = 1$, and let K be as in (49), (51), and (53), respectively. Time response of the state variables is depicted in Figures 2–4, respectively.

Remark 11. Applying [12, Theorem 2 (28)] to Example 2 gives the same results as in Example 2 (II).

5. Conclusion

In this paper, the robust asymptotical stability of fractional-order interval systems with the fractional-order α belonging to $1 \leq \alpha < 2$ has been studied. The results on stability check for uncertain FO-LTI systems with interval coefficients of dimension n only need to solve one $4n$-by-$4n$ LMI. LMI stability conditions for fractional systems are proposed. Numerical examples have shown the effectiveness of our results. To the best of our knowledge, the idea of introducing free parameters is used for the first time to derive an analytical design of the stabilizing controllers for fractional-order

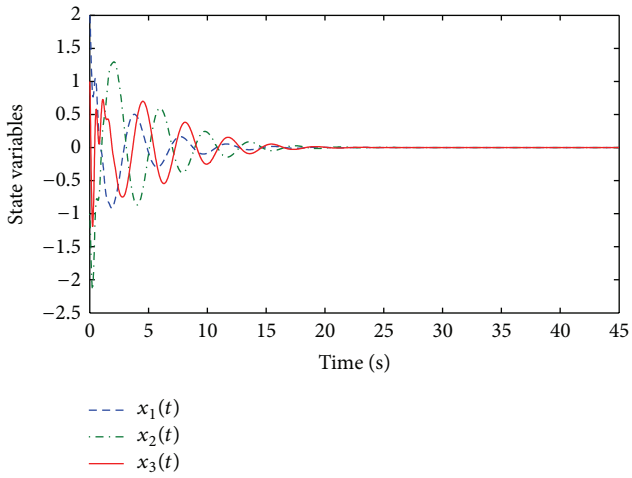

Figure 4: Time response of the state variables when K is as in (53).

dynamic interval systems. Working towards relaxing the requirements for the knowledge of system uncertainties and applying the proposed control methods to fractional-order nonlinear systems while maintaining the simplicity of the controller design are our further investigation directions.

Conflict of Interests

The authors declare that they have no competing interests.

Acknowledgments

The authors would like to thank the referees for their helpful comments and suggestions. The work of authors was supported in part by the Natural Science Foundation of China (Grant nos. 11401243 and 61403157) and the Science Foundation of Huainan Normal University (no. 2014xj45).

References

[1] E. Ahmed and A. S. Elgazzar, "On fractional order differential equations model for nonlocal epidemics," *Physica A*, vol. 379, no. 2, pp. 607–614, 2007.

[2] A. A. Kilbas, H. M. Srivastava, and J. J. Trujillo, *Theory and Application of Fractional Differential Equations*, Elsevier, New York, NY, USA, 2006.

[3] Y. Ma, J.-G. Lu, W. Chen, and Y. Chen, "Robust stability bounds of uncertain fractional-order systems," *Fractional Calculus and Applied Analysis*, vol. 17, no. 1, pp. 136–153, 2014.

[4] I. Podlubny, *Fractional Differential Equations*, Academic Press, New York, NY, USA, 1999.

[5] I. N'Doye, M. Darouach, M. Zasadzinski, and N.-E. Radhy, "Robust stabilization of uncertain descriptor fractional-order systems," *Automatica*, vol. 49, no. 6, pp. 1907–1913, 2013.

[6] M. Moze, J. Sabatier, and A. Oustaloup, "LMI characterization of fractional systems stability," in *Advances in Fractional Calculus: Theoretical Developments and Applications in Physics and Engineering*, pp. 419–434, Springer, New York, NY, USA, 2007.

[7] M. Moze and J. Sabatier, "LMI tools for stability analysis of fractional systems," in *Proceedings of the International Design Engineering Technical Conferences & Computers and Information in Engineering Conference*, Long Beach, Calif, USA, 2005.

[8] I. Petráš, Y. Q. Chen, and B. M. Vinagre, "Robust stability test for interval fractional order linear systems," in *Unsolved Problems in the Mathematics of Systems and Control*, Princeton University Press, Princeton, NJ, USA, 2004.

[9] I. Petráš, Y. Q. Chen, B. M. Vinagre, and I. Podlubny, "Stability of linear time invariant systems with interval fractional orders and interval coefficients," in *Proceedings of the 2nd IEEE International Conference on Computational Cybernetics (ICCC '04)*, pp. 341–346, IEEE, Vienna, Austria, 2004.

[10] H.-S. Ahn, Y. Q. Chen, and I. Podlubny, "Robust stability test of a class of linear time-invariant interval fractional-order system using Lyapunov inequality," *Applied Mathematics and Computation*, vol. 187, no. 1, pp. 27–34, 2007.

[11] Y. Q. Chen, H.-S. Ahn, and I. Podlubny, "Robust stability check of fractional order linear time invariant systems with interval uncertainties," *Signal Processing*, vol. 86, no. 10, pp. 2611–2618, 2006.

[12] J.-G. Lu and G. Chen, "Robust stability and stabilization of fractional-order interval systems: an LMI approach," *IEEE Transactions on Automatic Control*, vol. 54, no. 6, pp. 1294–1299, 2009.

[13] I. Podlubny, "Geometric and physical interpretation of fractional integration and fractional differentiation," *Fractional Calculus and Applied Analysis*, vol. 5, no. 4, pp. 367–386, 2002.

[14] D. Matignon and B. d'Andréa-Novel, *Observer-Based Controllers for Fractional Differential Systems*, SIAM, San Diego, Calif, USA, 1997.

[15] D. Matignon, "Stability result for fractional differential equations with applications to control processing," in *Computational Engineering in Systems Applications*, pp. 963–968, 1997.

[16] M. Chilali, P. Gahinet, and P. Apkarian, "Robust pole placement in LMI regions," *IEEE Transactions on Automatic Control*, vol. 44, no. 12, pp. 2257–2270, 1999.

[17] P. P. Khargonekar, I. R. Petersen, and K. Zhou, "Robust stabilization of uncertain linear systems: quadratic stabilizability and H_∞ control theory," *IEEE Transactions on Automatic Control*, vol. 35, no. 3, pp. 356–361, 1990.

[18] I. R. Petersen, "A stabilization algorithm for a class of uncertain linear systems," *Systems & Control Letters*, vol. 8, no. 4, pp. 351–357, 1987.

Hindawi Publishing Corporation
Mathematical Problems in Engineering
Volume 2015, Article ID 280251, 9 pages
http://dx.doi.org/10.1155/2015/280251

Research Article

A New Wavelet Threshold Determination Method Considering Interscale Correlation in Signal Denoising

Can He,[1] Jianchun Xing,[1] Juelong Li,[2] Qiliang Yang,[1] and Ronghao Wang[1]

[1] *College of Defense Engineering, PLA University of Science and Technology, Nanjing 210007, China*
[2] *Technical Management Office of Naval Defense Engineering, Beijing 100841, China*

Correspondence should be addressed to Jianchun Xing; xjc893@163.com

Received 28 August 2014; Revised 8 October 2014; Accepted 8 October 2014

Academic Editor: Zheng-Guang Wu

Copyright © 2015 Can He et al. This is an open access article distributed under the Creative Commons Attribution License, which permits unrestricted use, distribution, and reproduction in any medium, provided the original work is properly cited.

Due to simple calculation and good denoising effect, wavelet threshold denoising method has been widely used in signal denoising. In this method, the threshold is an important parameter that affects the denoising effect. In order to improve the denoising effect of the existing methods, a new threshold considering interscale correlation is presented. Firstly, a new correlation index is proposed based on the propagation characteristics of the wavelet coefficients. Then, a threshold determination strategy is obtained using the new index. At the end of the paper, a simulation experiment is given to verify the effectiveness of the proposed method. In the experiment, four benchmark signals are used as test signals. Simulation results show that the proposed method can achieve a good denoising effect under various signal types, noise intensities, and thresholding functions.

1. Introduction

Due to the combined impacts of the internal measurement system and the external environmental factors, measured signals are often contaminated by noise [1]. Therefore, signal denoising technology has been a hot topic in the field of signal processing. In a noisy signal, noise energy is generally concentrated in the high frequency region, and the spectrum of useful signal is distributed in the low frequency region [2]. According to this theory, a variety of signal denoising methods were put forward, such as mean filtering [3], median filtering [4] and Wiener filtering [5]. Most of these methods can be considered as low-pass filters essentially. However, in some signals, the high frequency region not only contains noise but also possesses a lot of useful information. Therefore, directly filtering out high frequency information is unreasonable. Recently, because of multiresolution and low entropy, wavelet transform has become a popular research topic in the signal denoising field. A number of methods based on wavelet theory have been proposed, such as wavelet coefficient modulus maxima method [6], wavelet correlation method [7], and wavelet threshold method [8]. The essence of these methods is nonlinear processing on the wavelet coefficients and then using the processed coefficients to reconstruct signals. Among these methods, wavelet threshold method has been used the most widely because of its simple calculation and good effect.

Wavelet threshold method was proposed by Donoho and Johnstone [8], whose main idea is to reconstruct signal on the basis of thresholding coefficients. The denoising effect of wavelet threshold method depends on threshold determination. If the selected threshold is too large, then some useful information is filtered out, and if the threshold is too small, then a certain amount of noise is retained. In order to solve this problem, many researchers studied the threshold determination methods. Donoho and Johnstone [8] presented a universal threshold by analyzing normal Gaussian noise model; Tao et al. [9] improved the universal threshold and indicated that the threshold should be adaptively changed with the scale alter. The defect in this kind of methods is that universal threshold is often set too large, which may lead to overkill the useful information. Chang et al. [10] assumed that the wavelet coefficients obeyed generalized Gaussian distribution and proposed a Bayesian threshold method; Lu and Loizou [11] considered the coefficients obeyed Gaussian distribution and presented

a new threshold based on maximum a posteriori probability; Li et al. [12] supposed the coefficients obeyed generalized Gamma distribution and put forward a threshold method based on Bayesian shrinkage. All of these methods are based on a particular coefficient distribution, but it may not satisfy the distribution to a specific signal. Donoho and Johnstone [13] proposed a new threshold method based on minimax criterion. However, this method requires the prior knowledge of the original signal, while the information of original signal is difficult to obtain in reality. Stein's unbiased risk estimate (SURE) criterion [8] and generalized cross validation (GCV) criterion [14] were presented based on the idea of parameter estimates, in which SURE criterion is unbiased estimate of the minimized mean square error (MSE) criterion, and GCV criterion is biased estimates of the minimized MSE criterion. Cai and Zhou [15] proposed a data-driven threshold determination method based on SURE criterion. Autin et al. [16] put forward a new idea by combining different threshold rules.

Although the wavelet threshold method has developed significantly, some deficiencies remain. The primary defect is that most of these methods ignore the relationship between the wavelet coefficients. According to wavelet correlation theory [7], the wavelet coefficients of a useful signal have a strong correlation in various decomposition scales, whereas the wavelet coefficients of noise are weakly correlated or uncorrelated. Therefore, analysis of the coefficients correlation can help distinguish useful information or noise. However, the existing threshold methods are mostly from the minimum error criterion or other optimization criteria that do not consider the coefficient correlation, and this defect may diminish the signal denoising effect.

The goal of this paper is to propose a new wavelet threshold determination method that considers the interscale correlation of coefficients. The method firstly adopts the universal threshold as the basic threshold. And then, a new correlation index is presented based on the wavelet correlation theory. At last, the new threshold is obtained using the correlation index to improve the basic threshold.

The remaining parts of the paper are organized as follows. Section 2 introduces the wavelet threshold denoising theory. Section 3 proposes a new correlation index and presents a new threshold determination method based on the new index and basic threshold. Section 4 provides a simulated experiment using four benchmark signals to verify the effectiveness of the new threshold. The conclusion is given in Section 5.

2. Wavelet Threshold Denoising Theory

In one-dimension noisy signals, noise acts on the original signal through linear superposition:

$$X(k) = S(k) + E(k), \tag{1}$$

where $X(k)$ is the noisy signal, $S(k)$ is the original signal, and $E(k)$ is white Gaussian noise, subject to $N(0, \sigma^2)$ distribution.

Wavelet transform is a linear transform. Therefore, wavelet coefficients obtained through wavelet transform of $X(k)$ still contain two parts. One part is from the original signal $S(k)$, and the other part is brought from the noise $E(k)$. Wavelet transform can concentrate signal energy on some large wavelet coefficients and distribute the noise energy throughout the whole wavelet domain. Thus, large amplitude wavelet coefficients may be produced by the useful signal, and the small amplitude is likely to represent the noise. According to this characteristics of wavelet coefficients, Donoho and Johnstone [8] proposed wavelet threshold method, which can be divided into three steps:

(1) choosing the appropriate wavelets basis and decomposition scale and computing the corresponding wavelet coefficients,

(2) selecting the proper threshold and thresholding function and obtaining the estimated values of the wavelet coefficients,

(3) reconstructing the signal based on the estimated values of wavelet coefficients by inverse wavelet transform.

In the wavelet threshold denoising method, a core issue is to determine the optimal threshold. Threshold can make a great influence on the denoising effect. If the threshold value is too small, then considerable noise will still exist, and if the threshold value is too large, then some important feature of signal may be filtered out. As mentioned in the introduction, many existing methods can determine the threshold. Among these methods, universal threshold is the most widely used because of its simpleness and effectiveness. The formula for the universal threshold is expressed as follows:

$$\lambda = \sigma\sqrt{2\ln(N)}, \tag{2}$$

where σ is the average variance of the noise and N is the signal length.

σ is calculated using median estimate method. The formula is as follows:

$$\sigma = \frac{\text{Median}\left(\left|W_{1,K}\right|\right)}{0.6745}, \tag{3}$$

where $W_{1,k}$ represent all the wavelet coefficients in scale 1.

Because universal threshold is the most widely used threshold method, therefore it is selected as basis to construct the new threshold in this paper.

Thresholding function reflects different estimation strategies to the wavelet coefficients. There are two well-known thresholding functions named hard thresholding function and soft thresholding function. Their main ideas are to both remove small wavelet coefficients and shrink large wavelet coefficients. Hard thresholding function shown in Figure 1(a) is defined as

$$\widehat{W_{j,k}} = \begin{cases} W_{j,k}; & \left|W_{j,k}\right| \geq \lambda \\ 0; & \left|W_{j,k}\right| < \lambda. \end{cases} \tag{4}$$

Soft thresholding function shown in Figure 1(b) is defined as

$$\widehat{W_{j,k}} = \begin{cases} \operatorname{sgn}\left(W_{j,k}\right)\left(\left|W_{j,k}\right| - \lambda\right); & \left|W_{j,k}\right| \geq \lambda \\ 0; & \left|W_{j,k}\right| < \lambda. \end{cases} \tag{5}$$

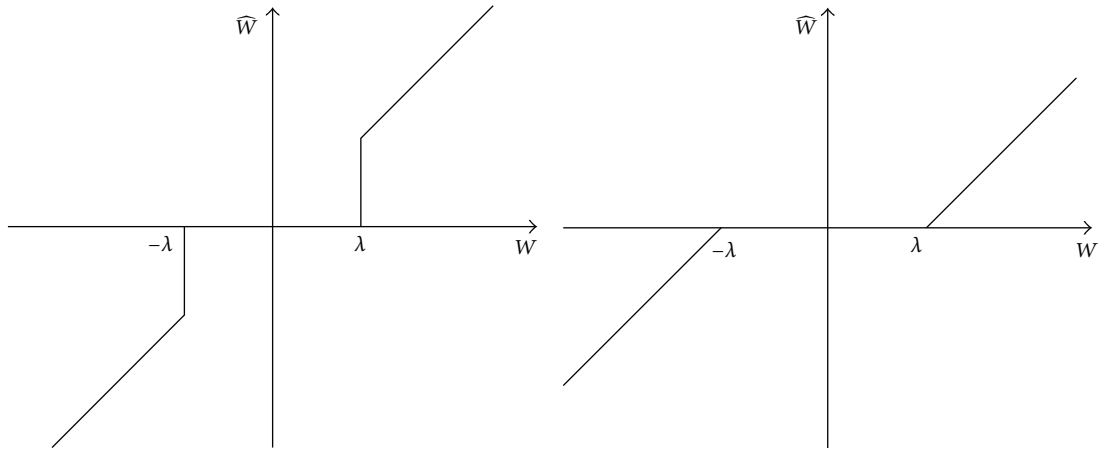

(a) Hard thresholding function (b) Soft thresholding function

Figure 1: Hard and Soft thresholding functions.

Some researchers focused on studying the thresholding function and proposed some new functions [17, 18]. Because the core issue of this study is to determine the threshold, the classical hard and soft thresholding functions are selected in the experimental section.

3. A New Wavelet Threshold Determination Method

3.1. Wavelet Correlation Denoising Theory. The propagation characteristics of wavelet coefficients show that signal has a strong correlation in various decomposition scales, while noise is weakly correlated or uncorrelated. Considering this feature, Xu et al. [7] proposed a classical wavelet correlation denoising method named spatially selective noise filtration. In this method, the correlation factors of different scales are calculated firstly. And then, the larger values are retained as useful information by comparing the correlation factors with original coefficients. Finally, the signal is reconstructed using the inverse wavelet transform.

In this method, the correlation of wavelet coefficients is measured using the normalised correlation index $N\mathrm{Cor}$:

$$N\mathrm{Cor}(j,n) = \mathrm{Cor}(j,n)\sqrt{\frac{PW(j)}{P\mathrm{Cor}(j)}}, \tag{6}$$

where $\mathrm{Cor}(j,n) = W_{j,n}W_{j+1,n}$ represents the coefficients correlation between $W_{j,n}$ and $W_{j+1,n}$; $W_{j,n}$ represents the coefficient in location point n and scale j; $P\mathrm{Cor}(j) = \sum_{n=1}^{N}\mathrm{Cor}(j,n)^2$ represents the correlation factor energy of scale j; $PW(j) = \sum_{n=1}^{N} W_{j,n}^2$ represents the coefficients energy of scale j.

$N\mathrm{Cor}$ can describe the correlation among the wavelet coefficients to a certain extent, but its calculation is complicated and inefficient. Therefore, it is necessary to propose a simple and efficient correlation index.

3.2. A New Interscale Correlation Index. Crouse et al. [19] found that the wavelet coefficients typically had the following distribution characteristics:

(1) clustering: if a particular wavelet coefficient is large/small, then adjacent coefficients are very likely to also be large/small;

(2) persistence across scale: large/small values of wavelet coefficients tend to propagate across scales.

According to this theory, a new index is proposed to measure the interscale correlation of wavelet coefficients in this paper:

$$K(n) = \frac{\max|W(:,n)| - \min|W(:,n)|}{\min|W(:,n)|}, \tag{7}$$

where $W(:,n)$ represents all the wavelet coefficients in location point n.

When $K(n) \in [0,r)$, the difference between maximum and minimum of the wavelet coefficients in location point n is little. It is considered that there is a strong correlation of wavelet coefficients in location point n. Therefore, the location point n is likely to be a signal point. A smaller value of the $K(n)$ means a bigger possibility to be a signal point for location point n. When $K(n) \in [r,+\infty)$, the difference between maximum and minimum of location point n is big. A weak correlation of wavelet coefficients is considered in location point n. Therefore, the location point n is likely to be a noise point.

r is an important parameter to measure the coefficients correlation. If the value is selected too small, it may result in overkilling some useful signal points. If the value is chosen too large, it may lead to retain some noise points. As a lot of experiments shown, when r takes 0.5 to 1.5, the denoising effect is good. Therefore, in the experiment of this paper, r is set 1.

3.3. A New Threshold Determination Strategy Considering Interscale Correlation. K is an index measuring the interscale

correlation of wavelet coefficients, which can represent the possibility of a certain point belonging to the signal point. Because universal threshold often has the risk of overkilling the useful information, therefore, when $K(n) \in [0, r)$, the threshold needs to be shrunk to retain location point n, and when $K(n) \in [r, +\infty)$, the threshold of location point n remains invariant. Based on a lot of experiments, a new threshold determination method considering interscale correlation is presented as follows:

$$T_{\text{new}} = \begin{cases} 0.7\lambda & k(n) \in [0, 0.5r) \\ 0.8\lambda & k(n) \in [0.5r, 0.8r) \\ 0.9\lambda & k(n) \in [0.8r, r) \\ \lambda & k(n) \in [r, +\infty), \end{cases} \tag{8}$$

where λ is universal threshold.

If $K(n) \in [0, 0.5r)$, then the correlation of the wavelet coefficients is considered to be very large, and the location n is very likely to be a signal point. Therefore, we set the threshold value $T_{\text{new}} = 0.7\lambda$. If $K(n) \in [0.5r, 0.8r)$, then the correlation of the wavelet coefficients is considered large, and the location point n is likely to be a signal point. Therefore, we set the threshold value $T_{\text{new}} = 0.8\lambda$. If $K(n) \in [0.8r, r)$, then the correlation of the wavelet coefficients is considered to be slightly large, and there is slight possibility for location n to be a signal point. Therefore, we set the threshold value $T_{\text{new}} = 0.9\lambda$. If $K(n) \in [r, +\infty)$, the correlation of the wavelet coefficients is considered very little, and there is almost no possibility for location n to be a signal point. Therefore, we set the threshold value $T_{\text{new}} = \lambda$.

4. Simulation Experiment

4.1. Experimental Parameter Settings and Experiment Results. In order to verify the validity of the new threshold, four classic benchmark signals, namely, Blocks, Bumps, Heavy Sine, and Doppler, are used as test signals. The length of the signal is 512 and r is set 1. Two strengths of white Gaussian noise $\sigma = 3$ and $\sigma = 5$ are added to the test signals in the experiments. The calculation process of the correlation index K requires that the number of wavelet coefficients to be the same in different decompositions. Therefore, stationary wavelet transform is used in this paper [20]. Wavelet basis adopts sym6 wavelet, wavelet decomposition scale is set to be 3, and hard and soft thresholding functions are chosen as thresholding functions. The traditional universal threshold is selected as comparative experiment. In order to measure the denoising effect under different thresholds, MSE and signal-to-noise-ratio (SNR) are selected as comparative index:

$$\begin{gathered} \text{MSE} = \frac{\sum_{k=1}^{N} [X(k) - S(k)]^2}{N}, \\ \text{SNR} = 10 \ln \frac{\sum_{k=1}^{N} S(k)^2}{\sum_{k=1}^{N} [X(k) - S(k)]^2}. \end{gathered} \tag{9}$$

Figures 2 and 3 show the denoising effects of the four test signals with $\sigma = 5$ Gaussian white noise and hard thresholding function. In the figures, OS represents the original signal, NS is the noisy signal, DSUT is reconstructed signal using universal threshold, DSPT expresses the reconstructed signal using the proposed threshold.

The denoising results of soft thresholding function are given in Figures 4 and 5.

In order to exclude the effect of noise intensity, experiment is retested with $\sigma = 3$ white Gaussian noise.

4.2. Result Analysis. As shown in Figure 2, when $\sigma = 5$ and hard thresholding function is selected, denoising signal obtained by the proposed method is closer to the original signal than universal threshold for all the four different signals. As shown in Figure 3, the proposed method can achieve a smaller MSE and a larger SNR than traditional method. In order to avoid the interference of thresholding function, Figures 4 and 5 show the denoising results under soft thresholding function. Comparing Figure 2 with Figure 4, denoising signal obtained by our method is closer to the original signal than universal threshold, regardless of which hard threshold function or soft threshold function is selected. From Figures 3 and 5, we find that no matter which thresholding function is selected, denoising signal using our method can obtain a smaller MSE and greater SNR. Experiment is retested with $\sigma = 3$ white Gaussian noise to exclude the effect of noise intensity. The experiment results are shown in Figures 6, 7, 8, and 9, which indicate that the denoising effect and index of the proposed method are superior to those of the universal threshold with both heavy and light noise.

5. Conclusion

A new method considering interscale correlation is presented to solve the problem of wavelet threshold determination. Firstly, a new index is proposed to measure the coefficients correlation. Then, a new threshold determination strategy is obtained using new index to improve universal threshold. Some conclusions are summarized as follows.

(1) According to the propagation characteristics of the wavelet coefficients, a new index is proposed to measure the coefficients correlation. Compared with traditional index NCor, the new index has the advantage of a simple structure and convenient calculation.

(2) Universal threshold has the defect of overkilling the useful information. In order to address the issue, interscale correlation is used to shrink the universal threshold. Experimental results show that the proposed method can achieve optimum denoising effect under different signal types, noise intensities, and thresholding functions. Therefore, this method is effective and superior in signal denoising.

Universal threshold is selected as the basic threshold in this paper. In theory, the proposed idea is also applicable to the other threshold methods. Future research will be conducted on using the proposed idea to improve other thresholds.

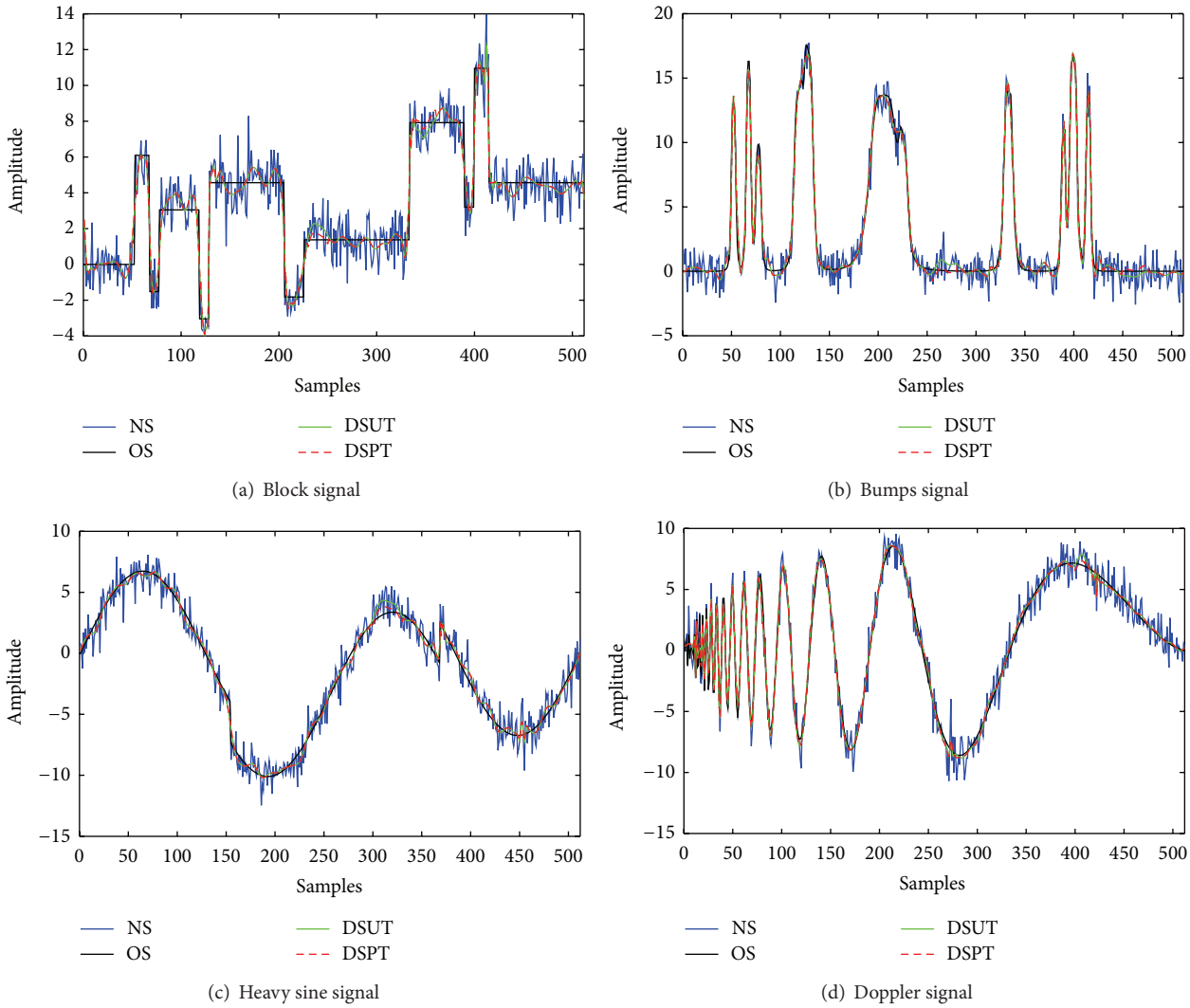

(a) Block signal

(b) Bumps signal

(c) Heavy sine signal

(d) Doppler signal

Figure 2: Denoising effect of $\sigma = 5$, hard thresholding function.

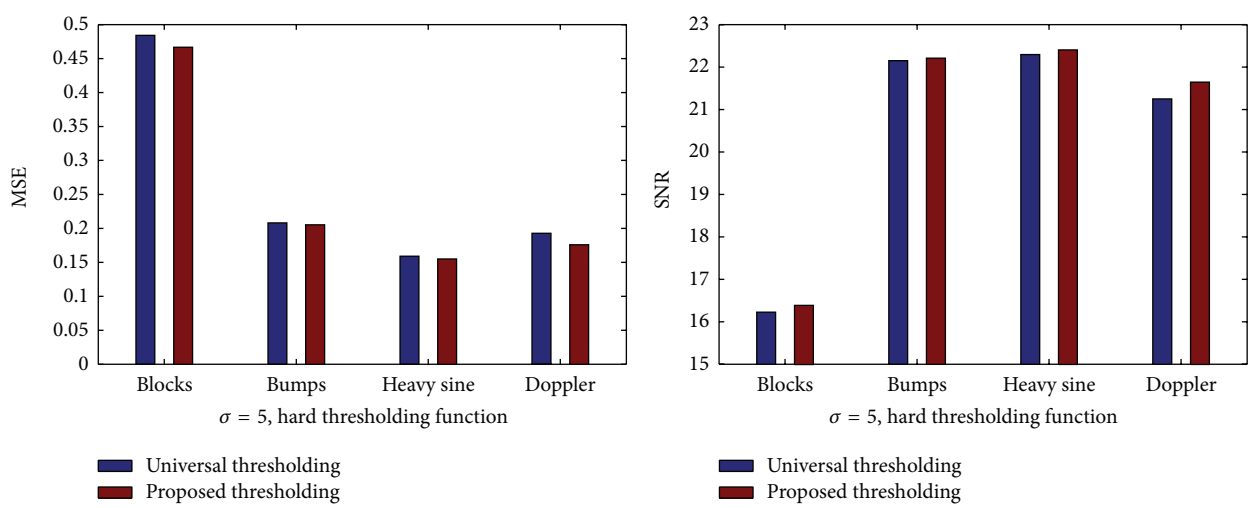

(a) MSE

(b) SNR

Figure 3: Denoising index of $\sigma = 5$, hard thresholding function.

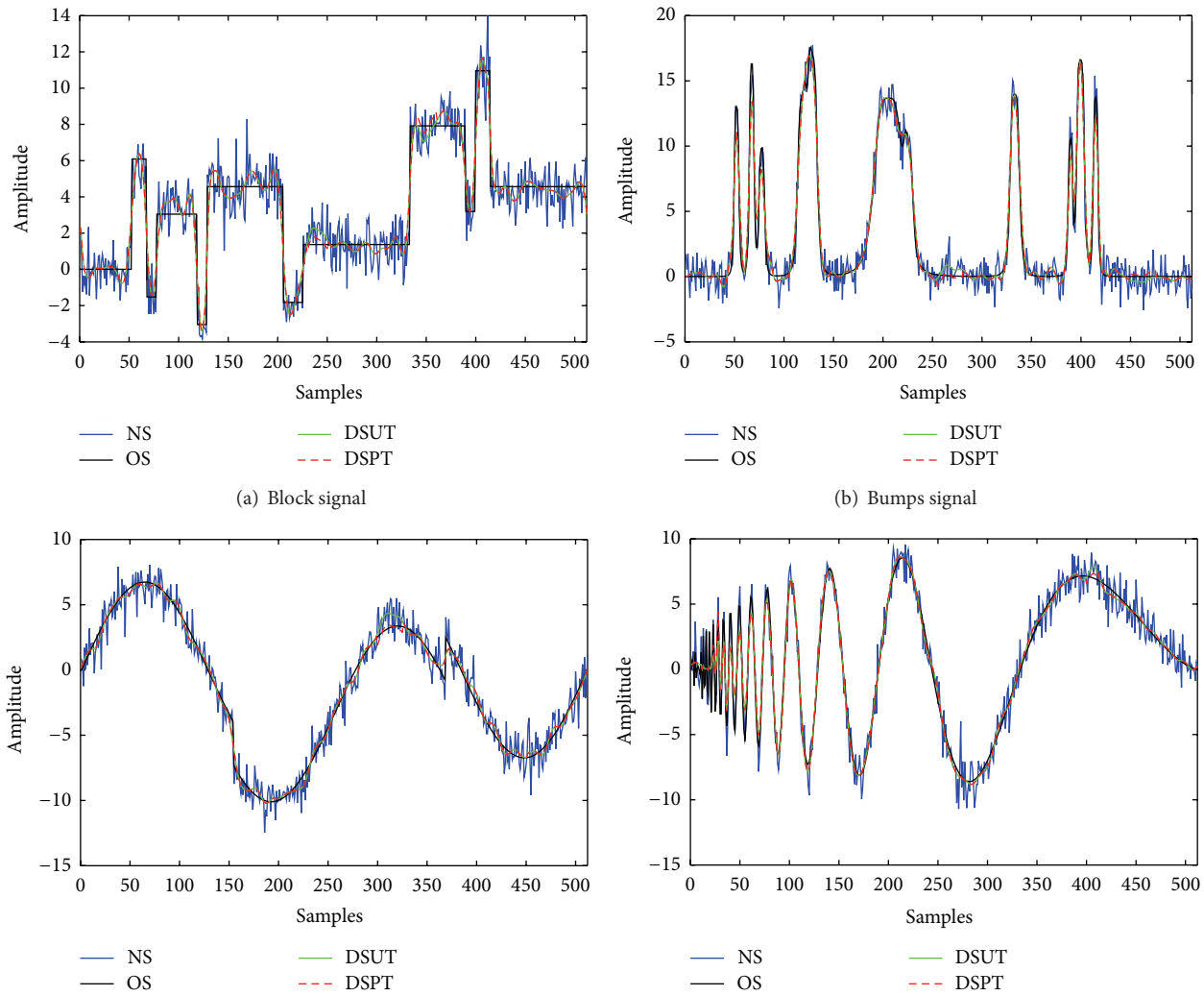

(a) Block signal

(b) Bumps signal

(c) Heavy sine signal

(d) Doppler signal

Figure 4: Denoising effect of $\sigma = 5$, soft thresholding function.

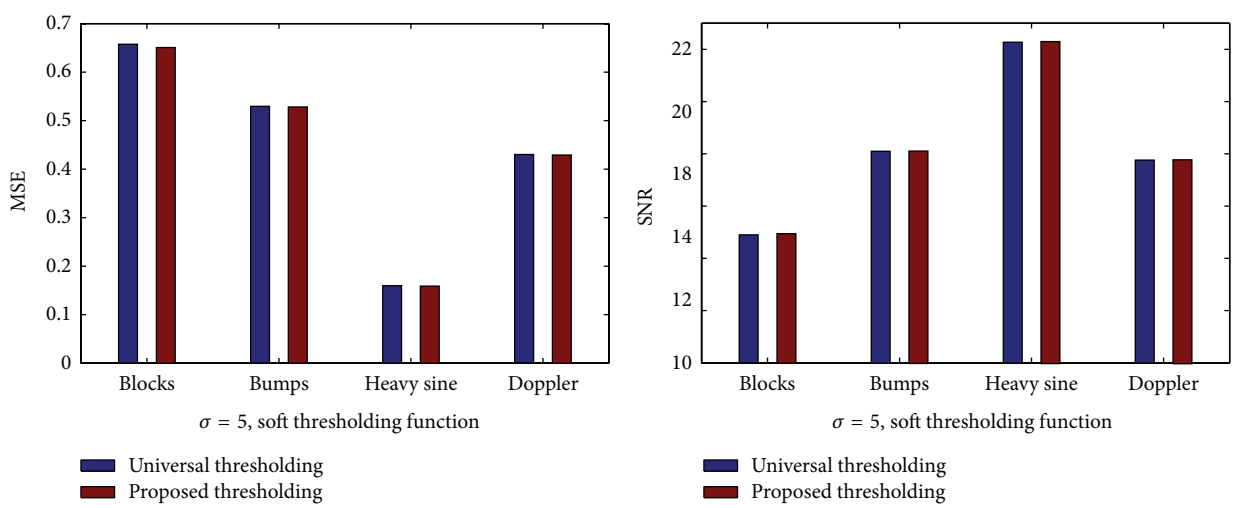

(a) MSE

(b) SNR

Figure 5: Denoising index of $\sigma = 5$, soft thresholding function.

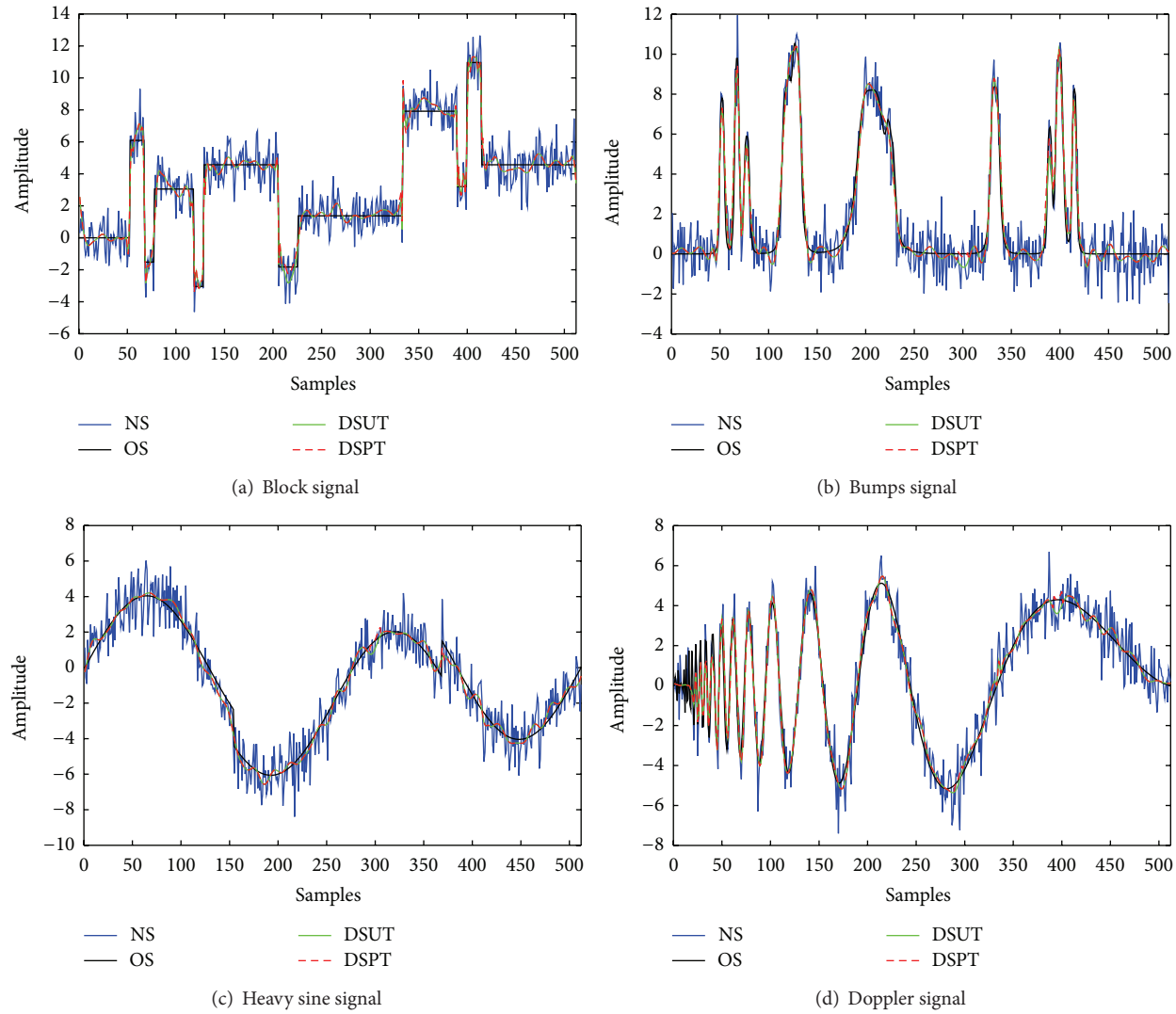

(a) Block signal

(b) Bumps signal

(c) Heavy sine signal

(d) Doppler signal

Figure 6: Denoising effect of $\sigma = 3$, hard thresholding function.

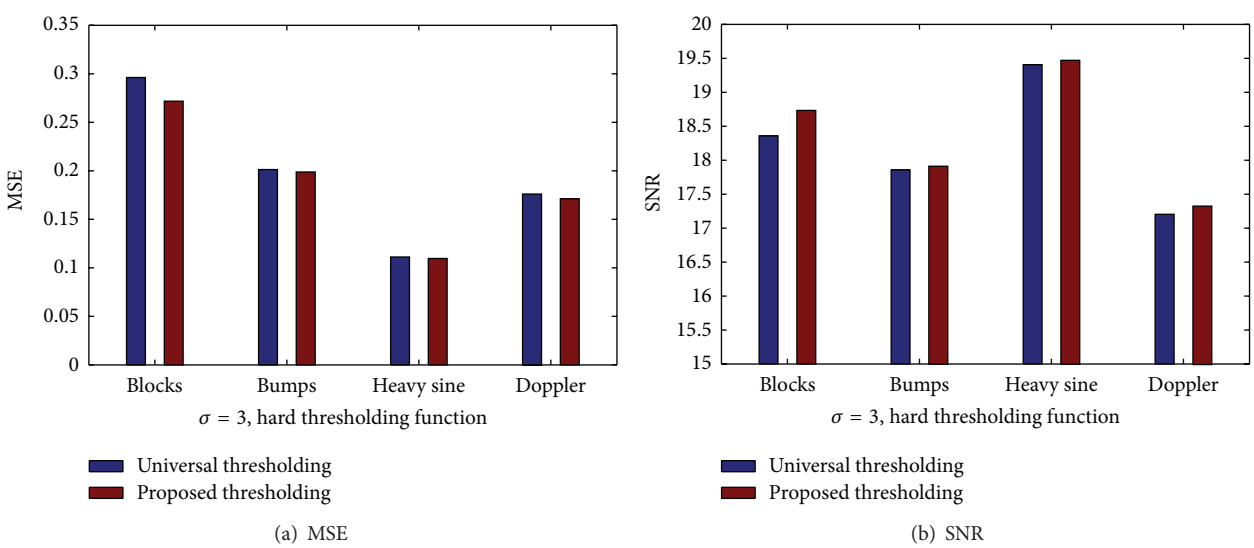

(a) MSE

(b) SNR

Figure 7: Denoising index of $\sigma = 3$, hard thresholding function.

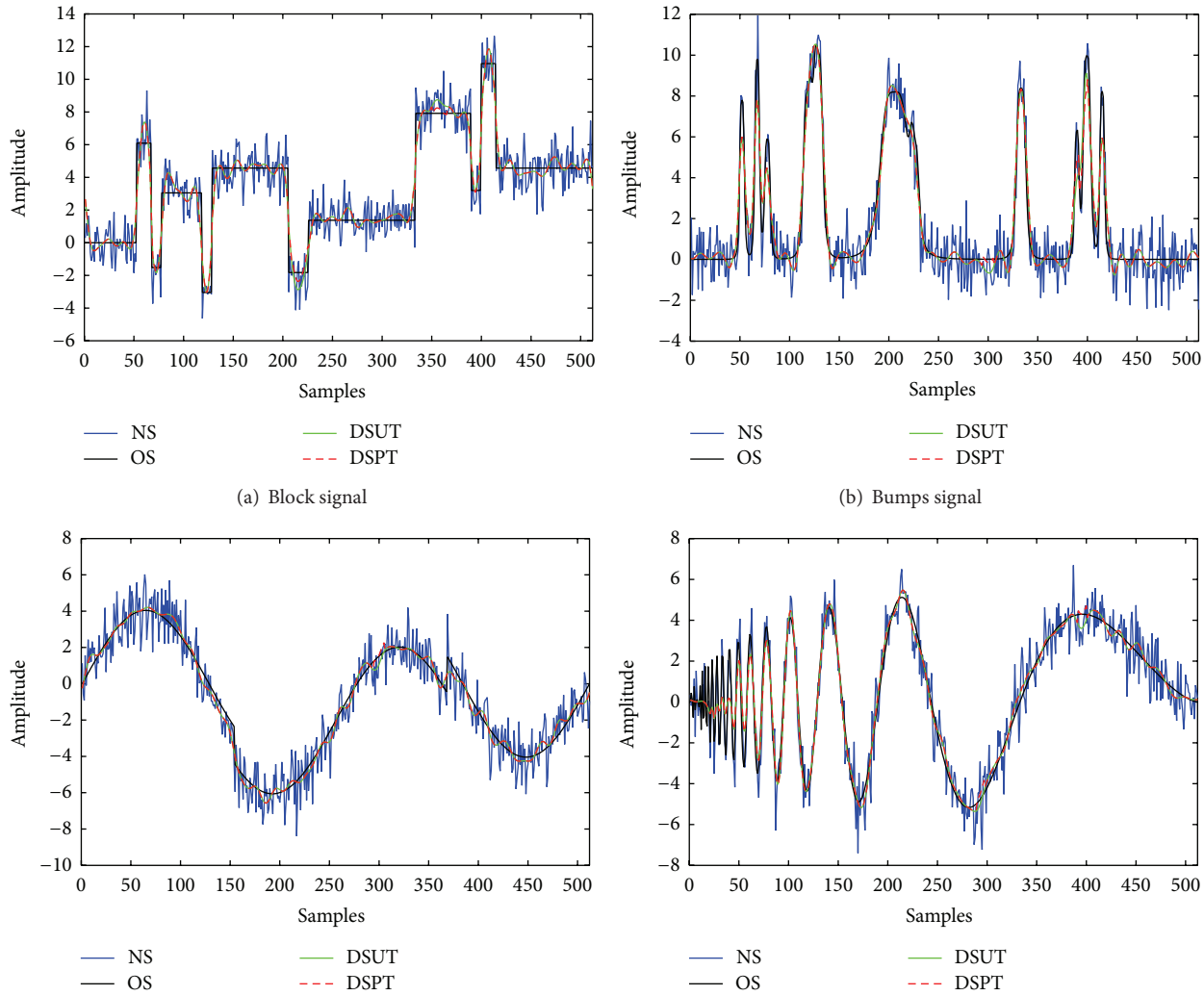

(a) Block signal

(b) Bumps signal

(c) Heavy sine signal

(d) Doppler signal

Figure 8: Denoising effect of $\sigma = 3$, soft thresholding function.

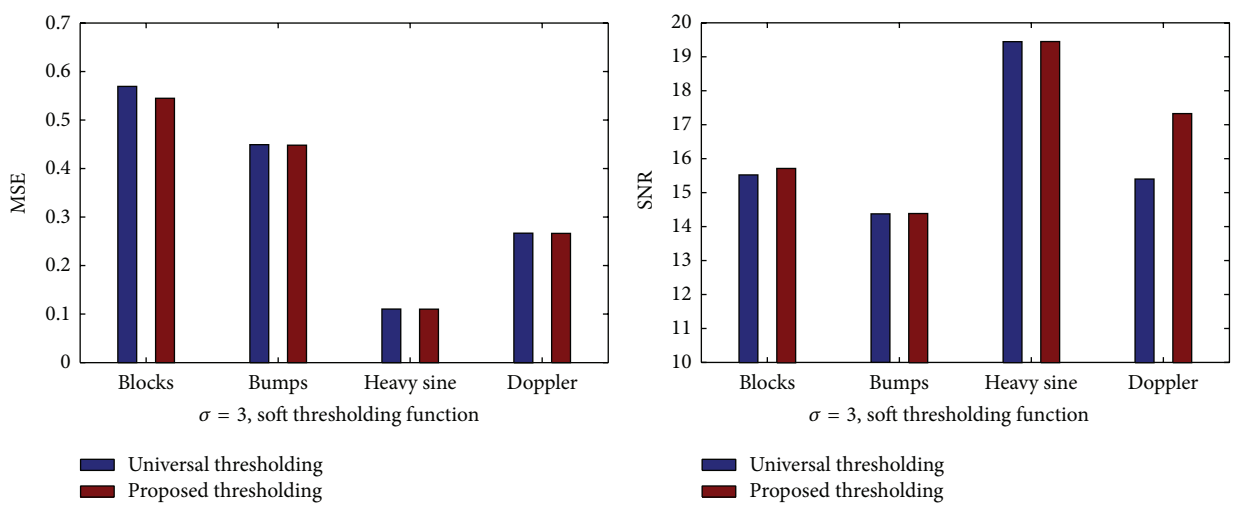

(a) MSE

(b) SNR

Figure 9: Denoising index of $\sigma = 3$, soft thresholding function

Conflict of Interests

The authors declare that there is no conflict of interests regarding the publication of this paper.

References

[1] T.-H. Yi, H.-N. Li, and X.-Y. Zhao, "Noise smoothing for structural vibration test signals using an improved wavelet thresholding technique," *Sensors*, vol. 12, no. 8, pp. 11205–11220, 2012.

[2] A. G. Bruce, D. L. Donoho, H. Y. Gao, and R. D. Martin, "Denoising and robust nonlinear wavelet analysis," in *Optical Engineering and Photonics in Aerospace Sensing*, Proceedings of SPIE, pp. 325–336, Orlando, Fla, USA, 1994.

[3] X. Zhang and Y. Xiong, "Impulse noise removal using directional difference based noise detector and adaptive weighted mean filter," *IEEE Signal Processing Letters*, vol. 16, no. 4, pp. 295–298, 2009.

[4] G. Gupta, "Algorithm for image processing using improved median filter and comparison of mean, median and improved median filter," *International Journal of Soft Computing and Engineering*, vol. 1, no. 5, pp. 2231–2307, 2011.

[5] K.-M. Chang and S.-H. Liu, "Gaussian noise filtering from ECG by Wiener filter and ensemble empirical mode decomposition," *Journal of Signal Processing Systems*, vol. 64, no. 2, pp. 249–264, 2011.

[6] B. Le, Z. Liu, and T. Gu, "Weak LFM signal detection based on wavelet transform modulus maxima denoising and other techniques," *International Journal of Wavelets, Multiresolution and Information Processing*, vol. 8, no. 2, pp. 313–326, 2010.

[7] Y. Xu, J. B. Weaver, D. M. Healy Jr., and J. Lu, "Wavelet transform domain filters: a spatially selective noise filtration technique," *IEEE Transactions on Image Processing*, vol. 3, no. 6, pp. 747–758, 1994.

[8] D. L. Donoho and I. M. Johnstone, "Ideal spatial adaptation by wavelet shrinkage," *Biometrika*, vol. 81, no. 3, pp. 425–455, 1994.

[9] Z. Tao, H.-M. Zhao, X.-J. Zhang, and D. Wu, "Speech enhancement based on the multi-scales and multi-thresholds of the auditory perception wavelet transform," *Archives of Acoustics*, vol. 36, no. 3, pp. 519–532, 2011.

[10] S. G. Chang, B. Yu, and M. Vetterli, "Adaptive wavelet thresholding for image denoising and compression," *IEEE Transactions on Image Processing*, vol. 9, no. 9, pp. 1532–1546, 2000.

[11] Y. Lu and P. C. Loizou, "Estimators of the magnitude-squared spectrum and methods for incorporating SNR uncertainty," *IEEE Transactions on Audio, Speech, and Language Processing*, vol. 19, no. 5, pp. 1123–1137, 2011.

[12] H.-C. Li, W. Hong, Y.-R. Wu, and P.-Z. Fan, "Bayesian wavelet shrinkage with heterogeneity-adaptive threshold for SAR image despeckling based on generalized gamma distribution," *IEEE Transactions on Geoscience and Remote Sensing*, vol. 51, no. 4, pp. 2388–2402, 2013.

[13] D. L. Donoho and I. M. Johnstone, "Minimax risk over l_p-balls for l_p-error," *Probability Theory and Related Fields*, vol. 99, no. 2, pp. 277–303, 1994.

[14] M. Jansen and A. Bultheel, "Multiple wavelet threshold estimation by generalized cross validation for images with correlated noise," *IEEE Transactions on Image Processing*, vol. 8, no. 7, pp. 947–953, 1999.

[15] T. T. Cai and H. H. Zhou, "A data-driven block thresholding approach to wavelet estimation," *The Annals of Statistics*, vol. 37, no. 2, pp. 569–595, 2009.

[16] F. Autin, J.-M. Freyermuth, and R. von Sachs, "Combining thresholding rules: a new way to improve the performance of wavelet estimators," *Journal of Nonparametric Statistics*, vol. 24, no. 4, pp. 905–922, 2012.

[17] A. Fathi and A. R. Naghsh-Nilchi, "Efficient image denoising method based on a new adaptive wavelet packet thresholding function," *IEEE Transactions on Image Processing*, vol. 21, no. 9, pp. 3981–3990, 2012.

[18] R. Yang and M. Ren, "Wavelet denoising using principal component analysis," *Expert Systems with Applications*, vol. 38, no. 1, pp. 1073–1076, 2011.

[19] M. S. Crouse, R. D. Nowak, and R. G. Baraniuk, "Wavelet-based statistical signal processing using hidden Markov models," *IEEE Transactions on Signal Processing*, vol. 46, no. 4, pp. 886–902, 1998.

[20] S. Zhong and S. O. Oyadiji, "Crack detection in simply supported beams using stationary wavelet transform of modal data," *Structural Control and Health Monitoring*, vol. 18, no. 2, pp. 169–190, 2011.

Hindawi Publishing Corporation
Mathematical Problems in Engineering
Volume 2015, Article ID 969702, 7 pages
http://dx.doi.org/10.1155/2015/969702

Research Article

Application of a New Wavelet Threshold Method in Unconventional Oil and Gas Reservoir Seismic Data Denoising

Guxi Wang,[1,2] Ling Chen,[1] Si Guo,[1,3] Yu Peng,[3] and Ke Guo[1]

[1] *Chengdu University of Technology, Chengdu 610059, China*
[2] *Nation Institute of Measurement and Testing Technology, Chengdu 610021, China*
[3] *CNPC Chuanqing Drilling Engineering Company Limited, Chengdu 610000, China*

Correspondence should be addressed to Ling Chen; chenl@cdut.edu.cn

Received 5 January 2015; Accepted 27 February 2015

Academic Editor: Yun-Bo Zhao

Copyright © 2015 Guxi Wang et al. This is an open access article distributed under the Creative Commons Attribution License, which permits unrestricted use, distribution, and reproduction in any medium, provided the original work is properly cited.

Seismic data processing is an important aspect to improve the signal to noise ratio. The main work of this paper is to combine the characteristics of seismic data, using wavelet transform method, to eliminate and control such random noise, aiming to improve the signal to noise ratio and the technical methods used in large data systems, so that there can be better promotion and application. In recent years, prestack data denoising of all-digital three-dimensional seismic data is the key to data processing. Contrapose the characteristics of all-digital three-dimensional seismic data, and, on the basis of previous studies, a new threshold function is proposed. Comparing between conventional hard threshold and soft threshold, this function not only is easy to compute, but also has excellent mathematical properties and a clear physical meaning. The simulation results proved that this method can well remove the random noise. Using this threshold function in actual seismic processing of unconventional lithologic gas reservoir with low porosity, low permeability, low abundance, and strong heterogeneity, the results show that the denoising method can availably improve seismic processing effects and enhance the signal to noise ratio (SNR).

1. Introduction

The study area is located in the middle of Sulige gas field, with small effective reservoir thickness, expressed as "thin, more scattered, and miscellaneous" feature on the vertical of reservoir; therefore, to remove noise in seismic data, which improves the reliability of the signal, is particularly important for reservoir prediction in later work, as it is always the goal of geophysical workers.

Random noise cannot seek a unified time pattern, with wide bandwidth, and cannot be determined by its apparent velocity and direction of propagation, thus removing random noise and the key point is to improve its SNR. In order to effectively remove random noise, various denoising methods have been proposed; thereinto, the wavelet transform method works better in recent years. Wavelet transform theory developed in mid and late eighties of last century [1], and it can make multiscale decomposition of seismic signals.

Since desired signal and random noise have different characteristics on different wavelet scales, such as during valid signal occurs within a short time, instantaneous modulus maxima of the wavelet coefficients occurs, and with the decomposition scale increment, wavelet coefficients and dense maxima of random noise in desired signal will decrease while decomposition scale increasing [2, 3]. Wavelet denoising method separates desired signal and random noise by this opposite characteristic between them. In 1995, Donoho proposed wavelet threshold method, and soon it became one of the most widely used methods for it is easy to implement and with fast calculation speed.

But hard and soft threshold methods commonly used in wavelet threshold methods have some shortcomings, such as the following: remodeling factor in hard threshold processing occurs intermittently at the threshold point; the reconstructed signal is prone to Pseudo-Gibbo phenomenon; while although reconstruction coefficient of soft threshold has good overall continuity, there is always a constant bias between reconstructed coefficients and decomposition coefficients [4]. These all impact the wavelet threshold effect. This paper gives a new threshold function, which not only is easy

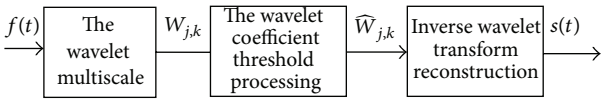

Figure 1: The flow of wavelet threshold.

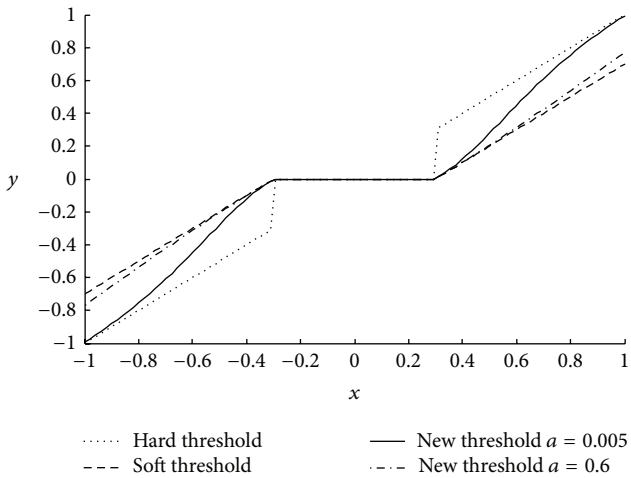

Figure 2: The new threshold.

to compute, but also has excellent mathematical properties and a clear physical meaning. The significant effect of the new threshold function will show in simulation results and practical applications.

2. An Improved Method of Threshold Function

Consider the following observation signal:

$$f(t) = s(t) + n(t). \tag{1}$$

$f(t)$ is noisy random signal. $s(t)$ is original signal. $n(t)$ obeys Gaussian white noise distribution, means $N(0,\sigma^2)$ distribution. For one-dimensional random signal $f(t)$, we first discretize samples to give N points of discrete signal $f(n), n = 0, 1, 2, \ldots, N-1$. Then we have a wavelet transform:

$$Wf(j,k) = 2^{-j/2} \sum_{n=0}^{N-1} f(n)\, \psi\left(2^{-j}n - k\right), \tag{2}$$

where $Wf(j,k)$ are wavelet coefficients, abbreviated as $W_{j,k}$ to simplify the calculation, Making discrete wavelet transform for noisy random signals as $f(t) = s(t) + n(t)$, for wavelet transform is a linear transformation, the obtained $W_{j,k}$ are still composed by two parts: wavelet coefficients corresponding to desired signal $s(t)$, denoted by $U_{j,k}$, and wavelet coefficients corresponding to noise $n(t)$, denoted by $V_{j,k}$.

Wavelet threshold method based on the minimum mean square error (MSE) proposed by Donoho has been widely used. The basic flow is shown in Figure 1 [5].

Hard threshold function is

$$\widehat{W}_{j,k} = \begin{cases} W_{j,k}, & \left|W_{j,k}\right| \geq k, \\ 0, & \left|W_{j,k}\right| < k. \end{cases} \tag{3}$$

Soft threshold function is

$$\widehat{W}_{j,k} = \begin{cases} \operatorname{sgn}\left(W_{j,k}\right) \cdot \left(\left|W_{j,k}\right| - \lambda\right), & \left|W_{j,k}\right| \geq \lambda, \\ 0, & \left|W_{j,k}\right| < \lambda. \end{cases} \tag{4}$$

The value λ of formulas (3) and (4) is the preset threshold. $\operatorname{Sgn}(*)$ in formula (4) means the sign function.

A weighted average threshold estimation method is given in literatures [6, 7]; that is,

$$\widehat{W}_{j,k} = \begin{cases} (1-\mu)\, W_{j,k} + \mu \operatorname{sgn}\left(W_{j,k}\right)\left(\left|W_{j,k}\right| - \lambda\right), & \left|W_{j,k}\right| \geq \lambda, \\ 0, & \left|W_{j,k}\right| < \lambda. \end{cases} \tag{5}$$

Traditional weighted average methods generally set the weighting factor μ to 0.5, and the constant μ can overcome soft and hard threshold disadvantages in a certain extent, but it still has flaw: first threshold function is still not a continuous function, followed by a fixed bias which is still existent between estimate value and original value of wavelet coefficients, but the deviation is less than 0.5. In order to better show advantages of weighted average threshold estimation method, this paper presents a new weighting factor calculation formula:

$$\mu = \alpha^{(|W_{j,k}|-\lambda)^2}, \quad (0 \leq \alpha \leq 1),\ 0 \leq \mu \leq 1. \tag{6}$$

The new threshold function has the following characteristics:

(1) When $\alpha \to 0$ is the hard threshold function, $\alpha \to 1$ is the soft threshold function.

(2) $|\widehat{W}_{j,k}|$ will be gradually increased as $|W_{j,k}|$ is increasing; when $|W_{j,k}| \to \infty$, then $\widehat{W}_{j,k} \to W_{j,k}$.

(3) When $|W_{j,k}| = \lambda, \widehat{W}_{j,k} = 0$; when $|W_{j,k}| \to \lambda, \widehat{W}_{j,k} \to 0$; so $\widehat{W}_{j,k}$ is consecutive when $|W_{j,k}| = \lambda$.

This shows that the new threshold function is an adjustable function between hard and soft threshold function (Figure 2). As long as there is a proper sizing α, we can get a better denoising effect, and it also has a very clear physical meaning.

3. Simulation and Comparison

To verify effect of the new threshold denoising function, we use Matlab toolbox containing Gaussian noise Heavisine signals. Using traditional hard and soft threshold function and the new threshold function make denoising tests. Then comparative analysis of results, select sym6 to make wavelet

Table 1: Methods of signal to noise ratio (SNR/dB) and mean square error (MSE).

Threshold	Plus noise signal	Hard threshold	Soft threshold function	The new threshold
SNR	14.8606	24.7590	25.2749	26.5035
RMSE	1.0324	0.3303	0.3113	0.2702

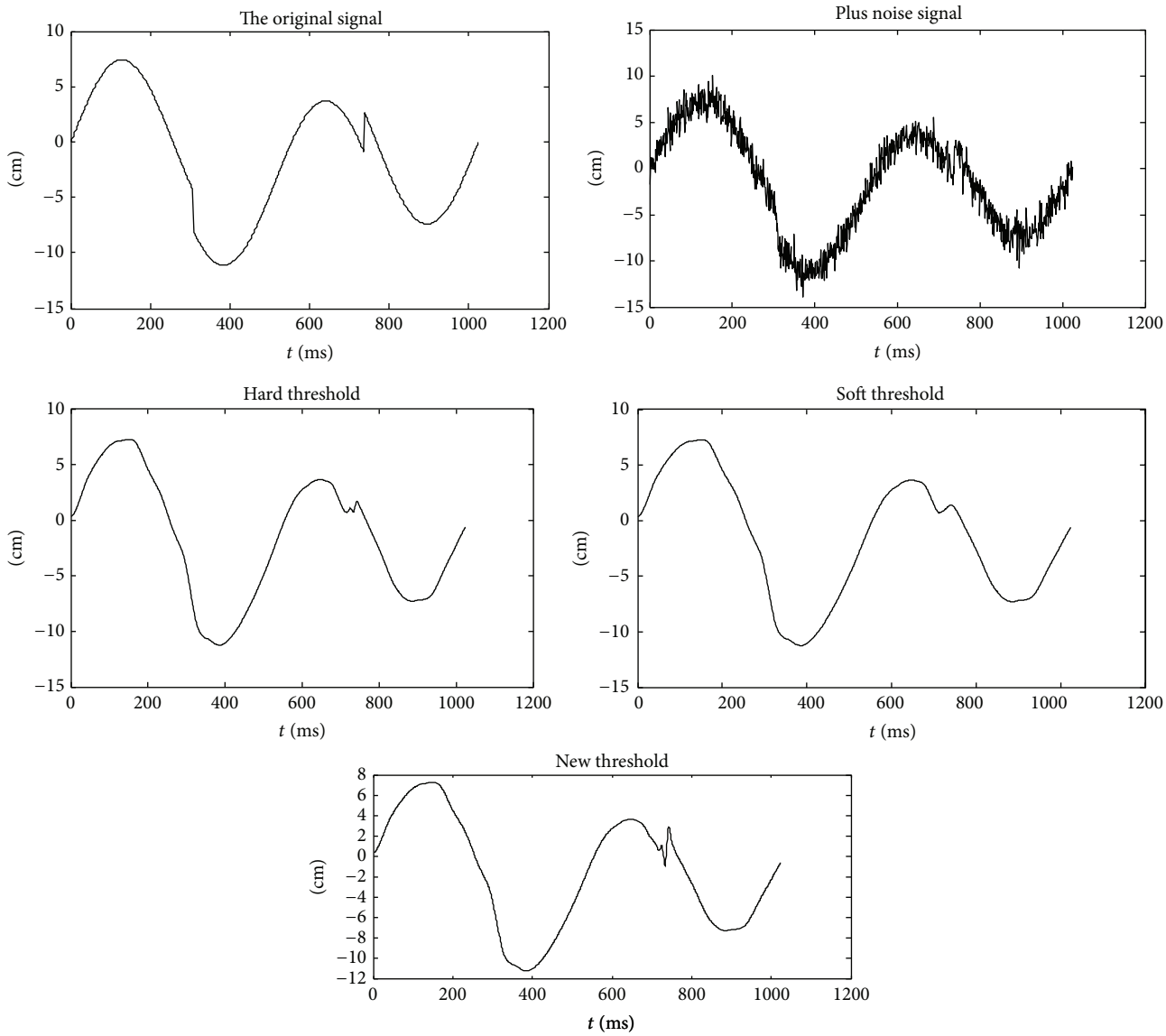

Figure 3: The effect diagram of different threshold function.

decomposition, the maximum resolution scale J is taken as 5, the selected threshold value of $\lambda = \sigma\sqrt{2\log N}/\log(j+1)$, wherein the noise variance σ, and N is a discrete signal sampling length. The simulation results shown in Figure 3, SNR, and MSE of denoising signal are shown in Table 1.

By the numerical denoising effect evaluation in 3–1 one can see several improved threshold function denoising effects showing soft, hard threshold method is better than the classical one note. We note that the denoising effects of exponential threshold function are better than other kinds of methods; and the method of the new threshold function in root mean square error slightly inferior to the exponential threshold function, but in the signal to noise ratio of this index, is obviously better than the exponential threshold method [5].

4. Noising Seismic Data and Application

4.1. Original Data Analysis

4.1.1. Shot Record Quality Analysis. Typical analysis from the original records, shot records SNR differences, higher SNR

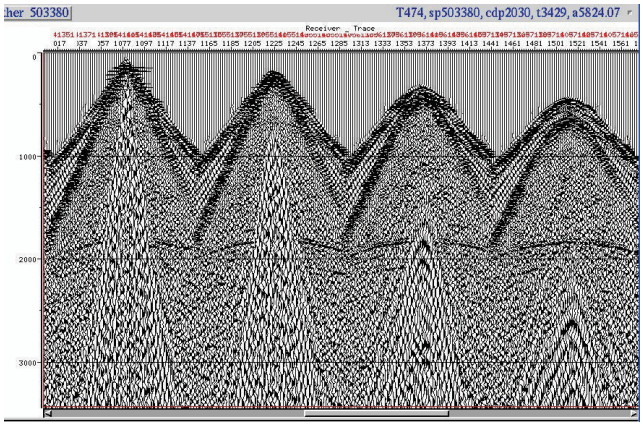

Figure 4: Better quality of the original single shot.

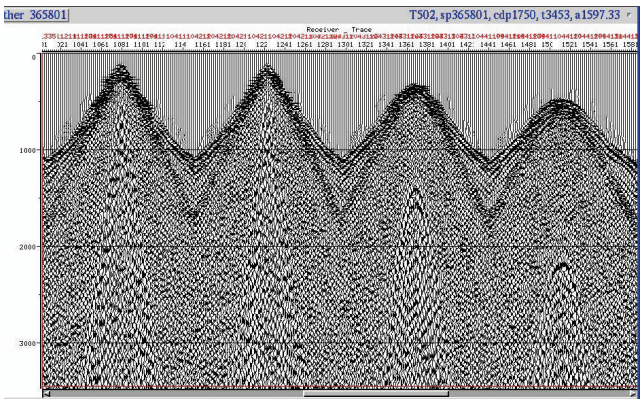

Figure 5: Poor quality of the original single shot.

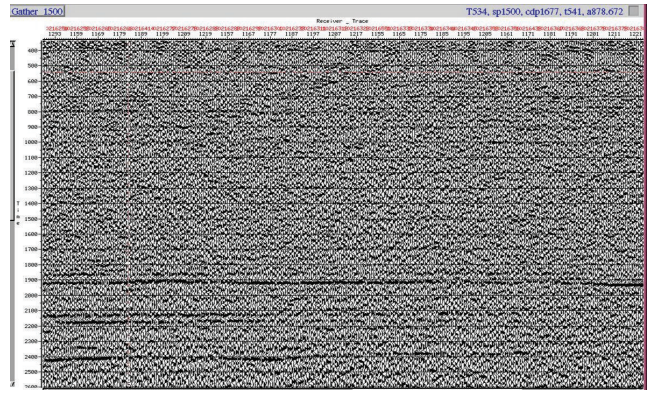

Figure 6: Stacked section INLINE551 CDP691–961.

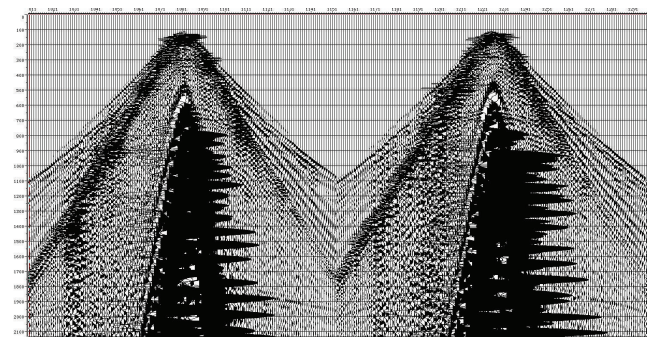

Figure 7: Refracted waves, multiple refraction, direct waves, surface waves, and sound waves.

from 1.8 s to 2.1 s, the whole region can continuously track mark phase axis, with good quality single shot, shallow, mid-wave group is complete, 2.5 s or less energy loss is more serious. Poor quality single shot shallow, deep SNR poor record serrated early to beat poor continuity (Figures 4 and 5).

4.1.2. Analysis of the Entire Work Area Stacked Section. Since the surface area of seismic and geological conditions is complex, the entire work area accounts for about 7% of Salt Lake wetlands; desert area is about 50%; grass and sand grass are about 35%; rock outcrop is about 8%. Overall, qualities of collected data are quite different; SNR and continuous quality display banded regional variation, and desert zone data was poor, which is shown in Figure 6. This requires us to do information processing, especially denoising before and after stacking, and parameters should be targeted to ensure data consistency.

4.1.3. Interference Wave Analysis. The original single shot shows that work area noise is relatively developed (Figure 7), which can be grouped into several categories:

(1) Mechanical interference: performance on the record is outliers and abnormal trace, and characteristics of such interference is with strong randomness distribution and different stimulation time; different positions have different distributions, easily recognizable from the amplitude [8].

(2) Linear ramp interference: it includes multiple refraction, surface wave, acoustic and some secondary oblique interference, multiple refraction, and secondary oblique interference which are with larger apparent velocity on the record, generally more than 1000 m/s, with low-frequency surface waves, mainly distributed in the gun point neighborhood, single shot on the record as low apparent velocity, generally not more than 800 m/s, with high sound waves frequency and strong energy.

(3) Random interference.

Combined with the above analysis of raw data, we can see that interference of three-dimensional low-frequency surface wave is strong in the study area, effective reflections on the original record are full inundated by surface wave, with low SNR; in addition, shallow direct wave interference is strong, with broad band distribution, which seriously interferes with shallow reflection signals [6]. During the processing, we should focus on the basis of noise characteristics analysis, take a targeted approach for noise pressure, carry out noise suppression in a multidomain, and improve SNR of data. Minimizing the effective wave damage in the process of

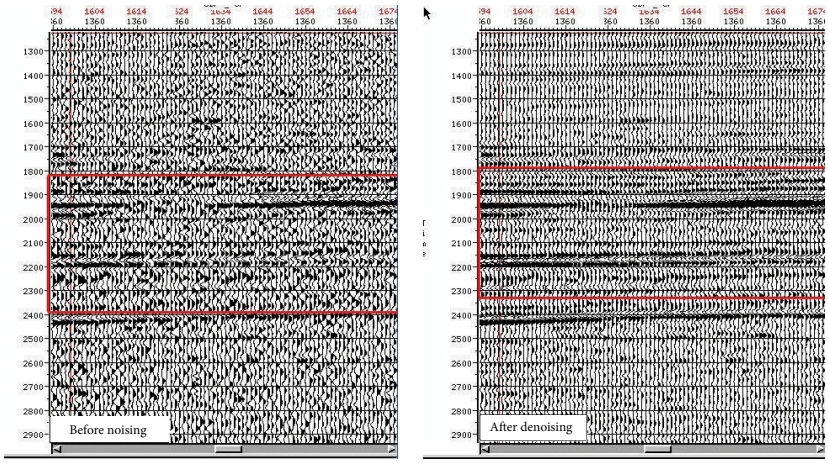

(a) (b)

Figure 8: Actual seismic records.

denoising and achieving high-fidelity denoising is another difficulty and emphasis of three-dimensional processing.

4.2. Analysis of the Actual Processing Effect. To illustrate the effectiveness of the proposed denoising method, we selected a small cross-sectional view of seismic data of a work area to actual test. Where Figure 8(a) is actual seismic data with random noise, Figure 8(b) is seismic data denoising with a new threshold method.

The premise of denoising is without prejudice to the effective reflection information, for low SNR data; if it cannot well suppress noise, it is difficult to have effectively phase axis. In order to achieve better denoising effect, after several trials comparing, one finds that using this method is superior to conventional denoising methods [7, 9]. By comparing the two figures, we can see that the noise is significantly reduced after processing the new threshold; meanwhile the resolution has been improved. Thus the new method of denoising seismic data has some practical significance.

From the results, the data for the effective band are from 10 to 70 Hz; frequency ranges are from 13 to 45 Hz, which reached the processing demands and meet the requirements of seismic data interpretation and reservoir inversion. To the whole cross section, the processing result is ideally effective, and SNR of profile and resolution are moderate, with natural wave, and the main target layer wave groups characteristics are distinct, clear, stable, reliable, and with good profile backgrounds, which achieve good results. This confirms the effectiveness of using data denoising algorithm for the complex seismic and geological conditions blocks. (Figures 9 and 10).

To further verify compliance between denoising method and actual seismic exploration, we selected well tie cross section of two representative wells in the area to calibrate and analyze, and we found that synthesis record and main borehole-side well layer are highly consistent. Results show that processing outcome and actual drilling revealing geological features is very accordant (Figures 11 and 12).

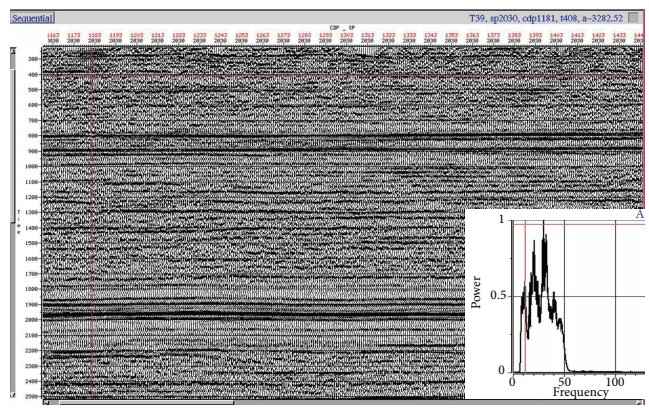

Figure 9: Stacked section INLINE1081.

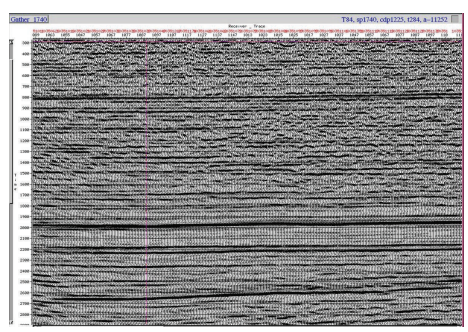

Figure 10: Poststack migration profile (INLINE791 CDP194–476).

5. Conclusions

Based on wavelet threshold methods proposed by D. L. Dohono and I. M. Johnstone, we present a new threshold function, which enables the superiority of threshold wavelet transform method fully realized. In order to test the effectiveness of the proposed method, we first made ideal synthetic seismograms and achieved the desired results. Finally, we

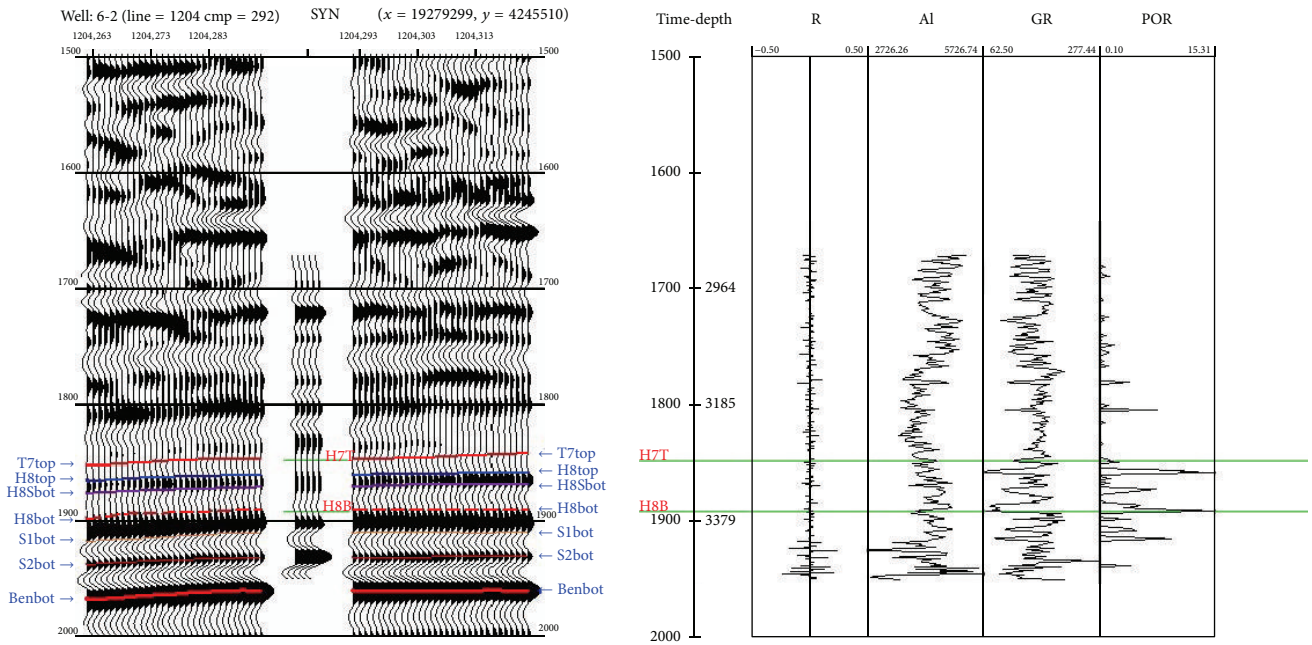

Figure 11: X Wells calibration results.

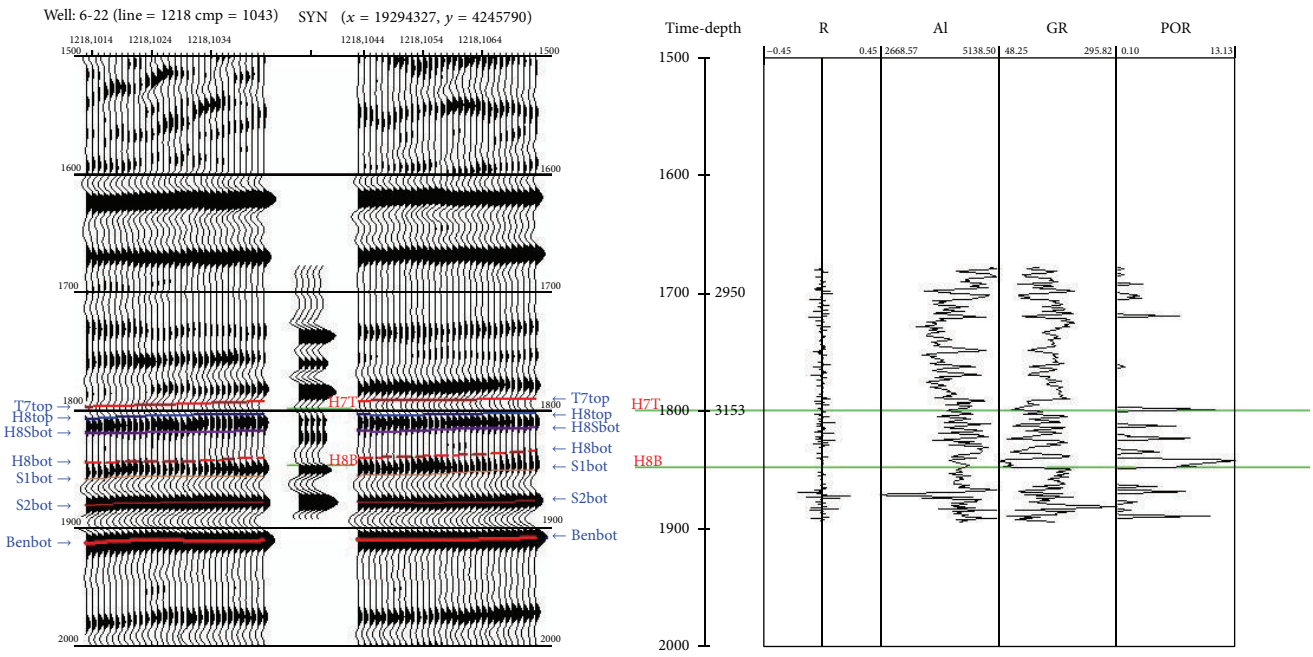

Figure 12: Y Wells calibration results.

used the method for denoising actual seismic data, and the results show that this method can effectively remove random noise in original seismic data and improve SNR of seismic data, which provides high quality data for the later work of stratigraphic interpretation and has some practical significance.

Conflict of Interests

The authors declare that there is no conflict of interests regarding the publication of this paper.

Acknowledgments

Foundation item: The Joint Specialized Research Fund for the Doctoral Program of Higher Education (20135122110010) and National Natural Science Foundation of China (4127236).

References

[1] K. Guo and S. Guo, "A method of multiple blind separation based on ICA," *Progress in Geophysics*, vol. 25, no. 3, pp. 1075–1080, 2010 (Chinese).

[2] D. P. Xu and K. Guo, "Reservoir identification generalized S transform and JADE algorithm," *Geophysical Prospecting for Petroleum*, vol. 4, 2011.

[3] K. Guo, L. Chen, H. Chen, and W. Yang, "The method of seismic random noise blind separation based on JADE," *Earth Science Frontiers*, no. 3, pp. 302–309, 2011.

[4] S. G. Mallat, "Theory for multiresolution signal decomposition: the wavelet representation," *IEEE Transactions on Pattern Analysis and Machine Intelligence*, vol. 11, no. 7, pp. 674–693, 1989.

[5] S. Mallat and W. L. Hwang, "Singularity detection and processing with wavelets," *IEEE Transactions on Information Theory*, vol. 38, no. 2, pp. 617–643, 1992.

[6] T. Liu, X. L. Zeng, and J. Zeng, *Getting Practical Wavelet Analysis*, National Defense Industry Press, Beijing, China, 2006.

[7] J. Peng, *Sensors and Detection Technology*, Xidian University Publisher, Xian, China, 2003.

[8] D. L. Donoho, "De-noising by soft-thresholding," *IEEE Transactions on Information Theory*, vol. 41, no. 3, pp. 613–627, 1995.

[9] Z. X. Cheng, *Wavelet Analysis Algorithms and Applications*, Xi'an Jiaotong University, Xi'an, China, 1998.

Hindawi Publishing Corporation
Mathematical Problems in Engineering
Volume 2015, Article ID 528656, 10 pages
http://dx.doi.org/10.1155/2015/528656

Research Article

A New Wavelet Thresholding Function Based on Hyperbolic Tangent Function

Can He,[1] Jianchun Xing,[1] Juelong Li,[2] Qiliang Yang,[1] and Ronghao Wang[1]

[1] *College of Defense Engineering, PLA University of Science and Technology, Nanjing 210007, China*
[2] *Technical Management Office of Naval Defense Engineering, Beijing 100841, China*

Correspondence should be addressed to Jianchun Xing; xjc893@163.com

Received 11 October 2014; Accepted 27 November 2014

Academic Editor: Kun Liu

Copyright © 2015 Can He et al. This is an open access article distributed under the Creative Commons Attribution License, which permits unrestricted use, distribution, and reproduction in any medium, provided the original work is properly cited.

Thresholding function is an important part of the wavelet threshold denoising method, which can influence the signal denoising effect significantly. However, some defects are present in the existing methods, such as function discontinuity, fixed bias, and parameters determined by trial and error. In order to solve these problems, a new wavelet thresholding function based on hyperbolic tangent function is proposed in this paper. Firstly, the basic properties of hyperbolic tangent function are analyzed. Then, a new thresholding function with a shape parameter is presented based on hyperbolic tangent function. The continuity, monotonicity, and high-order differentiability of the new function are theoretically proven. Finally, in order to determine the final form of the new function, a shape parameter optimization strategy based on artificial fish swarm algorithm is given in this paper. Mean square error is adopted to construct the objective function, and the optimal shape parameter is achieved by iterative search. At the end of the paper, a simulation experiment is provided to verify the effectiveness of the new function. In the experiment, two benchmark signals are used as test signals. Simulation results show that the proposed function can achieve better denoising effect than the classical hard and soft thresholding functions under different signal types and noise intensities.

1. Introduction

Signals are often contaminated by noise during their acquisition, processing, and transmission because of the measurement system error and the environment interference. In order to solve this classical problem, a variety of signal denoising methods, such as median filtering [1], particle filtering [2] and H-infinity filtering [3, 4], were proposed. Recently, due to multiresolution and low entropy, wavelet transform has become an effective technology to study signal denoising. Many methods based on wavelet theory were proposed [5–8], such as wavelet coefficients modulus maxima method, wavelet correlation method, and wavelet threshold method. Among these methods, wavelet threshold denoising has been the most widely used, because of its simple calculation and good effect. Wavelet threshold method was proposed by Donoho and Johnstone, whose main idea is to reconstruct signal on the basis of thresholding coefficients. Therefore, thresholding function is one of the factors that affect the denoising effect. Donoho and Johnstone [8] considered that only a small number of wavelet coefficients were necessary to reconstruct the signal and proposed a classical method, namely, hard thresholding function. In this function, coefficients with absolute values smaller than the threshold were set to zero, and the bigger coefficients remained unchanged. Sanam and Shahnaz [9] supposed that forcedly setting the small coefficients to zero was unreasonable and presented an improved hard thresholding function. In order to make thresholding function continuous, Donoho [10] proposed a soft thresholding function that required the wavelet coefficients to minus the threshold to achieve the new coefficients. Phinyomark et al. [11] modified the soft thresholding function and proposed a thresholding function based on hyperbolic function. By combining the advantages of hard and soft thresholding functions, Sanam and Shahnaz [12] presented a semisoft thresholding function. From the view of fuzzy theory, Shark and Yu [13] used the fuzzy membership function to process the wavelet coefficients between the

fixed form threshold and the Stein unbiased risk estimate (SURE) threshold. Jia et al. [14] divided the threshold interval into several subintervals and adopted different thresholding functions in different subintervals. On the basis of analyzing the properties of the sigmoid function, Yi et al. [15] proposed an improved wavelet thresholding function based on sigmoid function. Tang et al. [16] considered that the reconstructed signal would be smoother, if the thresholding function had high-order derivatives. According to this idea, a new function having high-order derivatives was constructed as the thresholding function in [16].

Although the research of wavelet thresholding functions made great development, a few deficiencies still exist. In the classical hard and soft thresholding functions, hard thresholding function is discontinuous and the reconstructed signal may give rise to ringing and pseudo-Gibbs phenomenon. Fixed bias exists between original and estimated wavelet coefficients in soft thresholding function, and it may lead to a big error in the reconstructed signal. The methods provided by [13–16] can improve the classical methods to some extent, but these new functions introduce new parameters, and there are few references on how to set these parameters.

The goal of this paper is to propose a new thresholding function and solve the problem of new parameters determination. Firstly, a new thresholding function is presented on the basis of hyperbolic tangent function, and the continuity, monotonicity, and high-order differentiability of the new function are proved in theory. Then, artificial fish swarm algorithm (AFSA), which uses mean square error (MSE) as the objective function, is adopted to achieve the optimal shape parameter. At last, the final form of the new function is determined on the basis of the two abovementioned steps.

The remaining parts of the paper are organized as follows. Section 2 proposes the new thresholding function and proves the continuity, monotonicity, and high-order differentiability of the function. A parameter optimization strategy based on AFSA is presented in Section 3. Section 4 provides a simulated experiment using two benchmark signals to verify the effectiveness of the new thresholding function. The conclusion is given in Section 5.

2. Description of the New Thresholding Function

2.1. Introduction of Hyperbolic Tangent Function. Hyperbolic tangent function (tanh) is defined as (see Figure 1):

$$\tanh = \frac{e^{x} - e^{-x}}{e^{x} + e^{-x}}. \tag{1}$$

The properties of hyperbolic tangent function are as follows.

(1) Domain and range: the domain of the function is $(-\infty, +\infty)$, and its range is $(-1, 1)$.

(2) Continuity: tanh is a continuous function in its domain.

(3) Monotonicity: tanh is a monotone increasing function in its domain.

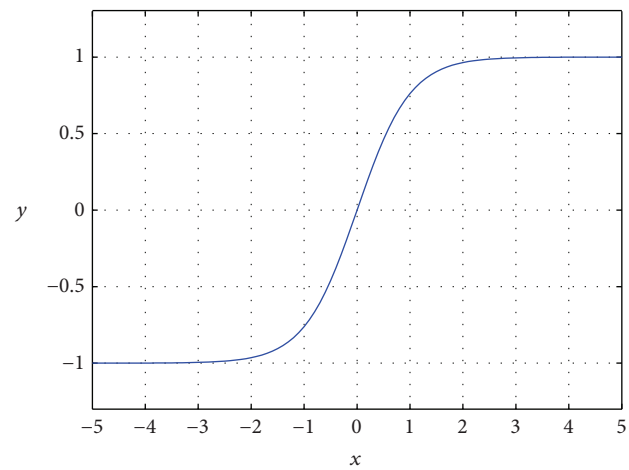

Figure 1: Curve of hyperbolic tangent function.

(4) Parity: tanh is an odd function in its domain.

(5) Asymptote: tanh has two horizontal asymptotes, namely, $y = 1$ and $y = -1$.

(6) Differentiability: tanh is differentiable in its domain, and its derivative is deduced as follows:

$$(\tanh)' = \frac{4}{(e^{x} + e^{-x})^{2}}, \tag{2}$$

where $(\tanh)'$ is an even function in its domain and obtains its maximum at $x = 0$.

2.2. A New Thresholding Function and Its Properties. On the basis of analyzing the hyperbolic tangent function, a new thresholding function is proposed in this paper:

$$\widetilde{w} = f(w) = \begin{cases} w - T + T\left(\dfrac{e^{\alpha((w-T)/T)} - e^{-\alpha((w-T)/T)}}{e^{\alpha((w-T)/T)} + e^{-\alpha((w-T)/T)}}\right), & w > T \\ 0, & |w| \le T \\ w + T + T\left(\dfrac{e^{\alpha((w+T)/T)} - e^{-\alpha((w+T)/T)}}{e^{\alpha((w+T)/T)} + e^{-\alpha((w+T)/T)}}\right), & w < -T, \end{cases} \tag{3}$$

where $\alpha \in (0, +\infty)$ is the shape parameter of the thresholding function, $T = \sigma\sqrt{2\ln(N)}$ is universal threshold, σ is the average variance of the noise, and N is the signal length.

The new thresholding function can be flexibly adjusted by changing the shape parameter α. When $\alpha \to 0$, this function approximately transfers into soft thresholding function. If $\alpha \to +\infty$, the new function corresponds to hard thresholding function. Figure 2 illustrates the comparison between soft, hard, and proposed thresholding functions.

The new thresholding function $f(w)$ has the following properties.

Theorem 1. *$f(w)$ is a continuous function in the domain of $(-\infty, +\infty)$.*

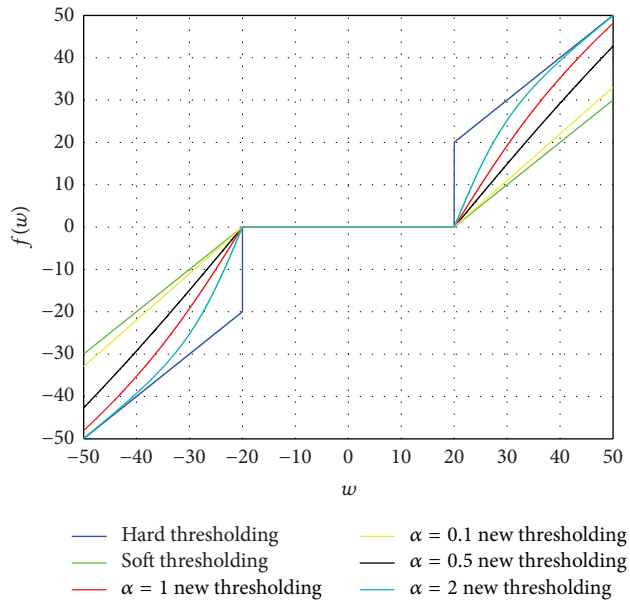

FIGURE 2: Comparison of soft, hard, and proposed thresholding functions with $T = 20$.

Proof. When

$$w > T,$$
$$f(w) = w - T + T\left(\frac{e^{\alpha((w-T)/T)} - e^{-\alpha((w-T)/T)}}{e^{\alpha((w-T)/T)} + e^{-\alpha((w-T)/T)}}\right). \tag{4}$$

So,

$$\begin{aligned}\lim_{w\to T^+} f(w) &= \lim_{w\to T^+} w - T + T\left(\frac{e^{a((w-T)/T)} - e^{-a((w-T)/T)}}{e^{a((w-T)/T)} + e^{-a((w-T)/T)}}\right)\\ &= T - T + T\left(\frac{e^0 - e^0}{e^0 + e^0}\right)\\ &= 0.\end{aligned} \tag{5}$$

When

$$|w| \le T, \qquad f(w) = 0. \tag{6}$$

Thus,

$$\lim_{w\to T^-} f(w) = 0, \qquad f(T) = 0. \tag{7}$$

Considering (5) and (7), we obtain $\lim_{w\to T^-} f(w) = \lim_{w\to T^+} f(w) = f(T)$.

Therefore, $f(w)$ is a continuous function at $w = T$.

Following above proof line, we can obtain that $f(w)$ is also continuous at $w = -T$.

That is, $f(w)$ is a continuous function in the domain of $(-\infty, +\infty)$.

Proof is completed. □

Remark 2. According to Theorem 1, $f(w)$ is a continuous function in its domain. In signal denoising, this property helps avoid pseudo-Gibbs phenomenon caused by function discontinuity.

Theorem 3. *$f(w)$ is a monotonous function in the domain of $(-\infty, +\infty)$.*

Proof. When

$$w > T,$$
$$f(w) = w - T + T\left(\frac{e^{\alpha((w-T)/T)} - e^{-\alpha((w-T)/T)}}{e^{\alpha((w-T)/T)} + e^{-\alpha((w-T)/T)}}\right). \tag{8}$$

So,

$$f(w)' = 1 + \frac{4\alpha}{(e^x + e^{-x})^2}. \tag{9}$$

Considering $\alpha \in (0, +\infty)$, we can obtain $f(w)' > 0$.

That is, $f(w)$ is a monotonous function in the domain of $(T, +\infty)$.

Following above proof line, we can obtain that $f(w)$ is also a monotonous function in the domain of $(-\infty, -T)$.

When

$$|w| \le T, \qquad f(w) \equiv 0, \tag{10}$$

Consider $f(w)$ is a continuous function in the domain of $(-\infty, +\infty)$.

Thus, $f(w)$ is a monotonic nondecreasing function in the domain of $(-\infty, +\infty)$.

Proof is completed. □

Remark 4. According to Theorem 3, $f(w)$ is a monotonic nondecreasing function in its domain, which ensures that $f(w)$ has the same variation trend of hard and soft thresholding functions.

Theorem 5. *$f(w)$ is a high-order differentiable function in the domain of $(-\infty, -T)$ and $(T, +\infty)$, respectively.*

Proof. When

$$w > T,$$
$$f(w) = w - T + T\left(\frac{e^{\alpha((w-T)/T)} - e^{-\alpha((w-T)/T)}}{e^{\alpha((w-T)/T)} + e^{-\alpha((w-T)/T)}}\right). \tag{11}$$

Thus, $f(w)$ is an elementary function.

According to the property of elementary function, we can obtain that $f(w)$ is a high-order differentiable function in the domain of $(T, +\infty)$.

Following above proof line, we can obtain that $f(w)$ is also high-order differentiable in the domain of $(-\infty, -T)$.

That is, $f(w)$ is a high-order differentiable function in the domain of $(-\infty, -T)$ and $(T, +\infty)$, respectively.

Proof is completed. □

Remark 6. According to Theorem 5, $f(w)$ is the high-order differentiable function in the domain of $(-\infty, -T)$ and $(T, +\infty)$ respectively. This advantage can make the reconstructed signal smooth.

3. A Shape Parameter Optimization Strategy Based on AFSA

3.1. Introduction of AFSA. Shape parameter α helps improve the flexibility of the new thresholding function. However, it also brings a problem on setting α. In the existed method, the shape parameter is determined by trial and error, which is subjective and lacks theoretical guidance. In order to solve this problem, AFSA is adopted to achieve the optimal shape parameter. AFSA is proposed by Li et al. [17] in 2002. It is considered as an effective global optimization algorithm that mainly simulates fish schooling behaviors of preying, swarming, and following. Compared with other optimization algorithms [18, 19], AFSA has the following advantages.

(1) Swarming behavior can make the algorithm get rid out of the local extremum and obtain global optimal value.

(2) Following behavior helps an individual move fast to the optimal value. Therefore, it can improve the optimization speed.

(3) After evaluating three behaviors, AFSA automatically selects the optimal behavior. This step assists the algorithm to obtain optimization results efficiently and rapidly.

3.2. Objective Function. The aim of shape parameter optimization is to improve the signal denoising effect. Several indicators are employed to measure the denoising effect, such as MSE, signal-to-noise-ratio (SNR), and smoothness. Given that MSE can accurately reflect the deviation between the reconstructed signal and the original signal, therefore, it is used most widely:

$$\mathrm{MSE} = \frac{\sum_{k=1}^{N} [X(k) - S(k)]^2}{N}, \tag{12}$$

where $X(k)$ is the noisy signal, $S(k)$ is the original signal, and N is the length of signal.

When the MSE index is small, it is close between the reconstructed signal and the original signal. In this case, the denoising effect is good. If MSE index is big, the deviation between reconstructed signal and the original signal deviation is large. Here, the denoising effect is poor.

In AFSA, the actual meaning of objective function is food concentration, and it is usually a maximum function. Therefore, the objective function based on MSE is constructed as follows:

$$F(x) = \frac{1}{\mathrm{MSE}(x)}, \tag{13}$$

where $\mathrm{MSE}(x)$ represents the MSE between reconstructed signal and the original signal deviation with shape parameter equal to x.

If MSE between the reconstructed signal and the original signal is small, the denoising effect is good. Here, the object function value is big. If MSE is big, the denoising effect is poor, and the object function value is small in this case.

3.3. Algorithm Initialization. Suppose that X is the current position of an artificial fish (AF), fish swarm including P AFes (P is the number of the artificial fish) is randomly generated as $(X_1 \cdots X_p)$. $Y = F(X)$ is the objective function of X, which represents food concentration of position X. The AF realizes external perception by its vision. Visual represents the visual distance of an AF. Step is the length of moving step, M is the maximum of preying try number, and W is the crowd factor $(0 < W < 1)$.

3.4. Description of AF Behavior

3.4.1. Preying Behavior. Suppose that an AF's current state is X_i. A new state X_j is selected randomly in its visual field according to the following equation:

$$X_j = X_i + \mathrm{Rand}(\cdot) * \mathrm{Visual}, \tag{14}$$

where $\mathrm{Rand}(\cdot)$ is a random function in the range $[0, 1]$.

If $Y(X_j) > Y(X_i)$, the AF satisfies the condition of moving forward and it moves towards X_j as follows:

$$X_i^{t+1} = X_i^t + \mathrm{Rand}(\cdot) * \mathrm{Step} * \frac{X_j - X_i^t}{\left\| X_j - X_i^t \right\|}, \tag{15}$$

where X_i^{t+1} represents the next state of the AF with the current state X_i^t and $d_{i,j} = \|X_j - X_i^t\|$ is the Euclidean distance between X_i and X_j.

By contrast, if $Y(X_j) \le Y(X_i)$, a new state X_j is selected according to (14), and then whether the new X_j satisfies the forward condition or not is judged. If after trying M times, it still did not achieve the condition of moving forward, AF is forced to move one step according to the following equation:

$$X_i^{t+1} = X_i + \mathrm{Rand}(\cdot) * \mathrm{Visual}. \tag{16}$$

3.4.2. Swarming Behavior. The current state of the AF is X_i, and n_f is the number of individual within its visual distance. The centre position of neighborhood individual can be calculated as follows:

$$X_c = \frac{\sum_{j=1}^{n_f} X_j}{n_f}, \tag{17}$$

where X_j represents the individual within AF's visual distance.

If $Y(X_c) > Y(X_i)$ and $n_f/p < W$ (where P is the total number of AF and W is the crowd factor), this means that the centre X_c has the higher food concentration and its surrounding is not crowded. Thereafter, the AF's state at the next iteration is calculated as follows:

$$X_i^{t+1} = X_i^t + \mathrm{Rand}(\cdot) * \mathrm{Step} * \frac{X_c - X_i^t}{\left\| X_c - X_i^t \right\|}. \tag{18}$$

3.4.3. Following Behavior. The current state of the AF is X_i, and X_b is the individual with the biggest food concentration within AF's visual distance. If $Y(X_b) > Y(X_i)$ and $n_f/p < W$, then the next state of AF can be computed as follows:

$$X_i^{t+1} = X_i^t + \text{Rand}(\cdot) * \text{Step} * \frac{X_b - X_i^t}{\left\| X_b - X_i^t \right\|}. \quad (19)$$

3.5. Behavior Selection. In this paper, three biological behaviors of AF are analyzed, namely, preying behavior, swarming behavior, and following behavior. Trial method has been frequently employed to simulate the three behaviors of AF, and the behavior which can obtain the biggest food concentration is selected to be implemented.

3.6. Bulletin. Bulletin is used to record the optimal state of the AF and the optimal value of objective function. Every AF compares its own state with the bulletin after making movements. If the current state of AF is better, then the value on the bulletin will be replaced.

3.7. Termination Condition. There are two different termination methods of AFSA. One method is to set an object function value. When the value is obtained, AFSA finishes. The other method is to set a maximum of iteration number. When this number is reached, the algorithm ends. According to the characteristics of our problem, the second method should be selected. That is because the first method requires a fixed object function value. However, how to determine the suitable value is a difficult problem.

3.8. Steps of Shape Parameter Optimization Strategy Based on AFSA. The steps of shape parameter optimization strategy based on AFSA are provided as follows.

(1) A fish swarm is randomly generated, and algorithm parameters are set including population size P, maximum iteration number N, visual distance *Visual*, the moving length *Step*, the largest try number of preying M, and crowding factor W.

(2) Preying behavior, swarming behavior, and following behavior are simulated by AF, and the behavior which can obtain the biggest food concentration is implemented.

(3) Objective function value of every AF is calculated as (13). Each AF compares its own state with the bulletin after making movements. If the current state of AF is better, then the value on the bulletin will be replaced.

(4) Iteration number num = num + 1.

(5) Judge whether the maximum iteration number N is reached. If reached, output the bulletin and the corresponding AF. Otherwise, go to step (2).

Flowchart of shape parameter optimization strategy based on AFSA is shown in Figure 3.

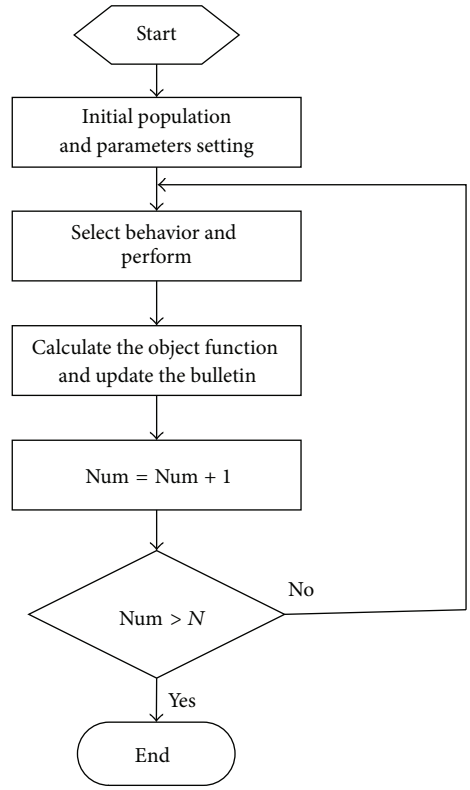

Figure 3: Flowchart of shape parameter optimization strategy based on AFSA.

Table 1: Parameters setting.

P	N	M	Visual	W	Step
100	50	100	1	0.618	0.05

4. Simulation Experiment

4.1. Shape Parameter Determination. To verify the denoising effect of the new thresholding function, we must firstly determine the shape parameter. AFSA is adopted to search the optimal shape parameter. The analysis of main parameters in AFSA is given as follows.

4.1.1. Visual Distance (Visual) and Moving Length (Step). Large *Visual* is of benefit to quick global optimization. But if *Visual* is set too large, the optimization process may be premature convergence. Small *Step* is better for local optimization, while it may decrease the velocity of evolution.

4.1.2. Crowd Factor (W). If W is set too large, the velocity of evolution will increase, but AFSA has a risk of premature convergence in this case.

4.1.3. Number of AF (P). When the number of AF is large, the capacity of getting out of local extremum is strong, but computational amount of every iteration will increase.

Based on the analysis above, the parameters in AFSA are set as in Table 1.

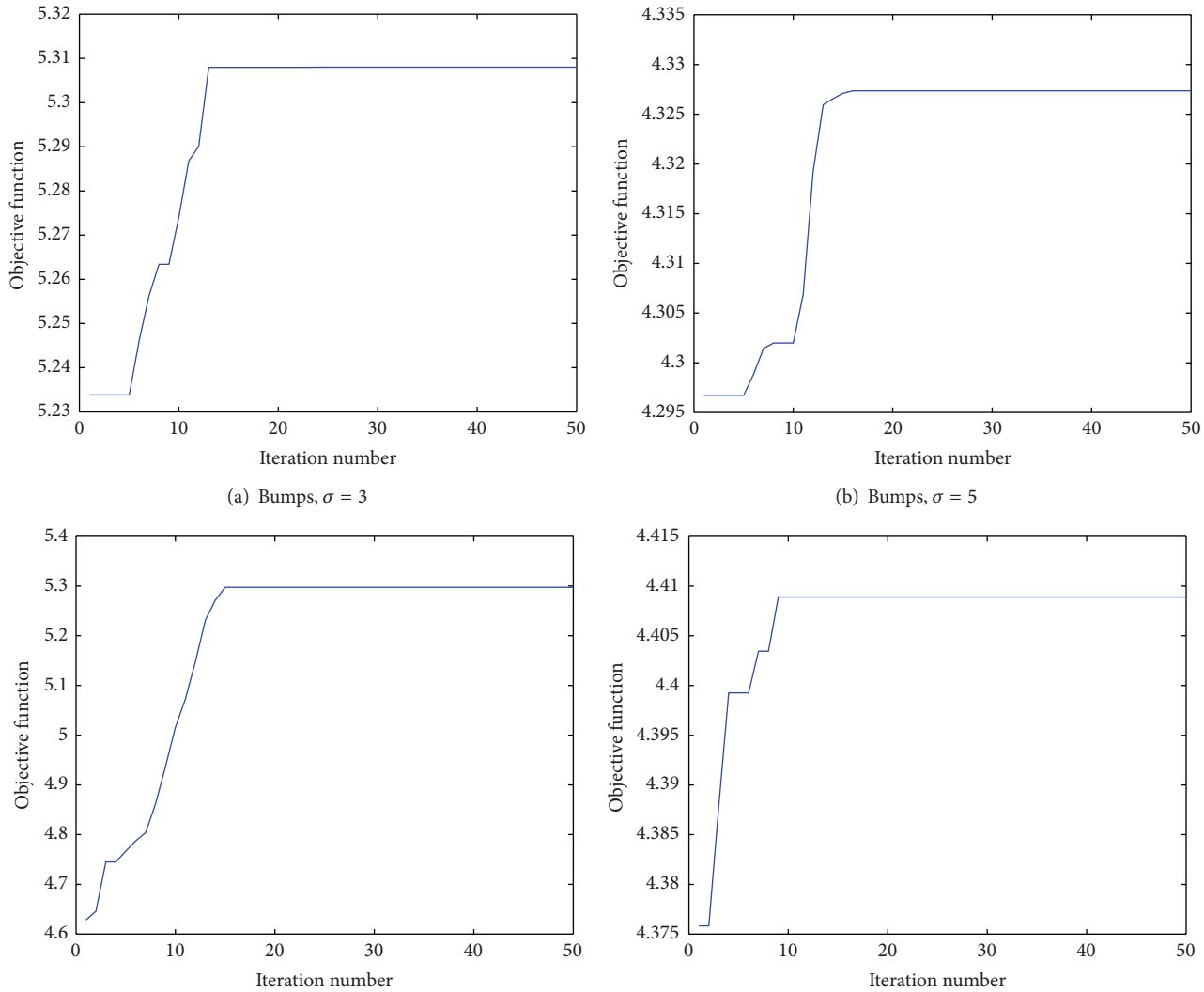

(a) Bumps, $\sigma = 3$

(b) Bumps, $\sigma = 5$

(c) Doppler, $\sigma = 3$

(d) Doppler, $\sigma = 5$

Figure 4: Curves of different signals.

Table 2: Optimal shape parameters.

	Bumps, $\sigma = 3$	Bumps, $\sigma = 5$	Doppler, $\sigma = 3$	Doppler, $\sigma = 5$
α	0.95	2.85	0.70	1.35

Two classic benchmark signals, namely, Bumps signal and Doppler signal, are used as test signals. Two strengths of white Gaussian noise, that is, $\sigma = 3$ and $\sigma = 5$, are added to the test signals in the experiments. The steps of shape parameter optimization strategy are provided in Figure 3. The optimization algorithm is run 100 times. The optimal shape parameters of different signals are obtained as in Table 2. Their iteration curves are shown in Figure 4.

4.2. Denoising Effect Verification of the New Thresholding Function. In this experiment, the test signals are selected the same as in Section 4.1. Stationary wavelet transform is adopted in this paper [20], wavelet basis adopts sym6 wavelet [21], and wavelet decomposition scale is set to be 3. Universal threshold is selected as the standard threshold. The proposed function is used as thresholding function in the experiment of wavelet threshold denoising. In order to verify the superiority of the proposed function, the classical hard and soft thresholding functions are chosen as comparative functions. The detailed steps of wavelet threshold denoising experiment were given by [8]. All the experiments were calculated on the same computer with the CPU frequency of 2 GHz, and Matlab 7.0 is used as the computation software.

In order to measure the denoising effects of different thresholding functions, MSE (equation (12)) and SNR are selected as comparative index:

$$\mathrm{SNR} = 10 \ln \frac{\sum_{k=1}^{N} S(k)^2}{\sum_{k=1}^{N} [X(k) - S(k)]^2}. \tag{20}$$

When $\sigma = 3$, the denoising effect of two test signals is shown in Figures 5 and 6. In the figures, NS expresses

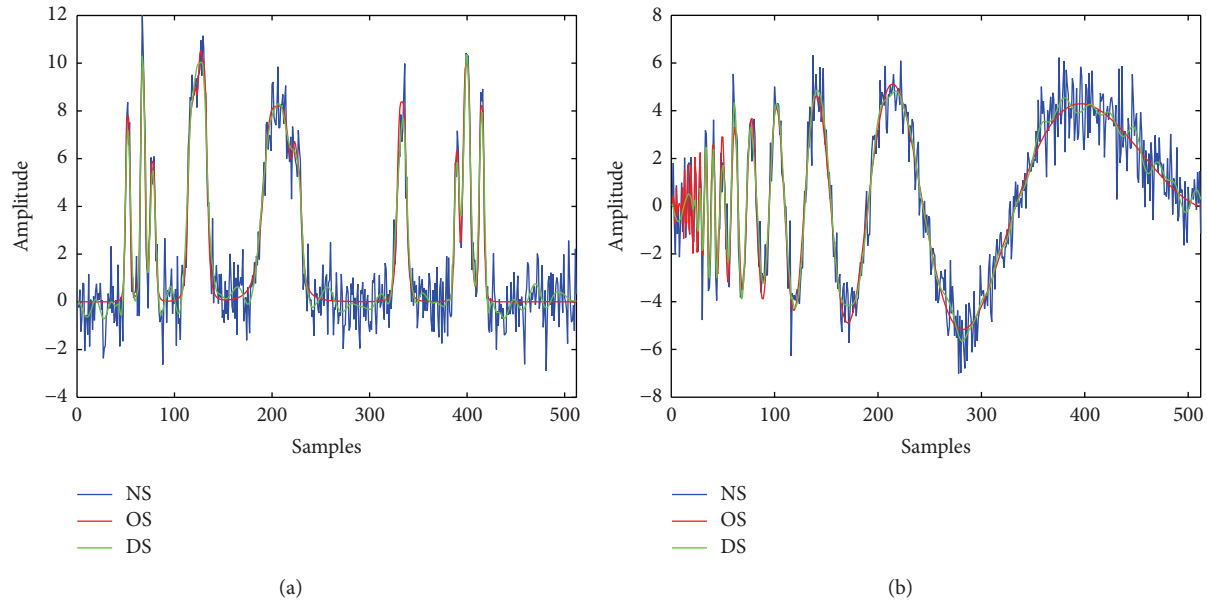

Figure 5: Denoising effect of different signals when $\sigma = 3$.

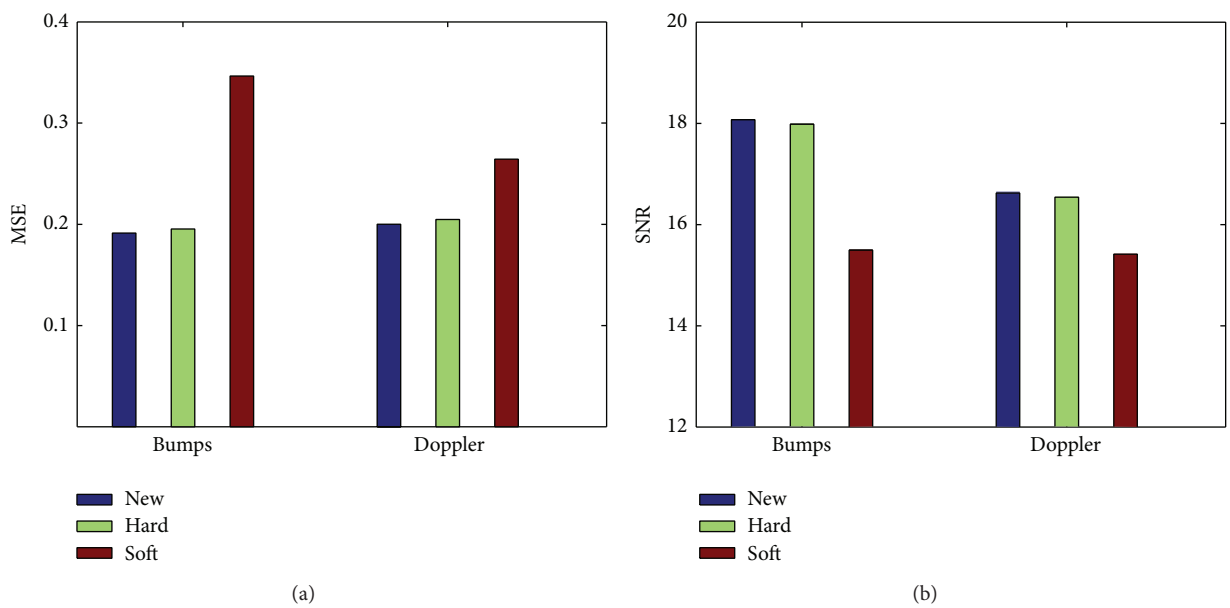

Figure 6: Effect index of different signals when $\sigma = 3$.

the noisy signals, OS represents the original signals, DS is the denoising signals using the new thresholding function, *New* represents the effect index of the new thresholding function, *Hard* is the effect index of hard thresholding function, and *Soft* expresses the effect index of soft thresholding function.

In order to exclude the effect of noise intensity, experiment is retested with $\sigma = 5$ white Gaussian noise (see Figures 7 and 8).

In order to prove the superiority of the optimal shape parameter, a comparative experiment between thresholding function with optimal shape parameter and thresholding function with nonoptimal shape parameter ($\alpha = 1$) is provided under $\sigma = 5$ white Gaussian noise. The denoising effect of nonoptimal shape parameter is shown in Figure 9. The denoising index of two methods is provided in Figure 10. NSP represents denoising index of thresholding function with nonoptimal shape parameter and OSP represents denoising index of thresholding function with optimal shape parameter.

4.3. Results Analysis. As shown in Figure 4, the parameter optimization method based on AFSA can quickly converge to the optimal objective function value. As it is shown in

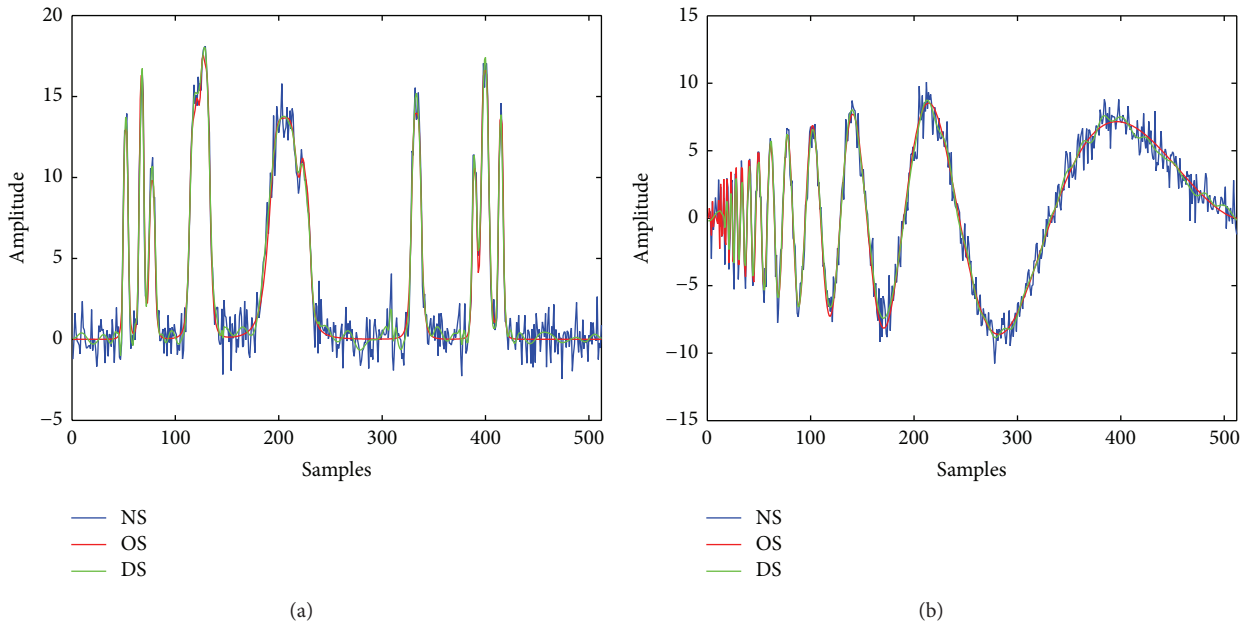

Figure 7: Denoising effect of different signals when $\sigma = 5$.

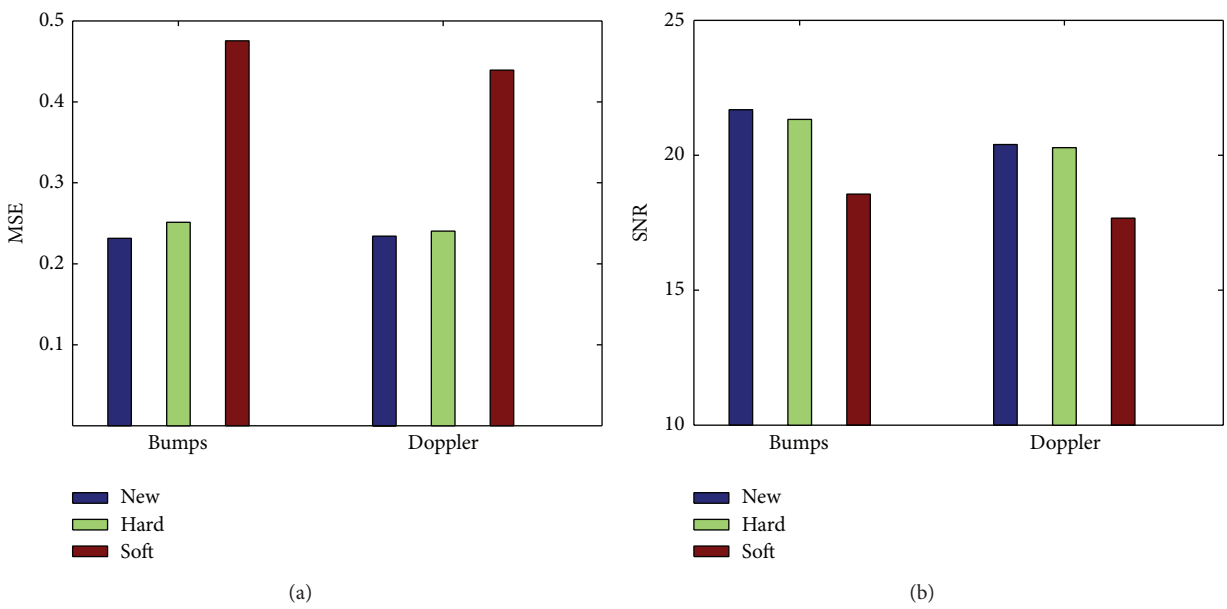

Figure 8: Effect index of different signals when $\sigma = 5$.

Figure 5, when $\sigma = 3$, denoising signal obtained by the proposed method is closer to the original signal than hard and soft thresholding functions for both signals. From Figure 6, we can see that the proposed method can achieve smaller MSE and larger SNR than traditional methods. To avoid the interference of noise intensity, experiment is retested with $\sigma = 5$ white Gaussian noise. The experiment results are provided in Figures 7 and 8. Comparing Figure 6 with Figure 8, it can be seen that the denoising effect and index of our method are better than hard and soft thresholding functions with both heavy noise and light noise. The results in Figures 9 and 10 show that thresholding function with optimal shape parameter has a better denoising effect than nonoptimal shape parameter.

5. Conclusion

In order to make up for the deficiency of the existing wavelet thresholding functions, a new thresholding function with a shape parameter based on hyperbolic tangent function is presented. Then, a shape parameter optimization method based on AFSA is proposed on the basis of analyzing the advantage of the AFSA. With the case analysis, some conclusions are summarized as follows.

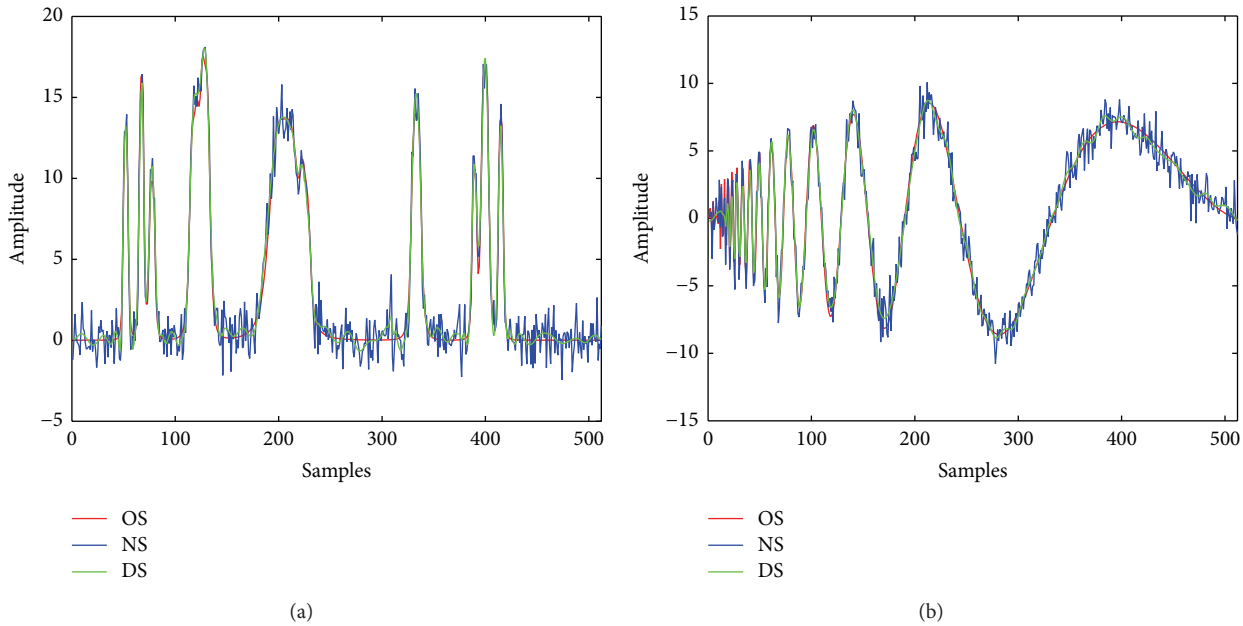

Figure 9: Denoising effect of nonoptimal shape parameter when $\sigma = 5$.

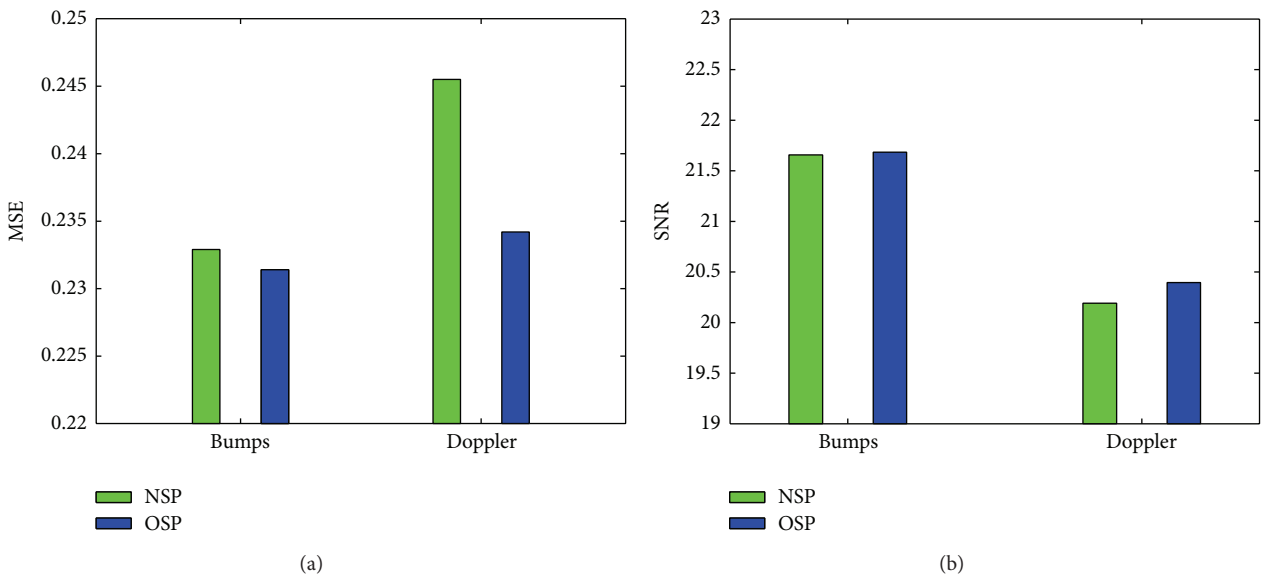

Figure 10: Denoising index of two methods when $\sigma = 5$.

(1) By improving the hyperbolic tangent function, a new thresholding function is presented in this paper. The new function has continuity, monotonicity, and high-order differentiability, which assist the new function to improve the denoising effect. The experiment results show that the proposed function can obtain better denoising effect than the classical hard and soft thresholding functions.

(2) Traditionally, trial and error method is adopted to determine shape parameter. This method depends on expert experience and lacks theoretical guidance. In order to solve this problem, AFSA is presented to search the optimal shape parameter. The experiment results show that AFSA can rapidly obtain the optimal shape parameter. It helps achieve the effective and quick signal denoising.

Conflict of Interests

The authors declare that there is no conflict of interests regarding the publication of this paper.

References

[1] G. Gupta, "Algorithm for image processing using improved median filter and comparison of mean, median and improved median filter," *International Journal of Soft Computing and Engineering*, vol. 1, pp. 2231–2307, 2011.

[2] T.-H. Yi, H.-N. Li, and M. Gu, "Characterization and extraction of global positioning system multipath signals using an improved particle-filtering algorithm," *Measurement Science and Technology*, vol. 22, no. 7, Article ID 075101, 2011.

[3] R. Lu, Y. Xu, and A. Xue, "H_∞ filtering for singular systems with communication delays," *Signal Processing*, vol. 90, no. 4, pp. 1240–1248, 2010.

[4] R. Lu, H. Li, A. Xue, J. Zheng, and Q. She, "Quantized H_∞ filtering for different communication channels," *Circuits, Systems, and Signal Processing*, vol. 31, no. 2, pp. 501–519, 2012.

[5] T.-H. Yi, H.-N. Li, and M. Gu, "Wavelet based multi-step filtering method for bridge health monitoring using GPS and accelerometer," *Smart Structures and Systems*, vol. 11, no. 4, pp. 331–348, 2013.

[6] B. Le, Z. Liu, and T. Gu, "Weak LFM signal dectection based on wavelet transform modulus maxima denoising and other techniques," *International Journal of Wavelets, Multiresolution and Information Processing*, vol. 8, no. 2, pp. 313–326, 2010.

[7] Y. Xu, J. B. Weaver, D. M. Healy Jr., and J. Lu, "Wavelet transform domain filters: a spatially selective noise filtration technique," *IEEE Transactions on Image Processing*, vol. 3, no. 6, pp. 747–758, 1994.

[8] D. L. Donoho and J. M. Johnstone, "Ideal spatial adaptation by wavelet shrinkage," *Biometrika*, vol. 81, no. 3, pp. 425–455, 1994.

[9] T. F. Sanam and C. Shahnaz, "Noisy speech enhancement based on an adaptive threshold and a modified hard thresholding function in wavelet packet domain," *Digital Signal Processing*, vol. 23, no. 3, pp. 941–951, 2013.

[10] D. L. Donoho, "De-noising by soft-thresholding," *IEEE Transactions on Information Theory*, vol. 41, no. 3, pp. 613–627, 1995.

[11] A. Phinyomark, C. Limsakul, and P. Phukpattaranont, "Optimal wavelet functions in wavelet denoising for multifunction myoelectric control," *ECTI Transactions on Electrical Engineering, Electronics, and Communications*, vol. 8, no. 1, pp. 43–52, 2010.

[12] T. F. Sanam and C. Shahnaz, "A semisoft thresholding method based on Teager energy operation on wavelet packet coefficients for enhancing noisy speech," *EURASIP Journal on Audio, Speech, and Music Processing*, vol. 2013, article 25, 2013.

[13] L.-K. Shark and C. Yu, "Denoising by optimal fuzzy thresholding in wavelet domain," *Electronics Letters*, vol. 36, no. 6, pp. 581–582, 2000.

[14] H.-R. Jia, X.-Y. Zhang, and J. Bai, "A continuous differentiable wavelet threshold function for speech enhancement," *Journal of Central South University*, vol. 20, no. 8, pp. 2219–2225, 2013.

[15] T.-H. Yi, H.-N. Li, and X.-Y. Zhao, "Noise smoothing for structural vibration test signals using an improved wavelet thresholding technique," *Sensors*, vol. 12, no. 8, pp. 11205–11220, 2012.

[16] J.-Y. Tang, W.-T. Chen, S.-Y. Chen, and W. Zhou, "Wavelet-based vibration signal denoising with a new adaptive thresholding function," *Journal of Vibration and Shock*, vol. 28, no. 7, pp. 118–121, 2009 (Chinese).

[17] X.-L. Li, Z.-J. Shao, and J.-X. Qian, "Optimizing method based on autonomous animats: fish-swarm algorithm," *System Engineering: Theory & Practice*, vol. 22, no. 11, pp. 32–38, 2002 (Chinese).

[18] T.-H. Yi, H.-N. Li, and X.-D. Zhang, "Sensor placement on Canton Tower for health monitoring using asynchronous-climb monkey algorithm," *Smart Materials and Structures*, vol. 21, no. 12, Article ID 125023, 2012.

[19] G. D. Zhou, T. H. Yi, and H. N. Li, "Sensor placement optimization in structural health monitoring using cluster-in-cluster firefly algorithm," *Advances in Structural Engineering*, vol. 17, no. 8, pp. 1103–1116, 2014.

[20] S. Zhong and S. O. Oyadiji, "Crack detection in simply supported beams using stationary wavelet transform of modal data," *Structural Control and Health Monitoring*, vol. 18, no. 2, pp. 169–190, 2011.

[21] C. He, J. C. Xing, and Q. L. Yang, "Optimal wavelet basis selection for wavelet denoising of structural vibration signal," *Applied Mechanics and Materials*, vol. 578, pp. 1059–1063, 2014.